Role of Southern Ocean sea ice on deep ocean circulation and carbon cycle at the Last Glacial Maximum

Fanny Lhardy

université
PARIS-SACLAY

Role of Southern Ocean sea ice on deep ocean circulation and carbon cycle at the Last Glacial Maximum

Rôle de la glace de mer australe sur la circulation océanique profonde et le cycle du carbone au Dernier Maximum Glaciaire

Thèse de doctorat de l'université Paris-Saclay

École doctorale n° 129, Sciences de l'Environnement d'Ile-de-France SEIF
Spécialité de doctorat: océan, atmosphère, climat et observations spatiales
Unité de recherche: Université Paris-Saclay, CNRS, CEA, UVSQ,
Laboratoire des Sciences du Climat et de l'Environnement, 91191, Gif-sur-Yvette, France
Référent: Université de Versailles-Saint-Quentin-en-Yvelines

**Thèse présentée et soutenue à Paris-Saclay,
le 27 Septembre 2021, par**

Fanny Lhardy

Composition du jury

Matthieu Roy-Barman Professeur des universités, UVSQ	Président
Agatha de Boer Associate Professor, rang A, Stockholm University	Rapportrice et examinatrice
Samuel Jaccard Professeur, rang A, University of Bern	Rapporteur et examinateur
Tatiana Ilyina Associate Professor, rang A, MPI Hamburg	Examinatrice
Kazuyo Tachikawa Directrice de Recherche CNRS, CEREGE	Examinatrice
Martin Vancoppenolle Chargé de Recherche CNRS, LOCEAN	Examinateur

Direction de la thèse

Didier Roche Directeur de Recherche CNRS, LSCE	Directeur de thèse
Nathaëlle Bouttes Chargée de Recherche CNRS, LSCE	Co-encadrante et examinatrice

Thèse de doctorat

NNT: 2021UPASJ013

Résumé

La période froide du Dernier Maximum Glaciaire était caractérisée, en regard de notre climat moderne, par une couverture de glace de mer australe accrue, une circulation profonde Atlantique moins profonde et une plus faible concentration en CO_2 dans l'atmosphère. Ces différences sont bien connues grâce aux observations indirectes mais difficiles à représenter dans les simulations issues des modèles de climat. En effet, ces modèles simulent fréquemment une concentration en CO_2 atmosphérique trop élevée, une circulation océanique trop profonde dans l'Atlantique et une banquise présentant une distribution trop circulaire dans l'océan austral ainsi qu'une étendue hivernale et une amplitude saisonnière trop faibles. Ces désaccords modèle-données observés au Dernier Maximum Glaciaire remettent en cause la représentation numérique de certains processus climatiques essentiels. Plusieurs études soulignent le rôle majeur de la glace de mer australe sur la capacité de stockage de carbone de l'océan et la circulation océanique profonde. Je me suis donc focalisée sur cette région pour mieux comprendre les processus associés à ce stockage. Grâce aux simulations réalisées avec le modèle système terre iLOVECLIM, j'ai pu démontrer que les incertitudes liées à la représentation des calottes polaires ont un impact limité sur les variables examinées ici. En revanche, d'autres choix de conditions aux limites (affectant le volume de l'océan, l'ajustement de l'alcalinité) peuvent entraîner des modifications importantes du contenu total en carbone de l'océan. Je montre également que l'utilisation d'une paramétrisation simple de la plongée des saumures résultant de la formation de glace de mer permet d'améliorer significativement la simulation de la glace de mer australe, de la circulation océanique profonde et de la concentration en CO_2 atmosphérique. Un ensemble de simulations incluant l'impact de différentes paramétrisations océaniques est utilisé pour montrer que la circulation océanique très profonde simulée par notre modèle ne peut être attribuée à une glace de mer australe insuffisante. En revanche, les processus de convection dans l'océan austral semblent clefs pour améliorer à la fois la glace de mer australe, la circulation océanique profonde et la concentration en CO_2 atmosphérique au Dernier Maximum Glaciaire.

Abstract

Compared to the present-day climate, the cold period of the Last Glacial Maximum was characterized by an expanded sea-ice cover in the Southern Ocean, a shoaled Atlantic deep ocean circulation and a lower atmospheric CO_2 concentration. These changes are well-documented by indirect observations but difficult to represent in simulations of climate models. Indeed, these models tend to simulate a too high atmospheric CO_2 concentration, a too deep Atlantic deep ocean circulation, and a sea-ice cover with a too circular distribution in the Southern Ocean and a too small winter extent and seasonal amplitude. The model-data discrepancies observed at the Last Glacial Maximum call into question the model representation of some important climate processes. Several studies have underlined the crucial role of the Southern Ocean sea ice on ocean carbon storage capacity and deep circulation. I have therefore focussed on this region to improve our understanding of the processes associated with this storage. Thanks to simulations performed with the Earth System Model iLOVECLIM, I have demonstrated that the uncertainties related to ice sheet reconstructions have a limited impact on the variables examined in this study. In contrast, other choices of boundary conditions (influencing the ocean volume and alkalinity adjustment) can yield large changes of carbon sequestration in the ocean. I also show that a simple parameterization of the sinking of brines consequent to sea-ice formation significantly improves the simulated Southern Ocean sea ice, deep ocean circulation and atmospheric CO_2 concentration. A set of simulations including the effects of diverse ocean parameterizations is used to show that the too deep ocean circulation simulated by our model cannot be attributed to an insufficient sea-ice cover, whereas convection processes in the Southern Ocean seem crucial to improve both the Southern Ocean sea ice, the deep ocean circulation and the atmospheric CO_2 concentration at the Last Glacial Maximum.

Remerciements

My thesis would not have been possible without my excellent supervisors, Didier and Nathaëlle, who offered valuable insight to guide me throughout this 3-year work and taught me how to navigate the (peculiar) research field. I truly feel grown from the experience.

I would like to express my gratitude to my jury members, for their rich questions and scientific exchanges. I have enjoyed my defense very much.

My thesis was done in a very nurturing and instructive environment. I would like to thank the lab members and CLIM team for their warm welcome. Thanks a lot Aurélien, Jean-Yves, Masa, Didier P., Gilles, Pierre, Jean-Claude, and many others, for many things. Thank you Juliette for your advice. Thank you Will for your infectious enthusiasm in our scientific discussions. Thank you Florence, Catherine, Cécile, François, Gaëlle, among others, for the significant support provided by the IT and administrative teams. PhD students are very lucky to work in such an environment.

I have also had the chance to interact with external colleagues from various expertises, who lavishly shared their vast knowledge. My particular thanks to Xavier, Claire, Casimir, Martin, Pepijn. I've learnt a lot from you.

Before the pandemic hit, I have also had many opportunities to "get out of the lab". Thank you Nada and Alain for offering me to participate in outreach activities. Thank you Matthieu for your total trust in my teachings.

I would also like to thank and encourage the PhD students who are embarked on the same adventure: Marie, Julia, Gaëlle, Stella, Alizée & Alizée, Tiphaine, Isma, Victor, Clément... and those who have completed their journey before me: Lise, Thomas, Audrey, Vincent, Tristan, Aglaé, Anta, Cyril, Florentin, Kristan. Thank you also Sophie and Yann, even if you belong to neither of these categories. Thank you to those of you who have listened during impromptu biology lectures.

Thank you Marie and Fanny for saving me during the tedious work of printing my manuscript. Special thanks to Peter for proofreading the whole thing. That was brave.

Merci bien sûr et surtout à mes proches, à commencer par mes parents, Chloé, Antonio, la famille Hursin, Pauline, Inès, Daphné, Aurélie. Merci aussi aux coureurs de l'OC Gif pour ces moments de défoulement partagés. Merci enfin à ceux que j'oublie.

Contents

Introduction

Paleoclimatology is a field of research dedicated to the study of past climatic variations. In the context of current and future climate change, studying the past allows us to better understand the processes behind natural variations of a complex climate system. Although the present-day climate is largely influenced by anthropogenic emissions of carbon since the pre-industrial (PI), astronomical forcing is in the Milankovitch theory a dominant control on the Quaternary climate. Indeed, periodic fluctuations of orbital parameters (i.e. eccentricity, obliquity and climatic precession) have induced glacial-interglacial cycles which, in the last million years, have lasted around 100,000 years. The most recent glacial period culminated with the Last Glacial Maximum (LGM) around 23,000 − 19,000 years ago [Mix et al., 2001].

The LGM was characterized by cold temperatures (~ -4°C relative to the PI, according to Annan and Hargreaves [2013]), large ice sheets over the Northern Hemisphere and an associated low sea level (around -130 m, Lambeck et al. [2014]). These differences with the PI climate were also accompanied by other changes in the climatic system, which are well-documented by various paleoclimate indicators. Our knowledge of the LGM sea-ice cover, deep ocean circulation, and atmospheric CO_2 concentration relies on these proxy data. The Southern Ocean sea-ice cover, for example, can be reconstructed using the abundance of sea-ice linked diatoms in marine cores [Gersonde et al., 2005], which suggest an extensive winter sea-ice extent and enhanced seasonal amplitude at the LGM, along with a northward displacement of the sea-ice edge particularly pronounced in the Atlantic and Indian sectors. The deep ocean circulation can also be inferred from marine cores, thanks to measurements of geochemical tracers such as the δ^{13}C of benthic foraminifera species − among others [Adkins, 2013, Lynch-Stieglitz et al., 2007]. The reconstructions based on such paleotracers tend to indicate that the Atlantic Meridional Overturning Circulation (AMOC) was shoaled at the LGM, with a shallower North Atlantic Deep Water (NADW) and an expanded, more sluggish, and denser Antarctic Bottom Water (AABW) [Curry and Oppo, 2005, Howe et al., 2016, Böhm et al., 2015, Skinner et al., 2017, Homola et al., accepted, 2021, Adkins, 2013, Sigman et al., 2010]. Finally, a low atmospheric CO_2 concentration at the LGM ($\sim$ 190 ppm) is well-constrained by gas measurements in ice core bubbles [Bereiter et al., 2015].

The LGM is a period of interest to modellers. Indeed, this recent period is a good target to investigate how Earth System Models (ESMs) respond to different forcings [Eyring et al., 2016, Kageyama et al., 2017]. In addition, the amount of available paleoproxy data enables modellers to test the performance of models − designed for modern times − under a climate very different from today's, thus allowing more confidence in future projections [Braconnot et al., 2012].

The identification of significant model biases and of their origin is facilitated by the existence of a common experimental design to run standardized LGM simulations. Indeed, the Paleoclimate Modelling Intercomparison Project (PMIP) enables multimodel comparisons of climate

variables in a coherent framework. Now in its fourth phase, the PMIP protocol is described in Kageyama et al. [2017]. Authors detail the forcings and boundary conditions to implement in all models to simulate this glacial climate: low greenhouse gases concentrations and slightly different orbital parameters (forcings), but also extensive ice sheets in the Northern Hemisphere and a low sea level (boundary conditions). They explain the necessary technical steps to follow in order to properly generate these boundary conditions on the atmosphere (orography, ice sheet extent) and ocean (bathymetry, coastlines) component. Finally, since some PMIP models now simulate the carbon cycle, Kageyama et al. [2017] also recommend an adjustment of biogeochemical variables (Dissolved Inorganic Carbon, alkalinity, nutrients) that results from the relative ocean volume change.

Following such an experimental design, various models have been run under glacial conditions during the previous phases of the PMIP project. Several model intercomparison studies have notably examined the simulated Southern Ocean sea-ice cover and the Atlantic deep ocean circulation, while intercomparison studies of coupled carbon-climate simulations at the LGM are yet to be made (see Sect. 2.3.2 of chapter 2). These studies report a large intermodel spread and model-data disagreements in the deep ocean circulation, with a majority of PMIP2 and PMIP3 models simulating an intensified and deepened NADW, contrasting with inferences from proxy-based reconstructions [Otto-Bliesner et al., 2007, Weber et al., 2007, Muglia and Schmittner, 2015]. PMIP models also simulate significant biases of Antarctic sea-ice cover with respect to data inferences, as they frequently show an underestimated winter sea-ice extent with an oval-shaped distribution in the Southern Ocean [Roche et al., 2012, Goosse et al., 2013, Marzocchi and Jansen, 2017]. Furthermore, models including the carbon cycle tend to simulate much higher CO_2 concentration than the measured 190 ppm in ice core data for the LGM, probably due to insufficient ocean sequestration [Hain et al., 2010, Oka et al., 2011, Kobayashi and Oka, 2018, Marzocchi and Jansen, 2019, Morée et al., 2021].

Despite decades of model development, this recurrent difficulty of most models to simulate well-known aspects of this cold period calls into question the model representation of the physical processes at play. As they are numerous and difficult to disentangle, the source of model-data discrepancies regarding sea ice, deep ocean circulation and CO_2 concentration at the LGM remains hard to pinpoint in models. These model biases are however likely interdependent, and related to a critical role of the Southern Ocean.

Indeed, brine rejection consequent to sea-ice formation locally increases the density of surface water, a process which can induce deep water formation. As a result, variations in the Southern Ocean sea-ice cover affect deep water formation rates and the resulting characteristics of the deep water mass of Southern origin (AABW). As deep water masses arrange themselves according to density gradients, the surface conditions at high latitudes actually influence the deep ocean circulation on a global scale. Furthermore, the Southern Ocean is also an important region of carbon uptake. As the carbon content of sinking waters may get isolated from the atmosphere for hundreds to thousands of years, the global carbon sink that is the ocean is influenced by deep ocean circulation, among other processes [Sigman et al., 2010]. In fact, Ferrari et al. [2014] suggest that the residence time of carbon in the deep ocean is increased at the LGM thanks to the expansion of the Southern Ocean sea-ice cover. The authors argue that such an expansion leads to a more voluminous, isolated, and carbon-rich AABW, due to less mixing with the overlying NADW and less outgassing in the Southern Ocean.

Consequently, the absence of a NADW shoaling and the overestimation of the atmospheric CO_2 concentration in most models may be related to a too small glacial AABW density. Rare

estimates of deep temperature and salinity inferred from pore fluid measurements of chloride concentration [Adkins et al., 2002] evidence an underestimated density of bottom water in the South Atlantic in most PMIP2 and PMIP3 models [Otto-Bliesner et al., 2007, Muglia and Schmittner, 2015]. Using the NCAR-CCSM model, Shin et al. [2003] attribute the weaker and shallower NADW at the LGM to an increased haline density flux in the Southern Ocean, triggered by brine release consequent to an increased sea-ice formation. These results support a dominant control of the Southern Ocean sea ice on the NADW circulation, over the Northern Hemisphere influence. Following this line of reasoning, insufficient sea-ice formation in the Southern Ocean may be linked to an underestimated buoyancy loss and ocean stratification, and ultimately to a too deep and strong NADW [Ferrari et al., 2014, Jansen and Nadeau, 2016]. This causal chain is statistically tested in Marzocchi and Jansen [2017], who produced both a multimodel comparison of the Atlantic deep ocean circulation and a model-data comparison of the Antarctic sea-ice extent simulated by PMIP3 models at the LGM. Relying on correlations and principal components analysis, this study shows that the link between Antarctic sea ice and deep ocean circulation is statistically significant (about half of the variance). As seven out of eight PMIP3 models underestimate the sea-ice extent with respect to proxy data, Marzocchi and Jansen [2017] partly attribute the depth and intensity of the simulated deep ocean circulation to an insufficient sea-ice formation, though the influence of other drivers of the AMOC (tidal mixing, Southern Hemisphere and North Atlantic westerlies) is also discussed.

Other studies have suggested an influence on the simulated deep ocean circulation of tidal mixing changes and vertical diffusivity parameterization [Schmittner et al., 2015, De Boer and Hogg, 2014], of Southern Ocean [Toggweiler et al., 2006, Marshall and Speer, 2012] and North Atlantic westerly winds [Sherriff-Tadano et al., 2018, Muglia and Schmittner, 2015]. In particular, the latter are sensitive to ice sheet boundary conditions, and mainly to the elevation of the Laurentide ice sheet [Sherriff-Tadano et al., 2018, Ullman et al., 2014, Klockmann et al., 2016]. Yet ice sheet reconstructions are still associated with large uncertainties. One novelty of the PMIP4 protocol [Kageyama et al., 2017] is to account for these uncertainties by proposing to modelling groups the use of three different ice sheet reconstructions.

The aim of this study is thus to investigate the model representation of the Southern Ocean sea ice, deep ocean circulation, and carbon storage at the LGM, as well as the simulated link between these three key variables.

In this thesis, chapter 1 is dedicated to the state of the art, followed in chapter 2 by a description of the methods and tools.

Chapter 3 then focuses on the quantification of the effects of a boundary conditions change on the simulated carbon content. I first approach this topic by implementing the boundary conditions associated with the LGM climate in the iLOVECLIM model in an automated way. Since the glacial ice sheets were much more extensive over the Northern Hemisphere than today's, the sea level was consequently lower at the LGM [Lambeck et al., 2014]. To account for these changes, I generate on the model grids both the atmosphere (i.e. orography, ice sheet extent) and ocean (i.e. bathymetry, coastlines) boundary conditions associated with the two most recent ice sheet reconstructions recommended in the PMIP4 protocol [Kageyama et al., 2017]. After these technical steps, I evaluate the impact on the simulated carbon sequestration of two modelling choices related to an ocean boundary conditions change: the total ocean volume and the adjustment of biogeochemical variables (Dissolved Inorganic Carbon, nutrients, alkalinity) recommended in the PMIP4 experimental design. To this end, I perform sensitivity tests at the LGM with the iLOVECLIM model to quantify the carbon content variations induced by

the ocean boundary conditions change and by each recommended adjustment. In addition, I produce a multimodel comparison of the ocean volume and carbon content simulated by models participating in the PMIP-carbon project. The results of this study are presented in Lhardy et al. [2021a].

In chapter 4, I use the different glacial boundary conditions generated in chapter 3 to identify the surface conditions biases in the Southern Ocean and their consequences on the simulated deep ocean circulation and carbon content at the LGM. For this purpose, I evaluate the various surface conditions (Sea Surface Temperature, sea ice) obtained using a set of LGM simulations with diverse modelling choices in the iLOVECLIM model (boundary conditions and/or sensitivity tests related to sea ice) against proxy data and identify systematic biases. I then explore the impact of these modelling choices on the deep ocean circulation by examining the water mass distribution in the Atlantic, and its agreement with respect to paleotracer data (δ^{13}C), as well as the consequent carbon content of the ocean. Part of the content of chapter 4 is published in Lhardy et al. [2021b].

In the course of chapter 5, I quantify the effects of vertical mixing on the same climate variables (sea ice, deep ocean circulation, carbon content). To do so, we replace the traditional Bryan and Lewis diffusivity profile with a more sophisticated parameterization, either a stratification-dependant mixing scheme or a parameterization of internal wave-driven mixing – which takes into account the energy input by tidal and geostrophic motions interacting with topography [de Lavergne et al., 2020], to which we combine geothermal fluxes. My motivation to test a vertical diffusivity of varying complexity lies in the fact that De Boer and Hogg [2014] demonstrate its critical role on AABW formation rate, while Friedrich et al. [2011] and Bouttes et al. [2011] also underline a significant impact of these schemes on ocean biogeochemistry and carbon content.

Finally, the aim of chapter 6 is to further investigate the relationships between sea-ice biases, deep ocean circulation and carbon content using the large range of LGM simulations ran within this study. Since the Southern Hemisphere westerlies influence Ekman transport and therefore the upwelling of deep water masses, I first focus on the effects of an additional set of sensitivity tests with a modified wind tension in the Southern Ocean. Then, I synthesize the model-data agreements regarding surface conditions, water mass distribution, and atmospheric CO_2 concentration using this diversity of LGM simulations. This allows me to examine the consistency of biases and to discuss the model representation of the link between the Southern Ocean sea ice, deep ocean circulation and CO_2 concentration.

Chapter 1

Sea ice, ocean dynamics and carbon cycle under glacial conditions

Chapter aims:

1. Introduce the main variables examined in this thesis: sea ice, deep ocean circulation, atmospheric CO_2 concentration; present their interplay and importance in the climate system
2. Describe their glacial state reconstructed from proxy data; illustrate the common model-data disagreements underlined in the literature of modelling studies at the LGM; present a few potential causes of these discrepancies
3. Justify my regional focus on the Southern Ocean sea ice and Atlantic deep ocean circulation at the LGM

Highlights:

↪ Local sea-ice formation at high latitudes of the Southern Ocean influences the large-scale deep ocean circulation (via density processes), as well as the global carbon storage capacity of the ocean (via various physical and biogeochemical effects). However, this influence is difficult to disentangle from other climate variables (e.g. winds, mixing).

↪ Proxy-based reconstructions suggest an expanded winter sea-ice cover in the glacial Southern Ocean associated with an enhanced seasonality; a weak and shallow AMOC relative to the present-day; a $80 - 100$ ppm pCO_2 drawdown with respect to the pre-industrial CO_2 concentration.

↪ Significant intermodel spread and model-data discrepancies are frequently observed in terms of sea-ice extent, distribution and seasonal amplitude; AMOC strength and depth; bottom water properties; CO_2 concentration. These recurring issues calls into question the representation in paleoclimate models of the processes involved.

Sea ice, deep ocean circulation, and atmospheric CO_2 concentration are key players of the Earth climate. Paleoclimatic archives suggest that they have significantly varied at the scale of glacial−interglacial cycles, inducing large differences between the Last Glacial Maximum (LGM) and the pre-industrial (PI) or present-day climates. In this first chapter, I present these variables and some of their characteristics and interplays, with a focus on the Southern Ocean sea-ice cover, Atlantic Meridional Overturning Circulation (AMOC), and carbon sequestration in the ocean. I then describe their glacial state, as inferred from proxy-based reconstructions or as typically simulated by paleoclimate models, such as those participating in the Paleoclimate Modelling Intercomparison Project (PMIP). Potential causes of the observed model-data discrepancies have been identified in the literature, pointing out where model representation may be lacking, but no consensus has been reached yet. Given the complexity of the climate system, the objective of this chapter is clearly not to be comprehensive, only to give contextual elements for the following study.

1.1 Three essential elements of the climate system

1.1.1 Sea ice

The climate system is characterized by numerous variables and multiple interactions and feedback effects involving them. These interactions can play out on different time scales (e.g. seasonal cycle, glacial-interglacial cycle, geological time scale) and between different components (atmosphere, oceans, cryosphere...). As a result, the thin layer of ice situated at the interface of the ocean and atmosphere at high latitudes is a particularly reactive element of this system. It is influenced by heat fluxes from both components, and consequently shows large seasonal variations. Furthermore, the dramatic sea-ice decline in the present-day Arctic, due to an especially intense warming in this region, is one of the most visible impact of climate change. The recent evolution of the Southern Ocean sea ice is, however, more variable and difficult to interpret [Maksym, 2019, Meehl et al., 2019, Hobbs et al., 2016].

Sea ice grows in winter, when the sea surface water freezes due to a temperature reaching its freezing point. It usually reaches its maximal extent in February−March, or September in the Southern Ocean (and the opposite for its minimal extent). A large part of the Artic and Antarctic sea ice melts in summer (boreal and austral respectively), but it does not completely disappear. Contrary to volume changes in ice sheets and glaciers, these variations do not impact the sea level.

Sea ice forms a dynamic and heterogeneous pack, transported by oceanic currents and winds. Drifting ice can collide and build ridges according to its rheology, therefore increasing its thickness, or form openings such as leads and polynias. The ice dynamics is fairly different in the Arctic or Southern Oceans. Indeed, the Arctic is a polar ocean surrounded by land, which notably constrains ice export through narrow straits (e.g. Fram and Bering Strait). On the other hand, Antarctica is a polar continent surrounded by water, the Southern Ocean sea ice having no northern boundary. In addition, strong katabatic winds, flowing down the ice cap, tend to push sea ice away from the Antarctic coast, therefore enhancing sea-ice formation in the newly opened areas and expanding the sea-ice cover, while strong westerly winds create an eastward ice drift at the sea-ice edge.

Although influenced by both the ocean and atmosphere thermodynamics and dynamics, sea ice is also an active player of the climate system with impacts in both of these components, allowing feedback effects to occur. For example, due to its white surface, sea ice has a high albedo, meaning that it reflects a much larger part of the solar fluxes than the ocean does. This allows for a positive feedback effect as a surface cooling tends to enhance sea-ice formation, therefore leading up to a higher regional albedo and to further cooling − consequently amplifying the initial perturbation. Such feedback mechanisms involving sea ice are assessed in Goosse et al. [2018]. Two of them are of particular interest in this study as they also involve the ocean (excerpt from Table 1, Goosse et al. [2018]):

> "Ice production−entrainment (−) (mostly active in Southern Ocean): Brine rejection during sea ice formation induces an ocean mixed layer deepening that brings to the surface warmer water from deeper levels, melting a part of the ice initially formed and inhibiting further ice production."

> "Ice production−ocean heat storage (+) (mostly active in Southern Ocean): Anomalous sea ice production induces vertical exchanges of salt, a higher stratification, storage of heat at depth and finally lower oceanic heat fluxes that favor further ice production."

As described, these mechanisms rely on density processes. Indeed, a sea-ice characteristic which is essential in the context of this study is its low salinity. As such, sea-ice melting induces a surface freshening. On the other hand, sea-ice formation entails a brine rejection process, which increases the density of residual surface waters and locally triggers deep water formation, especially in the Southern Ocean [Shin et al., 2003]. As a result, local sea-ice processes at high latitudes influence the large-scale deep ocean circulation.

The impacts of sea ice on the climate system are however not restricted to density and stratification effects. Indeed, sea ice insulates the ocean surface from the atmosphere, reducing heat loss to the atmosphere and therefore also impeding its own growth. This sea-ice capping also reduces evaporation and − more importantly for this study − carbon fluxes. Moreover, it affects marine productivity through its effects on sunlight and nutrient availability [Sun and Matsumoto, 2010, Abelmann et al., 2015]. Therefore, it is to be noted that sea ice may have direct or indirect effects on carbon sequestration into the ocean.

Despite its relative inaccessibility, the present-day sea ice is well-monitored through satellite observations (Fig. 1.1). Past sea-ice changes on longer time scales than the recent decades can only be reconstructed through the use of proxy data. Several decades of research have resulted in the identification and development of various proxies, though each of them have their own limitations and are not necessarily associated with a large amount of data [de Vernal et al., 2013]. These proxies typically rely on the abundance of specific microfossils or biomarkers in marine cores, and therefore depend on the species habitat. In the Southern Ocean, the sea-ice cover can be reconstructed thanks to the existence of sea-ice linked diatoms [Gersonde and Zielinski, 2000]. Compilation of numerous marine core data can allow for the inferrence of a sea-ice edge at the LGM, though the sparsity of data in some sectors due to the uneven coverage of coring sites do not constrain it well in summer (see Fig. 1.2 from Gersonde et al. [2005]). From this reconstruction, Gersonde et al. [2005] point out that the winter sea-ice extent at the

LGM was much larger than the present-day one (Fig. 1.1 and 1.2), with a sea-ice edge reaching close to 47°S in the Atlantic and Indian sectors due to a northward (displacement of $7-10°$ in latitude. In constrast, the limited data tend to support only a minor expansion of the summer extent, hence an increased sea-ice seasonality at the LGM.

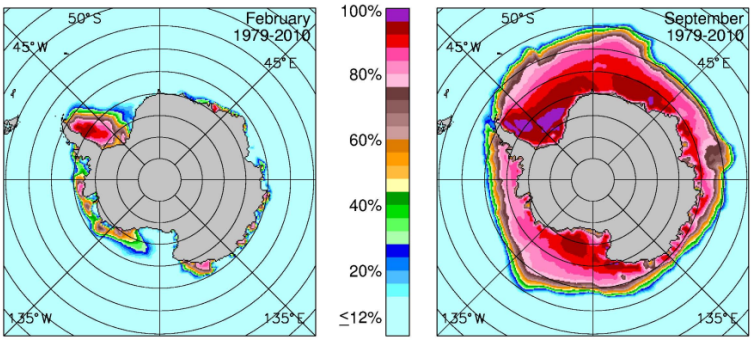

Figure 1.1: Figure from Parkinson and Cavalieri [2012], showing the sea-ice concentrations measured through satellite data, averaged over the years 1979−2010

(a) Austral summer

(b) Austral winter

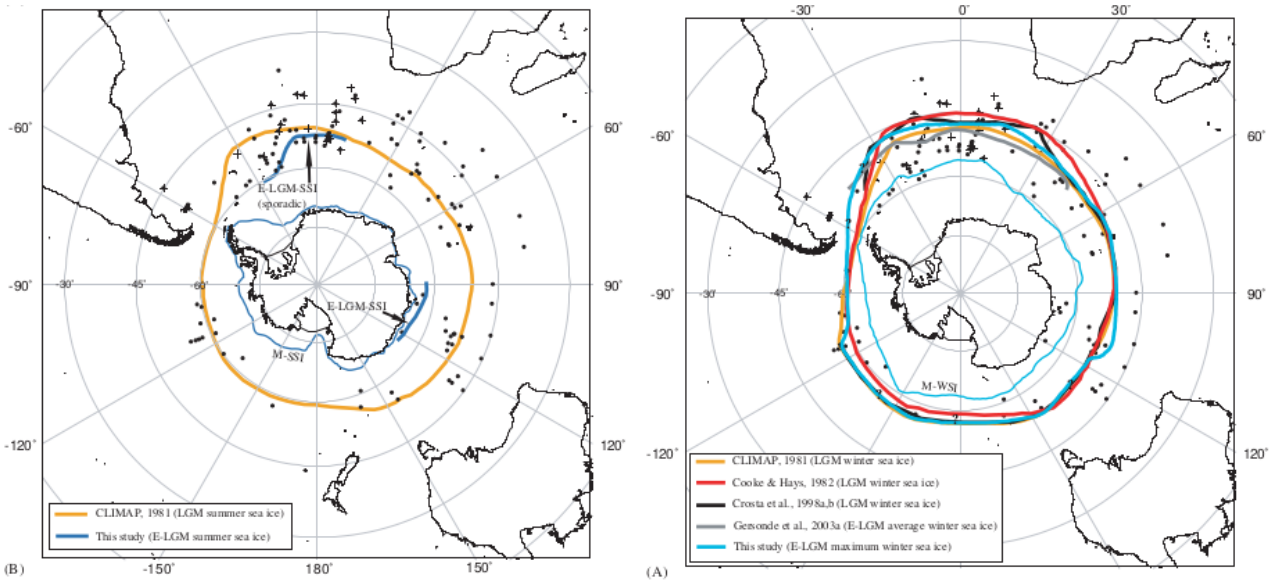

Figure 1.2: Figure from Gersonde et al. [2005], showing the reconstructed (a) summer and (b) winter sea-ice edge at the LGM according to their study (blue contours) compared to previous reconstructions

1.1.2 Deep ocean circulation: AMOC

The ocean circulation is a dominant feature of our climate system. On account of the sheer surface of the oceans ($\sim$ 70% of the Earth surface) and of the high heat capacity of water, the ocean plays an important role in storing and redistributing heat between different seasons and latitudes, though with higher inertia than the atmosphere. The ocean circulation plays an important part in explaining regional climates and is key in interannual variability such

as El Niño−Southern Oscillation (ENSO). It can be decomposed into a surface wind-driven gyre circulation and a thermohaline circulation (Fig. 1.3), driven by density gradients. Sometimes called the "conveyor belt", the latter can isolate deep water masses from the atmosphere for thousands of years, hence the large residence time of carbon in the deep ocean (see Fig. 1.5).

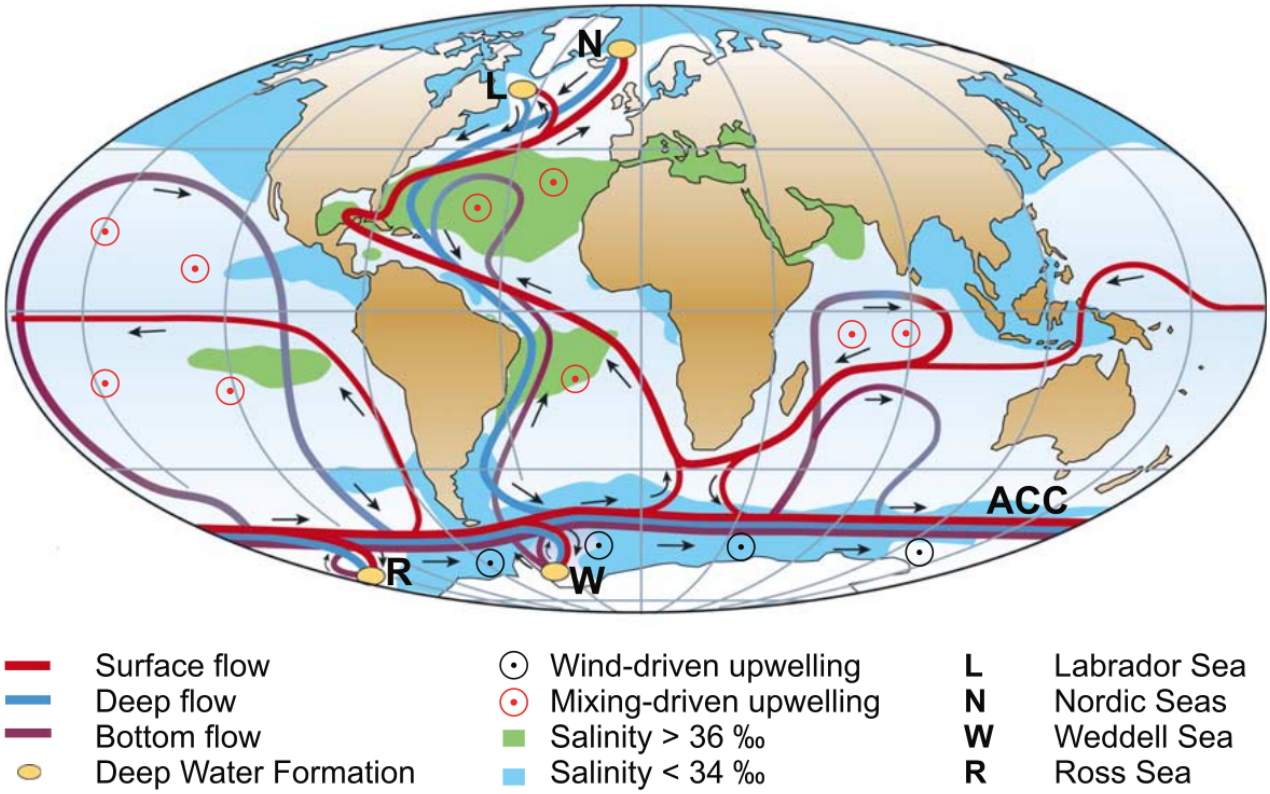

Figure 1.3: Simplified schematic of the global overturning circulation, as adapted from Rahmstorf [2002] in Kuhlbrodt et al. [2007]. Mixing-driven upwelling occurs over extensive areas and wind-driven upwelling along the Antarctic Circumpolar Current (ACC), whereas deep water formation sites are very few and localized.

The thermohaline circulation is influenced by surface buoyancy as heat and freshwater fluxes can lead to a density increase of surface waters. Sometimes, this increase is enough to trigger deep water formation at a few rare locations in the ocean, thus explaining the importance of brine release consequent to sea-ice formation. At larger and more numerous locations, deep water can also upwell as a result of the Ekman divergence (wind-driven upwelling), notably in the Southern Ocean where strong westerly winds flow. Upwellings also occur along the west Peruvian and African coasts, increasing local marine productivity as nutrients become more available. In addition to winds, mixing processes play an important role: the breaking of waves such as internal tides interacting with the ocean floor provides turbulent energy, causing dense deep waters to lose their properties and upwell [de Lavergne et al., 2016].

Since the deep water formation sites are localized in the Nordic seas and Southern Ocean, the Atlantic Ocean is unique in having both a main southern-sourced bottom water mass (i.e. AABW) and a northern-sourced deep water mass (i.e. NADW), arranged according to density gradients between them. As a result, fluctuations in the surface water density at high latitudes can significantly impact the deep ocean circulation strength and geometry in this particular

basin, also called the Atlantic Meridional Overturning Circulation (AMOC, Fig. 1.4b, top panel).

(a) δ^{13}C distribution [Curry and Oppo, 2005] (b) AMOC structure [Howe et al., 2016]

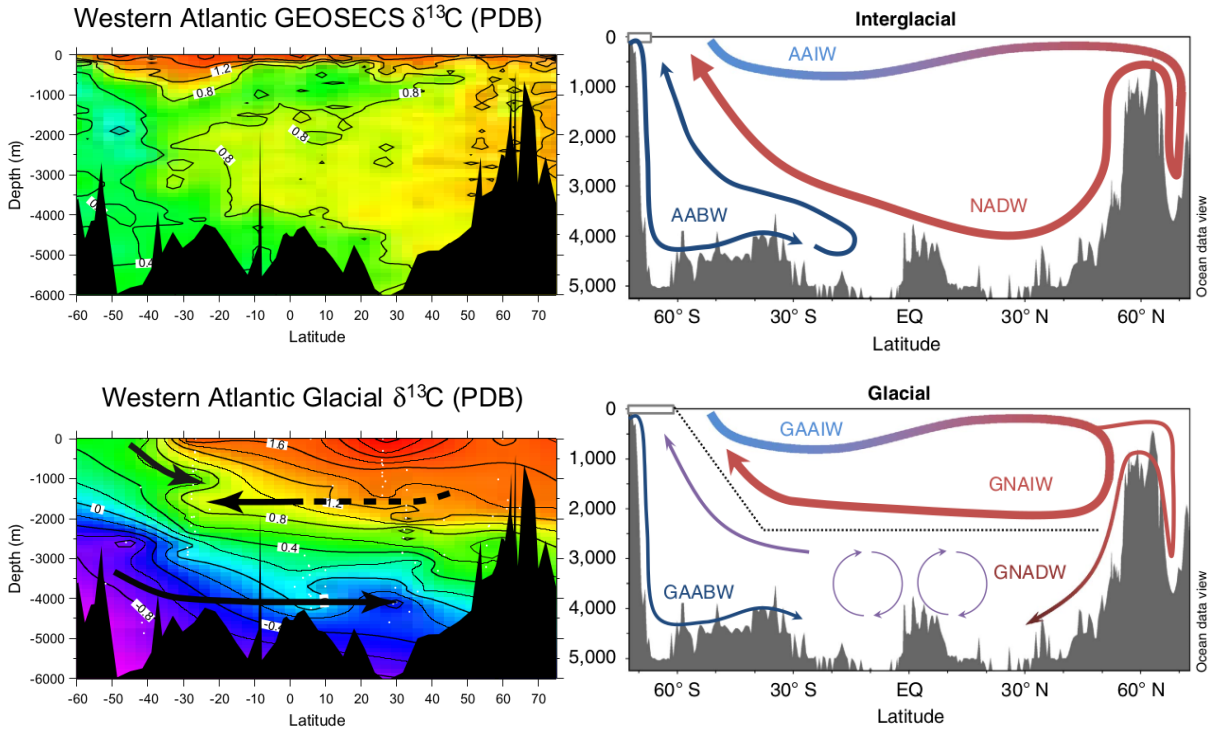

Figure 1.4: (a) δ^{13}C distribution in the Western Atlantic at the present-day (top) and LGM (bottom) inferred from marine core data in Curry and Oppo [2005]. (b) Schematics of the AMOC during the Holocene (top) and LGM (bottom) with a sluggish abyssal overturning, inferred from paleotracer data in Howe et al. [2016]. Are indicated AAIW: Antarctic Intermediate Water, AABW: Antarctic Bottom Water, NADW: North Atlantic Deep Water, and their glacial counterparts (G).

Studying the mechanisms, stability, past variations, and model representations of the AMOC is critical as it is considered a tipping point of the climate system [Wunderling et al., 2021], whose collapse is possible [Castellana et al., 2019]. Modern-day observations are monitoring the AMOC strength, for example thanks to the RAPID array at 26.5°N since 2004 [McCarthy et al., 2015]. These observations show an initial decline [Smeed et al., 2014] leading to a reduced state [Smeed et al., 2017]. The internal variability of the ocean may explain these fluctuations, and possibly even a future recovery of the AMOC [Moat et al., 2020]. The Intergovernmental Panel on Climate Change [2014] still announces as "very likely" an overall weakening of the AMOC over the coming century.

Past variations of the AMOC are documented thanks to numerous paleotracer data [Adkins, 2013], which evidence a shallower and weaker AMOC at the LGM, as well as abrupt AMOC changes during climatic events on shorter time scales (e.g. Younger Dryas, Heinrich and Dansgaard-Oeschger events, Lynch-Stieglitz [2017]). Proxy-based reconstructions include data from different types of proxy, developed using marine core measurements of geochemical tracers such as carbon and oxygen isotopes in benthic foraminifera [Ravelo and Hillaire-Marcel, 2007], neodymium isotopes, or atomic ratios (Cd/Ca, Mg/Ca, ^{231}Pa/^{230}Th, Adkins [2013]) –

though less conventional proxies also exist [Beny et al., 2020]. Multiple studies have been conducted using diverse records of $\delta^{13}C$ (Curry and Oppo [2005], Fig. 1.4a), radiocarbon ages [Freeman et al., 2016, Skinner et al., 2017], ϵ_{Nd} [Howe et al., 2016, Gu et al., 2017, Wilson et al., 2020] and $^{231}Pa/^{230}Th$ [Lippold et al., 2012, Böhm et al., 2015, Bradtmiller et al., 2014, Lippold et al., 2016]. Each of these proxies is associated with its own strengths and limitations [Gu et al., 2017, Muglia and Schmittner, 2021]. A majority of them tend to describe an AMOC at the LGM with a shoaled upper overturning cell (i.e. clockwise cell with a shoaled NADW), and an expanded and more sluggish abyssal cell due to denser and more saline AABW (see Fig. 1.4b, bottom panel). A very saline AABW is supported by a few pore-fluid measurements evidencing an enhanced, salinity-driven stratification at the LGM [Adkins et al., 2002].

In the following study, I will assume these aspects of the LGM circulation to be true, even though the ambiguity of the proxy signals remains debated [Gebbie, 2014, Pöppelmeier et al., 2020]. I will rely on $\delta^{13}C$ records [Peterson et al., 2014] specifically, which consist of numerous marine core data in all ocean basins (Sect. 2.4.3). In addition, $\delta^{13}C$ is explicitly computed by the Earth System Model used in this study (see Sect. 2.1.1). This indicator which can be expressed as [Ravelo and Hillaire-Marcel, 2007]:

$$\delta^{13}C = \frac{\frac{^{13}C}{^{12}C}_{sample} - \frac{^{13}C}{^{12}C}_{standard}}{\frac{^{13}C}{^{12}C}_{standard}} \times 1000$$

This indicator is a good tracer of water mass distribution, since the $\delta^{13}C$ in the ocean interior is influenced by the source of deep waters, as well as convection and mixing processes [Duplessy et al., 1988]. Indeed, isotopic fractionation occurs during photosynthesis (favoring the uptake of light isotopes), which is why an intense marine productivity leads to a high $\delta^{13}C$ of surface waters. On the other hand, remineralization in the ocean interior lowers the $\delta^{13}C$ value of water. Therefore, different water masses carry distinct $\delta^{13}C$ signatures (e.g. high values of NADW, see Fig. 1.4a) depending on their source and ventilation. These past signatures can be recorded in shells of some epibenthic foraminifera, such as those of the *Cibicidoides* genus. Especially low $\delta^{13}C$ values (Fig. 1.4a, bottom panel) measured in marine cores drilled in the Southern Ocean, suggest that the AABW was particularly isolated during the LGM, supporting the view of a highly stratified, poorly mixed bottom ocean. These records can also evidence interbasin differences, highlighting a potential role of the Drake Passage sill depth relative to the NADW shoaling [Sikes et al., 2017].

1.1.3 Atmospheric CO_2 concentration

Greenhouse gas concentrations play an essentiel role on the climate. Anthropogenic emissions since the pre-industrial era are responsible for the present-day and future climate change. Due to their physical properties, greenhouse gases tend to absorb and re-emit in all directions part of the longwave radiations emitted back to space by the Earth, but not the incoming shortwave solar radiations, causing a warming of the atmosphere. Although this greenhouse effect is perfectly natural, the increase of greenhouse gas concentrations observed today in the atmosphere modifies the Earth climate, which did not show much variation during the Holocene.

Among the different greenhouse gases, one of the most important is CO_2. The concentration of CO_2 in the atmosphere is determined by variations in the carbon cycle (Fig. 1.5), depending on the exchanges with much larger carbon reservoirs (e.g. ocean, terrestrial biosphere, lithosphere). The carbon fluxes between reservoirs relies on various physical (e.g. atmosphere and

ocean circulations), chemical (e.g. dissolution of CO_2 at the ocean surface), geological (e.g. sedimentation, weathering, volcanic activity) and biological (e.g. photosynthesis, respiration) processes, all playing out at different time scales. Some of these processes depend themselves on climate, for example as the CO_2 solubility varies with temperature. This allows for feedback effects to amplify or lessen initial perturbations, which notably complicates our understanding of the climate system.

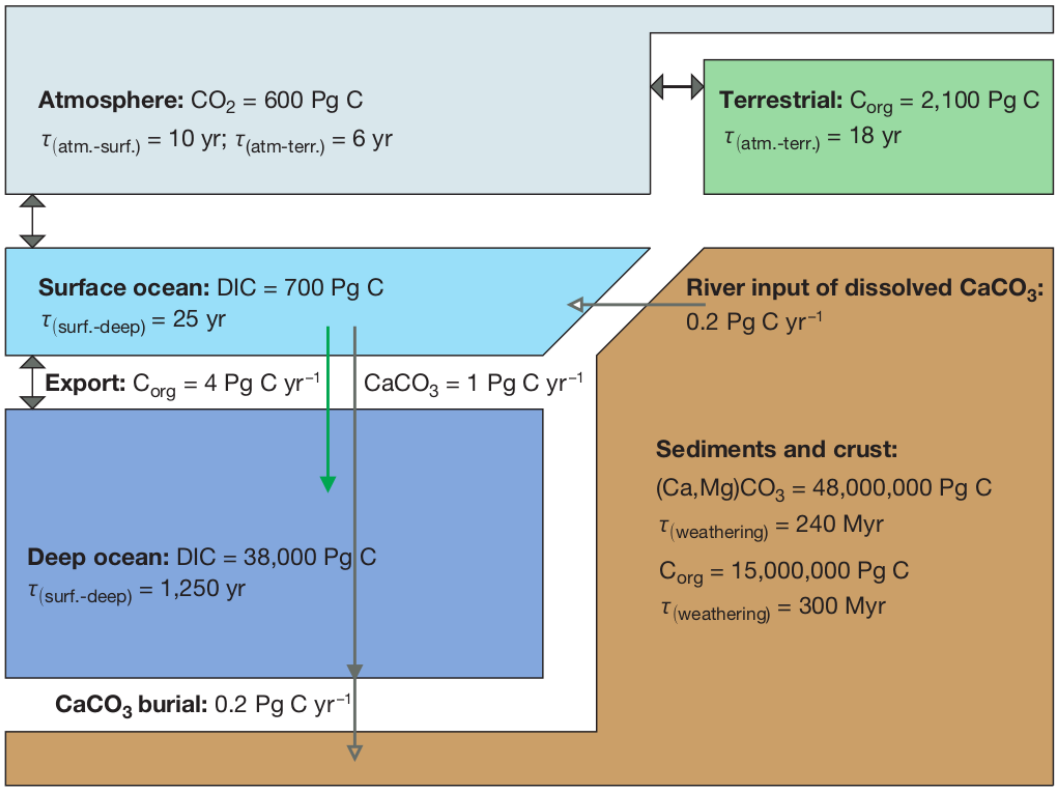

Figure 1.5: Simplified schematic of the PI carbon cycle (figure from Sigman and Boyle [2000]). The different reservoirs are indicated in boxes, with their corresponding carbon content and residence time (τ). Arrows show the main carbon fluxes between reservoirs (on the scale of glacial-interglacial variations).

Variations of the atmospheric CO_2 concentration at the scale of orbitally-driven glacial-interglacial cycles have been recorded by natural archives. Indeed, this concentration can be measured in air bubbles contained in ice cores [Bereiter et al., 2015] such as those drilled in the Antarctic or Greenland ice sheets. Such records clearly show variations with an amplitude of about 80−100 ppm, associated with the most recent glacial-interglacial cycles of 100 kyr (Fig. 1.6). As a result, the atmospheric CO_2 concentration during the LGM 21,000 years ago was around 190 ppm [Bereiter et al., 2015], constrasting the pre-industrial concentration of $\sim$ 280 ppm and the present-day one, now above 400 ppm.

These variations are still poorly understood, though there is a relative consensus on a large role played by the ocean. Such a role makes sense considering that the ocean represents the largest ($\sim$38,000 GtC) carbon reservoir available to exchange carbon with the atmosphere on a millenial scale. An increased carbon storage in the LGM ocean is needed to explain both a low atmospheric CO_2 concentration of $\sim$190 ppm (i.e. a pCO_2 drawdown of 80−100 ppm), and less carbon in the terrestrial biosphere (due to the extensive ice sheets, low temperatures, and a reduced CO_2 fertilization effect).

However, the mechanisms explaining a larger carbon sequestration in the ocean at the LGM are still subject to debate. Both physical and biological processes can explain an enhanced storage, through what are called the "solubility pump", "soft tissue pump", and "carbonate pump" [Kohfeld and Ridgwell, 2009]. Indeed, the temperature and salinity influence the solubility of CO_2, which is enhanced in colder waters ("solubility pump"). In the photic zone, photosynthesis allows for a decrease of Dissolved Inorganic Carbon (DIC) and a subsequent export of organic carbon into the deep ocean, where it is largely remineralized ("soft tissue pump"). In addition, certain species of phytoplankton also trap carbon in their shells in the form of calcium carbonate. The consequent sinking of $CaCO_3$ drives an opposite effect on CO_2 due to a reduced alkalinity in surface waters ("carbonate pump" or "counter pump", Kohfeld and Ridgwell [2009], Sigman et al. [2010]). Nonetheless, the exact contributions of temperature, salinity, ocean circulation, marine productivity (e.g. through iron fertilization) and carbonate compensation changes (i.e. variations in the amount of $CaCO_3$ preserved and buried in sediments, driven by the DIC and alkalinity budget) are far from being elucidated.

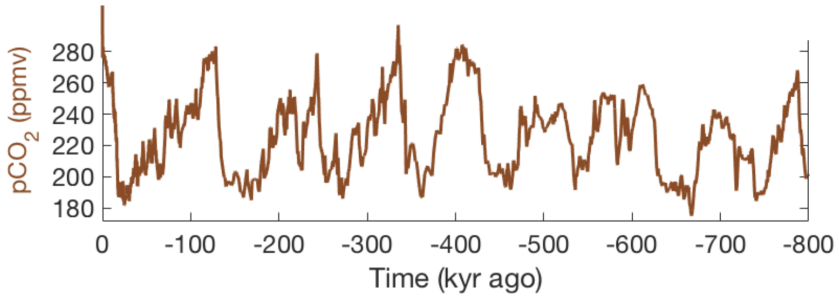

Figure 1.6: Atmospheric CO_2 variations during the past 800 ka as measured in ice cores [Bereiter et al., 2015]. Figure adapted from [Berends et al., 2021].

1.2 Modelling the Southern Ocean sea ice, AMOC and pCO_2 drawdown at the LGM

1.2.1 Paleoclimate models

Considering the complexity of the climate system, models represent valuable tools to investigate the potential relationships between the Southern Ocean sea-ice cover, deep ocean circulation, and carbon sequestration at the LGM. Models allow for a numerical resolution of physical, chemical, and biological laws on a grid mesh (Fig. 1.7). Depending on their spatial resolution, models resolve the coded equations of their dynamical core and approximate a solution, but have to rely on parameterizations to represent small-scale processes. These parameterizations are generally a source of uncertainty. They introduce a certain number of poorly constrained parameters, which can be adjusted to reduce the discrepancies with a selected set of observations, in what is called the tuning of a climate model [Hourdin et al., 2017].

Models are typically tuned for the present-day, while the same code is used to run paleoclimate simulations. Modellers only apply different forcings and/or boundary conditions (Fig. 1.7, and Sect. 2.3) in order to prescribe changes in orbital configuration, greenhouse gas concentrations, coastlines... While "boundary conditions" generally designate model inputs which

are fixed during the run, the definition of these two terms can be ambiguous [Goosse, 2015]. In any case, these prescribed inputs enable simulations with very different background climates than today's (e.g. the LGM with cold temperatures due to low greenhouse gas concentrations and extensive ice sheets in the Northern Hemisphere). This is why paleoclimate runs can be especially useful to evaluate model performance, as long as the target period is well-documented by proxy data (e.g. the LGM). Models which perform well in past warm periods (e.g. Last Interglacial) tend to give relatively more confidence in their ability to simulate the future climate. In addition to this rather technical objective, paleoclimate simulations may also improve our understanding of the processes involved in the climate system, as they give a more comprehensive view into the model response to forcings, uncovering potential nonlinear behaviour of said processes (e.g. CO_2 forcing influence on AABW volume, Galbraith and de Lavergne [2019]).

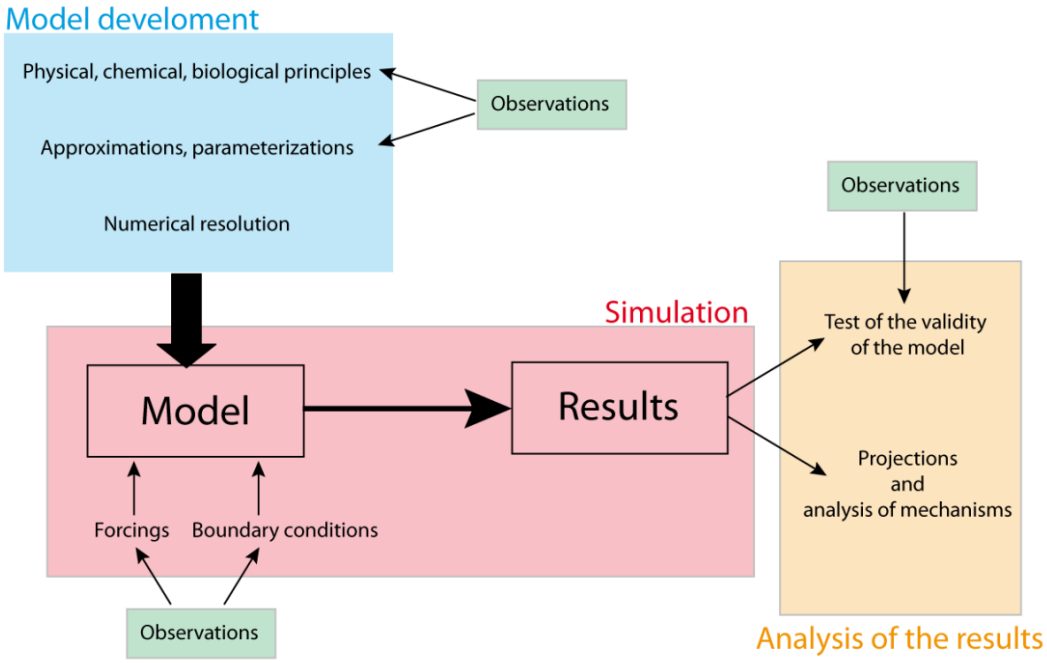

Figure 1.7: Simplified inputs and outputs of a climate model (figure from Goosse [2015])

During the last decades, models have evolved from stand-alone components (e.g. AGCM, OGCM) to coupled models (e.g. AOGCM) and then on to complex ESMs including multiple components (vegetation, sea ice, carbon cycle, atmospheric chemistry...). Thanks to advances in supercomputing, the calculation cost of high resolution models have also been reduced. However, models of diverse resolution (and diverse complexity of the physical processes represented) still find their use, from conceptual models to EMICs and higher resolution GCMs [Claussen et al., 2002]. Paleoclimate modelling in particular often requires runs on a millenial to multi-millenial timescale, which is why the models used tend to have a comparatively lower resolution than modelling studies at modern times (e.g. IPSL-CM5A2 version of the IPSL model, [Sepulchre et al., 2020]).

This diversity of models is an asset, especially in the context of modelling intercomparison projects (MIPs). It is essential to assess uncertainties, and identify processes which are robustly simulated, systematically biased or a source of intermodel spread. Such interpretations are not easy, and may even be further complicated by the interdependances observed in the genealogy of CMIP5 models [Knutti et al., 2015].

1.2.2 Modelling the glacial Southern Ocean sea ice

Model intercomparison studies have analyzed outputs of LGM simulations run in the framework of previous PMIP phases (PMIP2 and PMIP3, while PMIP4 is still ongoing). In particular, Roche et al. [2012], Goosse et al. [2013] and Marzocchi and Jansen [2017] have focussed on the Southern Ocean sea ice, examining its distribution and/or extent in both seasons (see Fig. 1.8, 1.9, and Sect. 6.4). These studies underline three recurring biases with respect to proxy-based reconstructions:

- A fairly round-shaped sea-ice distribution around Antarctica, in disagreement with proxy data evidencing an oval-shaped sea-ice cover [Gersonde et al., 2005] (see Fig. 1.8).
- An underestimated winter sea-ice extent simulated by a majority of PMIP2 (5 out of 8) and PMIP3 (7 out of 8) models, relative to the reconstructed extent estimate in Roche et al. [2012] (see Fig. 1.9 and Sect. 6.4).
- An underestimated seasonal range, staying fairly close to the PI one although proxy data suggest an enhanced seasonality at the LGM (see Sect. 6.4).

As a result, "models fail to represent the sea-ice distribution in the Southern Ocean for the LGM both in shape and in seasonal range, calling for a detailed assessment of mechanisms driving sea-ice changes over such timescales" [Goosse et al., 2013]. The authors point out that the LGM is a key period to investigate the contrasted response of models in Southern Ocean sea ice, especially as both Goosse et al. [2013] and Roche et al. [2012] observe a link between LGM biases and PI ones. I also note that the Southern Ocean sea ice is still poorly represented (and usually underestimated) in present-day conditions, even in the most recent intercomparison exercise (CMIP6, Beadling et al. [2020]).

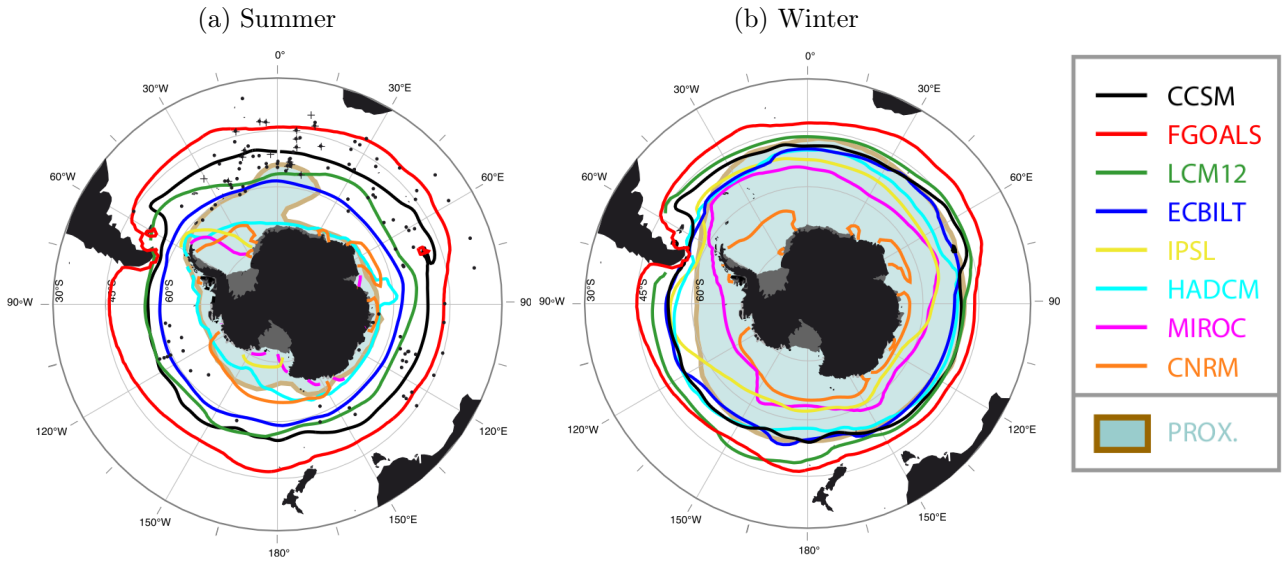

Figure 1.8: (a) Summer and (b) winter sea-ice edges (defined at 15% of sea-ice concentration) in the Southern Ocean, as simulated at the LGM by PMIP2 models (figure adapted from Roche et al. [2012]). The blue area indicates the sea-ice distribution reconstructed in Gersonde et al. [2005], with the location of their marine core data displayed by black points and crosses.

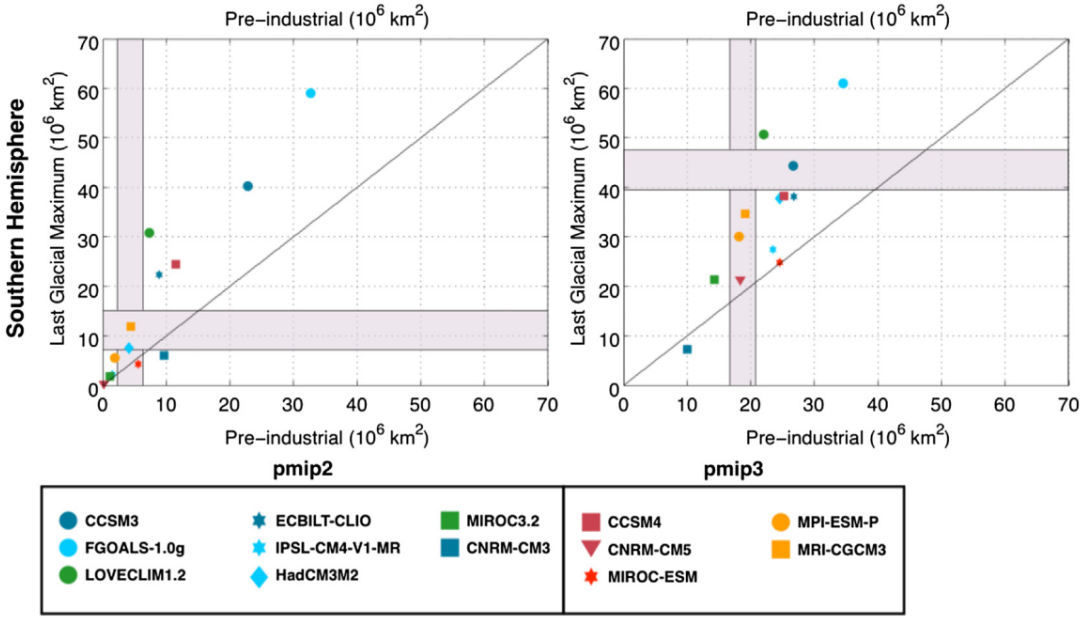

Figure 1.9: Minimal (summer, left) and maximal (winter, right) sea-ice extent in the Southern Ocean, as simulated by PMIP2-3 models at the PI (x-axis) and LGM (y-axis). Horizontal bars shows the LGM estimates of Roche et al. [2012] and vertical bars the satellite observations for modern times (1979−2000, Fetterer et al. [2012]). Figure from Goosse et al. [2013].

While it has been suggested that model-data disagreements in terms of sea-ice seasonality in the glacial Southern Ocean may be linked to a too weak stratification near the surface [Roche et al., 2012], Marzocchi and Jansen [2017] point out that an insufficient sea-ice formation may lead to a too weakly stratified Atlantic ocean and a consequently deep AMOC.

1.2.3 Modelling the glacial AMOC

In the context of previous PMIP phases, model intercomparison studies have also focussed on the AMOC simulated by the PMIP2 and PMIP3 ensembles [Otto-Bliesner et al., 2007, Muglia and Schmittner, 2015, Weber et al., 2007]. This meridional overturning can be portrayed by the streamfunction, which shows the integrated transport of water masses computed in the Atlantic basin on a latitude-depth plot (Fig. 1.10 and 1.11). The upper clockwise cell (with positive values) is the one associated with the NADW formation in the North Atlantic and Nordic seas, while the bottom counterclockwise cell (with negative values) encompasses the AABW northward transport until its consumption.

A large intermodel spread in terms of the AMOC strength and depth simulated at the LGM is a recurring issue in PMIP exercises (Fig. 1.10 and 1.11), although substantial discrepancies in the PI streamfunctions are also visible. Furthermore, half of the PMIP2 models and the overwhelming majority of PMIP3 models display a deep and intense NADW overturning cell at the LGM, sometimes even reaching down to the ocean floor in the North Atlantic (e.g. MIROC, ECBILT-CLIO). Muglia and Schmittner [2015] quantified that on average, PMIP3 models simulate both an increase ($41 \pm 26\%$) and deepening (663 ± 550 m) of the AMOC. This is in clear disagreement with the AMOC reconstructed from proxy data (Sect. 1.1.2), which is associated with a NADW shoaling.

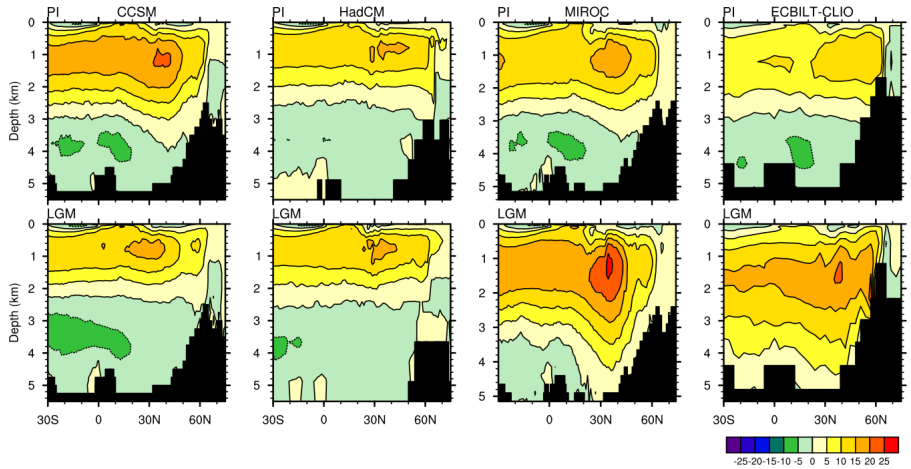

Figure 1.10: Atlantic meridional streamfunction (Sv) simulated by four PMIP2 models at the PI (top) and LGM (bottom). Figure from Otto-Bliesner et al. [2007].

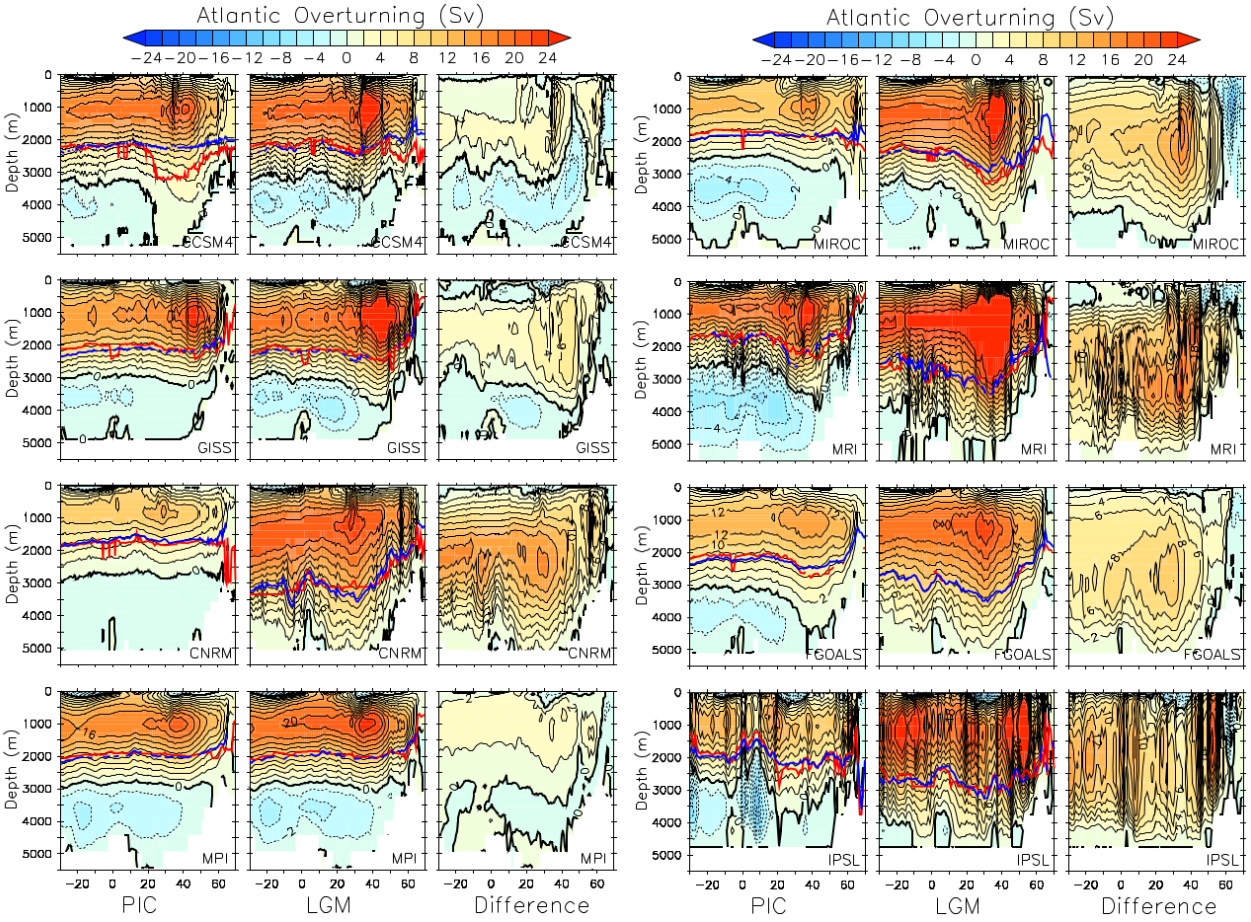

Figure 1.11: Atlantic meridional streamfunction simulated by eight PMIP3 models (figure from Muglia and Schmittner [2015], SI). Legend from Muglia and Schmittner [2015]: "First column corresponds to PI simulations, middle to LGM, and third to the difference between them. Each row corresponds to a different PMIP3 model. Isoline difference is 4 Sv. The red line is the depth of the AMOC calculated as the middle depth between $\psi = \psi_{\max}$ and $\psi = 0$, and the blue line is the depth where $\psi = \frac{\psi_{\max}}{2}$".

Model-data comparison studies using LGM simulations and sensitivity tests run with a proxy-enabled model have specifically examined the agreement with different types of proxy data (δ^{13}C, Δ^{14}C, ϵ_{Nd}, ^{231}Pa/^{230}Th). These studies show a consistent picture of an improved agreement with proxy data when an upper cell shoaling ($>$ 500 m) is simulated [Gu et al., 2020, Hesse et al., 2011, Muglia et al., 2018, Kurahashi-Nakamura et al., 2017, Tagliabue et al., 2009, Menviel et al., 2017, 2020]. On the other hand, they show more conflicted results in terms of AMOC strength. Hesse et al. [2011], Gu et al. [2020] and Muglia and Schmittner [2021] all underline that the proxy data used (in particular carbon isotopes) do not constrain well the AMOC strength. In addition, it is difficult to generate simulations with similar depths but different strengths, as these two characteristics of the AMOC often co-vary [Muglia and Schmittner, 2021, Gu et al., 2020]. As a result, the simulation with the closest match to proxy data may show a weak overturning (5 Sv in Tagliabue et al. [2009], 6−9 Sv in Muglia et al. [2018], 8−12 Sv in Hesse et al. [2011]), a moderate one (10−15 Sv in Menviel et al. [2017], 14.7 Sv in Menviel et al. [2020], 9.9−17.6 Sv in Gu et al. [2020]) or even a stronger overturning than at the PI (22 Sv in Kurahashi-Nakamura et al. [2017]).

(a) PMIP2 [Otto-Bliesner et al., 2007] (b) PMIP3 [Muglia and Schmittner, 2015]

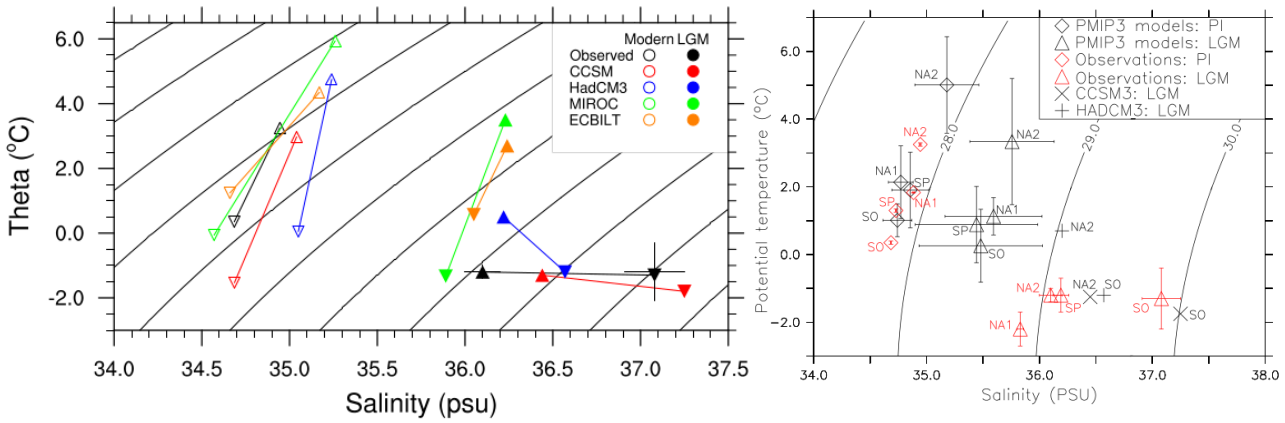

Figure 1.12: Bottom potential temperature and salinity simulated by (a) PMIP2 models and (b) the PMIP3 multimodel average at the PI and LGM, at the locations of the four sites of pore-fluid measurements [Adkins et al., 2002], indicated in black in (a) and red in (b). These sites are situated in the North Atlantic (triangle or NA1 and NA2), South Pacific (SP), Atlantic sector of the Southern Ocean (upside down triangle or SO). The two PMIP2 models with similarities with the reconstructed bottom temperature and salinity are CCSM3 (red or $\times$) and HADCM3 (blue or $+$).

Looking into the potential causes of the overestimated AMOC depth in most PMIP models, Otto-Bliesner et al. [2007] and Muglia and Schmittner [2015] have compared the simulated bottom temperature and salinity to the rare pore-fluid measurements of Adkins et al. [2002] (Fig. 1.12). They show that most models largely fail to simulate the density gradient between the deep Southern Ocean and North Atlantic at the LGM. According to Adkins et al. [2002], this gradient is essentially due to differences in bottom salinity, with very saline (and thus very dense) bottom waters in the Atlantic sector of the Southern Ocean. However, this gradient tends to retain its PI pattern in PMIP models (with the exception of CCSM3). These results suggest that the properties of bottom waters are not well simulated at the LGM, and especially those of AABW. Both Weber et al. [2007] and Galbraith and de Lavergne [2019] have suggested

that the surface density difference between AABW and NADW deep water formation sites is a dominant control on the AABW volume and AMOC depth.

The relative inability of PMIP models to simulate an Atlantic deep ocean circulation in good agreement with paleotracer data under a different background climate than today's calls into question the model representation of the AMOC drivers. Physical oceanography studies have identified several significant drivers: winds [Kuhlbrodt et al., 2007, Johnson et al., 2019, Baker et al., 2021], mesoscale eddies [Marshall and Speer, 2012, Johnson et al., 2019], vertical mixing processes [Kuhlbrodt et al., 2007, Baker et al., 2021, De Boer and Hogg, 2014] and surface buoyancy [Johnson et al., 2019, Baker et al., 2020] − though their relative contribution is difficult to elucidate.

In LGM studies, the surface buoyancy of the Southern Ocean in particular has received some attention [Shin et al., 2003, Ferrari et al., 2014, Watson et al., 2015, Jansen, 2017, Marzocchi and Jansen, 2017], as increased sea-ice cover induced by the drop of surface temperatures may have caused enhanced brine-induced stratification (and thus a denser AABW). Other studies have also pointed out the influence of surface buoyancy and winds over the North Atlantic [Oka et al., 2011, Sherriff-Tadano et al., 2018, Muglia and Schmittner, 2015], as well as the impact on the AMOC of freshwater budget changes caused by the Bering Strait closure [Hu et al., 2010]. However, the wind stress changes in the Northern Hemisphere associated with high LGM ice sheets tend to deepen the AMOC, while the Southern Ocean buoyancy fluxes may counterbalance this effect in some models (MPI-ESM, Klockmann et al. [2016]). I also note that, although rarely implemented in PMIP models [De Boer and Hogg, 2014], LGM tidal mixing changes would tend to significantly strenghten the AMOC [Wilmes et al., 2019, Schmittner et al., 2015]. Finally, the Southern Ocean upwelling (and eddy-induced circulation) could be affected by a shift of latitude and strength of the westerly winds, which seem to be poorly represented in PMIP models [Gray et al., in review, 2021] − but also poorly resolved by conflicting paleodata records [Kohfeld et al., 2013].

Considering these different drivers, their often poor LGM representation (or even lack thereof), and their contrasted effects in interplay (e.g. feedback and nonlinear effects underlined in Oka et al. [2011], Galbraith and de Lavergne [2019], Sherriff-Tadano and Abe-Ouchi [2020]), it is no wonder that simulating an AMOC in good agreement with paleotracer data is challenging.

1.2.4 Modelling the glacial pCO_2 drawdown

Up until now, carbon outputs have not been examined by PMIP intercomparison studies, despite a growing number of carbon-enabled models. Therefore, differences between results from different studies may be linked to the experimental design (LGM forcings and boundary conditions − a smaller ocean volume is responsible for a ∼16 ppm increase in Morée et al. [2021]), in addition to model differences (e.g. coupled model vs stand-alone ocean models), resolution [Gottschalk et al., 2020], simulated climate (e.g. large range of simulated global mean SAT anomaly in PMIP4 models, Kageyama et al. [2021]), and representation of the carbon cycle (e.g. with carbonate compensation, permafrost, iron dust). Still, a few tendencies have emerged from various modelling studies:

- The LGM pCO_2 drawdown of ∼-90 ppm (according to ice core data) is very difficult to simulate. Most studies quantify a largely underestimated drawdown in LGM simulations (e.g. -20.8 ppm in Morée et al. [2021], -40 ppm in Marzocchi and Jansen [2019], -38.66 ppm in Kobayashi and Oka [2018], -42.1 ppm in Oka et al. [2011], -34−43 pmm in Brovkin et al. [2007], -32 ppm in Stein et al. [2020]...), hence an overestimated CO_2 concentration. I however stress here that these numbers can hardly be compared due to various model settings and additional processes taken into account.

- As a result, modellers have to resort to some adjustments in sensitivity tests to simulate a more realistic pCO_2 drawdown and/or test the impact of various processes. Typically, they stimulate the biological pump via increased nutrients [Morée et al., 2021, Brovkin et al., 2007, Oka et al., 2011, Bouttes et al., 2011, Tagliabue et al., 2009, Menviel et al., 2012] or other biogeochemistry changes (e.g. increased depth of remineralization, export production of particulate organic carbon, and decreased export production of inorganic carbon in Buchanan et al. [2016]). Some of these changes are justified by iron fertilization due to increased aeolian dust fluxes at the LGM. Conversely, modelling studies have also focussed on changes in the physical pump through an increased stratification [Kobayashi and Oka, 2018], a parameterized sinking of brines [Bouttes et al., 2010, Menviel et al., 2012], or a change of vertical diffusivity [Bouttes et al., 2011, Kobayashi and Oka, 2018].

- Studies have suggested an influence from various physical and biogeochemical processes (Fig. 1.13 and 1.14), including changes in the Southern Ocean sea-ice cover. The potential contribution of these processes has been reviewed in Kohfeld and Ridgwell [2009] and Gottschalk et al. [2020]. As underlined in Lhardy et al. [2021a]:

  > "Despite the identification of these processes, their contribution to the pCO_2 drawdown is still much debated. Modelling studies tend to show a large effect of the biological pump and a moderate effect of circulation changes [Khatiwala et al., 2019, Buchanan et al., 2016, Yamamoto et al., 2019, Tagliabue et al., 2009, Hain et al., 2010, Menviel et al., 2012], but model disagreements remain. Iron fertilization seems to explain a relatively small part (∼15 ppm) of the LGM pCO_2 drawdown [Bopp et al., 2003, Tagliabue et al., 2014, Kohfeld and Ridgwell, 2009, Muglia et al., 2017]. Accounting for carbonate compensation in models also seems to significantly reduce the simulated atmospheric CO_2 concentrations [Kobayashi and Oka, 2018, Brovkin et al., 2007]. However, review studies show that the amplitude of the CO_2 variation caused by each process is not well constrained [Kohfeld and Ridgwell, 2009, Gottschalk et al., 2020]. Moreover, sensitivity tests underline that, due to the interactions of both these physical and biogeochemical processes, isolating their effect remains challenging [Hain et al., 2010, Kobayashi and Oka, 2018, Ödalen et al., 2018]. The emerging common view is that the LGM pCO_2 drawdown cannot be explained by a single mechanism, but by a combination of different intrinsic processes [Kohfeld and Ridgwell, 2009, Hain et al., 2010]."

  Kohfeld and Ridgwell [2009] also point out that a linear sum of the contributions from the different identified processes does not explain the full amplitude of the LGM pCO_2 drawdown (Fig. 1.14).

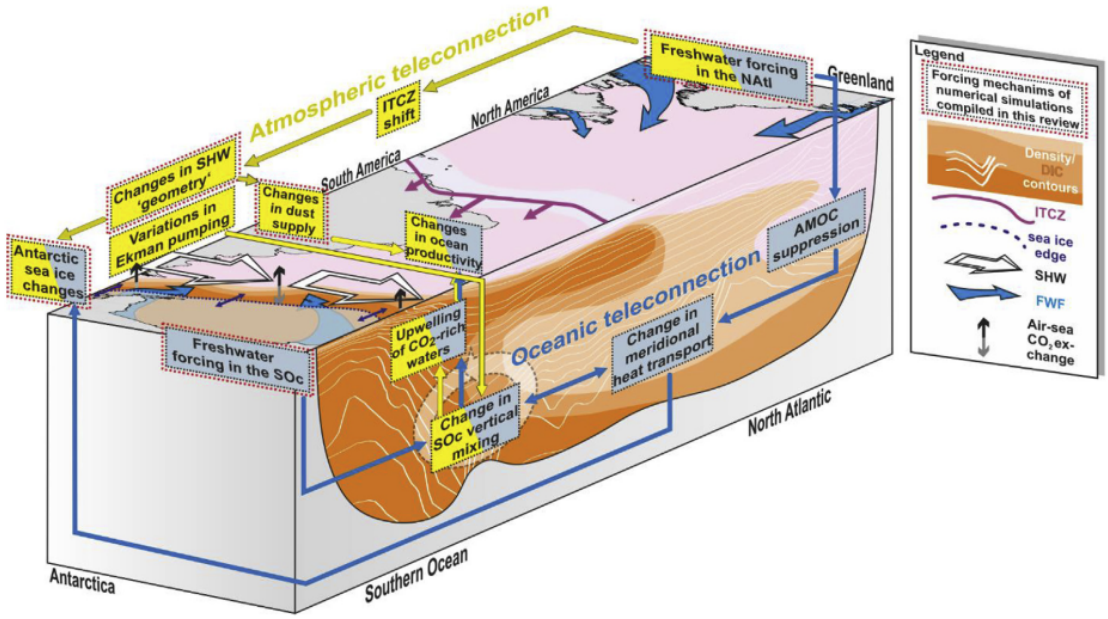

Figure 1.13: Potential mechanisms contributing to millenial-scale atmospheric CO_2 concentration variations, proposed and tested by models in the literature reviewed in Gottschalk et al. [2020]. The six forcing mechanisms include: changes in freshwater fluxes (in the North Atlantic or Southern Ocean), in the strength and position of Southern Hemisphere westerly winds, in Southern Ocean sea-ice extent, and in aeolian dust fluxes. Figure from Gottschalk et al. [2020].

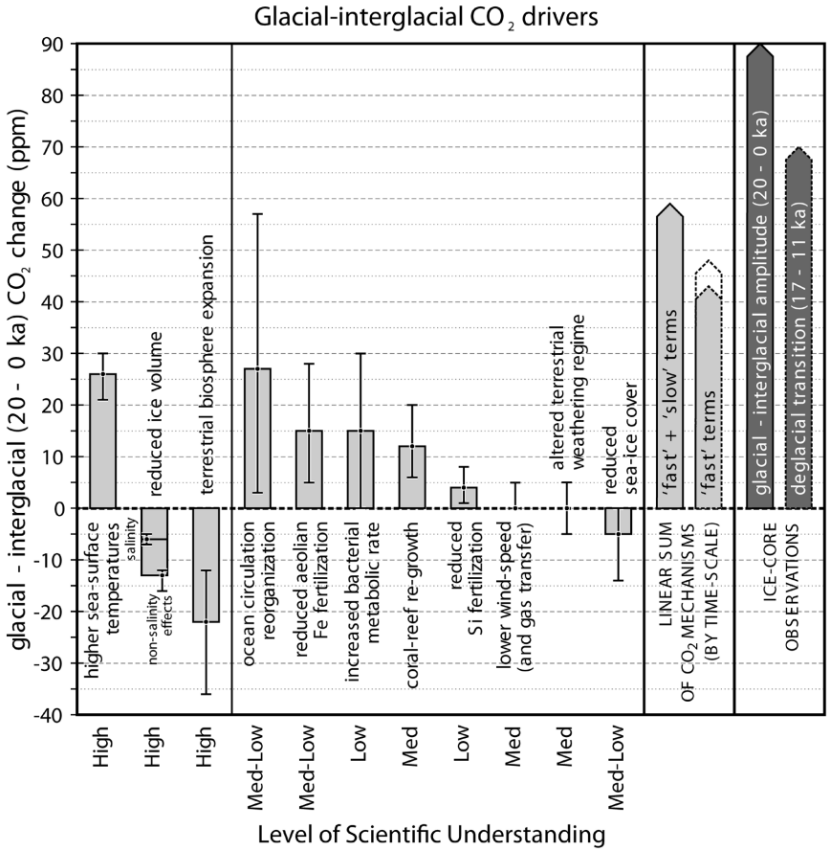

Figure 1.14: Estimated impact of mechanisms contributing to variations of atmospheric CO_2 concentration at the scale of glacial-interglacial cycles (figure from Kohfeld and Ridgwell [2009])

1.3 The strategic Southern Ocean

The present study largely focusses on the Southern Ocean. It may be useful to justify this choice here, considering that the biases assessed in the following chapters either concerns the Antarctic sea-ice cover (Arctic sea ice is not examined), the deep ocean circulation (at the scale of the Atlantic basin), or the pCO_2 drawdown (at a global scale) simulated at the LGM. What makes the Southern Ocean so special? How can local processes occurring in the Southern Ocean be related to large-scale processes, such as ocean circulation and sequestration?

As mentioned before, Antarctica is a polar continent completely surrounded by water. This geographic situation has consequences, as there are few landmasses and topographic barriers limiting winds and currents. Strong westerly winds flow eastward, pushing the largest current on Earth (the Antarctic Circumpolar Current). The ACC connects the Atlantic, Indian, and Pacific oceans, and is associated with considerable turbulent energy (mesoscale eddies) and strong fronts (e.g. polar front). As a result, the Antarctic continent is particularly isolated, which helps maintaining a huge ice sheet even in the present-day climate change. In addition, this geography causes significant differences between Arctic and Antarctic sea ice [Maksym, 2019]: the latter is not constrained by a northern boundary, and its export towards lower latitudes is enhanced by katabatic winds flowing down the slope of the ice cap.

As shown in Fig. 1.3, the Southern Ocean is also the location of rare deep water formation sites. Filling the bottom ocean, the AABW is originated from sea-ice formation, which leads to brine release and therefore dense waters on the Antarctic continental shelf, then to an overflow along the continental slope. Other vertical advection of water masses includes the Southern Ocean upwelling, caused by westerly winds leading to a strong Ekman divergence − but with a notable influence of the eddy-induced circulation [Marshall and Speer, 2012]. As a result, exchanges between the surface and deep ocean are particularly significant in the Southern Ocean.

Carbon fluxes are among such exchanges. Partly because of its low SSTs and SSSs, the Southern Ocean represents a carbon sink region, accounting for a major uptake into the ocean. When this dissolved carbon load sinks into bottom waters, it may be isolated from the atmosphere on the long run.

Because of these characteristics, the Southern Ocean can be a critical region of ice-ocean-wind-carbon feedbacks, especially at the LGM [Ferrari et al., 2014, Stein et al., 2020]. Modelling studies suggest that an enhanced sea-ice formation due to colder temperatures can lead to an increased brine-induced stratification, associated with a weaker and shallower AMOC [Marzocchi and Jansen, 2017, Shin et al., 2003, Klockmann et al., 2016, Jansen, 2017]. While the expansion of poorly ventilated AABW could increase the ocean carbon storage capacity [Skinner, 2009, Muglia et al., 2018], colder temperatures in LGM waters would also yield a higher CO_2 solubility. A third effect on the physical pump has been proposed by Ferrari et al. [2014], who argue that the AABW may experience less mixing with the overlying NADW as a result of a displaced sea-ice edge and of a limited reach of topography-enhanced mixing (Fig. 1.15). In addition, the northward expansion of the sea-ice cover also means that less CO_2 outgassing could occur as a result of a reduced atmospheric exposure time of freshly upwelled surface waters [Stein et al., 2020]. However, it is difficult to disentangle the sea-ice capping effects, from this decreased outgassing, to an increased stratification, and a reduced marine productivity due to less light availability. Sun and Matsumoto [2010], Stephens and Keeling [2000], Stein et al. [2020] and Khatiwala et al. [2019] have quantified very different drawdowns associated with this sea-ice capping. Finally, Watson et al. [2015] have also underlined that a northward

displacement of the upwelling could be associated with a significant increase of carbon sequestration in the ocean.

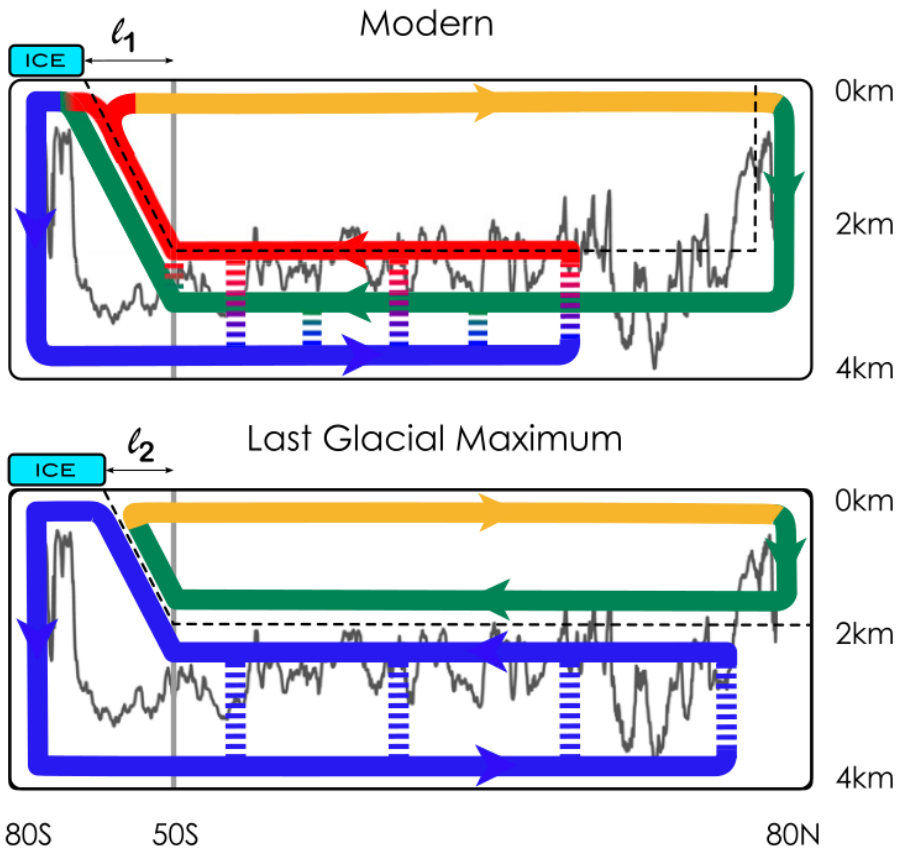

Figure 1.15: Figure and legend from Ferrari et al. [2014]: *(Upper)* Schematic of the overturning circulation for the modern climate. The ribbons represent a zonally averaged view of the circulation of the major water masses; blue is AABW, green is NADW, red are IDW and PDW, and orange are Antarctic Intermediate Waters. The dashed vertical lines represent mixing-driven upwelling of AABW into NADW and IDW/PDW respectively. There is also some mixing between NADW and IDW/PDW in the Southern Ocean. The dashed black line represents the isopycnal that separates the upper and lower overturning branches present in the Southern Ocean. l_1 is the distance between the northernmost latitude reached by the ACC, indicated by a solid gray line, and the quasi-permanent sea ice line. The ragged gray line is the crest of the main bathymetric features of the Pacific and Indian ocean basins: mixing is enhanced below this line. *(Lower)* Schematic of the overturning circulation for the LGM. The extent of the quasi-permanent sea ice line has shifted equatorward compared with modern climate ($l_2 < l_1$). Mixing-driven upwelling of abyssal waters is confined below 2 km and it cannot lift waters high enough to upwell north of the ice line. As a result the abyssal overturning circulation closes on itself, leaving above a small overturning cell of North Atlantic waters.

I also note that even in present-day conditions, the Southern Ocean is the location of significant model biases in SSTs, sea ice, winds, ocean transport, etc. [Hyder et al., 2018, Park et al., 2014, Downes et al., 2015], despite some improvements in the recent CMIP phases [Beadling et al., 2020, Meijers, 2014]. Heuzé et al. [2013], Heywood et al. [2014] and Heuzé [2021] also show large disagreements between the Southern Ocean bottom densities simulated by coupled models (CMIP5 or CMIP6) and climatological values from historical data (Fig.

1.16). They relate these bottom water properties to the inaccurate representation of slope processes in models. Indeed, observations suggest that AABW formation occurs as a result of a spilling of dense shelf water off the Antarctic continental shelf. On the other hand, open-ocean convection is a rarely occuring process. Yet, all CMIP5 models and the overwhelming majority of CMIP6 models (except those relying on an overflow parameterization) simulate an AABW formation via an open-ocean convection [Heuzé et al., 2013, Heuzé, 2021], noted to be "too deeply, too often, and/or over too large an area" by Heuzé [2021]. It is likely that the production of AABW through an unrealistic process may also impact the AABW density under a different background climate, such as the LGM [Klockmann et al., 2016].

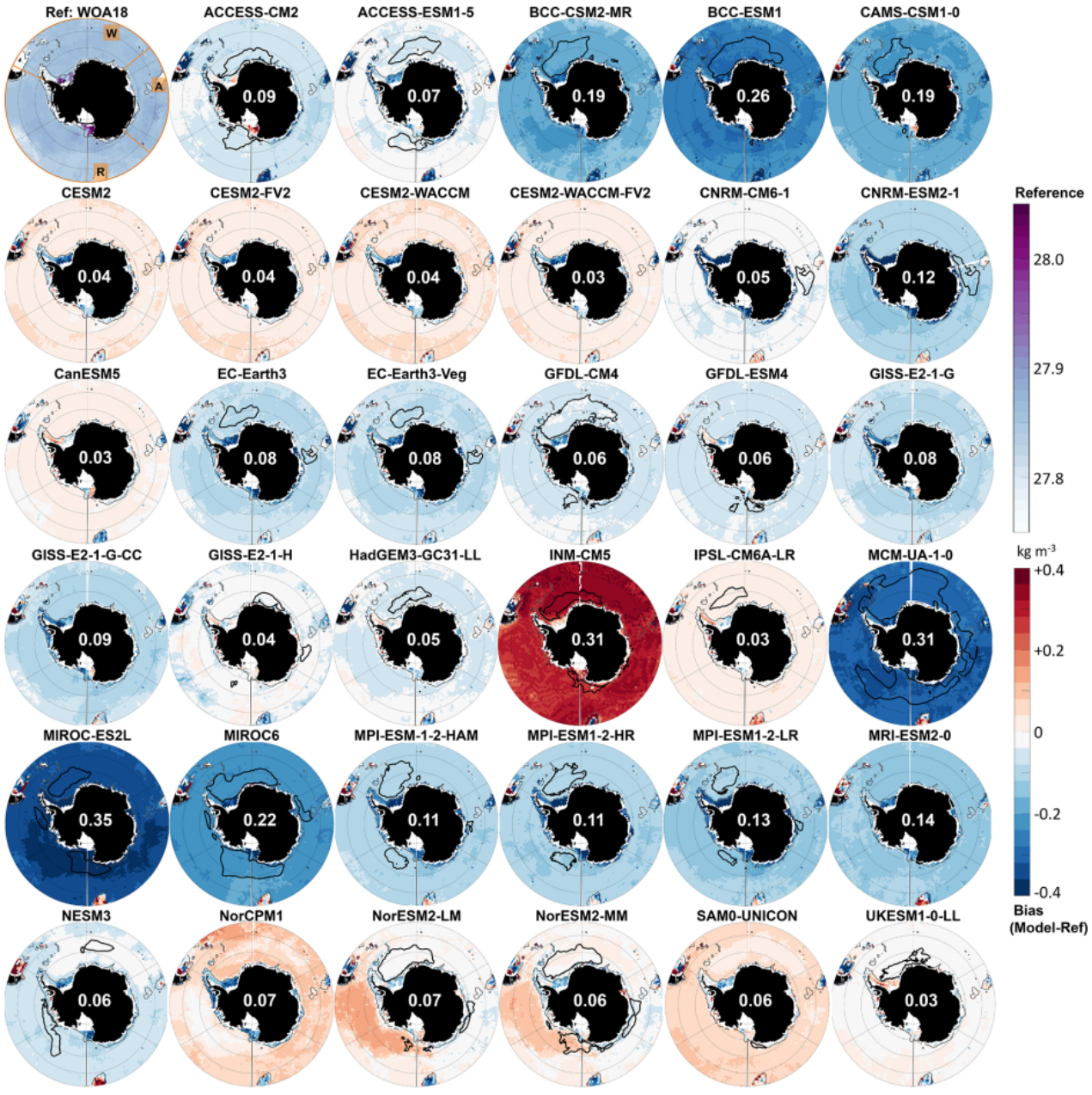

Figure 1.16: (top left panel) Reference bottom density in the Southern Ocean. (all other panels) Bottom density bias over 1985−2014 with respect to the reference for each CMIP6 model (figure from Heuzé [2021]). The RMSE over the deep (>1000 m) Southern Ocean is indicated in white. The black line indicates where the maximum mixed layer reaches 2000 m.

1.4 Résumé du chapitre en français

L'objectif de ce premier chapitre est de placer mon sujet de thèse dans un contexte scientifique plus général. Je décris pour cela mes trois objets d'étude (à savoir la glace de mer, la circulation océanique profonde, et le carbone atmosphérique), leur importance dans le système climatique, ainsi que certaines de leur interactions avec d'autres variables du climat. L'océan Austral présente un intérêt particulier dans l'étude combinée de ces trois variables, étant notamment le lieu de formation de l'AABW et un puits de carbone majeur. Les différences entre l'état moderne ou pré-industriel (PI) de ces trois variables et leur état au cours du Dernier Maximum Glaciaire (DMG, il y a 21 000 ans environ) sont relativement bien connues grâce à de nombreux enregistrements paléoclimatiques [Gersonde et al., 2005, Adkins, 2013, Bereiter et al., 2015]. Ces enregistrements témoignent d'une glace de mer australe très étendue en hiver, d'une circulation de retournement moins profonde qu'à l'actuel et d'une concentration en CO_2 atmosphérique très faible au DMG.

En revanche, les modèles paléoclimatiques tels que ceux utilisés dans le cadre du projet PMIP simulent dans les conditions du DMG une glace de mer australe, une circulation océanique profonde, et une concentration en CO_2 atmosphérique présentant des désaccords importants avec les enregistrements paléoclimatiques. En particulier, la glace de mer simulée au DMG dans l'océan Austral semble présenter à la fois des biais en terme d'étendue, d'amplitude saisonnière, et de distribution régionale [Roche et al., 2012, Goosse et al., 2013, Marzocchi and Jansen, 2017]. Dans l'Atlantique, la circulation profonde simulée par les modèles PMIP est souvent trop intense et profonde, associée à une AABW moins volumineuse du fait d'une NADW plus profonde qu'au PI, alors que les enregistrements paléoclimatiques tendent à suggérer le contraire [Otto-Bliesner et al., 2007, Muglia and Schmittner, 2015]. Enfin, la concentration en CO_2 atmosphérique en sortie des modèles intégrant le cycle du carbone au DMG est souvent très supérieure à la valeur mesurée dans les carottes de glace ($\sim$ 90 ppm), et n'explique donc pas l'amplitude de la différence avec celle du PI ($80 - 100$ ppm, Kohfeld and Ridgwell [2009]).

Plusieurs études rendent compte d'un lien physique fort entre ces trois variables [Shin et al., 2003, Ferrari et al., 2014, Marzocchi and Jansen, 2017]. Théoriquement, les biais mentionnés peuvent ainsi être liés. Toutefois, le système climatique est complexe et de nombreuses autres variables (ex. vents, mélange profond, pompe biologique) peuvent influencer celles citées. La représentation dans les modèles PMIP2 de ces trois variables est donc potentiellement limitée par différents facteurs. Certains d'entre eux seront étudiés dans le cadre de cette thèse.

Chapter 2

Methods

Chapter aims:

1. Present the Earth system model of intermediate complexity (iLOVECLIM) used in this thesis; its assets and limitations; briefly describe its components
2. Introduce two parameterizations of the ocean model whose effects are evaluated in chapters 4 and 5; their motivations and methods
3. Present the experimental design which is implemented in chapter 3 in order to run LGM simulations in the framework of the PMIP project
4. Briefly characterize the proxy data used in the following to perform model-data comparisons in terms of sea ice, SST and water mass distribution

Highlights:

↪ Despite its relatively coarse resolution, the proxy- and carbon-enabled iLOVECLIM model is fully suitable to study the large-scale deep ocean circulation and global carbon content in reservoirs at the LGM, and may pave the way for more complex and computationally expensive models.

↪ Parameterizations are needed to account for two key processes (i.e. sinking of brines, topography-enhanced mixing). Both have been implemented in the iLOVECLIM model prior to this study and are tested in chapter 4 and 5.

↪ The standardized experimental design of PMIP4 defines the LGM forcings and boundary conditions to implement in PMIP models. For the first time, modelling groups are urged to explicitely consider differing boundary conditions due to the uncertainty of ice sheet reconstructions.

In this chapter, I give an overview of the various tools (i.e. model, modelling choices, data) used in this study. The modelling results presented in chapter 3 to 6 are mainly from pre-industrial (PI) and Last Glacial Maximum (LGM) simulations. These simulations were

run with the iLOVECLIM model, though chapter 3 also includes model outputs from other PMIP-carbon models. I present here the iLOVECLIM model, in particular its ocean module called CLIO and the carbon cycle model embedded into it. The model was run under different modelling choices, of which there are 3 types: (1) forcings, (2) boundary conditions, and (3) model parameter and parameterization choices. I briefly describe the forcings and boundary conditions associated with glacial conditions, which are specified by the PMIP protocol and implemented in the model in chapter 3. I also present here two parameterizations of the ocean model which are of interest to this study. The effects of their use and of related parameter choice are explored in chapters 4 and 5. Finally, we introduce the experimental proxy data used to carry out model-data comparisons in the following chapters.

2.1 iLOVECLIM model

2.1.1 General description

The LOVECLIM model, previously known as ECBILT-CLIO, was first developed in the 90s in Louvain-la-Neuve, Belgium, in collaboration with the Royal Netherlands Meteorological Institute (KNMI) in the Netherlands. As a three-dimensional Earth system Model of Intermediate Complexity (EMIC), its spatial resolution is coarser than state-of-the-art General Circulation Models (GCMs) and the physical processes included are described in a more parametrized way. It therefore occupies a quite specific location in the spectrum of model types, "bridging the gap" between conceptual and comprehensive models [Claussen et al., 2002]. The most obvious advantage of using an EMIC lies in its computation time. The LOVECLIM model is fast enough (5000 years run in ∼54 hours) to enable long-term simulations of thousands of years or even a full glacial cycle. On the other hand, it is not suitable to study high resolution processes. Since this study mainly focuses on large-scale ocean circulation, the relatively coarse resolution of the model can be seen as an asset rather than a drawback. Indeed, it gives us the opportunity to explore various approaches with a number of equilibrated simulations (e.g. to test the impact of model parameter choices) which are unaffordable in a GCM. As a result, EMICs may be useful for "providing guidance for more detailed investigations to be undertaken by GCMs" [Claussen et al., 2002].

The low computation time of the LOVECLIM model mostly originates from the simplicity of its atmospheric component, called ECBILT, in which a land surface model is also included. As a 3-level quasi-geostrophic model on a T21 grid, the spatial resolution of ECBILT is $\sim 5.6°$ in latitude and longitude [Goosse et al., 2010]. ECBILT was first developed by Opsteegh et al. [1998] before it was coupled to the CLIO (Coupled Large-scale Ice Ocean) model [Goosse et al., 1997a,b, Goosse and Fichefet, 1999], thus becoming ECBILT-CLIO [Goosse et al., 2010]. The CLIO model itself was the product of the coupling of a comprehensive thermodynamic-dynamic sea-ice model [Fichefet and Morales Maqueda, 1997] to an ocean general circulation model [Campin, 1997, Campin and Goosse, 1999]. Shortly after, the terrestrial biosphere model VECODE joined ECBILT-CLIO [Brovkin et al., 2002a]. This vegetation model is also quite simple, as it simulates the evolution of only two plant functional types (tree and grass), in addition to desert. The components of the LOVECLIM model are detailed by Goosse et al. [2010], who also evaluated the model performance under different climate states and specifically

underlined important biases at low latitudes. Since sea ice and convection processes occur at high latitudes, these biases may not be too consequential in the context of this study.

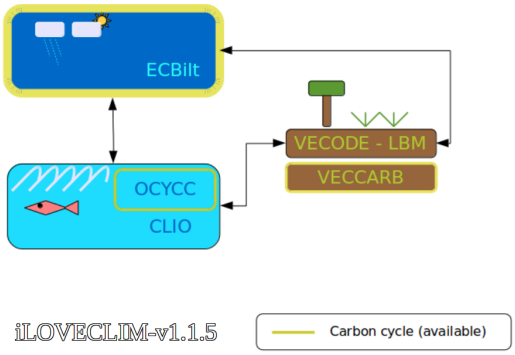

Figure 2.1: Model version used in this study: Atmosphere-Ocean-Vegetation base components, with the carbon cycle included (figure from Roche, pers. com.)

The iLOVECLIM model is at its core composed by the same components as its parent model LOVECLIM, but has significantly diverged from it over time. Notable model developments include the implementation of an ocean carbon cycle model [Bouttes et al., 2015], a permafrost module [Kitover et al., 2019] and an ice sheet model [Roche et al., 2014], the reimplementation of the iceberg model [Bügelmayer et al., 2015] and the inclusion of a dynamical downscaling of temperature and precipitation fields [Quiquet et al., 2018]. In addition, a more complex vegetation model than VECODE, called CARAIB, can now be coupled to iLOVECLIM [Extier, 2019]. Substantial efforts have also been made into forward modelling, with the inclusion of oxygen isotopes [Roche, 2013, Roche and Caley, 2013, Caley and Roche, 2013], carbon isotopes [Bouttes et al., 2015] and Pa/Th ratio [Missiaen et al., 2020a]. Although these features are not all activated in the simulations run in this study (see Fig. 2.1), they illustrate the potential of this model as a tool to study paleoclimates as well as the relevance of undertaking further developments (see Sect. 1 of chapter 3).

On a practical level, the iLOVECLIM model is developed and run by a small but active team based at either *Laboratoire des Sciences du Climat et de l'Environnement* or *Vrije Universiteit Amsterdam*. Its documentation is freely accessible at `http://forge.ipsl.jussieu.fr/ludus/wiki/` and its Fortran code is collaboratively shared and updated thanks to the Subversion software. Substantial changes to the code have been made since the beginning of this thesis, with more than 500 revisions in less than 3 years. While part of this model evolution has been crucial to this study, limitations (with respect to multiproxy model-data comparison in particular) have also arisen, with:

- The discovery of an unsolved bug related to oxygen isotopes. As a result, I could not run simulations with both the carbon cycle and oxygen isotopes throughout most of this thesis (or, for that matter, with the FAME module simulating planktonic foraminifers of Roche et al. [2018]).
- The emergence of significant differences between model versions, after revisions influencing the global mean surface air temperature, marine productivity, etc. These differences entailed a retuning of the carbon cycle in PI conditions before re-running LGM simula-

tions. As a result, I actually ran and used in this study two batches of LGM simulations, which I call v1 and v2 for simplicity. However, on account of the abnormally long equilibration time of radiocarbon ($\sim 30,000$ years), the PI restart of my second batch of LGM simulations was not fully equilibrated in terms of ^{14}C because of time limitations. For that reason, I did not carry out model-data comparisons of $\Delta^{14}C$ and reservoir time as planned.

- The absence of particulate fields ($CaCO_3$, particulate organic carbon and biogenic silica) corresponding to LGM conditions. The iLOVECLIM model does not explicitely simulate the opal cycle and therefore has to rely on prescribed particle concentration fields to compute the Pa/Th ratio. In Missiaen et al. [2020a], the authors prescribed the fields simulated by the PISCES-NEMO model under its PI state. Since this model had not run under LGM conditions at the time of my simulations, I had no LGM particulate fields to prescribe. I still ran some of my LGM simulations (v1) with the PI particulate fields, but the significant effects of particle concentrations [Missiaen et al., 2020b] challenge the validity of model-data comparisons using the Pa/Th ratio.

2.1.2 Ocean model: CLIO

The CLIO model is an ocean general circulation model which solves the primitive equations with classical approximations [Campin, 1997]. Its horizontal discretization is on a B-grid in the classification of Arakawa [Mesinger and Arakawa, 1976], with a resolution of $3° \times 3°$ in latitude and longitude. This means that tracer and velocity fields are staggered by 1.5° [Goosse et al., 2010], a fact which has to be taken into consideration when generating land-sea masks (see Sect. 3.1). Actually, two spherical grids are associated to form the CLIO grid in order to avoid the North-Pole singularity. While the first one has classical coordinates, the second one is rotated and encompasses both the North Atlantic and Arctic ocean. The two grids are connected in the equatorial Atlantic. As a result, the Pacific and Arctic oceans are not directly connected: the transport across the Bering Strait is parameterized [Goosse et al., 1997a]. As for the vertical discretization, CLIO is a z-coordinate model, with 20 irregular vertical levels. While the top vertical level is 5 m deep and 10 m wide, the bottom grid cells are much larger (close to 750 m) when reaching a depth as high as 5000 m. This has consequences for the ocean volume considerations made in Lhardy et al. [2021a] (see Sect. 3.2 and Fig. S2).

Because of its relatively coarse resolution, the CLIO model has to rely on parameterizations to represent vertical mixing [Goosse and Fichefet, 1999], the eddy-induced advection term Gent and McWilliams [1990], or the downsloping currents originated from dense shelf water overflows [Campin and Goosse, 1999], among others. Some of these parameterizations will be further addressed in this chapter.

As mentioned before, a thermodynamic-dynamic sea-ice model [Fichefet and Morales Maqueda, 1997] is embedded into CLIO. Described in Goosse et al. [2010], this model simulates on the same horizontal grid a sea ice of uniform thickness, with visco-plastic rheology. These characteristics are quite unsophisticated but remain similar to a number of models also used in PMIP [Goosse et al., 2013].

2.1.3 Carbon cycle in iLOVECLIM

A carbon cycle module has been fully implemented in iLOVECLIM in Bouttes et al. [2015]. In fact, the vegetation model VECODE [Brovkin et al., 1997] already computed the terrestrial biosphere carbon content in four plant compartments (leaf, wood, litter and soil), but the authors further included the carbon isotopes, and an ocean carbon cycle model already in use in the CLIMBER-2 model [Brovkin et al., 2002a,b, 2007].

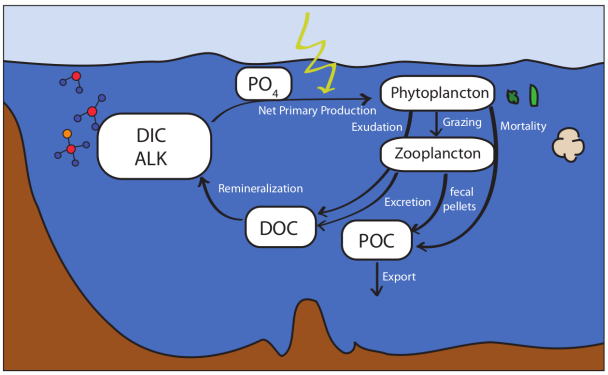

Figure 2.2: The ocean carbon cycle in iLOVECLIM (schematic from Bouttes et al. [2015])

Based on a NPZD ecosystem model [Six and Maier-Reimer, 1996], this ocean module enables the computation of nutrients (phosphate and nitrate), alkalinity, O_2, Dissolved Inorganic Carbon (DIC), carbon isotopes (^{13}C and ^{14}C) as well as six variables which are part of the organic carbon pool: Dissolved Organic Carbon (DOC), slow DOC, particulate organic carbon, $CaCO_3$, phytoplankton and zooplankton (see Fig. 2.2). As a result, thirteen tracers are transported via the advection-diffusion scheme of iLOVECLIM when the carbon cycle is activated, which significantly increases the computation time (5000 years run in ∼184 hours). To this day, sedimentary processes are however not included, with the coupling to a sediment model being ongoing work.

Bouttes et al. [2015] have also validated the simulated carbon cycle against observational data and reported a good agreement with modern observations for both the surface and the ocean interior, though the Atlantic distribution of some variables such as alkalinity tends to be poorer than other models.

2.2 Parameterizations of interest

Parameterizations in models are meant to account for processes which are not explicitly computed in the dynamical core [Goosse, 2015], typically because they occur on a subgrid level. I present here two parameterizations recently included in the iLOVECLIM model, which are of interest to the present study. Indeed, the brine release and sinking process is crucial to account for the influence of sea-ice formation on deep water formation and properties [Shin et al., 2003, Marzocchi and Jansen, 2017, Klockmann et al., 2016]. The effects of a parameterized sinking of brines are described in chapter 4. Studies have also underlined the importance of vertical diffusivity to AABW characteristics, such as its volume and formation rate [De Boer and Hogg, 2014], isolation and carbon content [Ferrari et al., 2014]. Various vertical diffusivity parameterizations (e.g. including tidal mixing) are tested in chapter 5.

2.2.1 Sinking of brines

Paleotracer data tend to indicate a glacial ocean with an enhanced and salt-driven stratification [Adkins, 2013, Homola et al., accepted, 2021]. Rare pore-fluid measurements evidenced colder and saltier deep waters, in particular in the Southern Ocean [Adkins et al., 2002]. Modelling studies also underlined the importance of haline density fluxes originated in the Southern Ocean in setting the glacial deep ocean circulation [Shin et al., 2003]. In this context, an accurate representation of the brine sinking process in models seems crucial. The sinking of brines occurs when and where sea ice forms, so mostly in leads or areas of thin sea-ice cover, such as around the Antarctic coast where strong catabatic winds blow away the newly formed ice. As sea ice is mostly composed of freshwater, salt tends to get rejected into the surrounding waters, along with other ions. Enriched in salt, these surface waters can form dense plumes sinking down to the ocean floor.

Since model resolution is generally insufficient to resolve this very local process, both GCMs and EMICs have to rely on parameterizations to account for its effect. Indeed, the rejected salt tends to get diluted in the surface grid cells where sea ice is forming. Due to the dimensions of these grid cells ($3° \times 3° \times 10$ m in iLOVECLIM), the consequent salinity increase of surface waters may either not be enough to entail deep water formation, or lead to large-scale convection rather than localized salt plumes. To account for the effect of brine sinking in the Southern Ocean on glacial stratification, Bouttes et al. [2010] parameterized a simple brine sinking mechanism in the CLIMBER-2 model. They evaluated the simulated $\delta^{13}C$ distribution in the Atlantic and deep ocean salinity, and showed an improved agreement with reconstructions from sediment cores with it, as well as a substantial drop of atmospheric CO_2 concentration (-52 ppm at most). The effect of this parameterization on atmospheric CO_2 and $\delta^{13}C$ was also tested in combination with other modelling choices (with respect to iron fertilization or stratification-dependent diffusion) in the CLIMBER-2 model [Bouttes et al., 2011], demonstrating notably that low glacial CO_2 levels ($\sim$ 190 ppm) can be simulated when combining these three mechanisms.

The brine sinking parameterization described in Bouttes et al. [2010] has been coded into the iLOVECLIM model, using the same simple formulation to account for a transfer of salt from the surface to the bottom level in the Southern Ocean. As explained in Lhardy et al. [2021b] (chapter 4):

> This parameterization allows for a fraction of the salt content of the surface grid cell to be transferred to the deepest grid cell underneath the location of sea-ice formation. As a result, the salinity and density of the bottom cells increase while the salinity and density of the surface grid cells decrease, without congruent motion of water masses. The modification of the salinity depends on the rate of sea-ice formation, as well as the chosen fraction parameter. [...] This simple parameterization is relatively different than a downsloping current one as it is not confined to the continental slope and does not create mixing along the way of the sinking brines. While "this brine mechanism is idealized, it reflects the impact of intense Antarctic sea-ice formation during the LGM" [Bouttes et al., 2010] on the AABW density.

However with such a formulation, the brine mechanism does not depend on the water depth. In contrast, Paillard and Parrenin [2004] argued that brine rejection is favored above continental shelves, but hindered by a strong negative feedback in open ocean areas. The authors suggest that this difference may be critical during glacial terminations, when the continental shelves are made smaller by the large Antarctic ice sheet.

This parameterization is illustrated in Fig. 2.3. The $frac$ parameter can be varied from 0 (standard model version) to 1 (none of the rejected salt is diluted, all is transferred to the bottom ocean), but Bouttes et al. [2010] showed that intermediate values (around 0.5) represent the most plausible parameter choices.

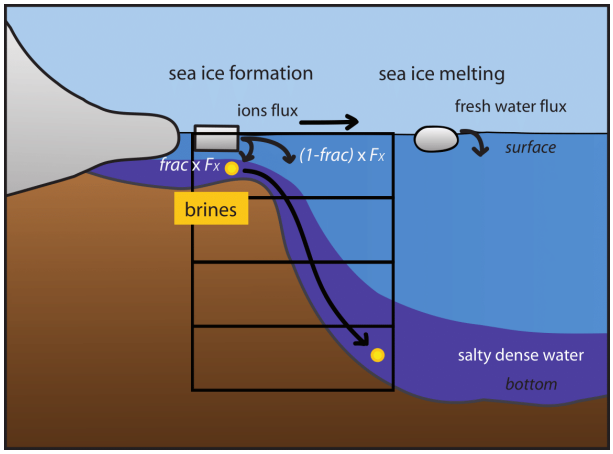

Figure 2.3: Brine sinking mechanism (schematic from Bouttes et al. [2010]). F_X represents the flux of salt, and the parameter $frac$ is the fraction of surface salt content being transferred to the deepest grid cells.

Usually tested in the Southern Ocean under LGM conditions (see chapter 4), this parameterization usually allows for both a transfer of salt and of other biogeochemical variables (DIC, DOC, alkalinity, nutrients, oxygen, ^{13}C and ^{14}C) to the bottom ocean, though their effects have been decomposed and analyzed in Bouttes et al. [2010]. The same $frac$ is used, and the same enrichment is assumed when these biogeochemical variables are rejected into the surface waters as a consequence of sea-ice formation.

2.2.2 Tidal mixing and geothermal fluxes

In ocean models, vertical mixing is a key mechanism with a notable influence on the large-scale circulation and heat transport. Vertical mixing processes include mainly a wind-driven mixing in the thermocline and a tidal-driven mixing below, and are more or less explicitely computed or parameterized depending on the model resolution. The processes which cannot be resolved are represented by a background diffusivity. Typically for most paleoclimate models [De Boer and Hogg, 2014], the background diffusivity is imposed with a fixed vertical profile, such as the one used by Bryan and Lewis [1979]. This is the case of the CLIO model, whose vertical diffusivity (see Fig. 2.4) is adapted from the Bryan and Lewis [1979] profile below

-150 m [Goosse et al., 2000, 1999]. Following a tangent function, the vertical diffusivity is low (10^{-5} $m^2.s^{-1}$) in the upper layers of the ocean and high (10^{-4} $m^2.s^{-1}$) at depth, with a rather sharp increase at mid-depths ($\sim$ 2500 m). As a result, the vertical diffusivity in the deep ocean (>3000 m) is almost constant.

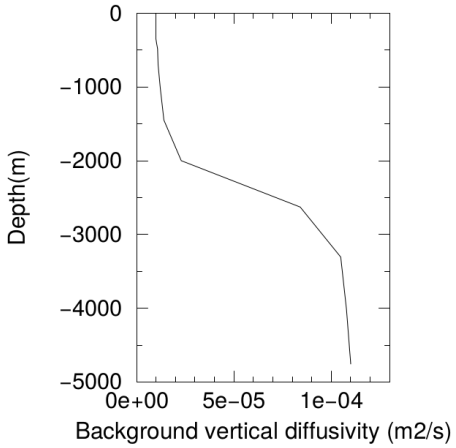

Figure 2.4: Vertical profile of the background diffusivity in the CLIO model (figure from Goosse et al. [2000])

The effects of the mixing scheme choice on climate, circulation and water mass characteristics have been investigated at the present-day with a diversity of models [Hieronymus et al., 2019, Heuzé et al., 2015, Friedrich et al., 2011]. However, such studies are rather less frequent at the LGM. Bouttes et al. [2011] have run multiple LGM simulations with a stratification-dependent vertical diffusivity profile imposed in the CLIMBER-2 model. They notably quantified the effects of the associated model parameter choice on the simulated CO_2 and $\delta^{13}C$. Nonetheless, studies focussing on the impact of vertical mixing at the LGM seem especially relevant as most models struggle to simulate a deep ocean circulation in good agreement with paleotracer data [Otto-Bliesner et al., 2007, Weber et al., 2007, Marzocchi and Jansen, 2017]. Indeed, De Boer and Hogg [2014] have suggested that eight out of nine PMIP2 models are unable to simulate a weaker yet more voluminous bottom water cell because of their vertical diffusivity parameterization, which did not decrease linearly away from the bottom.

In this context, we have collaborated with Casimir de Lavergne in order to test in the iLOVECLIM model the effects of a more complex vertical mixing parameterization than a uniform diffusivity profile. de Lavergne et al. [2020] have indeed produced 3D maps of the mixing induced by the breaking of internal tides. These maps can be used to implement an energy-constrained tidal mixing parameterization in models, which takes into account local dissipation resulting from the sloping or rough topography. In addition, such an approach has the advantage of abiding by energy conservation, which is not the case of a constant vertical diffusivity.

Using this approach, four static 2D maps of de Lavergne et al. [2020], which represent different source terms of energy dissipation (see Fig. 2.5), have been interpolated on the CLIO grid along with their corresponding vertical structure. To complete the picture, the energy injected from geothermal heat fluxes can now also be taken into account (Fig. 2.6).

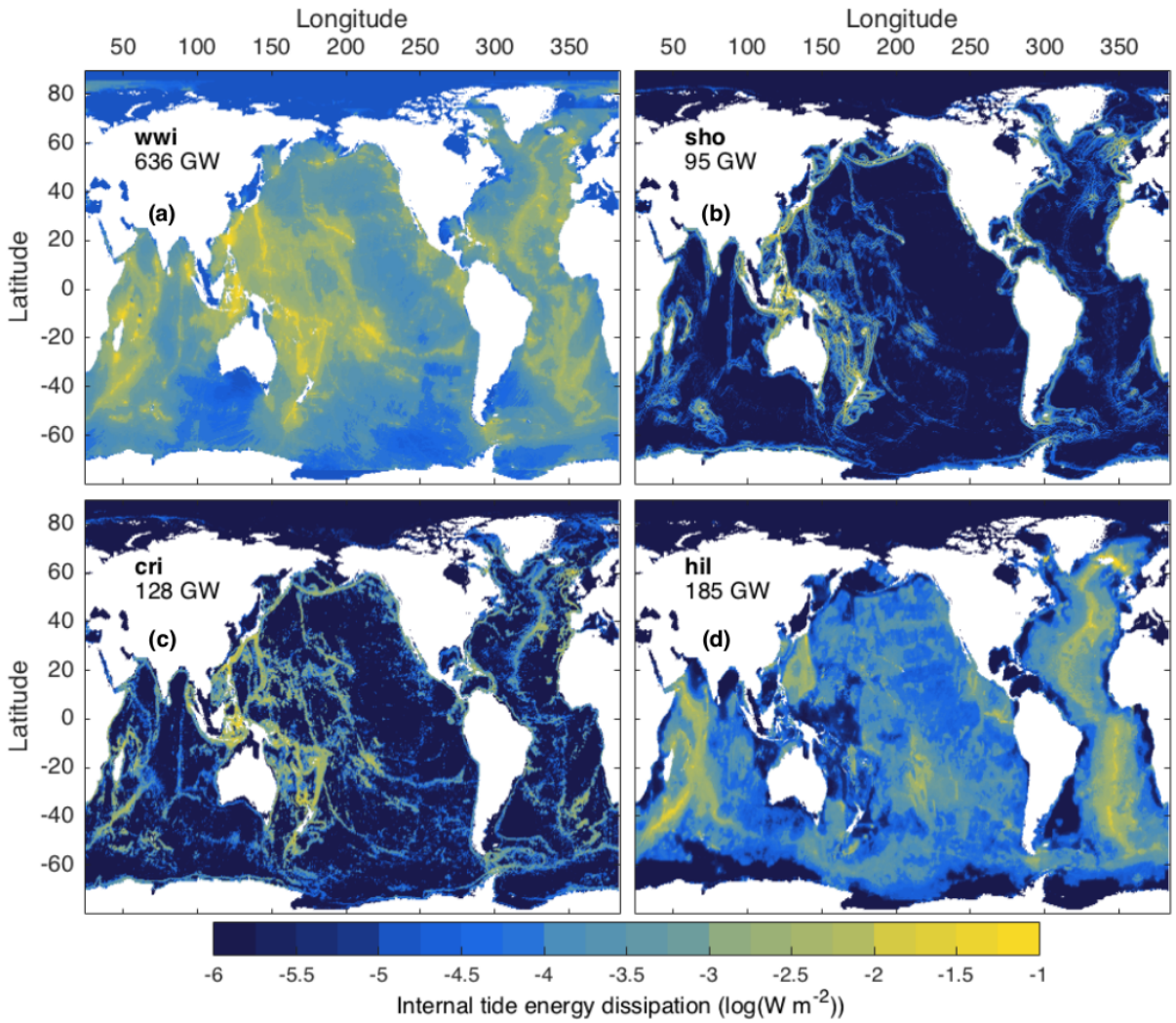

Figure 2.5: The four 2D maps accounting for the dissipation of tidal energy by wave-wave interactions (*wwi*), breaking through shoaling (*sho*), critical slopes (*cri*), or scattering at abyssal hills (*hil*) (figure from de Lavergne et al. [2020])

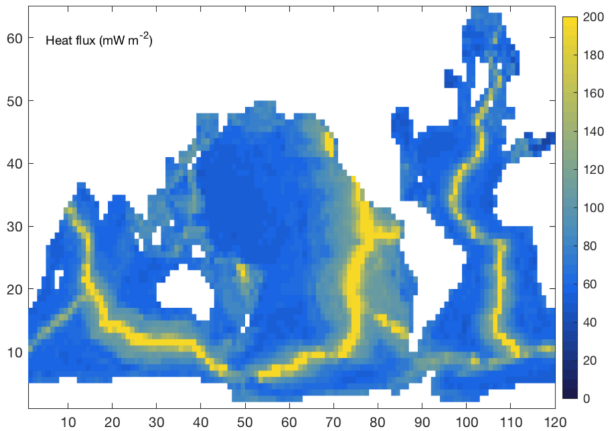

Figure 2.6: Geothermal heat fluxes from Lucazeau [2019], regridded on the CLIO grid (figure from de Lavergne, pers. com). The Arctic ocean is deformed due to the rotated CLIO grid.

This tidal mixing parameterization is already implemented in a GCM of much higher resolution (i.e. IPSL model), in a model version which is not used for paleoapplications. Therefore, this implementation into the iLOVECLIM model may allow for an assessment of its effect under a coarser resolution, but also at the LGM. However, we note that the four maps used in this parameterization have been generated using the present-day sea level. A low sea level of around -130 m will affect to some extent the energy dissipation terms. Both Schmittner et al. [2015] and Wilmes et al. [2019] have estimated that tidal energy dissipation in the deep ocean was strongly enhanced during the LGM, resulting in an increased vertical diffusivity and a strengthened and deepened AMOC, in contrast with the common view inferred from the majority of paleotracer data. Nonetheless, using this parameterization in a glacial setting remains an interesting sensitivity test.

2.3 PMIP experimental design

The Paleoclimate Modelling Intercomparison Project (PMIP) represents a coordinated effort in paleoclimate modelling which has been going on for more than 20 years. This project is phased with the Coupled Model Intercomparison Project (CMIP, e.g. PMIP3-CMIP5, PMIP4-CMIP6) endorsed by the World Climate Research Program (WCRP) and iterated with each assessment report of the IPCC. The PMIP project has now entered its fourth phase [Kageyama et al., 2018]. Enriched by the experiences of previous phases (PMIP1: Joussaume and Taylor [1995]; PMIP2: Braconnot et al. [2007]; PMIP3: Braconnot et al. [2012]), it has grown along:

- the complexity of Earth System Models (ESMs), with the inclusion of the dynamical representation of ocean, sea ice, land surface, vegetation, carbon cycle...
- the targeted scientific questions [Kageyama et al., 2017]
- the number of target periods (five in PMIP4-CMIP6: *lgm*, *midHolocene*, *past1000*, *lig127k* and *midPliocene-eoi400*), in addition to those of specific working groups (e.g. *deglaciation*) [Kageyama et al., 2018]
- the explicit consideration of uncertainties in boundary conditions, with Kageyama et al. [2017] notably advising modelling groups to choose from three different ice sheet reconstructions and calling for studies testing this impact at the LGM.

The LGM, defined at $\sim$ 21 ka, has been one of the benchmark periods of PMIP since its inception. Its study is motivated by the fact that the LGM climate is well-documented, yet radically different from the present-day climate. Indeed, it is characterized by low greenhouse gases concentrations, a maximal continental ice extent, and a consequent low sea level [Lambeck et al., 2014]. These characteristics influence both the atmospheric and oceanic circulations, the radiative budget and vegetation, involving different feedback effects. As such, the LGM is a good target period to evaluate the performance of models (which are typically *not* tuned to produce better paleoclimates), as well as investigate the model-dependent response to forcings. With this dual purpose, modelling studies at the LGM may actually address two of the scientific questions of CMIP6 defined in Eyring et al. [2016]: "What are the origins and consequences of systematic model biases?" and "How does the Earth System respond to forcing?" [Kageyama et al., 2017]. In addition, studies of the LGM are insightful in the context of climate change,

with the PI − LGM global mean temperature difference being of the same amplitude as projected changes at the end of the century. Recent studies specifically underline the relevance of using paleoclimate modelling to constrain climate sensitivity or future climate projections [Schmidt et al., 2014, Bracegirdle et al., 2019, Sherwood et al., 2020].

2.3.1 Description of the PMIP4 protocol

In the framework of PMIP4, Kageyama et al. [2017] provide practical guidelines on how to run LGM simulations to motivated modelling groups (see Table 2.1).

Table 2.1: Summary of model forcings and boundary conditions recommended by the PMIP4 protocol for LGM simulations (adapted from Kageyama et al. [2017] and Ivanovic et al. [2016])

Forcings	Variable	LGM value	References
Trace gases	Carbon dioxide (CO_2)	190 ppm	Bereiter et al. [2015]
	Methane (CH_4)	375 ppb	Loulergue et al. [2008]
	Nitrous oxide (N_2O)	200 ppb	Schilt et al. [2010]
	Methane (CFC)	0	
	Ozone (O_3)	PI (10 DU)	
Insolation	Eccentricity	0.018994	Berger [1978]
	Obliquity	22.949°	"
	Perihelion - 180°	114.42°	"
	Vernal equinox	Noon, 21 March	"
	Solar constant	PI (1361.0 ± 0.5 W.m^{-2})	Matthes et al. [2017]
Ice sheets	Ice sheet extent	ICE-6G-C, GLAC-1D, or PMIP3	ICE-6G-C: Peltier et al. [2015], Argus et al. [2014]
	Orography	"	GLAC-1D: Ivanovic et al. [2016]
	Coastlines	"	PMIP3: Abe-Ouchi et al. [2015]
	Bathymetry	"	
	Global salinity	+1 psu from PI	

The authors define a standardized experimental design in order to enable subsequent multimodel comparison studies. To simulate the LGM climate, modelling groups following this PMIP4 protocol are required to implement the same forcings (e.g. greenhouse gas concentrations, orbital parameters) and the boundary conditions (e.g. orography, continental ice extent, coastlines and bathymetry) associated with one of the three proposed ice sheet reconstructions (namely PMIP3, ICE-6G-C and GLAC-1D). The greenhouse gas concentrations of this recent paleoclimate are relatively well constrained thanks to ice core measurements. Due to their cyclicity, the orbital parameters of the LGM are also well-known and the resulting insolation is not vastly different from the present-day (which is not the case of other target periods of PMIP, such as the *midHolocene* or *lig127k* experiments). This is convenient, as modelling groups do not have to redefine the seasons of the calendar during analysis. However, the uncertainties of ice sheet reconstructions are high, as they stem from different reconstruction approaches [Ivanovic et al., 2016]. Indeed, the boundary conditions associated with the three proposed ice sheet reconstructions show significant differences, in particular in the elevation of the Laurentide and Fennoscandian ice sheets (see Fig. 2.7). The GLAC-1D ice sheet reconstruction for example displays a lower altitude than the other two, and is consequently associated with a higher sea level due to the ice volume trapped on land. As a result, small differences in the

observed coastlines (aka "land-sea mask") and bathymetry are also emerging, though some of them are simply due to the grid resolution on which these boundary conditions are provided.

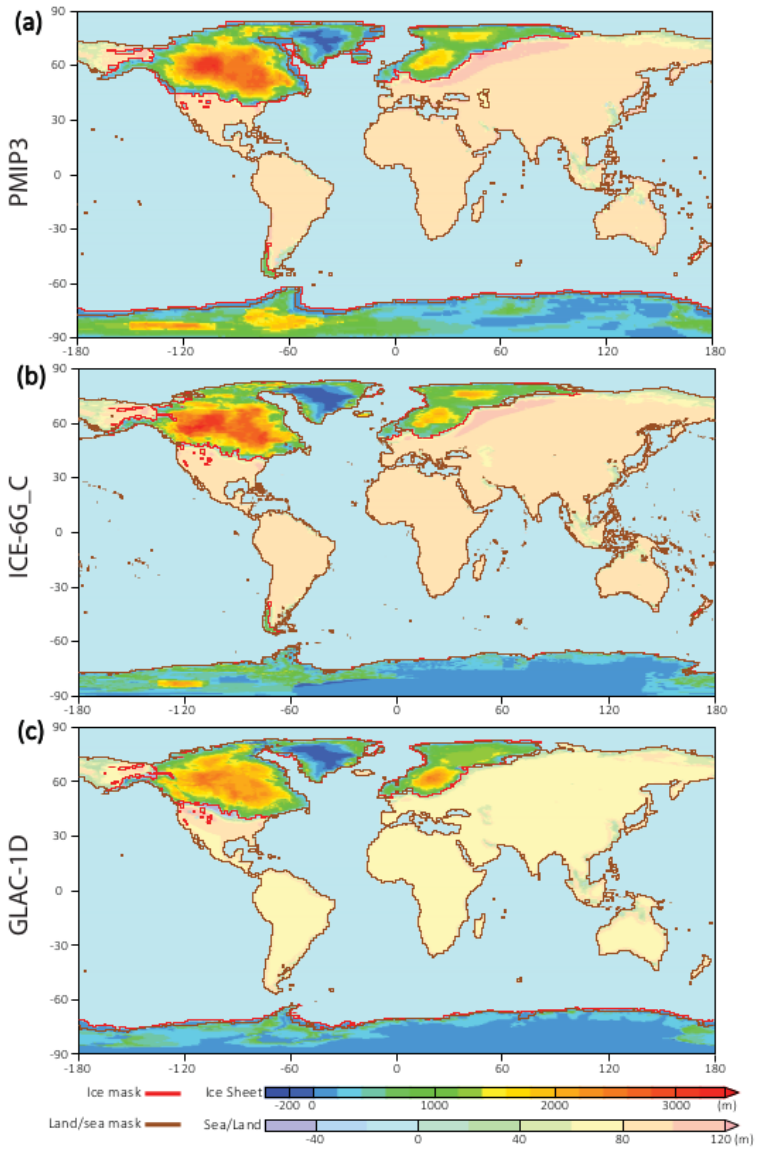

Figure 2.7: Elevation anomalies, continental ice extent and coastlines associated with the three proposed ice sheet reconstructions: (a) PMIP3, (b) ICE-6G-C and (c) GLAC-1D (figure from Kageyama et al. [2017])

Since these boundary conditions are interpolated on model grids of varying resolutions, Kageyama et al. [2017] also provide recommendations on how to implement the LGM orography, bathymetry, land-sea mask and ice mask within the climate model. In order to ensure consistency with the deglaciation protocol [Ivanovic et al., 2016], modelling groups are advised to apply the LGM orography and bathymetry as an anomaly added to those of the PI. The authors also underline that specific adjustments in straits and key passages are often required:

> "There are two options for implementing the changes in bathymetry. The first option is to use the bathymetry anomalies obtained from step 0 directly and add them to the bathymetry used for the *piControl* simulations. However, given that the resolution of the ocean models often decreases with depth, this may not be necessary, and a simpler option is to modify the present-day bathymetry by subtracting the mean sea-level drop corresponding to the chosen ice-sheet reconstruction. In this second option, special treatment will be required for straits that are crucial for the ocean circulation and for which the change in bathymetry is significantly different from the mean sea-level drop. The Denmark and Davis straits and the Iceland–Faeroe Rise, for example, must be treated with care, as these are often locations at which the bathymetry for *piControl* is also adjusted to obtain realistic oceanic currents."

The definition of this standardized experimental design is useful to carry out intercomparison studies and explore the intermodel spread and model-data discrepancies in a coherent framework. Significant improvements have been made with the different phases of the PMIP project, but important model biases also remain [Braconnot et al., 2012, Kageyama et al., 2021], for example in terms of the simulated deep ocean circulation [Otto-Bliesner et al., 2007, Marzocchi and Jansen, 2017]. This project is also not freed from limitations, especially as it concerns a relatively small number of models [Bracegirdle et al., 2019] which share some degree of interdependence [Knutti et al., 2015].

2.3.2 Specifications for the PMIP-carbon project

The PMIP-carbon project is a new initiative which is related to the deglaciation working group of PMIP and coordinated by Nathaëlle Bouttes. As more and more PMIP models are now carbon-enabled, the objective of this ongoing project is to conduct the first multimodel comparison of coupled climate-carbon simulations, starting at the LGM.

A protocol was defined and participating modelling groups were requested to perform an equilibrated PI and LGM experiments with no change of code in between. The simulations were typically run with an atmospheric CO_2 concentration which is prescribed (at 190 ppm for the LGM and 280 ppm for the PI) in the radiative code, but freely-evolving − if possible − in the carbon cycle. Running such experiments, with two separate CO_2 variables (as opposed to a fully interactive run), is a common modelling choice in paleoclimate modelling as models are struggling to simulate the pCO_2 drawdown. Modelling groups were also asked to follow the PMIP4 protocol or an experimental design as close to PMIP4 as possible, with modified greenhouse gases concentrations, orbital parameters, and ice sheets. Since the priority was to collect many model outputs, the established protocol was deliberately not very restrictive and model outputs which were not fully conformed to PMIP4 experimental design were also accepted.

Thanks to that, we managed to collect outputs (climate, carbon, and fixed fields) from eight models, either GCMs or EMICs (MIROC4m-COCO, CESM, IPSL-CM5A2, MIROC-ES2L, CLIMBER-2, iLOVECLIM, LOVECLIM, UVic). Additional outputs from the MPI, Bern3D-LPX, and NorESM-OC models can also be expected. However, the effects of this choice of protocol have to be seriously considered, as pointed out by Ivanovic et al. [2016]:

> "Many palaeoclimate model intercomparison projects have been designed to facilitate the robust comparison of results from the same "experiment" (i.e. simulation set) across a range of different models, usually taking a prescriptive approach to model set-up to ensure that any differences observed in the results are attributable to differences in model structure and not to differences in chosen "boundary conditions" and climate forcings."

In particular, the effects of the modelling choices associated with a change of ocean boundary conditions (e.g. bathymetry and coastlines) are assessed in Lhardy et al. [2021a] (see chapter 3). These modelling choices concern either:

- the implementation of the bathymetry and land-sea mask, described in the previous section, which can impact the ocean volume along with the model resolution
- the related adjustments of biogeochemical variables (DIC, alkalinity, nutrients), which are recommended in Kageyama et al. [2017] as follows: "The global amount of dissolved inorganic carbon, alkalinity, and nutrients should be initially adjusted to account for the change in ocean volume. This can be done by multiplying their initial value by the relative change in global ocean volume."

2.4 Experimental proxy data

In a few decades of research, the use of proxy data has considerably expanded our knowledge of the past climate variations, way past the short period of direct observations. In particular, our knowledge of the Southern Ocean sea-ice cover, deep ocean circulation, and CO_2 concentration at the LGM was established by well-documented proxy-based reconstructions (see chapter 1). From a paleoclimate modelling point of view, this type of data is extremely valuable to evaluate model biases. I briefly present here the Southern Ocean sea ice, SST, and $\delta^{13}C$ compilations of proxy data which are used in the following chapters to perform several model-data comparisons. Robust datation and calibration methods have been used in these published marine core records to constrain the LGM values.

2.4.1 Southern Ocean sea-ice proxy data compilation

Past sea-ice variations in the Southern Ocean can be inferred from diatom assemblages found in the sediments. This phototrophic algae is widely distributed in the Southern Ocean, and some of its taxa reflects a sea-ice presence [Gersonde and Zielinski, 2000]. We use in Lhardy et al. [2021b] a compilation of Southern Ocean sea ice proxy data recently updated by Xavier Crosta. It is based on the work from Gersonde et al. [2005], to which the experimental data of several studies [Allen et al., 2011, Ferry et al., 2015, Benz et al., 2016, Xiao et al., 2016, Nair et al., 2019] are also added. This compilation include three types of proxies:

- a quantitative proxy of yearly sea-ice duration [Crosta et al., 2004]
- a quantitative proxy of the winter (September) or summer (February) sea-ice concentration [Esper and Gersonde, 2014]

- a qualitative proxy of sea-ice presence, based on the relative abundance of sea-ice linked diatoms *Fragilariopsis curta* and *F. cylindrus* (in winter) and *F. obliquecostata* (in summer) [Gersonde and Zielinski, 2000].

Quantitative estimates rely on diatom-based transfer functions, using the modern analog technique [Crosta et al., 2004, Esper and Gersonde, 2014]. As the three proxies are not always in agreement, we have built an integrated index indicating how certain the sea-ice presence is. This index is shown in Fig. 2.8, and ranges from 0 to 3 in winter and 0 to 2 in summer, depending on the number of qualitative or quantitative proxy value above the error of the calibration step [Gersonde and Zielinski, 2000, Crosta et al., 2004, Esper and Gersonde, 2014].

Summer and winter sea-ice contours have also been drawn, locating the likely delimitation of sea-ice presence when considering all marine core data. However, proxy data in key regions are too scarce in summer to robustly constrain the summer sea-ice edge.

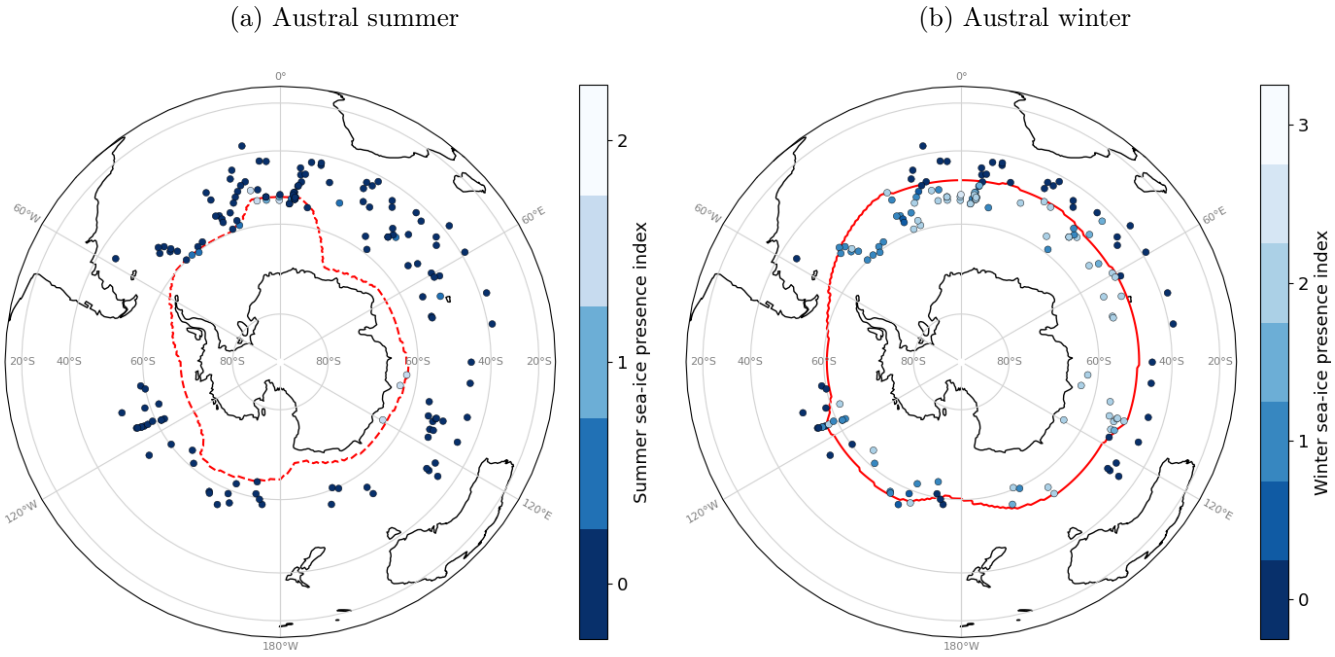

Figure 2.8: Austral summer (a) and winter (b) sea-ice lines inferred from the proxy data compilation. The summer sea-ice contour is represented by a dashed red line as it is not well-constrained. The sea-ice presence suggested by marine core data is represented as an arbitrary index on a blue to white scale, where blue denotes no indication of sea ice in proxies, and white denotes agreement of several proxies on the presence of sea ice.

2.4.2 SST proxy data from MARGO Project Members [2009]

Global sea-surface temperature reconstructions at the LGM (23−19 ka) have been developed since the 70s/80s, with the CLIMAP project (Climate Long-Range Investigation, Mapping and Prediction). Following this first initiative, the Multiproxy Approach for the Reconstruction of the Glacial Ocean Surface (MARGO) provided a widely used synthesis of SSTs (at 10 m depth) at the LGM [MARGO Project Members, 2009]. This reconstruction combines 696 individual

records, using either geochemical palaeothermometers (alkenones, foraminifera Mg/Ca ratio) or transfer functions based on microfossils (planktonic foraminifera, diatom, dinocysts, and radialoria). In contrast, Tierney et al. [2020] relies on a more recent compilation (956 individual SST records) of geochemical proxies only (alkenones, foraminifera Mg/Ca ratio, $\delta^{18}O$ and TEX_{86}), excluding marine assemblage data with the argument that: "Although including marine assemblage data would improve spatial coverage, the outstanding no-analogue problems and lack of comparable Bayesian models prevent us from using these data in the framework presented here." As such a choice would exclude most of the Southern Ocean data points, a region of interest in this study, I chose to use the SST reconstruction from MARGO Project Members [2009].

The MARGO proxy records are associated with diverse regional and seasonal distribution (Fig. 2.9), but combined in a final regridded product (Fig. 2.10) by averaging all seasonal proxy data falling into the same $5° \times 5°$ cell, weighted by a reliability index [MARGO Project Members, 2009]. Still, this procedure results in a patchy coverage, with a good amount of data in the Southern Ocean (in austral summer), in the tropics and in the North Atlantic.

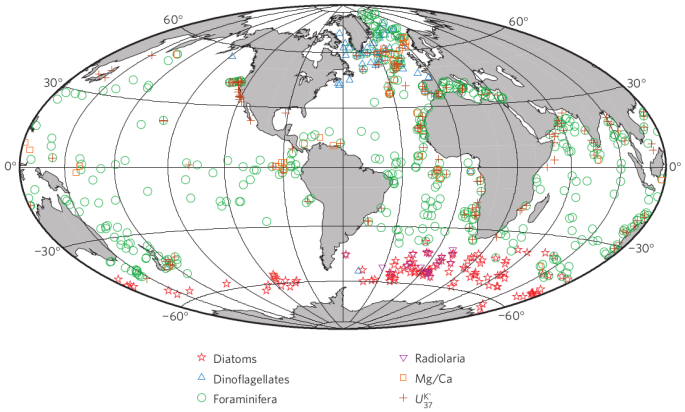

Figure 2.9: Distribution of SST proxy data points (figure from MARGO Project Members [2009])

(a) Austral summer

(b) Austral winter

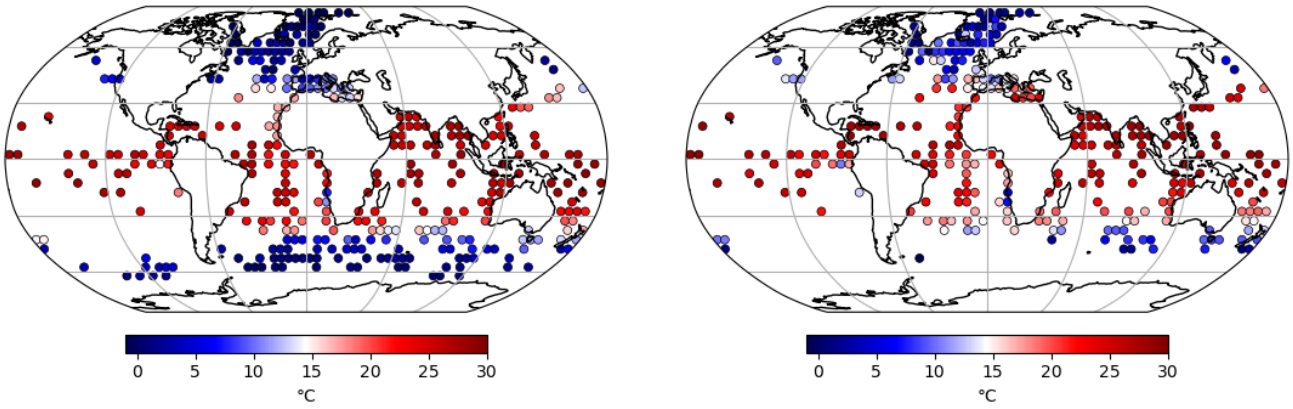

Figure 2.10: Austral summer (a) and winter (b) SST data from the regridded product of MARGO Project Members [2009]

2.4.3 δ^{13}C proxy data from Peterson et al. [2014]

As explained in chapter 1, δ^{13}C represents a useful paleotracer to constrain the water mass distribution in models. I use in the course of the next chapters a compilation of benthic foraminiferal δ^{13}C data [Peterson et al., 2014]. This compilation is based on 480 marine core measurements of late Holocene and LGM δ^{13}C using *Cibicidoides species*, which are epibenthic foraminiferas (i.e. living at the sediment-water interface) known to reflect the δ^{13}C signature of the DIC of surrounding water [Mackensen et al., 1993]. However, I note that Gottschalk et al. [2016] have recently observed significant offsets in *Cibicides kullenbergi* and *Cibicides wuellerstorfi* δ^{13}C, with possible implications for the interpretation very light values in the South Atlantic at the LGM (see Fig. 2.11b).

This compilation shows a relatively good coverage in the Atlantic Ocean, though data tend to be scarce in large areas of the ocean interiors, where sediment rates or carbonate preservation are insufficient.

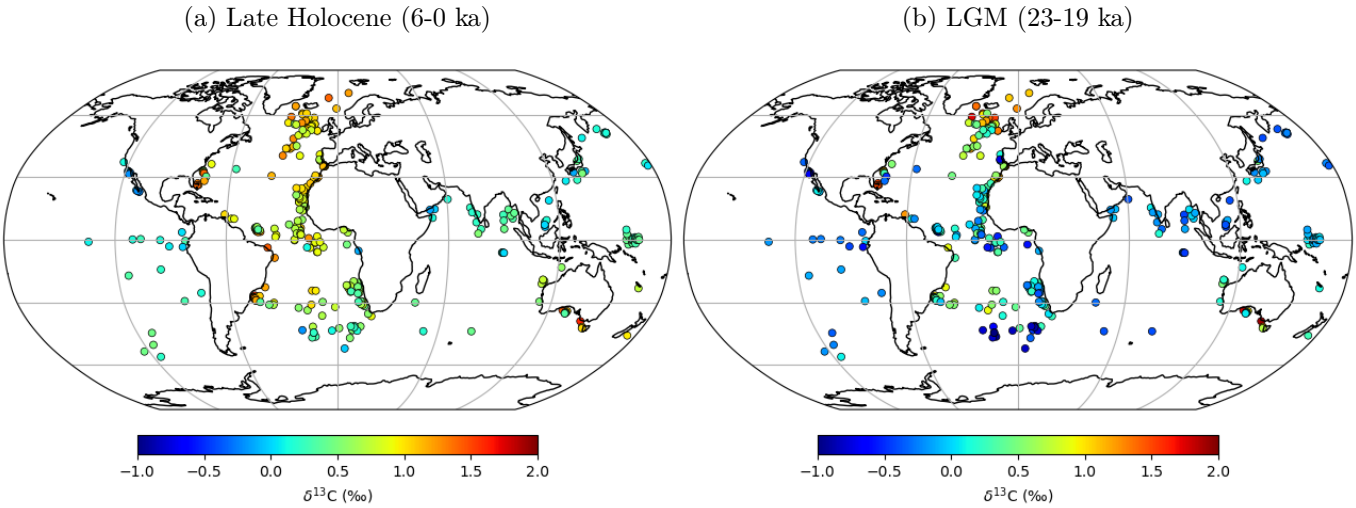

Figure 2.11: Late Holocene (a) and LGM (b) δ^{13}C data from Peterson et al. [2014]

2.5 Résumé du chapitre en français

Dans ce chapitre 2, je présente les outils déjà développés que j'utilise dans le cadre de cette thèse. Il s'agit du modèle du climat de complexité intermédiaire iLOVECLIM, intégrant en particulier de deux paramétrisations d'intérêt pour cette étude, permettant une représentation simple de la plongée des saumures ou bien du mélange vertical induit par le déferlement d'ondes de marée. Je décris également le protocole PMIP4, qui définit les forçages et conditions aux limites à implémenter lors des simulations du DMG. Pour la première fois, ce protocole PMIP recommande l'utilisation de différentes reconstructions de calottes, afin de prendre en compte leur incertitude. L'implémentation des conditions aux limites associées, nécessaire aux études d'intercomparison auxquelles iLOVECLIM participe, est présentée dans le chapitre suivant. Ce protocole est également celui recommandé dans le cadre du tout nouveau projet PMIP-carbon, dont les premiers résultats font l'objet d'une publication. Enfin, les enregistrements paléoclimatiques (de glace de mer, SST, δ^{13}C) servant à mener par la suite des comparaisons modèle-données sont brièvement exposés.

Je souligne dans ce chapitre que malgré certaines limitations telles que sa résolution, le modèle iLOVECLIM est tout à fait adéquat pour examiner la circulation profonde de grande échelle et le contenu carbone de l'océan. En effet, il intègre un module de cycle du carbone et simule directement certains proxies tels que le δ^{13}C. De plus, son faible temps de calcul permet de réaliser un grand nombre de simulations équilibrées, et ainsi d'explorer diverses directions concernant l'influence des processus tels que la plongée des saumures (chapitre 4), la diffusion verticale (chapitre 5), ou bien l'effet des vents (chapitre 6) et des conditions aux limites imposées (chapitre 3 et 4).

Chapter 3

Changing boundary conditions: consequences on carbon sequestration in the ocean

Chapter aims:

1. Describe the semi-automated generation of ocean boundary conditions on the model grid, a method developed in this thesis in order to notably test the influence of the choice of ice sheet reconstruction on the examined variables
2. Evaluate the impact of this method on the PI climate and ocean circulation
3. Quantify the carbon sequestration simulated in the ocean by PMIP-carbon models (including iLOVECLIM) as a consequence of modelling choices which relate to differing implementations of LGM ocean boundary conditions (or lack thereof)

Highlights:

↪ The technical development undertaken allows for an easy generation of the iLOVECLIM model bathymetry and coastlines from any topographic file, including those recommended by the PMIP4 protocol. Straits and key passages still have to be checked, and a limited number of adjustments manually enforced.

↪ At the PI, the newly generated ocean boundary conditions yield a slight deterioration of some climate variables (e.g. Drake transport), but a major improvement of the ocean volume.

↪ Comparison with other PMIP models demonstrates that the ocean volume tends to be overlooked during the implementation of the LGM experimental design in models, yet it is a dominant control on carbon sequestration. In addition, the adjustment of biogeochemical variables (e.g. alkalinity) to account for a change of volume must be carefully considered due to its large effect on ocean carbon content. Future PMIP and PMIP-carbon protocols may wish to draw more attention on these modelling choices.

In chapter 2, I have outlined the methods used in this study, which basically amounts to running multiple simulations and sensitivity tests at the Last Glacial Maximum (LGM) with the carbon-enabled iLOVECLIM model to explore the relationship between the simulated sea ice, deep ocean circulation, and CO_2 concentration. I chose to do it in the coherent framework of the PMIP4 project. Following this protocol indeed allows a participation of the iLOVECLIM model in multimodel intercomparison studies [Kageyama et al., 2021, Lhardy et al., 2021a], but also to update the LGM boundary conditions implemented in the iLOVECLIM model, which dates back to PMIP2 [Roche et al., 2007]. This gives me the opportunity to assess whether the significant differences in the recommended boundary conditions of PMIP4 compared to previous phases result in any improvement of the simulated sea ice and deep ocean circulation, previously evaluated in Roche et al. [2012] and Otto-Bliesner et al. [2007]. As recommended by Kageyama et al. [2017], I chose to run simulations with the boundary conditions associated with the two most recent ice sheet reconstructions (GLAC-1D and ICE-6G-C) to evaluate the impact of ice sheet uncertainties [Ivanovic et al., 2016] in the iLOVECLIM model. To facilitate the use of both reconstructions and to enable future work on transient simulations with an interactive bathymetry (as in Meccia and Mikolajewicz [2018]), I have developed a semi-automated method to generate and update boundary conditions on the model grid.

In this chapter 3, I first describe these developments and their validation at the pre-industrial (PI), as well as the underlying modelling choices. Secondly, I evaluate the consequences of modelling choices which relates to a change of ocean boundary conditions on the simulated CO_2 concentration. These results, presented in [Lhardy et al., 2021a], are obtained using both sensitivity tests with the iLOVECLIM model and preliminary results from the PMIP-carbon project, whose protocol is described in chapter 2. The effects of the choice of boundary conditions on the simulated sea ice and deep ocean circulation at the LGM are examined in chapter 4 [Lhardy et al., 2021b].

3.1 Implementation of boundary conditions in the iLOVECLIM model

I have developed a new method to implement the boundary conditions (e.g. orography, ice sheet extent, coastlines, bathymetry) associated with each ice sheet reconstruction on the atmosphere and ocean grids of iLOVECLIM. This semi-automated method allows for consistency between LGM, PI, and ongoing transient runs with an updated bathymetry. I chose to use both GLAC-1D and ICE-6G-C ice sheet reconstructions to generate these boundary conditions, and I compare these results to the ones obtained with the ICE-5G reconstruction [Peltier, 2004] recommended in the PMIP2 protocol, which was used in the former version of iLOVECLIM in its LGM configuration [Roche et al., 2007]. As the iLOVECLIM model did not take part in the PMIP3 phase, there was no need to generate the boundary conditions associated with the ice sheet reconstruction produced for PMIP3, which is a composite of three individual reconstructions (ICE-6G v2.0, GLAC-1a, ANU − see Abe-Ouchi et al. [2015]). Both the GLAC-1D [Tarasov and Peltier, 2002, Tarasov et al., 2012, Briggs et al., 2014, Ivanovic et al., 2016] and the ICE-6G-C [Peltier et al., 2015, Argus et al., 2014] reconstructions are more recent and also recommended in the deglaciation protocol [Ivanovic et al., 2016]. However, the advantage of this semi-automated method is that new boundary conditions can be easily implemented if need be.

3.1.1 Generation of atmosphere boundary conditions

To generate the atmosphere boundary conditions (e.g. orography, land-ice fraction), I interpolated the variables provided with each ice sheet reconstruction on the T21 grid of ECBilt (see Fig. 3.1). Although the resolution of this atmospheric component is coarse, the elevation of the Laurentide ice sheet in particular remains significantly lower in GLAC-1D than in ICE-6G-C boundary conditions. As recommended by Kageyama et al. [2017], I implemented the LGM orography by adding the 21 ka − 0 ka anomaly on the PI orography. This enables consistency between the LGM, PI, and first and last steps of transient runs of the last deglaciation.

(a) GLAC-1D orography (21 ka)

(b) ICE-6G-C orography (21 ka)

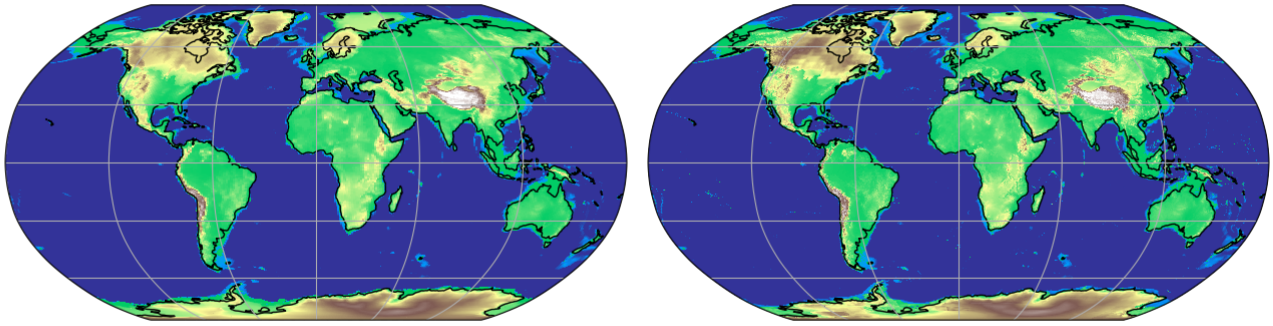

(c) GLAC-1D interpolated orography (21 ka)

(d) ICE-6G-C interpolated orography (21 ka)

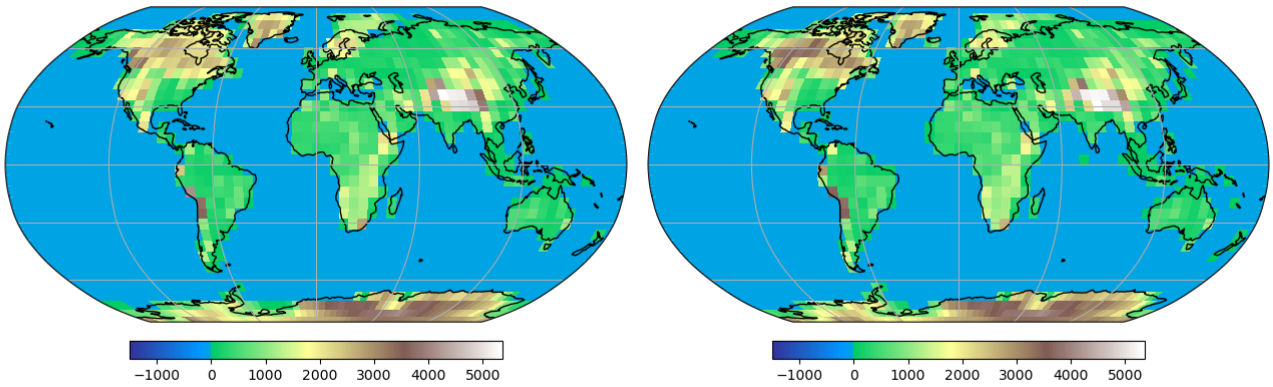

(e) Generated anomaly (GLAC-1D − ICE-6G-C)

(f) Generated anomaly (ETOPO1 − ICE-6G-C)

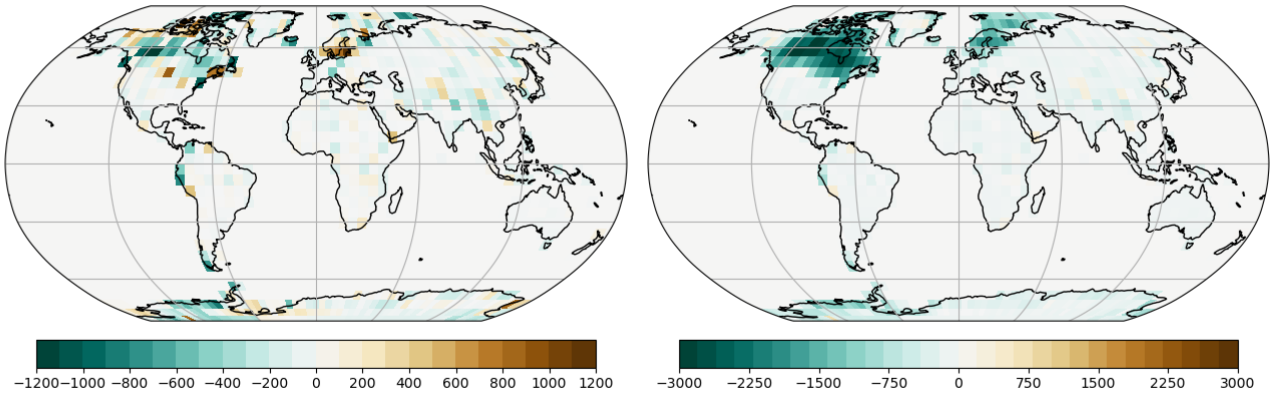

Figure 3.1: The GLAC-1D and ICE-6G-C orographies at 21 ka before (a, b) and after (c, d) interpolation on the T21 grid of ECBilt. Anomaly in the orography generated from GLAC-1D (e) or ETOPO1 (f) with respect to the one from ICE-6G-C.

The same was done for the continental ice extent (see Fig. 3.2), though with an additional step. Indeed, in the files containing the GLAC-1D and ICE-6G-C ice sheet reconstructions, the ice extent variable (*sftgif*) is provided as a point-value mask, typically as an ice fraction with values equal to 0 (i.e no ice) or 1 (100% ice) [Kageyama et al., 2017]. Such a variable − regridded on the ECBilt grid − is also what the model needs to read in an input file. However, the interpolation sometimes results in intermediate values at the border of the ice sheets. Therefore, a threshold has to be enforced to implement only 0 or 1 values. This threshold can be arbitrarily chosen at 0.5 (50% ice in a grid cell), but since the interpolation entails a decrease of the total continental surface area with a high albedo, I chose a lower threshold (20%). As a result, this 'white' continental area remains close to the one computed before interpolation (see Table 3.1).

Table 3.1: Quantification of the continental surface area with a high albedo (i.e. 0.85), before and after interpolation on the T21 grid

'White' continental surface area (millions of km^2)	GLAC-1D	ICE-6G-C
Raw data from each ice sheet reconstruction	38.9	39.0
After interpolation (integration of grid cell area weighted by the ice fraction)	38.4	37.6
Threshold at 0.50 (integration of grid cell area where ice fraction $>$ 50%)	38.3	37.3
Threshold at 0.01 (integration of grid cell area where ice fraction $>$ 1%)	39.2	40.2
Threshold at 0.20 (integration of grid cell area where ice fraction $>$ 20%)	39.0	39.0

(a) GLAC-1D land ice fraction

(b) ICE-6G-C land ice fraction

(c) 'Ice mask' generated from GLAC-1D

(d) 'Ice mask' generated from ICE-6G-C

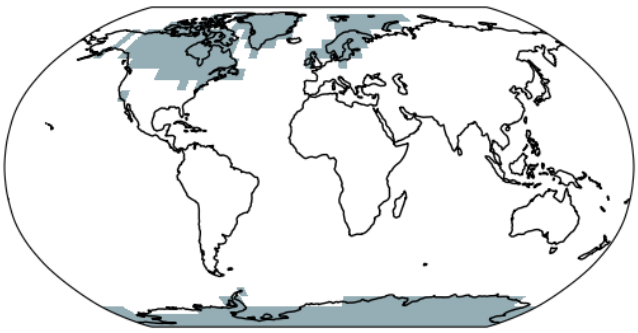

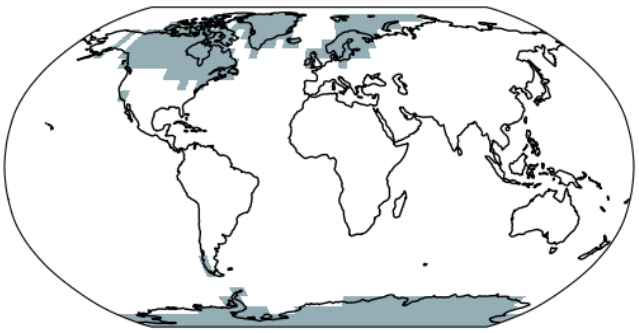

Figure 3.2: The GLAC-1D and ICE-6G-C land ice fraction, and the resulting boundary condition on the ECBilt grid (after interpolating the land ice fraction, applying a 20% threshold and adding the 21 ka − 0 ka anomaly on the PI ice mask)

3.1.2 Generation of ocean boundary conditions

Generating the ocean boundary conditions (e.g. bathymetry, coastlines) is a more delicate step. As pointed out by Kageyama et al. [2017], the large ice sheets and the lower sea level of the LGM, around -130 m relative to the present-day [Lambeck et al., 2014], lead to shallow continental shelves being either emerged (e.g. Sunda shelf, Sahul shelf) or covered by land ice (e.g. Hudson Bay, Barents and Kara seas), along with the closure of major straits (e.g. Bering strait). As a result, the coastlines (i.e. 'land-sea mask') in these areas have to be defined with care, in addition to the locations where the bathymetry is also adjusted for the PI (typically, Gibraltar Strait and Greenland-Iceland-Scotland ridge). This manual polishing is unavoidable in order to get realistic ocean transport in straits which are often too narrow to be open considering the ocean model resolution.

In the iLOVECLIM model, the ocean boundary conditions used to be constructed manually [Roche et al., 2007]. The coastlines were redefined to account for the low sea level and the bathymetry was adjusted in shallow areas, but no modifications were made in open ocean areas such as the abyssal plains. This was justified by the irregular vertical resolution of the CLIO model, which exceeds 700 m in deep grid cells. As these changes are rather tedious, I chose to develop a semi-automated method to generate bathymetries and land-sea masks on the CLIO grid from any topographic file, allowing a systematic procedure using input variables from either GLAC-1D or ICE-6G-C reconstructions (at 21 ka, or at any step of the deglaciation). Moreover, this development enabled the update of the ocean boundary conditions at the PI, which were generated (and heavily-tuned) from a rather old topographic file (ETOPO5 [1986], see Campin [1997]). This generation method, also described in the appendix of Lhardy et al. [2021b], is completed in several steps.

First step: The LGM bathymetry anomaly (21 ka − 0 ka) is added to the PI bathymetry (ETOPO1, Amante and Eakins [2009]), after interpolation on the ETOPO1 grid.
Second step: A connectivity program (Paillard, pers. com.) is run using this topographic data. This program provides the bathymetry, the hypsometry and the connections between ocean basins on the two CLIO grids (either regular or rotated). To do so, the lowest sill between any points is computed thanks to a tree structure, then aggregated on the ocean grid of coarser resolution (see Appendix B of Lhardy et al. [2021b]).
Third step: The two grids are combined in a program which generates both the land-sea mask (using the hypsometry from the previous step) and the vertical depth at any location (using the bathymetry). The program produces an output file containing this bathymetric data with the land-sea mask applied on it as a mask (defining 0 in land grid cells).
Fourth step: As the coastlines are first defined for the ocean model, the fraction of land and ocean on the atmospheric grid is computed in an additional pre-processing step, as well as the interpolation points between the CLIO and ECBilt grids.

This procedure is largely automated, though the land-sea mask and bathymetry are manually defined for a few grid cells in the third step. In more details, this step includes:

1. Generation of the land-sea mask

- *The hypsometry method.* Using the hypsometry (produced on the CLIO grid in the second step), the program computes the altitude at which a certain percentage of ocean is reached within each grid cell, and compares it to the given sea level. To illustrate this, I can take the hypothetical exemple of a coastal grid cell. This grid cell may be divided between land and ocean on a subgrid level, with 20% of its surface being land and 80% ocean, at the present-day sea level. Therefore, it makes sense for this particular cell to be assigned as ocean in the PI land-sea mask. However, depending on the subgrid topography, this grid cell may be composed of 90% land and 10% ocean at the LGM considering the low sea level, thus defined as land in the LGM land-sea mask.
  I point out that in this computation, two modelling choices come into play: both a sea level and a threshold need to be defined. I chose to use the sea level reconstructed by Lambeck et al. [2014], whose evolution is constrained by numerous observations. However, I note that the ice volume trapped on land in the GLAC-1D and ICE-6G-C reconstructions is not completely consistent with the sea level inferred by Lambeck et al. [2014], which is -134 m at 21 ka. As for the threshold, I defined as ocean any grid cell with a surface area composed of at least 40% ocean at the given sea level. I note that a 50% value was chosen in the IPSL model [Kageyama et al., 2017]. Nonetheless, a 40% threshold is consistent with the previous generation of boundary conditions in the CLIO model [Campin, 1997], and has the advantage of limiting the number of grid cells which have to be manually defined as ocean (see example in Fig. 3.3). Still, it remains a subjective choice.

- *Automated elimination of isolated grid cells.* Then, the ocean grid cells with 3 or 4 neighbouring cells defined as land are forced as land in a few iterations, in order to fill closed seas and eliminate isolated cells on the coast. I mean by 'isolated' that single ocean grid cells on the coast are dynamically isolated (i.e. no horizontal transport can reach them) since the CLIO grid is of B-type on the classification of Arakawa. Due to the staggered tracer and velocity fields, the isolated grid cells need to be eliminated or else the model crashes (due to incoherency in the divergence computation).

- *Manual changes.* The land-sea mask is further modified to enable model runs and realistic ocean currents. Some grid cells are manually defined as land or ocean in order to completely close or open straits and channels which are not wide enough (see examples in Fig. 3.3). Indeed, no ocean transport can occur in channels with only one ocean grid cell, due to the B-grid type of the CLIO model. The manual changes are kept to a minimum (10 grid cells at the PI, 17 at the LGM using ICE-6G-C and 16 using GLAC-1D). These changes concern Gibraltar Strait (4 to 5 problematic grid cells) and Denmark Strait (1 to 2) at both the PI and LGM ; in addition to Fram Strait (1), Davis Strait (2), Gulf of Mexico outlet (5) and Sulawesi island (2) at the LGM ; and the Hudson Bay (2) and Baffin Bay outlets (1) at the PI only. Since a perspective of this work is to run deglacial transient runs with an interactive bathymetry, I note that it is not trivial to decide when these passages should be forced open.

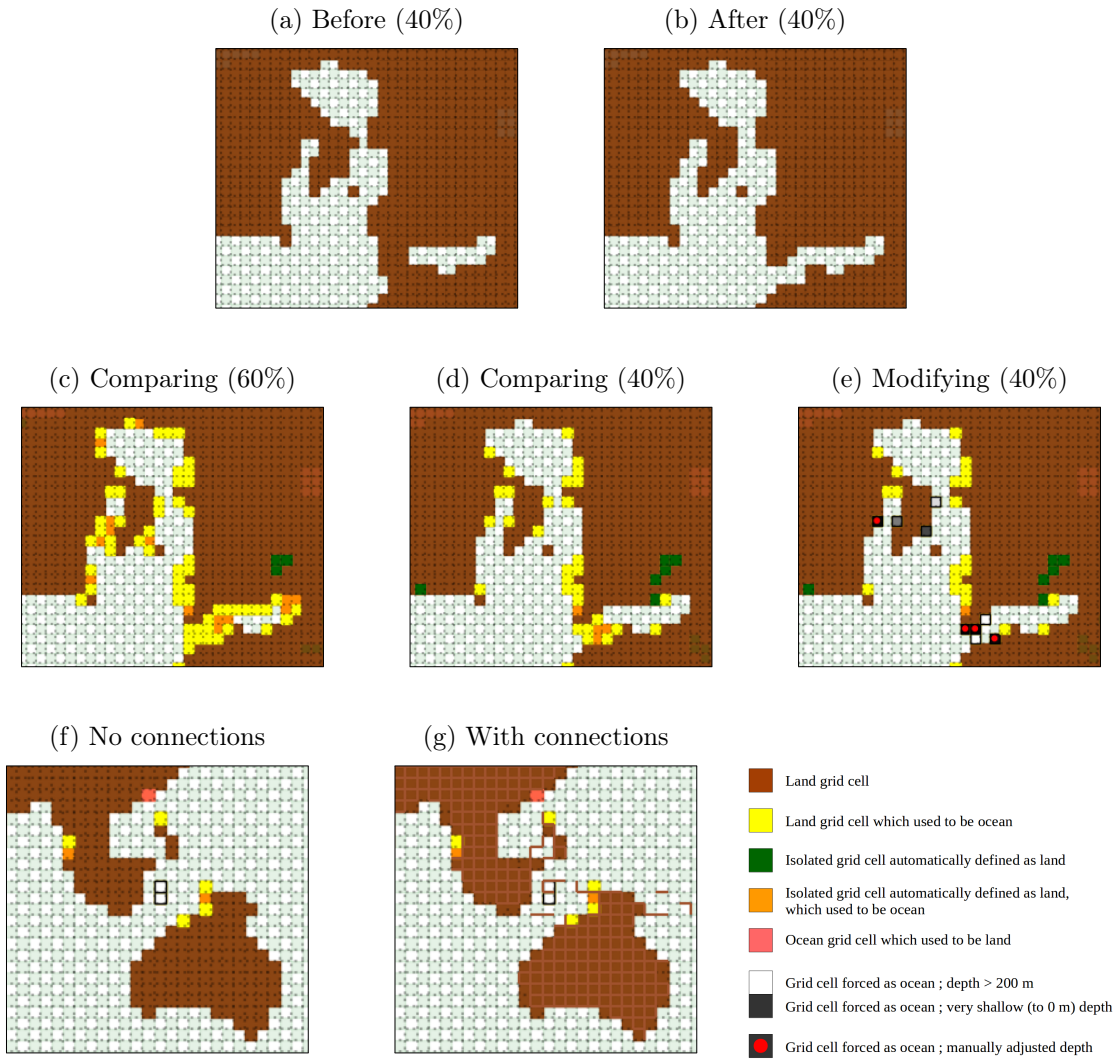

Figure 3.3: Land-sea masks produced at the LGM on the CLIO grid[1]

[1]The examples shown here are for the North Atlantic (a to e) or the Indonesian region (f, g). Note that the Arctic ocean is deformed due to the rotated CLIO grid. I show in (a) that without manual changes, the Mediterranean sea is closed, and no ocean transport can occur in Denmark, Davis, or Fram straits. I obtain (b) by manually forcing as ocean 9 grid cells, which are shown in (e) on a black (depth close to 0 m) to white (at least 200 m) scale. Among these grid cells, 4 of them are not deep enough to simulate a realistic transport at Gibraltar or Davis Strait, so their bathymetry also has to be manually adjusted (red dots). In addition, I compare in (c to g) the land-sea mask generated by this method to the former LGM land-sea mask (PMIP2, Roche et al. [2007]): grid cells which used to be ocean and are now land appear in yellow (and the reverse in light red). The automated elimination of isolated cells produces land grid cells in green (also formerly land) or orange (formerly ocean). I show with (c) that using a threshold of 60% in the hypsometry method entails much more problematic land grid cells (yellow cells in straits) than (d) and also generates more isolated grid cells (in orange). In (e), the land grid cells in yellow which are not problematic for ocean transport are kept as land, keeping the manual changes to a minimum. Finally, I show in (g) that computing the connections (in the second step of the procedure) is useful to make informed choices in (e). The grid cell borders where no ocean transport is supposed to occur are shown in brown. I chose to define as ocean two grid cells (corresponding to Sulawesi island) to eliminate the too narrow channel west of it, where the connectivity still shows that ocean transport is possible. On the other hand, I chose to keep as land a brown grid cell which blocks ocean transport between Sundaland and the Philippines, isolating the South China sea at the South as suggested by the connections shown in (g).

2. Generation of the bathymetry

- The program interpolates the bathymetric data produced in the second step on the irregular vertical levels of the CLIO grid.
- The bathymetry of a few grid cells is adjusted in critical straits and passages (see Fig. 3.3e). These manual changes concern 9 grid cells, at Gibraltar Strait (3 cells), Hudson Bay outlet (2) and Greenland-Iceland-Scotland ridge (4) for the PI, and Gibraltar Strait (3), Davis Strait (1), Gulf of Mexico outlet (1) and Greenland-Iceland-Scotland ridge (4) for the LGM. The bathymetry of these 9 grid cells is deepened and set equal to their depth on the former CLIO grid (i.e. at the PI: $\sim$ 350 m at Gibraltar, $\sim$ 1450 m at the Greenland-Iceland-Scotland ridge, as in Campin [1997]). Without these adjustments, the Norwegian Sea remains too isolated from the North Atlantic [Campin, 1997] and the salinity of the Mediterranean Sea diverges.
- Then, the program also eliminates isolated grid cells. Indeed, as the model cannot deal with ocean grid cells with only one vertical level (e.g. ocean floor at 10 m), the bathymetry of these few cells is either forced at vertical level 2 or they are defined as land. In addition, I adjust the bathymetry of grid cells which are vertically isolated (e.g. deeper than their neighbours) by applying a fonction similar to a smoothing filter. As a result, the deepest grid cells share the same depth as some of their neighbours, in groups of at least 4 cells (see Fig. 3.5).

(a) Generated anomaly (GLAC-1D − ICE-6G-C)

(b) Generated anomaly (ETOPO1 − ICE-6G-C)

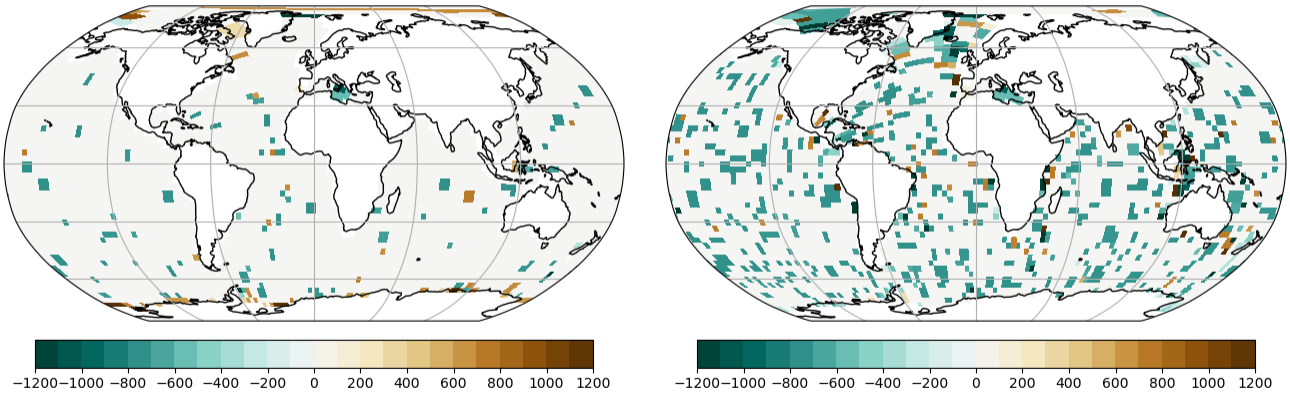

Figure 3.4: Anomaly in the bathymetry generated from (a) GLAC-1D or (b) ETOPO1 with respect to the one from ICE-6G-C. Deeper grid cells (than the bathymetry generated from ICE-6G-C) are indicated in blue and shallower grid cells in brown.

The bathymetry generated with this method using both GLAC-1D or ICE-6G-C topographic data is shown in Fig. 3.5. I note that they are largely similar, with noticeable differences along the Antarctic coast for example (also see Fig. 3.4a). Plotting the anomaly with the PI bathymetry (Fig. 3.4b), I underline that despite the coarse vertical resolution at depth (reaching $\sim$ 750 m in the deepest vertical level), the interpolation results in shallower grid cells at the LGM (relative to the PI) in a significant number of grid cells, even in abyssal plains. As a result, the ocean volume is strongly impacted by the use of this semi-automated method. In the following section, I will quantify the change in ocean volume (see Fig. 1b and S2 of Lhardy et al. [2021a]) and elaborate on the consequences on the simulated carbon content.

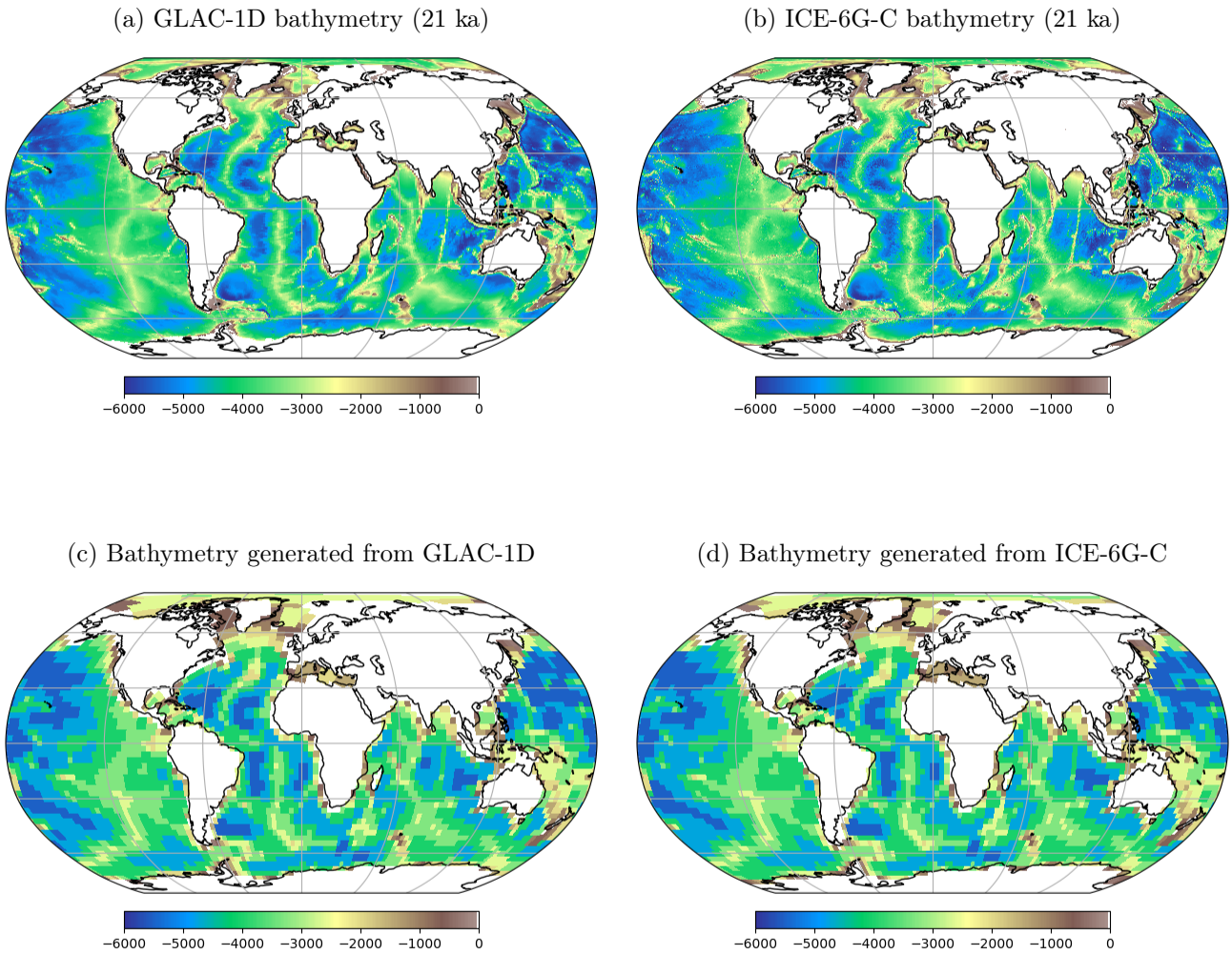

Figure 3.5: The GLAC-1D and the ICE-6G-C bathymetries, and the bathymetries generated from each ice sheet reconstruction on the CLIO grid

3.1.3 Model runs with an automated change of ocean boundary conditions

The boundary conditions generated in the previous sections are implemented in the model during the initialization of runs. I initialize LGM runs with the same equilibrated simulation at the PI (i.e. 'restart' simulation), which is a common practice of modellers to reduce spin-up duration [Kageyama et al., 2017]. Since I also generated new ocean boundary conditions for the PI standard run (using ETOPO1 from Amante and Eakins [2009], in replacement to those of Campin [1997]), with a large effect on ocean volume [Lhardy et al., 2021a], we first retuned the carbon cycle. The total carbon content was adjusted (by 632 GtC, i.e. ∼-1.5%) in order to get the PI atmospheric CO_2 concentration to equilibrate at ∼ 280 ppm. We also got $\delta^{13}C_{atm}$ values close to -6.48‰[Lourantou et al., 2010] and $\Delta^{14}C$ values close to 0‰. The model code is kept identical between PI and LGM standard runs, with the exception of the ocean transport through Bering Strait. Since this transport is enabled via a pipe due to the limitation of the

CLIO grid, it is explicitely set to 0 in LGM runs. Using this PI restart with a larger ocean volume, a few adjustments had to be made to ensure mass conservation.

We developed the initialization code of the CLIO model in order to enable an automated change of ocean boundary conditions. New ocean grid cells (e.g. during deglacial transient runs) are now detected by comparing the current boundary conditions with the ones from the restart run. In order to quickly equilibrate the model, their tracer content (e.g. temperature, salinity) is initialized at the average value of the neighbouring ocean grid cells. We pay specific attention to conservative tracers. First, we ensure that the oxygen isotopes are initialized with a Standard Mean Ocean Water (SMOW) of +1‰. Secondly, we conserve salt by computing the difference between the total salt content in the restart and during initialization (after dealing with new ocean grid cells). The salinity in each grid cell is homogeneously modified below 1000 m to account for this difference. While LGM runs are usually initialized with a salinity of +1 psu to account for a sea level of -134 m compared to the PI [Kageyama et al., 2017], our modelling choice allows for salt conservation, regardless of the sea level change. Considering the realistic relative volume change [Lhardy et al., 2021a], this automated modification amounts to a similar salinity change relative to the PI salinity (+0.96 psu for GLAC-1D boundary conditions and +1.11 psu for ICE-6G-C). In addition, Kageyama et al. [2017] also recommend specific adjustments for ocean biogeochemistry models, concerning DIC, alkalinity, and nutrients. We chose to conserve the total quantities of these variables in a similar manner as the salinity adjustment previously described, instead of multiplying the initial values by a relative volume change of around 3%. These adjustments and their effects on the simulated carbon are described in Lhardy et al. [2021a].

Finally, Kageyama et al. [2017] also underline that the models should be spun up until equilibrium. While different criterias have been advised in previous PMIP phases (mean SST drift < 0.05°C/century, net carbon uptake by the biosphere < 0.01 GtC/year, small drift in zonal mean sea salinity in the Southern Ocean, see Kageyama et al. [2017]), Marzocchi and Jansen [2017] point out the importance of deep-ocean equilibration in multimodel comparisons of PMIP simulations at the LGM. Indeed, they observe a significant long-term drift in the AMOC strength and depth in one of the PMIP models. The authors warn that: "Discrepancies between models and paleodata can be further amplified by short integration times, as the transient response to cooling is expected to be associated with a stronger and deeper AMOC." Since the AMOC is of particular interest to this study, I have standardly run simulations of 3000 (v1) or 5000 (v1, v2) years to ensure a quasi-equilibrated state of the deep ocean despite its inertia. This is made possible by the low computation cost of iLOVECLIM, with such simulations ending in little more than one week. To evaluate this equilibration, the drift of the deep ocean temperature has been quantified in my first batch of simulations (v1), and happens to be less than 2×10^{-4} °C per century for any individual simulation at the end of it. I standardly analyze the last 100 years of each simulation.

3.1.4 Evaluation of the consequences of the semi-automated ocean boundary conditions generation method on the PI climate and ocean circulation

After generating the boundary conditions associated with the ETOPO1 [Amante and Eakins, 2009] or PMIP4 (GLAC-1D and ICE-6G-C, Kageyama et al. [2017]) topographies and adding related developments to the initialization code, I ran simulations at both the PI and LGM. Then, I evaluated whether the iLOVECLIM model produces a reasonable climate and ocean circulation with these new boundary conditions. The differences caused by the use of this generation method at the LGM are notably assessed in Lhardy et al. [2021b] (see chapter 4), where I examined global mean temperature, SST, Southern Ocean sea ice and Atlantic streamfunction, which are variables of particular interest to this study.

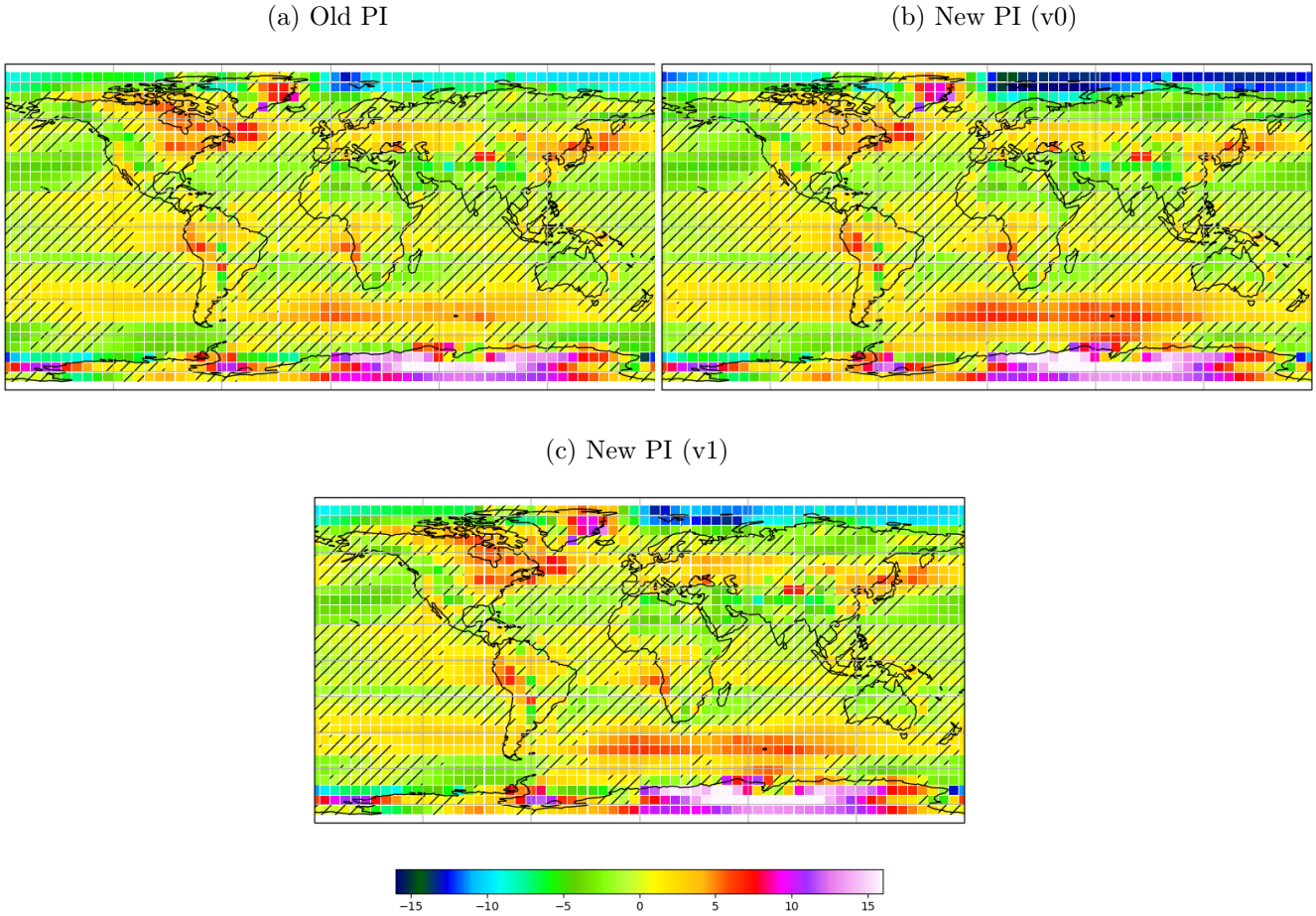

Figure 3.6: Surface temperature anomaly with respect to model reanalysis (ERA-interim), for PI simulations run with (a) former ocean boundary conditions (ETOPO5 [1986], Campin [1997]), or newly-generated coastlines and bathymetry (b) without or (c) with adjusting the depth of the Greenland-Iceland-Scotland ridge. Grid cells in good agreement with ERA-interim data are hatched.

In this section, I therefore focus on the PI climate and ocean circulation, using a few variables which were helpful to determine some of the modelling choices described above. I compared the usual climatic fields (SAT, ST, SS), but also outputs from the carbon cycle [Bouttes et al., 2015] to results obtained with the former boundary conditions (simulation called 'Old PI').

It quickly appeared that the negative anomaly of surface temperature (with respect to ERA-interim) in the Arctic strongly deteriorates with the change of ocean boundary conditions to automated ones (in simulation 'New PI (v0)', see Fig. 3.6a and b). In simulation 'New PI (v1)', I managed to lower to some extent this anomaly by deepening 4 grid cells at the Greenland-Iceland-Scotland ridge (Fig. 3.6c), which is also a modelling choice documented in Campin [1997]. Despite numerous tests in this region, I could not further reduce this anomaly. In addition, we wished to keep manual changes of the bathymetry to a minimum. As a result, I note that the agreement with the ERA-interim surface temperatures slightly deteriorates with the new ocean boundary conditions in two regions: the Arctic Ocean (and in particular at proximity of Fram Strait), and in parts of the Southern Ocean (Atlantic and Indian sectors).

I also compared the simulated ocean fields (ST, SS, biogeochemical variables) to WOA2009 [Locarnini et al., 2010, Antonov et al., 2010] or GLODAP [Key et al., 2004] data. This data is the same as the one used in Bouttes et al. [2015], in which the PI results from the carbon cycle implemented in the iLOVECLIM model are fully evaluated, and compared to CMIP5 model outputs (their Fig. 20 to 22). Using the same graphical representation, I quantified statistical differences (in terms of root mean square error, correlation coefficient, and standard deviation) between my three PI simulations in Taylor diagrams (Fig. 3.8). Though the differences remain small, the simulated fields in the Atlantic are generally in better agreement with observations in 'Old PI', indicating again a slight deterioration of the simulated variables when using the ocean boundary conditions generated semi-automatically. However, I note that the adjustment of the Greenland-Iceland-Scotland threshold partly compensates this difference, with the values from 'New PI (v1)' generally lying in-between 'Old PI (v0)' and 'New PI (v1)'.

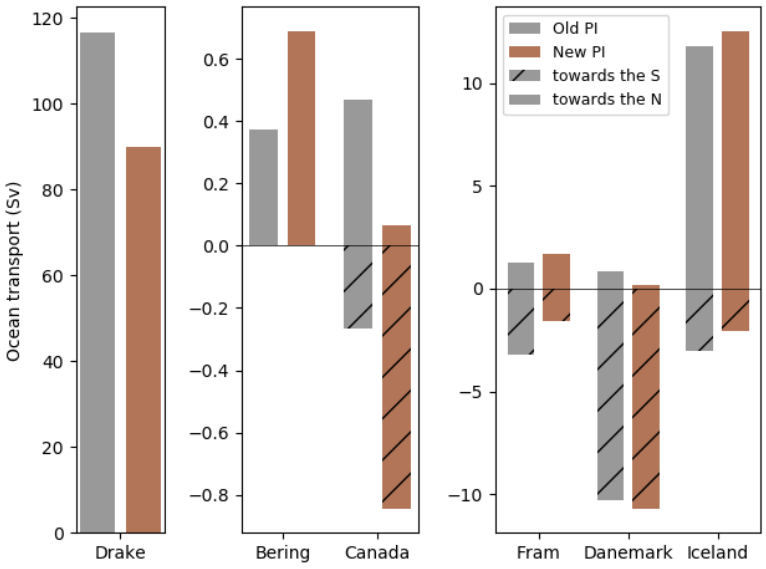

Figure 3.7: Ocean transport through key straits, in PI simulations with the former ocean boundary conditions ('Old PI') or the newly-generated ones ('New PI (v1)')

In addition, I examined more specifically the ocean transport through key straits (e.g. Drake Passage, Bering Strait, Canadian archipelago, Fram Strait, Denmark Strait, and Iceland-Norway passage). This transport is quantified in Sverdrup (i.e. 1×10^6 $m^3.s^{-1}$) in Fig. 3.7. Significant differences are arising, in particular in narrow regions where no manual adjustments were made to the bathymetry (e.g. Canadian archipelago, Drake Passage).

(a) Temperature

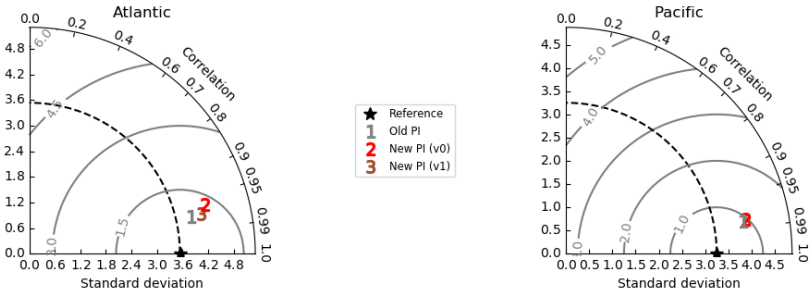

(b) Salinity

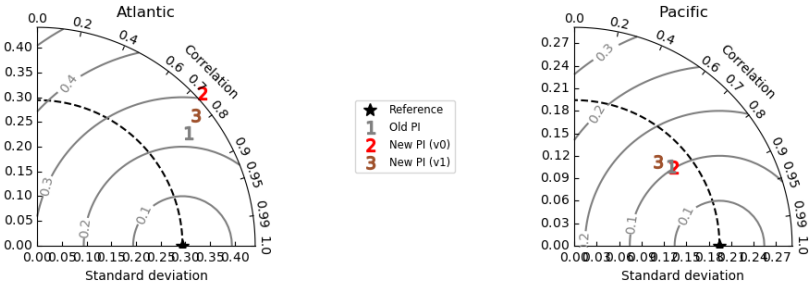

(c) DIC

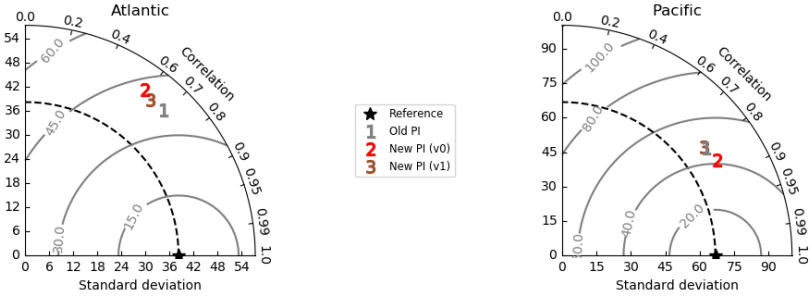

(d) Phosphate

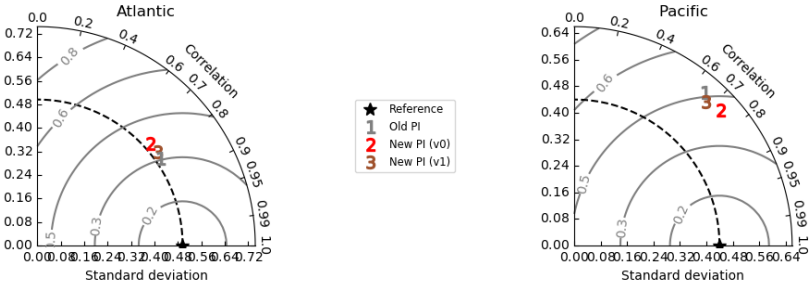

(e) O_2

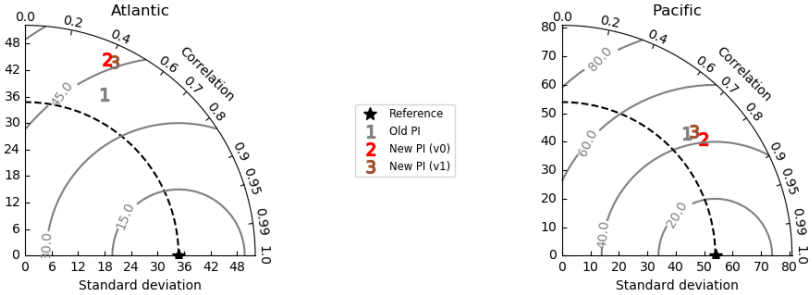

Figure 3.8: Taylor diagrams obtained using the zonally averaged ST, SS, DIC, phosphate and O_2, and data from WOA2009 or GLODAP.

I note that I simulate a lower Drake Passage transport with the new ocean boundary conditions (90 Sv), though this transport was already strongly underestimated with the former bathymetry (117 Sv), considering the observational estimate of Donohue et al. [2016] (173.3 ± 10.7 Sv). I realised that Bering transport was also underestimated compared to a climatology mean of 0.8 Sv [Roach et al., 1995], so I adjusted the pipe to get a much closer value (0.69 Sv, against 0.37 Sv previously). Still, this ocean transport remains quite low if I consider the more recent climatology from Woodgate [2018] (1 Sv). The influence of this particular transport on the freshwater budget and ocean circulation was examined in iLOVECLIM in Goosse et al. [1997a].

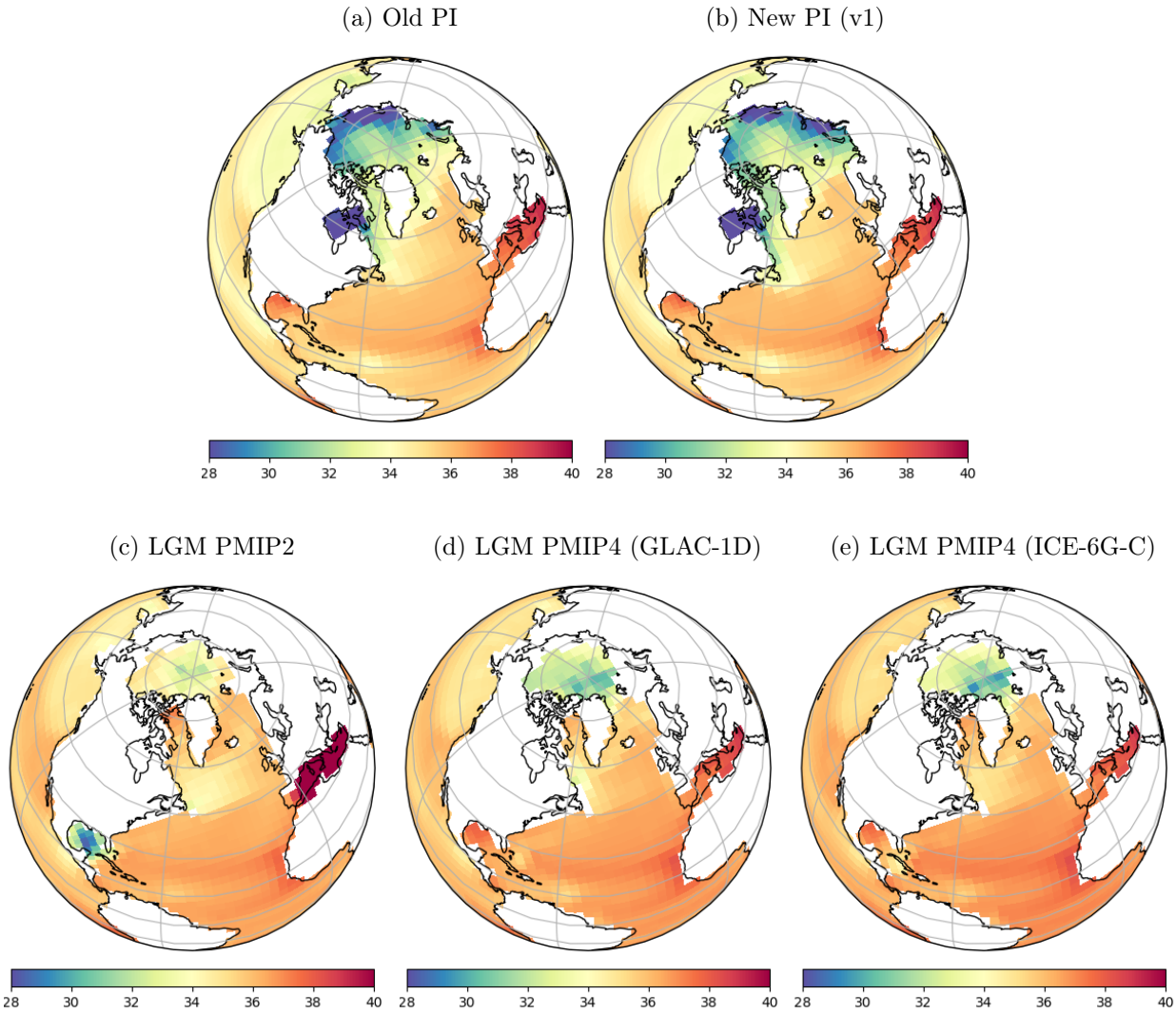

Figure 3.9: Sea surface salinity (SSS) in the North Atlantic − Arctic region

Finally, regional differences in sea surface salinity (SSS) can also be related to some of my modelling choices. Indeed, I have adjusted the bathymetry of a few grid cells at the Gulf of Mexico outlet and at Gibraltar Strait in my LGM (PMIP4) simulations. As a result, these simulations shows more moderate surface salinities in the Mediterraneen Sea (Fig. 3.9). The larger ocean transport at Bering Strait in the 'New PI (v1)' simulation also produces noticeable differences in the salinities of the Arctic ocean at the PI. However, the general pattern remains unchanged.

3.2 *Article 1: A first intercomparison of the simulated LGM carbon results within PMIP-carbon: role of the ocean boundary conditions*

I now quantify the consequences of modelling choices related to a change of ocean boundary conditions on the simulated ocean sequestration and CO_2 concentration. In contrast to the rest of this thesis, this is done in the framework of a model intercomparison study, thanks to preliminary results from the PMIP-carbon project. In the following article, I use both PMIP-carbon model outputs and sensitivity tests with the iLOVECLIM model (v2), enabled by the developments described in this chapter.

My findings underline the importance of the relative ocean volume change between the PI and LGM simulations, which is rarely accurately represented in PMIP models. In the case of the iLOVECLIM model, the ocean volume at both the PI and LGM is considerably improved by the semi-automated method developed here to generate ocean boundary conditions. In addition, the related adjustment of biogeochemical variables recommended by the PMIP4 protocol (Kageyama et al. [2017], see Sect. 2.3) also has a large impact on the ocean carbon content. Yet both of these elements (ocean volume change and alkalinity adjustment in particular) are not consistently implemented in the PMIP-carbon model ensemble. While this complicates intercomparison of existing carbon-enabled model outputs, raising these technical issues at the start of the PMIP-carbon project will allow us to revise the protocol going forward.

Paleoceanography and Paleoclimatology®

RESEARCH ARTICLE
10.1029/2021PA004302

Key Points:

- Ocean volume is a dominant control on Last Glacial Maximum (LGM) carbon sequestration and must be accurately represented in models
- Adjusting the alkalinity to account for the relative change of volume at the LGM induces a large increase of oceanic carbon (of ~250 GtC)
- Paleoclimate Modeling Intercomparison Project-carbon models standardly simulate high LGM CO_2 levels (over 300 ppm) despite a larger proportion of carbon in the ocean at LGM than pre-industrial

Supporting Information:

Supporting Information may be found in the online version of this article.

Correspondence to:

F. Lhardy,
fanny.lhardy@lsce.ipsl.fr

Citation:

Lhardy, F., Bouttes, N., Roche, D. M., Abe-Ouchi, A., Chase, Z., Crichton, K. A., et al. (2021). A first intercomparison of the simulated LGM carbon results within PMIP-carbon: Role of the ocean boundary conditions. *Paleoceanography and Paleoclimatology*, *36*, e2021PA004302. https://doi.org/10.1029/2021PA004302

Received 7 MAY 2021
Accepted 10 SEP 2021

A First Intercomparison of the Simulated LGM Carbon Results Within PMIP-Carbon: Role of the Ocean Boundary Conditions

F. Lhardy[1], N. Bouttes[1], D. M. Roche[1,2], A. Abe-Ouchi[3], Z. Chase[4], K. A. Crichton[5], T. Ilyina[6], R. Ivanovic[7], M. Jochum[8], M. Kageyama[1], H. Kobayashi[3], B. Liu[6], L. Menviel[9], J. Muglia[10], R. Nuterman[8], A. Oka[3], G. Vettoretti[8], and A. Yamamoto[11]

[1]Laboratoire des Sciences du Climat et de l'Environnement, CEA-CNRS-UVSQ, Gif-sur-Yvette, France, [2]Department of Earth Sciences, Earth and Climate Cluster, Faculty of Science, Vrije Universiteit Amsterdam, Amsterdam, The Netherlands, [3]Atmosphere and Ocean Research Institute, The University of Tokyo, Kashiwa, Japan, [4]University of Tasmania, Hobart, Australia, [5]School of Geography, Exeter University, Exeter, UK, [6]Max Planck Institute for Meteorology, Hamburg, Germany, [7]University of Leeds, Leeds, UK, [8]Niels Bohr Institute, University of Copenhagen, Copenhagen, Denmark, [9]Climate Change Research Centre, The University of New South Wales, Sydney, Australia, [10]Centro para el Estudio de los Sistemas Marinos, CONICET, Puerto Madryn, Argentina, [11]Japan Agency for Marine-Earth Science and Technology, Yokohama, Japan

Abstract Model intercomparison studies of coupled carbon-climate simulations have the potential to improve our understanding of the processes explaining the pCO_2 drawdown at the Last Glacial Maximum (LGM) and to identify related model biases. Models participating in the Paleoclimate Modeling Intercomparison Project (PMIP) now frequently include the carbon cycle. The ongoing PMIP-carbon project provides the first opportunity to conduct multimodel comparisons of simulated carbon content for the LGM time window. However, such a study remains challenging due to differing implementation of ocean boundary conditions (e.g., bathymetry and coastlines reflecting the low sea level) and to various associated adjustments of biogeochemical variables (i.e., alkalinity, nutrients, dissolved inorganic carbon). After assessing the ocean volume of PMIP models at the pre-industrial and LGM, we investigate the impact of these modeling choices on the simulated carbon at the global scale, using both PMIP-carbon model outputs and sensitivity tests with the iLOVECLIM model. We show that the carbon distribution in reservoirs is significantly affected by the choice of ocean boundary conditions in iLOVECLIM. In particular, our simulations demonstrate a ~ 250 GtC effect of an alkalinity adjustment on carbon sequestration in the ocean. Finally, we observe that PMIP-carbon models with a freely evolving CO_2 and no additional glacial mechanisms do not simulate the pCO_2 drawdown at the LGM (with concentrations as high as 313, 331, and 315 ppm), especially if they use a low ocean volume. Our findings suggest that great care should be taken on accounting for large bathymetry changes in models including the carbon cycle.

1. Introduction

The mechanisms of the atmospheric CO_2 variations at the scale of glacial-interglacial cycles are not fully understood. Ice core records have shown CO_2 variations with an amplitude of about 100 ppm for the last four or five cycles (Lüthi et al., 2008). In particular, the atmospheric CO_2 is known to have reached concentrations as low as 190 ppm (Bereiter et al., 2015) at 23–19 kaBP, during the Last Glacial Maximum (LGM). Compared to pre-industrial (PI) levels of around 280 ppm, this LGM pCO_2 drawdown is commonly thought to be mainly linked to an increase in carbon sequestration in the ocean (Anderson et al., 2019).

The total carbon content of this large reservoir currently holding ~38,000 GtC (Sigman & Boyle, 2000) is influenced by both physical and biogeochemical processes (Bopp et al., 2003; Kohfeld & Ridgwell, 2009; Ödalen et al., 2018; Sigman et al., 2010). Physical processes include changes in the solubility pump: a glacial cooling is associated with higher CO_2 solubility, though counteracted by the effect of an increased salinity. They also encompass changes of Southern Ocean sea ice (Marzocchi & Jansen, 2019; Stephens & Keeling, 2000), ocean stratification (Francois et al., 1997), and circulation (Aldama-Campino et al., 2020; Menviel et al., 2017; Ödalen et al., 2018; Schmittner & Galbraith, 2008; Skinner, 2009; Watson et al., 2015).

Biogeochemical processes rely on changes in the $CaCO_3$ cycle (Brovkin et al., 2007, 2012; Kobayashi & Oka, 2018; Matsumoto & Sarmiento, 2002) or an increased efficiency of the biological pump (Morée et al., 2021), through increased iron inputs from aeolian dust for example (Bopp et al., 2003; Oka et al., 2011; Tagliabue et al., 2009, 2014; Yamamoto et al., 2019).

Despite the identification of these processes, their contribution to the pCO_2 drawdown is still much debated. Modeling studies tend to show a large effect of the biological pump and a moderate effect of circulation changes (Buchanan et al., 2016; Hain et al., 2010; Khatiwala et al., 2019; Menviel et al., 2012; Tagliabue et al., 2009; Yamamoto et al., 2019), but model disagreements remain. Iron fertilization seems to explain a relatively small part (~ 15 ppm) of the LGM pCO_2 drawdown (Bopp et al., 2003; Kohfeld & Ridgwell, 2009; Muglia et al., 2017; Tagliabue et al., 2014). Accounting for carbonate compensation in models also seems to significantly reduce the simulated atmospheric CO_2 concentrations (Brovkin et al., 2007; Kobayashi & Oka, 2018). However, review studies show that the amplitude of the CO_2 variation caused by each process is not well constrained (Gottschalk et al., 2020; Kohfeld & Ridgwell, 2009). Moreover, sensitivity tests underline that, due to the interactions of both these physical and biogeochemical processes, isolating their effect remains challenging (Hain et al., 2010; Kobayashi & Oka, 2018; Ödalen et al., 2018). The emerging common view is that the LGM pCO_2 drawdown cannot be explained by a single mechanism, but by a combination of different intrinsic processes (Hain et al., 2010; Kohfeld & Ridgwell, 2009). Gaining a better understanding of these mechanisms, which depend on the background climate, is critical to accurately project future climate (Yamamoto et al., 2018).

As a result, it is hardly surprising that models struggle to simulate the LGM pCO_2 drawdown, especially in their standard version. Previous studies show that models simulate a large range of pCO_2 drawdown, with most modeling studies accounting for one third to two thirds of the 90–100 ppm change inferred from ice core data (Brovkin et al., 2007, 2012; Buchanan et al., 2016; Hain et al., 2010; Khatiwala et al., 2019; Kobayashi & Oka, 2018; Marzocchi & Jansen, 2019; Matsumoto & Sarmiento, 2002; Morée et al., 2021; Oka et al., 2011; Stephens & Keeling, 2000; Tagliabue et al., 2009). The discrepancies between models can be partly linked to resolution (Gottschalk et al., 2020) and representation of ocean and atmosphere physics, completeness of the carbon cycle model (including sediments, permafrost...) (Kohfeld & Ridgwell, 2009), and simulated climate and ocean circulation (Menviel et al., 2017; Ödalen et al., 2018). Ödalen et al. (2018) also highlights that differences in the initial equilibrium states (which depend on the model tuning strategy at the PI) may lead to different pCO_2 drawdown potentials in models. In this context, we could learn a lot from a multimodel comparison study of standardized LGM experiments. Such studies are now common for modern and future climates: the Coupled Climate Carbon Cycle Model Intercomparison Project (C4MIP, Jones et al., 2016) aims to quantify climate-carbon interactions in General Circulation Models (GCMs). Since the LGM is a benchmark period of the Paleoclimate Modeling Intercomparison Project (PMIP, Kageyama et al., 2018), the stage is set for a similar study focused on the LGM. Indeed, the PMIP project is now in its phase 4 and a standardized experimental protocol has been designed for the LGM (Kageyama et al., 2017). Although more and more PMIP models now also simulate the carbon cycle, outputs describing the carbon cycle have not been shared through Earth System Grid Federation systematically and no systematic multimodel analysis of coupled climate-carbon LGM experiments has been done so far. The purpose of the new PMIP-carbon project is therefore to compare outputs of various models in order to better understand the mechanisms behind past carbon cycle changes. As a first step, the project focusses on the model response to LGM conditions.

In this study, the preliminary results of the PMIP-carbon project gives us the opportunity to examine LGM carbon outputs of a roughly consistent model ensemble for the first time. We evaluate the impact of modeling choices related to the ocean boundary conditions change on the simulated carbon. We assess specifically the impacts of the total ocean volume change and associated adjustments, two elements which are not the focus of the PMIP protocol. Since the PMIP-carbon project is ongoing, this first look is especially useful to draw a few conclusions which will help refine the PMIP-carbon protocol.

2. Modeling Choices in PMIP-Carbon Models and Resulting Ocean Volumes

2.1. The PMIP-Carbon Protocol

The PMIP-carbon project, which falls under the auspices of the "Deglaciations" working group in the PMIP structure, aims at the first multimodel comparison of coupled climate-carbon experiments at the LGM. Participating modeling groups ran both a PI and a LGM simulation with the same code, following the PMIP4 experimental design as far as possible, but model outputs obtained using the PMIP2 or PMIP3 protocol were also accepted. These standardized protocols specify modified forcing parameters (greenhouse gas concentrations and orbital parameters) and different boundary conditions (e.g., elevation, land ice extent, coastlines, and bathymetry). Indeed, the LGM was a cold period with extensive ice sheets over the Northern Hemisphere. Due to the quantity of ice trapped on land, the eustatic sea level was around −134 m below its present value (Lambeck et al., 2014). To account for the related changes of topography (which encompasses changes of elevation, albedo, coastlines and bathymetry) in models, Kageyama et al. (2017) define the PMIP4 protocol and provide guidelines on how to implement the LGM boundary conditions on the atmosphere and ocean grids. Given the uncertainty of ice sheet reconstructions, the PMIP4 protocol lets modeling groups choose from three different topographies: GLAC-1D (Ivanovic et al., 2016), ICE-6G-C (Argus et al., 2014; Peltier et al., 2015), or PMIP3 (Abe-Ouchi et al., 2015), whereas the PMIP3 protocol relied on the PMIP3 ice sheet reconstructions (https://wiki.lsce.ipsl.fr/pmip3/doku.php/pmip3:design:21k:final) and the PMIP2 protocol relied on the ICE-5G topography (Peltier, 2004). To account for the sea level difference between the LGM and PI, the protocol underlines that a higher salinity of 1 psu should be ensured during the initialization of the ocean. We expect that this would partly compensate for the temperature effect by reducing the CO_2 solubility.

For ocean biogeochemistry models specifically, Kageyama et al. (2017) also recommend that "the global amount of dissolved inorganic carbon (DIC), alkalinity, and nutrients should be initially adjusted to account for the change in ocean volume. This can be done by multiplying their initial value by the relative change in global ocean volume." The implicit modeling choice here is to ensure the mass conservation of these tracers. Running a LGM experiment from a PI restart, adjusting these variables will induce an increase of their concentration. We expect that this will impact the carbon storage capacity of the ocean. Indeed, increased nutrient concentrations can boost marine productivity and consequently affect the biological pump. In addition, an increase of alkalinity lowers atmospheric CO_2 concentrations by displacing the acid-base equilibriums of inorganic carbon in favor of CO_3^{2-} (Sigman et al., 2010). These adjustments are typically done by assuming a −3% decrease in total ocean volume (Brovkin et al., 2007), or a decrease close to this value (Bouttes et al., 2010; Morée et al., 2021). However, it should be noted that these adjustments are meant to account for the sea level change at a global scale, and do not reflect local processes such as corals or shelf erosion (Broecker, 1982). Studies suggest in particular that the reduced continental shelf area during glacial times may have led to an elevated whole ocean alkalinity via reduced carbonate deposition on shelves (Kerr et al., 2017; Rickaby et al., 2010). While changes in the alkalinity budget during glacial cycles remain debated, assuming a conserved inventory is a simple and frequent choice in models which do not include sediments.

2.2. The PMIP-Carbon Model Outputs

Five General Circulation Models (GCMs: MIROC4m-COCO, CESM, MPI-ESM, IPSL-CM5A2, MIROC-ES2L) and four Earth System Models of intermediate complexity (EMICs: CLIMBER-2, iLOVECLIM, LOVECLIM, UVic) have performed carbon-cycle enabled LGM simulations submitted to the PMIP-carbon project. Most of them did not include additional glacial mechanisms (e.g., sediments, permafrost, brines, iron fertilization...) when running their LGM simulation, with the exception of MPI-ESM which includes an embedded sediment module (Ilyina et al., 2013), and MIROC4m-COCO, MIROC-ES2L, MPI-ESM and IPSL-CM5A2 in which dust-induced iron fluxes were changed at the LGM. These models and the characteristics of their LGM simulations are summed up in Table 1.

This table shows that PMIP-carbon model outputs result from differing modeling choices in terms of model resolution, boundary conditions, and CO_2 forcing (either prescribed at 190 ppm in both the radiative code and carbon cycle model, or prescribed in the radiative code but freely evolving in the carbon cycle part). In

Table 1
Characteristics of the Last Glacial Maximum Simulations of Paleoclimate Modeling Intercomparison Project (PMIP)-Carbon Models

Model name	Ocean resolution lat × lon (levels)	Atmospheric CO_2	Ice sheet reconstruction	Ocean boundary conditions	Adjustment of DIC, alkalinity, nutrients
MIROC4m	~ 1° × 1° × (43)	Freely evolving	ICE-5G	Unchanged	No
CLIMBER-2	2.5° × 3 basins (21)	Freely evolving	ICE-5G	Unchanged	Yes (−3.3%)
CESM	~ 400 – 40 km (60)	Freely evolving	ICE-6G-C	Changed	Yes (−5.7%)
iLOVECLIM	3° × 3° (20)	Freely evolving	GLAC-1D, ICE-6G-C	Changed	Yes (see Section 3.2)
MPI-ESM	3° × 3° (40)	Prescribed	GLAC-1D	Changed	Yes (see Supporting Information S1)
IPSL-CM5A2	2° – 0.5° (31)	Prescribed*	PMIP3	Changed	Yes (−3%)
MIROC-ES2L	1° × 1° (63)	Prescribed*	ICE-6G-C	Changed	Yes (−3%)
LOVECLIM	3° × 3° (20)	Prescribed*	ICE-6G-C	Unchanged	Yes (−3.3%)
UVic	3.6° × 1.8° (19)	Prescribed*	GLAC-1D, ICE-6G-C, PMIP3	Changed	No

Note. * indicates that the CO_2 concentration in both the radiative and the carbon cycle code is prescribed to 190 ppm, following the PMIP4 protocol which recommended a slight change of atmospheric CO_2 (compared to 185 ppm in PMIP3) to ensure consistency with the deglaciation protocol (Ivanovic et al., 2016). DIC, dissolved inorganic carbon.

particular, the effects of a lower sea level are accounted for differently by the models. Ocean boundary conditions (i.e., bathymetry and coastlines) are not updated in three of the LGM experiments. Furthermore, the recommended initial adjustment of ocean biogeochemistry variables (Kageyama et al., 2017) to account for the change in ocean volume is not consistently applied. Indeed, when these three variables are adjusted, it is often according to a theoretical value of around −3%, rather than according to the relative volume change imposed in models. However, considering that the ocean boundary conditions stem from different ice sheet reconstructions and are interpolated on ocean grids of various resolution, the resulting ocean volumes and relative volume change may not always be equal to this theoretical value. These differing modeling choices give us the opportunity to evaluate their impact on the simulated carbon at the LGM.

2.3. Evaluating the Ocean Volume in PMIP Models

We now focus on the total ocean volume, which conditions both the size of this carbon reservoir and the adjustment of biogeochemical variables. In models, topographic data are typically used to implement boundary conditions for the LGM (e.g., GLAC-1D, ICE-6G-C reconstructions) or PI (e.g., etopo1, Amante & Eakins, 2009). To quantify the impact of modeling choices related to the implementation of ocean boundary conditions on the ocean volume, we computed the ocean volumes of PMIP-carbon models for both the LGM and PI period. Then, we compared these values to the ocean volumes computed using topographic data (Figure 1).

2.3.1. The Ocean Volume From Topographic Data

We computed the ocean volume from the ICE-6G-C and GLAC-1D topographies, both at 21 kyr and at 0 kyr (see dotted and dashed lines in Figure 1). The ocean volume from the etopo1 topography was computed by Eakins and Sharman (2010): 1.335×10^{18} m^3 (±1%). These topographic data are of medium to high resolution: the ICE-6G-C topography is provided on a (1,080, 2,160) points grid and the GLAC-1D topography on a (360, 360) one. The etopo1 relief data have a 1 arc-minute resolution. Considering the high resolution of these data, we assume a relatively negligible error in the computed ocean volumes (with respect to reality). We use these reference values to quantify the differences (Δ) linked with the interpolation on a coarser grid and/or with modeling choices made during the implementation of boundary conditions (Table 2).

We observe that the ocean volumes associated with the ICE-6G-C and GLAC-1D topographies at 0 kyr are similar to the etopo1 ocean volume (see dotted lines on Figure 1). However, there is a difference of around 1×10^{16} m^3 between the volumes computed at the LGM (see dashed lines on Figure 1): we found 1.299×10^{18} m^3 (GLAC-1D), 1.292×10^{18} m^3 (ICE-6G-C), and 1.288×10^{18} m^3 (ICE-5G). This difference stems from the uncertainties in ice sheet reconstructions. As the Laurentide ice sheet is higher in the ICE-6G-C

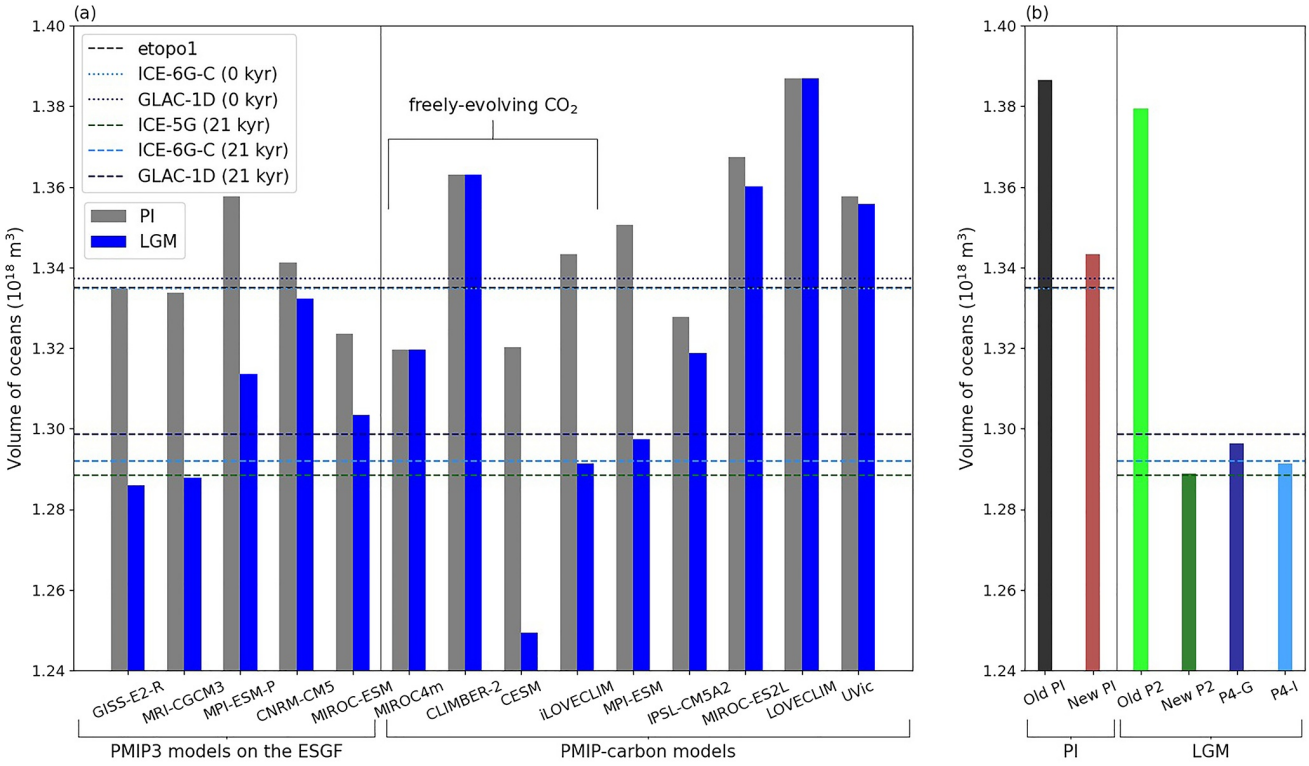

Figure 1. Ocean volume in (a) Paleoclimate Modeling Intercomparison Project (PMIP) models and (b) iLOVECLIM simulations. The iLOVECLIM reference simulations in (a) are "New pre-industrial (PI)" and "P4-I." The dashed and dotted lines represent the ocean volume computed from high-resolution topographic files (etopo1, ICE-5G, GLAC-1D, and ICE-6G-C). LGM, Last Glacial Maximum.

Table 2
Quantification in Paleoclimate Modeling Intercomparison Project (PMIP) Models of Pre-Industrial (PI) and Last Glacial Maximum (LGM) Ocean Volumes, as Well as the Volume Changes Between the LGM Simulation and Its PI Restart (LGM−PI, That Is to Say a PI-to-LGM Change)

Project	Model name	PI (10^{18} m^3)	LGM (10^{18} m^3)	Δ PI (%)	Δ LGM (%)	LGM−PI (10^{16} m^3)	Δ LGM−PI (%)	Relative change (%)
PMIP3	GISS-E2-R	1.335	1.286	−0.02	−0.48	−4.89	+13.73	−3.66
	MRI-CGCM3	1.334	1.288	−0.09	−0.33	−4.59	+6.92	−3.44
	MPI-ESM-P	1.358	1.313	+1.70	+1.66	−4.42	+2.93	−3.26
	CNRM-CM5	1.341	1.332	+0.47	+3.11	−0.91	−78.91	−0.68
	MIROC-ESM	1.323	1.303	−0.86	+0.88	−2.01	−53.32	−1.52
PMIP-carbon	MIROC4m	1.320	1.320	−1.16	+2.13	0	−100	0
	CLIMBER-2	1.363	1.363	+2.10	+5.49	0	−100	0
	CESM	1.320	1.249	−1.12	−3.25	−7.10	+65.34	−5.38
	iLOVECLIM	1.343	1.291	+0.62	−0.05	−5.19	+20.85	−3.87
	MPI-ESM	1.351	1.297	+1.17	+0.40	−5.33	+24.08	−3.95
	IPSL-CM5A2	1.328	1.319	−0.54	+2.07	−0.90	−79.05	−0.68
	MIROC-ES2L	1.367	1.360	+2.42	+5.26	−0.73	−83.09	−0.53
	LOVECLIM	1.387	1.387	+3.90	+7.35	0	−100	0
	UVic	1.358	1.356	+1.70	+4.93	−0.20	−95.33	−0.15

Note. Their differences (Δ) with respect to the ocean volume computed from PI (etopo1) and/or from LGM topographic data (ICE-6G-C, 21 kyr) are shown, indicating when an overestimated PI volume (Δ PI > 0%), LGM volume (Δ LGM > 0%), or volume change (Δ LGM−PI > 0%) seems to be observed. The relative volume change in models can also be compared to the one computed from topographic data: −2.88% (GLAC-1D) or −3.19% (ICE-6G-C).

reconstruction than in the GLAC-1D one (Kageyama et al., 2017), the ocean volume calculated from ICE-6G-C is consistent with a lower sea level. From these reconstructions, we computed a LGM−PI volume difference of around -4.30 $\times 10^{16}$ m^3 (ICE-6G-C−etopo1). We note that running LGM simulations from a PI restart entails in theory a relative volume change of −2.72% (GLAC-1D), −3.22% (ICE-6G-C), or −3.48% (ICE-5G) when this volume change is computed relative to the PI ocean volume from etopo1 topography; or −2.88% (GLAC-1D) and −3.19% (ICE-6G-C) when considering the ICE-6G-C and GLAC-1D topographies at 0 kyr. These values are close to the −3% change enforced in the initial adjustment of biogeochemical variables in some PMIP-carbon models (Table 1).

2.3.2. The Ocean Volume Implemented in PMIP Models

We used the fixed fields for each PMIP-carbon model to compute the total integrated ocean volume. To provide more elements of comparison, we also computed the ocean volumes of additional PMIP3 models. We chose the GISS-E2-R, MRI-CGCM3, MPI-ESM-P, CNRM-CM5, and MIROC-ESM models since both their LGM and PI fixed fields were available for download.

The PMIP models show a large range of ocean volumes for their PI and LGM states, and a range of LGM −PI volume changes (Figure 1a and Table 2). The difference (Δ) with the computed volume based on high-resolution topographic data (etopo1, ICE-6G-C) is significant for the majority of models: this difference amounts to less than 1% for only 6 models (out of 14) at the PI and for only 5 models at the LGM. The PMIP models with an ocean volume close to the high-resolution topographic data at both the PI and the LGM are MRI-CGCM3, GISS-E2-R, iLOVECLIM, and MPI-ESM (PMIP4). MPI-ESM-P (PMIP3) shows a slight overestimation (+ 1.7%) for both its PI and LGM volume but its relative volume change remains realistic (−3.26%). However, the LGM−PI difference is often largely underestimated (CNRM-CM5, MIROC-ESM, IPSL-CM5A2, MIROC-ES2L, UVic) or not implemented at all (MIROC4m-COCO, CLIMBER-2, LOVECLIM). As a result, these eight models significantly underestimate the relative volume change (−0% to −1.52%). Finally, CESM underestimates both the PI and the LGM volumes while being the only model largely overestimating the relative volume change (−5.38%). Although a majority of models substantially underestimate the relative volume change, the LGM−PI difference in ocean surface area is less frequently underestimated (Figure S1). This suggests that the coastlines associated with the low sea level of the LGM may have been set more carefully than the bathymetry.

We note that EMICs (CLIMBER-2, LOVECLIM, UVic) tend to substantially overestimate the PI ocean volume with respect to etopo1 data. They also show little to no change in ocean boundary conditions at the LGM (Figure 1a and Table 2). This is not the case of the iLOVECLIM model, which will be further detailed in Section 3.1 and in Figure 1b. Conversely, most GCMs also show discrepancies with the ocean volumes of topographic data at both the PI and LGM (CESM, MPI, and MIROC models) or mainly at the LGM (CNRM-CM5, IPSL-CM5A2). There is no obvious correlation between model spatial resolution and ocean volume accuracy.

Since PMIP-carbon models simulate various change of ocean volume, we expect different responses of the carbon cycle to these differing ocean boundary conditions. Indeed, the simulated ocean carbon concentrations, which depend both on mass and volume, may be merely affected by a reservoir size effect. In particular, models with a large ocean volume at the LGM may overestimate carbon storage in the ocean. Moreover, the adjustment of biogeochemical variables done in some LGM simulations (e.g., according to a theoretical − 3% change) is not necessarily consistent with the ocean volume change enforced in the models, which leads to a failed mass conservation of these tracers. It is difficult to assess the consequences of these bathymetry related modeling choices on the simulated carbon at the LGM by relying only on PMIP-carbon model outputs: these models also have differing carbon cycle modules, simulate different climate backgrounds, and do not all simulate a freely evolving CO_2 in the carbon cycle (Table 1). Therefore, we sought to evaluate the impact of these choices using additional sensitivity tests run with the iLOVECLIM model (see Appendix A).

Table 3
iLOVECLIM Simulations With Differing Ocean Boundary Conditions (BCs, i.e., Coastlines and Bathymetry), Hence the Differing Ocean Volumes Shown in Figure 1b

Simulation name	Old PI	New PI	Old P2	New P2	P4-G	P4-I
PMIP protocol	-	-	PMIP2	PMIP2	PMIP4	PMIP4
Ocean BCs from	etopo5 (1986)	etopo1 (2009)	ICE-5G	ICE-5G	GLAC-1D	ICE-6G-C
Generation method	Manual	Semi-automated	Manual	Semi-automated	Semi-automated	Semi-automated

Note. PI, pre-industrial; PMIP, Paleoclimate Modeling Intercomparison Project.

3. Evaluating the Impact of Bathymetry Related Modeling Choices on the Simulated Carbon at the LGM

3.1. Ocean Boundary Conditions in the iLOVECLIM Model and Resulting Ocean Volumes

As shown in Table 1, the iLOVECLIM LGM simulations were run with with a freely evolving CO_2 in the carbon cycle and following the PMIP4 experimental design (Kageyama et al., 2017). We used either the GLAC-1D or the ICE-6G-C ice sheet reconstruction to implement the boundary conditions (including the bathymetry and coastlines), thanks to the new semi-automated bathymetry generation method described in Lhardy et al. (2021). We also implemented new ocean boundary conditions for the PI, using a modern high-resolution topography file (etopo1) to replace the old bathymetry (adapted from etopo5, 1986). As this change of ocean boundary conditions has an impact on the ocean volume and therefore on the size of this carbon reservoir (Figure 1b), we retuned the total carbon content at the PI in order to get an equilibrated atmospheric CO_2 concentration of around 280 ppm. This content is now 632 GtC lower (41,016 GtC compared to 41,647 GtC previously). To ensure equilibrium, we then ran 5,000 years of LGM carbon simulation using this PI restart called "New PI." The two standard LGM simulations (run following the PMIP4 protocol, using either the GLAC-1D or ICE-6G-C topography) are called "P4-G" and "P4-I" respectively. To observe the effect of the semi-automated bathymetry generation method on the ocean volume, in our study, we use the fixed fields of simulations run with the former PI and LGM bathymetries (respectively "Old PI" and "Old P2"). As the latter was manually generated in the framework of the PMIP2 exercise, we also regenerated with this method the bathymetry and coastlines associated with the ICE-5G topography recommended in the PMIP2 protocol. The resulting "New P2" simulation is therefore more comparable to "Old P2" than the "P4-G" and "P4-I" simulations. All these simulations are also described in Table 3.

Figure 1b shows that with the implementation of manually tuned bathymetries, the former version of iLOVECLIM was run with overestimated ocean volumes at the PI (+ 3.86% for "Old PI") and especially at the LGM (+ 7.06% for "Old P2"). Most of the overestimation of the "Old P2" ocean volume is caused by differences in the deepest (deeper than 4 km) grid cells (Figure S2), rather than the slight overestimation of the ocean surface area (Figure S1b). As a result, iLOVECLIM used to simulate only 15% of the LGM–PI volume change (Table S1). However, we now have much more realistic ocean volume values in the current version of iLOVECLIM, both at the PI ("New PI") and at the three new LGM simulations ("New P2," "P4-G," and "P4-I"). Indeed, these values are all fairly close to their references (etopo1, ICE-5G, GLAC-1D, and ICE-6G-C respectively), though there is still a small overestimation of the PI ocean volume. Despite the interpolation of the bathymetry on a relatively coarse ocean grid, it is interesting to note that the differences (Δ) with respect to topographic data are now of the same order of magnitude as other GCMs of higher resolution (Table 1), and smaller than most models. Since this improvement can be attributed to the bathymetry generation method which notably leads to a reduced number of deep and voluminous grid cells in iLOVECLIM LGM runs (Figure S2), we speculate that the effect of the sea level drop in abyssal plain areas is regularly overlooked in models.

3.2. Modeling Choices Related to the Boundary Conditions Change and Set of LGM Simulations With iLOVECLIM

We made several modifications to the code of iLOVECLIM to allow for a change of ocean boundary conditions in an automated way. These developments allow us to run carbon simulations with the iLOVECLIM

model under any given change of ocean boundary conditions (PI, GLAC-1D, ICE-6G-C, or otherwise). First, we ensured a systematic conservation of salt. Indeed, the boundary conditions changes associated with a lower glacial sea level cause a loss of the salt contained in some grid cells such as the ones corresponding to the continental shelves. In LGM runs, 1 psu is usually added to the PI salinity to compensate for this loss (Kageyama et al., 2017). We computed the total salt content before and after initialization and the lost salt was added uniformly over the whole deep ocean (>1 km). In iLOVECLIM, this automated modification is equivalent to an addition of 0.96 psu (GLAC-1D boundary conditions) or 1.11 psu (ICE-6G-C) to the PI salinity. Second, we coded an automated adjustment of ocean biogeochemistry variables. We chose to conserve the total alkalinity, nitrate and phosphate concentrations, and DIC, instead of multiplying their initial values by a relative volume change. This choice allows us to take into account not only the global sea level change, but also the distribution patterns of the tracers which would have been lost during the change of boundary conditions. Finally, the change of bathymetry and coastlines from PI to LGM conditions can also cause a loss in the ocean organic carbon pools (i.e., phytoplankton, zooplankton, dissolved organic carbon, particulate organic carbon, and calcium carbonate). To account for it, we ensured an automated conservation of the total model carbon content. We computed the total carbon content before and after initialization and the carbon from organic pools which would have been lost was put into the atmosphere, which then re-equilibrated with the ocean during the run.

We aim at quantifying the impact of modeling choices which relate to the change of ocean boundary conditions on the simulated carbon, that is:

1. Adjustments of alkalinity, nutrients, DIC
2. Automated conservation of the total salt content
3. Automated conservation of the total carbon content, as described above

To do this, we ran sensitivity tests using the ICE-6G-C boundary conditions (like "P4-I") but without one or two of these choices: these simulations are called "alk-," "nut-," "DIC-/C-," "C-," and "salt-." To be clear, "alk," "nut," and "DIC" refer to the adjustments of alkalinity, nutrients and DIC, while "C" refers to the total carbon content conservation and "salt" to the total salt content conservation. We ran "DIC-/C-" both without the DIC adjustment and without the total carbon content conservation to be able to see the impact of the DIC adjustment. As a matter of fact, a "DIC-" simulation (not shown here) results in the same carbon distribution in reservoirs as the reference "P4-I," albeit after a longer equilibration time. Indeed, the total carbon content conservation – ensured by transferring the lost carbon to the atmosphere – makes up for the missing DIC adjustment, though the ocean and atmosphere need more time to re-equilibrate.

As the ocean boundary conditions are not always implemented in LGM simulations of PMIP-carbon models, we also ran a LGM simulation with the PI coastlines and bathymetry (called "PIbathy"). As a consequence, there was no change of ocean volume nor any adjustment of biogeochemical variables during the initialization of this simulation. Finally, this ensemble of simulations is completed by "PIbathy, alk+". In this LGM simulation with the PI ocean boundary conditions, we increased the initial alkalinity according to a theoretical relative change of volume, since this is a modeling choice of some PMIP-carbon models. All simulations and the modeling choices related to the change of boundary conditions are summed up in Table 4.

3.3. Simulated Carbon at the LGM

To assess the impact on the simulated carbon of these modeling choices which relates to the change of ocean boundary conditions, we computed the carbon content of each carbon reservoir (atmosphere, ocean, terrestrial biosphere) in PMIP-carbon models and iLOVECLIM sensitivity tests. Typically for the ocean, the concentration in each carbon pool (e.g., DIC, dissolved organic carbon, particulate carbon, phytoplankton...) was summed, integrated on the ocean grid (weighted by the grid cell volume), and converted into GtC. The equilibrated atmospheric CO_2 concentrations of PMIP-carbon models with freely evolving CO_2 in the carbon cycle are presented in Figure 2a. The interested reader will find the carbon content of all reservoirs and models in Figure S3.

Among the PMIP-carbon models, about half have thus far run with a freely evolving CO_2 for the carbon cycle (MIROC4m-COCO, CLIMBER-2, CESM, and iLOVECLIM). Furthermore, among this subset, only

Table 4
Bathymetry Related Modeling Choices of the Last Glacial Maximum Simulations With iLOVECLIM

Simulation name	P4-G	P4-I	Salt-	C-	DIC-/C-	Nut-	Alk-	PIbathy	PIbathy, alk+
Ocean BCs	G	I	I	I	I	I	I	PI	PI
Salt conservation	×	×	No	×	×	×	×	–	–
Carbon conservation	×	×	×	No	No	×	×	–	–
DIC adjustment	×	×	×	×	No	×	×	–	–
Nutrients adjustment	×	×	×	×	×	No	×	–	–
Alkalinity adjustment	×	×	×	×	×	×	No	–	Yes

Note. Ocean boundary conditions (BCs, i.e., coastlines, bathymetry, and the resulting ocean volume) are specified by the letters G (GLAC-1D), I (ICE-6G-C), or PI (etopo1). Crosses indicate that the automated conservation of salt and carbon and adjustment of biogeochemical variables are done according to the relative change of volume (here relative to the PI restart). Hyphens indicate that these adjustments are inactive due to the absence of ocean boundary conditions change. "No" indicates in which simulation these adjustments are deliberately switched off and "yes" when they are done according to a theoretical value (−3.22%, the relative change of volume between from etopo1 to ICE-6G-C). DIC, dissolved inorganic carbon; PI, pre-industrial.

CESM and iLOVECLIM are fully comparable in terms of carbon outputs, as they both have run with LGM ocean boundary conditions and include a vegetation model. We observe that these two models both typically simulate high CO_2 concentrations at the LGM (331 and 315 ppm respectively, see Figure 2a). These values are very far from the CO_2 levels inferred from data (~190 ppm, Bereiter et al., 2015; Ivanovic et al., 2016) as they are even higher than the PI levels (280 ppm).

3.3.1. In iLOVECLIM

Looking at the carbon distribution simulated in the different reservoirs by the iLOVECLIM model (Table 5), we observe that although the ocean volume is smaller, the ocean is effectively trapping more carbon at the LGM (+272 GtC for "P4-I" compared to "New PI"). However, the terrestrial biosphere sink is also less efficient due to lower temperatures and the presence of large ice sheets (−344 GtC). Overall, it results in higher atmospheric concentrations as the ocean sink is not enhanced enough to compensate for the smaller terrestrial biosphere sink. The carbon outputs from the two standard LGM simulations ("P4-G" and "P4-I") suggest that the ice sheet reconstruction (GLAC-1D or ICE-6G-C) chosen to implement the boundary conditions has a small impact on the simulated carbon (as well as the ocean volume, see Figure 1b and Table S1).

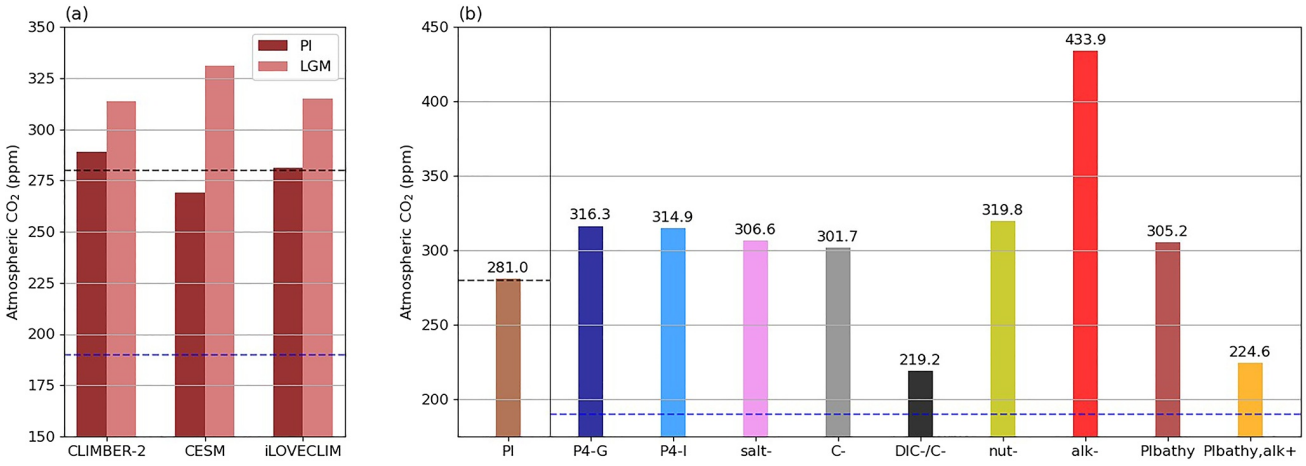

Figure 2. Atmospheric CO_2 (ppm) in (a) Paleoclimate Modeling Intercomparison Project-carbon models with a freely evolving CO_2 in the carbon cycle (excluding the ocean-only MIROC4m-COCO) and (b) iLOVECLIM simulations. The iLOVECLIM reference simulations in (a) are "New pre-industrial (PI)" and "P4-I." The gray and blue dashed lines represents the atmospheric CO_2 concentrations at the PI (280 ppm) and Last Glacial Maximum (LGM) (190 ppm, Bereiter et al., 2015).

Table 5
Quantification in iLOVECLIM Simulations of the Carbon Content in Reservoirs (GtC) and Differences (GtC) With Respect to "P4-I"

Simulation name	New PI	P4-G	P4-I	Salt-	C-	DIC-/C-	Nut-	Alk-	PIbathy	PIbathy, alk+
Atmosphere (GtC)	599	674	671	653	643	467	681	924	650	478
Ocean (GtC)	38,480	38,728	38,753	38,767	38,627	37,599	38,742	38,499	39,020	39,191
Vegetation (GtC)	1,937	1,615	1,593	1,596	1,593	1,593	1,593	1,593	1,347	1,347
Atmosphere difference	−72	+3	0	−18	−28	−204	+10	+254	−21	−192
Ocean difference	−272	−25	0	+14	−126	−1153	−10	−253	+267	+439
Vegetation difference	+344	+22	0	+3	0	0	0	0	−246	−246

Note. DIC, dissolved inorganic carbon; PI, pre-industrial.

Using the iLOVECLIM sensitivity tests, we quantify the carbon content variations associated with the modeling choices made to accommodate the change of ocean boundary conditions. If the total salt content conservation is not ensured ("salt-"), we get slightly lower CO_2 concentrations (8 ppm lower), as the CO_2 solubility is greater when the salinity is lower. The total carbon content conservation apparently has a relatively small effect on the CO_2 (13 ppm lower), but is actually essential when the DIC adjustment is not done either ("DIC-/C-"): in this case, 1,357 GtC are lost, and the CO_2 concentration is much closer to the LGM data value but for the wrong reason, that is, a loss of total carbon from the system. Only 154 GtC are lost in the "C-" simulation, which amount to the lost organic carbon. Indeed, the DIC adjustment compensates for most of the lost carbon as the DIC is the largest carbon pool in the ocean. As for the other two recommended adjustments, the nutrient adjustment has a relatively small effect through a marine productivity boost (+5 ppm without it, see "nut-") whereas the alkalinity adjustment is much more critical. Indeed, the simulation without it ("alk-") has a CO_2 reaching as high as 434 ppm: an increased alkalinity reduces the atmospheric CO_2 concentration (by 254 GtC). Given the large effect of this adjustment, the method used to implement it is crucial.

In addition, we quantify the carbon content simulated at the LGM with no change of ocean boundary conditions in iLOVECLIM. We see from the "PIbathy" simulation that a larger ocean volume can significantly increase the ocean carbon content at the LGM (+267 GtC, close to a doubling of the LGM−PI difference), but in this instance at the expense of the terrestrial carbon (−246 GtC). This difference in terrestrial carbon content can be explained by the second ocean boundary condition, as the PI coastlines yield less available land surfaces to grow vegetation. While this compensation of errors causes a relatively small change of atmospheric CO_2 concentration, we argue here that not changing the bathymetry while performing LGM experiments significantly affects the carbon distribution since it can potentially trap twice as much carbon in the ocean. Furthermore, if this absence of ocean boundary conditions change is combined with the adjustment of alkalinity (considering the theoretical relative volume change between etopo1 and ICE-6G-C, see "PIbathy, alk+"), the carbon storage of the ocean is increased even more. This time, the drop of atmospheric CO_2 concentration is much more significant as there is no additional compensating effect of the terrestrial biosphere.

3.3.2. In PMIP-Carbon Models

Finally, since the ocean is thought to have played a major role in explaining the pCO_2 drawdown at the LGM, we now examine the ocean carbon content simulated by PMIP-carbon models in light of our findings on ocean volume. We know that PMIP-carbon models simulate various total carbon content (Figure S3b). To be able to compare their carbon content in the ocean, we therefore plotted in Figure 3 the percentage of carbon in the ocean at the PI and LGM, against the ocean volume. Figure 3 clearly shows four distinct model behaviors. CLIMBER-2 and LOVECLIM, which have run with no change of ocean boundary conditions, show a significantly larger proportion of carbon in the oceans under LGM conditions (+1.5% and +2.1% respectively). IPSL-CM5A2, MIROC-ES2L, and UVic have run with a limited change of ocean volume, and they also simulate a large increase of carbon storage in the oceans between their PI and LGM states (+2.6%, +2.1%, and 1.7% respectively). In contrast, the ocean carbon content of iLOVECLIM and CESM increases at the LGM, but this variation (+0.7% and +0.8%) is relatively smaller than in other models with no large

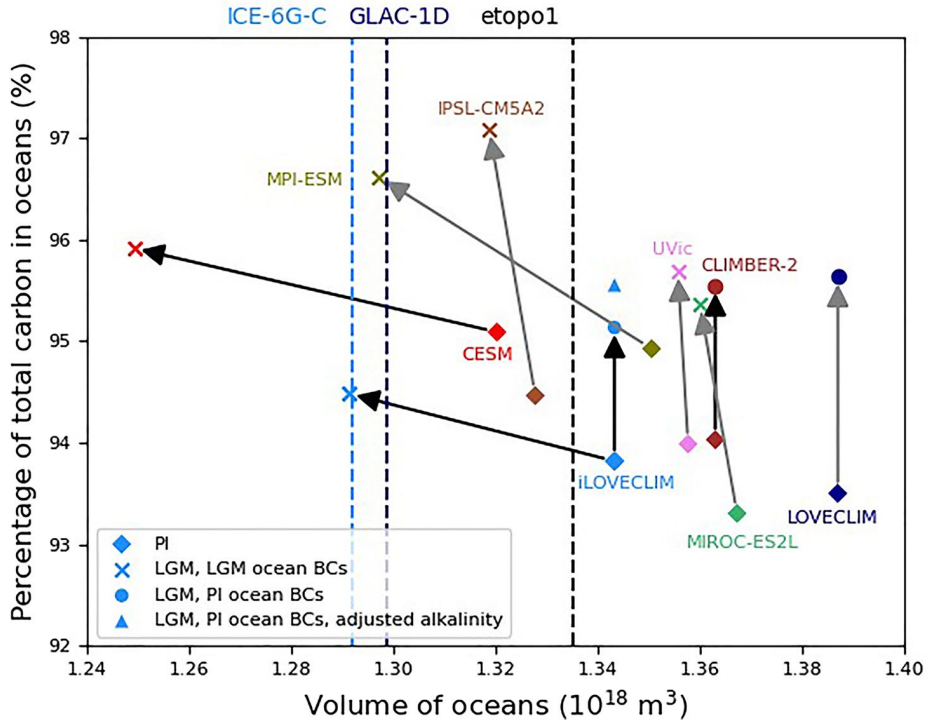

Figure 3. Ocean carbon versus ocean volume plot for a subset of Paleoclimate Modeling Intercomparison Project-carbon models (excluding the ocean-only MIROC4m-COCO) and iLOVECLIM simulations ("P4-I," "PIbathy," and "PIbathy, alk+"). The dashed lines represent the ocean volume computed from high-resolution topographic files (etopo1, GLAC-1D, ICE-6G-C). The pre-industrial (PI) to Last Glacial Maximum (LGM) changes are traced by the gray (prescribed CO_2) and black (freely evolving CO_2) arrows. BCs stands for boundary conditions.

change of ocean boundary conditions. The exception is MPI-ESM, which displays both a large change of ocean volume and carbon storage (+1.7%). It is however not fully comparable to iLOVECLIM and CESM models as it also ran with a prescribed CO_2 in the carbon cycle. Finally, we underline that the two iLOVECLIM simulations with no change of ocean volume show a larger increase of carbon storage in the oceans (+1.3% and +1.7% for "PIbathy" and "PIbathy, alk+" respectively). Therefore, it is likely that other models would also simulate lower carbon sequestration in the oceans and high atmospheric CO_2 concentration values (much larger than 190 ppm, if freely evolving) if they had a lower ocean volume at the LGM.

4. Discussion and Conclusion

In this study, we use preliminary results of the PMIP-carbon project and sensitivity tests run with the iLOVECLIM model at the LGM to quantify the consequences of bathymetry related modeling choices on the simulated carbon at the global scale. We consider the effects of the ocean volume change and of the resulting biogeochemical variables adjustments recommended in Kageyama et al. (2017).

We show that the implementation of ocean boundary conditions in PMIP models rarely results in accurate ocean volumes. We suggest that this may not be primarily related to the model resolution, since we get a much more realistic ocean volume in iLOVECLIM after developing a new method to generate the bathymetry despite the relatively coarse resolution of its ocean model. In fact, the ocean boundary conditions (i.e., bathymetry, coastlines) associated with the low sea level of the LGM are not systematically generated in models. When they are, modeling groups often mostly concentrate on setting the coastlines ("land-sea mask") and the bathymetry of shallow grid cells in order to simulate a reasonable ocean circulation. However, the ocean volume is mostly affected by the bathymetry of deep grid cells in models with irregular vertical levels. Setting the bathymetry of these deep grid cells to account for a sea level of −134 m (Lambeck et al., 2014) at the LGM, even if the vertical resolution exceeds such a value, will move up the ocean floor

here and there depending on the outcome of vertical interpolation. As a result, the overall volume of deep levels should be closer to reality. It is therefore important to account for the −134 m sea level change before the vertical interpolation done to generate the bathymetry in order to implement a realistic volume change between PI and LGM.

While these modeling choices may have little consequences on the climate variables usually examined in PMIP intercomparison papers, we argue that their effects on the simulated carbon cannot be overlooked, considering the role of the deep ocean on carbon storage (Skinner, 2009). In the iLOVECLIM model, the carbon distribution in reservoirs is significantly affected when the low sea level is not taken into account. Indeed, in the absence of a change of ocean boundary conditions in LGM runs, the carbon sequestration in the ocean is increased twofold due to the larger size of this reservoir. In contrast, more carbon is lost in the terrestrial biosphere as the coastlines of the PI do not allow for emerged continental shelves to grow vegetation. While different model biases may limit carbon sequestration in the ocean (e.g., underestimated stratification, sea ice, efficiency of the biological pump), an overestimated ocean volume at the LGM has an opposite effect. It is therefore even more challenging for models with a realistic ocean volume at the LGM to simulate the pCO_2 drawdown.

Kageyama et al. (2017) recommend an adjustment of DIC, nutrients, and alkalinity to account for the change of ocean volume between the PI and the LGM. We quantify the effects of each on the simulated carbon at the LGM in the iLOVECLIM model. The DIC adjustment shortens the equilibration time but is not essential as long as carbon conservation is otherwise ensured. We observe a limited effect of the nutrients adjustment but adjusting the alkalinity yields a large increase of carbon sequestration in the ocean (~ 250 GtC). As a result, this last adjustment should be cautiously made. Multiplying the initial alkalinity by a theoretical value of around 3% which is potentially far from the implemented relative change of volume can significantly decrease the atmospheric CO_2 concentration.

The quantified effects of these modeling choices in iLOVECLIM depend on the carbon cycle module and on the simulated climate (e.g., surface temperatures, deep ocean circulation, sea ice). In that respect, quantifications using other models would be useful to assess the robustness of these results, which can be affected by model biases. Further studies using coupled carbon-climate models including sediments may be especially desirable to be able to compute the alkalinity budget from riverine inputs and $CaCO_3$ burial (Sigman et al., 2010), as accounting for this mechanism may significantly increase the simulated pCO_2 drawdown (Brovkin et al., 2007, 2012; Kobayashi & Oka, 2018). Still, these results give us a sense of the magnitude of each effect. We stress here that the ocean volume and the alkalinity adjustment should be both carefully considered in coupled carbon-climate simulations at the LGM as there is a risk of simulating a low CO_2 for the wrong reasons.

At present, PMIP-carbon models with a freely evolving CO_2 are all simulating an increased carbon sequestration into the ocean at the LGM, but also high atmospheric concentrations (>300 ppm). Overall, the enhanced carbon sink of the ocean is therefore not compensating for the loss of carbon in the terrestrial biosphere due to the lower temperatures and extensive ice sheets. Causes for the glacial CO_2 drawdown can be sought inside (e.g., physical and biogeochemical biases, Morée et al. (2021)) or outside (e.g., iron, terrestrial vegetation, sediments, permafrost) of the modeled ocean. However, investigating the processes behind the pCO_2 drawdown at the LGM and their limitations in model representation remains a challenge insofar as model outputs are hardly comparable. Our findings emphasize the need for documenting the ocean volume in models and defining a stricter protocol for PMIP-carbon models with the view of improving coupled climate-carbon simulations intercomparison potential. One practical recommendation in future PMIP protocols could be to enforce an alkalinity adjustment based on the actual (rather than theoretical) change of ocean volume implemented in biogeochemistry models at the LGM. Explicit guidelines concerning the change of ocean volume and related modeling choices may also be relevant for other target periods of paleoclimate modeling.

Appendix A: Description of the iLOVECLIM Model Under the PMIP Experimental Design

The iLOVECLIM model (Goosse et al., 2010) is an EMIC. Its standard version includes an atmospheric component (ECBilt), a simple land vegetation module (VECODE) and an ocean general circulation model named CLIO, of relatively coarse resolution ($3° \times 3°$ and 20 irregular vertical levels). In addition, a carbon cycle model is fully coupled to these components. Originated from a NPZD ecosystem model (Six & Maier-Reimer, 1996), it was further developed in the CLIMBER-2 model (Brovkin, Bendtsen, et al., 2002; Brovkin et al., 2007; Brovkin, Hofmann, et al., 2002) before it was also implemented in iLOVECLIM (Bouttes et al., 2015).

The iLOVECLIM model is typically used to simulate past climates such as the LGM, and contributed to previous PMIP exercises (Otto-Bliesner et al., 2007; Roche et al., 2012) under its PMIP2 version (Roche et al., 2007), as well as to the current PMIP4 exercise (Kageyama et al., 2021). The LGM simulations run with iLOVECLIM follow the standardized experimental design described in the PMIP4 protocol (Kageyama et al., 2017). In order to assess the impact of the ice sheet reconstruction choice, we implemented the boundary conditions associated with the two most recent reconstructions (GLAC-1D and ICE-6G-C, both recommended in Ivanovic et al., 2016) in the iLOVECLIM model, using a new semi-automated bathymetry generation method described in Lhardy et al. (2021). The change of bathymetry and coastlines was automated for the most part, with a few unavoidable manual changes in straits and key passages. We also implemented new ocean boundary conditions for the PI, using a modern high-resolution topography file (etopo1, Amante & Eakins, 2009) to replace the old bathymetry (adapted from etopo5, 1986).

Acknowledgments
F. Lhardy, N. Bouttes, and D. M. Roche designed the research. N. Bouttes coordinated the PMIP-carbon project and obtained funding. Participating modeling groups all performed a PI and a LGM simulation, provided their model outputs and the relevant metadata and computed the equilibrated carbon content in reservoirs. These modeling groups included AA-O, HK, and AO (MIROC4m-COCO); KC (CLIMBER-2); MJ, RN, GV, and ZC (CESM); BL and TI (MPI-ESM); MK (IPSL-CM5A2); AY (MIROC-ES2L); LM (LOVECLIM); JM and AS (UVic). F. Lhardy, D. M. Roche, and N. Bouttes generated new boundary conditions in the iLOVECLIM model. N. Bouttes and D. M. Roche developed the automated adjustments to allow for a change of ocean boundary conditions. F. Lhardy ran the iLOVECLIM simulations and analyzed both the iLOVECLIM and the PMIP-carbon outputs under supervision of N. Bouttes and D. M. Roche. F. Lhardy wrote the manuscript with the inputs from all co-authors. This study was supported by the French National program LEFE (Les Enveloppes Fluides et l'Environnement). F. Lhardy is supported by the Université Versailles Saint-Quentin-en-Yvelines (UVSQ). N. Bouttes and D. M. Roche are supported by the Centre national de la recherche scientifique (CNRS). In addition, D. M. Roche is supported by the Vrije Universiteit Amsterdam. B. Liu and T. Ilyina are supported by the German Federal Ministry of Education and Research (PalMod initiative, FKZ: 420 grant no. 01LP1919B). L. Menviel acknowledges funding from the Australian Research Council grant FT180100606. A. Yamamoto acknowledges funding from the Integrated Research Program for Advancing Climate Models (TOUGOU) Grant Number JPMXD0717935715 from the Ministry of Education, Culture, Sports, Science and Technology (MEXT), Japan. The authors acknowledge the use of the LSCE storage and computing facilities. The authors thank Théo Mandonnet for his preliminary work on the PMIP-carbon project. Last but not least, the authors thank the two anonymous reviewers for their help with this manuscript.

Conflict of Interest

The authors declare no conflicts of interest relevant to this study.

Data Availability Statement

The model outputs of PMIP-carbon models and iLOVECLIM simulations are available for download online (doi: 10.5281/zenodo.5464162). The fixed fields of GISS-E2-R, MRI-CGCM3, MPI-ESM-P, CNRM-CM5, and MIROC-ESM models can also be found at https://esgf-node.llnl.gov/projects/cmip5/. Descriptions of the PMIP-carbon models can be found in Kobayashi and Oka (2018) (MIROC4m-COCO), Petoukhov et al. (2000) and Ganopolski et al. (2001) (CLIMBER), Bouttes et al. (2015) and Lhardy et al. (2021) (iLOVECLIM), Liu et al. (2021), Mauritsen et al. (2019) and references therein (MPI-ESM), Ohgaito et al. (2021) and Hajima et al. (2020) (MIROC-ES2L).

References

Abe-Ouchi, A., Saito, F., Kageyama, M., Braconnot, P., Harrison, S. P., Lambeck, K., et al. (2015). Ice-sheet configuration in the CMIP5/PMIP3 Last Glacial Maximum experiments. *Geoscientific Model Development*, *8*, 3621–3637. https://doi.org/10.5194/gmd-8-3621-2015

Aldama-Campino, A., Fransner, F., Ödalen, M., Groeskamp, S., Yool, A., Döös, K., & Nycander, J. (2020). Meridional ocean carbon transport. *Global Biogeochemical Cycles*, *34*. https://doi.org/10.1029/2019GB006336

Amante, C., & Eakins, B. W. (2009). *ETOPO1 1 arc-minute global relief model: Procedures, data sources and analysis* (NOAA Technical Memorandum NESDIS NGDC-24). National Geophysical Data Center, NOAA. Retrieved from https://www.ngdc.noaa.gov/mgg/global/global.html

Anderson, R. F., Sachs, J. P., Fleisher, M. Q., Allen, K. A., Yu, J., Koutavas, A., & Jaccard, S. L. (2019). Deep-sea oxygen depletion and ocean carbon sequestration during the last ice age. *Global Biogeochemical Cycles*, *33*, 301–317. https://doi.org/10.1029/2018GB006049

Argus, D. F., Peltier, W. R., Drummond, R., & Moore, A. W. (2014). The Antarctica component of postglacial rebound model ICE-6G-C (VM5a) based on GPS positioning, exposure age dating of ice thicknesses, and relative sea level histories. *Geophysical Journal International*, *198*, 537–563. https://doi.org/10.1093/gji/ggu140

Bereiter, B., Eggleston, S., Schmitt, J., Nehrbass-Ahles, C., Stocker, T. F., Fischer, H., et al. (2015). Revision of the EPICA Dome C CO_2 record from 800 to 600 kyr before present. *Geophysical Research Letters*, *42*, 542–549. https://doi.org/10.1002/2014GL061957

Bopp, L., Kohfeld, K. E., Le Quéré, C., & Aumont, O. (2003). Dust impact on marine biota and atmospheric CO_2 during glacial periods. *Paleoceanography*, *18*(2). https://doi.org/10.1029/2002PA000810

Bouttes, N., Paillard, D., & Roche, D. M. (2010). Impact of brine-induced stratification on the glacial carbon cycle. *Climate of the Past*, *6*(5), 575–589. https://doi.org/10.5194/cp-6-575-2010

Bouttes, N., Roche, D. M., Mariotti, V., & Bopp, L. (2015). Including an ocean carbon cycle model into iLOVECLIM (v1.0). *Geoscientific Model Development*, *8*, 1563–1576. https://doi.org/10.5194/gmd-8-1563-2015

Broecker, W. S. (1982). Ocean chemistry during glacial time. *Geochimica et Cosmochimica Acta*, *46*, 1689–1705. https://doi.org/10.1016/0016-7037(82)90110-7

Brovkin, V., Bendtsen, J., Claussen, M., Ganopolski, A., Kubatzki, C., Petoukhov, V., & Andreev, A. (2002). Carbon cycle, vegetation, and climate dynamics in the Holocene: Experiments with the CLIMBER-2 model. *Global Biogeochemical Cycles*, *16*. https://doi.org/10.1029/2001GB001662

Brovkin, V., Ganopolski, A., Archer, D., & Munhoven, G. (2012). Glacial CO_2 cycle as a succession of key physical and biogeochemical processes. *Climate of the Past*, *8*, 251–264. https://doi.org/10.5194/cp-8-251-2012

Brovkin, V., Ganopolski, A., Archer, D., & Rahmstorf, S. (2007). Lowering of glacial atmospheric CO_2 in response to changes in oceanic circulation and marine biogeochemistry. *Paleoceanography*, *22*, PA4202. https://doi.org/10.1029/2006PA001380

Brovkin, V., Hofmann, M., Bendtsen, J., & Ganopolski, A. (2002). Ocean biology could control atmospheric $\delta^{13}C$ during glacial-interglacial cycle. *Geochemistry, Geophysics, Geosystems*, *3*(1027), 1–15. https://doi.org/10.1029/2001GC000270

Buchanan, P. J., Matear, R. J., Lenton, A., Phipps, S. J., Chase, Z., & Etheridge, D. M. (2016). The simulated climate of the Last Glacial Maximum and insights into the global marine carbon cycle. *Climate of the Past*, *12*, 2271–2295. https://doi.org/10.5194/cp-12-2271-2016

Eakins, B., & Sharman, G. (2010). *Volumes of the world's oceans from ETOPO1*. NOAA National Geophysical Data Center. Retrieved from https://www.ngdc.noaa.gov/mgg/global/etopo1_ocean_volumes.html

Francois, R., Altabet, M. A., Yu, E.-F., Sigman, D. M., Bacon, M. P., Frankk, M., et al. (1997). Contribution of Southern Ocean surface-water stratification to low atmospheric CO_2 concentrations during the last glacial period. *Nature*, *389*, 929–935. https://doi.org/10.1038/40073

Ganopolski, A., Petoukhov, V., Rahmstorf, S., Brovkin, V., Claussen, M., Eliseev, A., & Kubatzki, C. (2001). CLIMBER-2: A climate system model of intermediate complexity. Part II: Model sensitivity. *Climate Dynamics*, *17*(10), 735–751. https://doi.org/10.1007/S003820000144

Goosse, H., Brovkin, V., Fichefet, T., Haarsma, R., Huybrechts, P., Jongma, J., et al. (2010). Description of the Earth system model of intermediate complexity LOVECLIM version 1.2. *Geoscientific Model Development*, *3*(2), 603–633. https://doi.org/10.5194/gmd-3-603-2010

Gottschalk, J., Battaglia, G., Fischer, H., Frölicher, T. L., Jaccard, S. L., Jeltsch-Thömmes, A., et al. (2020). Mechanisms of millennial-scale atmospheric CO_2 change in numerical model simulations. *Quaternary Science Reviews*, *220*, 30–74. https://doi.org/10.1016/j.quascirev.2019.05.013

Hain, M. P., Sigman, D. M., & Haug, G. H. (2010). Carbon dioxide effects of Antarctic stratification, North Atlantic Intermediate Water formation, and subantarctic nutrient drawdown during the last ice age: Diagnosis and synthesis in a geochemical box model. *Global Biogeochemical Cycles*, *24*, GB4023. https://doi.org/10.1029/2010GB003790

Hajima, T., Watanabe, M., Yamamoto, A., Tatebe, H., Noguchi, M. A., Abe, M., et al. (2020). Development of the MIROC-ES2L Earth system model and the evaluation of biogeochemical processes and feedbacks. *Geoscientific Model Development*, *13*, 2197–2244. https://doi.org/10.5194/gmd-13-2197-2020

Ilyina, T., Six, K. D., Segschneider, J., Maier-Reimer, E., Li, H., & Núñez Riboni, I. (2013). Global ocean biogeochemistry model HAMOCC: Model architecture and performance as component of the MPI-Earth system model in different CMIP5 experimental realizations. *Journal of Advances in Modeling Earth Systems*, *5*, 287–315. https://doi.org/10.1029/2012MS000178

Ivanovic, R. F., Gregoire, L. J., Kageyama, M., Roche, D. M., Valdes, P. J., Burke, A., et al. (2016). Transient climate simulations of the deglaciation 21–9 thousand years before present (version 1)—PMIP4 Core experiment design and boundary conditions. *Geoscientific Model Development*, *9*, 2563–2587. https://doi.org/10.5194/gmd-9-2563-2016

Jones, C. D., Arora, V., Friedlingstein, P., Bopp, L., Brovkin, V., Dunne, J., et al. (2016). C4MIP—The Coupled Climate–Carbon Cycle Model Intercomparison Project: Experimental protocol for CMIP6. *Geoscientific Model Development*, *9*, 2853–2880. https://doi.org/10.5194/gmd-9-2853-2016

Kageyama, M., Albani, S., Braconnot, P., Harrison, S. P., Hopcroft, P. O., Ivanovic, R. F., et al. (2017). The PMIP4 contribution to CMIP6—Part 4: Scientific objectives and experimental design of the PMIP4-CMIP6 Last Glacial Maximum experiments and PMIP4 sensitivity experiments. *Geoscientific Model Development*, *10*, 4035–4055. https://doi.org/10.5194/gmd-10-4035-2017

Kageyama, M., Braconnot, P., Harrison, S. P., Haywood, A. M., Jungclaus, J. H., Otto-Bliesner, B. L., et al. (2018). The PMIP4 contribution to CMIP6—Part 1: Overview and over-arching analysis plan. *Geoscientific Model Development*, *11*, 1033–1057. https://doi.org/10.5194/gmd-11-1033-2018

Kageyama, M., Harrison, S. P., Kapsch, M.-L., Löfverström, M., Lora, J. M., Mikolajewicz, U., et al. (2021). The PMIP4-CMIP6 Last Glacial Maximum experiments: Preliminary results and comparison with the PMIP3-CMIP5 simulations. *Climate of the Past*. https://doi.org/10.5194/cp-2019-169

Kerr, J., Rickaby, R., Yu, J., Elderfield, H., & Sadekov, A. Y. (2017). The effect of ocean alkalinity and carbon transfer on deep-sea carbonate ion concentration during the past five glacial cycles. *Earth and Planetary Science Letters*, *471*, 42–53. https://doi.org/10.1016/j.epsl.2017.04.042

Khatiwala, S., Schmittner, A., & Muglia, J. (2019). Air-sea disequilibrium enhances ocean carbon storage during glacial periods. *Science Advances*, *5*(6), eaaw4981. https://doi.org/10.1126/sciadv.aaw4981

Kobayashi, H., & Oka, A. (2018). Response of atmospheric CO_2 to glacial changes in the southern ocean amplified by carbonate compensation. *Paleoceanography and Paleoclimatology*, *33*, 1206–1229. https://doi.org/10.1029/2018PA003360

Kohfeld, K. E., & Ridgwell, A. (2009). Glacial-interglacial variability in atmospheric CO_2. In Surface ocean-lower atmosphere processes Vol. (187, pp. 251–286). https://doi.org/10.1029/2008GM000845

Lambeck, K., Rouby, H., Purcell, A., Sun, Y., & Sambridge, M. (2014). Sea level and global ice volumes from the Last Glacial Maximum to the Holocene. *Proceedings of the National Academy of Sciences*, *111*(43), 15296–15303. https://doi.org/10.1073/pnas.1411762111

Lhardy, F., Bouttes, N., Roche, D. M., Crosta, X., Waelbroeck, C., & Paillard, D. (2021). Impact of Southern Ocean surface conditions on deep ocean circulation at the LGM: A model analysis. *Climate of the Past*. https://doi.org/10.5194/cp-2020-148

Liu, B., Six, K. D., & Ilyina, T. (2021). Incorporating the stable carbon isotope ^{13}C in the ocean biogeochemical component of the Max Planck Institute Earth System Model. *Biogeosciences*, *18*, 4389–4429. https://doi.org/10.5194/bg-18-4389-2021

Lüthi, D., Le Floch, M., Bereiter, B., Blunier, T., Barnola, J.-M., Siegenthaler, U., et al. (2008). High-resolution carbon dioxide concentration record 650,000–800,000 years before present. *Nature*, *453*, 379–382. https://doi.org/10.1038/nature06949

Marzocchi, A., & Jansen, M. F. (2019). Global cooling linked to increased glacial carbon storage via changes in Antarctic sea ice. *Nature Geoscience*, *12*, 1001–1005. https://doi.org/10.1038/s41561-019-0466-8

Matsumoto, K., & Sarmiento, J. L. (2002). Silicic acid leakage from the Southern Ocean: A possible explanation for glacial atmospheric pCO_2. *Global Biogeochemical Cycles*, *16*(3). https://doi.org/10.1029/2001GB001442

Mauritsen, T., Bader, J., Becker, T., Behrens, J., Bittner, M., Brokopf, R., et al. (2019). Developments in the MPI-M Earth System Model version 1.2 (MPI-ESM1.2) and its response to increasing CO_2. *Journal of Advances in Modeling Earth Systems*, *11*, 998–1038. https://doi.org/10.1029/2018MS001400

Menviel, L., Joos, F., & Ritz, S. P. (2012). Simulating atmospheric CO_2, ^{13}C and the marine carbon cycle during the Last Glacial-Interglacial cycle: Possible role for a deepening of the mean remineralization depth and an increase in the oceanic nutrient inventory. *Quaternary Science Reviews*, *56*, 46–68. https://doi.org/10.1016/j.quascirev.2012.09.012

Menviel, L., Yu, J., Joos, F., Mouchet, A., Meissner, K. J., & England, M. H. (2017). Poorly ventilated deep ocean at the Last Glacial Maximum inferred from carbon isotopes: A data-model comparison study. *Paleoceanography*, *32*, 2–17. https://doi.org/10.1002/2016PA003024

Morée, A. L., Schwinger, J., Ninnemann, U. S., Jeltsch-Thömmes, A., Bethke, I., & Heinze, C. (2021). Evaluating the biological pump efficiency of the Last Glacial Maximum ocean using $\delta^{13}C$. *Climate of the Past*, *17*, 753–774. https://doi.org/10.5194/cp-17-753-2021

Muglia, J., Somes, C. J., Nickelsen, L., & Schmittner, A. (2017). Combined effects of atmospheric and seafloor iron fluxes to the glacial ocean. *Paleoceanography*, *32*, 1204–1218. https://doi.org/10.1002/2016PA003077

Ödalen, M., Nycander, J., Oliver, K. I. C., Brodeau, L., & Ridgwell, A. (2018). The influence of the ocean circulation state on ocean carbon storage and CO_2 drawdown potential in an Earth system model. *Biogeosciences*, *15*, 1367–1393. https://doi.org/10.5194/bg-15-1367-2018

Ohgaito, R., Yamamoto, A., Hajima, T., O'ishi, R., Abe, M., Tatebe, H., et al. (2021). PMIP4 experiments using MIROC-ES2L Earth system model. *Geoscientific Model Development*, *14*, 1195–1217. https://doi.org/10.5194/gmd-14-1195-2021

Oka, A., Abe-Ouchi, A., Chikamoto, M. O., & Ide, T. (2011). Mechanisms controlling export production at the LGM: Effects of changes in oceanic physical fields and atmospheric dust deposition. *Global Biogeochemical Cycles*, *25*, GB2009. https://doi.org/10.1029/2009GB003628

Otto-Bliesner, B. L., Hewitt, C. D., Marchitto, T. M., Brady, E., Abe-Ouchi, A., Crucifix, M., et al. (2007). Last Glacial Maximum ocean thermohaline circulation: PMIP2 model intercomparisons and data constraints. *Geophysical Research Letters*, *34*(12), 1–6. https://doi.org/10.1029/2007GL029475

Peltier, W. R. (2004). Global glacial isostasy and the surface of the ice-age Earth: The ICE-5G (VM2) model and GRACE. *Annual Review of Earth and Planetary Sciences*, *32*, 111–149. https://doi.org/10.1146/annurev.earth.32.082503.144359

Peltier, W. R., Argus, D. F., & Drummond, R. (2015). Space geodesy constrains ice age terminal deglaciation: The global ICE-6G-C (VM5a) model. *Journal of Geophysical Research: Solid Earth*, *120*, 450–487. https://doi.org/10.1002/2014JB011176

Petoukhov, V., Ganopolski, A., Brovkin, V., Claussen, M., Eliseev, A., Kubatzki, C., & Rahmstorf, S. (2000). CLIMBER-2: A climate system model of intermediate complexity. Part I: Model description and performance for present climate. *Climate Dynamics*, *16*(1), 1–17. https://doi.org/10.1007/PL00007919

Rickaby, R. E. M., Elderfield, H., Roberts, N., Hillenbrand, C.-D., & Mackensen, A. (2010). Evidence for elevated alkalinity in the glacial Southern Ocean. *Paleoceanography*, *25*, PA1209. https://doi.org/10.1029/2009PA001762

Roche, D. M., Crosta, X., & Renssen, H. (2012). Evaluating Southern Ocean sea-ice for the Last Glacial Maximum and pre-industrial climates: PMIP-2 models and data evidence. *Quaternary Science Reviews*, *56*, 99–106. https://doi.org/10.1016/j.quascirev.2012.09.020

Roche, D. M., Dokken, T. M., Goosse, H., Renssen, H., & Weber, S. L. (2007). Climate of the Last Glacial Maximum: Sensitivity studies and model-data comparison with the LOVECLIM coupled model. *Climate of the Past*, *3*(2), 205–224. https://doi.org/10.5194/cp-3-205-2007

Schmittner, A., & Galbraith, E. D. (2008). Glacial greenhouse-gas fluctuations controlled by ocean circulation changes. *Nature*, *456*, 373–376. https://doi.org/10.1038/nature07531

Sigman, D. M., & Boyle, E. A. (2000). Glacial/interglacial variations in atmospheric carbon dioxide. *Nature*, *407*, 859–869. https://doi.org/10.1038/35038000

Sigman, D. M., Hain, M. P., & Haug, G. H. (2010). The polar ocean and glacial cycles in atmospheric CO_2 concentration. *Nature*, *466*, 47–55. https://doi.org/10.1038/nature09149

Six, K. D., & Maier-Reimer, E. (1996). Effects of plankton dynamics on seasonal carbon fluxes in an ocean general circulation model. *Global Biogeochemical Cycles*, *10*, 559–583. https://doi.org/10.1029/96gb02561

Skinner, L. C. (2009). Glacial-interglacial atmospheric CO_2 change: A possible "standing volume" effect on deep-ocean carbon sequestration. *Climate of the Past*, *5*, 537–550. https://doi.org/10.5194/cp-5-537-2009

Stephens, B. B., & Keeling, R. F. (2000). The influence of Antarctic sea ice on glacial-interglacial CO_2 variations. *Nature*, *404*, 171–174. https://doi.org/10.1038/35004556

Tagliabue, A., Aumont, O., & Bopp, L. (2014). The impact of different external sources of iron on the global carbon cycle. *Geophysical Research Letters*, *41*, 920–926. https://doi.org/10.1002/2013GL059059

Tagliabue, A., Bopp, L., Roche, D. M., Bouttes, N., Dutay, J.-C., Alkama, R., et al. (2009). Quantifying the roles of ocean circulation and biogeochemistry in governing ocean carbon-13 and atmospheric carbon dioxide at the last glacial maximum. *Climate of the Past*, *5*, 695–706. https://doi.org/10.5194/cp-5-695-2009

Watson, A. J., Vallis, G. K., & Nikurashin, M. (2015). Southern Ocean buoyancy forcing of ocean ventilation and glacial atmospheric CO_2. *Nature Geoscience*, *8*, 861–864. https://doi.org/10.1038/NGEO2538

Yamamoto, A., Abe-Ouchi, A., Ohgaito, R., Ito, A., & Akira Oka, A. (2019). Glacial CO_2 decrease and deep-water deoxygenation by iron fertilization from glaciogenic dust. *Climate of the Past*, *15*(3), 981–996. https://doi.org/10.5194/cp-15-981-2019

Yamamoto, A., Abe-Ouchi, A., & Yamanaka, Y. (2018). Long-term response of oceanic carbon uptake to global warming via physical and biological pumps. *Biogeosciences*, *15*, 4163–4180. https://doi.org/10.5194/bg-15-4163-2018

3.3 Résumé du chapitre en français

Dans ce chapitre, j'expose les développements du modèle iLOVECLIM que j'ai réalisés afin de :

- générer les conditions aux limites du DMG correspondant aux recommandations du protocole PMIP4 [Kageyama et al., 2017] sur la grille du modèle iLOVECLIM. Le terme conditions aux limites fait ici référence à l'élévation et l'étendue des calottes glaciaires, mais aussi à un tracé de ligne de côte et une bathymétrie correspondant à la baisse de niveau marin observée au DMG. Le suivi de ce protocole standardisé permet ensuite au modèle iLOVECLIM de participer aux études d'intercomparaison des modèles PMIP (par exemple, Kageyama et al. [2021]).

- automatiser au maximum la génération des conditions aux limites du modèle océan (ligne de côte, bathymétrie). La méthode développée permet ainsi de générer facilement les conditions aux limites associées aux récentes reconstructions de calottes recommandées dans le protocole PMIP4 (GLAC-1D, ICE-6G-C), mais ouvre aussi d'autres perspectives pour des périodes de temps différentes du DMG (par exemple, des simulations transitoires de la dernière déglaciation, avec bathymétrie interactive). Cette méthode reste toutefois semi-automatique, certaines zones clefs telles que les détroits nécessitant un ajustement particulier afin d'obtenir une circulation océanique réaliste. Les choix associés sont détaillés ici de façon transparente.

- automatiser l'implémentation de ces conditions aux limites dans le modèle océan. En effet, un changement de conditions aux limites implique une variation du volume des océans. Il convient alors de développer l'initialisation du modèle afin d'assurer la conservation de masse des traceurs, tels que le contenu de carbone ou de sel des océans.

Les conséquences de cette méthode sont d'abord évaluées au PI, dont les conditions aux limites océan (issues de ETOPO5 [1986]) ont également été remplacées par une topographie plus récente. Je constate alors une légère détérioration de certaines variables climatiques (ex. température de surface, débit au niveau du passage de Drake), mais une amélioration très nette du volume de l'océan [Lhardy et al., 2021a].

Malgré sa résolution limitée, le modèle iLOVECLIM présente donc désormais grâce à ma méthode une variation de volume entre PI et LGM (-3.9%, contre -0.5% auparavant) proche de celle suggérée par les reconstructions de calottes (-3.2%), ce qui n'est pas le cas de nombreux modèles PMIP. Ce n'est pas sans conséquence pour la capacité de stockage de carbone des océans. En effet, la comparaison des résultats préliminaires du projet PMIP-carbon et de certains tests de sensibilité du modèle iLOVECLIM suggère que la variation de volume de l'océan et les choix de modélisation associés (tels qu'un ajustement de l'alcalinité) exercent un contrôle majeur sur le contenu total de carbone de l'océan. Ces résultats d'intercomparaison font l'objet d'un article [Lhardy et al., 2021a], et de certaines perspectives concernant une possible révision du protocole PMIP-carbon.

Chapter 4

Identification of sea-ice biases in the Southern Ocean and their consequences on deep ocean circulation and CO_2 concentration

Chapter aims:

1. Identify and quantify the model biases in Southern Ocean surface conditions (SST, sea-ice), Atlantic water mass distribution and CO_2 concentration at the LGM
2. Assess the impact of differing LGM boundary conditions and of a parameterized sinking of brines

Highlights:

↪ The iLOVECLIM model under the PMIP4 protocol simulates the same type of biases as in PMIP2, with respect to proxy data: a warm Southern Ocean ($\sim$40$-$50°S) with a circular sea-ice distribution, an underestimated seasonal amplitude of the sea-ice extent, a very deep and intense AMOC, and high CO_2 concentration.

↪ However, we have estimated a reconstructed winter sea-ice extent of 32.9×10^6 km^2, constrasting with the previous estimate of 43.5×10^6 km^2 [Roche et al., 2012]. On this basis, the simulated sea-ice extent is only slightly underestimated in winter.

↪ The choice of ice sheet reconstruction used to generate the boundary conditions yields only small effects on the examined variables. The boundary conditions associated with a cold Southern Ocean tend to show a further intensified AMOC.

↪ The parameterization of the sinking of brines leads to reduced biases in surface conditions (cold Southern Ocean, enhanced sea-ice seasonality), water mass distribution (shallower NADW) and CO_2 concentration (up to a $\sim$60 ppm drop). However, the regional pattern of surface biases remains. These improvements do not necessarily co-occur, suggesting different causes (stratified surface ocean, denser AABW).

As explained in chapter 1, simulating a sea-ice cover and a deep ocean circulation at the LGM in good agreement with proxy data remains challenging to this day. Model intercomparison studies during previous PMIP phases underline recurrent and large intermodel spread and model-data disagreements [Roche et al., 2012, Marzocchi and Jansen, 2017, Otto-Bliesner et al., 2007, Muglia and Schmittner, 2015].

Indeed, a majority of PMIP3 models simulate a strengthening and a deepening of the Atlantic Meridional Overturning Circulation (AMOC), contrasting with the common view inferred from most paleotracer data [Curry and Oppo, 2005, Böhm et al., 2015, Skinner et al., 2017]. This is also the case of the former version of the iLOVECLIM model (PMIP2), which is among those with a NADW overturning cell reaching the ocean floor in the North Atlantic [Otto-Bliesner et al., 2007]. Some modelling studies attribute an increased AMOC to wind stress changes in the Northern Hemisphere due to the influence of high altitude ice sheets at the LGM [Oka et al., 2012, Sherriff-Tadano et al., 2018, Klockmann et al., 2016, Muglia and Schmittner, 2015]. As this suggests a potentially significant impact of uncertainties in ice sheet boundary conditions [Ullman et al., 2014], it becomes apparent that the recommended ice sheet reconstructions of the PMIP4 protocol may induce some change in the simulated AMOC with respect to previous phases. Indeed, the ICE-6G-C and GLAC-1D ice sheets are significantly lower than the boundary conditions implemented in the framework of previous PMIP phases [Kageyama et al., 2017]. They also differ from each other, which provides the opportunity to run LGM simulations with the boundary conditions associated with both reconstructions in order to assess − to some extent − the impact of uncertainties in ice sheet reconstructions on deep ocean circulation.

As for the Southern Ocean sea ice, the PMIP2-PMIP3 ensemble demonstrates that most models fail to reproduce the LGM sea-ice distribution inferred from proxy data, both in terms of extent, seasonal range, and shape [Roche et al., 2012, Goosse et al., 2013, Marzocchi and Jansen, 2017]. With their different experimental design (and recent model developments) notably inducing a change of the global mean temperature anomaly (LGM − PI, Kageyama et al. [2021]), it remains to be seen whether PMIP4 models still show these three types of biases (Vadsaria et al., in prep).

In this chapter, I evaluate the surface conditions (SST, sea-ice cover), deep ocean circulation and carbon content simulated by the iLOVECLIM model at the LGM, using proxy data to carry out model-data comparisons of SST, sea-ice distribution, and $\delta^{13}C$ (see Sect. 2.4 of chapter 2). To relate to some extent the identified biases, I use simulations with different boundary conditions and/or sensitivity tests resulting in various surface conditions. Some of these simulations test the parameterization of the sinking of brines described in Sect. 2.2.1 of chapter 2. Published in part in Lhardy et al. [2021b], this work also gives me the opportunity to evaluate the climatic consequences of the LGM boundary conditions generated using the new and largely automated method described in chapter 3.

4.1 *Article 2: Impact of Southern Ocean surface conditions on deep ocean circulation at the LGM: a model analysis*

In this article, I follow an inverse methodology approach, using multiple LGM simulations which display contrasting climates. This approach is useful to evaluate the effect of differing boundary conditions and sensitivity tests related to the Southern Ocean sea ice, as well as to investigate potential relationships between the identified biases. In addition, it allows me to highlight which biases seem systematically simulated by the iLOVECLIM model. Since this article is chronologically the first I wrote, these results were obtained using the first batch of my simulations (v1), whereas the following sections and chapters all consider more recent (v2) model ouputs.

Clim. Past, 17, 1139–1159, 2021
https://doi.org/10.5194/cp-17-1139-2021

Climate of the Past
Open Access
EGU

Impact of Southern Ocean surface conditions on deep ocean circulation during the LGM: a model analysis

Fanny Lhardy[1], Nathaëlle Bouttes[1], Didier M. Roche[1,2], Xavier Crosta[3], Claire Waelbroeck[4], and Didier Paillard[1]

[1]Laboratoire des Sciences du Climat et de l'Environnement, LSCE/IPSL, CEA-CNRS-UVSQ-Université Paris-Saclay, 91198 Gif-sur-Yvette, France
[2]Vrije Universiteit Amsterdam, Faculty of Science, Cluster Earth and Climate, de Boelelaan 1085, 1081HV Amsterdam, the Netherlands
[3]Université de Bordeaux, CNRS, EPHE, UMR 5805 EPOC, 33615 Pessac, France
[4]Laboratoire d'Océanographie et du Climat: Expérimentation et Approches Numériques (LOCEAN), IPSL, Université Pierre et Marie Curie, 75005 Paris, France

Correspondence: Fanny Lhardy (fanny.lhardy@lsce.ipsl.fr)

Received: 13 November 2020 – Discussion started: 21 November 2020
Revised: 22 April 2021 – Accepted: 27 April 2021 – Published: 7 June 2021

Abstract. Changes in water mass distribution are considered to be a significant contributor to the atmospheric CO_2 concentration drop to around 186 ppm recorded during the Last Glacial Maximum (LGM). Yet simulating a glacial Atlantic Meridional Overturning Circulation (AMOC) in agreement with paleotracer data remains a challenge, with most models from previous Paleoclimate Modelling Intercomparison Project (PMIP) phases showing a tendency to simulate a strong and deep North Atlantic Deep Water (NADW) instead of the shoaling inferred from proxy records of water mass distribution. Conversely, the simulated Antarctic Bottom Water (AABW) is often reduced compared to its pre-industrial volume, and the Atlantic Ocean stratification is underestimated with respect to paleoproxy data. Inadequate representation of surface conditions, driving deep convection around Antarctica, may explain inaccurately simulated bottom water properties in the Southern Ocean. We investigate here the impact of a range of surface conditions in the Southern Ocean in the iLOVECLIM model using nine simulations obtained with different LGM boundary conditions associated with the ice sheet reconstruction (e.g., changes of elevation, bathymetry, and land–sea mask) and/or modeling choices related to sea-ice export, formation of salty brines, and freshwater input. Based on model–data comparison of sea-surface temperatures and sea ice, we find that only simulations with a cold Southern Ocean and a quite extensive sea-ice cover show an improved agreement with proxy records of sea ice, despite systematic model biases in the seasonal and regional patterns. We then show that the only simulation which does not display a much deeper NADW is obtained by parameterizing the sinking of brines along Antarctica, a modeling choice reducing the open-ocean convection in the Southern Ocean. These results highlight the importance of the representation of convection processes, which have a large impact on the water mass properties, while the choice of boundary conditions appears secondary for the model resolution and variables considered in this study.

1 Introduction

The Southern Ocean is a major climate player. Due to its specific geographical setting, it acts as a heat exchanger and buffer between the southern polar regions and the subtropics but also connects the other oceanic basins. Furthermore, it is one of the few oceanic regions where deep water formation takes place. Indeed, cold surface temperatures and brine rejection consecutive to sea-ice formation allow for a large and localized density increase of surface waters triggering deep convection. As a result, the dense southern-sourced Antarctic Bottom Water (AABW) fills the bottom of the world ocean. Density gradients between this water mass and others – such as its counterpart, the northern-sourced North Atlantic Deep Water (NADW) – determine the water mass distribution and

the large-scale circulation. Rearrangement of water masses explains part of past changes in the carbon storage capacity of the oceans (Buchanan et al., 2016; Khatiwala et al., 2019; Yu et al., 2016), which stresses the importance of correctly simulating the processes affecting the deep ocean circulation.

Multimodel studies using outputs from previous Paleoclimate Modelling Intercomparison Project (PMIP) phases showed that models simulate different responses of the Atlantic Meridional Overturning Circulation (AMOC) to the same Last Glacial Maximum (LGM) experimental design. Only a minority of PMIP2 models produce a shoaling of the NADW (Otto-Bliesner et al., 2007; Weber et al., 2007), while most PMIP3 models produce an intensified and deepened NADW (Muglia and Schmittner, 2015), at odds with reconstructions from paleotracer data which display a shallower NADW along with a denser, more voluminous and possibly more sluggish AABW during the last glacial compared to pre-industrial (PI) era and modern times (Curry and Oppo, 2005; Howe et al., 2016). Models rarely simulate bottom water temperatures and salinities close to the ones suggested by the few pore-fluid measurements in the deep glacial Atlantic (Adkins et al., 2002; Otto-Bliesner et al., 2007). Moreover, Heuzé et al. (2013) showed that, even in present-day conditions, models generally simulate inaccurate bottom water temperatures, salinities, and densities. Even when they do simulate relatively accurate modern bottom water properties, they tend to form AABW via the wrong process (namely open-ocean deep convection), whereas the largest proportion of AABW currently results from brine-dominated formation of dense shelf waters, overflowing in the deep ocean (Orsi et al., 1999; Williams et al., 2010). While some high-resolution CMIP6 models now simulate dense shelf waters, Heuzé (2021) observed no obvious export of these waters, and open-ocean deep convection remains a much-too-widespread and frequently occurring process.

As both the sea-surface temperature (SST) and salinity related to sea-ice formation in the Southern Ocean influence the surface density and therefore the AABW formation and properties, any surface condition bias has the potential to impact the deep ocean circulation. Studies on the historical period have underlined important model biases in the Southern Ocean SSTs (Hyder et al., 2018) and sea ice (Downes et al., 2015), which could also affect paleoclimate simulations. And indeed, PMIP models struggle to reproduce the glacial sea-ice extent suggested by sea-ice proxy data and especially its seasonality (Roche et al., 2012; Goosse et al., 2013; Marzocchi and Jansen, 2017). While Ferrari et al. (2014) have shown a dynamical link between the deep ocean circulation and Antarctic sea ice, Shin et al. (2003) have highlighted the major role played by Antarctic sea ice on the glacial AMOC by quantifying the haline density flux increase at the LGM in the Community Climate System Model (CCSM). Moreover, Marzocchi and Jansen (2017) have quantitatively attributed part of the observed discrepancies of the AMOC simulated by PMIP3 models to insufficient sea-ice formation and export. Therefore, targeting sea-ice biases in models may be necessary to improve the simulated water mass distribution. It is also crucial to better understand and simulate the interplay between surface and deep conditions, especially as some processes – such as brine rejection (Bouttes et al., 2010) and downsloping currents (Campin and Goosse, 1999) – are inherently limited by the resolution of the models.

In this study, we use an intermediate complexity model under PMIP2 or PMIP4 experimental design and several bathymetries to generate a set of simulations computed with different boundary conditions. In addition to these simulations displaying contrasted surface conditions, three sensitivity tests of Southern Ocean conditions for sea-ice export, formation of brines, and freshwater input further document the role of sea ice in the deep ocean circulation. This variety of simulations allows us to investigate the respective effects of the many possible choices for boundary conditions and other experimental settings on the simulated surface conditions and associated deep water formation. We hereafter focus on Southern Ocean surface conditions and evaluate them using proxy data for both SSTs and sea ice. We rely on the principle of a simplified inverse methodology: we assess what improves the simulated temperatures and sea ice in the Southern Ocean, as evaluated against proxy data, and we analyze the associated impact on deep ocean circulation.

2 Methods

2.1 Model description

The iLOVECLIM model is a coupled Earth system model of intermediate complexity (Claussen et al., 2002). Its relatively low computation time allows us to run multiple simulations and to test the effect of different modeling choices and boundary conditions on surface conditions. Over time, iLOVECLIM has significantly diverged from its parent model LOVECLIM (Goosse et al., 2010) but is still composed in its core of an atmospheric component (ECBilt), a simple land vegetation model (VECODE), and an oceanic general circulation model (CLIO). With 20 irregular vertical levels and a horizontal resolution of $3° \times 3°$, CLIO is able to simulate the large-scale circulation, which is of interest to us in this study. It also includes a thermodynamic–dynamic sea-ice component described by Fichefet and Morales Maqueda (1997). This component simulates a viscoplastic rheology but no sea-ice thickness distribution, which is relatively classic compared to other PMIP models (see Table 1 of Goosse et al., 2013) but far from the complexity of more recently developed sea-ice components (Rousset et al., 2015).

2.2 The PMIP boundary conditions and their implementation

PMIP provides standardized boundary conditions for paleoclimate simulations, enabling robust multimodel compar-

isons for periods of interest such as the LGM. The atmospheric gas concentrations and orbital parameters are prescribed to set values (e.g., a forcing parameter of 186 ppm for the glacial CO_2 concentration), based on data from Bereiter et al. (2015), Loulergue et al. (2008), Schilt et al. (2010), and Berger (1978). Since the ice sheet reconstructions are still associated with large uncertainties, Kageyama et al. (2017) describe the common experimental design for LGM experiments in the current phase (phase 4) of the project but let modeling groups choose from three different ice sheet reconstructions: GLAC-1D (Tarasov et al., 2012), ICE-6G-C (Peltier et al., 2015; Argus et al., 2014), or PMIP3 (Abe-Ouchi et al., 2015). To see the impact of such a choice, we have implemented in this study the boundary conditions (e.g., elevation, bathymetry, land–sea mask) associated with the first two options since these reconstructions are the most recent. We have also considered the results obtained with the previous LGM version of the model (PMIP2) described in Roche et al. (2007), which was generated with the boundary conditions associated with ICE-5G (Peltier, 2004), a previous reconstruction with notably higher elevation of the Northern Hemisphere ice sheets.

We have implemented the elevation associated with either GLAC-1D or ICE-6G-C topography at 21 000 years ago on the T21 grid of ECBilt in the Northern Hemisphere. The bathymetry of the CLIO grid has been modified according to the same topography and to a low sea level of −133.9 m (Lambeck et al., 2014). The bathymetry of the previous LGM version of iLOVECLIM was manually generated, while we now use a semi-automated method for our PMIP4 runs (see more detailed explanations in Appendix A). The land–sea mask is computed using the hypsometry discretized on the CLIO grid. A grid cell is defined as ocean if, at the subgrid level, the fraction of this cell below sea level exceeds a set threshold of 40 %. The land–sea mask is manually defined in a few key regions (Strait of Gibraltar, Greenland–Iceland–Scotland threshold, etc.). We take particular care of this step, relying on knowledge of the sea level change and of the straits' geography at the LGM, and also by running a connectivity program (see Appendix B) computing sills to make informed choices.

2.3 Set of simulations

Thanks to the implementation of the PMIP boundary conditions and to the related development of the model, we have a set of five LGM simulations (Table 1) displaying contrasted climates (Fig. 1). Indeed, we ran two simulations under the PMIP4 experimental design ("P4-G" and "P4-I", both also used in Kageyama et al., 2021) and three under the PMIP2 one ("New P2", "Cold P2", and "Warm P2"). We used different boundary conditions and/or modeling choices to obtain them. The boundary conditions (elevation, bathymetry, and land–sea mask) associated with the GLAC-1D, ICE-6G-C, or ICE-5G topography were implemented to obtain "P4-G", "P4-I", and "New P2", respectively. The elevation associated with the ICE-5G topography was also implemented for the other two PMIP2 simulations ("Cold P2" and "Warm P2") but with the former manual bathymetry instead of the one generated using our new semi-automated method. Finally, we made different modeling choices with respect to the glacial temperature profiles used in the radiative code of ECBilt for these last two simulations ("Cold P2" and "Warm P2"). Indeed, due to the coarse vertical resolution of ECBilt, the model uses general circulation model (GCM) vertical linearizations which are region dependent. We kept the default continental profile in the first case and used the Greenland profile for all ice-covered regions in the Northern Hemisphere in the second one, resulting in a large difference in the global mean temperature of these two simulations.

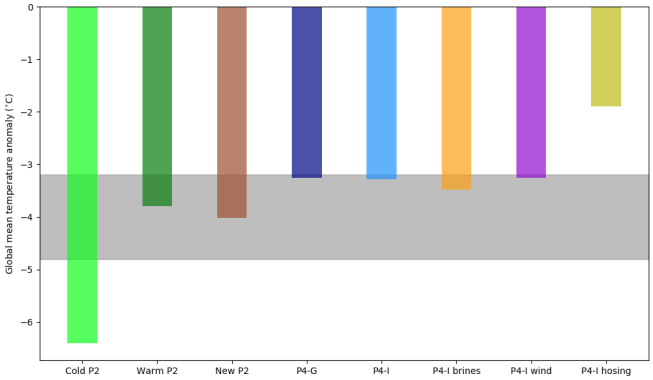

Figure 1. Global mean surface air temperature anomalies (LGM – PI). The gray bar shows the anomaly (-4 ± 0.8 °C) estimated by Annan and Hargreaves (2013).

We added three sensitivity tests to this set. The boundary conditions associated with ICE-6C-G were arbitrarily chosen as the standard in these tests, which is why the simulation "P4-I" is considered as a LGM reference in the following sections. Sensitivity tests using the simulation "P4-G" as reference (i.e., GLAC-1D boundary conditions) yield fairly similar results (not shown here). In "P4-I wind", we multiplied – in the Southern Ocean only – the meridional wind tension on ice by a coefficient of 3 in order to boost the sea-ice export in the Southern Hemisphere and therefore explore the possible impact of the Antarctic sea-ice dynamics. We ran "P4-I brines" using the parameterization of the sinking of brines described by Bouttes et al. (2010). The objective of this parameterization is to account for the sinking of dense water rejected during sea-ice formation. Indeed, this process is often limited by the horizontal resolution of models, as the rejected salt tends to get diluted in the surface grid cells where sea ice is forming. This parameterization allows for a fraction of the salt content of the surface grid cell to be transferred to the deepest grid cell underneath the location of sea-ice formation. As a result, the salinity and density of the bottom cells increase, while the salinity and

Table 1. Short description of the iLOVECLIM simulations.

Simulation	Duration (years)	Forcing parameters	Topography	Bathymetry	Comments on the experimental setting
PI	5000	PI	default	semi-automated[a]	Reference simulation for the pre-industrial climate
Cold P2	5000	PMIP2	ICE-5G	manual	With the default profile, yielding a very cold climate
Warm P2	3000	PMIP2	ICE-5G	manual	With the Greenland profile allocated to all ice-covered regions in the Northern Hemisphere
New P2	5000	PMIP2	ICE-5G	semi-automated	Reference LGM simulation with boundary conditions associated with PMIP2
P4-G	5000	PMIP4	GLAC-1D	semi-automated	Reference LGM simulation with boundary conditions associated with GLAC-1D[b]
P4-I	5000	PMIP4	ICE-6G-C	semi-automated	Reference LGM simulation with boundary conditions associated with ICE-6G-C[b]
P4-I brines	5000	PMIP4	ICE-6G-C	semi-automated	Sensitivity test with the parameterization of the sinking of brines
P4-I wind	3000	PMIP4	ICE-6G-C	semi-automated	Sensitivity test with the multiplication by 3 of the meridional wind tension on ice
P4-I hosing	3000	PMIP4	ICE-6G-C	semi-automated	Sensitivity test with hosing (+0.6 Sv) around Antarctica

[a] Generated using etopo1 (Amante and Eakins, 2009). [b] Both simulations are also part of Kageyama et al. (2021).

density of the surface grid cells decrease, without congruent motion of water masses. The modification of the salinity depends on the rate of sea-ice formation, as well as the chosen fraction parameter. Here, the fraction was chosen at 0.8 to allow for a large effect of this sensitivity test, but the gradual effect of this parameter choice on the streamfunction is shown in Fig. S5 in the Supplement, as well as the impact of this parameterization on the PI streamfunction (and deep water mass properties; see "PI brines" simulation in Fig. S6). This simple parameterization is relatively different from a downsloping current one as it is not confined to the continental slope and does not create mixing along the way of the sinking brines. While "this brine mechanism is idealized, it reflects the impact of intense Antarctic sea-ice formation during the LGM" (Bouttes et al., 2010) on the AABW density. In contrast to this transfer of salt, an addition of a freshwater flux (of 0.6 Sv) around Antarctica was done in the "P4-I hosing" experiment, as described by Roche et al. (2010).

The simulations are briefly described in Table 1. Each simulation has been run either 3000 or 5000 years to ensure a quasi-equilibrium state. The drift for any individual simulation is less than 2×10^{-4} °C per century for the deep ocean temperature (global mean of all oceans below 2000 m depth). The last 100 years are analyzed. We use this set of simulations to (a) compare the simulated sea-surface temperatures and sea-ice extent to their distribution in the Southern Ocean inferred from data and (b) explore the impact of these surface conditions on deep ocean circulation.

2.4 Experimental data

The simulated surface conditions are first compared with the LGM sea-surface temperatures reconstructed by MARGO Project Members (2009). Thanks to the use of multiple proxies (diatoms, radiolaria, dinoflagellates, foraminifera, Mg/Ca, and alkenones), this dataset, combining 696 individual records, provides a synthesis of our knowledge of the LGM ocean surface temperature. However, it should be noted that most proxies are calibrated against summer SST (Esper and Gersonde, 2014; Cortese and Prebble, 2015) or annual SST (Sikes et al., 1997; Prahl et al., 2000). Only planktonic foraminifera allow for the estimation of winter SST (Howard and Prell, 1992) but their growth is hampered, and restricted to a couple of species, south of the polar front (Bé and Hutson, 1977). As such, there are only a few winter SST estimates to compare with the simulated ones. As for the model–data comparison of the PI SSTs, we relied on the modern World Ocean Atlas (WOA) data (World Ocean Atlas, 1998) since they are used by MARGO Project Members (2009).

Secondly, to evaluate the glacial Antarctic sea-ice distribution, we compiled sea-ice proxy data from Gersonde et al. (2005), Allen et al. (2011), Ferry et al. (2015), Benz et al. (2016), Xiao et al. (2016), Nair et al. (2019), and Ghadi et al. (2020). In this compilation, LGM data include three types of proxies: a quantitative proxy of yearly sea-ice duration, a quantitative proxy of the winter (September) or summer (February) sea-ice concentration, and finally a qualitative proxy (based on the relative abundance of diatoms *Fragilariopsis curta* and *F. cylindrus* for winter sea-ice presence

and *F. obliquecostata* for summer sea-ice presence). To integrate these different types of measurements, an index is built based on the number of proxies agreeing on the sea-ice presence (ranging from 0 to 3 in winter and 0 to 2 in summer, with halved values when a proxy is not very conclusive). The presence of sea ice at a given location is accepted when the qualitative or quantitative value is above the error on the calibration step (Gersonde and Zielinski, 2000; Crosta et al., 2004; Esper and Gersonde, 2014). Taking into account all marine cores, we draw the likely delimitation of sea-ice presence in austral winter. Unfortunately, there are too-few proxy data available to robustly constrain the location of the austral summer sea-ice edge. We thus extrapolated the modern relationship between summer sea-ice extent and SST, whereby summer sea ice lies south of the 0 °C isotherm (Nicol et al., 2000) to the LGM. Caution is therefore needed when using the results, as this summer contour is not well constrained.

We then estimated the sea-ice extent inferred from this data compilation: we imported these contours on a 360×360 points grid (of $1° \times 0.5°$ in longitude and latitude), computed the surface area contained within (summing the weighted area of each grid cell on a perfect sphere) and subtracted an estimated surface of the Antarctic continent (i.e., land and grounded ice sheet areal extent) at the LGM. Results are discussed in Sect. 3.3. We estimated a glacial Antarctica of 16.8×10^6 km^2 by computing the total area of the continent and of the continental shelves (up to -1000 m) on a high-resolution (16×16 km) modern topographic dataset (Fretwell et al., 2013). This value falls close to a GIS surface area estimate of 16.4×10^6 km^2 using Bentley et al. (2014) Antarctic maps at 20 ka on a Lambert projection. To put this value into perspective, the modern Antarctic continent has a surface area of 13.9×10^6 km^2 (Fretwell et al., 2013), due to a smaller areal extension of the Antarctic ice sheet and a higher sea level. For the indicative error in the sea-ice surface extent computed, we have chosen the values of 15 % (in winter) and 30 % (in summer) for two reasons. First of all, it is difficult to estimate the uncertainty linked to the extrapolation of the sea-ice edges using marine core data, and it makes sense for this uncertainty to be larger in summer than it is in winter due to the scarcity of data. Secondly, another uncertainty is arising from the subtracted surface area of Antarctica at the LGM, which affects the estimated sea-ice extent (but not its seasonality). Its continental limit is speculative in some regions (Bentley et al., 2014), while the discretization of this limit as a land–sea mask on a coarse-resolution grid may induce an additional error. More precisely, with the ICE-6G-C and the GLAC-1D topographic files (with their 1080×2160 and 360×360 grid point resolutions, respectively), we find a 21 ka Antarctic surface of 15.0×10^6 and 17.1×10^6 km^2, respectively. An uncertainty of this order of magnitude (2 million km^2) represents 6 % and 20 % of the sea-ice extent estimated in winter and summer, respectively. If we further discretize the contours of the winter and summer sea-ice edges and of the ICE-6G-C Antarctic continent on the $3° \times 3°$ CLIO grid, we underestimate the sea-ice extent by 3.4×10^6 km^2 (in winter) and 1.7×10^6 km^2 (in summer), that is, by 10 % and 16 %, respectively. Considering the order of magnitude of these alternative estimates, error bars of 15 % and 30 % seem reasonable. Still, these estimates are only indicative of the order of magnitude of the error.

Finally, to also evaluate the simulated PI sea-ice extent, we used sea-ice data for the period 1979–2010 from Parkinson and Cavalieri (2012), who computed a mean extent of 18.5×10^6 km^2 (in September) and 3.1×10^6 km^2 (in February) – though it should be noted that the sea-ice extent we simulated in our pre-industrial run is not fully comparable with these modern values because of climate change over the last century.

3 Results

3.1 Global mean surface air temperature anomaly

Six out of eight of our runs display a global mean surface air temperature anomaly (LGM mean SAT – PI mean SAT) in the range of -4 ± 0.8 °C (Fig. 1) estimated by Annan and Hargreaves (2013), though three of them fall close to its upper limit. The average climate of "Cold P2" is too cold and "P4-I hosing" is too warm to agree with this range. With a LGM cooling of around -3.3 °C, we also note that the PMIP4 boundary conditions (with lower ice sheets compared to PMIP2) lead to a significantly warmer climate than the PMIP2 boundary conditions (see "P4-G" and "P4-I" compared to "New P2"). Compared to other PMIP4 models, iLOVECLIM simulates a quite-warm glacial climate, in agreement with previous evaluations (Roche et al., 2007): Kageyama et al. (2021) shows that half of the PMIP4 models simulate a LGM cooling in the -3.7 to -4 °C range, while three colder models simulate a larger global SAT anomaly (up to -6.8 °C). We note that the LGM mean SAT anomaly was recently re-evaluated at -6.1 ± 0.4 °C (Tierney et al., 2020) due to lower SAT in the tropics than previously reconstructed. Both iLOVECLIM and most of the other PMIP4 models simulate relatively modest SAT anomalies which do not compare well with such a large LGM mean SAT anomaly. Nonetheless, this estimation was obtained thanks to a field reconstruction of LGM temperatures using data assimilation in the Community Earth System Model (CESM), an innovative method which is not freed from potential model biases, with CESM being the coldest model out of the PMIP4 ensemble in Kageyama et al. (2021).

3.2 Sea-surface temperatures

Figure 2 shows that our set of simulations yields a variety of sea-surface temperatures, with some significant regional differences. The pre-industrial SSTs are obviously warmer than the ones simulated by the reference LGM simulation "P4-I", with a marked anomaly in the North Atlantic and in the

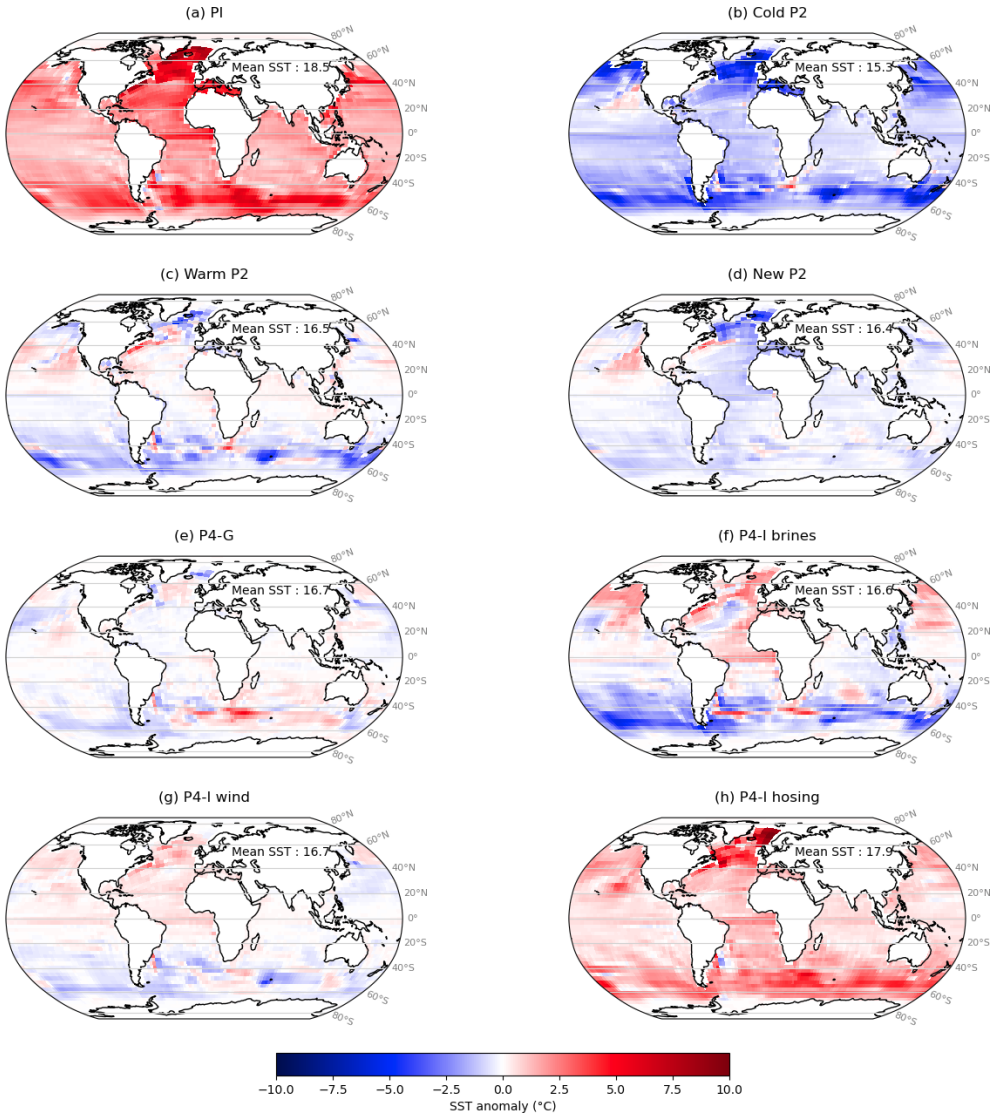

Figure 2. Anomaly in simulated mean sea-surface temperature (°C) relative to simulation "P4-I" (mean SST of 15.2 °C). Due to the vertical resolution of iLOVECLIM, the sea-surface temperature is defined as the temperature of the first 10 m of the water column.

Southern Ocean (Fig. 2a). Overall, the three PMIP2 simulations show colder SSTs than "P4-I" (Fig. 2b, c, d). The differences between "P4-G" and "P4-I" are small (Fig. 2e), with the exception of the eastern Atlantic and western Indian sectors of the Southern Ocean, south of the African continent, where "P4-G" displays warmer SSTs. This positive anomaly is related to a southward shift of the Antarctic Circumpolar Current. Larger differences exist between "P4-I" and its sensitivity tests, especially in the North Atlantic and in the Southern Ocean. We note that the transfer of salt to the bottom of the ocean leads to a cooling of the Southern Ocean ("P4-I brines"; Fig. 2f), while the opposite occurs with the addition of a freshwater flux around Antarctica ("P4-I hosing", Fig. 2h). Observed in ice-free regions (i.e., where the SSTs are not necessarily at the freezing point value), this cooling is probably a consequence of the enhanced stratification, since a well-mixed water column in upwelling regions would tend to dampen the effect of low winter surface temperatures on the SSTs. The third sensitivity test ("P4-I wind") only yields small differences with "P4-I", except around the Kerguelen Islands. A latitudinal gradient along the Atlantic is sometimes visible in the SST anomalies ("New P2", "P4-I wind"), suggesting a change in the meridional heat transport, possibly due to the influence of the choice of boundary conditions and of the sensitivity tests on the AMOC (see Sect. 3.4).

We now explore which of these surface conditions agree best with the proxy data from MARGO Project Members (2009). To quantify the model–data agreement, we compute the root mean square errors (RMSEs) for each ocean basin, for both the austral summer (JFM) and winter (JAS) seasons.

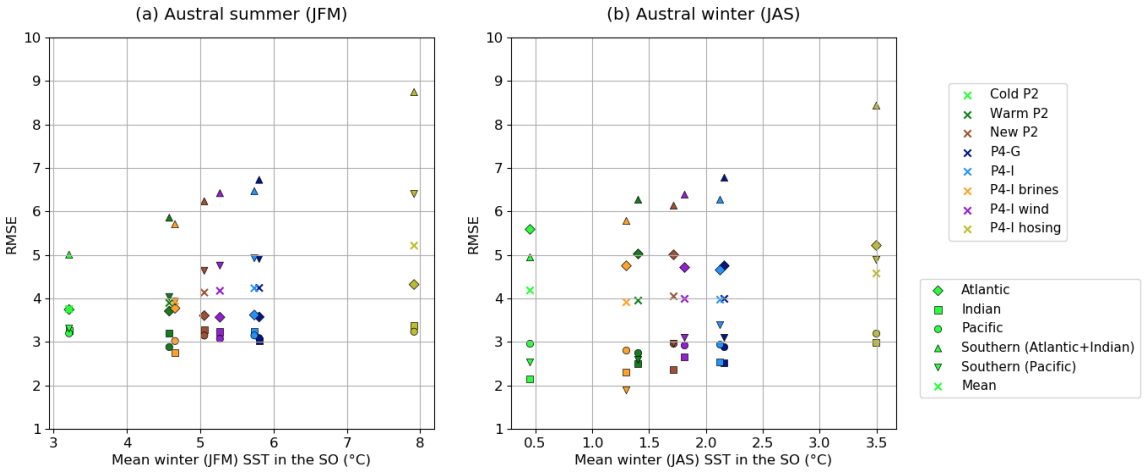

Figure 3. Relationship between the model–data agreement and the overall temperature of the Southern Ocean, in austral summer **(a)** and winter **(b)**. The mean value of the Southern Ocean SSTs (averaged up to 36° S) of each simulation is plotted on the x axis. The y axis represents the root mean square error computed using the SST data from MARGO Project Members (2009), which is small when the agreement is good. This value was computed for each basin and each simulation, as shown by the marker style and color, respectively.

We choose to plot these values against the mean SST of the Southern Ocean (Fig. 3), to show the potential relationships between the model–data agreement computed for each simulation and a cold or warm Southern Ocean. We also choose to compute individual RMSEs for each ocean basin according to the core locations of the Multiproxy Approach for the Reconstruction of the Glacial Ocean Surface (MARGO) data, separating the Southern Ocean into two sectors (Atlantic and Indian sectors versus Pacific sector). The poorest agreement is observed in the Southern Ocean, especially in the Atlantic and Indian sectors of the Southern Ocean. The simulations with a colder Southern Ocean ("Cold P2", "P4-I brines") show a better agreement with the SST data, as indicated by smaller RMSEs computed for the Southern Ocean (see triangles in Fig. 3). However, "Cold P2" is not the simulation with the lowest mean RMSE (see crosses in Fig. 3b), as it notably shows a higher RMSE in the Atlantic basin in winter (see diamonds).

To better understand the discrepancies between data and model, we analyze next the SSTs in a data versus model diagram for the summer and winter months with superimposed information about their latitudinal location. A set of representative simulations is presented in Fig. 4; the interested reader can find similar plots for all simulations in Fig. S2. In general, the simulated LGM SSTs in austral winter (Fig. 4d, f, h) agree reasonably well with MARGO data. Although data are scarce in the Southern Ocean for these winter months, it seems that simulations with a cold Southern Ocean ("P4-I brines") yield a better agreement with data (compared to "P4-I" or "P4-I hosing"). However, during the austral summer months, a clear trend with latitude is observed for all LGM simulations (Fig. 4c, e, g), with the model–data disagreement peaking around 40–50° S. At these latitudes, the summer Southern Ocean is too warm to match the data, even when taking into account the uncertainties. We note that the simulated summer SSTs in the Pacific sector of the Southern Ocean seem less overestimated (compared to data) than in the Atlantic or Indian sectors. At higher latitudes ($\sim$ 60° S), the agreement with data improves (as shown by points closer to the 1 : 1 line), and cold simulations even simulate colder summer SSTs than the SST data in the high latitudes of the Pacific sector, which is where sea ice is also simulated (see white markers in Figs. 4e and S2c, or Fig. S1c). This trend with latitude is almost as clear for the pre-industrial (Fig. 4a), which simulates a slightly too-warm Southern Ocean compared to WOA98 data for most latitudes of the Southern Hemisphere and for both seasons – though the model–data disagreement is more pronounced in the summer months.

There is a clear anticorrelation between the simulated sea-surface temperature and sea-ice area in the Southern Ocean (Fig. S3), which suggests a thermodynamic control prevailing over the influence of advection processes. Therefore, we can also use sea-ice proxy data to further constrain the surface conditions and examine whether our model–data evaluation using the sea-ice signal is consistent with our observations so far.

3.3 Sea ice

Analyzing correctly the sea-ice distribution requires distinguishing the summer and winter values. We here compare the simulated sea ice with data reconstructions for the austral summer (JFM) and winter (JAS) seasons, first in terms of sea-ice extent and then in terms of regional patterns. Only the sea-ice extent, defined as the surface with a sea-ice concentration over 15 %, is strictly comparable to our data estimates. We however chose to present both the simulated sea-ice ex-

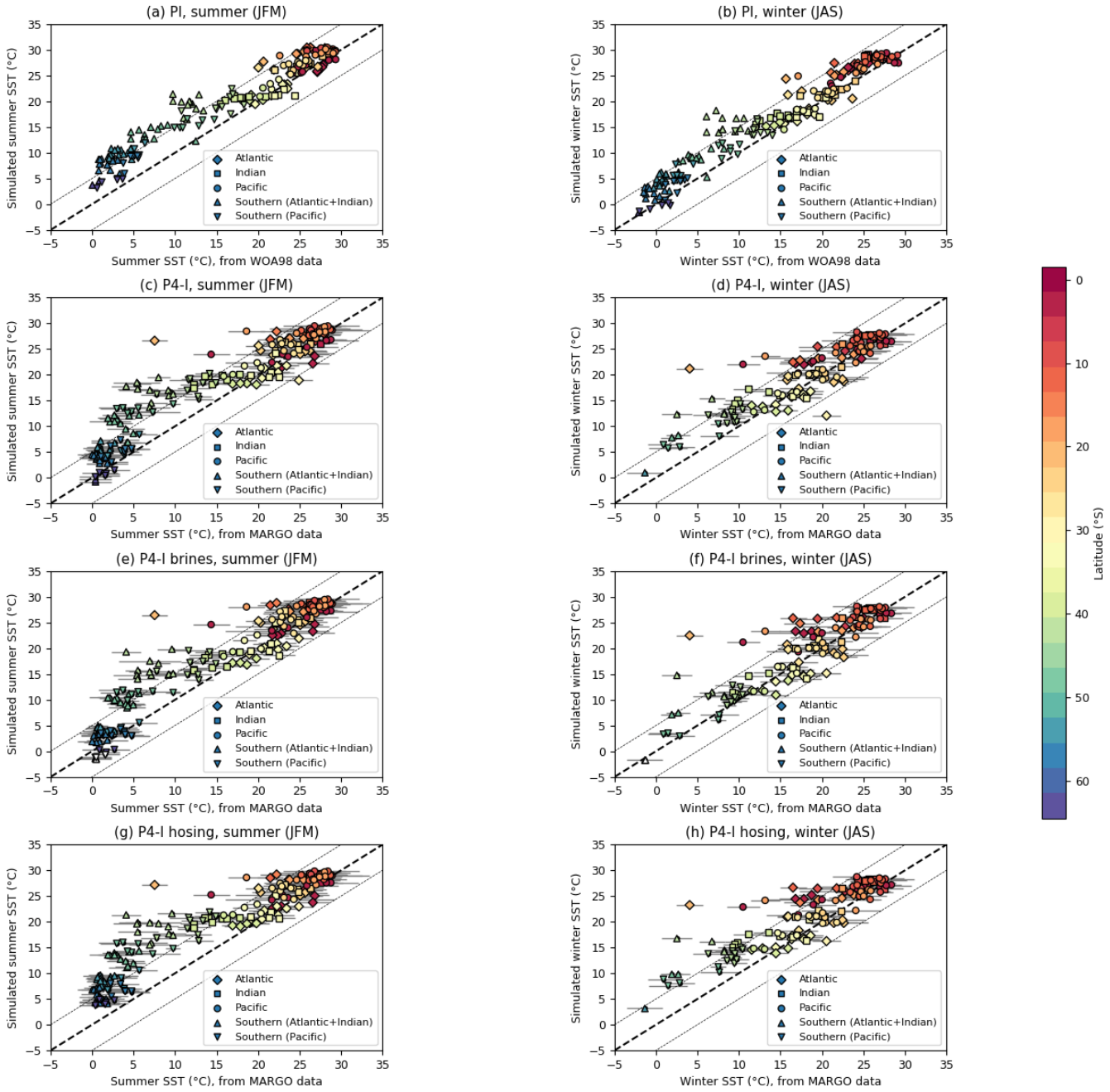

Figure 4. Austral summer (JFM) and winter (JAS) sea-surface temperatures of the Southern Hemisphere in a model versus data diagram, for a sample of our simulations (see Fig. S2 for the complete results). The simulated SSTs are plotted against the SST data from the regridded product (MARGO Project Members, 2009 or World Ocean Atlas, 1998) thanks to the aggregation of the coordinates on the nearest ocean grid cell. The 1 : 1 line features a perfect model–data agreement (dashed black line), while the dotted gray lines feature a 5 °C departure from it. The marker style indicates the ocean basin of each core. The marker color shows the latitude of the core, except it is white where the model simulates sea ice in the Southern Ocean. The uncertainties associated with the SST data are plotted with the horizontal gray bars.

tent (here, the total surface between the northernmost 15 % concentration limit and the Antarctic continent) and area (the sea-ice concentration multiplied by the area of the grid cell for all ocean cells south of the Equator) in Fig. 5.

Using the method described in Sect. 2.4 to integrate the sea-ice proxy data, we estimated a minimal (in austral summer) sea-ice extent of $\sim 10.2 \times 10^6$ km^2 and a maximal (in austral winter) extent of $\sim 32.9 \times 10^6$ km^2. This last value is significantly lower than previous studies (39×10^6 km^2 in

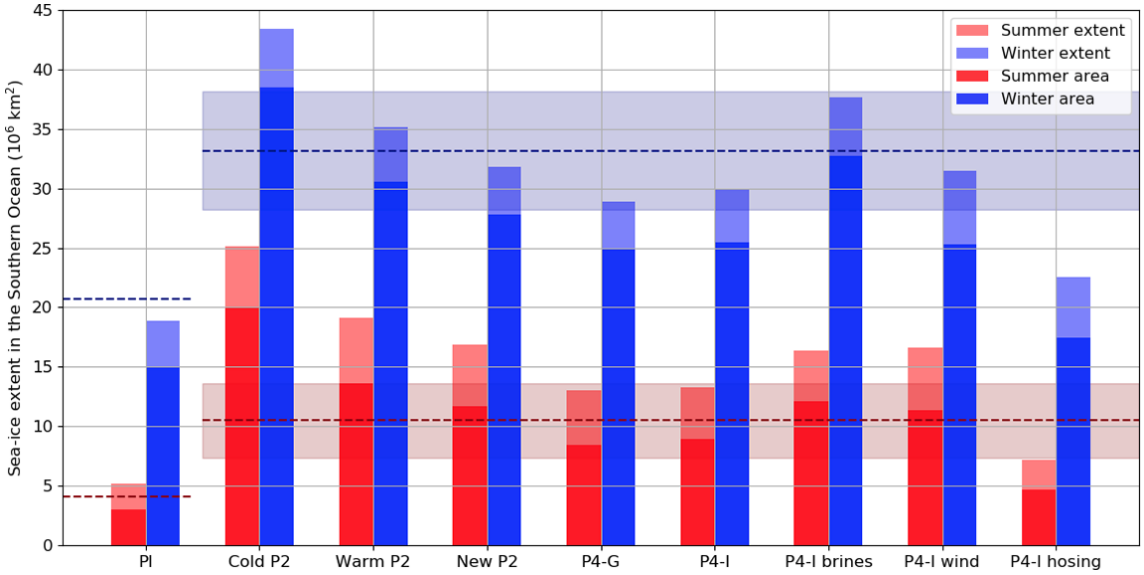

Figure 5. Austral summer (JFM) and winter (JAS) sea-ice areas and extents in the Southern Ocean. The LGM sea-ice extent estimated using the proxy data compilation is represented by the dashed red (summer) and the blue (winter) lines (with an indicative error bar of 30 % and 15 %, respectively). The modern values (dashed lines on the left) are mean values on the period 1979–2010 published in Parkinson and Cavalieri (2012).

Gersonde et al., 2005 and 43.5×10^6 km^2 in Roche et al., 2012). While our estimates inherit the uncertainties linked to proxy data and to the extrapolation of sea-ice edges, this computation does not rely on a specific projection on a map. Given the limited change in the area enclosed in the contours, we estimate that the value of 43.5×10^6 km^2 of Roche et al. (2012) (which was also used in Marzocchi and Jansen, 2017 to evaluate the simulated sea-ice extent of PMIP3 models) was overestimated. It is difficult to pinpoint the exact cause of this overestimation, but two factors certainly had a significant impact: first, the use of a stereographic projection for the areal estimation, and second the use of the modern surface area of the Antarctic continent instead of the LGM one.

Comparing now these data reconstructions with our model outputs, Figs. 5 and S3a show that most simulations overestimate the LGM summer sea-ice extent – a tendency which is also noticeable for pre-industrial conditions (Fig. 5), despite the warm bias observed in Fig. 4a. Conversely, the sea-ice extent of most simulations falls close to the reconstructed winter sea-ice extent of 32.9×10^6 km^2. The warmest simulation ("P4-I hosing"; see Fig. 1) is the only one to show both a winter and a summer sea-ice extent under the data estimates. However, simulations which are closer to the -4 °C anomaly estimate (such as "Warm P2" and "New P2") show an overestimated minimal extent, yet a reasonable maximal extent, while warm simulations which are almost out of the -4 ± 0.8 °C range (such as "P4-G" and "P4-I") show both a small underestimation in winter and a small overestimation in summer. This suggests that the enhanced seasonality of the LGM Southern Ocean sea ice (22.7×10^6 km^2 according to our proxy reconstructions, compared to the modern seasonal range of 15.4×10^6 km^2), is not entirely simulated by the model, a result already observed in Roche et al. (2012). Two sensitivity tests show opposite results: "P4-I brines" shows a larger seasonality (21.3×10^6 km^2) and "P4-I wind" (14.9×10^6 km^2) a reduced one compared to their parent simulation "P4-I" (16.7×10^6 km^2). It should be noted that, if we compared the simulated sea-ice area (instead of the extent) to our data estimates, we would rather conclude of a reasonable estimation of the sea-ice cover in summer for most simulations and of an almost-systematic underestimation in winter. Indeed, the simulated sea-ice areas fall under the sea-ice extent values by 5 millions km^2 approximately, a difference enhanced in "P4-I wind" due to the multiplication of the wind stress on ice.

Figure 6 presents the simulated sea-ice edges alongside the sea-ice contours based on marine core data, using the reconstruction method described in Sect. 2.4. The sea-ice edge – set at 15 % of sea-ice concentration by convention (US National Snow and Ice Data Center) – of all LGM simulations shows a roughly circular regional distribution around Antarctica (also see Fig. S4). While the scarcity of summer LGM sea-ice indicators does not allow us to make firm statements for the minimum extent, the circular shape does not compare well with the more oval-shaped proxy reconstruction in winter (Fig. 6b). Indeed, while cold simulations seem close to the reconstruction in the Atlantic and Indian sectors, they overestimate sea ice in the Pacific sector compared to proxy data. In summer (Fig. 6a), we observe a similar trend with less available proxy data: the simulated sea ice seems too extensive in

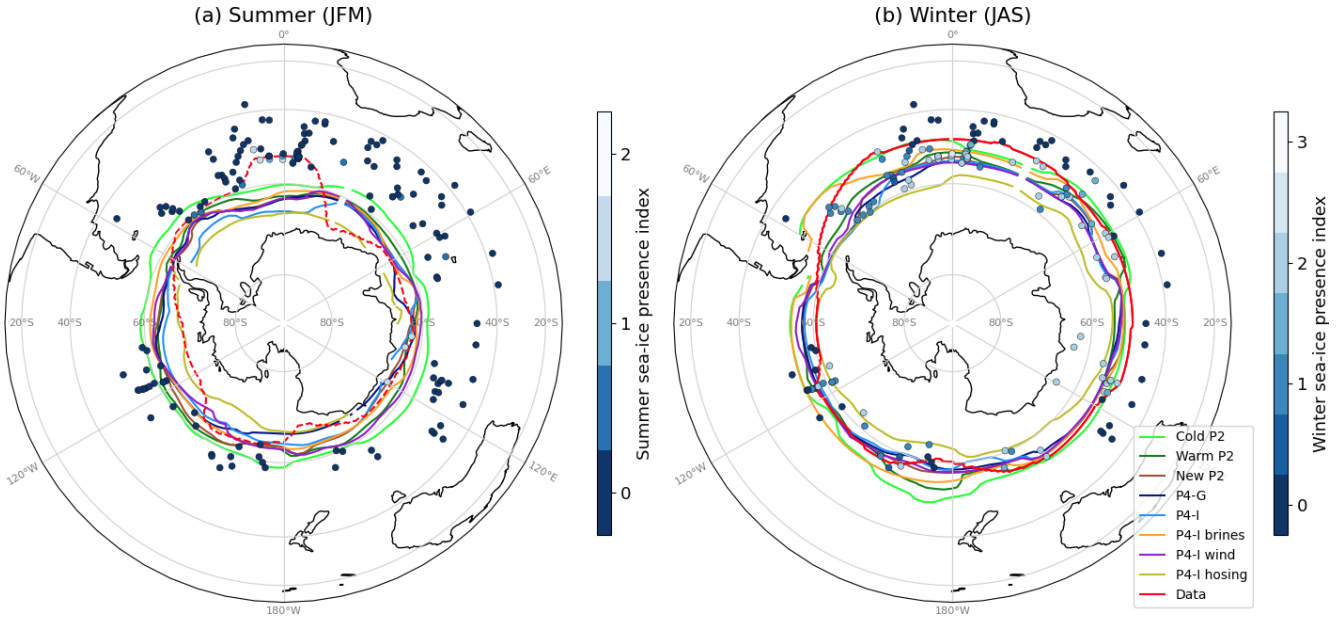

Figure 6. Austral summer **(a)** and winter **(b)** sea-ice edges (at 15 % of sea-ice concentration, enclosing the total ocean surface defined as the sea-ice extent) in the Southern Ocean for the LGM simulations. The sea-ice presence suggested by marine core data is represented as an arbitrary index on a blue to white scale, where blue denotes no indication of sea ice in proxies, and white denotes agreement of several proxies on the presence of sea ice. The red lines mark the likely delimitation of the sea-ice presence according to the proxy data (compilation of data from Gersonde et al., 2005; Allen et al., 2011; Ferry et al., 2015; Benz et al., 2016; Xiao et al., 2016; Nair et al., 2019; and Ghadi et al., 2020). We used a solid red line in panel **(b)** but a dashed line in panel **(a)** as the summer contour is not well constrained (see Sect. 2.4).

the Pacific sector for cold simulations but cannot match some of the sea-ice presence indications in marine cores (reaching as far as 50° S in a few cores of the Atlantic sector). As the high southern latitudes of the Pacific are also where the model tends to simulate colder SSTs than MARGO data – on the contrary to the warm bias around latitudes of 40–50° S in the Atlantic and Indian sectors (Figs. 4 and S1), the observed discrepancies in sea-ice distribution seem consistent with the SST signal.

Both the SST and the sea-ice model–data comparison suggest that a cold Southern Ocean, with an relatively extensive winter sea-ice cover (which is present in some of our simulations), but also with both a large seasonal amplitude (simulated to a certain extent by one of our simulations) and a large interbasin contrast (shown by none of our simulations), would agree best with proxy data. Now that we have clarified what an improvement of the simulated surface conditions with respect to proxy data means, we can further use their variety to examine whether improved surface conditions would be linked to a more realistic water mass distribution.

3.4 Deep ocean circulation

Although all of our simulations broadly show the same biases in the seasonal and regional patterns of the Southern Ocean surface conditions, they simulate a variety of SST and sea-ice extent. We can expect these differences to have an impact on the density of surface waters and possibly on deep water formation. Additionally, since these surface conditions are simulated using different boundary conditions and/or forcings or model parameter choices (in the sensitivity tests), we take this opportunity to investigate the relative impact of these modeling choices and boundary conditions on the simulated deep ocean circulation.

We can examine the impact of the different modeling choices on the streamfunction along a meridional section of the Atlantic and Southern Ocean basins (Fig. 7). The AMOC depth and strength in our PI simulation are within the PMIP3/PMIP4 ensemble (see Figs. S1 and S2 of Kageyama et al., 2021). In more details, the streamfunction of iLOVECLIM is fairly comparable to the pre-industrial streamfunctions of HadCM3, AWIESM2, MIROC-ESM, and CNRM-CM5, and actually stronger and deeper than that of IPSL-CM5A2 (and IPSL-CM5A-LR). However, the pre-industrial AMOC strength simulated by the iLOVECLIM model is underestimated compared to modern observational data. Since 2004, the RAPID array at 26° N has measured an AMOC within the range of 13.5 to 20.9 Sv, when interannual variability is accounted for (Moat et al., 2020), with a mean estimate of 17.2 Sv (McCarthy et al., 2015). The simulated AMOC strength at this latitude does not fall into this range in any of our PI simulations, which show a maximum of 10.1 Sv ("PI") and 11.2 Sv ("PI brines"; Fig. S5), with both maxima occurring at a depth of 1225 m.

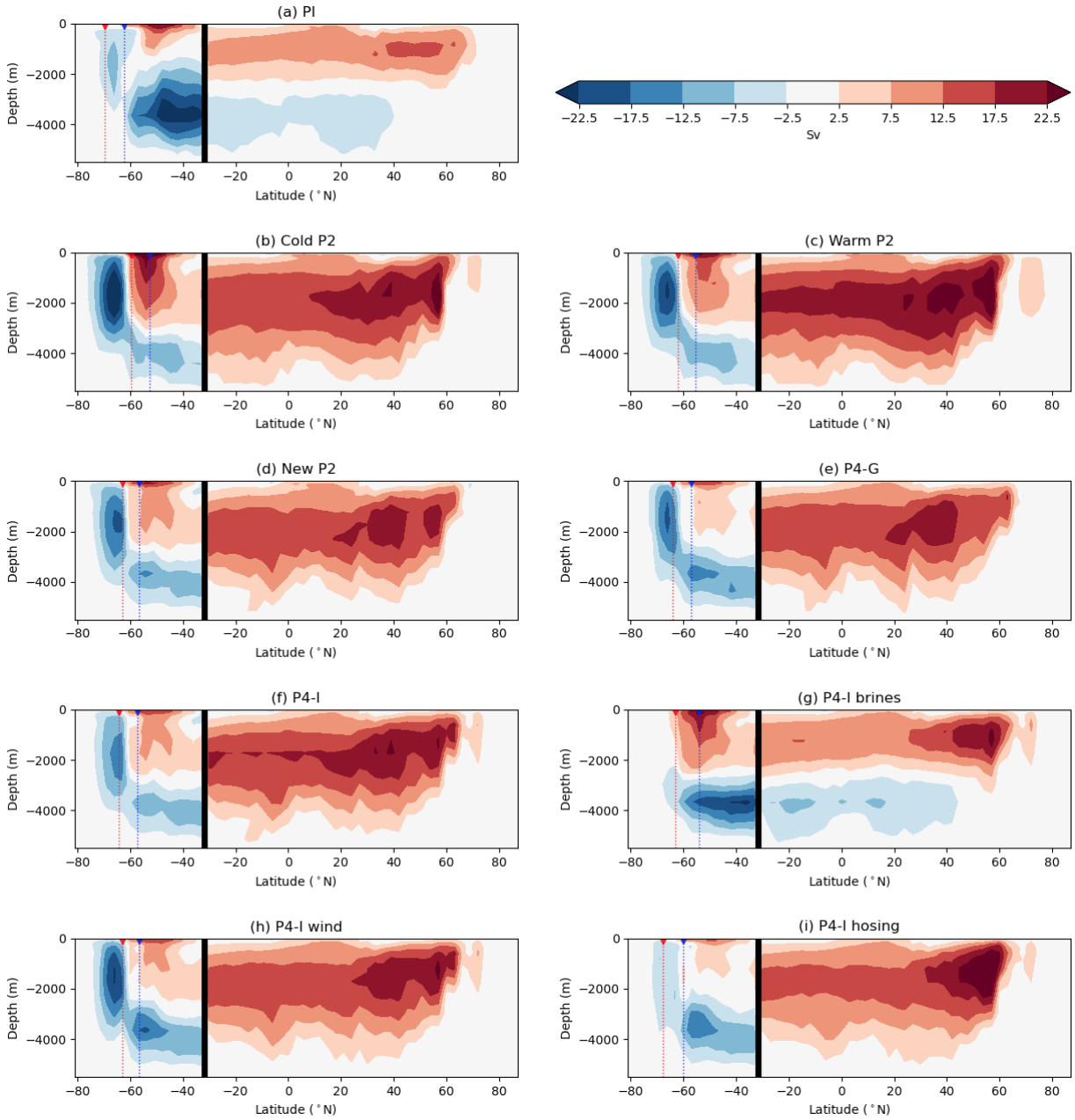

Figure 7. Streamfunctions (Sv) in the Atlantic (north of 32° S) and Southern Ocean basins (south of 32° S). The vertical black line represents the limit between these two basins, chosen at 32° S. The thin dotted lines show the latitude of the average sea-ice edge in austral summer (red) and winter (blue) for each simulation.

A clockwise cell can be observed in the Atlantic, which relates to the formation of NADW. In the Southern Ocean, we choose to define two counterclockwise cells – one which is located around 60–80° S and another which is located both deeper and further north – but which do not always penetrate into the Atlantic Ocean. We name these three overturning cells the NADW cell, the Southern Ocean cell, and the bottom cell, respectively. As Otto-Bliesner et al. (2007) have shown, iLOVECLIM is among the models which simulate a very strong glacial NADW cell at the expense of the bottom cell (as is also the case here for almost all experimental settings; see Fig. 7b, c, d, e, f, h, i), a response which is not consistent with the shallower glacial NADW and the more voluminous AABW inferred from paleotracer data (Curry and Oppo, 2005; Howe et al., 2016; Böhm et al., 2015; Lynch-Stieglitz et al., 2007).

We first observe an effect of the boundary conditions choice. For example, the use of the new bathymetry genera-

tion method reduces the LGM NADW cell slightly: its overturning is more intense for "Warm P2" than for "New P2". We also notice differences between the "P4-G" and "P4-I" streamfunctions, with a slight enhancement of the bottom overturning cell in the "P4-G" simulation associated with GLAC-1D (compared to the "P4-I" simulation with ICE-6G-C) but not enough to counterweight the massive NADW cell. However, we note that the choice of forcings and model parameters seems to have a stronger impact than the boundary conditions, as evidenced by the contrasting results between the three sensitivity tests and their parent simulation "P4-I". The bottom cell is strongly enhanced by the use of the parameterization of the sinking brines, an experimental setting which allows for the penetration of AABW in the Atlantic. On the other hand, the Southern Ocean cell is enhanced for "P4-I wind" but moderately ("P4-I hosing") or strongly ("P4-I brines") suppressed for the other sensitivity tests. These results could be due to the fact that the experimental setting of "P4-I wind" – with the multiplication of the meridional wind stress on ice – enhances sea-ice export, which leads to an increased sea-ice formation and its consequent brine rejection (Shin et al., 2003). In "P4-I brines", the Southern Ocean overturning is not fully explicitly computed due to the parameterization, leading to these very low values. Finally, it is no surprise that the addition of a freshwater flux ("P4-I hosing") leads to less overturning as it decreases the density of surface waters.

To single out the impact of surface conditions on the convection, we plot the relationship between the mean SST in the Southern Ocean and the maximum intensity of the three overturning cells in Fig. 8, for all simulations except the two with modeling choices affecting the density processes ("P4-I brines" and "P4-I hosing", plotted in Fig. S7). The correlation coefficients R are very significant (with $|R| \geq 0.83$ for all plots), showing that simulations with a colder Southern Ocean tend to be associated with a stronger Southern Ocean cell, a weaker bottom cell, and a more intense NADW cell. While this relationship holds, modeling choices yielding colder SST in the Southern Ocean (thus in better agreement with the data) do not lead to more realistic water mass distributions. Instead, a Southern Ocean cooling seems associated with an intensification of the open-ocean convection, with a negative effect on stratification.

4 Discussion

4.1 What is the relative impact of boundary conditions and modeling choices?

With this set of simulations, we make use of the recent evolution of the iLOVECLIM model (regarding the recommended PMIP4 experimental design and its implementation; see Sect. 2.2) to investigate the relative impact of boundary conditions and of other modeling choices (related to forcings or model parameter choices) on the simulated surface conditions and deep ocean circulation. Given the uncertainties in the ice sheet reconstructions, Kageyama et al. (2017) gave several options to modeling groups in the current phase (phase 4) of PMIP and advised the use of the new ICE-6G-C and GLAC-1D topographies (either one or, ideally, both). We have implemented both topographies in the relatively coarse-resolution iLOVECLIM model, and we show here that these two boundary conditions yield only small differences on the variables observed in this study. The use of the PMIP2 (ICE-5G) ice sheet reconstruction – with a higher elevation – causes an overall colder climate compared to PMIP4 but differences in simulated surface conditions and deep ocean circulation remain relatively small. In contrast, the modeling choices made in sensitivity tests can cause much larger differences (e.g., between "Cold P2" and "Warm P2", or "P4-I" and "P4-I brines", or "P4-I" and "P4-I hosing"). In particular, the differences between "Cold P2" and "Warm P2" suggest that, while iLOVECLIM generally simulates a more modest global SAT anomaly than other PMIP4 models (Kageyama et al., 2021), modeling choices related to the glacial temperature profiles used in the radiative code can induce a very significant change. Moreover, thanks to the use of proxy data to evaluate our simulations, this inverse methodology approach is useful to highlight systematic biases in the simulated surface conditions of the Southern Ocean. In the iLOVECLIM model, it seems that the recurrent biases are larger than the differences related to the choice of boundary conditions. It is therefore particularly important to investigate and understand the origin of these biases, while different ice sheet reconstructions have a relatively smaller impact and may not all be implemented during the PMIP4 exercise. Nonetheless, it should be noted that Galbraith and de Lavergne (2019) have investigated the effects of a broader range of forcings (greenhouse gas concentrations and orbital parameters in addition to changes in ice sheet size) on the deep water masses and they notably highlighted the nonlinear responses of their volume to varying forcings (e.g., with different global temperatures). Therefore, the choice of ice sheet reconstruction could potentially yield more significant differences in deep ocean circulation under different time periods or simulated global temperature.

4.2 What is the "best" simulation and why?

Our analysis suggests that in terms of surface conditions, the PMIP2 boundary conditions yield a better agreement than the PMIP4 ones with SST and sea-ice geological data. However, among our set of eight simulations, the sensitivity test with the parameterization of the sinking of the dense water ("P4-I brines") is the one with the best overall agreement with data. This parameterization allows for the simulation of a cold Southern Ocean, an extensive winter sea-ice cover along with an enhanced seasonality of sea ice (close to the data estimate) compared to other simulations. This parameterization also impacts the AABW density and therefore the deep ocean

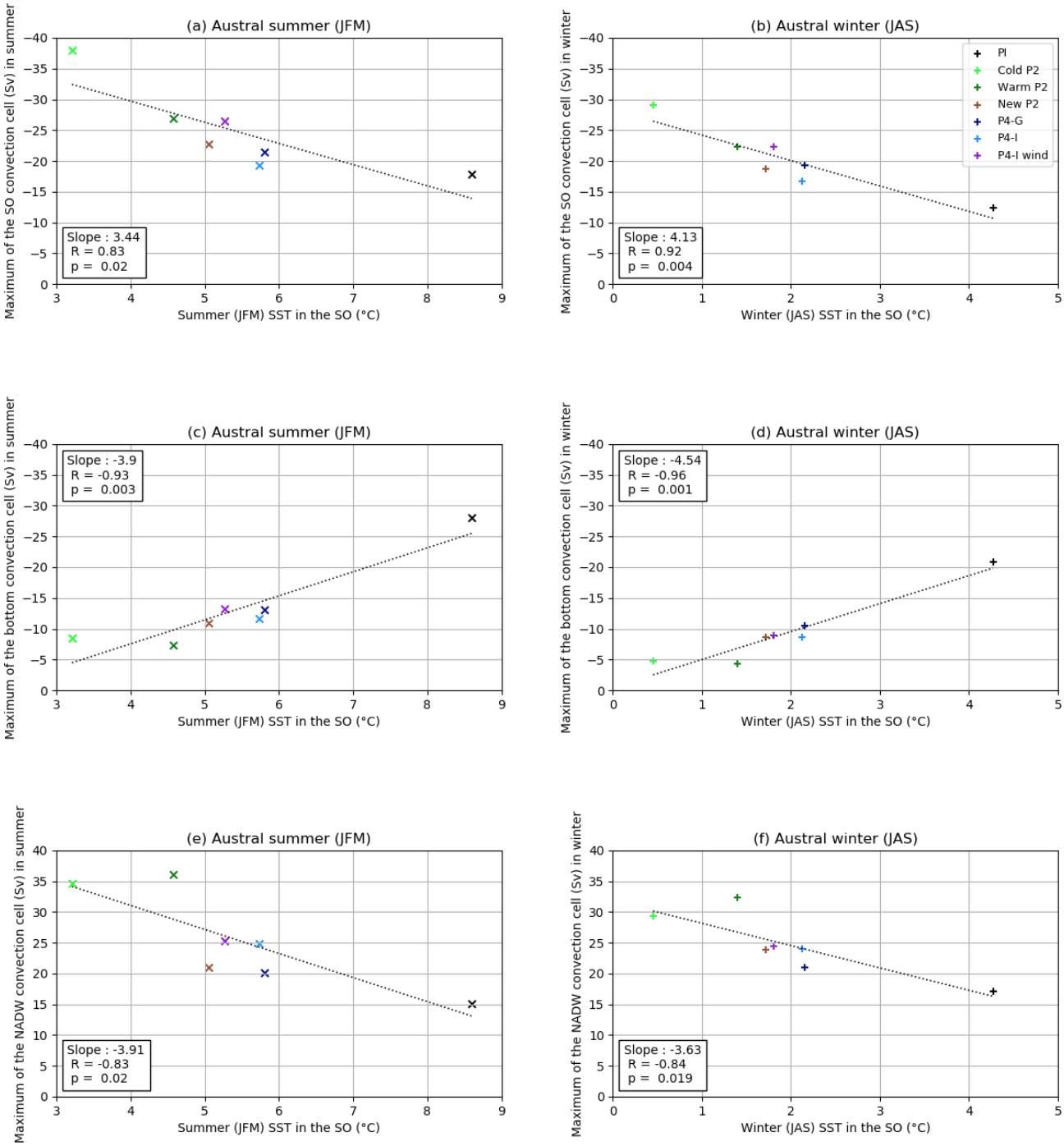

Figure 8. Relationships between the mean SST in the Southern Ocean (averaged up to 36° S) and the Southern Ocean **(a, b)**, bottom **(c, d)**, or NADW **(e, f)** overturning cell maximum, for all simulations except "P4-I brines" and "P4-I hosing". The *y* axis is inverted for the two counterclockwise cells **(a–d)**. The dotted line represents the linear fit to the model results plotted here.

circulation. Among our set of simulations, it is the only one simulating a water mass distribution which is reconcilable with reconstructions from paleoproxies. Nonetheless, this experimental design (like all the others tested in this study) does not result in a shoaling of the AMOC between the PI and LGM state (see Fig. S5), as inferred from the majority of the proxy data (Curry and Oppo, 2005; Böhm et al., 2015; Skinner et al., 2017; Gebbie, 2014). In contrast, Morée et al. (2021) were able to simulate with the NorESM-OC model a shoaled and slightly weaker AMOC at the LGM compared

to their PI state. As the radiocarbon ages simulated in southern source waters were too young compared to data, they suggested however that the ventilation at the LGM was still overestimated, possibly in relation to a too-small Antarctic sea-ice extent in their LGM simulation (their Fig. S12, displaying a sea-ice extent of $\sim 4.94 \times 10^6$ km^2 in summer and $\sim 32.95 \times 10^6$ km^2 in winter). However, if we consider our new estimates of $\sim 10.2 \times 10^6$ and $\sim 32.9 \times 10^6$ km^2 (respectively, for the summer and winter sea-ice extent inferred from proxy data), instead of the ones presented in Roche et al. (2012), the sea-ice extent simulated by Morée et al. (2021) is underestimated only in summer. Therefore, additional processes might be involved to explain the weak ventilation of Southern Ocean sourced deep water at the LGM.

Artificially sinking dense waters is motivated by the fact that, due to the coarse resolution of the model, the salt linked to brine rejection during sea-ice formation tends to get diluted in the surface grid cells rather than allow the sinking of dense water along the continental slope (Bouttes et al., 2010). Though legitimate, this parameterization is quite crude: a fraction (here chosen as 0.8) of the salt content of the surface grid cells is directly transferred to the deepest grid cell beneath them, without explicitly computing the convection.

However, we can argue that the open-ocean convection in the Southern Ocean is actually hindering the simulation of a realistic water mass distribution. Indeed, while paleotracer data suggest a dense, stratified glacial deep ocean, the simulation of cold conditions in the Southern Ocean is rather associated with an intense convection in the Southern Ocean (therefore well mixed) and a deep NADW (Figs. 7 and 8). As underlined by Heuzé et al. (2013), models struggle to simulate the correct bottom water properties even in the present-day conditions, as they tend to form AABW by open-ocean convection, a process rarely observed, instead of the overflow of dense continental shelf water. While none of the CMIP5 models were able to simulate the latter, Heuzé (2021) showed that a few CMIP6 models are now able to simulate AABW formation via shelf processes, notably thanks to the development of an overflow parameterization. Despite this progress, the issue remains, as "the large majority of climate models form deep water via open ocean deep convection, too deep, too often, over too large an area" (Heuzé, 2021).

Our results suggest that, even if we were able to simulate surface conditions in perfect agreement with proxy data, it would probably not be sufficient to simulate a deep ocean circulation in good agreement with paleotracer data, unless the convection and mixing processes are realistically represented by the model. Accounting for the sinking of brines rejected during sea-ice formation using a parameterization may be one way of tackling this issue, but other authors have also put forward the importance of a realistic vertical mixing scheme (De Boer and Hogg, 2014; de Lavergne et al., 2017). Topography-dependent mixing parameterizations, linked to the energy received by water masses due to geothermal fluxes and interactions of tidal waves with the ocean floor, have been recently developed in some high-resolution models (de Lavergne et al., 2019). Their effects on the simulated deep ocean circulation in a coarser-resolution z-level model such as iLOVECLIM may be of interest for further studies.

4.3 What are the systematic biases?

Still, even in the sensitivity test with the parameterization of the sinking of the dense water ("P4-I brines"), which yields the best model–data agreement among our set of simulations, the model results show the same biases than in all the other simulations. We observe several systematic biases, linked to seasonal or regional patterns of SSTs and sea ice. First of all, the simulated seasonal amplitude of sea ice is too small with respect to the proxy data estimates, which suggest a sea-ice seasonality of 22.7×10^6 km^2 ($\pm 8.0 \times 10^6$ km^2 based on 15 % and 30 % error bars on winter and summer sea-ice extent, respectively). Secondly, the simulated winter sea-ice extent seems too small (compared to data) in the Atlantic and Indian sectors ($\sim$ 40–50° S), and too large in the Pacific sector ($\sim$ 60° S) for cold simulations. The model simulates round sea-ice distributions, while proxy data suggest more oval-shaped winter and summer covers, as observed today. Thirdly, the simulated summer SSTs are too high in the Atlantic and Indian sectors ($\sim$ 40–50° S) with respect to MARGO data, while they sometimes seem slightly too low in the high latitudes of the Pacific sector. This is true at least for the summer months, as data are scarce in the winter months.

We note that the model underestimates the interbasin contrasts, as it struggles to simulate a large winter sea-ice cover in the Atlantic and Indian sectors. While a good representation of sea-ice advection by the Antarctic Circumpolar Current may be hard to achieve in key areas (e.g., Weddell Sea, Ross Sea, Kerguelen Plateau where strong oceanic gyres exist) due to the discretization of the coasts on a 3° × 3° land–sea mask, this difficulty could be largely attributed to the warm bias observed in the Southern Ocean. The clear zonal trend of this bias may stem from an underestimated polar amplification, and/or of the SST gradients across the oceanic fronts (whose location may also be wrong). This type of bias is not surprising considering the relatively coarse spatial resolution of iLOVECLIM. Interestingly, diverse modeling studies have also pointed out distinctive regional patterns in the Southern Ocean with significant differences between the Pacific sector and the other two sectors, whether it considered freshwater fluxes linked to icebergs and their influence on sea ice (Merino et al., 2016), zonal asymmetries of the Southern Hemisphere westerly jet trends (Waugh et al., 2021), or the sea-ice retreat scenario with the best agreement with the Antarctic ice core δ^{18}O records at the last interglacial period (Holloway et al., 2017).

Identifying the origin of a bias is always a challenge. It might be an especially hard task to identify the origin of biases in the simulated sea-ice cover, considering the sheer

number of feedbacks involved (Goosse et al., 2018). What can be noticed is that the simulated sea-ice seasonal cycle is affected by some of our modeling choices (increased in "P4-I brines", reduced in "P4-I wind"). Alongside, the Southern Ocean convection is suppressed in the first sensitivity test and enhanced in the second. In a climatological mean in our model, there seems to be a link between reduced Southern Ocean convection and increased sea-ice seasonal cycle. In opposition to this observation, Heuzé et al. (2013) have underlined the fact that CMIP5 models with a large sea-ice seasonality are also the ones simulating open-ocean convection over extensive areas at modern times, arguing that strong sea-ice formation could precondition the ocean for open-ocean deep convection. This questions the relative importance of the different simulated mechanisms at play linking the ocean convection and the sea-ice seasonal cycle, an aspect that is present in several studies (Marshall and Speer, 2012; Behrens et al., 2016; Ma et al., 2020).

5 Conclusions

Using diverse boundary conditions and sensitivity tests, we are able to simulate a variety of LGM climates and in particular different surface conditions in the Southern Ocean among our set of simulations. We assess the model–data agreement in terms of both SSTs and sea-ice extent, and we explore the associated impact on deep ocean circulation.

In this study, we underline that simulated cold surface conditions in the Southern Ocean are overall in better agreement with proxy data. A detailed analysis shows that there are seasonal and spatial distribution patterns which are associated with systematic discrepancies between our simulations and both sea-ice and SST reconstructions. All simulations underestimate the sea-ice seasonal range (with a simulated sea-ice extent range equal to 65 % to 94 % of the range inferred from the proxy reconstructions). Model–data comparisons also consistently suggest that the simulated SSTs of the Pacific sector of the Southern Ocean ($\sim 60^\circ$ S) are slightly too low, while those of the Atlantic and Indian sectors (~ 40–50° S) are too high, which may explain why the model is not able to reproduce the reconstructed oval-shaped distributions of sea ice. Overall, the model results exhibit a mean warm bias of 2 to 6 °C over the Southern Ocean with respect to MARGO data.

Yet, colder conditions in the Southern Ocean would not necessarily lead to a more realistic water mass distribution. Our study shows that colder conditions rather tend to intensify the Southern Ocean open-ocean convection, a process which leads to inaccurate AABW properties, as it does not account for the overflow of dense continental shelf water but instead creates a well-mixed water column. The parameterization of the sinking of brines is the only experimental setting we used which accommodates a better representation of both the surface conditions and the deep ocean circulation. For the variables analyzed in this study, it would therefore seem that the improved simulation of convection processes is paramount and far more important than the choice of ice sheet reconstruction used to implement the orography and bathymetry.

Appendix A: Description of the semi-automated method to generate CLIO bathymetries

This method replaces the tedious manual changes that have been done on the CLIO grid in the past, in order to be able to generate a CLIO bathymetry quickly from any topography file – a technical development which fastens the start of new PMIP phases and enables the run of transient simulations with an interactive bathymetry. It has been used here to (re)generate a pre-industrial bathymetry (using the high-resolution etopo1 topography), a PMIP2 bathymetry (using the ICE-5G reconstruction), and two PMIP4 bathymetries (using either the GLAC-1D or the ICE-6G-C reconstruction).

This development has been done in several pre-processing steps:

- Anomalies are computed using the PMIP2/PMIP4 topographies and then regridded on the etopo1 grid:

  LGM topography = PI (etopo1) + LGM Peltier (ICE-6G-C, 21 kyr) − PI Peltier (ICE-6G-C, 0 kyr).

- A connectivity program (see Appendix B) writes the mean bathymetry and hypsometry into a text file, either on the rotated or regular CLIO grid. It also produces the connections between ocean basins thanks to the computation of subgrid sills.

- In a second program, the two grids are first put together.

- Then, the mask is generated using the hypsometry, a chosen sea level (−0.5 m for the PI, −133.9 m for the LGM, according to Lambeck et al., 2014), and a chosen threshold (% of surface of a grid cell above which the cell is defined as ocean – here 40 %). Small isolated seas are closed. The mask of a few ocean grid cells is manually forced at the PI so that all the critical straits stay open. These manual points have to be redefined at the LGM. Indeed, while some stay the same (Strait of Gibraltar), others are not necessary anymore (Hudson Bay and Sea of Japan outlets), and a few new critical points appear (Fram Strait, Gulf of Mexico outlet). We take particular care of this step, using the connections computed earlier and our knowledge of the LGM ocean.

- The bathymetry is converted into the irregular vertical levels of the CLIO model. The new vertical levels are set equal to the former vertical levels for a few problematic grid cells in order to get realistic salinity values in the Mediterranean Sea and Hudson Bay. Vertical level 1 is avoided (either forced to 0 or 2), because the model cannot deal with these very shallow grid cells. As the model also cannot deal with isolated oceanic grid cells for which the deepest vertical level is isolated (e.g., deep grid cells with shallower neighbors), a process similar to a smoothing filter is applied.

- Finally, this program writes a text file containing the bathymetry with the land–sea mask (0 in every land grid cell).

- Two additional pre-processing steps are required to generate the necessary input files (one containing the fraction of ocean seen by the T21 grid cells and another containing the interpolation points between the CLIO and the T21 grids).

- In order to be able to quickly equilibrate the model when running a simulation with a different bathymetry than its restart, the initialization code of iLOVECLIM has been modified to generate realistic values of the tracer content of new oceanic grid cells. To achieve this, the initialization of all the restart variables in new ocean grid cells is done by averaging the values in neighboring oceanic grid cells when necessary. The conservation of the total content of conservative variables (salt, carbon, etc.) is ensured.

Appendix B: Description of the connectivity program

The "topo_connect" software was developed in order to compute the connection between ocean basins directly from topography/bathymetry data. The basic idea is rather simple, though its implementation is not trivial. The algorithm builds a global tree structure from the topographic data file, with each leaf corresponding to a local minimum in the topographic data, with the trunk corresponding to the entire domain, and with branching occurring for each sill between two (or more) sub-basins. From this tree structure, it is then easy to find the lowest sill connecting any two points by finding the first common branch to which they belong.

More precisely, the algorithm starts by finding the local minima in the topographic domain. For each minimum, it builds the set of points belonging to this minimum basin by adding the lowest (uphill) neighbor and continues to do so up to finding a sill. This sill corresponds to a branching between two (or more) basins. The algorithm then continues the same procedure from this sill, up to the next one, and so on, until all basins (branches) are connected to a single trunk, which represents the whole domain. Building this tree structure is the most computationally demanding task. Then, for any two points in the domain, it is easy to use this tree structure and to find the level (and the location) of the lowest sill connecting them. For a given sea level, this allows us to decide if two ocean basins are connected or not, according to topographic data. This information is then aggregated in a new grid system, typically an ocean model grid with a much lower resolution, in order to decide whether model cells are connected or not.

The implementation requires caution, since non-trivial cases can arise. For example, there may be flat areas in the domain and/or multiple sills at the same level therefore con-

necting more than two basins at the same time. The implementation relies therefore not on simple traditional "arrays" but on more flexible structures like "lists" or "priority_queues" available in standard C++. The execution time is a few minutes on a desktop computer when using bathymetric data at the resolution of 1 arcmin (etopo1). Higher resolution could be useful to resolve some canyons, in particular to compute the possible extent of lakes on land, but this was not investigated so far.

Data availability. The model outputs and reconstructed sea-ice limits are available for download online (https://doi.org/10.5281/zenodo.4576026, Lhardy, 2020).

Supplement. The supplement related to this article is available online at: https://doi.org/10.5194/cp-17-1139-2021-supplement.

Author contributions. FL, NB, and DMR designed the study. DP developed the connectivity program. DMR, FL, and NB developed the semi-automated bathymetry generation method, and the iLOVECLIM model to accommodate new boundary conditions. FL performed the simulations and analyzed the outputs under supervision of NB and DMR. XC compiled existing sea-ice proxy data, inferred the reconstruction of LGM sea-ice edges, and provided expert knowledge on sea-ice processes. CW contributed expert knowledge on SST data. FL wrote the manuscript with contributions from all co-authors.

Competing interests. The authors declare that they have no conflict of interest.

Special issue statement. This article is part of the special issue "Reconstructing Southern Ocean sea-ice dynamics on glacial-to-historical timescales". It is not associated with a conference.

Acknowledgements. The authors acknowledge the support from the French National program LEFE (Les Enveloppes Fluides et l'Environnement). Fanny Lhardy acknowledges the use of the LSCE storage and computing facilities. Didier M. Roche, Nathaëlle Bouttes, Claire Waelbroeck, and Xavier Crosta are supported by the Centre national de la recherche scientifique (CNRS). Didier M. Roche is also supported by the Vrije Universiteit Amsterdam. Didier Paillard is supported by the Commisariat à l'énergie atomatique et aux énergies alternatives (CEA) and Fanny Lhardy by the Université Versailles Saint-Quentin-en-Yvelines (UVSQ). Claire Waelbroeck acknowledges the support from the European Research Council. We thank Aurélien Quiquet for scientific discussions and technical support on the use of iLOVECLIM. We also thank Masa Kageyama and Jean-Yves Peterschmitt for their technical help. Last but not least, we thank the two anonymous reviewers for their help with the manuscript.

Financial support. This research has been supported by the European Research Council (ERC), Seventh Framework Programme (ACCLIMATE; grant no. 339108) and the French National program LEFE (Les Enveloppes Fluides et l'Environnement, project GLACOCEAN).

Review statement. This paper was edited by Alice Marzocchi and reviewed by two anonymous referees.

References

Abe-Ouchi, A., Saito, F., Kageyama, M., Braconnot, P., Harrison, S. P., Lambeck, K., Otto-Bliesner, B. L., Peltier, W. R., Tarasov, L., Peterschmitt, J.-Y., and Takahashi, K.: Ice-sheet configuration in the CMIP5/PMIP3 Last Glacial Maximum experiments, Geosci. Model Dev., 8, 3621–3637, https://doi.org/10.5194/gmd-8-3621-2015, 2015.

Adkins, J. F., McIntyre, K., and Schrag, D. P.: The salinity, temperature, and $\delta^{18}O$ of the glacial deep ocean, Science, 298, 1769–1773, https://doi.org/10.1126/science.1076252, 2002.

Allen, C. S., Pike, J., and Pudsey, C. J.: Last glacial-interglacial sea-ice cover in the SW Atlantic and its potential role in global deglaciation, Quaternary Sci. Rev., 30, 2446–2458, https://doi.org/10.1016/j.quascirev.2011.04.002, 2011.

Amante, C. and Eakins, B. W.: ETOPO1 1 Arc-Minute Global Relief Model: Procedures, Data Sources and Analysis, National Geophysical Data Center, NOAA, NOAA Technical Memorandum NESDIS NGDC-24, https://doi.org/10.7289/V5C8276M, 2009.

Annan, J. D. and Hargreaves, J. C.: A new global reconstruction of temperature changes at the Last Glacial Maximum, Clim. Past, 9, 367–376, https://doi.org/10.5194/cp-9-367-2013, 2013.

Argus, D. F., Peltier, W. R., Drummond, R., and Moore, A. W.: The Antarctica component of postglacial rebound model ICE-6G-C (VM5a) based on GPS positioning, exposure age dating of ice thicknesses, and relative sea level histories, Geophys. J. Int., 198, 537–563, https://doi.org/10.1093/gji/ggu140, 2014.

Behrens, E., Rickard, G., Morgenstern, O., Martin, T., Osprey, A., and Joshi, M.: Southern Ocean deep convection in global climate models: A driver for variability of subpolar gyres and Drake Passage transport on decadal timescales, J. Geophys. Res.-Oceans, 121, 3905–3925, https://doi.org/10.1002/2015JC011286, 2016.

Bentley, M. J., Cofaigh, C. O., Anderson, J. B., et al.: A community-based geological reconstruction of Antarctic Ice Sheet deglaciation since the Last Glacial Maximum, Quaternary Sci. Rev., 100, 1–9, https://doi.org/10.1016/j.quascirev.2014.06.025, 2014.

Benz, V., Esper, O., Gersonde, R., Lamy, F., and Tiedemann, R.: Last Glacial Maximum sea surface temperature and sea-ice extent in the Pacific sector of the Southern Ocean, Quaternary Sci. Rev., 146, 216–237, https://doi.org/10.1016/j.quascirev.2016.06.006, 2016.

Bereiter, B., Eggleston, S., Schmitt, J., Nehrbass-Ahles, C., Stocker, T. F., Fischer, H., Kipfstuhl, S., and Chappellaz, J.: Revision of the EPICA Dome C CO_2 record from 800 to 600 kyr before present, Geophys. Res. Lett., 42, 542–549, https://doi.org/10.1002/2014GL061957, 2015.

Berger, A.: Long-term variations of daily insolation and quaternary climatic changes, J. Atmos. Sci., 35, 2362–2367, https://doi.org/10.1175/1520-0469(1978)035<2362:LTVODI>2.0.CO;2, 1978.

Bouttes, N., Paillard, D., and Roche, D. M.: Impact of brine-induced stratification on the glacial carbon cycle, Clim. Past, 6, 575–589, https://doi.org/10.5194/cp-6-575-2010, 2010.

Buchanan, P. J., Matear, R. J., Lenton, A., Phipps, S. J., Chase, Z., and Etheridge, D. M.: The simulated climate of the Last Glacial Maximum and insights into the global marine carbon cycle, Clim. Past, 12, 2271–2295, https://doi.org/10.5194/cp-12-2271-2016, 2016.

Bé, A. W. H. and Hutson, W. H.: Ecology of planktonic foraminifera and biogeographic patterns of life and fossil assemblages in the Indian Ocean, Micropaleontology, 23, 369–414, https://doi.org/10.2307/1485406, 1977.

Böhm, E., Lippold, J., Gutjahr, M., Frank, M., Blaser, P., Antz, B., Fohlmeister, J., Frank, N., Andersen, M. B., and Deininger, M.: Strong and deep Atlantic meridional overturning circulation during the last glacial cycle, Nature, 517, 73–76, https://doi.org/10.1038/nature14059, 2015.

Campin, J.-M. and Goosse, H.: Parameterization of density-driven downsloping flow for a coarse-resolution ocean model in z-coordinate, Tellus A, 51, 412–430, https://doi.org/10.3402/tellusa.v51i3.13468, 1999.

Claussen, M., Mysak, L. A., Weaver, A. J., Crucifix, M., Fichefet, T., Loutre, M. F., Weber, S. L., Alcamo, J., Alexeev, V. A., Berger, A., Calov, R., Ganopolski, A., Goosse, H., Lohman, G., Lunkeit, F., Mohkov, I. I., Petoukhov, V., Stone, P., and Wang, Z.: Earth System Models of Intermediate Complexity: closing the gap in the spectrum of climate system models, Clim. Dynam., 18, 579–586, https://doi.org/10.1007/s00382-001-0200-1, 2002.

Cortese, G. and Prebble, J.: A radiolarian-based modern analogue dataset for palaeoenvironmentalreconstructions in the southwest Pacific, Mar. Micropaleontol., 118, 34–49, https://doi.org/10.1016/j.marmicro.2015.05.002, 2015.

Crosta, X., Sturm, A., Armand, L., and Pichon, J.-J.: Late Quaternary sea ice history in the Indian sector of the Southern Ocean as recorded by diatom assemblages, Mar. Micropaleontol., 50, 209–223, https://doi.org/10.1016/S0377-8398(03)00072-0, 2004.

Curry, W. B. and Oppo, D. W.: Glacial water mass geometry and the distribution of $\delta^{13}C$ of $\sum CO_2$ in the western Atlantic Ocean, Paleoceanography, 20, 317–341, https://doi.org/10.1029/2004PA001021, 2005.

De Boer, A. M. and Hogg, A. M. C.: Control of the glacial carbon budget by topographically induced mixing, Geophys. Res. Lett., 41, 4277–4284, https://doi.org/10.1002/2014GL059963, 2014.

de Lavergne, C., Madec, G., Roquet, F., Holmes, R. M., and McDougall, T. J.: Abyssal ocean overturning shaped by seafloor distribution, Nature, 551, 181–186, https://doi.org/10.1038/nature24472, 2017.

de Lavergne, C., Falahat, S., Madec, G., Roquet, F., Nycander, J., and Vic, C.: Toward global maps of internal tide energy sinks, Ocean Model., 137, 52–75, https://doi.org/10.1016/j.ocemod.2019.03.010, 2019.

Downes, S. M., Farneti, R., Uotila, P., Griffies, S. M., Marsland, S. J., Bailey, D., Behrens, E., Bentsen, M., Bi, D., Biastoch, A., Böning, C., Bozec, A., Canuto, V. M., Chassignet, E., Danabasoglu, G., Danilov, S., Diansky, N., Drange, H., Fogli, P. G., Gusev, A., Howard, A., Ilicak, M., Jung, T., Kelley, M., Large, W. G., Leboissetier, A., Long, M., Lu, J., Masina, S., Mishra, A., Navarra, A., George Nurser, A. J., Patara, L., Samuels, B. L., Sidorenko, D., Spence, P., Tsujino, H., Wang, Q., and Yeager, S. G.: An assessment of Southern Ocean water masses and sea ice during 1988–2007 in a suite of interannual CORE-II simulations, Ocean Model., 94, 67–94, https://doi.org/10.1016/j.ocemod.2015.07.022, 2015.

Esper, O. and Gersonde, R.: New tools for the reconstruction of Pleistocene Antarctic sea ice, Palaeogeography, Palaeoclimatology, Palaeoecology, 399, 260–283, https://doi.org/10.1016/j.palaeo.2014.01.019, 2014.

Ferrari, R., Jansen, M. F., Adkins, J. F., Burke, A., Stewart, A. L., and Thompson, A. F.: Antarctic sea ice control on ocean circulation in present and glacial climates, P. Natl. Acad. Sci. USA, 111, 8753–8758, https://doi.org/10.1073/pnas.1323922111, 2014.

Ferry, A. J., Crosta, X., Quilty, P. G., Fink, D., Howard, W., and Armand, L. K.: First records of winter sea ice concentration in the southwest Pacific sector of the Southern Ocean, Paleoceanography, 30, 1525–1539, https://doi.org/10.1002/2014PA002764, 2015.

Fichefet, T. and Morales Maqueda, M. A.: Sensitivity of a global sea ice model to the treatment of ice thermodynamics and dynamics, J. Geophys. Res., 102, 12609–12646, https://doi.org/10.1029/97JC00480, 1997.

Fretwell, P., Pritchard, H. D., Vaughan, D. G., Bamber, J. L., Barrand, N. E., Bell, R., Bianchi, C., Bingham, R. G., Blankenship, D. D., Casassa, G., Catania, G., Callens, D., Conway, H., Cook, A. J., Corr, H. F. J., Damaske, D., Damm, V., Ferraccioli, F., Forsberg, R., Fujita, S., Gim, Y., Gogineni, P., Griggs, J. A., Hindmarsh, R. C. A., Holmlund, P., Holt, J. W., Jacobel, R. W., Jenkins, A., Jokat, W., Jordan, T., King, E. C., Kohler, J., Krabill, W., Riger-Kusk, M., Langley, K. A., Leitchenkov, G., Leuschen, C., Luyendyk, B. P., Matsuoka, K., Mouginot, J., Nitsche, F. O., Nogi, Y., Nost, O. A., Popov, S. V., Rignot, E., Rippin, D. M., Rivera, A., Roberts, J., Ross, N., Siegert, M. J., Smith, A. M., Steinhage, D., Studinger, M., Sun, B., Tinto, B. K., Welch, B. C., Wilson, D., Young, D. A., Xiangbin, C., and Zirizzotti, A.: Bedmap2: improved ice bed, surface and thickness datasets for Antarctica, The Cryosphere, 7, 375–393, https://doi.org/10.5194/tc-7-375-2013, 2013.

Galbraith, E. and de Lavergne, C.: Response of a comprehensive climate model to a broad range of external forcings: relevance for deep ocean ventilation and the development of late Cenozoic ice ages, Clim. Dynam., 52, 653–679, https://doi.org/10.1007/s00382-018-4157-8, 2019.

Gebbie, G.: How much did Glacial North Atlantic Water shoal?, Paleoceanography, 29, 190–209, https://doi.org/10.1002/2013PA002557, 2014.

Gersonde, R. and Zielinski, U.: The reconstruction of late Quaternary Antarctic sea-ice distribution–the use of diatoms as a proxy for sea-ice, Palaeogeogr. Palaeocl., 162, 263–286, https://doi.org/10.1016/S0031-0182(00)00131-0, 2000.

Gersonde, R., Crosta, X., Abelmann, A., and Armand, L.: Sea-surface temperature and sea ice distribution of the Southern Ocean at the EPILOG Last Glacial Maximum – a circum-Antarctic view based on siliceous microfossil records, Quaternary Sci. Rev., 24, 869–896, https://doi.org/10.1016/j.quascirev.2004.07.015, 2005.

Ghadi, P., Nair, A., Crosta, X., Mohan, R., Manoj, M., and Meloth, T.: Antarctic sea-ice and palaeoproductivity variation over the last 156,000 years in the Indian sector of Southern Ocean, Mar. Micropaleontol., 160, 101894, https://doi.org/10.1016/j.marmicro.2020.101894, 2020.

Goosse, H., Brovkin, V., Fichefet, T., Haarsma, R., Huybrechts, P., Jongma, J., Mouchet, A., Selten, F., Barriat, P.-Y., Campin, J.-M., Deleersnijder, E., Driesschaert, E., Goelzer, H., Janssens, I., Loutre, M.-F., Morales Maqueda, M. A., Opsteegh, T., Mathieu, P.-P., Munhoven, G., Pettersson, E. J., Renssen, H., Roche, D. M., Schaeffer, M., Tartinville, B., Timmermann, A., and Weber, S. L.: Description of the Earth system model of intermediate complex-

ity LOVECLIM version 1.2, Geosci. Model Dev., 3, 603–633, https://doi.org/10.5194/gmd-3-603-2010, 2010.

Goosse, H., Roche, D. M., Mairesse, A., and Berger, M.: Modelling past sea ice changes, Quaternary Sci. Rev., 79, 191–206, https://doi.org/10.1016/j.quascirev.2013.03.011, 2013.

Goosse, H., Kay, J. E., Armour, K. C., Bodas-Salcedo, A., Chepfer, H., Docquier, D., Jonko, A., Kushner, P. J., Lecomte, O., Massonnet, F., Park, H.-S., Pithan, F., Svensson, G., and Vancoppenolle, M.: Quantifying climate feedbacks in polar regions, Nat. Commun., 9, 1–13, https://doi.org/10.1038/s41467-018-04173-0, 2018.

Heuzé, C.: Antarctic Bottom Water and North Atlantic Deep Water in CMIP6 models, Ocean Sci., 17, 59–90, https://doi.org/10.5194/os-17-59-2021, 2021.

Heuzé, C., Heywood, K. J., Stevens, D. P., and Ridley, J. K.: Southern Ocean bottom water characteristics in CMIP5 models, Geophys. Res. Lett., 40, 1409–1414, https://doi.org/10.1002/grl.50287, 2013.

Holloway, M. D., Sime, L. C., Allen, C. S., Bunch, P., Wolff, E., and Valdes, P. J.: The Spatial Structure of the 128 ka Antarctic Sea Ice Minimum, Geophys. Res. Lett., 44, 129–139, https://doi.org/10.1002/2017GL074594, 2017.

Howard, W. R. and Prell, W. L.: Late Quaternary surface circulation of the Southern Indian Ocean and its relations to orbital variations, Paleoceanography, 7, 79–117, https://doi.org/10.1029/91PA02994, 1992.

Howe, J. N. W., Piotrowski, A. M., Noble, T. L., Mulitza, S., Chiessi, C. M., and Bayon, G.: North Atlantic Deep Water Production during the Last Glacial Maximum, Nat. Commun., 7, 1–8, https://doi.org/10.1038/ncomms11765, 2016.

Hyder, P., Edwards, J. M., Allan, R. P., Hewitt, H. T., Bracegirdle, T. J., Gregory, J. M., Wood, R. A., Meijers, A. J. S., Mulcahy, J., Field, P., Furtado, K., Bodas-Salcedo, A., Williams, K. D., Copsey, D., Josey, S. A., Liu, C., Roberts, C. D., Sanchez, C., Ridley, J., Thorpe, L., Hardiman, S. C., Mayer, M., Berry, D. I., and Belcher, S. E.: Critical Southern Ocean climate model biases traced to atmospheric model cloud errors, Nat. Commun., 9, 3625, https://doi.org/10.1038/s41467-018-05634-2, 2018.

Kageyama, M., Albani, S., Braconnot, P., Harrison, S. P., Hopcroft, P. O., Ivanovic, R. F., Lambert, F., Marti, O., Peltier, W. R., Peterschmitt, J.-Y., Roche, D. M., Tarasov, L., Zhang, X., Brady, E. C., Haywood, A. M., LeGrande, A. N., Lunt, D. J., Mahowald, N. M., Mikolajewicz, U., Nisancioglu, K. H., Otto-Bliesner, B. L., Renssen, H., Tomas, R. A., Zhang, Q., Abe-Ouchi, A., Bartlein, P. J., Cao, J., Li, Q., Lohmann, G., Ohgaito, R., Shi, X., Volodin, E., Yoshida, K., Zhang, X., and Zheng, W.: The PMIP4 contribution to CMIP6 – Part 4: Scientific objectives and experimental design of the PMIP4-CMIP6 Last Glacial Maximum experiments and PMIP4 sensitivity experiments, Geosci. Model Dev., 10, 4035–4055, https://doi.org/10.5194/gmd-10-4035-2017, 2017.

Kageyama, M., Harrison, S. P., Kapsch, M.-L., Lofverstrom, M., Lora, J. M., Mikolajewicz, U., Sherriff-Tadano, S., Vadsaria, T., Abe-Ouchi, A., Bouttes, N., Chandan, D., Gregoire, L. J., Ivanovic, R. F., Izumi, K., LeGrande, A. N., Lhardy, F., Lohmann, G., Morozova, P. A., Ohgaito, R., Paul, A., Peltier, W. R., Poulsen, C. J., Quiquet, A., Roche, D. M., Shi, X., Tierney, J. E., Valdes, P. J., Volodin, E., and Zhu, J.: The PMIP4 Last Glacial Maximum experiments: preliminary results and comparison with the PMIP3 simulations, Clim. Past, 17, 1065–1089, https://doi.org/10.5194/cp-17-1065-2021, 2021.

Khatiwala, S., Schmittner, A., and Muglia, J.: Air-sea disequilibrium enhances ocean carbon storage during glacial periods, Science Advances, 5, eaaw4981, https://doi.org/10.1126/sciadv.aaw4981, 2019.

Lambeck, K., Rouby, H., Purcell, A., Sun, Y., and Sambridge, M.: Sea level and global ice volumes from the Last Glacial Maximum to the Holocene, P. Natl. Acad. Sci. USA, 111, 15296–15303, https://doi.org/10.1073/pnas.1411762111, 2014.

Lhardy, F.: Model outputs for figures in Climate of the Past "Impact of Southern Ocean surface conditions on deep ocean circulation at the LGM: a model analysis" (Version 2), Zenodo [data set], https://doi.org/10.5281/zenodo.4576026, 2020.

Loulergue, L., Schilt, A., Spahni, R., Masson-Delmotte, V., Blunier, T., Lemieux, B., Barnola, J. M., Raynaud, D., Stocker, T. F., and Chappellaz, J.: Orbital and millennial-scale features of atmospheric CH4 over the past 800 000 year, Nature, 453, 383–386, https://doi.org/10.1038/nature06950, 2008.

Lynch-Stieglitz, J., Adkins, J. F., Curry, W. B., Dokken, T., Hall, I. R., Herguera, J. C., Hirschi, J. J.-M., Ivanova, E. V., Kissel, C., Marchal, O., Marchitto, T. M., McCave, I. N., McManus, J. F., Mulitza, S., Ninnemann, U., Peeters, F., Yu, E.-F., and Zahn, R.: Atlantic Meridional Overturning Circulation During the Last Glacial Maximum, Science, 316, 66–69, https://doi.org/10.1126/science.1137127, 2007.

Ma, L., Wang, B., and Cao, J.: Impacts of atmosphere–sea ice–cean interaction on Southern Ocean deep convection in a climate system model, Clim. Dynam., 54, 4075–4093, https://doi.org/10.1007/s00382-020-05218-1, 2020.

MARGO Project Members: Constraints on the magnitude and patterns of ocean cooling at the Last Glacial Maximum, Nat. Geosci., 2, 127–132, https://doi.org/10.1038/ngeo411, 2009.

Marshall, J. and Speer, K.: Closure of the meridional overturning circulation through Southern Ocean upwelling, Nat. Geosci., 5, 171–180, https://doi.org/10.1038/ngeo1391, 2012.

Marzocchi, A. and Jansen, M. F.: Connecting Antarctic sea ice to deep-ocean circulation in modern and glacial climate simulations, Geophys. Res. Lett., 44, 6286–6295, https://doi.org/10.1002/2017GL073936, 2017.

McCarthy, G. D., Smeed, D. A., Johns, W. E., Frajka-Williams, E., Moat, B. I., Rayner, D., Baringer, M. O., Meinen, C. S., Collins, J., and Bryden, H. L.: Measuring the Atlantic Meridional Overturning Circulation at 26° N, Prog. Oceanogr., 130, 91–111, https://doi.org/10.1016/j.pocean.2014.10.006, 2015.

Merino, N., Le Sommer, J., Durand, G., Jourdain, N. C., Madec, G., Mathiot, P., and Tournadre, J.: Antarctic icebergs melt over the Southern Ocean: Climatology and impact on sea ice, Ocean Model., 104, 99–110, https://doi.org/10.1016/j.ocemod.2016.05.001, 2016.

Moat, B. I., Smeed, D. A., Frajka-Williams, E., Desbruyères, D. G., Beaulieu, C., Johns, W. E., Rayner, D., Sanchez-Franks, A., Baringer, M. O., Volkov, D., Jackson, L. C., and Bryden, H. L.: Pending recovery in the strength of the meridional overturning circulation at 26° N, Ocean Sci., 16, 863–874, https://doi.org/10.5194/os-16-863-2020, 2020.

Morée, A. L., Schwinger, J., Ninnemann, U. S., Jeltsch-Thömmes, A., Bethke, I., and Heinze, C.: Evaluating the biological pump efficiency of the Last Glacial Maximum ocean using

δ^{13}C, Clim. Past, 17, 753–774, https://doi.org/10.5194/cp-17-753-2021, 2021.

Muglia, J. and Schmittner, A.: Glacial Atlantic overturning increased by wind stress in climate models, Geophys. Res. Lett., 42, 9862–9869, https://doi.org/10.1002/2015GL064583, 2015.

Nair, A., Mohan, R., Crosta, X., Manoj, M., Thamban, M., and Marieu, V.: Southern Ocean sea ice and frontal changes during the Late Quaternary and their linkages to Asian summer monsoon, Quaternary Sci. Rev., 213, 93–104, https://doi.org/10.1016/j.quascirev.2019.04.007, 2019.

Nicol, S., Pauly, T., Bindoff, N. L., Wright, S., Thiele, D., Hosie, G. W., Strutton, P. G., and Woehler, E.: Ocean circulation off east Antarctica affects ecosystem structure and sea-ice extent, Nature, 406, 504–507, https://doi.org/10.1038/35020053, 2000.

Orsi, A. H., Johnson, G. C., and Bullister, J. L.: Circulation, mixing, and production of Antarctic Bottom Water, Prog. Oceanogr., 43, 55–109, https://doi.org/10.1016/S0079-6611(99)00004-X, 1999.

Otto-Bliesner, B. L., Hewitt, C. D., Marchitto, T. M., Brady, E., Abe-Ouchi, A., Crucifix, M., Murakami, S., and Weber, S. L.: Last Glacial Maximum ocean thermohaline circulation: PMIP2 model intercomparisons and data constraints, Geophys. Res. Lett., 34, L12706, https://doi.org/10.1029/2007GL029475, 2007.

Parkinson, C. L. and Cavalieri, D. J.: Antarctic sea ice variability and trends, 1979–2010, The Cryosphere, 6, 871–880, https://doi.org/10.5194/tc-6-871-2012, 2012.

Peltier, W. R.: Global glacial isostasy and the surface of the ice-age Earth: the ICE-5G (VM2) model and GRACE, Annu. Rev. Earth Pl. Sc., 32, 111–149, https://doi.org/10.1146/annurev.earth.32.082503.144359, 2004.

Peltier, W. R., Argus, D. F., and Drummond, R.: Space geodesy constrains ice age terminal deglaciation: The global ICE-6G-C (VM5a) model, J. Geophys. Res.-Sol. Ea., 120, 450–487, https://doi.org/10.1002/2014JB011176, 2015.

Prahl, F., Herbert, T. D., Brassell, S., Ohkouchi, N., Pagani, M., Rosell-Melé, A., Repeta, D., and Sikes, E.: Status of alkenone paleothermometer calibration: Report from Working Group 3, Geochem. Geophy. Geosy., 1, 1034, https://doi.org/10.1029/2000GC000058, 2000.

Roche, D. M., Dokken, T. M., Goosse, H., Renssen, H., and Weber, S. L.: Climate of the Last Glacial Maximum: sensitivity studies and model-data comparison with the LOVECLIM coupled model, Clim. Past, 3, 205–224, https://doi.org/10.5194/cp-3-205-2007, 2007.

Roche, D. M., Wiersma, A. P., and Renssen, H.: A systematic study of the impact of freshwater pulses with respect to different geographical locations, Clim. Dynam., 34, 997–1013, https://doi.org/10.1007/s00382-009-0578-8, 2010.

Roche, D. M., Crosta, X., and Renssen, H.: Evaluating Southern Ocean sea-ice for the Last Glacial Maximum and pre-industrial climates: PMIP-2 models and data evidence, Quaternary Sci. Rev., 56, 99–106, https://doi.org/10.1016/j.quascirev.2012.09.020, 2012.

Rousset, C., Vancoppenolle, M., Madec, G., Fichefet, T., Flavoni, S., Barthélemy, A., Benshila, R., Chanut, J., Levy, C., Masson, S., and Vivier, F.: The Louvain-La-Neuve sea ice model LIM3.6: global and regional capabilities, Geosci. Model Dev., 8, 2991–3005, https://doi.org/10.5194/gmd-8-2991-2015, 2015.

Schilt, A., Baumgartner, M., Schwander, J., Buiron, D., Capron, E., Chappellaz, J., Loulergue, L., Schüpbach, S., Spahni, R., Fischer, H., and Stocker, T. F.: Atmospheric nitrous oxide during the last 140 000 years, Earth Planet. Sc. Lett., 300, 33–43, https://doi.org/10.1016/j.epsl.2010.09.027, 2010.

Shin, S.-I., Liu, Z., Otto-Bliesner, B. L., Kutzbach, J. E., and Vavrus, S. J.: Southern Ocean sea-ice control of the glacial North Atlantic thermohaline circulation, Geophys. Res. Lett., 30, 1096, https://doi.org/10.1029/2002GL015513, 2003.

Sikes, E. L., Volkman, J. K., Robertson, L. G., and Pichon, J.-J.: Alkenones and alkenes in surface waters and sediments of the Southern Ocean: Implications for paleotemperature estimation in polar regions, Geochim. Cosmochim. Ac., 61, 1495–1505, https://doi.org/10.1016/S0016-7037(97)00017-3, 1997.

Skinner, L. C., Primeau, F., Freeman, E., de la Fuente, M., Goodwin, P. A., Gottschalk, J., Huang, E., McCave, I. N., Noble, T. L., and Scrivner, A. E.: Radiocarbon constraints on the glacial ocean circulation and its impact on atmospheric CO_2, Nat. Commun., 8, 16010, https://doi.org/10.1038/ncomms16010, 2017.

Tarasov, L., Dyke, A. S., Neal, R. M., and Peltier, W. R.: A data-calibrated distribution of deglacial chronologies for the North American ice complex from glaciological modeling, Earth Planet. Sc. Lett., 315-316, 30–40, https://doi.org/10.1016/j.epsl.2011.09.010, 2012.

Tierney, J. E., Zhu, J., King, J., Malevich, S. B., Hakim, G. J., and Poulsen, C. J.: Glacial cooling and climate sensitivity revisited, Nature, 584, 569–573, https://doi.org/10.1038/s41586-020-2617-x, 2020.

US National Snow and Ice Data Center (NSIDC): https://nsidc.org/, last access: 16 May 2021.

Waugh, D. W., Banerjee, A., Fyfe, J. C., and Polvani, L. M.: Contrasting recent trends in Southern Hemisphere Westerlies across different ocean basins, Geophys. Res. Lett., https://doi.org/10.1002/essoar.10503156.1, in review, 2021.

Weber, S. L., Drijfhout, S. S., Abe-Ouchi, A., Crucifix, M., Eby, M., Ganopolski, A., Murakami, S., Otto-Bliesner, B., and Peltier, W. R.: The modern and glacial overturning circulation in the Atlantic ocean in PMIP coupled model simulations, Clim. Past, 3, 51–64, https://doi.org/10.5194/cp-3-51-2007, 2007.

Williams, G. D., Aoki, S., Jacobs, S. S., Rintoul, S. R., Tamura, T., and Bindoff, N. L.: Antarctic Bottom Water from the Adélie and George V Land coast, East Antarctica (140–149° E), J. Geophys. Res., 115, C04027, https://doi.org/10.1029/2009JC005812, 2010.

World Ocean Atlas: http://ingrid.ldeo.columbia.edu/SOURCES/.NOAA/.NODC/.WOA98/ (last access: 18 January 2009), 1998.

Xiao, W., Esper, O., and Gersonde, R.: Last glacial-Holocene climate variability in the Atlantic sector of the Southern Ocean, Quaternary Sci. Rev., 135, 115–137, https://doi.org/10.1016/j.quascirev.2016.01.023, 2016.

Yu, J., Menviel, L., Jin, Z. D., Thornalley, D. J. R., Barker, S., Marino, G., Rohling, E. J., Cai, Y., Zhang, F., Wang, X., Dai, Y., Chen, P., and Broecker, W. S.: Sequestration of carbon in the deep Atlantic during the last glaciation, Nat. Geosci., 9, 319–324, https://doi.org/10.1038/NGEO2657, 2016.

4.2 Complement A – Quantification of biases in Southern Ocean sea ice, deep ocean circulation and CO_2 concentration: effects of a boundary conditions change

In this complement to article 2, I describe and quantify the deep ocean circulation, water mass characteristics and the carbon content simulated by a set of six simulations with different boundary conditions. I now use in the rest of this thesis the second batch of my simulations (v2), keeping the same simulation names for simplicity. While some differences (e.g. larger global mean SAT LGM−PI anomaly) between v1 and v2 arise due to substantial model development in between, the surface biases highlighted in Lhardy et al. [2021b] are still valid. My set of simulations now consists of a PI run ('New PI (v2)') and two standard LGM runs obtained using either the GLAC-1D or the ICE-6G-C boundary conditions ('P4-G' and 'P4-I' respectively). In addition, I complement the 'P4-I brines' simulation – whose v1 notably led to large changes in deep ocean circulation – with a 'P4-G brines' simulation (same *frac* parameter of 0.8, hence a large transfer of salt to the bottom grid cell when sea-ice formation occurs). This is done to see whether the ice sheet reconstruction chosen to implement the boundary conditions has larger effects in the context of a more stratified ocean with a shallower NADW overturning cell (see Fig. 7 of Lhardy et al. [2021b]) than in standard runs. Finally, I add to this set a 'P4-I PIbathy' simulation to single out the effects of a change of ocean boundary conditions (i.e. bathymetry, coastlines) on other variables than the carbon content. Indeed, this simulation was also used in article 1 in comparison with PMIP-carbon model outputs with no update of ocean boundary conditions at the LGM in order to underline the importance of ocean volume on carbon storage.

I first examine the effects of boundary condition changes on the streamfunction simulated in the Southern and Atlantic oceans (see meridional sections shown in Fig. 4.1). As underlined in Lhardy et al. [2021b] and Kageyama et al. [2021] (v1), standard LGM runs with the iLOVECLIM model yield a very deep and intense upper overturning cell (i.e. NADW cell), reaching down to the Atlantic ocean floor. Despite model developments and the update of boundary conditions to those of PMIP4, the simulated AMOC remains as deep as the PMIP2 version of iLOVECLIM shown in Otto-Bliesner et al. [2007].

In contrast, multimodel comparison studies for successive PMIP phases produced somewhat different conclusions: Weber et al. [2007] analyzed outputs from nine models of the PMIP1.5-PMIP2 ensemble and showed an AMOC slow down (or intensification) at the LGM in about half of the models. A large intermodel spread was also observed in Otto-Bliesner et al. [2007] within the PMIP2 ensemble. However, Muglia and Schmittner [2015] found using eight PMIP3 models that a majority of them simulate a strengthening and a deepening of the NADW cell. Among this ensemble, only the CCSM4 model simulate a NADW shoaling. Finally, the most recent PMIP results show that PMIP4 models tend to simulate limited changes or a slight increase in terms of AMOC strength and depth between their PI and glacial states (see Fig. 4.2 from Kageyama et al. [2021]). This difference between PMIP3 and PMIP4 studies can be related to changes in the atmospheric circulation due to the use of lower ice sheet reconstructions or changes in the freshwater balance [Kageyama et al., 2021], though results may also differ purely due to the fact that the PMIP3 and PMIP4 ensembles are of fairly different composition.

iLOVECLIM is therefore one of the two PMIP4 outliers (along with the IPSL-CM5A2 model) still showing an AMOC response comparable to the PMIP3 ensemble. I also observe that the NADW cell simulated at the PI is among the weakest of the PMIP3-PMIP4 ensemble

(Fig. 4.2) whereas the bottom cell is the strongest (reaching ~ -5 Sv), two characteristics which are not unlike those of IPSL-CM5A2 and IPSL-CM5A-LR again. As a result, exploring the AMOC response to differing modelling choices in such an EMIC to identify where model representation may be lacking remains useful to pave the way for more complex models.

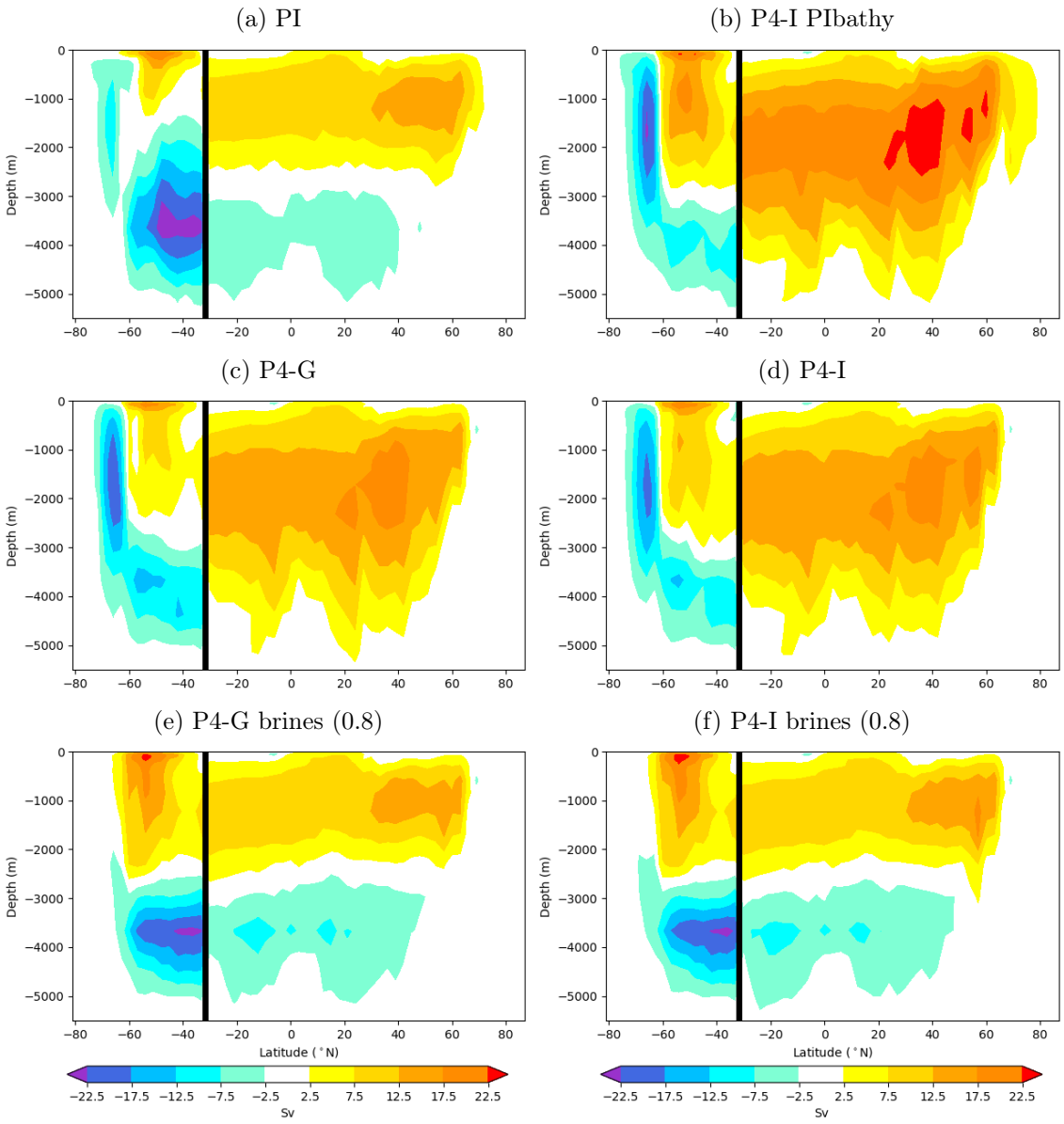

Figure 4.1: Streamfunctions in the Atlantic (North of 32°S) and Southern Ocean basins (South of 32°S). The black vertical line represents the limit between these two basins, chosen at 32°S.

Going back to Fig. 4.1, I observe that the streamfunction obtained using GLAC-1D boundary conditions ('P4-G') is fairly similar to the one of 'P4-I'. Small differences are still visible, for example in the North Atlantic where the NADW cell is more intense in 'P4-I' than in 'P4-G', which can be related to a higher ice sheet elevation in the ICE-6G-C reconstruction. This difference is also found when the parameterization of the sinking of brines is activated (Fig. 4.1e and f), though the overturning cells simulated by 'P4-I brines' and 'P4-G brines' mostly remain of similar depth and intensity. In addition, I observe in Fig. 4.1b that the use

of PI ocean boundary conditions in an otherwise LGM simulation (greenhouse gases, orbital parameters, ice sheet extent and elevation of the LGM) leads to an even stronger NADW cell. This strengthening may be partly due to the bathymetry of the Greenland-Iceland-Scotland threshold, but it is also likely that the land-sea mask influences ocean circulation and the freshwater budget. Indeed, the Arctic coastlines are quite different in a PI set-up compared to a LGM one (notably with more free surface to form sea ice, e.g. in the Barents sea).

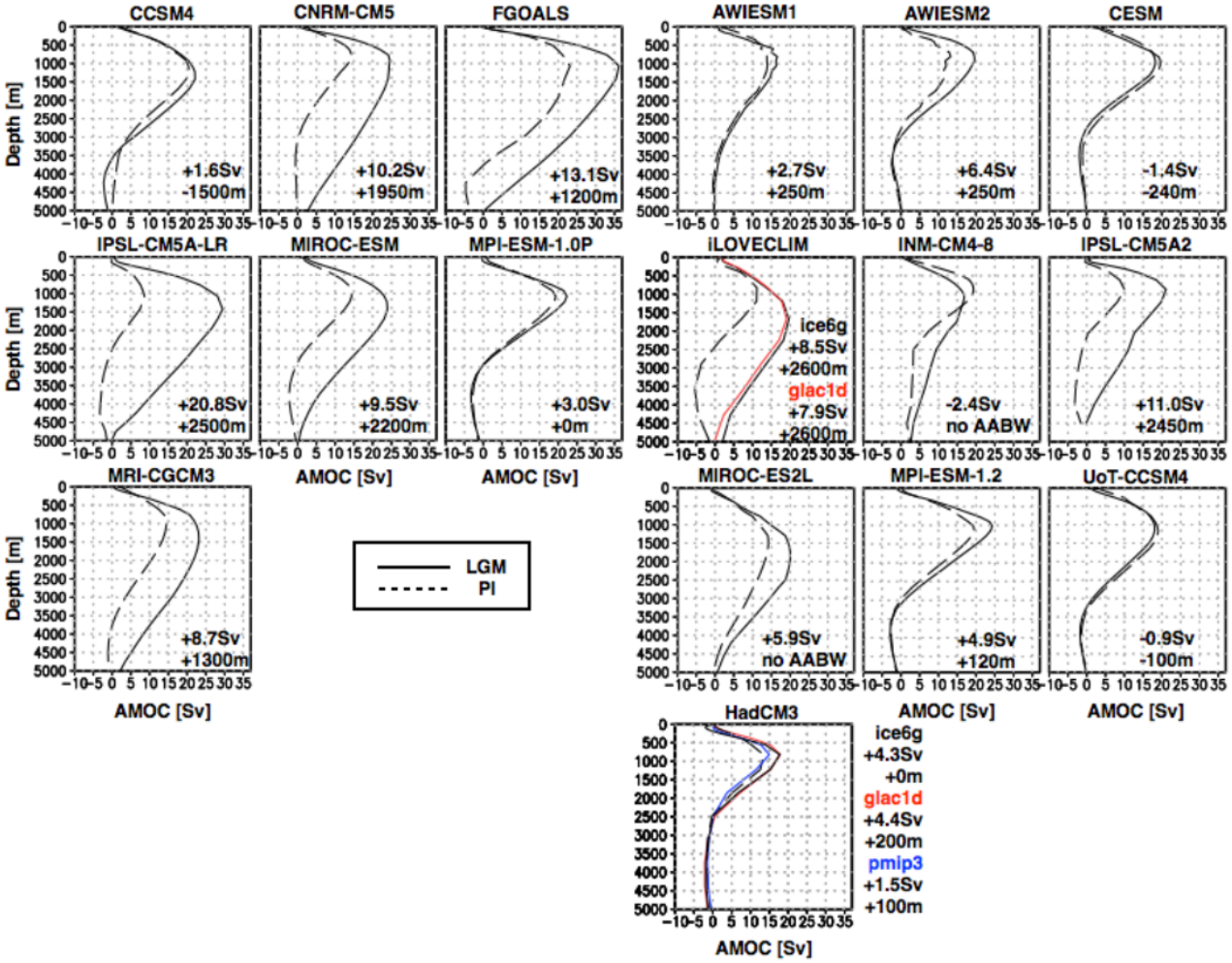

Figure 4.2: Mean Atlantic streamfunction at 30°N simulated by PMIP3 and PMIP4 models at the PI and LGM (figure taken from Kageyama et al. [2021]). The nominal values for the LGM − PI anomaly in terms of maximum streamfunction (Sv) and NADW vertical extent (m) are indicated. The two iLOVECLIM simulations are the same as in Lhardy et al. [2021b] (v1).

In addition to a NADW shoaling, proxy data tend to indicate an enhanced, salt-driven stratification at the LGM [Adkins, 2013]. Now observing potential density in the Atlantic ocean (Fig. 4.3), it is clear that the deep ocean (> 2000 m) remains very homogeneous in standard LGM runs (Fig. 4.3c and d), whereas the parameterization of the sinking of brines yields much more pronounced density gradients (Fig. 4.3e and f). I observe from the isoligns that the parameterized transfer of salt both depletes surface values and increases bottom water density in the Southern Ocean. This figure also shows the global effect of the automatised salt adjustment, which was not done in the 'P4-I PIbathy' run (as no change of ocean volume occurred). I noted in article 1 that this adjustment was a little more pronounced in 'P4-I' (+ 1.11 psu) than in 'P4-G' (+0.96 psu), since the higher ice sheet elevation of the ICE-6G-C

reconstruction entails a lower ocean volume than GLAC-1D [Lhardy et al., 2021a]. This reason should explain the overall potential density differences between 'P4-I' and 'P4-G' (or 'P4-I brines' and 'P4-G brines') while their distribution pattern remains similar.

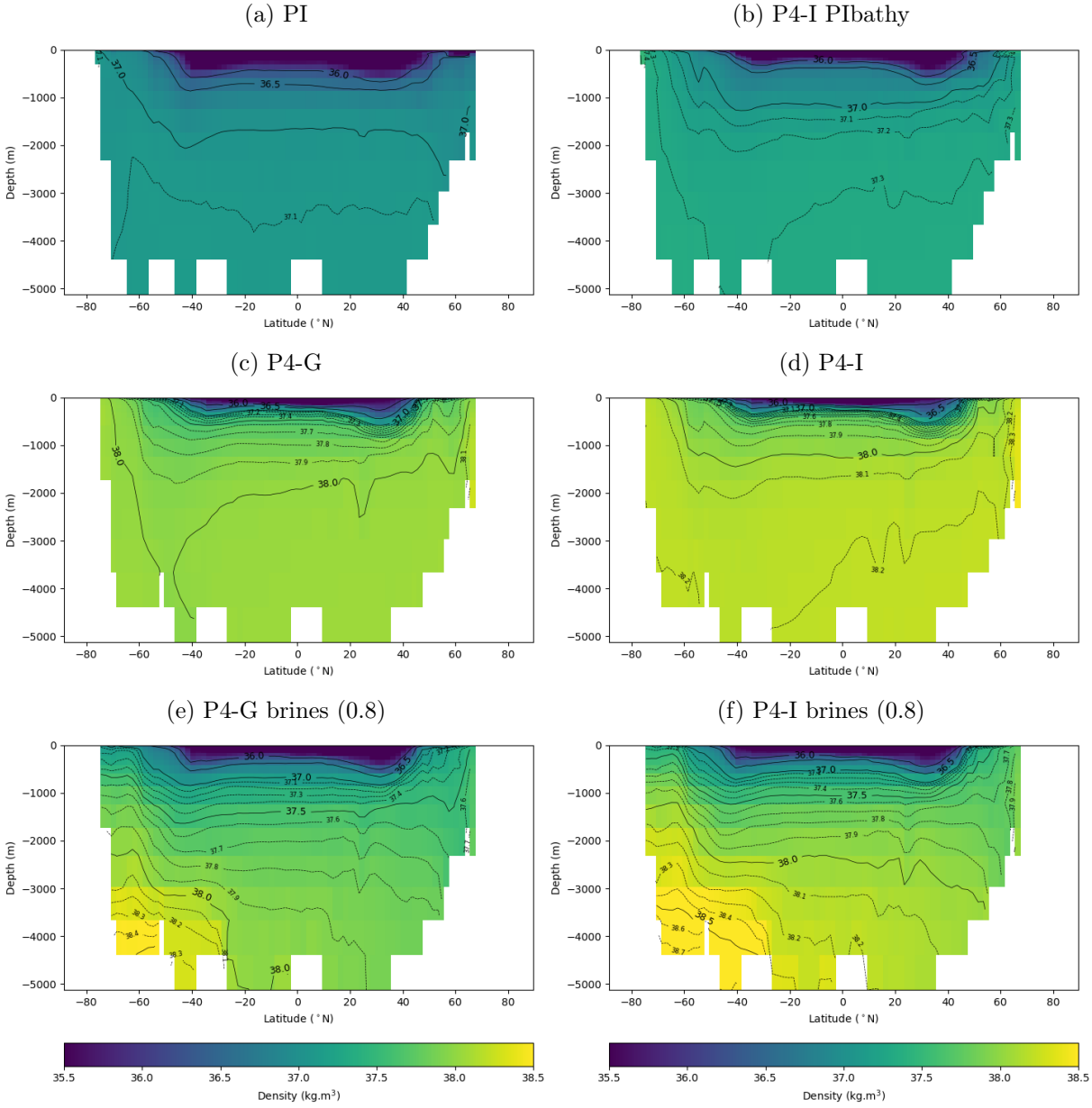

Figure 4.3: Mean zonal potential density σ_2 (referenced to 2000 m)

δ^{13}C is a useful paleotracer to track water mass distribution, as it is sensitive to ventilation changes in the ocean [Curry and Oppo, 2005]. This indicator is directly simulated by the carbon-enabled iLOVECLIM model, in a forward modelling approach [Bouttes et al., 2015]. As a result, model-data comparisons with large δ^{13}C records at the LGM [Peterson et al., 2014] are done to identify biases and examine which simulations are associated with a more realistic water mass distribution. Model-data discrepancies are also quantified using the Root Mean Square Error (RMSE), which indicates an improved agreement when it decreases. I show in Fig. 4.4 the distribution of δ^{13}C in the Atlantic ocean (and in the Indian and Pacific oceans in Fig. 6.17 and Fig. 6.18, see Appendix). A clear vertical gradient in δ^{13}C data is visible from

the deep Southern Ocean (δ^{13}C $\sim$ -1‰) to the shallower depths of the North Atlantic (δ^{13}C $>$ 1‰). The simulated δ^{13}C does not reproduce this gradient well in standard LGM runs (Fig. 4.4c and d), as positive δ^{13}C values are simulated in the Atlantic deep ocean due to the NADW reaching the ocean floor. As a result, model-data agreement is poorer at the LGM (Atlantic RMSE = 0.64) than at the PI. In contrast, the changes in deep ocean circulation induced by the parameterization of the sinking of brines shape the Atlantic distribution of δ^{13}C: the resurgence of AABW in the Atlantic explains lower values in the deep ocean, whereas the positive values of the NADW are more confined to shallower depths ($\sim$ 2000-2500 m). The δ^{13}C extrema are also enhanced as lower δ^{13}C are simulated in the deep Southern Ocean while higher δ^{13}C appear in the North Atlantic intermediate depths. These changes are associated with a significant improvement of model-data agreement (Atlantic RMSE = 0.42).

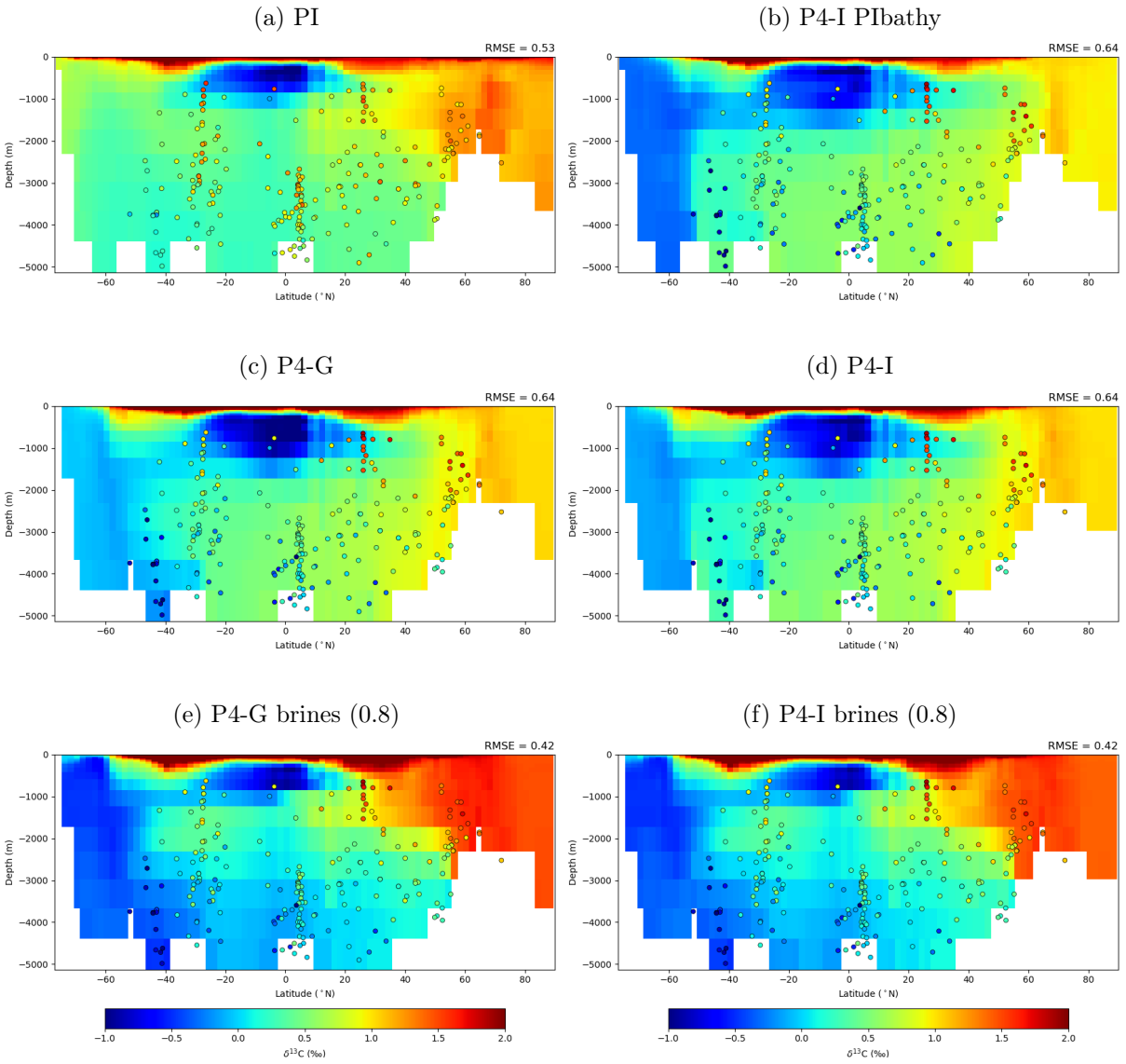

Figure 4.4: Mean zonal distribution of the simulated δ^{13}C (‰) in the Atlantic (and Arctic) Ocean. The superimposed dots represents the δ^{13}C data from Peterson et al. [2014], obtained using benthic foraminifera in 480 marine cores. The values are estimated by averaging all measurements in the late Holocene (0-6 ka) or LGM (19-23 ka) time windows. The RMSE computed with respect to this δ^{13}C data in the Atlantic is indicated in the top right corner.

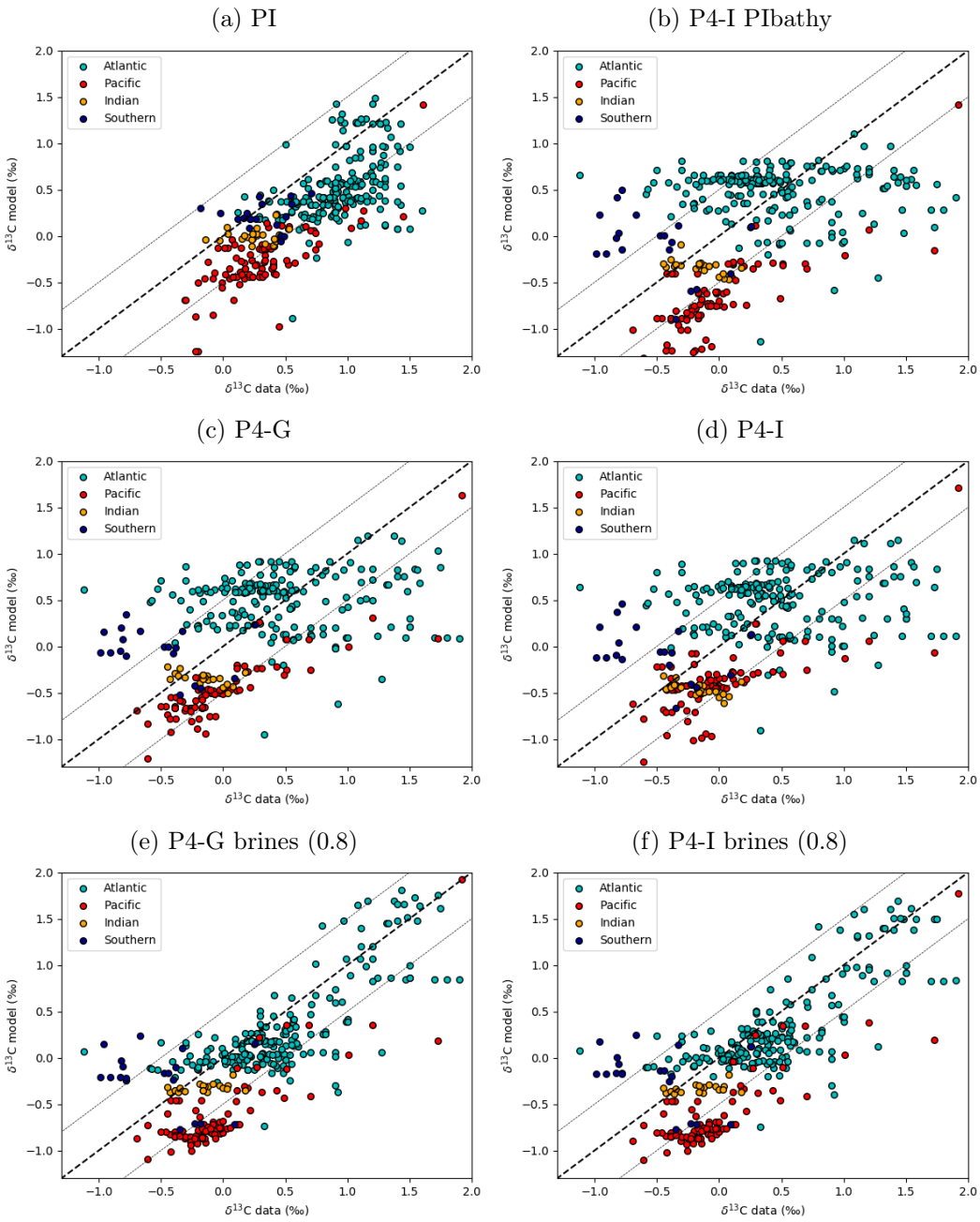

Figure 4.5: δ^{13}C in a model versus data diagram. The simulated δ^{13}C is plotted against the δ^{13}C data from Peterson et al. [2014], thanks to the aggregation of the coordinates on the nearest ocean grid cell. The 1:1 line features a perfect model-data agreement (black dashed line), while the grey dotted lines features a 0.5‰ departure from it. The marker color indicates the ocean basin of each core.

The model-data discrepancies can also be represented in a data versus model diagram of δ^{13}C (Fig. 4.5). In this diagram, points with a close match between the marine core data and the simulated value in the nearest ocean grid cell get aligned close to the 1:1 line. I note that the simulated δ^{13}C at the PI is slightly biased towards low values (Fig. 4.5a). However, an in-depth evaluation of this bias would require the use of denser pre-industrial data (e.g. Eide et al. [2017]) instead of the late Holocene record of Peterson et al. [2014] and is not the point of this study. As for the LGM standard runs (Fig. 4.5c and d), they both also show a slight bias

towards low δ^{13}C values in the Indian and Pacific oceans, but the largest discrepancies between model and data occur in the Atlantic and Southern Ocean basins. Indeed, I observe from the blue cluster of points that the simulated δ^{13}C are mostly between 0‰ and 1‰, whereas measurements on benthic foraminifera suggest a much larger spread of δ^{13}C values in the Atlantic. This spread is much more closely reproduced in 'brines' simulations in which the NADW is shallower than in standard runs (Fig. 4.5e and f). As a stronger vertical gradient is simulated, δ^{13}C points are more aligned to the 1:1 line and a better agreement with data is achieved. In the Southern Ocean however, the simulated δ^{13}C do not reach the very low values inferred from benthic foraminifera measurements (up to $\sim$ -1‰). While this bias could be attributed to a too ventilated AABW, I am also aware of δ^{13}C offsets between different *Cibicides* species which may question to some extent the interpretation of these very light values [Gottschalk et al., 2016]. Finally, I underline again that the δ^{13}C distribution simulated with ICE-6G-C or GLAC-1D boundary conditions are largely similar.

To restate the observed biases and relate them whenever possible, I summarize in Table 4.1 different quantifications made until this point for the simulations with differing boundary conditions, as well as the two simulations with a strong parameterized sinking of brines ($frac = 0.8$). I observe that the simulated global mean SAT anomaly is in the lower part of the range estimated by Annan and Hargreaves [2013] (-4 ± 0.8 °C) for all LGM simulations. Considering also the global warm bias of the iLOVECLIM model under its PI state, it is likely that it also simulates a too warm LGM climate. This observation is consistent with the higher RMSE computed at the LGM using SST data, which is mostly due to a large warm bias observed in summer in the Southern Ocean (see Fig. 4 of Lhardy et al. [2021b]). The winter RMSE is not optimal either, but is also linked to a cold bias in the Northern seas (not shown here).

Table 4.1: Summary of the quantified surface conditions, overturning cells, and carbon content. I indicate the global mean Surface Air Temperature (SAT) anomaly, the RMSE computed with respect to MARGO Project Members [2009] data (or WOA98 for the PI) in terms of austral summer (JFM) and winter (JAS) SST, the summer and winter sea-ice extent in the Southern Ocean and the maximum intensity of each overturning cells. All of these indicators are described and analyzed in more detail in Lhardy et al. [2021b]. I also quantify the global RMSE computed with respect to Peterson et al. [2014] δ^{13}C data and the carbon content of the ocean, terrestrial biosphere, and atmosphere (also given in Table 4 of Lhardy et al. [2021a]).

Simulation	LGM-PI SAT (°C)	RMSE SST		Sea-ice extent (10^6 km^2)		Overturning cells maximum (Sv)			RMSE δ^{13}C	Ocean carbon (GtC)	Terrestrial carbon (GtC)	CO_2 (ppm)
		JFM	JAS	JFM	JAS	SO	Bottom	NADW				
PI	-	3.43	2.98	6.6	21.2	-13.96	-23.97	17.76	0.56	38,480	1,937	281.0
P4-I PIbathy	-3.60	3.77	3.87	18.7	34.3	-24.32	-10.89	25.84	0.69	39,020	1,347	305.2
P4-G	-3.49	4.12	4.08	13.8	29.9	-22.94	-11.60	20.19	0.65	38,728	1,615	316.3
P4-I	-3.83	4.01	4.07	14.0	31.8	-20.27	-9.85	21.80	0.65	38,753	1,593	314.9
P4-G brines	-3.68	3.87	4.08	14.0	35.5	-13.01	-22.81	18.56	0.52	38,830	1,621	265.4
P4-I brines	-3.95	3.84	4.09	17.5	38.3	-13.23	-21.17	20.82	0.52	38,840	1,609	266.2

As for the sea-ice extents simulated in the Southern Ocean at the LGM, they can be compared to the minimal extent of $\sim 10.2 \times 10^6$ km^2 and maximal extent of $\sim 32.9 \times 10^6$ km^2 estimated in Lhardy et al. [2021b] using a recent compilation of marine core data. Therefore, it seems that the standard LGM runs overestimate the summer sea-ice extent and underestimate the winter sea-ice extent, thus underestimating its seasonal amplitude to a significant degree ($\sim 16.1 \times 10^6$ km^2 in 'P4-G' and $\sim 17.8 \times 10^6$ km^2 in 'P4-I', with respect to $\sim 22.7 \times 10^6$ km^2

according to our estimates). Still, these quantified extents do not translate well the regionality of biases, since I observed in Lhardy et al. [2021b] (Fig. 6) that standard LGM runs (v1, same with v2) simulate an overestimated equatorward displacement of the sea-ice edges in the Pacific sector while the sea-ice edges remain too far South in the Atlantic and Indian sectors. These regional and seasonal sea-ice biases are consistent with the observed latitudinal and regional trend of the Southern Ocean warm bias (Fig. 4 of article 2).

The standard LGM runs also show a significant increase of the Southern Ocean and NADW overturning cells, while the bottom cell is weakened in the Southern Ocean and even disappears in the Atlantic basin. These characteristics are associated with a weakly stratified Atlantic deep ocean and with a $\delta^{13}C$ distribution in poor agreement with marine core data. It is therefore likely that at least part of the reason why iLOVECLIM simulates such high atmospheric CO_2 concentrations ($\sim$ 315 ppm, contrasting with the 190 ppm from Bereiter et al. [2015]) is due to a deep ocean circulation which does not produce a voluminous, isolated, and poorly-ventilated AABW.

Comparing the quantifications between 'P4-G' and 'P4-I', it appears that the ice sheet reconstruction used to generate the boundary conditions have small effects (e.g. lower mean SAT and slightly stronger NADW cell in 'P4-I') but that the observed biases remains the same. Larger differences are quantified between 'P4-I' and 'P4-I PIbathy': while the latter simulation is globally warmer, it also shows warmer SSTs in the North Atlantic and slightly colder SSTs in the Atlantic sector of the Southern Ocean, possibly due to a Drake transport effect. These two differences in the SST pattern are associated with a lower RMSE in both seasons. Nonetheless, the warmer global mean SAT of 'P4-I PIbathy' can be related to a conflict between ice sheet and ocean boundary conditions in this set-up: wherever the land-sea mask designates a grid cell as ocean, the corresponding albedo is enforced even if the 'ice mask' would have designated the grid cell as 'white' (e.g. in Hudson Bay, Barents sea). The Southern Ocean cooling leads to a larger sea-ice extent and to a stronger Southern Ocean overturning cell, though I also note that the retreat of coastlines associated with the PI land-sea mask also liberates some free space for sea-ice formation, especially in the Arctic. Finally, while the agreement with $\delta^{13}C$ data further deteriorates in 'P4-I PIbathy', a lower CO_2 is also simulated. I argued in Lhardy et al. [2021a] that this slight improvement of the simulated atmospheric concentration is actually due the effects of the chosen ocean boundary conditions on the carbon distribution in reservoirs.

Both simulations using the parameterization of the sinking of brines show a slightly colder global mean SAT and colder SSTs in the Southern Ocean, associated with a lower RMSE in summer. Despite this improvement, I showed in article 2 that this experimental design still shows the same latitudinal trend of the warm bias. The simulated sea-ice extents in the Southern Ocean are consequently larger (overestimated in comparison to both our summer and winter data estimates), inverting the winter sea-ice bias. On the other hand, the seasonal amplitude is also increased, reducing this seasonal bias. Nonetheless, the sea-ice distribution remains fairly round in comparison to the oval-shaped sea-ice line inferred from marine core data. This parameterization yields in both simulations a reduced SO cell, an enhanced bottom cell and a slightly weakened but more importantly shallower NADW cell. It also induces an increased stratification (Fig. 4.3) and an Atlantic water mass distribution in better agreement with $\delta^{13}C$ data (Fig. 4.4). Finally, I also quantify a significant drop of CO_2 concentration of about 50 ppm, mostly due to an increased ocean sequestration (of $\sim 90 - 100$ GtC). As a result and despite some systematic regional patterns, this parameterization overall lessens the observed biases in surface conditions, but also water mass distribution and carbon content. Using this

experimental design, I still observe a very limited influence of the choice of the ice sheet reconstruction on the variables examined here.

To summarize, I described in chapter 3 how I generated the boundary conditions associated with the ice sheet reconstructions recommended by the PMIP protocol (in PMIP4: GLAC-1D and ICE-6G-C, notably lower than the ICE-5G reconstruction used in PMIP2). Although studies suggest an important influence of the high ice sheets of the Northern Hemisphere on the AMOC [Oka et al., 2012, Sherriff-Tadano et al., 2018, Klockmann et al., 2016, Muglia and Schmittner, 2015], I still simulate with the iLOVECLIM model a strong and deep NADW overturning cell using both the GLAC-1D and ICE-6G-C boundary conditions. This result contrast with the AMOC simulated by the PMIP4 ensemble [Kageyama et al., 2021], which differ quite a bit from the AMOC simulated by most PMIP3 models [Muglia and Schmittner, 2015]. When evaluating the biases in surface conditions, water mass characteristics, and carbon distribution, I only observe limited effects resulting from the choice of ice sheet reconstruction. The use of the parameterization of the sinking of brines has comparatively a much larger influence on the observed biases. For the most part, these biases form a coherent picture. Yet, I underline in article 2 that excluding the 'brines' simulations, I do not observe in iLOVECLIM simulations the inference of Marzocchi and Jansen [2017], that: "models simulating large sea-ice formation also exhibit strong deep-ocean stratification and a shallower AMOC, consistent with the geological record". Conversely, I find it difficult to exclusively attribute the strong and deep AMOC to insufficient Southern Ocean sea ice, for two reasons. First, I demonstrate that the winter sea-ice extent estimated using marine core data was probably overestimated in Roche et al. [2012] and is still associated with large and poorly-constrained uncertainties. However, I acknowledge that while the maximum sea-ice extent may not be as underestimated in standard LGM runs as previously thought, the underestimated seasonality (and overestimated quasi-permanent sea ice) still entails that sea-ice formation was probably inadequately represented throughout the year. Secondly, my LGM simulations show that a Southern Ocean cooling with more sea ice tends to be associated with a stronger SO and NADW overturning cells. I suggest that open-ocean convection may be detrimental to the establishment of a well-stratified water column in the Southern Ocean, with a formation of dense AABW. The parameterization of the sinking of brines is the only modelling choice tested so far which seems to reconcile a more realistic water mass distribution and a lower CO_2 concentration with reduced surface conditions biases. As a result, I propose to further explore the effects of the parameterization of the sinking of brines in the following section.

4.3 Complement B – Quantification of biases in Southern Ocean sea ice, deep ocean circulation and CO_2 concentration: effects of choices related to the parameterization of the sinking of brines

Up to this point, I used a fixed parameter ($frac = 0.8$) to examine the effects of the parameterization of the sinking of brines on the simulated sea ice, deep ocean circulation, and carbon storage. However, considering the low computation time of the iLOVECLIM model, this parameter choice can be easily varied, like Bouttes et al. [2010] in the CLIMBER-2 model.

I performed ten 'brines' simulations with a fraction of salt released by sea-ice formation varying between 0.1 and 1. The LGM simulation chosen as reference ('P4-I') represents a parameter choice of $frac = 0$. With such simulations, I can investigate how gradual the response of the different examined variables to a varying *frac* is, whether there are any threshold, whether different biases are reduced for the same parameter choice, and which parameter choice ultimately yields the best agreement with the proxy data used in this study.

In addition to these ten simulations, I test other modelling choices related to this parameterization:

- In my simulations (v2), this parameterization allows for a transfer of salt to the bottom ocean, as well as a transfer of other biogeochemical variables (DIC, alkalinity, nutrients, etc.). I turned off the transfer of these variables in the 'only salt' simulation. The effect of the transfer of each variable was more extensively explored in Bouttes et al. [2010].

- In addition, this parameterization is by default only active in the Southern Ocean. Therefore, I tested a 'brines + North' set-up in which it is also activated in the Northern Hemisphere.

- Since this parameterization does not depend on water depth, it can indiscriminately transfer salt to the bottom ocean in open ocean areas or continental shelves. Following Paillard and Parrenin [2004] who argued that brine rejection is favored only above continental shelves, I ran two simulations in which *frac* is not a scalar but a 2D input field computed using the subgrid topography in each ocean grid cell. In 'topofrac(min)', we related the *frac* number to the percentage of continent shelf (> 200 m) in the total grid cell surface. However, in 'topofrac(max)', we more drastically enforced a *frac* of 1 in all grid cells in which a portion of continental shelf was detected on a subgrid level.

- Finally, I tested the impact of a different transfer of salt in the water column where sea-ice formation occurs. In simulation 'shallow brines', instead of transfering the fraction of salt (still 0.8) to the deepest grid cell, I only transfered it to a shallower depth (200 m at most), therefore limiting this transfer to the subsurface in open ocean areas. Whether this dense water continues to sink to form deep water or not is then up to the dynamical code.

In Fig. 4.6, I show the Atlantic streamfunction for a subset of these simulations. The model simulates with a lower *frac* parameter of 0.4 the same trends for each overturning cells as in the 'P4-I brines (0.8)' but to a lesser extent (Fig. 4.6b and c). Indeed, with respect to 'P4-I', this simulation produces a reduced SO cell, an enhanced bottom cell and a somewhat shallower NADW cell, pushed back by the resurgence of a small bottom cell in the Atlantic. However with this parameter choice, the NADW cell remains quite deep in the North Atlantic. When the parameterization of the sinking of brines is also activated in the Northern Hemisphere, I observe a reduced overturning in both the bottom and the NADW cells (Fig. 4.6d and e), and a slightly shallower NADW cell in the North Atlantic when a large *frac* parameter (0.8) is used. As for the last two streamfunctions shown here, they still display a deep and intense NADW cell. A *frac* parameter which is tied to the presence of continental shelves (Fig. 4.6f) only causes a small reduction of the SO and NADW cells and increase of the bottom cell, with no significant impact on their geometry. Finally, the 'shallow brines' set-up only influences the geometry of the SO cell at shallow depths (Fig. 4.6g).

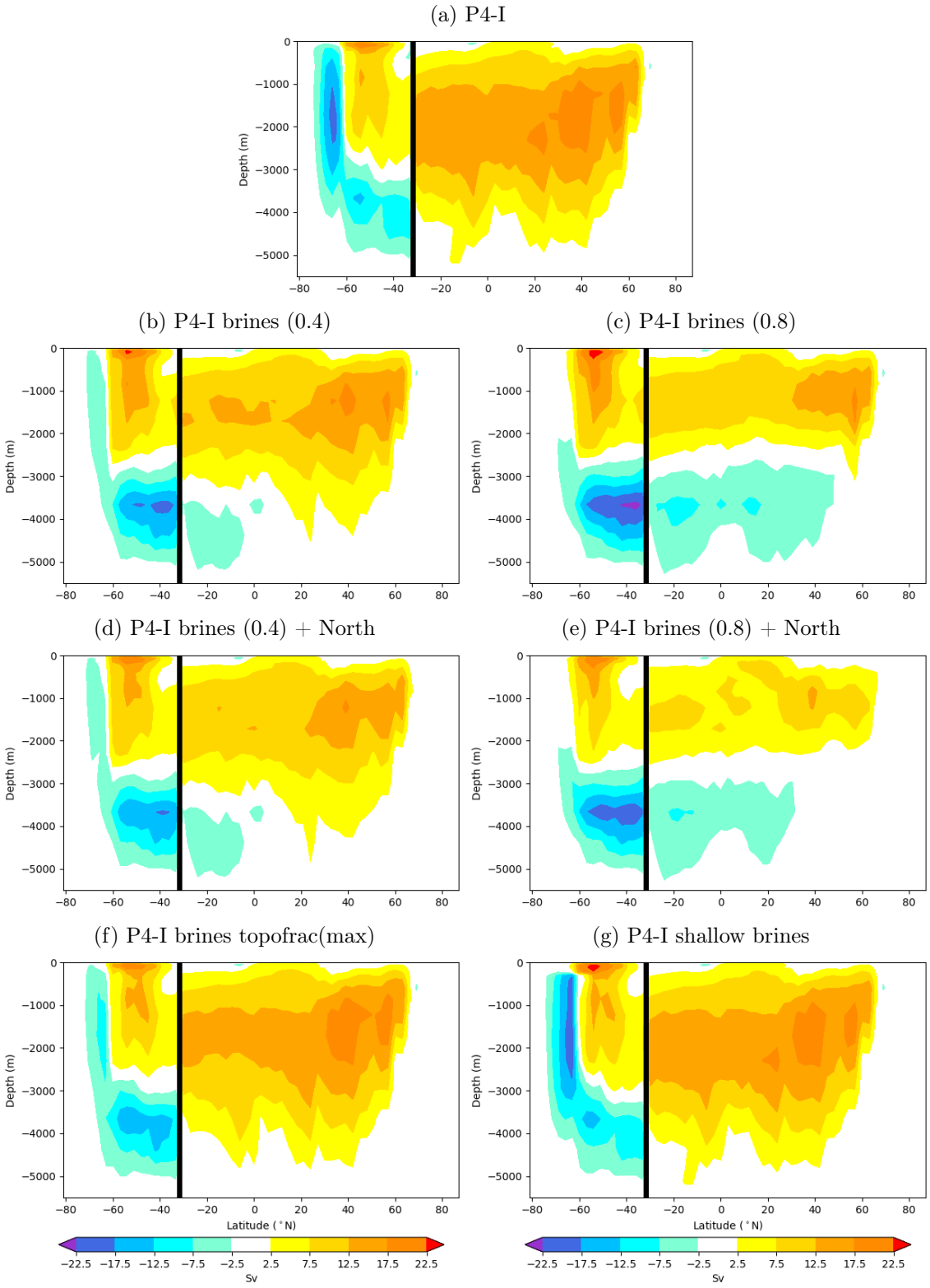

Figure 4.6: Streamfunctions in the Atlantic (North of 32°S) and Southern Ocean basins (South of 32°S). The black vertical line represents the limit between these two basins, chosen at 32°S.

(a) P4-I

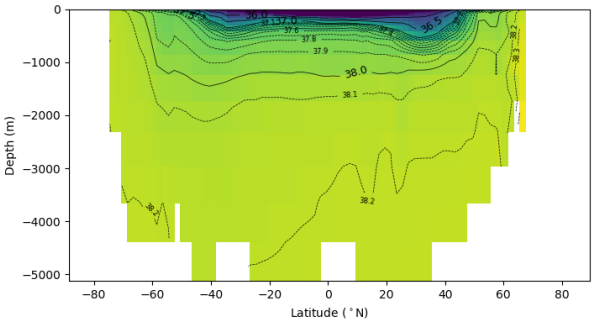

(b) P4-I brines (0.4)

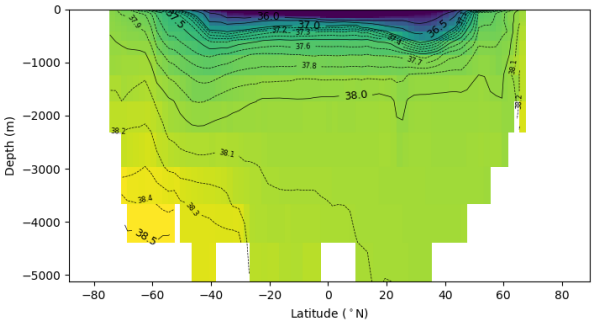

(c) P4-I brines (0.8)

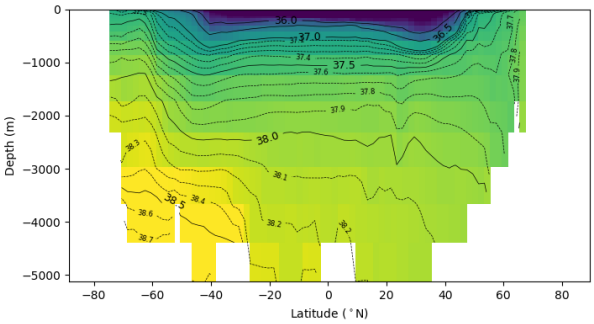

(d) P4-I brines (0.4) + North

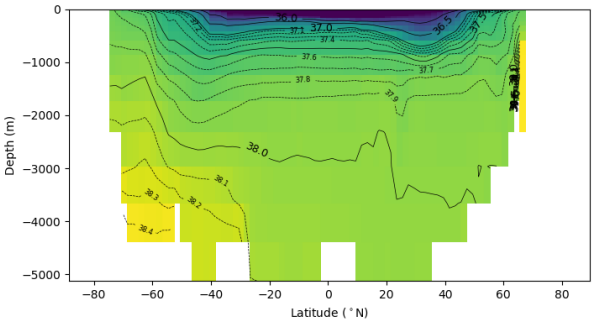

(e) P4-I brines (0.8) + North

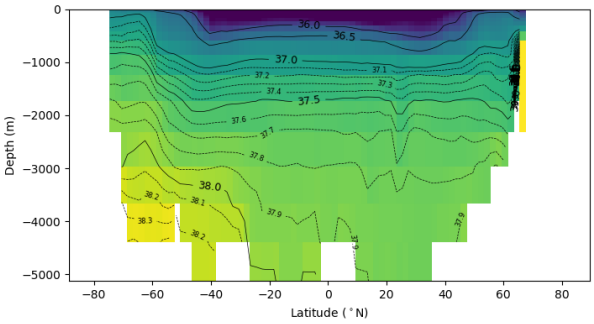

(f) P4-I brines topofrac(max)

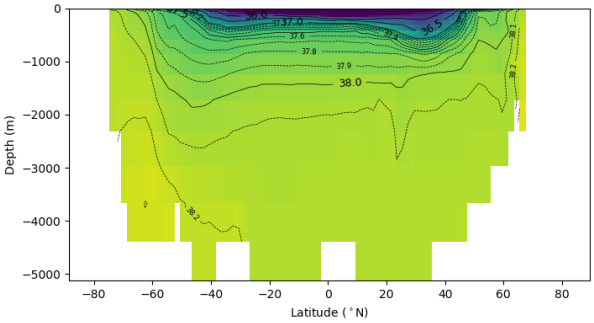

(g) P4-I shallow brines

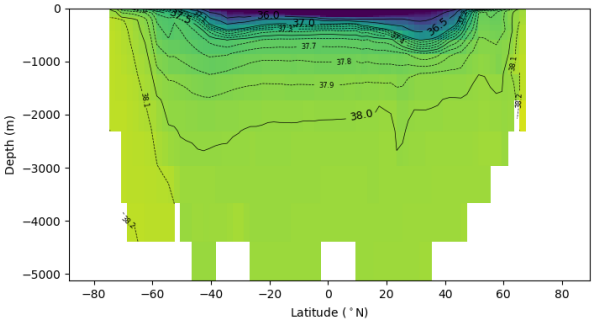

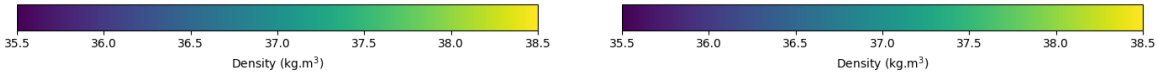

Figure 4.7: Mean zonal potential density σ_2 (referenced to 2000 m)

Examining the simulated potential density for the same subset of simulations in Fig. 4.7, I observe that the 'brines' parameter choice affects the maximal densities in the deep Southern Ocean and the surface values, as well as the slope of isoligns in the deep Atlantic (Fig. 4.7b and c). Two reasons can potentially explain why a *frac* of 0.4 is not enough to shoal the NADW cell: either the resultant AABW is still not dense enough or it loses its characteristics (through mixing) and upwells too quickly as it travels North. Comparatively, the densification effects of the parameterization in the Northern Hemisphere seems to mostly concern the Northern seas and to be limited by the Greenland-Iceland-Scotland threshold (Fig. 4.7d and e). In the rest of the Atlantic basin, I observe reduced values as the additional use of this parameterization in the North depletes the surface salinities. The last two simulations shown here have relatively small effects on the density simulated in the Southern Ocean (Fig. 4.7f and g).

Then, I examine how the quantifications which relates either to surface conditions, deep ocean circulation, or carbon behave as a function of the parameter choice (Fig. 4.8). The effects of the different modelling choices tested in various 'brines' simulations are observed. First, the use of the GLAC-1D ice sheet reconstruction in 'P4-G brines (0.8)' slightly warms the Southern Ocean, entailing both a worsened model-data agreement with SST data and a reduced sea-ice extent, in better agreement with our estimates. The bottom cell is also slightly enhanced and the maximum intensity of the NADW overturning is reduced. However, no significant changes are observed in the δ^{13}C RMSE or in the simulated CO_2 concentration, as already pointed out in the previous section.

Turning off the transfer of biogeochemical variables to keep only the parameterized transfer of salt does not yield any effect in the surface conditions and deep ocean circulation quantified here. Still, I simulate with 'only salt' a small increase of CO_2 (3.8 ppm), suggesting that the main driver of the CO_2 decrease in 'brines' simulations is the transfer of salt while the transfer of biogeochemical variables only causes a small additional drawdown (comparatively smaller than in Bouttes et al. [2010]).

On the other hand, activating the parameterization in the Northern Hemisphere has a relatively larger impact on the model-data agreement in terms of SST (worsened) and sea-ice extent (reduced, in closer agreement with our estimates). The enhanced sea-ice seasonality observed when using this parameterization remains the same. This modelling choice also slightly lowers the atmospheric CO_2 concentration (-8 ppm if $frac = 0.8$) but this small drop does not seem linked to a different water mass distribution. I also observe a reduced intensity of both the NADW and bottom cell in 'brines + North' simulations, and the depth at which the maximal intensity and the sign change (i.e. NADW vertical extent, as defined by Kageyama et al. [2021]) of the streamfunction are detected increases in 'P4-I brines + North (0.4)'.

As for the 'shallow brines' simulation, it is associated with very little change in terms of deep ocean circulation and water mass distribution (with respect to the 'P4-I' reference), yet it already shows a significant drop of CO_2 concentration (-20.8 ppm, mostly due to an increased ocean sequestration). I also observe that the quantified surface conditions are closer to 'P4-I brines' than 'P4-I', notably reducing the sea ice bias in seasonality. As a result, it seems that isolating the Southern Ocean surface from the subsurface has a significant effect both on one of the observed bias in sea ice and on the high atmospheric CO_2 values. This suggests that the changes in deep ocean stratification and circulation simulated with 'P4-I brines' only explain part of the increased carbon sequestration using this parameterization ($\sim$ 58 GtC).

I observe that the 'topofrac' simulations influence the variables quantified here in the same way as a simulation with a small *frac* does. They seem equivalent to a parameter of about

0.2-0.3 for 'topofrac(max)' and <0.1 for 'topofrac(min)'. These simulations do not significantly improve the model biases observed in this study.

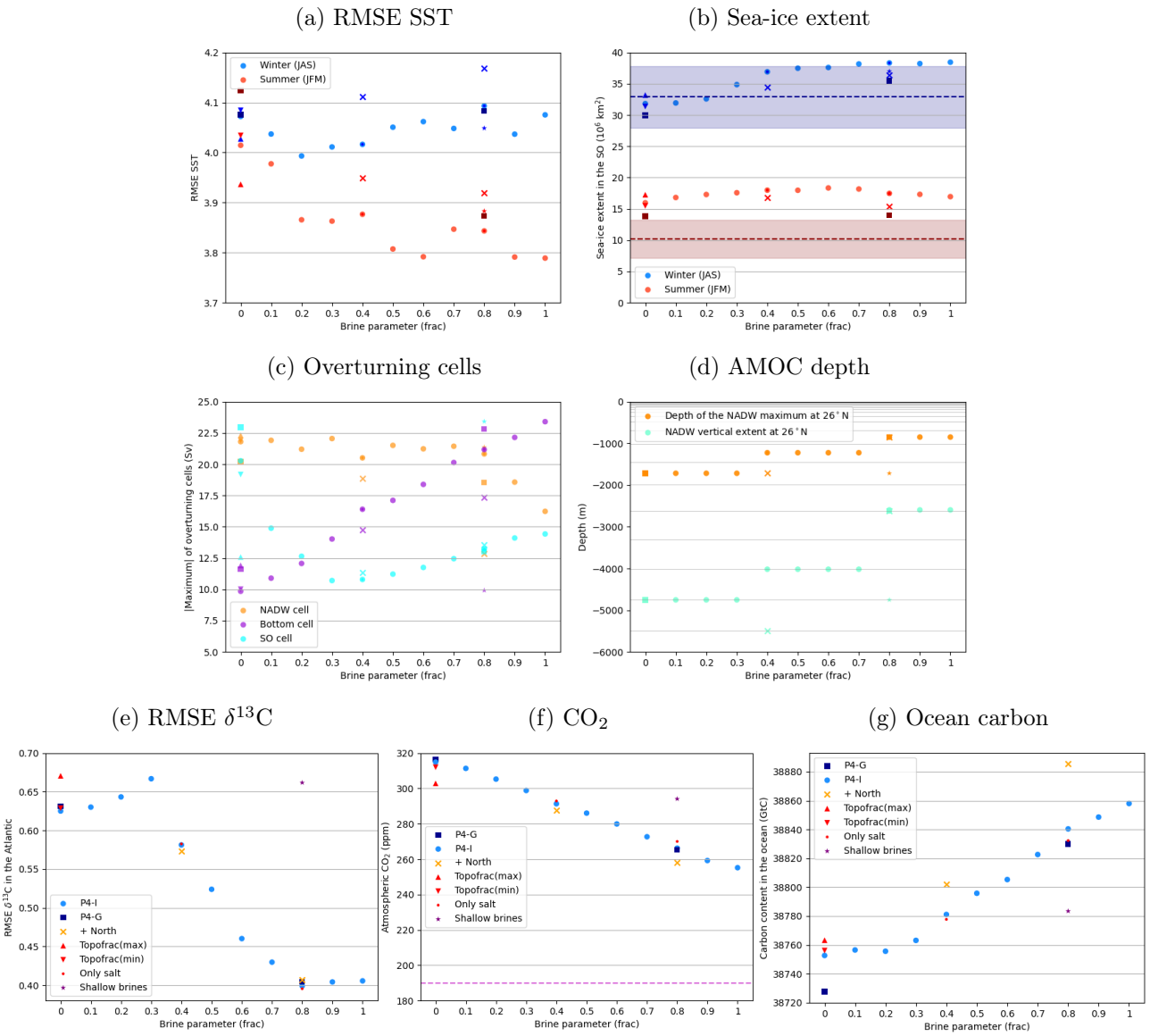

Figure 4.8: Effects of the modelling choices related to the parameterization of the sinking of brines on the quantified (a) RMSE computed with respect to SST data [MARGO Project Members, 2009], (b) sea-ice extent, (c) maximum intensity of each overturning cell, (d) depth of the maximal streamfunction and its sign change at 26°N, (e) RMSE computed with respect to δ^{13}C data [Peterson et al., 2014], (f) atmospheric CO_2 concentration and (g) ocean carbon. The x-axis represents the parameter choice (fraction of salt released by sea-ice formation). The marker style designates each type of simulation. The dashed lines indicate (in b) the summer (red) and winter (blue) sea-ice extent estimated in Lhardy et al. [2021b] or (in f) the CO_2 concentration at the LGM (magenta).

Finally commenting on the evolution of these quantifications with an increased transfer of salt, I do not observe a clear trend in the RMSE computed using SST data (Fig. 4.8a), though a low *frac* seems associated with an improved agreement in both seasons while a high *frac* only reduces the RMSE in summer. This seems related to the systematic latitudinal trend of the observed SST biases [Lhardy et al., 2021b]. A clearer and nonlinear trend is observed in the quantified sea-ice extent (Fig. 4.8b), as an increased *frac* produces a larger winter sea-ice extent without changing the summer sea-ice extent much. The simulated winter sea-ice extent agrees best with our estimate for a low *frac*, then exceeds it. However, the seasonal amplitude continues to increase at higher parameter choices, therefore getting closer to the one inferred from marine core data. Still, it seems that a low *frac* already has a significant impact on sea-ice biases, probably as it isolates the Southern Ocean surface in winter from a warmer subsurface. On the contrary, only a high *frac* value is able to achieve the water mass distribution associated with an improved model-data agreement of $\delta^{13}C$ (Fig. 4.8e), which seems to cap at $frac > 0.8$. Nonetheless, the simulated atmospheric CO_2 concentrations show a steady decrease with increased *frac* values while ocean sequestration only increases, albeit with two small slope discontinuities. While the CO_2 drop simulated using this parameterization is significant (-59.7 ppm with respect to 'P4-I' at most), the simulated concentration is still far from the 190 ppm value measured in ice core data [Bereiter et al., 2015] and it is likely that additional processes than ocean circulation changes (e.g. permafrost, sediments) need to be accounted for to simulate such a low LGM value. I also observe slope discontinuities in the simulated intensity of each overturning cell (Fig. 4.8c). The Southern Ocean overturning slows down quite drastically for low *frac* values, then recovers a bit at higher *frac*. On the other hand, the NADW cell intensity only decreases at high parameter values (> 0.8), whereas the bottom cell rises quite steadily. These discontinuities are perhaps more significant when considering the irregular vertical resolution of the iLOVECLIM model, which is particularly coarse in the deep ocean (Fig. 4.8d). As a consequence, it seems that the response of the NADW depth to an increased parameter choice is not gradual.

4.4 Résumé du chapitre en français

Dans ce chapitre 4, j'identifie les (dés)accords modèle-données concernant les températures des eaux de surface, la glace de mer australe, la distribution des masses d'eau profondes et la concentration en CO_2 atmosphérique. Pour ce faire, j'utilise plusieurs simulations réalisées avec le modèle iLOVECLIM, équipé de différentes conditions aux limites (PMIP2, GLAC-1D, ICE-6G-C) et/ou de certains choix de paramétrisation (liés à la plongée des saumures). Ces conditions de simulation variées mènent à différentes conditions de surface dans l'océan austral, ce qui est l'occasion de :

- évaluer l'impact des conditions de surface simulées (température, glace de mer) sur la circulation de retournement Atlantique.
- mesurer les conséquences des choix de modélisation liés aux conditions aux limites et/ou à la paramétrisation de la plongée des saumures sur les températures des eaux de surface, la glace de mer australe, la distribution des masses d'eau profondes et la concentration de CO_2 atmosphérique – et leur accord avec les enregistrements paléoclimatiques.
- identifier les biais systématiques.

J'observe alors que le modèle iLOVECLIM simule au DMG :

1. un biais chaud dans l'océan austral, dépendant nettement de la latitude (maximal à $\sim 40 - 50°S$).
2. une glace de mer australe présentant des désaccords avec les enregistrements paléoclimatiques, en terme d'étendue hivernale (légèrement sous-estimée), estivale (surestimée), amplitude saisonnière (sous-estimée), et de distribution (trop zonale). Toutefois, j'ai estimé à partir d'une récente compilation de données de carottes marines une étendue de glace de mer hivernale de 32.9×10^6 km^2, bien inférieure à une estimation précédente [Roche et al., 2012] utilisée dans le cadre des études d'intercomparaison PMIP [Roche et al., 2012, Marzocchi and Jansen, 2017]. Sur cette base, la glace de mer hivernale n'est que *légèrement* sous-estimée, tandis que la précédente estimation (de 43.5×10^6 km^2) suggérait une *large* sous-estimation de la glace de mer australe simulée par le modèle iLOVECLIM (et *a fortiori* par la plupart des modèles PMIP).
3. une circulation profonde Atlantique très intense et profonde, entraînant une distribution des masses d'eau en désaccord avec les données de $\delta^{13}C$.
4. une concentration en CO_2 atmosphérique bien supérieure à celle mesurée dans les carottes de glace.

Ainsi, je caractérise des biais semblables à ceux observés au cours des précédentes phases du projet PMIP, et dans de nombreux modèles. Entre PMIP2 et PMIP4, le modèle iLOVECLIM ne présente pas d'amélioration significative des variables examinées ici. Les différentes conditions aux limites utilisées, générées selon la méthode exposée dans le chapitre 3 à partir de diverses reconstructions de calottes, n'engendrent que des différences mineures face à l'amplitude des biais observés.

En revanche, j'observe avec la paramétrisation de la plongée des saumures une réduction de certains biais de température (océan austral plus froid), de glace de mer australe (saisonnalité plus grande), de circulation (AMOC moins profonde, océan Atlantique davantage stratifié) et une diminution significative (bien qu'insuffisante) du CO_2 atmosphérique. Globalement en meilleur accord avec les enregistrements paléoclimatiques, les simulations réalisées avec cette paramétrisation ne montrent cependant pas d'amélioration notable concernant la distribution régionale des biais de conditions de surface, telle que la distribution très homogène de glace de mer australe. Je note également que la réduction de ces biais ne se produit pas pour les mêmes choix de paramètres, ce qui suggère des causes différentes. Toutefois, cette paramétrisation, qui stratifie à la fois la subsurface et l'océan profond, montre qu'une amélioration simultanée des biais de surface, de circulation, et de carbone est possible, alors que la relation observée entre température de l'océan austral et les cellules de convection (Fig. 8, Lhardy et al. [2021b]) tend à suggérer qu'un océan plus froid contribue à intensifier l'AMOC.

Chapter 5

Quantification of the effects of vertical mixing on deep ocean circulation and CO_2 concentration

Chapter aims:

1. Explore the role of diffusion on the simulated Atlantic deep ocean circulation at the LGM
2. Evaluate the impact of vertical diffusivity parameterization choices on the model biases quantified in chapter 4

Highlights:

↪ The abyssal overturning is slightly reduced with the tidal mixing parameterization, and enhanced when accounting for geothermal fluxes. As for the parameterization of a stratification-dependent vertical diffusivity, its effects depends on parameter choices. These modelling choices do not yield any significant reduction of the model biases characterized in chapter 4.

↪ A strong absyssal overturning seems to be residual in the iLOVECLIM model.

In chapter 4, I have characterized the biases in Southern Ocean sea-ice cover, deep ocean circulation, and CO_2 concentration simulated by the iLOVECLIM model at the LGM. I have shown that the parameter choices related to a simple parameterization of the sinking of brines can yield large changes in the simulated sea-ice extent, Atlantic streamfunction, and ocean sequestration of carbon. Despite remaining biases, this experimental design associated with a large transfer of salt to the bottom ocean when sea-ice formation occurs produces a water mass distribution in better agreement with $\delta^{13}C$ data and a lower atmospheric CO_2 concentration than in standard LGM runs. From a very large vertical extent reaching to the ocean floor in the North Atlantic, the simulated NADW overturning cell at the LGM shoals to about the same depth as in the PI state thanks to an increased AABW density. Such a change is achieved

as the upper clockwise cell is pushed back into shallower depths by a reinvigorated counter-clockwise bottom cell. As a result, simulations obtained using a large 'brines' parameter choice do not show the slower abyssal overturning which is surmised from some experimental proxy data [Adkins, 2013, Howe et al., 2016]. In addition, comparison with other PMIP4 models [Kageyama et al., 2021] indicates that the streamfunction simulated at 30°N by the iLOVECLIM model in PI conditions is particularly intense (~ -5 Sv, see Fig. 4.2). It is expected that an overestimated abyssal circulation may significantly affect residence time and therefore ocean sequestration.

Vertical mixing is recognised as one of the drivers of the AMOC [Kuhlbrodt et al., 2007]. In this context, De Boer and Hogg [2014] point out that it is not trivial for PMIP models to simulate an expanded yet weaker AABW cell at the LGM. The authors investigate in a theoretical box model the influence of different vertical mixing profiles and show that only the parameterization of a topography-dependent vertical diffusivity is able to produce a voluminous yet slower AABW when their model is forced with a Southern Ocean cooling. In constrast, a constant diffusivity or a Bryan and Lewis profile (which has a constant diffusivity in the deeper part of the ocean) are not able to yield the inverse relationship between AABW volume and production rate. Yet most of the PMIP1.5-2 models relied on these simpler options, including the iLOVECLIM model (see Sect. 2.2.2). It is therefore likely that such a modelling choice impacts the model ability to simulate a realistic deep ocean circulation at the LGM, as well as an increased ocean storage capacity of carbon. Ferrari et al. [2014] also argue that the abyssal overturning cell is much more isolated as the NADW cell shoals, since turbulent mixing is confined to the deep ocean where topographic features are crossed. The authors point out that the consequently decreased mixing between AABW and NADW is one of the factors enhancing the physical pump at the LGM, drawing down more carbon into the ocean.

Considering these results, I choose to investigate how modelling choices related to vertical mixing in the iLOVECLIM model influence deep ocean circulation and carbon storage into the ocean. To do so, I replace at depth the Bryan and Lewis diffusivity profile with two different mixing schemes (e.g. a stratification-dependent diffusivity profile, or a 3D energy-constrained parameterization of tidal mixing, supplemented by geothermal fluxes − see Sect. 2.2.2). While chapter 4 focussed on the Southern Ocean surface conditions and their impact on deep ocean circulation via convection processes entailing deep water formation, this chapter approaches the consumption of AABW via mixing processes, which erode stratification until AABW upwells.

5.1 Effects on the Atlantic streamfunction of varying diffusivity parameterizations

5.1.1 With a parameterization of a stratification-dependent vertical diffusivity

Bouttes et al. [2011] successfully simulate the LGM CO_2 drawdown when adding three mechanisms to a standard run with the carbon cycle represented in the CLIMBER-2 model (which includes carbonate compensation). These additional mechanisms encompass iron fertilisation, sinking of brines (with the same parameterization as the one described in Sect. 2.2.1), and a stratification-dependent diffusivity. This last paramaterization explains a minor yet significant part of the changes needed to reconcile the CO_2 and $\delta^{13}C$ signals with experimental data. To demonstrate and quantify this effect, Bouttes et al. [2011] implemented in the CLIMBER-2 model the parameterization introduced in Marzeion et al. [2007], who chose to write the vertical diffusivity as $K_z \sim N^{-\alpha}$, where N is the buoyancy frequency equal to $(-\frac{g}{\rho_0}\frac{\partial \rho}{\partial z})^{1/2}$ ($\frac{\partial \rho}{\partial z}$ being the vertical density gradient, ρ_0 a reference density and g the gravity acceleration). In their formulation, three parameters (α, K_0, N_0) come into play:

$$K_z = K_0 \left(\frac{N}{N_0}\right)^{-\alpha}$$

In particular, α controls the sensitivity of K_z to changes in stratification. In this section, I also use this formulation, varying α between 0 and 1 while setting N_0 and K_0 at the same values as Marzeion et al. [2007] ($N_0 = 7.3 \times 10^{-3}$ s^{-1} ; $K_0 = 2 \times 10^{-5}$ m^2.s^{-1}), at least for a start.

Figure 5.1 shows the streamfunction simulated in the Atlantic with such a parameterization, using as references the PI simulation (Fig. 5.1a), and at the LGM both the 'P4-I' or 'P4-I brines' simulations (Fig. 5.1b and c), since they are associated with a very different stratification. Simulations with $\alpha = 0$ (Fig. 5.1d, e and f) are not equivalent to these references as the Bryan and Lewis vertical profile was replaced by a constant diffusivity: $K_z = K_0 = 2 \times 10^{-5}$ m^2.s^{-1}. I observe a slightly lower overturning in the bottom cell with $\alpha = 0$ while the NADW cell is enhanced and the cells' vertical extent shows limited change. However with $\alpha = 1$ (Fig. 5.1k and l), the overturning strongly intensifies, and shows a clear deepening of the NADW cell when the parameterization of the sinking of brines ($frac = 0.8$) is used. As a result, it seems that the AMOC deteriorates with such parameter choices. Since simulating too much mixing can erode the stratification too quickly (and feed back into a larger diffusivity), I then ran simulations with a lower $K_0 = 1 \times 10^{-5}$ m^2.s^{-1}.

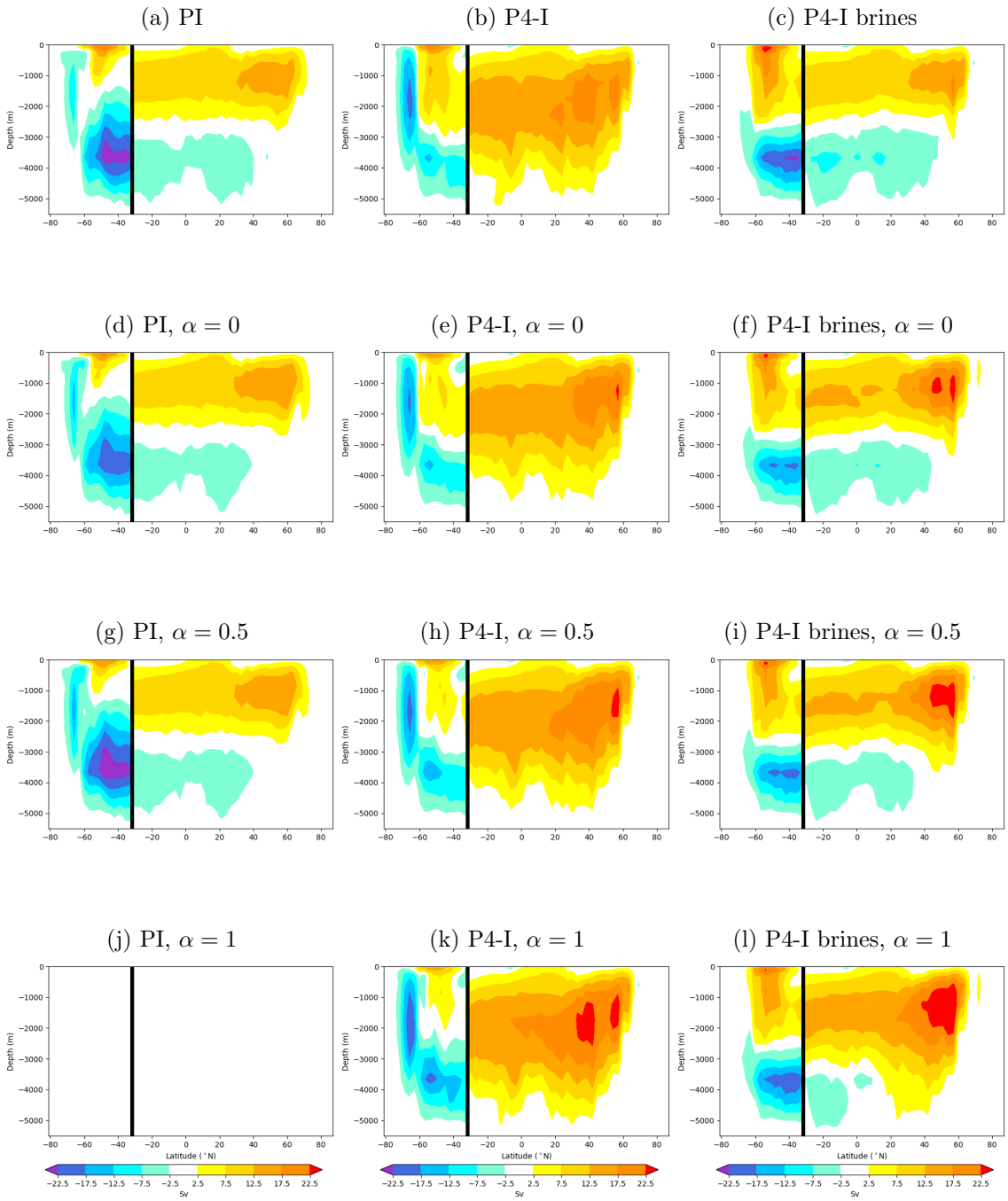

Figure 5.1: Streamfunctions in the Atlantic (North of 32°S) and Southern Ocean basins (South of 32°S), for a set of simulations with the parameterization of a stratification-dependent vertical diffusivity (varying α, K_0 set to 2×10^{-5} m^2.s^{-1}). Panel (j) is empty as the simulation crashed with NaN values. The black vertical line represents the limit between these two basins, at 32°S.

With a lower K_0, the changes in the streamfunction show the same trends but with a lower amplitude (Fig. 5.2). Even when the parameterization of the sinking of brines is also activated, inducing an increased stratification, the bottom cell does not display a significant reduction. Therefore, I ran simulations with a much lower $K_0 = 0.1 \times 10^{-5}$ m^2.s^{-1}.

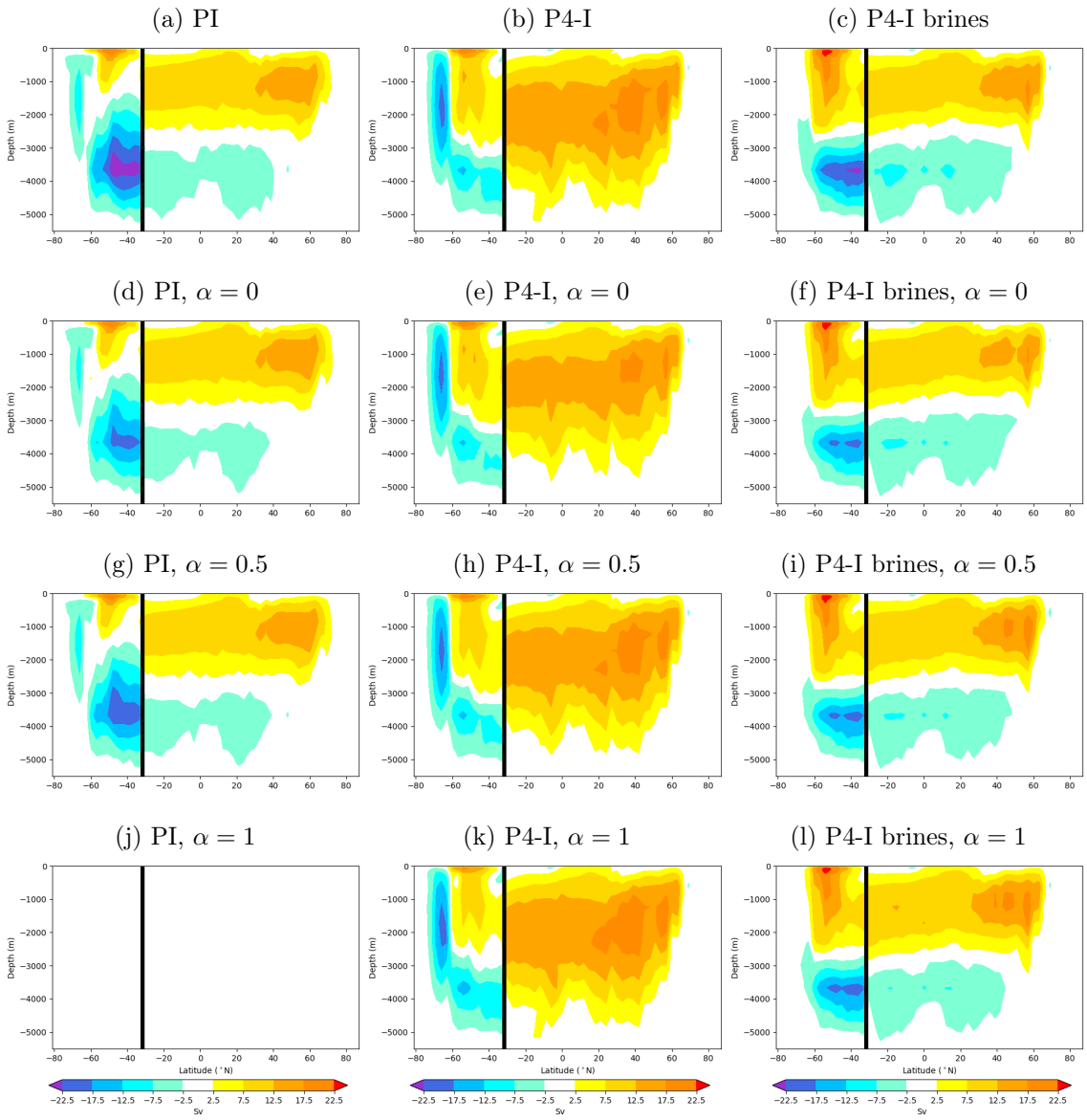

Figure 5.2: Streamfunctions in the Atlantic (North of 32°S) and Southern Ocean basins (South of 32°S), for a set of simulations with the parameterization of a stratification-dependent vertical diffusivity (varying α, K_0 set to 1×10^{-5} m^2.s^{-1}). Panel (j) is empty as the simulation crashed with NaN values. The black vertical line represents the limit between these two basins, at 32°S.

With a very low K_0 of 0.1×10^{-5} m^2.s^{-1}, I observe that a varying α does not yield much change anymore (Fig. 5.3). LGM simulations now show very limited changes compared to 'P4-I' without using the 'brines' parameterization. With it, the NADW cell is reduced and slightly less deep compared to 'P4-I brines'. However, the bottom cell is not further reduced compared to previous tests with a much higher K_0 and $\alpha = 0$, showing that this residual circulation may be robust. This suggests that other diffusion processes than the vertical diffusivity profile are responsible for this large overturning in the deep ocean, possibly even numerical diffusion. Further investigations are needed to identify the causes behind this relative absence of a bottom cell slowdown when changing the vertical diffusivity. For the time being, I have to settle for this set of simulations to observe the impact of a stratification-dependent diffusivity on the simulated carbon and on the quantified agreement with δ^{13}C proxy data.

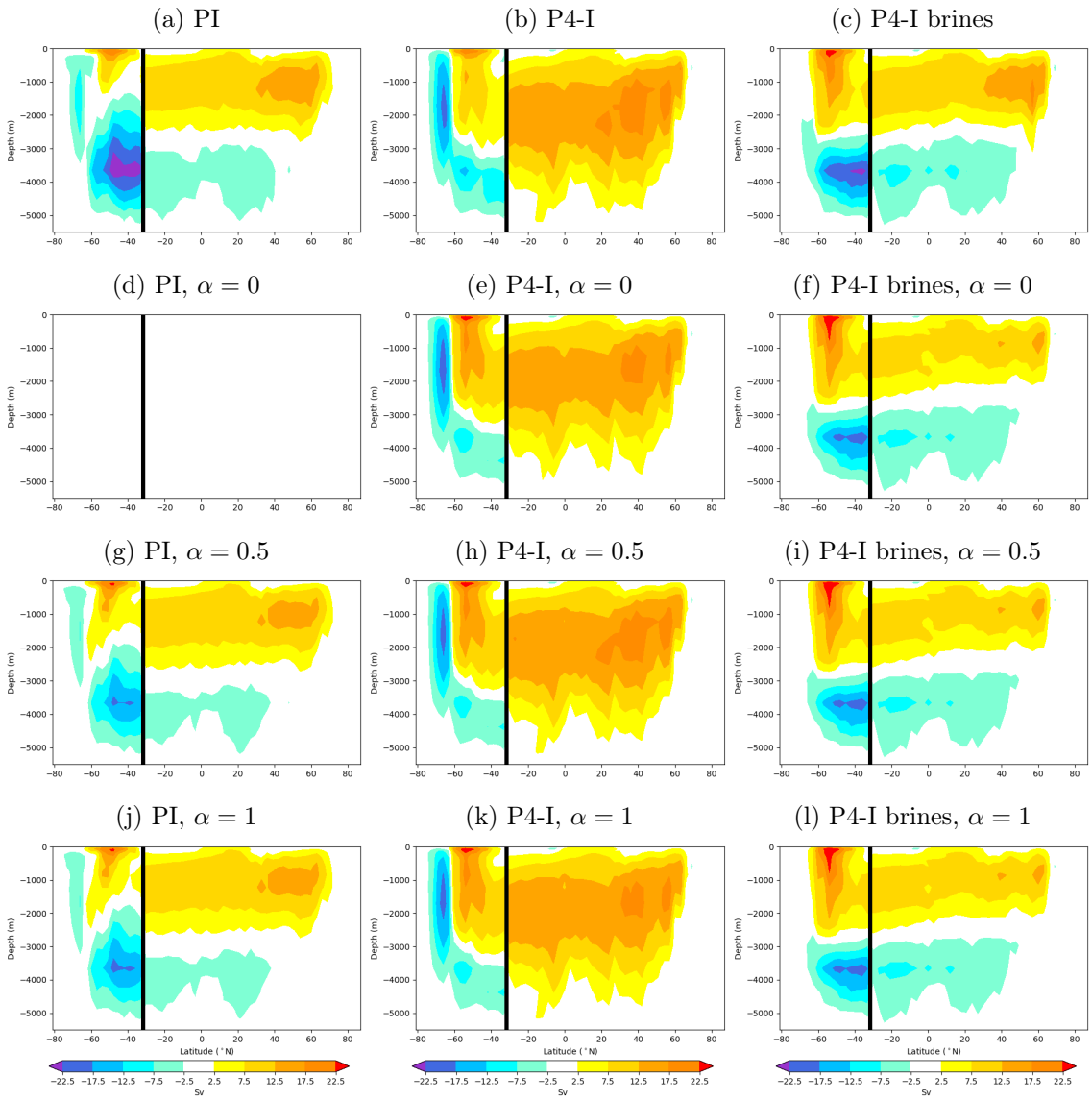

Figure 5.3: Streamfunctions in the Atlantic (North of 32°S) and Southern Ocean basins (South of 32°S), for a set of simulations with the parameterization of a stratification-dependent vertical diffusivity (varying α, K_0 set to 0.1×10^{-5} m^2.s^{-1}). Panel (d) is empty as the simulation crashed with NaN values. The black vertical line represents the limit between these two basins, at 32°S.

5.1.2 With a parameterization of tidal mixing and geothermal fluxes

As explained in Sect. 2.2.2, we also replaced the Bryan and Lewis profile with a more sophisticated and energy-constrained parameterization, developed by Casimir de Lavergne. This parameterization represents the mixing induced by the breaking of internal tides, which is topography-dependent. It considers four source terms implemented as 2D input maps and their associated vertical profile [de Lavergne et al., 2020]. In addition, I also test the effect of considering the heat received by bottom water masses from geothermal fluxes, which is largest at oceanic ridges. I ran simulations with the same three references, using either the parameterization of tidal mixing ('TM'), the geothermal fluxes ('G') or both ('TMG').

I observe very limited changes in the streamfunction simulated in the Atlantic basin (Fig. 5.4). However, the geothermal fluxes enhance abyssal overturning in the Pacific ocean (not shown here) and in the Southern Ocean (Fig. 5.4f and l) due to the large area of oceanic ridges [Emile-Geay and G. Madec, 2009, de Lavergne et al., 2016]. On the contrary, the tidal mixing parameterization slows down the abyssal overturning in the Southern Ocean (Fig. 5.4d and j) in comparison to 'PI' and 'P4-I brines' runs, while these modelling choices seem to have little effect in LGM runs when the 'brines' parameterization is not activated (Fig. 5.4g, h and i). In PI runs, the opposite effects of 'TM' and 'G' on the abyssal overturning partly balance each other out, whereas the 'P4-I brines TMG' simulation also shows a weaker abyssal overturning. The fact that I observe in Fig. 5.4j and k the same pattern in the bottom cell as in the runs of the previous section suggests that I may indeed have reached a residual overturning.

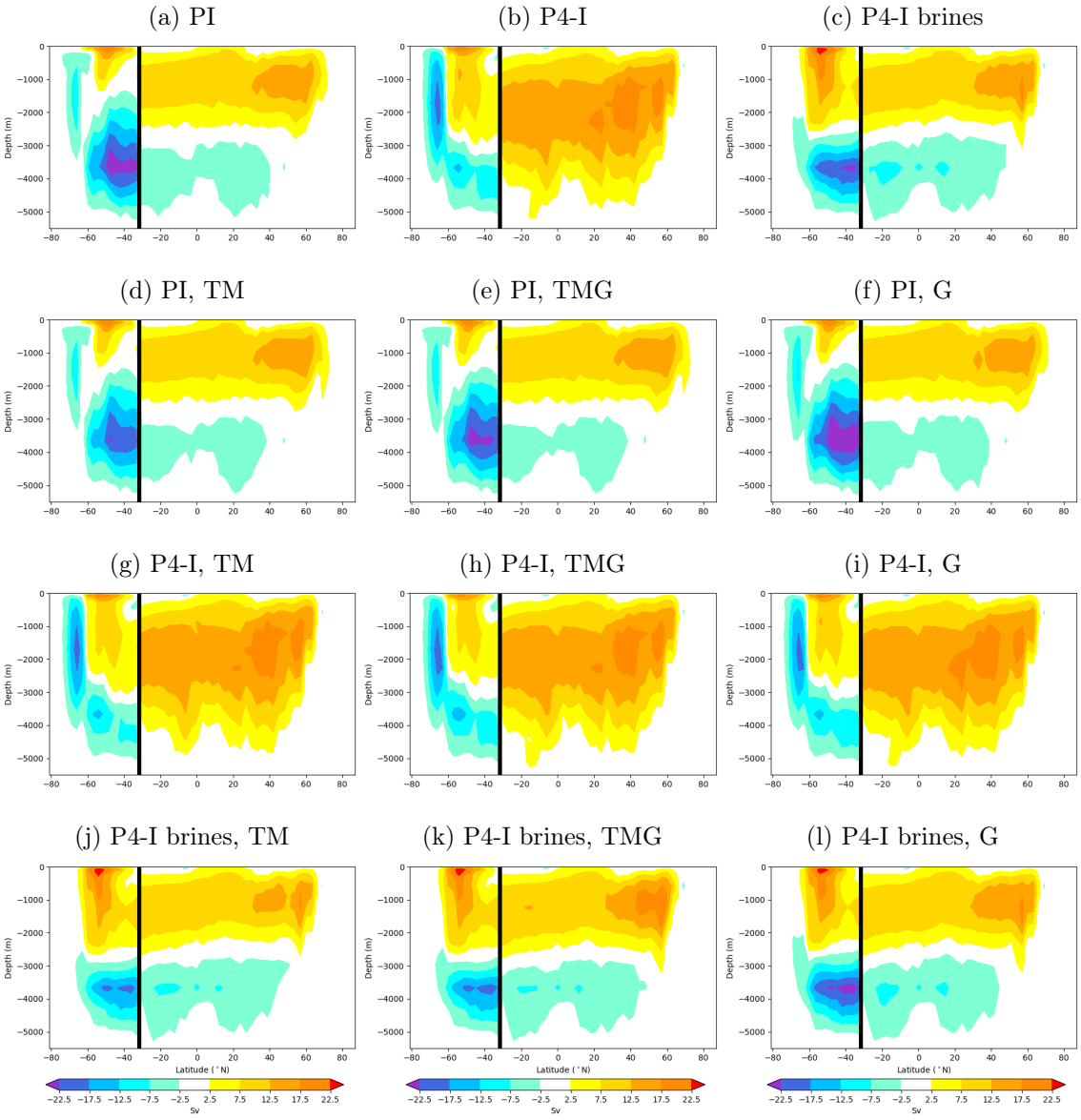

Figure 5.4: Streamfunctions in the Atlantic (North of 32°S) and Southern Ocean basins (South of 32°S). The black vertical line represents the limit between these two basins, chosen at 32°S.

5.2 Synthesis of quantifications related to Southern Ocean sea ice, deep ocean circulation and CO_2 concentration

I now examine the impact of these different parameterizations of vertical diffusivity on the quantifications already used in Sect. 4.3 to assess the model-data agreement obtained in terms of surface conditions (SST, sea ice), water mass distribution ($\delta^{13}C$), and atmospheric CO_2. Since biases may have regional or seasonal patterns (e.g. article 2), the chosen metrics have their limitations, but still ease first order comparison between multiple simulations.

Figure 5.5a shows that the parameterizations tested in this chapter tend to have relatively little effect on the model-data agreement with SST proxy data or to degrade it in summer (e.g. when the stratification-dependent diffusivity is used with a large K_0 and α), except for a very low K_0 (set to 0.1×10^{-5} $m^2.s^{-1}$). Compared to their references, these simulations tend to show a warming (in particular in the North Atlantic): for example, the use of a stratification-dependent diffusivity with a large K_0 yields a LGM$-$PI global mean SAT anomaly of $\sim -3.25°C$ $-$ almost outside of the range estimated by Annan and Hargreaves [2013], while the effect of the tidal mixing and geothermal fluxes is comparatively smaller. These simulations also show a consequently lower sea-ice extent in the Southern Ocean (Fig. 5.5b), which tends to bring the simulated summer extent closer to our estimate of $\sim 10.2 \times 10^6$ km^2, but without increasing the sea-ice seasonality as the 'brines' simulations did (see Sect. 4.3).

I observe in Fig. 5.5c and d that the NADW cell maximum is either increased or relatively unchanged (except with 'brines' and a very low K_0). The bottom cell maximum shows a limited decrease in simulations such as the ones with tidal mixing or a stratification-dependent diffusivity with a low K_0 or low α. These changes in the overturning intensity are not associated with large differences in the simulated water mass distribution, as suggested by the model-data agreement quantified for Atlantic $\delta^{13}C$ (Fig. 5.5e). The only exception is the 'P4-I brines, $\alpha = 1$, $K_0 = 2 \times 10^{-5}$ $m^2.s^{-1}$' simulation, which displays a much deeper NADW cell in the North Atlantic and therefore with a largely degraded agreement. The simulations with a lower K_0 are associated with a slighly improved agreement (when the 'brines' parameterization is also activated), possibly due to the reduced abyssal overturning. This is also the case of the 'P4-I brines TM' simulation, which again shows a small and opposite effect to 'P4-I brines G'.

Finally, I point out that the mixing schemes and vertical diffusivity parameter choices tested here entail either a higher or a relatively unchanged atmospheric CO_2 concentration. Again, the exception is when a very low K_0 is used in the stratification-dependent diffusivity parameterization, which then entails a lower CO_2 concentration (-6$-$14 ppm) and higher carbon sequestration in the ocean ($\sim$+30 GtC with 'brines'). While some other simulations (e.g.'P4-I brines TM') show a small decrease of a few ppm, it is imputable to a larger carbon content in the terrestrial biosphere (due to larger temperatures) and not to an increased ocean sequestration. On the other hand, simulations with an enhanced deep ocean circulation (e.g. '$\alpha = 1$, $K_0 = 2 \times 10^{-5}$ $m^2.s^{-1}$', Fig. 5.1) produce a larger increase of CO_2 concentrations of about $20 - 30$ ppm.

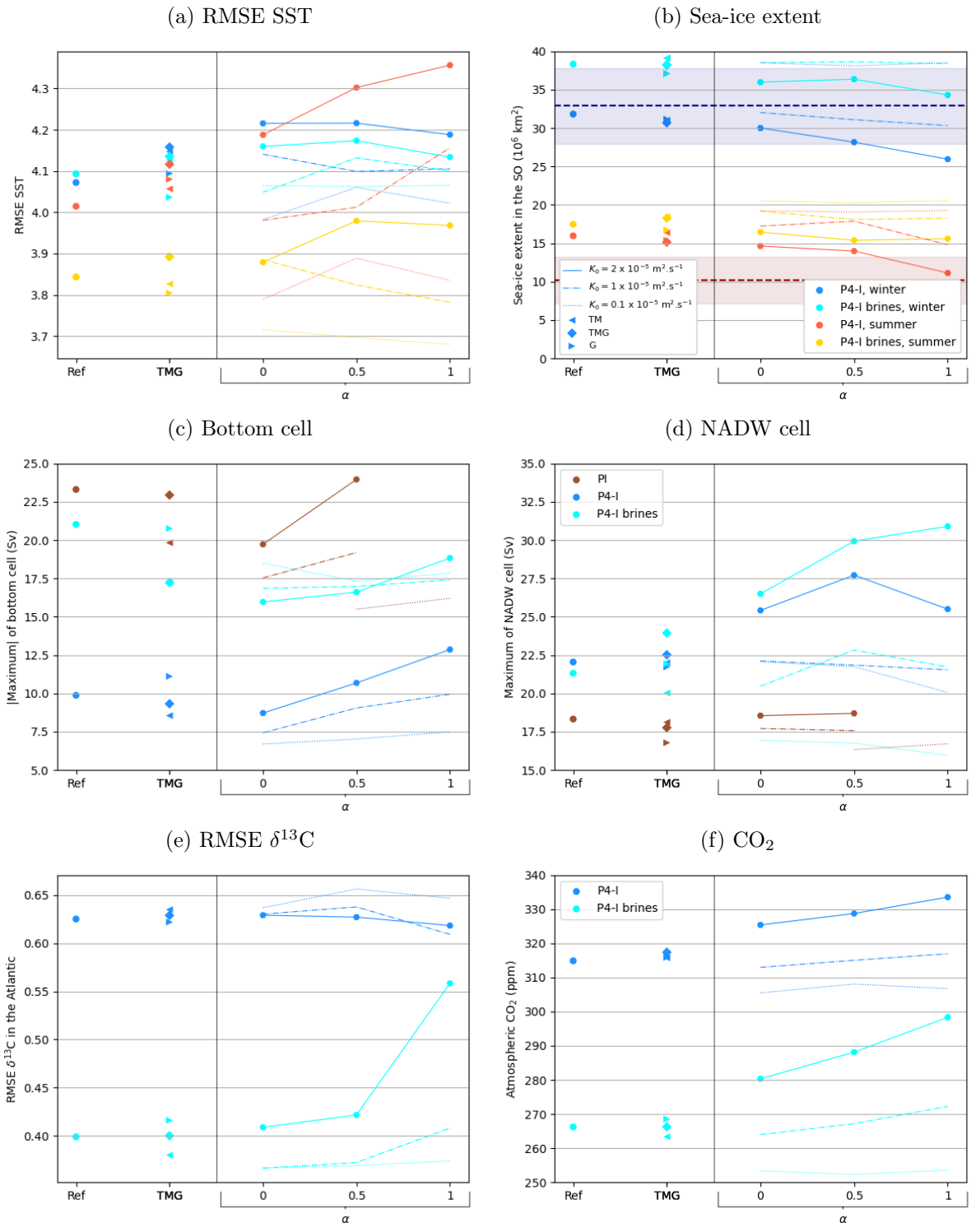

Figure 5.5: Effects of the modelling choices related to the vertical diffusivity parameterization on (a) RMSE computed with respect to SST data [MARGO Project Members, 2009], (b) sea-ice extent, maximum intensity of the (c) bottom and (d) NADW overturning cells, (e) RMSE computed with respect to δ^{13}C data [Peterson et al., 2014] and (f) atmospheric CO_2 concentration. The x-axis shows the different types of vertical diffusivity parameterization (reference, tidal mixing with/without geothermal fluxes, stratification-dependent diffusivity with a varying α). The dashed lines in panel (b) indicate the summer (red) and winter (blue) sea-ice extent estimated in Lhardy et al. [2021b].

Considering these results, it is unfortunate that I have not been able to test the effects of a much slower abyssal overturning, as there seems to be a strong residual overturning emerging in both types of parameterization tested here. In addition, simulating a slow abyssal overturning may be even more challenging if our tidal mixing parameterization had considered an enhanced tidal energy dissipation for the LGM [Schmittner et al., 2015, Wilmes et al., 2019]. One limitation of these results is the fact that we have implemented for now only the energy dissipation maps computed for the pre-industrial and modern era [de Lavergne et al., 2020]. The maps corresponding to the low sea level of the LGM will be generated and used in future LGM simulations.

5.3 Résumé du chapitre en français

Dans ce chapitre, j'explore non pas la formation de masses d'eau profonde (AABW) mais leur transformation, à l'aide de différentes paramétrisations de la diffusivité d'arrière-plan. En effet, la diffusion verticale paramétrisée dans les modèles paléoclimatiques suit souvent un profil simple, de type Bryan and Lewis [1979]. La diffusion imposée dans l'océan profond est alors quasi-uniforme, ne dépendant ni de la stratification des masses d'eau, ni de leur contact avec la topographie des fonds marins. En réalité, cette topographie importe pour éroder la stratification profonde et engendrer un upwelling de l'AABW, car elle permet d'injecter de l'énergie au mélange des masses d'eau grâce au déferlement d'ondes de marée et aux flux géothermiques. Il est possible que cette diffusivité d'arrière-plan, jamais très faible, explique l'absence de valeurs de δ^{13}C simulées dans l'océan austral proches de -1‰, comme mesurées dans les carottes marines (cf. Sect. 4.2). Or, il est essentiel pour bien représenter le temps de résidence du carbone dans l'océan de correctement simuler l'isolement des masses d'eau profondes. La circulation profonde simulée par le modèle iLOVECLIM dans le cadre du chapitre 4 présente une convection abyssale intense, à la fois au PI et avec la paramétrisation de la plongée des saumures, qui contraste avec les enregistrements paléoclimatiques suggérant à la fois une AABW plus volumineuse, mais aussi plus lente.

Ainsi, je teste dans ce chapitre 5 l'impact des choix de paramétrisation liés à la diffusivité d'arrière-plan, en remplaçant le profil de Bryan and Lewis par une diffusivité dépendante de la stratification, ou dépendante de l'énergie injectée par les ondes de marées et/ou par les flux géothermiques. Je réexamine la circulation océanique profonde simulée dans l'Atlantique et les biais déjà quantifiés dans le chapitre 4.

J'observe alors une convection abyssale légèrement réduite lorsque la diffusivité dépend des ondes de marées, et intensifiée quand elle dépend des flux géothermiques. Toutefois, ces variations sont petites, et une forte cellule résiduelle est observée même pour une diffusivité d'arrière-plan très faible. De plus, aucun des choix testés ne permet de réduire significativement les biais observés.

Ces résultats sont donc peu concluants à ce stade. Ils appellent donc diverses perspectives, telles que : (1) l'utilisation de métriques spécifiques à l'océanographie physique (telle qu'une fonction de courant en coordonnées isopycnales) pour préciser ce diagnostique ; (2) un examen détaillé du code dynamique afin d'identifier l'origine de la forte convection abyssale résiduelle ; (3) l'utilisation de cartes d'énergie dissipée correspondant à la topographie du DMG et non du PI dans la paramétrisation du mélange lié aux ondes de marées.

Chapter 6

Investigating the relationship between biases in Southern Ocean sea ice, deep ocean circulation and CO_2 concentration

Chapter aims:

1. Evaluate the impact of Southern Hemisphere westerly winds on the studied variables
2. Synthesize and compare the biases obtained with various modelling choices in terms of boundary conditions (chapter 3 and 4), parameter choices related to the sinking of brines (chapter 4) or vertical mixing (chapter 5), and wind stress (chapter 6)
3. Explore the relationships between Southern Ocean surface conditions, deep ocean circulation, water mass distribution, carbon sequestration and CO_2 concentration

Highlights:

↪ A reduced wind stress in the glacial Southern ocean yields a sea-ice cover in better agreement with proxy data and a slightly lower CO_2 concentration, but no improvement of Atlantic water mass distribution.

↪ A relationship is observed between sea-ice seasonality and open-ocean convection in the Southern Ocean. On this basis, the seasonality estimated from a proxy-based reconstruction would constrain a very low convection.

↪ An improved agreement with $\delta^{13}C$ data is associated with a NADW shoaling and an intense abyssal cell. However, $\delta^{13}C$ data do not constrain the AMOC strength.

↪ The maximal ocean sequestration simulated with a parameterized sinking of brines is only half as large as the one obtained when the LGM ocean boundary conditions are not implemented, underlining how crucial the ocean volume is.

↪ My simulations do not support an attribution of the AMOC depth to insufficient sea ice in the Southern Ocean.

In previous chapters, I have generated and implemented the boundary conditions associated with two different ice sheet reconstructions in order to run LGM simulations with the iLOVECLIM model under the PMIP4 protocol. I have then produced model-data comparisons and identified biases in the simulated Southern Ocean sea-ice cover, Atlantic water mass distribution, and atmospheric CO_2 concentration. I have characterized the biases obtained in simulations with different boundary conditions and parameterization choices (i.e sinking of brines, vertical diffusivity) in order to evaluate the impact of the ice sheet elevation (and related changes, e.g. on the ocean volume), artificial sinking of dense waters ensuing from sea-ice formation, and vertical mixing on these model biases.

I have uncovered the same kind of disagreements with proxy data as in most models and previous PMIP phases, that is to say a too round sea-ice cover in the Southern Ocean, associated with an underestimated seasonal amplitude and a marked warm bias at $\sim 40-50°S$, an Atlantic $\delta^{13}C$ distribution affected by a too deep NADW, and a too high atmospheric CO_2 concentration. However, we have re-estimated the sea-ice extent reconstructed from sea-ice linked diatoms in marine core data in the Southern Ocean. We have estimated a winter sea-ice extent of $\sim 32.9 \times 10^6$ km^2, largely reduced compared to the previous estimation from Roche et al. [2012] ($\sim 43.5 \times 10^6$ km^2). On the basis of our new estimates, the simulated sea-ice extent is likely only slightly underestimated in winter and overestimated in summer in my standard LGM runs (especially in v2).

As a result, it is not trivial to attribute a weak stratification and a deep AMOC to an insufficient sea-ice formation, as suggested by Marzocchi and Jansen [2017]. In theory, an insufficient sea-ice formation in the Southern Ocean could well be linked to a warm bias and entail an underestimated AABW density, hence the absence of a NADW shoaling in the Atlantic and of a carbon sequestration increase caused by a large and isolated AABW in the deep ocean. In this context, the biases appear to be broadly consistent with each other. However, the climate system is complex and influenced by numerous variables and feedback processes, which is why the observed biases may well have different origins. Using simulations with different boundary conditions, I have underlined in Lhardy et al. [2021b] that a cold Southern Ocean improves the overall agreement with SST and sea-ice proxy data (despite the remaining regional and seasonal patterns of model-data disagreements), but also tends to further increase the AMOC strength. As this is not the case for simulations with a parameterized sinking of brines, I have suggested that addressing the model representation of convection processes in the Southern Ocean may be key to reconcile both the surface conditions and the water mass distribution biases. Furthermore, simulations with various choices associated to this parameterization (e.g. different parameter choices, or the 'shallow brines' experiment, see Sect. 4.3) also demonstrate that the reductions of different biases do not necessarily co-occur.

Therefore, I examine in this chapter the potential relationships between the different observed biases and discuss the robustness of the link between the Southern Ocean SSTs and sea ice, the AMOC and Atlantic water mass distribution, and the atmospheric CO_2 concentration, as represented by the iLOVECLIM model (Sect. 6.3 and 6.4). These relationships are explored using my large set of simulations, obtained with different boundary conditions (chapter 3 and 4), parameter choices related to the sinking of brines (chapter 4) or to vertical mixing (chapter 5). This is an opportunity to compare the effects of each type of modelling choices on the quantified biases in a summary (Sect. 6.2). Nonetheless, my first step is to complete this set of simulations with sensitivity tests on the Southern Ocean winds (Sect. 6.1). Indeed, despite promising premises, my vertical mixing experiments gave little positive results, possibly due to a strong residual abyssal overturning (see chapter 5). However, mixing processes are not the sole driver of the AMOC: wind-driven processes, through their impact on the Ekman upwelling

in the Southern Ocean, also play an important role [Kuhlbrodt et al., 2007, Marshall and Speer, 2012, Baker et al., 2021]. Therefore, evaluating the impact of sensitivity tests on winds on the examined variables can also deepen our understanding of the AMOC behaviour, as well as of the potential relationship between sea-ice biases, sea-ice advection and deep ocean convection in the Southern Ocean (as discussed in article 2).

6.1 Evaluation of the effects of Southern Ocean winds on sea ice, deep ocean circulation and CO_2 concentration

6.1.1 Motivations and methods

Sensitivity tests on Southern Ocean winds are motivated by studies which suggest an important control of the strength and position of westerly winds at the LGM on the abyssal overturning rate and pCO_2 drawdown [Toggweiler et al., 2006, Gray et al., in review, 2021]. Recently, Gray et al. [in review, 2021] estimated using planktonic foraminifera $\delta^{18}O$ data a $\sim 25\%$ weakening and a $\sim 4.7°$ equatorward shift of Southern Ocean westerlies at the LGM, relative to the mid-Holocene. A shift of this magnitude is hardly represented by the PMIP3-4 ensemble (see Extended data 7, Gray et al. [in review, 2021]). Chavaillaz et al. [2013] also highlighted during the PMIP3 phase substantial intermodel spread both in terms of wind speed anomaly (LGM − PI) and direction of shift, with three models simulating a very small equatorward shift while three others display a moderate poleward shift ($\sim 1 - 1.5°$). Still, I note that data constraints on the winds strength and position remain elusive [Kohfeld et al., 2013].

Given this performance of the other PMIP models and the especially coarse resolution of the ECBILT atmospheric component, I can hardly expect the iLOVECLIM model to accurately represent the wind changes at the LGM (Fig. 6.2a). In fact, a comparison of the PI run with modern reanalysis data (ERA-interim, see Fig. 6.1) demonstrates that the PI westerlies are largely underestimated over the Southern Ocean, partly because of the low resolution. Exploring the impact of wind stress modifications on the AMOC and ocean sequestration via sensitivity tests is therefore a way of assessing the consequences of such wind biases.

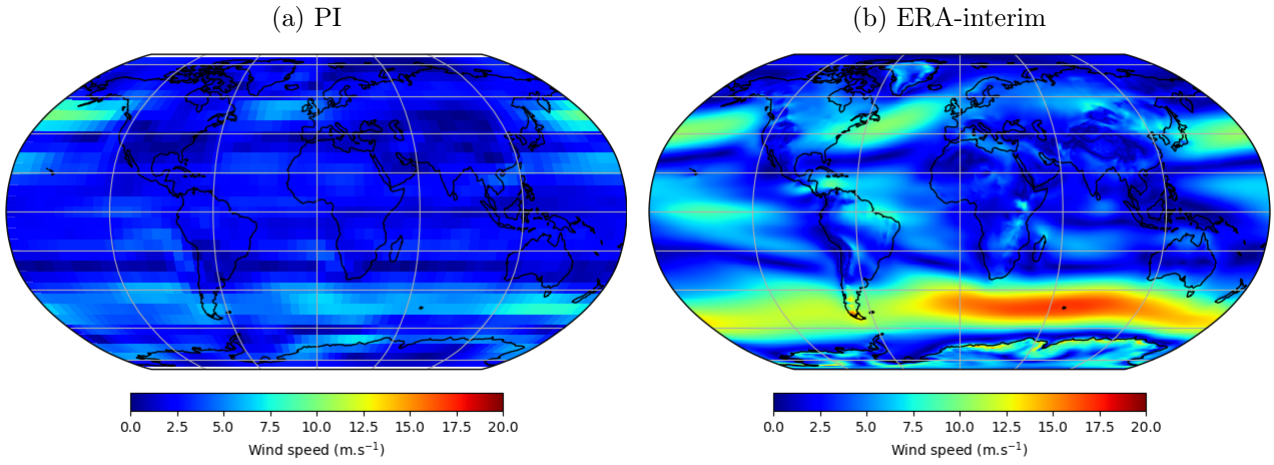

Figure 6.1: Wind speed simulated at 800 hPa at the PI by the iLOVECLIM model, compared to the ERA-interim reanalysis (1979-2016)

In addition, these tests can potentially also influence sea-ice biases, through a change of sea-ice export or Southern Ocean overturning. Studying the dynamics of the Southern Ocean upwelling branch, Marshall and Speer [2012] point out its importance as it "acts to connect the vast reservoirs of heat and carbon below the Southern Ocean mixed layer with the surface". As they explain, deep and warm waters can rise along the tilted density surfaces and melt sea ice, possibly controlling the sea-ice extent. The authors underline that the meridional residual flow of this upwelling results from both a wind-driven circulation (tilting density surface) and an eddy-driven circulation (flattening density surfaces). In this context, the surface heat fluxes can be influenced by westerly wind biases, as well as by the representation of the eddy-induced circulation. I note that as the iLOVECLIM model cannot resolve the latter, it relies on a parameterization [Gent and McWilliams, 1990] to account for its effects on isopycnal surfaces.

Therefore, I have performed sensitivity tests with a modified wind stress in the Southern Ocean (tests designed by Pepijn Bakker, pers. com.). The winds were left unchanged, but their effects on the ocean was modified by increasing (+20%, +50%), decreasing (-20%, -50%) or zonally shifting (3°S, 6°S, 3°N, 6°N) the peak of the zonal mean wind stress in the reference simulation (Fig. 6.2b). I respectively call these simulations 'plus20', 'plus50', 'minus20', 'minus50' and 'shift3S', 'shift6S', 'shift3N', 'shift6N' for simplicity. As the experimental set-up of these sensitivity tests allows for a feedback effect on the atmospheric winds, I observe minor changes in the zonal mean wind stress in 'shiftS' and a collapse in 'shiftN', possibly due to the geographical constraints of Drake Passage. Still, I kept the latter in this set of simulations, since it is interesting in itself to see the AMOC response of an absence of wind stress in the Southern Ocean. Finally, I also add to this set a simulation named 'a20S', which does not target wind stress but sea ice−ocean stress. Indeed, as pointed out by Ma et al. [2020], most climate models align ice and ocean velocities by prescribing a fixed turning angle of zero, while sea-ice observations suggest a more complex behaviour. Using an ESM, the authors evaluate the effects of a non-zero turning angle on the Southern Ocean, and show that a 20° angle induces an offshore sea-ice advection associated with a reduced open ocean convection. In addition, they obtain a reduced warm bias and an increased sea-ice seasonal amplitude, two effects which − considering the model biases identified in this study − caught my attention. Therefore, I performed a similar experiment (with a 20° turning angle in the Southern Hemisphere, hence 'a20S') under LGM conditions.

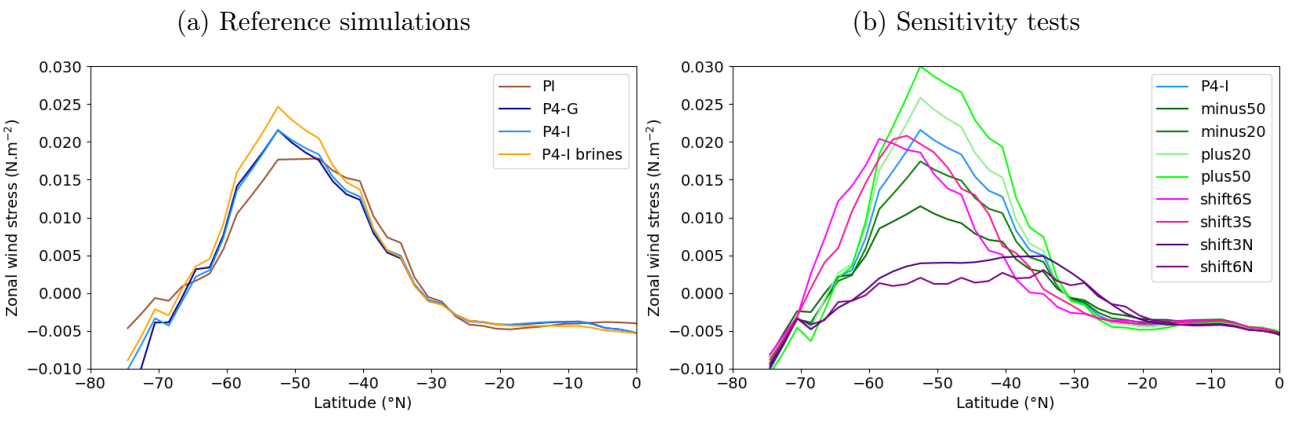

Figure 6.2: Mean zonal wind stress in the Southern Hemisphere, for (a) reference PI and LGM simulations, and (b) LGM sensitivity tests with a modified wind stress in the coupler

6.1.2 Sea-ice biases

First examining the effects of this set of experiments on the sea-ice extent in Fig. 6.3, I observe significant changes in the winter sea-ice extent and to a lesser degree in the summer one. Simulation 'a20S' displays a similar winter extent as in the reference 'P4-I', therefore slightly below our winter estimate of $\sim 32.9 \times 10^6$ km^2. However, it also shows a lower summer sea-ice extent than 'P4-I', thus much closer to our summer estimate of $\sim 10.2 \times 10^6$ km^2. Indeed, a non-zero turning angle enhances sea-ice advection towards lower latitudes and therefore melting. Still, this is in contrast with the results from Ma et al. [2020], which obtain a larger seasonal amplitude with a 20° turning angle essentially due to a larger winter sea-ice extent.

(a) P4-I (ICE-6G-C) (b) P4-G (GLAC-1D)

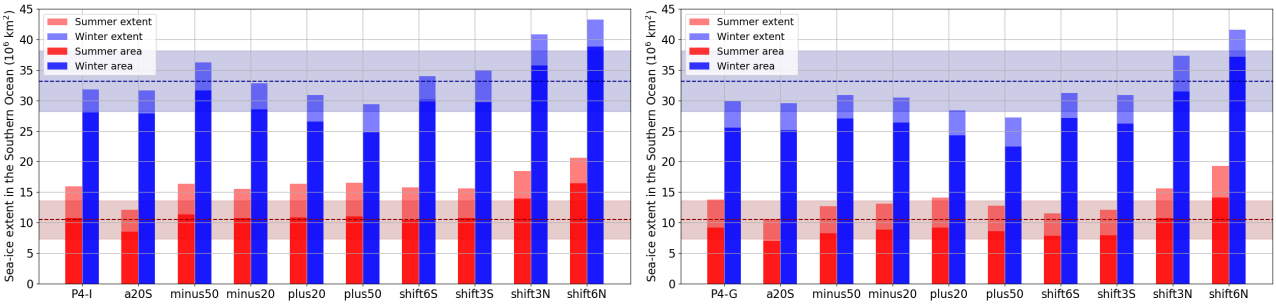

Figure 6.3: Austral summer (JFM) and winter (JAS) sea-ice areas and extents in the Southern Ocean, simulated at the LGM by (a) 'P4-I' and (b) 'P4-G' sensitivity tests on wind stress and sea ice−ocean stress. The LGM sea-ice extent estimated in Lhardy et al. [2021b] is represented by the dashed red (summer) and the blue (winter) dashed lines (with an indicative error bar of 30% and 15%, respectively).

The other sensitivity tests demonstrate that a reduced wind stress is associated with a larger winter sea-ice extent and seasonality, reducing to some degree the sea-ice biases. This is also the case of a poleward shift of the wind stress maximum, while the wind stress collapse observed in 'shiftN' simulations causes an overestimated sea-ice extent in both seasons, yet also an increased seasonal amplitude. The same simulations run with the GLAC-1D boundary conditions (Fig. 6.3b) broadly show the same trends relative to the 'P4-G' reference, though the simulated sea-ice extents are smaller due to an overall warmer Southern Ocean. I underline that the simulations showing the closest agreement with the estimates from marine core data are obtained with a poleward shift or a reduced wind stress, whereas PI winds are already largely biased towards low values (Fig. 6.1). However, it is entirely possible that the tuning of the atmosphere−ocean coupler was done accordingly, in order to simulate sufficient Ekman pumping even in this low wind situation. If true, I may overestimate here the sensitivity of the ocean model to wind stress changes.

Secondly, I assess the simulated sea-ice distribution using the same type of maps as in article 2 (Fig. 6.4). Again, regional biases are observed: the model still simulates a too round sea-ice distribution in the Southern Ocean to compare well with the sea-ice lines inferred from the marine core data compilation. Still, the 'minus50' simulation (in dark green) shows a visible improvement in winter, with a sea-ice edge reaching ~ 50°S in the Atlantic sector yet no further overestimation in the Pacific sector (in contrast to 'shift6N').

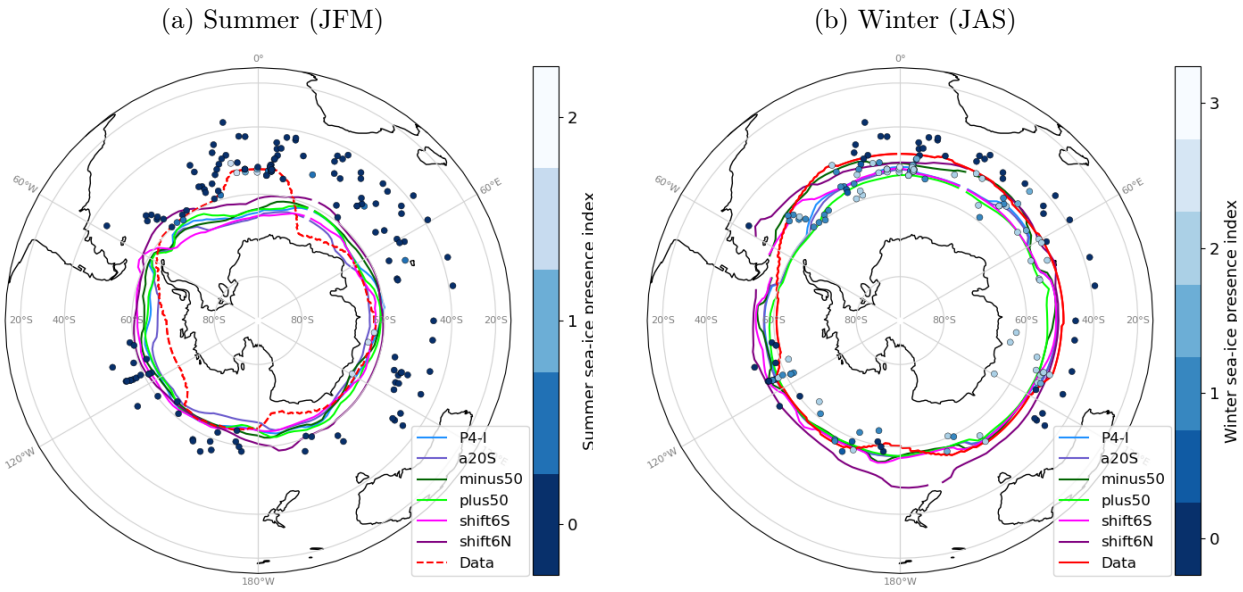

Figure 6.4: Austral summer (a) and winter (b) sea-ice edges (at 15% of sea-ice concentration, enclosing the total ocean surface defined as the sea-ice extent) in the Southern Ocean for a subset of the 'P4-I' sensitivity tests on wind stress and sea ice−ocean stress. The sea-ice presence suggested by marine core data is represented as an arbitrary index on a blue to white scale, where blue denotes no indication of sea ice in proxies, and white denotes agreement of several proxies on the presence of sea ice. The red lines mark the likely delimitation of the sea-ice presence according to the proxy data. The summer sea-ice contour is represented by a dashed red line as it is not well-constrained.

I can expect these modifications on wind and sea ice−ocean stress to influence convection processes in the Southern Ocean. And indeed, I observe in Fig. 6.5 that a non-zero turning angle significantly deepens the winter mixed layer depth (MLD) at several deep convection spots around the Antarctic coast, while the simulated sea-ice edge remains unchanged. Convection is largely enhanced in 'plus50', and suppressed in 'minus50'. Interestingly, this last simulation shows a much shallower MLD in the open ocean of the Atlantic sector ($\sim 55°S$) with respect to 'P4-I', whereas changes are not as pronounced in the Pacific sector. This contrasts with the MLD simulated in 'P4-I brines' (not shown here), which suppresses convection in the whole Southern Ocean. I underlined that 'minus50' shows reduced seasonal and regional biases with respect to sea-ice proxy data. Although heat fluxes need to be computed to perform a more in-depth analysis, I consider it likely that the northward displacement of the sea-ice edge in the Atlantic sector simulated with reduced wind stress is related to less heat brought to the surface by a less intense upwelling. As a result, it seems that regional biases in the sea-ice cover may be linked to convection processes. As for what could explain the oval-shaped sea-ice cover inferred from marine core data, I can hypothesize that an equatorward shift of the westerly winds at the LGM (of the amplitude suggested by Gray et al. [in review, 2021]) may well drive different upwelling rates in the Atlantic and Pacific sectors due to the geographical constraints of Drake Passage.

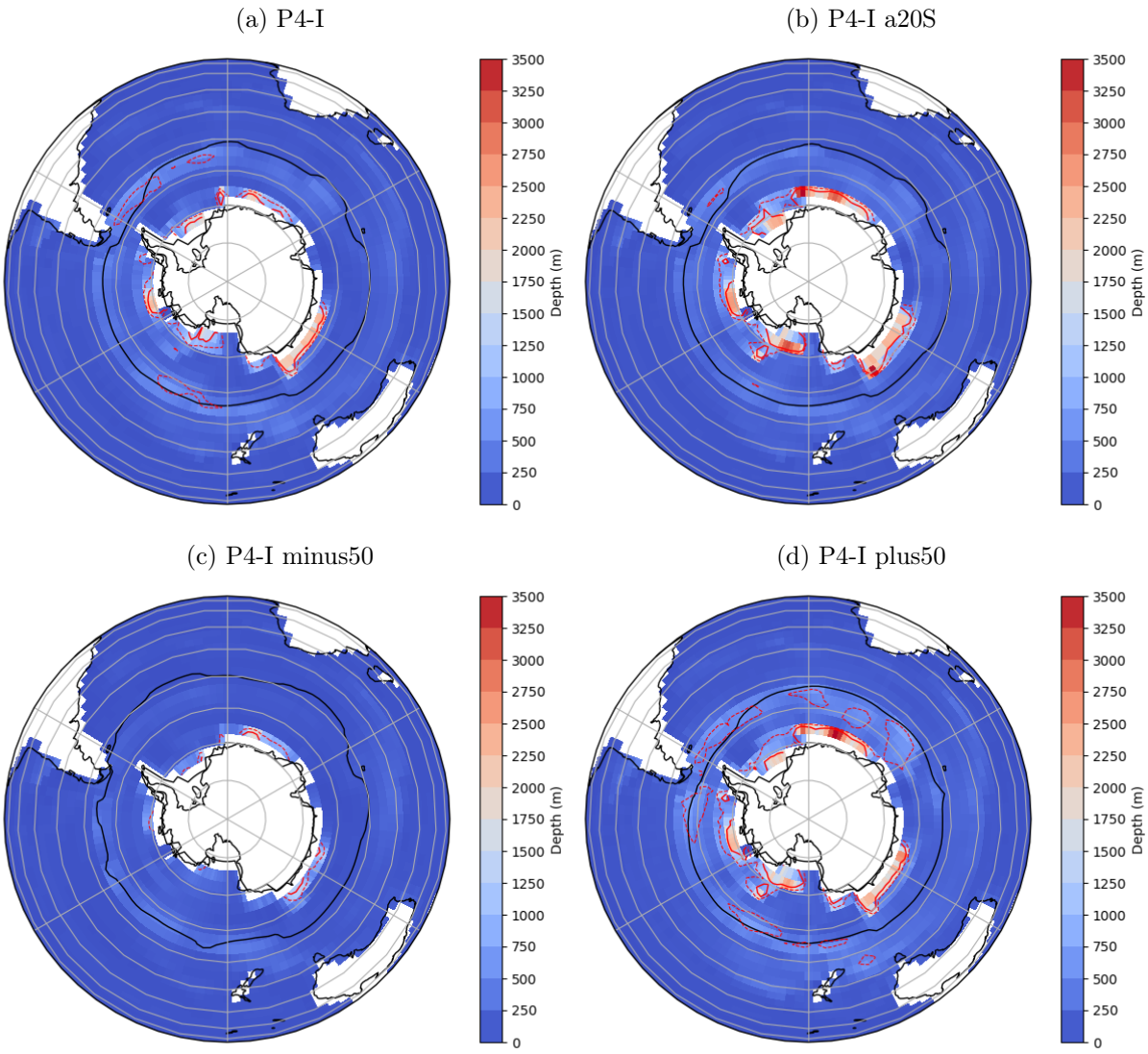

Figure 6.5: Austral winter (JAS) mixed layer depth (MLD) in the Southern Ocean for a subset of the 'P4-I' sensitivity tests on wind stress and sea ice−ocean stress. The black line indicates the simulated sea-ice edge. The red solid (dashed) line locates a MLD reaching 1000 m (500 m).

6.1.3 Southern Ocean and Atlantic streamfunction

These sensitivity tests on wind and sea ice−ocean stress impact the simulated streamfunction, through their effects on the Southern Ocean upwelling and sea-ice export. Figure 6.6 shows that the Southern Ocean overturning is suppressed in 'minus' simulations, with a very small reduction effect on the bottom and NADW cells. Conversely, the Southern Ocean overturning is significantly enhanced in 'plus' simulations. A non-zero turning angle in 'a20S' also induces an intensification of this overturning, which is consistent with the MLD observed previously. In contrast, 'shift' simulations shows that a zonal displacement of the westerly wind stress affects both the strength and geometry of the Southern Ocean overturning, which is largely stalled due to the wind stress collapse in 'shiftN'. Finally, I observe that the NADW cell remains very deep in all simulations.

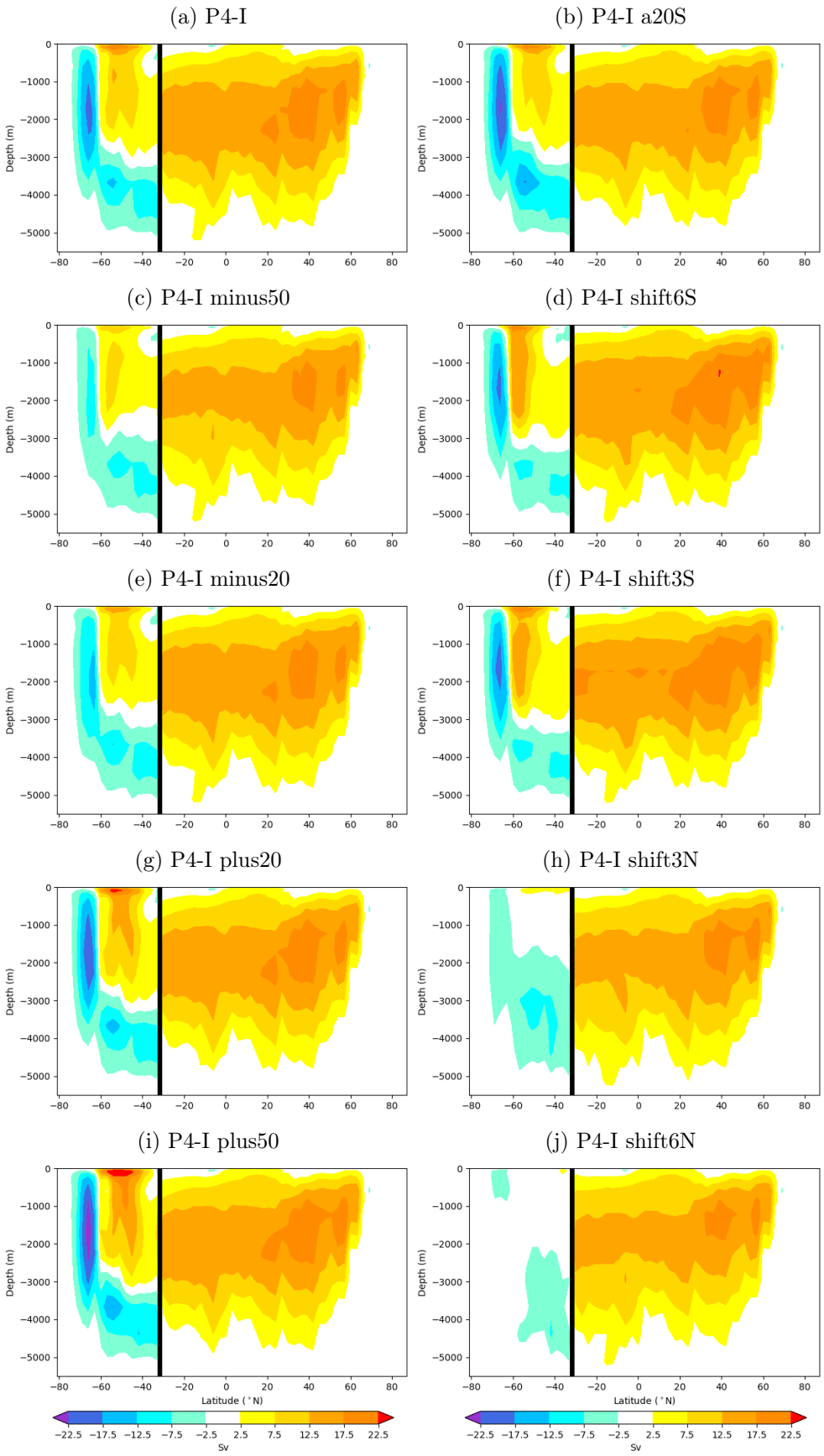

Figure 6.6: Streamfunctions (Sv) in the Atlantic (North of 32°S) and Southern Ocean basins (South of 32°S), simulated by 'P4-I' sensitivity tests on wind stress and sea ice−ocean stress.

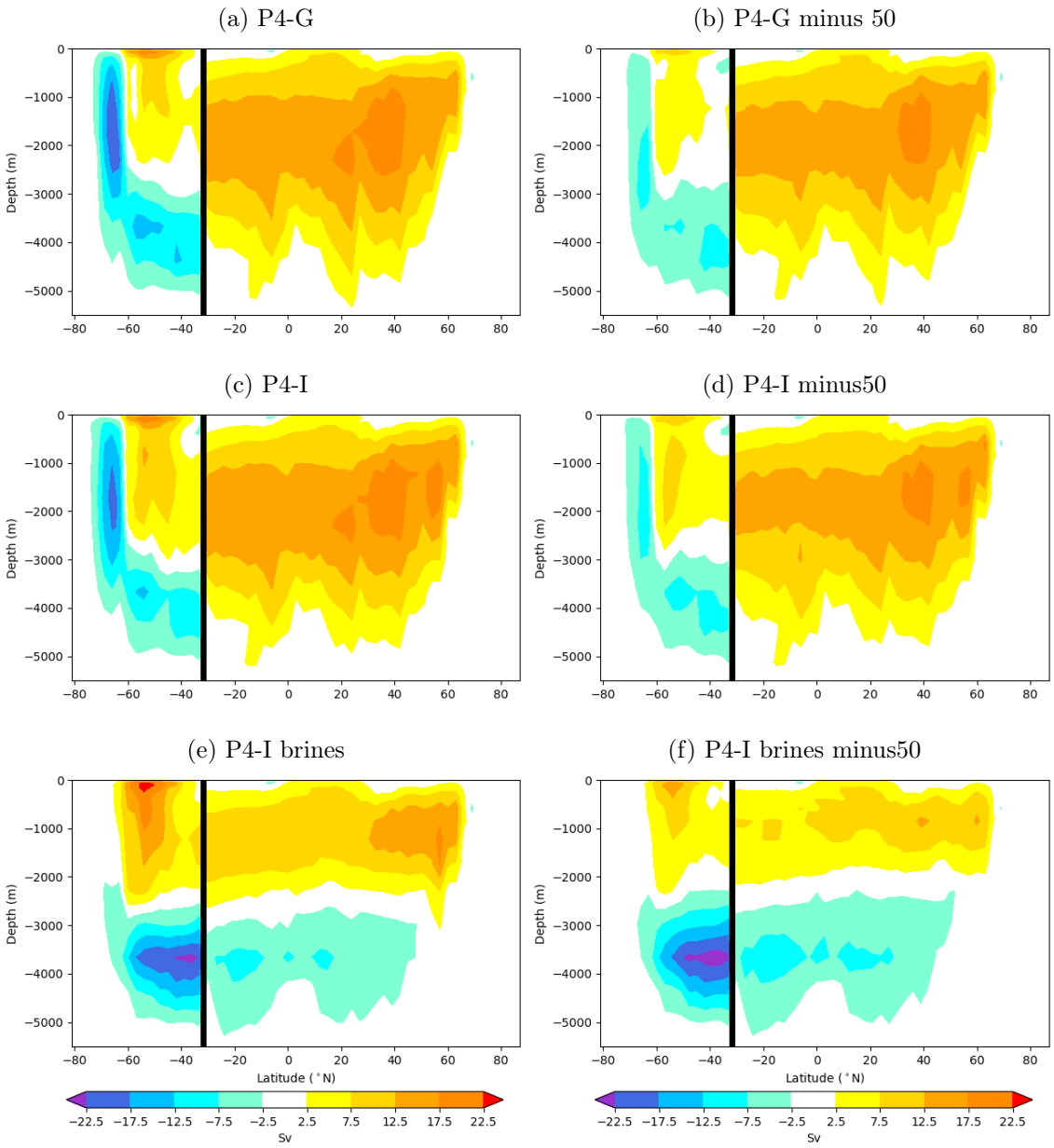

Figure 6.7: Streamfunctions (Sv) in the Atlantic (North of 32°S) and Southern Ocean basins (South of 32°S), simulated by reducing wind stress in different reference simulations.

It is interesting to note that the effect of the wind stress reduction is somewhat dependent on the reference simulation used to run these sensitivity tests (in Fig. 6.7, 'P4-G', 'P4-I' or 'P4-I brines'). For example, the 'P4-G minus50' simulation shows a relatively larger reduction of the Southern Ocean overturning (with respect to 'P4-G') than the 'P4-I' simulations. When the parameterization of the sinking of brines is activated, the reduction of wind stress also significantly impact the strength and depth of the NADW cell in the North Altantic (Fig. 6.7f).

6.1.4 Synthesis of quantifications related to Southern Ocean sea ice, deep ocean circulation and CO_2 concentration

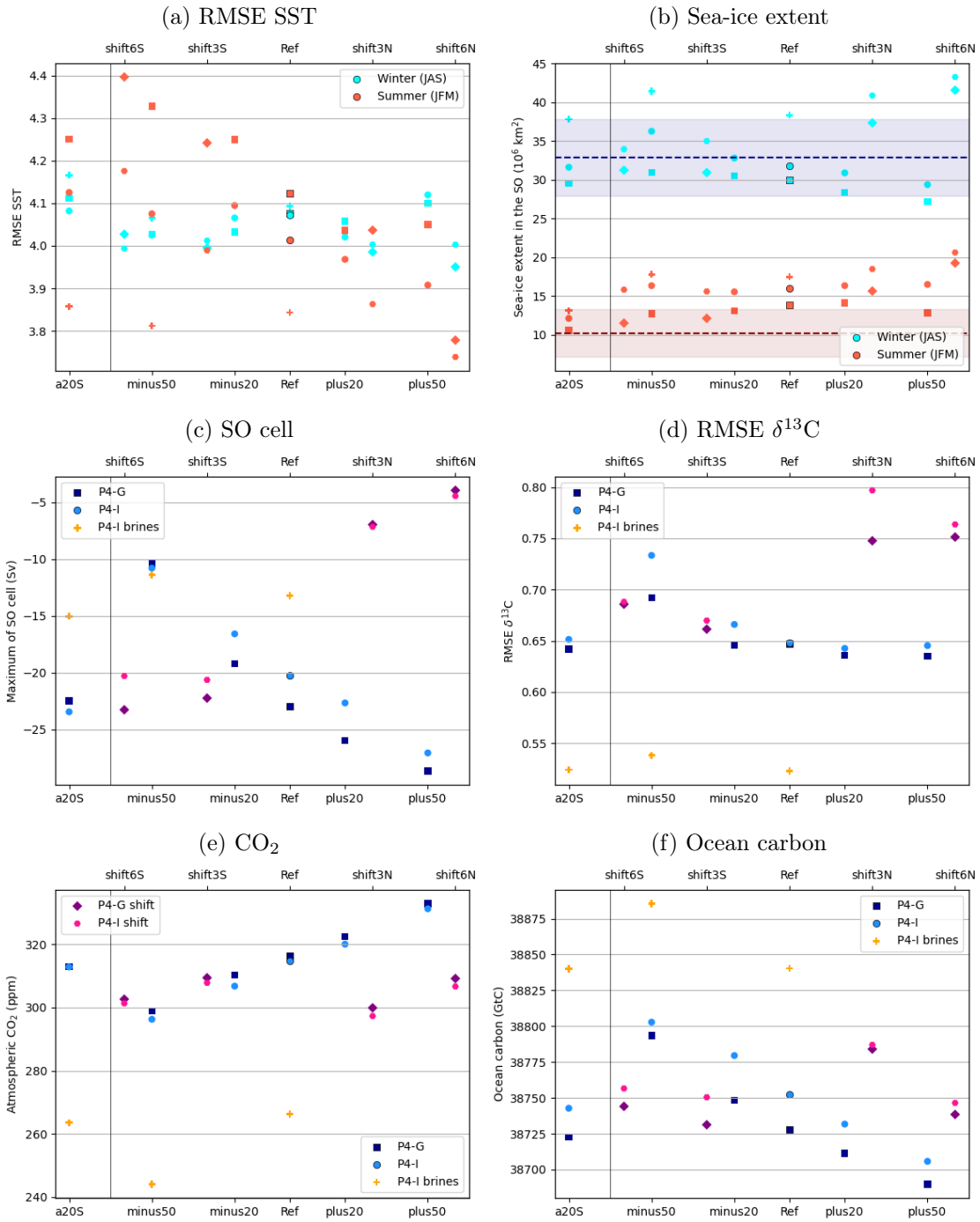

Figure 6.8: Effects of the sensitivity tests on wind stress and sea ice−ocean stress on the (a) RMSE computed with respect to SST data [MARGO Project Members, 2009], (b) sea-ice extent, (c) maximum intensity of the SO overturning cell, (d) RMSE computed with respect to δ^{13}C data [Peterson et al., 2014], (e) atmospheric CO_2 concentration and (f) ocean carbon content. The dashed lines in panel (b) indicate the summer (red) and winter (blue) sea-ice extent estimated in Lhardy et al. [2021b].

As in chapters 4 and 5, I examine how metrics related to surface conditions, deep ocean circulation and carbon content behave as a function of the wind stress modification in these sensitivity tests (Fig. 6.8). The RMSE computed with respect to SST data shows no clear relationship with wind stress (Fig. 6.8a). Sensitivity tests with a colder Southern Ocean ('shiftN') tend to show a smaller RMSE in summer, when the warm bias is distinct. However, the latitudinal pattern of this bias remains a systematic feature in my simulations.

While I already commented on most of the sea-ice extents presented in Fig. 6.8b, I note that a simulation with both a wind stress reduction and the sinking of brines in the Southern Ocean displays a larger winter sea-ice extent than 'minus50' and 'P4-I brines'. It is therefore likely that a wind stress reduction, via its impacts on the freshwater balance, influences the quantity of salt transferred to the bottom ocean by the 'brines' parameterization, hence the observed variations in the streamfunction (Fig. 6.7f).

The changes in the Southern Ocean overturning intensity are summarized in Fig. 6.8c. This overturning is decreased by about half when a 50% reduction of wind stress is applied. This decrease is relatively smaller in 'P4-I brines', but I point out that this parameterization induces a more seasonal overturning (not well represented by the annual mean).

Despite this impact on the Southern Ocean convection, none of these modified wind stress (and sea ice−ocean stress) simulations entails a water mass distribution with an improved agreement with δ^{13}C data (Fig. 6.8d). However, some of these sensitivity tests do simulate a lower CO_2 concentration (Fig. 6.8e), resulting from a larger ocean sequestration of carbon (Fig. 6.8f). In particular, a clear trend is observed when the wind stress intensity is varied: when the Southern Ocean westerly winds are reduced, more carbon is stored into the ocean as the reduced convection in the Southern Ocean allows for less CO_2 outgassing. This small improvement of the simulated pCO_2 drawdown therefore co-occurs with a sea-ice cover in better agreement with marine core data (see Sect. 6.1.2), but is not associated with an improved water mass distribution with respect to δ^{13}C data (Fig. 6.8d). When the 'brines' parameterization is also activated, a relatively low CO_2 concentration is simulated (244 ppm) due to the cumulative effect of 'brines ($frac = 0.8$)' (-49 ppm) and 'minus50' wind stress (-19 ppm). Therefore, physical changes in deep ocean stratification and circulation alone can potentially explain part of the pCO_2 drawdown at the LGM, as simulated by the iLOVECLIM model. If complemented by iron fertilization and carbonate compensation, we may actually be able to simulate a CO_2 concentration at the LGM much closer to 190 ppm.

6.1.5 Relationship between sea-ice seasonality and Southern Ocean convection

In contrast to simulations with different boundary conditions (see article 2), I observed in Fig. 6.3 that the sea-ice seasonal amplitude is largely modified by sensitivity tests on wind stress and sea ice−ocean stress. Considering how these simulations also impact the Southern Ocean overturning (Fig. 6.8c), I now look into how these two variables might correlate.

Figure 6.9 shows the relationship between the Southern Ocean overturning and sea-ice seasonality, which can be considered significant ($R = 0.83$ with a p-value < 0.01) for both 'P4-I' and 'P4-G' sensitivity tests. I observe that the sea-ice seasonal amplitude is reduced when the overturning rate is high. This relationship suggests that convection processes are a dominant control on sea-ice seasonality in the iLOVECLIM model, while advection processes may also play a role through sea-ice export towards lower latitudes (see 'a20S' and 'shiftS' simulations). Interestingly, the sea-ice seasonal amplitude which is inferred from our winter and summer

sea-ice extent estimates based on sea-ice proxy data in article 2 ($\sim 22.7 \times 10^6$ km^2) provides a constraint towards a very low Southern Ocean overturning.

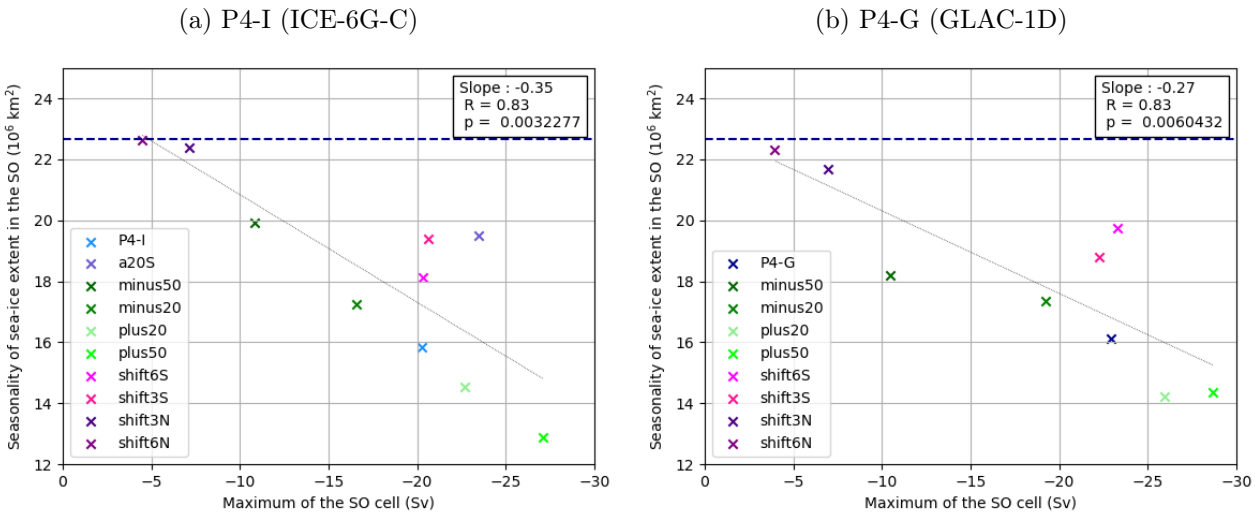

Figure 6.9: Relationship between the Southern Ocean overturning cell maximum and the sea-ice extent seasonal amplitude, simulated at the LGM by (a) 'P4-I' and (b) 'P4-G' sensitivity tests on wind stress and sea ice−ocean stress. The blue dashed line indicates the seasonal amplitude inferred in Lhardy et al. [2021b] from marine core data.

Considering this result, I underline that the convection process at the origin of AABW (i.e. open ocean convection, instead of dense shelf water overflows) may be key to both realistic bottom water densities [Heuzé et al., 2013] and reduced sea-ice biases. Indeed, even under present-day conditions (and the latest CMIP phase), a large majority of the CMIP6 models still form AABW "via open-ocean deep convection too deeply, too often, and/or over too large an area" [Heuzé, 2021]. Previously with CMIP5 models, Behrens et al. [2016] pointed out that biases in sea-ice variability may be linked to open ocean convection. However, Heuzé et al. [2013] conclude that "models with extensive deep convection are those with strong seasonality in sea ice", which is not what I observe in iLOVECLIM sensitivity tests with modified wind stress at the LGM.

In any case, it is likely that models which simulate an intense open ocean convection in the Southern Ocean do not represent the different ice−ocean feedbacks accurately. These positive or negative feedbacks are especially active in the Southern Ocean, and involve opposite effects on the mixed layer depth and heat transfer from the subsurface to the surface [Goosse et al., 2018, Goosse and Zunz, 2014], hence the importance of ocean heat storage and stratification. As a result, the simulated feedbacks may also be modulated under different forcings and boundary conditions (e.g. at the LGM), with possible consequences for the sea-ice biases. In addition, I note that a good representation of these feedbacks − such as the brine rejection effect on the MLD − can be especially tricky to achieve [Barthélemy et al., 2015].

6.2 Which processes reduce the quantified biases?

I now summarize and compare the effects of each type of modelling choices on the quantifications related to surface conditions, water mass distribution, and carbon content in Fig. 6.10.

I observe that the simulated global mean SAT anomaly (LGM − PI) of most simulations (v2) is well within the range estimated by Annan and Hargreaves [2013] (4 ± 0.8°C), though in its upper part. Considering the global warm bias at the PI, it is likely that my LGM simulations are a bit too warm. The simulation run with the ICE-6G-C boundary conditions ('P4-I') is colder than 'P4-G' by ~ 0.34°C. Alternate vertical mixing parameterizations to the Bryan and Lewis diffusivity profile entail a warmer climate, whereas simulations with a large *frac* in the 'brines' parameterization or reduced wind stress are closer to the center of the range.

On account of the largest SST bias (in the Southern Ocean in summer) identified in chapter 4, the RMSE with respect to summer MARGO data tends to be lower in simulations associated with a cold Southern Ocean. Warmer SSTs in the Nordic seas also improve the model-data agreement ('P4-I PIbathy') as explained in chapter 4. Still, these variations remain limited: for example, the latitudinal trend of the warm bias in the Southern Ocean (described in Lhardy et al. [2021b]) is a systematic feature of all of my simulations.

In terms of sea ice, I obtained various winter extents while the summer extents seem to be relatively overestimated in most simulations, with the exception of very warm simulations or the experiment with a non-zero turning angle in sea ice−ocean stress ('a20S'). However, our summer estimate of $\sim 10.2 \times 10^6$ km^2 is not well-constrained [Lhardy et al., 2021b]. Overall, these quantified extents tend to result from partly compensating regional biases, with an underestimated extent in the Atlantic and Indian sectors and an overestimated extent in the Pacific sector. Nonetheless, I still simulate various seasonal amplitudes with the 'brines' parameterization or modified wind stress, in contrast to my standard LGM simulations ('P4-I' and 'P4-G') which show a seasonality underestimated by $\sim 6.7 \times 10^6$ km^2 − if I am to believe our estimates despite their uncertainties.

As for the agreement with δ^{13}C data, only the 'brines' experiments show a significant improvement, associated with a shallower AMOC and enhanced stratification with respect to 'P4-I'. These simulations also show a lower atmospheric CO_2 concentration (~ -60 ppm at most, which is similar to the -52 ppm drop simulated in CLIMBER-2 by Bouttes et al. [2010]). Yet, this concentration (>244 ppm) remains very far from the 190 ppm value inferred from ice core data [Bereiter et al., 2015].

This drop is associated with enhanced ocean sequestration, which is also the case of simulations with a reduced wind stress, though to a lesser degree. Finally, I underline that the largest ocean sequestration by far is simulated by the 'P4-I PIbathy' simulation, in which the ocean boundary conditions of the LGM were not enforced. The impact of this modelling choice on the CO_2 concentration is limited because of an increased carbon storage in the terrestrial biosphere (linked with the unchanged land-sea mask). I suggest from this result that the ocean volume implemented in models may play a larger role on ocean sequestration than substantial circulation changes (such as those simulated between 'P4-I' and 'P4-I brines').

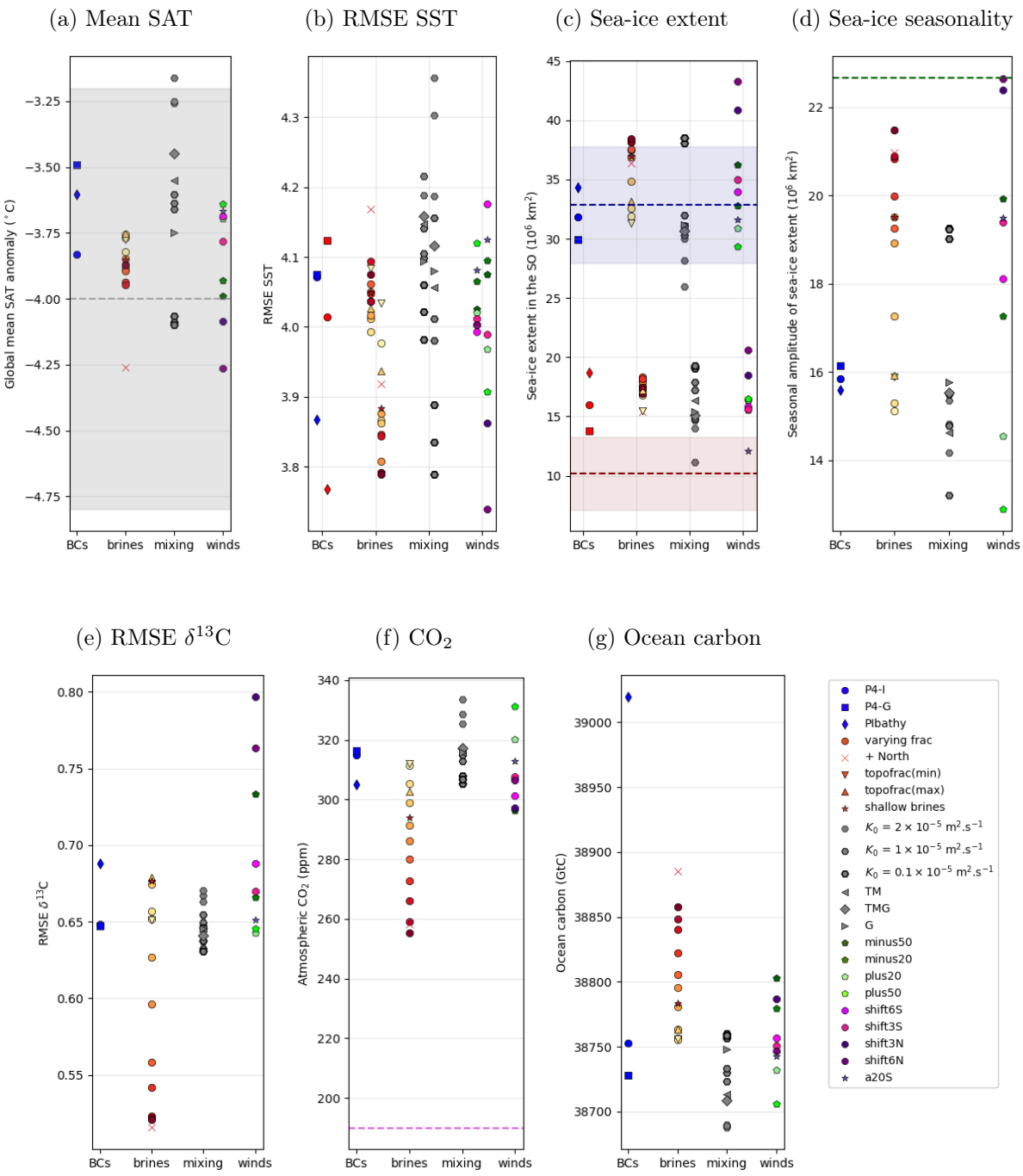

Figure 6.10: Summary of the effects of different types of modelling choices on the (a) global mean SAT anomaly (LGM − PI), (b) RMSE computed with respect to SST data [MARGO Project Members, 2009], sea-ice (c) extent and (d) seasonal amplitude, (e) RMSE computed with respect to δ^{13}C data [Peterson et al., 2014], (f) atmospheric CO_2 concentration and (g) ocean carbon content. The x-axis separates modelling choices related to boundary conditions (BCs), parameterized sinking of brines (brines), alternative parameterizations of the vertical diffusivity (mixing) and sensitivity tests with a modified wind tension in the Southern Hemisphere (winds). Both the austral winter (left) and summer (right) RMSEs and sea-ice extents are indicated in panels (b) and (c). The grey bar in panel (a) displays the mean SAT anomaly estimated by Annan and Hargreaves [2013]. The dashed lines in panels (c) and (d) shows the summer (red) and winter (blue) sea-ice extent estimated in Lhardy et al. [2021b].

6.3 What are the main drivers of changes in sea ice, water mass distribution and CO_2 concentration?

My multiple simulations may be especially useful to seek and highlight potential relationships between the variables quantified in this study, in order to better understand the model representation of key processes.

6.3.1 Ocean sequestration and atmospheric CO_2 concentration

Figure 6.11 clearly shows that in these simulations the CO_2 concentration is tightly linked to changes in the carbon content of the ocean, rather than of the terrestrial biosphere. According to the slope here, a pCO_2 drawdown of 90 ppm could be achieved if ocean sequestration were to increase by $\sim$ 250 GtC, relative to the standard LGM runs. As observed in article 1, simulations with no change of ocean volume compared to the PI ('P4-I PIbathy' and 'P4-I PIbathy brines') display a large ocean carbon content (anomaly >250 GtC).

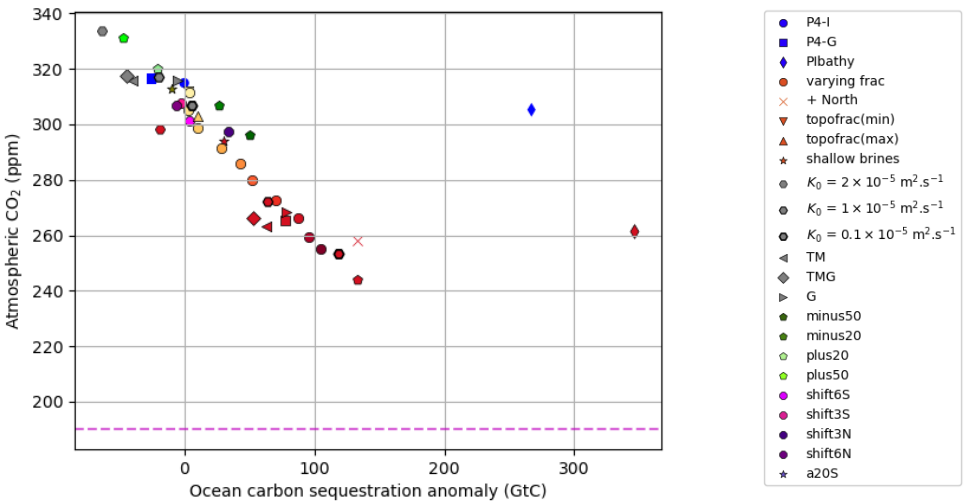

Figure 6.11: Relationship between the ocean sequestration anomaly (with respect to 'P4-I') and atmospheric CO_2 concentration, as simulated by my various simulations. The magenta dashed line indicates the CO_2 concentration at the LGM [Bereiter et al., 2015].

6.3.2 $\delta^{13}C$ model-data agreement and AMOC strength versus depth

My simulations also allow me to explore to some degree which circulation changes are associated with an improved agreement with paleotracer data. In that respect, Figure 6.12 shows the relationship between both the Atlantic overturning cells strength and depth and the quantified agreement with $\delta^{13}C$ data in the Atlantic. I observe that simulations with a large AABW in the Atlantic (obtained with the 'P4-I' parameterization) are associated with a lower RMSE (Fig. 6.12a). An improved agreement also seems to go hand in hand with an enhanced bottom cell in the Atlantic – a cell which is almost nonexistent in 'P4-I' (Fig. 6.12c). I point out again (see chapter 4 and Kageyama et al. [2021]) that this bottom cell is quite

intense in comparison to other PMIP3-4 models, even in PI runs. All the 'brines' simulations tested here (some in combination with other modelling choices) seem to show an enhanced stratification associated with a reinvigorated abyssal overturning. As a result, the iLOVECLIM model struggles to achieve both a voluminous and sluggish AABW at the LGM.

In contrast, Fig. 6.12b shows no relationship between the NADW cell strength and the agreement with δ^{13}C data in the Atlantic. This result is rather consistent with a more systematic study with the UVic model, in which Muglia and Schmittner [2021] underline that carbon isotopes alone are inadequate to constrain the AMOC transport well – whereas the model-data agreement in terms of both δ^{13}C and radiocarbon depends strongly on the AMOC depth.

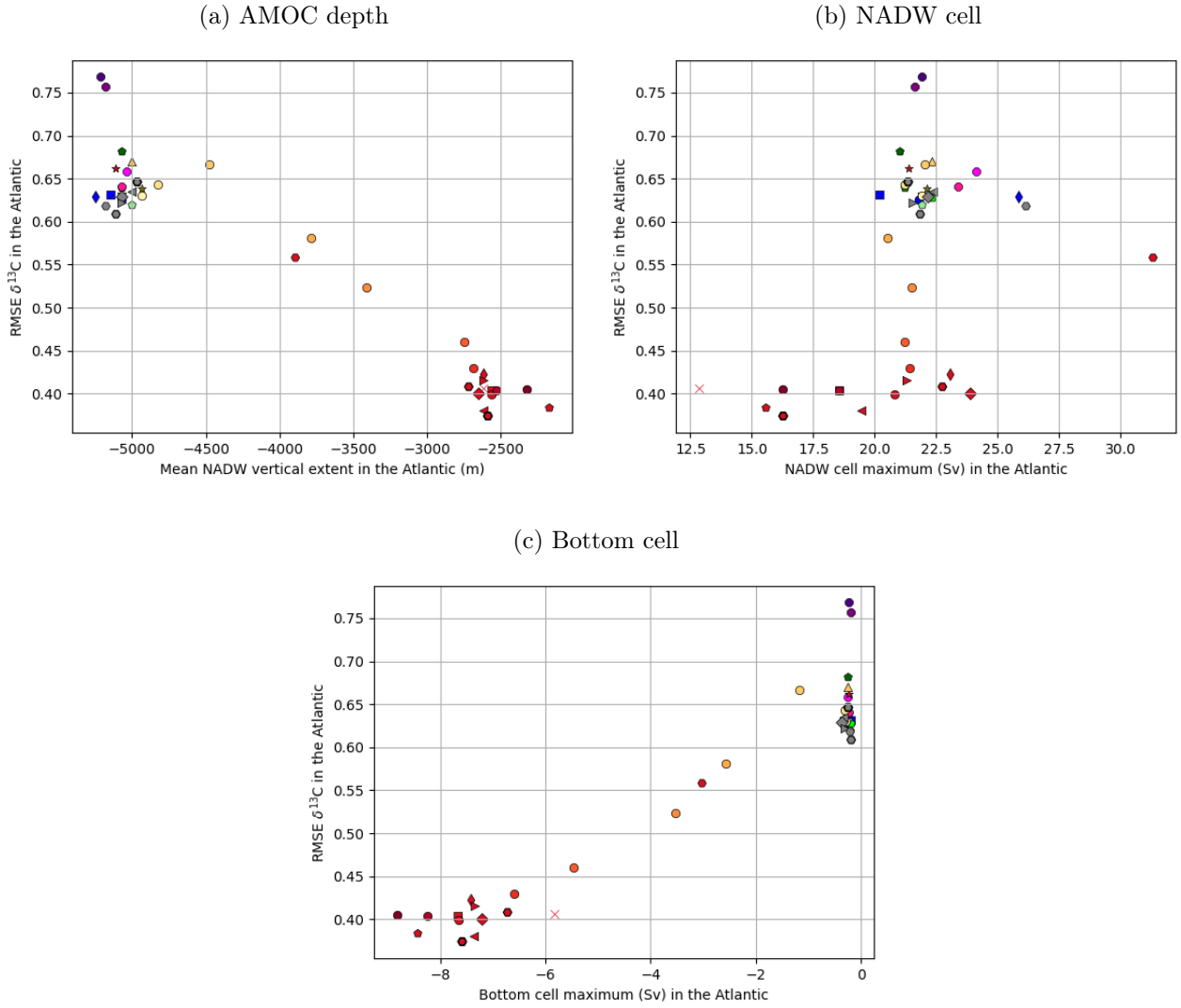

Figure 6.12: Relationship between the model-data agreement (RMSE) with respect to δ^{13}C data in the Atlantic [Peterson et al., 2014] and the (a) AMOC depth, or maximum overturning in the (b) NADW cell and (c) bottom cell in the Atlantic. The AMOC depth is approached here as the mean NADW vertical extent North of 32°S, with the vertical depth being detected at the sign change of the Atlantic streamfunction (as in Kageyama et al. [2021]). The marker colors and styles are the same as in Fig. 6.11.

6.3.3 Southern Ocean SST and sea-ice extent

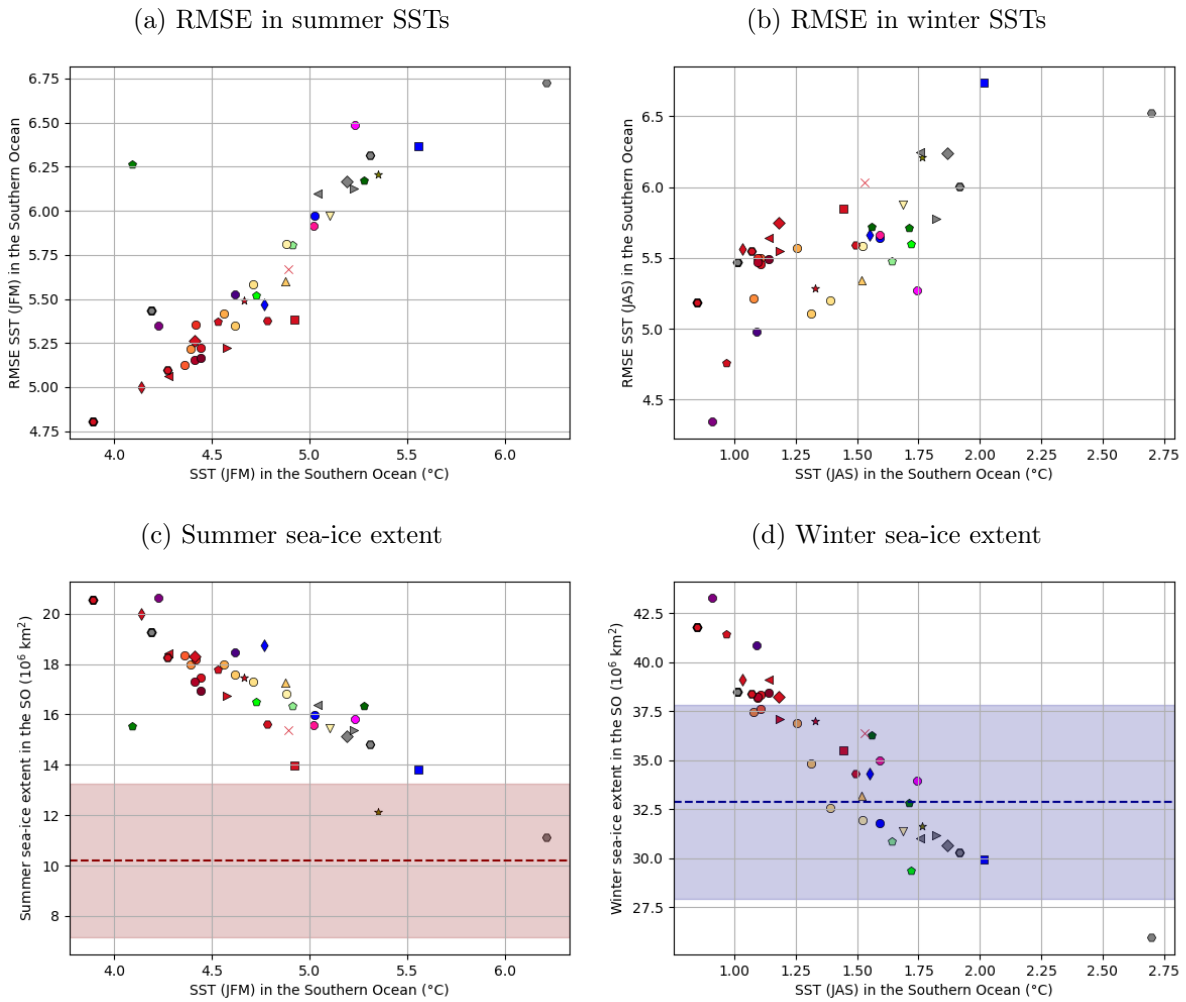

Figure 6.13: Relationship between the mean SST in the Southern Ocean (up to 36°S) and the (a) RMSE computed with respect to MARGO Project Members [2009] data, and (b) sea-ice extent in the Southern Ocean. The dashed lines in panels (c) and (d) shows the summer (red) and winter (blue) sea-ice extent estimated in Lhardy et al. [2021b]. The marker colors and styles are the same as in Fig. 6.11.

Figures 6.13a and b show that the agreement with SST data tends to improve when a cold Southern Ocean is simulated. This is especially the case in the summer season, when the warm bias in the Southern Ocean is clear (thanks to the availability of proxy data, see article 2). Conversely, both the summer and winter sea-ice extent increase with lower SSTs in the Southern Ocean, suggesting a dominant thermodynamic control. As a result, a colder Southern Ocean (than in my standard LGM runs) tends to be associated with an larger overestimation of the summer sea-ice extent with respect to our estimate. In winter, simulations with a colder Southern Ocean than 'P4-I' and 'P4-G' first show an extent closer to our estimate, then an overestimated one. Consequently, an improved agreement with SST data (i.e. colder Southern Ocean) does not necessarily go along with a sea-ice extents in closer match with the sea-ice proxy data reconstruction. However, I underlined in Lhardy et al. [2021b] that this apparent inconsistency may result from a compensation of regional biases: I have identified both a latitudinal trend of the SST bias, and significant interbasin contrasts in the sea-ice cover.

These characteristics are not well accounted for in the quantifications used here. In addition, I note that despite its warm bias, the PI simulation shows sea-ice extents in fairly good agreement with modern observations [Lhardy et al., 2021b]. This suggests that the sea-ice model may have been tuned accordingly. Tweaking tuning parameters (e.g. ice albedo) to reduce modern biases is a common practise of modellers. Such modelling choices, which are rarely well-documented, have consequences in simulations with a different background climate such as the LGM.

6.3.4 Sea-ice seasonality and Southern Ocean convection, $\delta^{13}C$ model-data agreement and CO_2 concentration

I now examine the relationships between the sea-ice seasonality and quantifications which relates to the overturning circulation and carbon. I have pointed out and discussed in Sect. 6.1.5 a relationship between the strength of the Southern Ocean overturning and the sea-ice seasonal amplitude in sensitivity tests with a modified wind stress. As shown in chapter 4 and Sect. 6.2, other simulations (those using the parameterization of the sinking of brines) also show various sea-ice seasonal amplitudes. Hence, I propose to revisit this relationship with a larger set of simulations in Fig. 6.14a.

I observe that the simulations with a large *frac* (orange to red colors) show a reduced Southern cell and enhanced sea-ice seasonality, and are therefore broadly aligned with the other sensitivity tests. However, simulations with a small *frac* (yellow to orange colors) rather show a reduced Southern Ocean convection (also see Sect. 4.3) which is not (yet) associated with a larger sea-ice seasonality. This could be related to the experimental design of these simulations, which allows for a direct transfer of salt from the surface to the bottom ocean without advection being explicitely computed. I can expect this modelling choice to seasonally impact the overturning strength, which reflects the integrated transport of water masses. I also acknowledge that although the maximum of each overturning cell and the streamfunction (as a function of depth) are practical metrics and representations, a more in-depth analysis of convection processes in the Southern Ocean especially would require a streamfunction plotted as a function of density. Indeed, the strong and deep overturning cell observed (also called Deacon cell) is essentially the result of an artifact of the projection in the latitude-depth space [Döös and Webb, 1994]. This remains − for now − perspectives of this work.

In addition, I observe that one 'brines' experiment ('shallow brines', red star) shows a significant increase of sea-ice seasonality without reducing the Southern Ocean cell. In this simulation, the transfer of salt was done from the surface (when sea-ice formation occurs) to a shallow grid cell of 200 m at most. Although this simulation does not increase stratification and improve the Atlantic water mass distribution with respect to paleotracer data (see Sect. 4.3), it does reduce to some degree the sea-ice biases, as it isolates the surface from the subsurface.

Figure 6.14b shows that modelling choices which yield a stronger seasonality in the Southern Ocean sea ice also tend to produce a lower CO_2 concentration than standard LGM runs. As a stronger sea-ice seasonality seems to often be associated with an intense convection in the Southern Ocean, I suggest that the consequently well-mixed water column favors CO_2 outgassing while the lower winter sea-ice extent also reduces the cap effect of the sea-ice cover. Although both of these effects may come into play, elucidating their relative contribution would require further investigation.

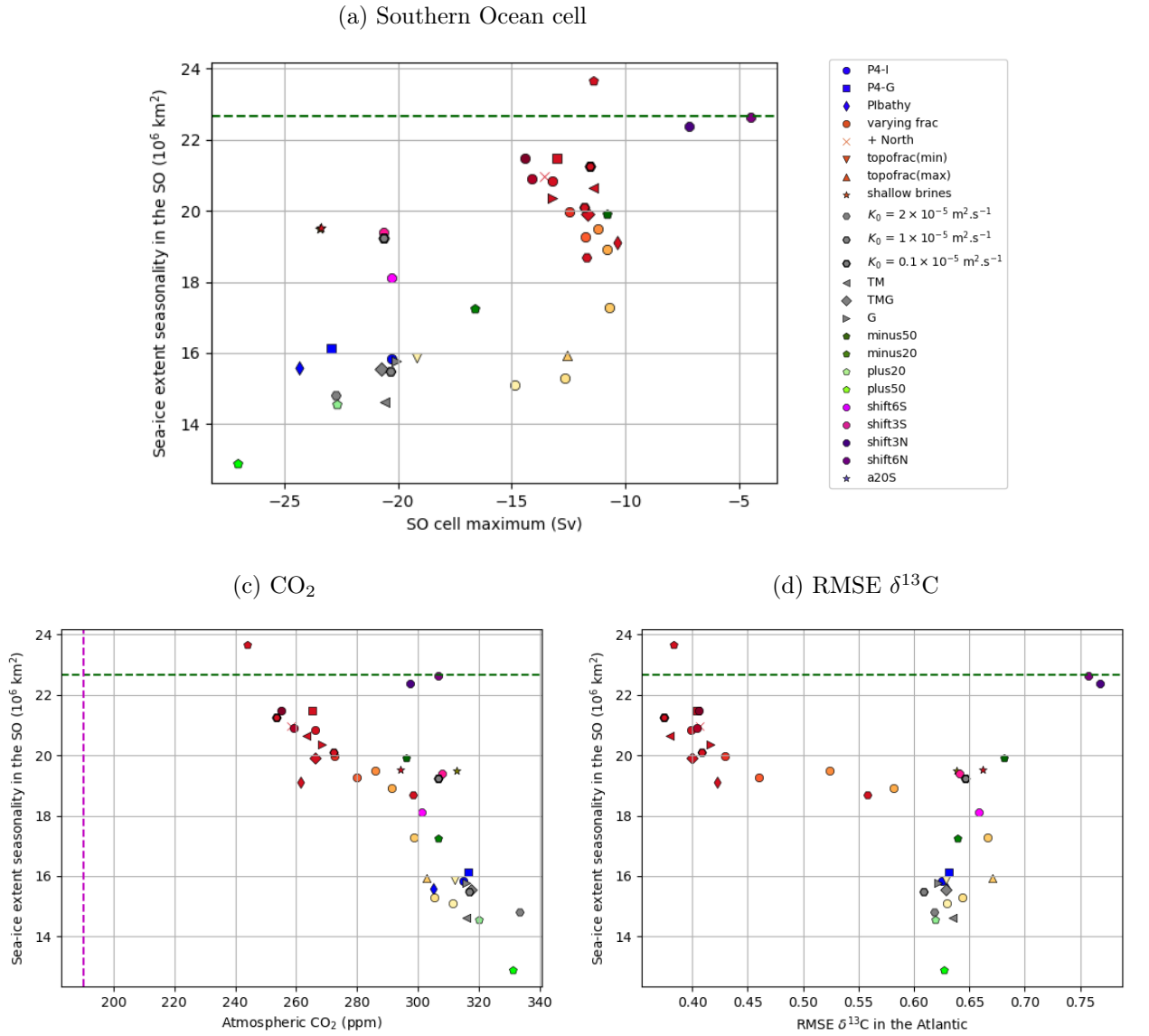

Figure 6.14: Relationship between the sea-ice extent seasonal amplitude and the (a) Southern Ocean overturning cell maximum, (b) atmospheric CO_2 concentration, and (c) model-data agreement (RMSE) with respect to δ^{13}C data in the Atlantic. The green dashed line indicates the seasonal amplitude inferred in Lhardy et al. [2021b] from marine core data.

Finally, Figure 6.14c shows no relationship between the Southern Ocean sea-ice seasonality and the model-data agreement in terms of δ^{13}C in the Atlantic. This rather suggests that although sea-ice and water mass distribution biases may potentially have similar causes (e.g. open ocean convection in the Southern Ocean, instead of overflows of dense shelf waters), a reduction of sea-ice biases may occur when the surface gets more isolated from the subsurface (e.g. through reduced wind stress, or 'shallow brines') whereas a NADW shoaling seems to be simulated only when the AABW density is increased. As a result, the 'brines' simulations which both increase the deep ocean and the subsurface stratification achieve a reduction of both biases. On the other hand, 'minus' simulations show a sea-ice cover in a closer match with sea-ice proxy data, yet no improvement of the AMOC and related water mass distribution.

6.4 Is the simulated AMOC too deep due to an underestimated sea-ice formation?

(a) Sea-ice extent in PMIP2 models

(b) Sea-ice seasonality in PMIP2 models

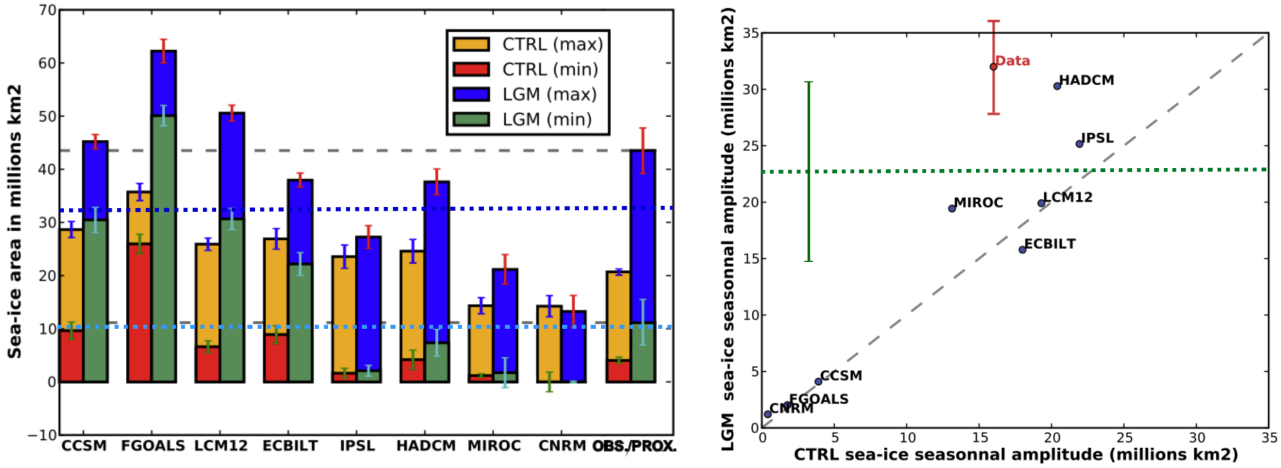

(c) Sea-ice extent in PMIP3 models

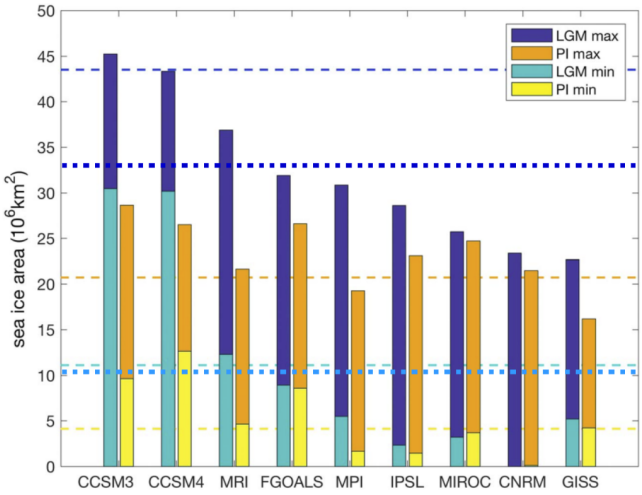

Figure 6.15: Minimal (summer) and maximal (winter) Southern Ocean sea-ice extent in PI and LGM simulations run with (a, b) PMIP2 and (c) PMIP3 models. Panel (b) shows the seasonal range in sea-ice extent in a LGM versus PI plot. Panels (a) and (b) are adapted from Roche et al. [2012] whereas panel (c) is from Marzocchi and Jansen [2017]. The grey (panel a) and blue (panel c) dashed lines indicate the extent reconstructed from sea-ice proxies in Roche et al. [2012], who estimated a sea-ice cover of $\sim 11.1 \pm 4 \times 10^6$ km^2 in summer and $\sim 43.5 \pm 4 \times 10^6$ km^2 in winter, hence a seasonal amplitude of $\sim 32.4 \times 10^6$ km^2 (panel b). In contrast, the thick dotted lines indicate our sea-ice extent estimates in winter (dark blue), summer (light blue) and seasonal amplitude (green) [Lhardy et al., 2021b].

A physical link between Southern Ocean sea ice and the AMOC has been proposed and discussed in several studies focussed on the LGM [Shin et al., 2003, Ferrari et al., 2014, Marzocchi and Jansen, 2017]. As sea-ice formation occurs, brines are rejected into the surrounding waters and may lead to deep water formation. Therefore, a more extensive (and seasonal) sea-ice cover in the glacial Southern Ocean is consistent with an increased AABW density, a consequent

NADW shoaling, and a higher carbon sequestration in the deep ocean. However, the processes which account for this link can be tricky to represent in state-of-the-art models, in particular as some of them occur on a subgrid level [Barthélemy et al., 2015]. Relying on correlations and principal component analysis, Marzocchi and Jansen [2017] demonstrate that the link between Southern Ocean sea ice and the AMOC depth is statistically significant in PMIP3 models. On this basis, they suggest that the weak stratification and deep AMOC simulated by a majority of PMIP3 models [Muglia and Schmittner, 2015] could be attributed to insufficient sea-ice formation. However, the authors rely on the sea-ice extent estimation inferred from sea-ice proxies in Roche et al. [2012], which is very likely to have been largely overestimated [Lhardy et al., 2021b].

Considering our new winter sea-ice extent estimate of $\sim 32.9 \times 10^6$ km^2 (and a seasonal amplitude of $\sim 22.7 \times 10^6$ km^2), some of the interpretations in Roche et al. [2012] and Marzocchi and Jansen [2017] need to be revisited ("most PMIP3 LGM simulations exhibit a considerably smaller maximum sea ice cover than estimated from the proxy data, even when their PI sea-ice extent is relatively close to observations"). Indeed, these authors performed a model-data comparison of the summer and winter sea-ice extents simulated by the PMIP2 and PMIP3 ensemble, respectively (see Fig. 6.15). They inferred from this comparison that the simulated winter sea-ice extent is underestimated in most PMIP models, with the exception of FGOALS (PMIP2), LCM12, and CCSM models. Roche et al. [2012] also observe that the sea-ice seasonality is underestimated in all PMIP2 models, except in HADCM. However, if I am to believe our new estimates despite their uncertainties, it is likely that FGOALS (PMIP2), LCM12 and the CCSM models overestimate the winter sea-ice extent in addition to the summer one. While the MIROC, CNRM, and GISS models still simulate an underestimated winter sea-ice extent, the other models (FGOALS (PMIP3), MPI, MRI, IPSL, ECBILT, and HADCM) show a relatively closer match to this new estimate. Furthermore, the sea-ice seasonal amplitude of PMIP3 models now appears to be either underestimated (CCSM, GISS), in close match with our estimate (FGOALS, MIROC, CNRM) or even slightly overestimated (MPI, IPSL), contrasting with the PMIP2 results from Roche et al. [2012].

As a result, the sea-ice extent simulated by the iLOVECLIM model under the PMIP4 boundary conditions falls well within this PMIP2-3 ensemble. Yet, it is still overestimated in summer, and slightly underestimated in winter, hence a quite significant underestimation of the seasonal amplitude. Potentially, the sea-ice formation may therefore be insufficient, hence the deep AMOC simulated in standard runs (according to the Marzocchi and Jansen [2017] statistical link).

Yet, I showed in Fig. 6.14c that this seasonal amplitude − which is underestimated in the large majority of my simulations − is not correlated with the δ^{13}C distribution in the Atlantic. As all sectors of the Southern Ocean are encompassed in this quantified seasonality of the sea-ice extent, I show in Fig. 6.16 the same plot, but for the sea-ice extent in the Atlantic sector. In this sector, the sea-ice extent seasonal amplitude seems to be less pronounced than in others. As a result, about half of my simulations now overestimate the seasonality, while standard runs underestimate it. Moreover, no correlation is still observed with the δ^{13}C model-data agreement in the Atlantic. I suggest with these results that it is difficult to attribute the deep and intense AMOC simulated at the LGM in the iLOVECLIM model to Southern Ocean sea-ice biases. My experiments rather indicate that the reduction of sea-ice biases will not be associated with a NADW shoaling as long as the processes which connect sea ice, deep water formation, and the AMOC (e.g. sinking of brines) are not accurately represented.

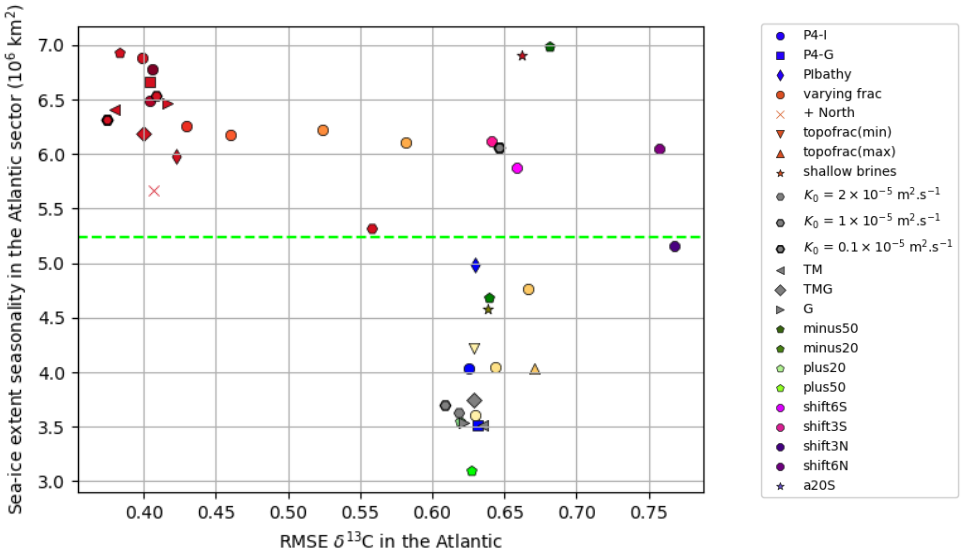

Figure 6.16: Relationship between the sea-ice extent seasonal amplitude in the Atlantic sector and the model-data agreement (RMSE) with respect to δ^{13}C data in the Atlantic. The light green dashed line indicates the seasonal amplitude in the Atlantic sector inferred from marine core data.

6.5 Résumé du chapitre en français

Dans ce dernier chapitre de thèse, j'examine tout d'abord l'impact des vents d'Ouest de l'Hémisphère Sud sur les biais quantifiés depuis le chapitre 4. En effet, ces vents représentent l'un des moteurs de l'AMOC, du fait de leur impact sur l'upwelling austral. Des tests de sensibilité sur les vents sont ainsi un moyen d'évaluer l'influence de la convection dans l'océan austral (dont l'importance est déjà suggérée par les résultats du chapitre 4) sur les variables climatiques examinées dans cette thèse. De plus, certaines études basées sur des données paléoclimatiques suggèrent une variation significative de l'amplitude de ces vents mais aussi de leur latitude au DMG, qui n'est pas reproduite par les modèles PMIP [Gray et al., in review, 2021]. Je note en particulier que le modèle iLOVECLIM, dont la composante atmosphérique est de résolution grossière, ne simule ni les variations suggérées par ces proxies au DMG, ni une amplitude réaliste de ces vents au PI.

Ce chapitre est également l'occasion de synthétiser et de comparer les différents biais (en terme de température, glace de mer australe, distribution des masses d'eau, et concentration de CO_2) obtenus à l'aide de différents choix de modélisation. Introduits progressivement au cours de cette thèse, ces différents choix sont liés aux conditions aux limites (chapitre 3 et 4), aux choix de paramétrisations associés à la plongée des saumures (chapitre 4) ou à la diffusivité d'arrière-plan (chapitre 5), et enfin à la tension de vent sur l'océan austral (chapitre 6). Enfin, je propose d'explorer à l'aide de ces différentes simulations les liens potentiels simulés entre conditions de surface dans l'océan austral, circulation océanique profonde, distribution des masses d'eau, et contenu des réservoirs de carbone.

Je montre dans ce chapitre qu'une tension de vent réduite sur l'océan austral permet de simuler une glace de mer en meilleur accord avec les données paléoclimatiques, et ce malgré le biais initial au PI. Par ailleurs, les tests de sensibilité liés aux vents n'ont que peu d'impact sur l'AMOC, bien qu'ils affectent significativement la convection australe. Ils nous permettent ainsi d'établir une première relation, entre l'intensité de la convection australe et la saisonnalité de la glace de mer. Plus cette convection est intense, et moins l'amplitude saisonnière de la glace de mer est marquée, ce qui est vraisemblablement lié à un apport hivernal de chaleur de la subsurface vers la surface du fait d'un océan peu stratifié. La saisonnalité estimée à partir de données paléoclimatiques semble alors contraindre une faible convection d'océan ouvert. Il est également constaté que certains paramètres du modèle (liés au couplage dynamique entre glace de mer et océan), peuvent influencer l'export et ainsi la saisonnalité de la glace de mer, en réduisant cette fois l'étendue estivale (surestimée).

Concernant la distribution des masses d'eau, un autre résultat émerge de cet ensemble de simulations, déjà souligné par Muglia and Schmittner [2021] : un meilleur accord modèle-données de $\delta^{13}C$ est obtenu quand une NADW peu profonde est simulée, mais ces données paléoclimatiques ne contraignent pas vraiment son intensité. Quant au contenu en carbone de l'océan, il est significativement augmenté dans certaines de mes simulations qui influencent la circulation profonde et la stratification de l'océan (à l'aide de la paramétrisation de la plongée des saumures), quoique moins largement que les tests conservant le volume pré-industriel de l'océan.

Pour finir, je souligne également que la simulation d'une AMOC très profonde au DMG avec le modèle iLOVECLIM ne semble pas liée aux biais de glace de mer australe observés, comme le suggère [Marzocchi and Jansen, 2017]. Ainsi, une amélioration significative des biais de glace de mer (telle que celle simulée avec une réduction de la tension de vent) n'induit pas nécessairement

une AABW plus volumineuse et stratifiée. Il est possible que le processus de formation d'eau profonde – par un débordement d'eau dense du plateau continental Antarctique et non pas par une convection d'océan ouvert (Heuzé et al. [2013], Heuzé [2021], Heywood et al. [2014], also see Sect. 1.3) – soit clef pour représenter correctement le rôle de la glace de mer sur la circulation océanique profonde et le contenu en carbone de l'océan.

Conclusions and perspectives

Context and research objectives

Paleoclimate modelling is dedicated to improving our understanding of complex processes which often depend on the background climate. In this respect, the Last Glacial Maximum (LGM) has been a period of interest for decades. The LGM allows modellers to investigate the model response to forcings [Eyring et al., 2016, Kageyama et al., 2017] corresponding to a very different climate from the present-day one and characterized by cold temperatures, low CO_2 concentration, large ice sheets in the Northern Hemisphere and an associated low sea level. It also enables them to perform model evaluations using numerous proxy records available for this time window. Such evaluations are facilitated by the common experimental design defined by the Paleoclimate Modelling Intercomparison Project (PMIP, Kageyama et al. [2017]), now in its phase 4.

The Southern Ocean is an important player of our climate system. It represents a carbon sink as well as one of the very few regions where deep water formation is triggered, as a result of cold temperatures and brine release consequent to sea-ice formation. The Southern Ocean sea-ice cover is able to influence both the large-scale overturning circulation and the carbon sequestration in the ocean, through its effect on water mass density and isolation. Several studies underline that this influence is crucial to explain a shoaling of the AMOC [Shin et al., 2003, Klockmann et al., 2016, Marzocchi and Jansen, 2017] and a lower CO_2 concentration [Ferrari et al., 2014, Stein et al., 2020] at the LGM, when the Southern Ocean sea ice was more extensive and more seasonal [Gersonde et al., 2005, Roche et al., 2012]. Considering that a majority of PMIP3 models simulate a deep and intense AMOC at the LGM [Muglia and Schmittner, 2015], in contrast with reconstructions inferred from paleotracer data, Marzocchi and Jansen [2017] suggest largely attributing this discrepancy and the large intermodel spread observed in the PMIP3 ensemble to "differing (and likely insufficient) Antarctic sea-ice formation". Indeed, compared to the reconstructed sea-ice extent estimated in Roche et al. [2012], most PMIP3 models largely underestimate the winter sea-ice extent [Marzocchi and Jansen, 2017]. To explain the remaining part of the intermodel spread, [Marzocchi and Jansen, 2017] briefly discuss other forcing mechanisms, which also represent drivers of the AMOC:

- the strength of the North Atlantic westerlies, which is linked to the elevation of the Northern Hemisphere ice sheets [Muglia and Schmittner, 2015, Klockmann et al., 2016]. As a result, the uncertainties in ice sheet reconstructions may impact the simulated AMOC [Ullman et al., 2014]. Considering these uncertainties, Kageyama et al. [2017] have recommended several ice sheet reconstructions in the PMIP4 experimental design.

- the strength and position of the Southern Ocean westerly winds [Toggweiler et al., 2006, Gray et al., in review, 2021].
- tidal mixing [Schmittner et al., 2015], which is not well accounted for in models with a simple vertical diffusivity profile [De Boer and Hogg, 2014].

As for carbon, several studies show a far from negligible impact of the Southern Ocean sea ice on the simulated pCO_2 drawdown [Stephens and Keeling, 2000, Marzocchi and Jansen, 2019, Stein et al., 2020], which differs from the rather minor role reported in Khatiwala et al. [2019]. However, it is difficult to interpret such differences, since these studies were made using various models and forcings.

I have therefore focussed on the role of Southern Ocean sea ice on the deep ocean circulation and carbon cycle at the LGM. I have run and analyzed LGM simulations with the proxy-enabled and carbon-enabled Earth System Model iLOVECLIM in order to:

1. identify and quantify model biases in terms of SST, Southern Ocean sea ice, Atlantic water mass distribution and CO_2 concentration. To do so, I have performed model-data comparison using existing proxy records [MARGO Project Members, 2009, Gersonde et al., 2005, Peterson et al., 2014].
2. assess the impact of the elevation of the Northern Hemisphere ice sheets on the examined variables. To this end, I have generated and implemented in a semi-automated way the boundary conditions associated with both the GLAC-1D and ICE-6G-C ice sheet reconstructions. As a result, LGM simulations with the iLOVECLIM model now follow the PMIP4 experimental design, enabling comparison with the previous LGM (PMIP2) version [Lhardy et al., 2021b] and with other PMIP4 models [Kageyama et al., 2021].
3. compare the carbon outputs of the iLOVECLIM model with results from the ongoing PMIP-carbon project [Lhardy et al., 2021a], aiming at the first intercomparison of coupled climate−carbon models.
4. compare the effects of various drivers of the AMOC, which either relate to sea ice (e.g. parameterized sinking of brines) or to the above-mentioned mechanisms (e.g. modified wind stress in the Southern Ocean, alternative parameterizations of the vertical diffusivity, including one accounting for tidal mixing).
5. explore the relationships between the simulated Southern Ocean sea ice, AMOC, water mass distribution and CO_2 concentration, using these various simulations and sensitivity tests.

Main findings

For the Southern Ocean sea ice, I identify three biases relative to the proxy data compilation described in Lhardy et al. [2021b]. First, the simulated sea-ice distribution around the Antarctic continent is quite circular, which does not compare well with the more oval-shaped reconstruction. Secondly, the winter sea-ice extent simulated in standard LGM simulations appears to be

slightly underestimated (while the summer sea-ice extent is likely overestimated) with respect to the reconstructed sea-ice extent estimated in Lhardy et al. [2021b]. This estimate (32.9×10^6 km^2) differs significantly from the previous one of Roche et al. [2012] (43.5×10^6 km^2). Thirdly, the simulated sea-ice seasonal range is underestimated with respect to our estimate of 22.7×10^6 km^2. These three model-data discrepancies have been observed in a majority of PMIP models during PMIP2 and PMIP3 intercomparison studies [Roche et al., 2012, Goosse et al., 2013, Marzocchi and Jansen, 2017]. As in PMIP2 [Otto-Bliesner et al., 2007, Weber et al., 2007], the iLOVECLIM model also standardly simulates at the LGM a very deep and intense NADW overturning cell, hardly allowing for AABW penetration in the Atlantic basin. As a result, the simulated δ^{13}C distribution does not reproduce the vertical gradient observed in δ^{13}C data [Peterson et al., 2014]. Finally, the simulated CO_2 concentrations ($\sim$315 ppm) are much higher than the one inferred from ice core data (190 ppm, Bereiter et al. [2015]).

I only observe a minor effect of the choice of ice sheet reconstruction (GLAC-1D, ICE-6G-G, or PMIP2) on the variables examined in this study (e.g. difference of 1.4 ppm in CO_2 concentration). This effect appears secondary compared to the magnitude of the observed biases. Still, I underline the importance of modelling choices which relate to the implementation of the boundary conditions associated with these reconstructions. Indeed, both the ocean volume and the related adjustment of alkalinity are dominant controls on the carbon sequestration in the ocean at the LGM [Lhardy et al., 2021a]. The semi-automated generation method of ocean boundary conditions developed in this thesis yields a significant improvement of both the PI and LGM ocean volumes despite the relative coarse resolution of the iLOVECLIM model. However, a low LGM ocean volume, in close agreement with the one computed using GLAC-1D or ICE-6G-C ice sheet reconstruction, entails a reduced carbon storage capacity of the ocean due to a lower size of this carbon reservoir. This effect makes it more difficult for carbon-enabled models to simulate a large pCO_2 drawdown (of $80-100$ ppm). Therefore, I argue that a consistent implementation of a realistic LGM$-$PI ocean volume change and of the related ajustment of biogeochemical variables is needed in the future of the PMIP-carbon intercomparison project.

I show that a large parameterized sinking of brines allows for a reduction of biases in terms of SSTs (colder Southern Ocean), sea ice (increased seasonality), water mass distribution (shallower NADW, more voluminous AABW) and carbon content (lower atmospheric concentration, increased storage in the ocean). Still, the regional pattern of biases in surface conditions (latitudinal trend of the SST bias, circular-shaped sea-ice distribution) remains unchanged. A more oval distribution around the Antarctic continent is simulated with reduced wind stress in the Southern Ocean. Wind stress, convection in the Southern Ocean, and sea-ice seasonality seem broadly related in my simulations, with reduced wind stress leading to less convection and an enhanced sea-ice seasonality in the Southern Ocean (in addition to a slightly reduced CO_2 concentration). However, experiments with a modified wind stress do not lead to an improved agreement with δ^{13}C data. This agreement improves as the NADW shoals, but does not seem related to the upper cell strength. Such a water mass distribution occurs when a strong bottom cell is also simulated, which contrasts with the more sluggish abyssal overturning inferred from some paleotracer data [Howe et al., 2016]. Simulations with various parameterizations of the vertical diffusivity suggest that a strong abyssal cell is residual in the iLOVECLIM model, with possible implications for the residence time of carbon.

My simulations do not support the attribution of the deep and intense AMOC to an insufficient sea-ice cover in the Southern Ocean, especially considering our new winter sea-ice extent estimate. Instead, the model representation of convection processes (influenced by the parameterized sinking of brines, or modified wind stress) seems crucial to simulate both an enhanced sea-ice seasonality and a dense and voluminous AABW at the LGM.

Perspectives

In this thesis, I have investigated the model representation of three key variables of the climate system, namely the Southern Ocean sea ice, Atlantic deep ocean circulation, and CO_2 concentration at the LGM. I have characterized their model-data discrepancies and how they relate to each other in order to better understand the processes which may be at the origin of these discrepancies. To do so, I have run LGM simulations with diverse modelling choices (e.g. different boundary conditions, parameterized sinking of brines and vertical diffusivity, modified wind stress in the Southern Hemisphere). While this study may call for various perspectives, I have chosen to outline here a few of them:

▶ Extending the analysis of model-data discrepancies

In this thesis, I have focussed on the Southern Ocean sea-ice cover and on the AMOC (see chapter 1). Still, the Arctic sea ice does also impact buoyancy fluxes, and therefore deep water formation in the Nordic seas [Liu and Fedorov, 2019]. I also acknowledge that compared to the Atlantic, the Pacific Ocean stores a comparatively larger amount of carbon due to its size. As a result, widening the focus of this study to also evaluate the Pacific deep ocean circulation and the Arctic sea-ice model biases at the LGM may lead to new insights.

In addition, I point out that a multiproxy analysis would notably allow for more robust results. To do so, the iLOVECLIM model is suitable as it is a proxy-enabled model which allows for direct comparison with paleotracer data. In particular, during the last decade, the model has been developed to compute the $\delta^{18}O$, $\delta^{13}C$, $\Delta^{14}C$, and Pa/Th ratio. It is however in constant evolution and considering the current limitations of the model versions used in this thesis (see Sect. 2.1.1), I only performed model-data comparisons using $\delta^{13}C$. Solving these issues is ongoing work in our group. In the future, the use of different types of paleotracer data is likely to provide additional constraint on the simulated deep ocean circulation, especially as carbon isotopes do not constrain well the strength of the NADW overturning (see chapter 6 and Muglia and Schmittner [2021]).

Furthermore, using my simulations and in particular sensitivity tests with a modified wind stress, I have shown that a reduced convection in the Southern Ocean tends to be associated with an enhanced sea-ice seasonality, and therefore with a closer agreement with our data estimate. While this can be explained by the Southern Ocean upwelling bringing to the surface heat stored at depth, a demonstration would require quantifying the ocean heat storage (especially in the Southern Ocean subsurface), and ice−ocean heat fluxes. It would also be interesting to examine whether the sea-ice seasonality of PMIP4 models (Vadsaria et al., in prep.) relates to convection in the Southern Ocean. Since I simply used the maximal intensity of the Southern Ocean overturning (i.e. Deacon cell, Döös and Webb [1994]), a change of metrics (e.g. plotting the streamfunction in a latitude−density space) may be desirable for a more in-depth analysis.

▶ Exploring the dynamical code in order to reduce model biases

I have shown in chapter 5 that even with a very low vertical diffusivity, a strong residual abyssal overturning seems to be simulated by the iLOVECLIM model, possibly also hindering the effects of a tidal mixing parameterization. To identify the reasons behind such a residual overturning, I would need to dig into the ocean dynamics code. Considering that convection processes in the Southern Ocean also seem crucial for the model biases observed at the LGM, this investigation may also provide the opportunity to reassess existing modelling choices (e.g. convective adjustment and downsloping currents parameterization, Goosse et al. [2010]) and the potentiality for new developments (e.g. overflow parameterization, [Heuzé, 2021]).

In addition, I have observed in my PI simulation a slightly underestimated sea-ice extent (with respect to Parkinson and Cavalieri [2012]) despite a warm bias in the Southern Ocean [Lhardy et al., 2021b]. This simulation also displays a large underestimation of the Southern Hemisphere westerly winds, relative to the ERA-interim reanalysis (see chapter 6). While temperatures and winds are likely to remain biased considering the resolution of the atmosphere and ocean components, the effects of tuning parameters in the sea-ice module and atmosphere−ocean coupler on sea-ice biases and Southern Ocean convection could be explored in sensitivity studies.

▶ Studying the carbon cycle at the scale of glacial-interglacial variations

In this thesis, I have only considered the total carbon content of reservoirs. I have not examined the carbon distribution in the global ocean, and how changes in carbon sequestration relate to the water mass distribution in the Atlantic. Still, an analysis of the carbon distribution in the ocean and its drivers, potentially with an explicit consideration of biological effects (e.g. iron fertilization, via increased dust fluxes) would be of interest to us, especially in the framework of the PMIP-carbon project.

Instead, I have focussed on the effect of the ocean volume when it emerged as a dominant control on carbon sequestration. This choice appeared relevant to us considering the model developments made in the context of this thesis and the preliminary results of the PMIP-carbon project [Lhardy et al., 2021a]. Indeed, this study has raised the importance for coupled climate−carbon models of modelling choices which relate to the ocean volume. Since the PMIP project first enabled intercomparison studies concerning physical changes at the LGM (such as those of the AMOC), modelling groups are used to produce a land-sea mask which is consistent with a low sea level, and to adjust the bathymetry in critical passages and shallow areas [Kageyama et al., 2017], but do not always account for this low level in open and deep areas (see chapter 3). A revision of protocols (PMIP and PMIP-carbon) may raise awareness about the importance of a realistic ocean volume for models including the carbon cycle. In addition, it would be desirable for all carbon-enabled models to include an alkalinity adjustment made according to the actual change in volume between the PI and LGM simulations rather than a pre-determined and theoretical change.

Thanks to the semi-automated method developed in this thesis, I have generated the boundary conditions associated with both the GLAC-1D and ICE-6G-C ice sheet reconstructions at the LGM. Therefore, I was able to consider the impact of their uncertainties on the Southern Ocean sea ice, deep ocean circulation, and CO_2 concentration. I have shown that the differences induced by the choice of ice sheet reconstruction remain small for these variables in LGM simulations run with the iLOVECLIM model. However, this may not be true for other models or time periods. In particular during the last deglaciation, freshwater fluxes depend on the chosen ice sheet reconstruction [Quiquet et al., 2021]. Following this development, the

boundary conditions associated with each time step of the reconstructions (each 100 years for GLAC-1D, and each 500 years for ICE-6G-C) were generated for the whole deglaciation. As a result, transient simulations of the last deglaciation, run with the iLOVECLIM model, the carbon cycle and an interactive bathymetry (notably allowing for a change of ocean volume) now represent ongoing work in our group. In the future, intercomparison studies of such simulations (as part of the 'Last Deglaciation' working group in the PMIP4 project) may improve our understanding of the processes driving the carbon cycle variations at such time scales, as well as their model representation.

Indeed, climate models under LGM conditions struggle to simulate the low atmospheric CO_2 concentration inferred from ice core data ($\sim$190 ppm), and are far from being able to run with an interactive CO_2. For example, PMIP-carbon models with a freely-evolving CO_2 (in the carbon cycle but not in the radiative code) simulate a very high CO_2 concentration ($>$310 ppm), in particular when considering a realistic ocean volume at the LGM [Lhardy et al., 2021a], if they do not take into account additional mechanisms (e.g. sediments, iron fertilization, and possibly permafrost, see Sect. 1.2.4). This difficulty calls into question the model representation of climate−carbon feedbacks which are also likely to be crucial for the accuracy of future projections. For that reason, modelling studies focussed on past climates provide a valuable opportunity to test out and identify which processes may explain the carbon cycle variations observed in paleoclimatic records.

Appendix

This appendix contains supplementary figures of chapter 4, showing the $\delta^{13}C$ distribution in the Indian and Pacific basins, as well as the supplementary materials of articles 1 and 2. The interactive discussion during peer review of article 2 [Lhardy et al., 2021b] can be found at: https://cp.copernicus.org/articles/17/1139/2021/cp-17-1139-2021-discussion.html.

In addition, this appendix also contains three co-authored publications. The first is an intercomparison study in which the iLOVECLIM model was able to participate thanks to the developments described in chapter 3. The other two studies were conducted by other members of the small team working with the iLOVECLIM model, since I have been an active player of this community. In more details, these publications consist of:

- a PMIP4 model intercomparison study [Kageyama et al., 2021], in which the PMIP4 simulations at the LGM are evaluated and compared to the PMIP3 ensemble. As changes in the simulated AMOC are notably examined, some of the results of this study are of particular interest in the context of this thesis (see chapter 4). The variations of some atmospheric variables are also presented, so the interested reader will be able to see where the iLOVECLIM model simulations (v1, 'P4-G' and 'P4-I') stand in the PMIP4 ensemble. I have contributed to this study by running PI and LGM simulations under the PMIP4 experimental design and providing the model outputs.

- a modelling study focussed on the Pa/Th ratio, as simulated by the proxy-enabled iLOVECLIM model. This study underlines the sensitivity of this paleotracer to particle fluxes. Thanks to her sensitivity tests, the first author argues that changes in particulate organic carbon, biogenic opal and calcium carbonate significantly affect the sedimentary Pa/Th and therefore complexify the interpretation of the Pa/Th signal in terms of circulation changes. As a result, this study tends to justify my choice of not using the Pa/Th simulated at the LGM with prescribed particle fields corresponding to the PI (see chapter 2). I have contributed to this study by assisting with model analysis [Missiaen et al., 2020b] and providing feedback on the first draft of this paper and on the revised manuscript.

- a modelling study [Quiquet et al., 2021] using the iLOVECLIM model coupled to an ice sheet model during the last deglaciation. The impacts of various modelling choices on the simulated deglacial climate and ice sheets are examined. In particular, the effects of freshwater fluxes and of a parameterized sinking of brines on the AMOC collapse observed during the transient run of the deglaciation are shown in Figure 3.
  I have contributed to this study by providing equilibrated LGM simulations to restart the model, as well as the LGM ocean boundary conditions (generated as explained in chapter 3), which are not (yet) interactively updated in the course of the transient runs. In addition, I have given feedback on the first and revised drafts of this paper.

Supplementary figures of chapter 4

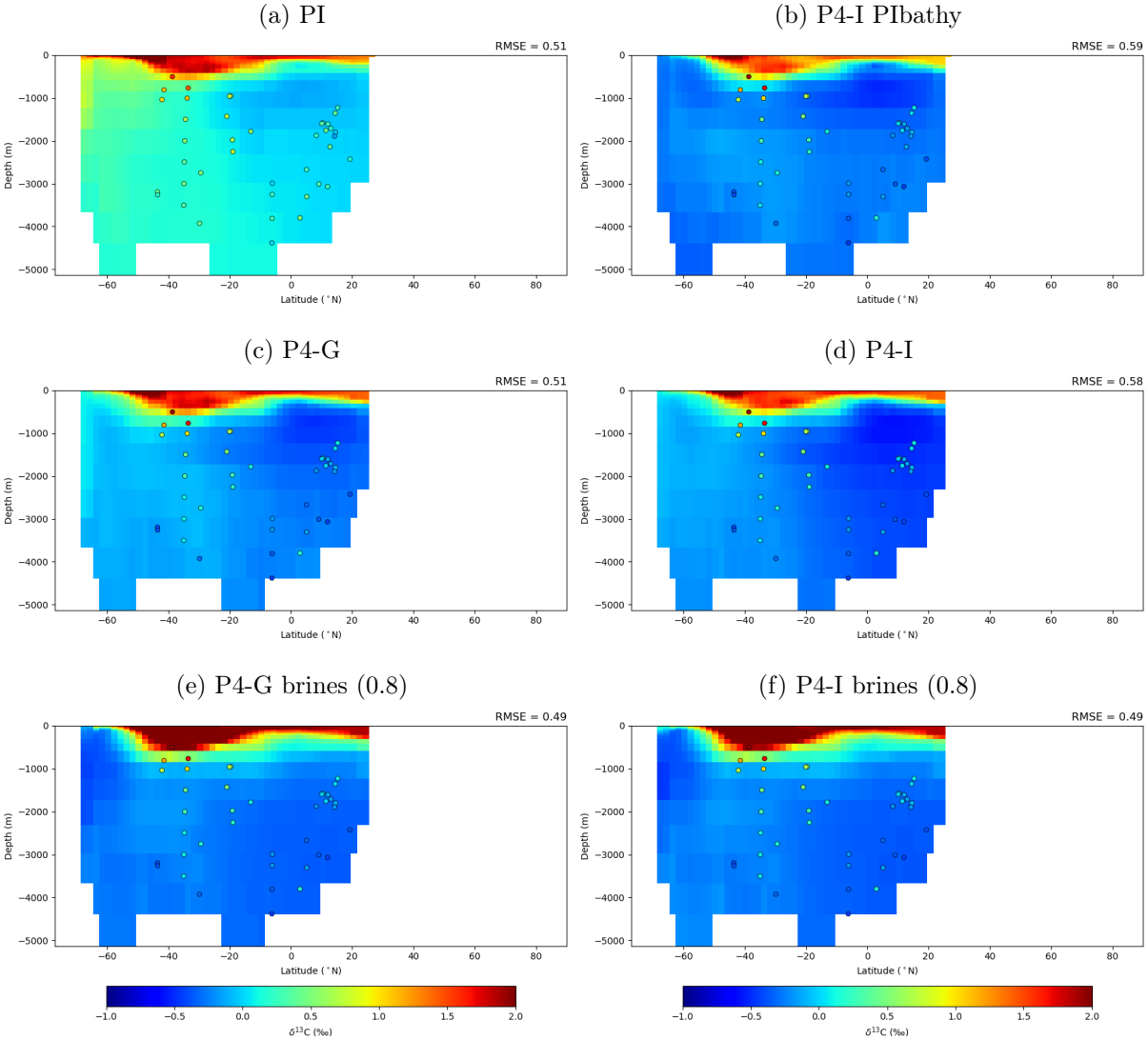

Figure 6.17: Mean zonal distribution of the simulated δ^{13}C (‰) in the Indian Ocean. The superimposed dots represents the δ^{13}C data from Peterson et al. [2014], obtained using benthic foraminifera in 480 marine cores. The values are estimated by averaging all measurements in the late Holocene (0-6 kyr) or LGM (19-23 kyr) time windows. The RMSE computed with respect to this δ^{13}C data in the Indian ocean is indicated in the top right corner.

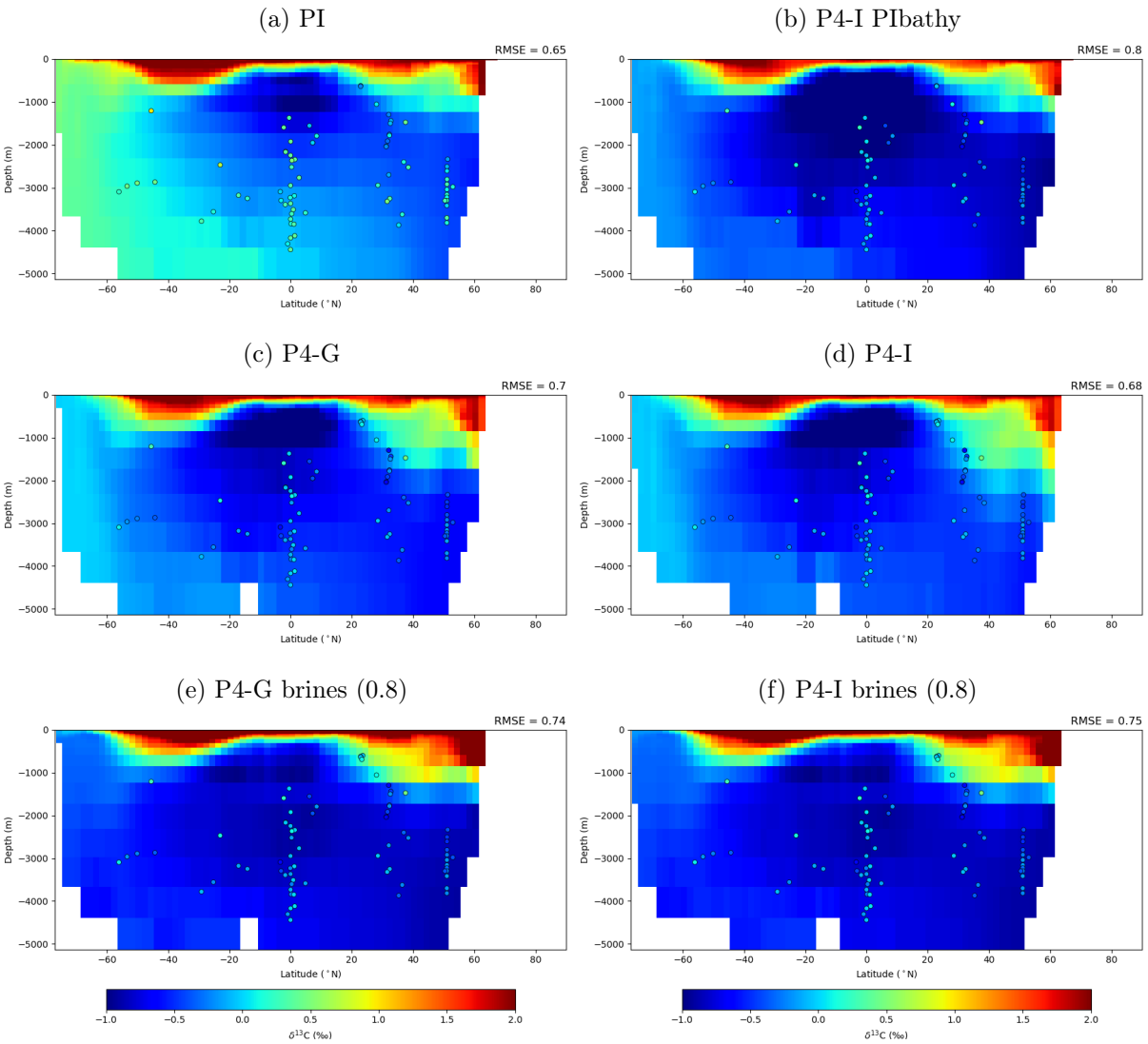

Figure 6.18: Mean zonal distribution of the simulated δ^{13}C (‰) in the Pacific ocean. The superimposed dots represents the δ^{13}C data from Peterson et al. [2014], obtained using benthic foraminifera in 480 marine cores. The values are estimated by averaging all measurements in the late Holocene (0-6 kyr) or LGM (19-23 kyr) time windows. The RMSE computed with respect to this δ^{13}C data in the Pacific is indicated in the top right corner.

Supporting Information for "A first intercomparison of the simulated LGM carbon results within PMIP-carbon: role of the ocean boundary conditions"

F. Lhardy[1], N. Bouttes[1], D. M. Roche[1,2], A. Abe-Ouchi[3], Z. Chase[4], K. A. Crichton[5], T. Ilyina[6], R. Ivanovic[7], M. Jochum[8], M. Kageyama[1], H. Kobayashi[3], B. Liu[6], L. Menviel[9], J. Muglia[10], R. Nuterman[8], A. Oka[3], G. Vettoretti[8], A. Yamamoto[11]

[1]Laboratoire des Sciences du Climat et de l'Environnement, CEA-CNRS-UVSQ, Gif-sur-Yvette, France

[2]Vrije Universiteit Amsterdam, Faculty of Science, Department of Earth Sciences, Earth and Climate cluster, Amsterdam, The Netherlands

[3]Atmosphere and Ocean Research Institute, The University of Tokyo, Kashiwa, Japan

[4]University of Tasmania, Hobart, Australia

[5]School of Geography, Exeter University, Exeter, UK

[6]Max Planck Institute for Meteorology, Hamburg, Germany

[7]University of Leeds, Leeds, UK

[8]Niels Bohr Institute, University of Copenhagen, Copenhagen, Denmark

[9]Climate Change Research Centre, the University of New South Wales, Sydney, Australia

[10]Centro para el Estudio de los Sistemas Marinos, CONICET, 2915 Boulevard Brown, U9120ACD, Puerto Madryn, Argentina

[11]Japan Agency for Marine-Earth Science and Technology, Yokohama, Japan

September 2, 2021, 4:26pm

Contents of this file

1. Text S1
2. Figures S1 to S3
3. Table S1

Introduction

Text S1 explains the adjustments of biogeochemical variables in the MPI-ESM model (additional details to Table 1).

Figure S1 shows the ocean surface area of PMIP models and iLOVECLIM simulations. It supplements the multimodel comparison of ocean volume presented in Fig. 1. The total surface was computed using the fixed fields ("areacello") of the same models, which are either PMIP3 models whose LGM and PI outputs were downloaded from the ESGF, PMIP-carbon models, or the iLOVECLIM model with different boundary conditions. The resulting values are compared to the high resolution topographic data described in Sect. 2.3. The characteristics of PMIP-carbon models are presented in Table 1 and the iLOVECLIM simulations are described in Sect. 3.1.

Figure S2 presents the surface area of the vertical levels in the iLOVECLIM simulations, which illustrates that most of the observed differences in ocean volume (Fig. 1b) stems from the deep (and large) vertical levels.

Table S1 supplements Table 2 as it quantifies the ocean volume and difference Δ (with

high resolution topographic data) in all iLOVECLIM simulations with different boundary conditions.

Figure S3 shows the carbon content of PMIP-carbon models computed in each reservoir (atmosphere, oceans, terrestrial biosphere, and total carbon) as mentioned in Sect. 3.3.

Text S1. Since the MPI-ESM model includes a sediment module, the adjustment of biogeochemical variables cannot be done simply by "multiplying their initial value by the relative change in global ocean volume" (Kageyama et al., 2017). Instead, the water-column inventory of alkalinity, phosphate and silicate at the LGM was kept as close as possible as the PI one thanks to several tunings in the course of the run. Although it is difficult to keep the ocean inventories identical between the PI and LGM simulations, a relative difference of 0.437% (phosphate), 0.531% (silicate) and 0.055% (alkalinity) was achieved at the end of the LGM run. We note that compared to a relative volume of 3.9% (see Table 2), the alkalinity difference is almost negligible.

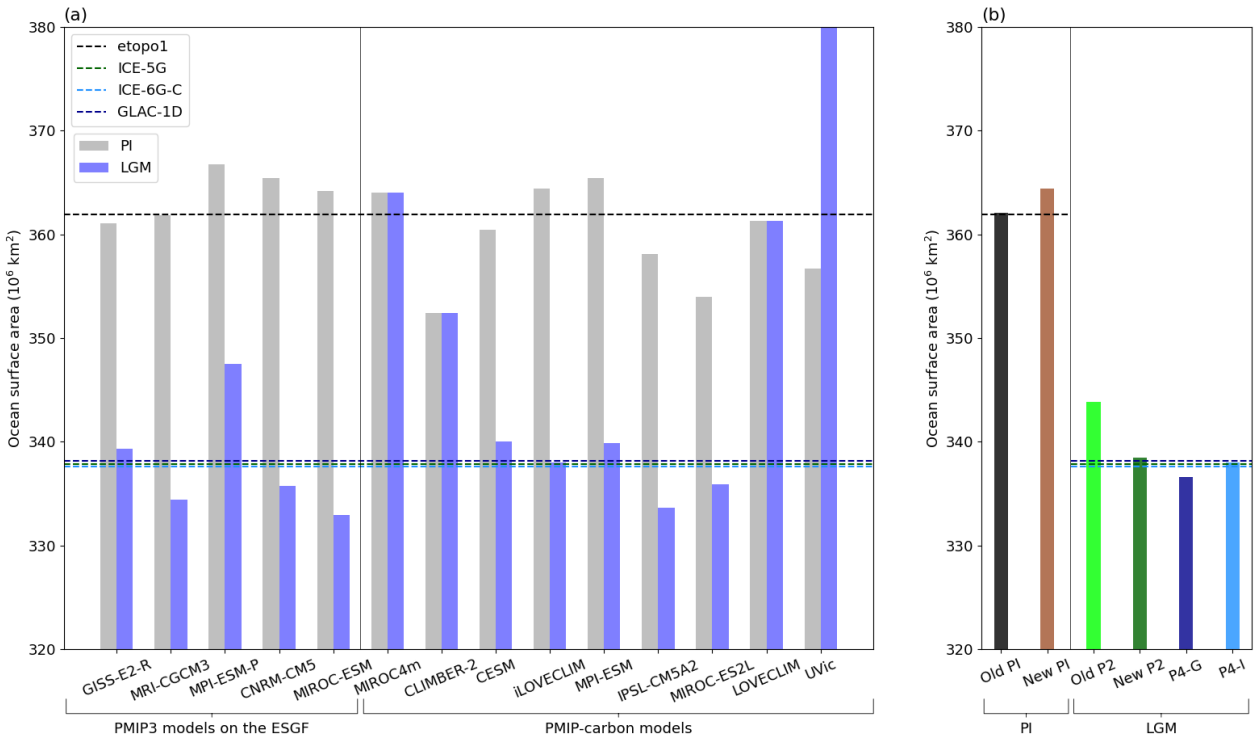

Figure S1. Ocean surface area in (a) PMIP models and (b) iLOVECLIM simulations. The iLOVECLIM reference simulations in (a) are 'New PI' and 'P4-I'. The horizontal dashed lines represent the ocean surface area computed from high resolution topographic data: etopo1 (361.9 millions of km^2), ICE-5G (337.9 millions of km^2), GLAC-1D (338.2 millions of km^2), and ICE-6G-C (337.6 millions of km^2).

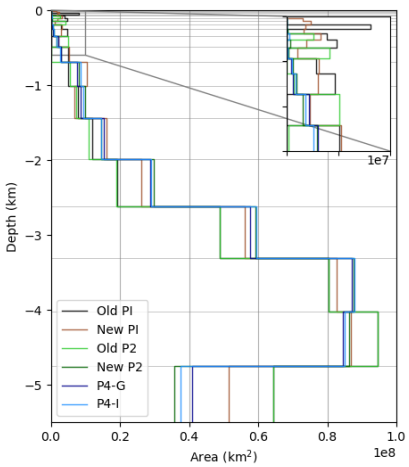

Figure S2. Surface area of each irregular vertical level in iLOVECLIM simulations.

Table S1. Quantification in iLOVECLIM simulations of PI and LGM ocean volumes, as well as the volume changes between each LGM simulation and its PI restart (LGM−PI, that is to say a PI-to-LGM change). Their differences (Δ) with respect to the ocean volume computed from PI (etopo1) and/or from LGM topographic data (ICE-5G, GLAC-1D or ICE-6G-C) are shown, indicating when an overestimated PI volume (Δ PI > 0%), LGM volume (Δ LGM > 0%), or volume change (Δ LGM−PI > 0%) seems to be observed. The relative volume change in simulations can also be compared to the one computed from topographic data: -2.88% (GLAC-1D) or -3.19% (ICE-6G-C).

Simulation name	Old PI	New PI	Old P2	New P2	P4-G	P4-I
Volume (10^{18} m^3)	1.387	1.343	1.379	1.289	1.296	1.291
Δ PI (%)	+3.86	+0.62				
Δ LGM (%)			+7.06	+0.02	-0.18	-0.05
LGM−PI (10^{16} m^3)			-0.72	-5.45	-4.70	-5.19
Δ LGM−PI (%)			-84.57	+17.14	+29.16	+20.85
Relative change (%)			-0.52	-4.06	-3.50	-3.87

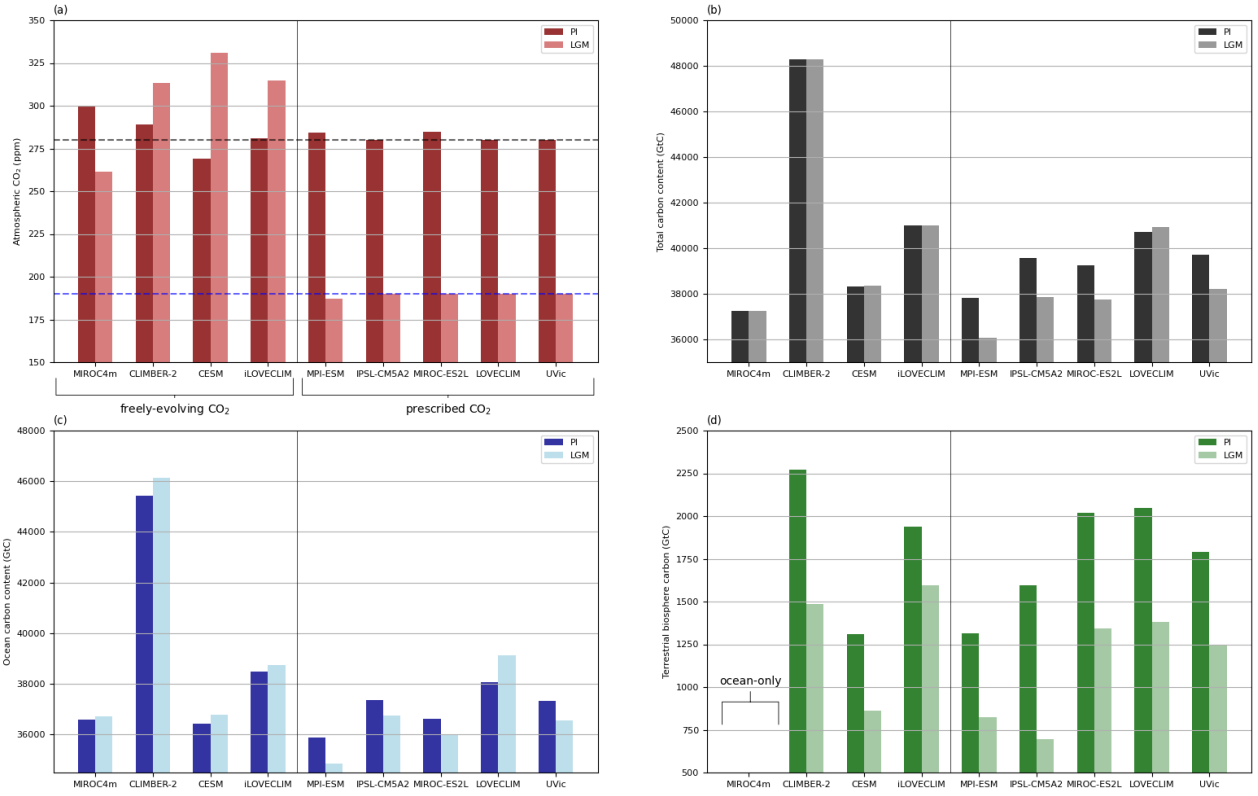

Figure S3. Carbon content of PMIP-carbon models in (a) atmosphere, (b) total system, (c) ocean and (d) terrestrial biosphere. The grey and blue dashed lines represents the atmospheric CO_2 concentrations at the PI (280 ppm) and LGM (190 ppm, Bereiter et al., 2015). Models have been run without accounting for additional processes at the LGM (e.g. permafrost, sediments, brines...), with the exception of MPI-ESM which includes an embedded sediment module, and MIROC4m-COCO, MIROC-ES2L, MPI-ESM and IPSL-CM5A2L in which dust-induced iron fluxes were changed at the LGM. The permafrost module is deliberately switched off in the CLIMBER-2(P) model, which is why we refer to it as CLIMBER-2 here. The carbon contained in sediments in MPI-ESM is not included in the total sum (b).

Supplementary information

(a) PI, summer (JFM)

(b) PI, winter (JAS)

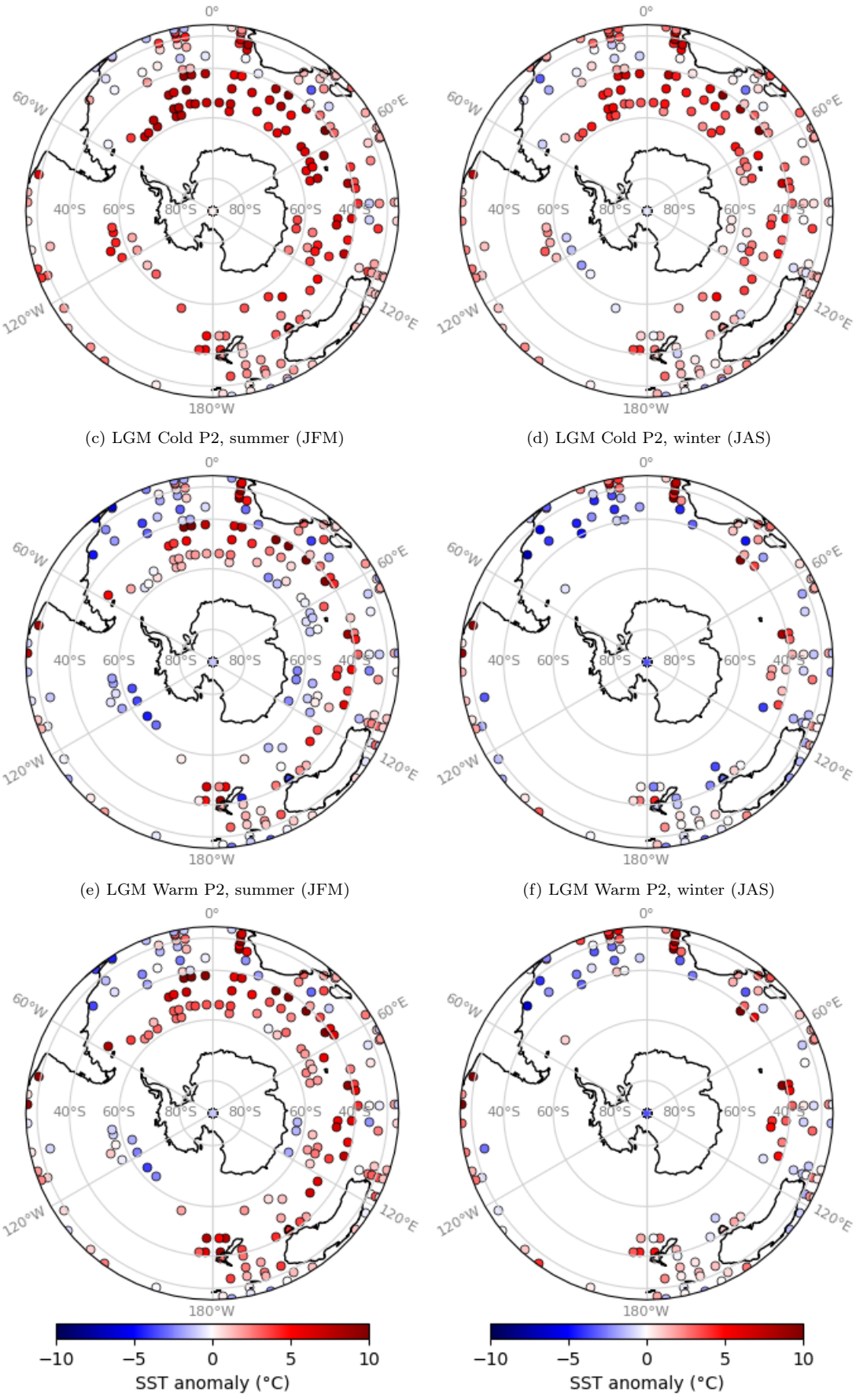

(c) LGM Cold P2, summer (JFM)

(d) LGM Cold P2, winter (JAS)

(e) LGM Warm P2, summer (JFM)

(f) LGM Warm P2, winter (JAS)

(g) LGM New P2, summer (JFM)

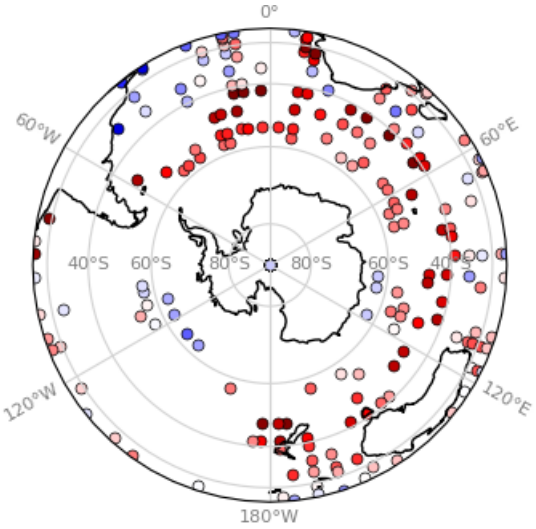

(h) LGM New P2, winter (JAS)

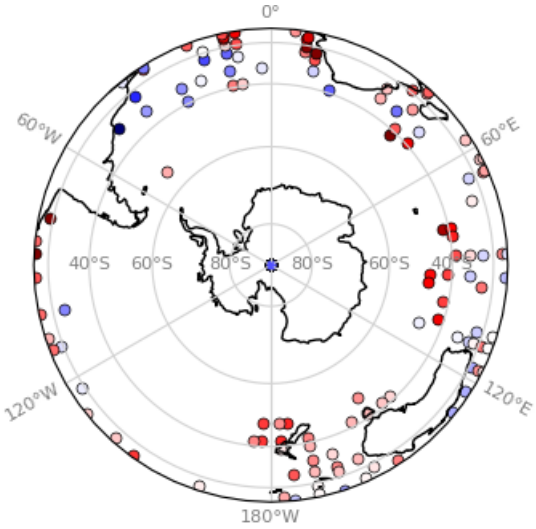

(i) LGM P4-G, summer (JFM)

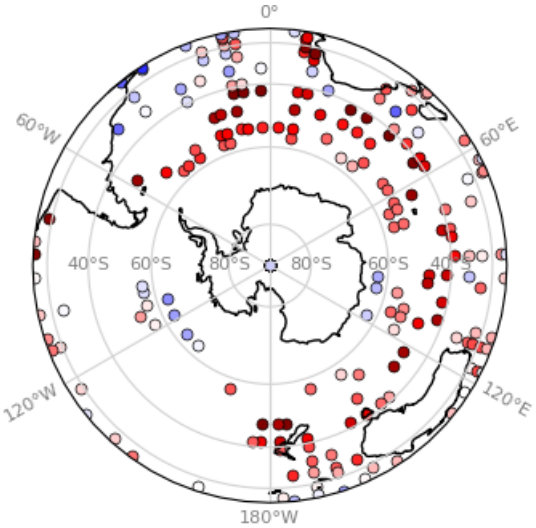

(j) LGM P4-G, winter (JAS)

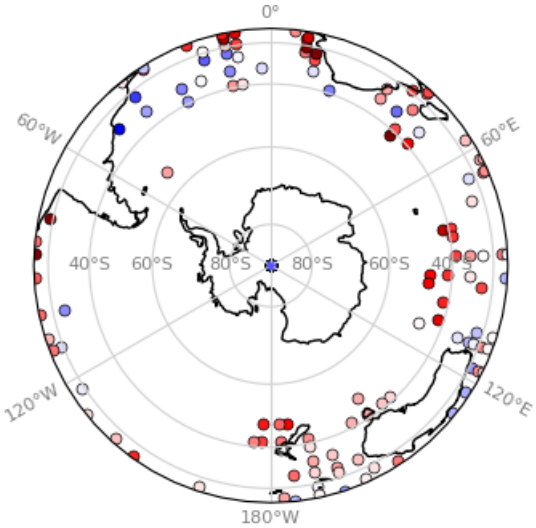

(k) LGM P4-I, summer (JFM)

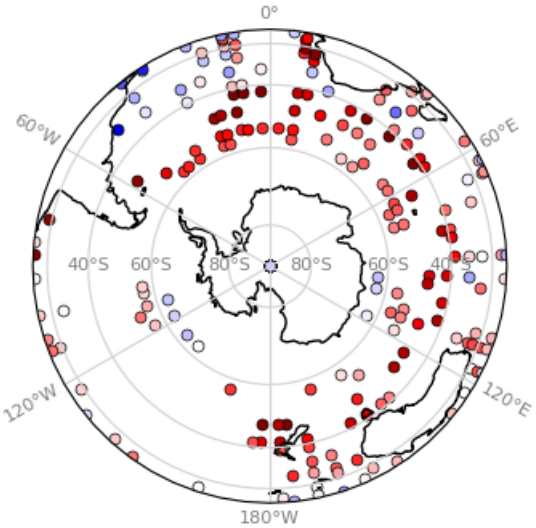

(l) LGM P4-I, winter (JAS)

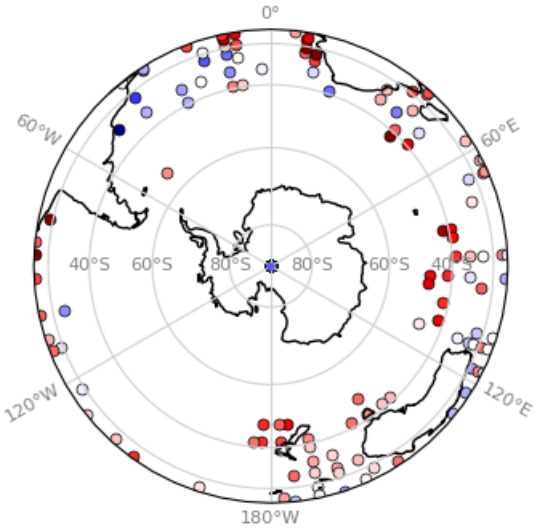

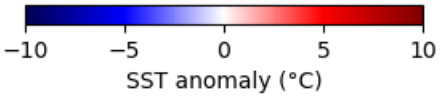

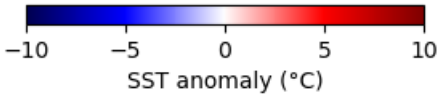

(m) LGM P4-I brines, summer (JFM)

(n) LGM P4-I brines, winter (JAS)

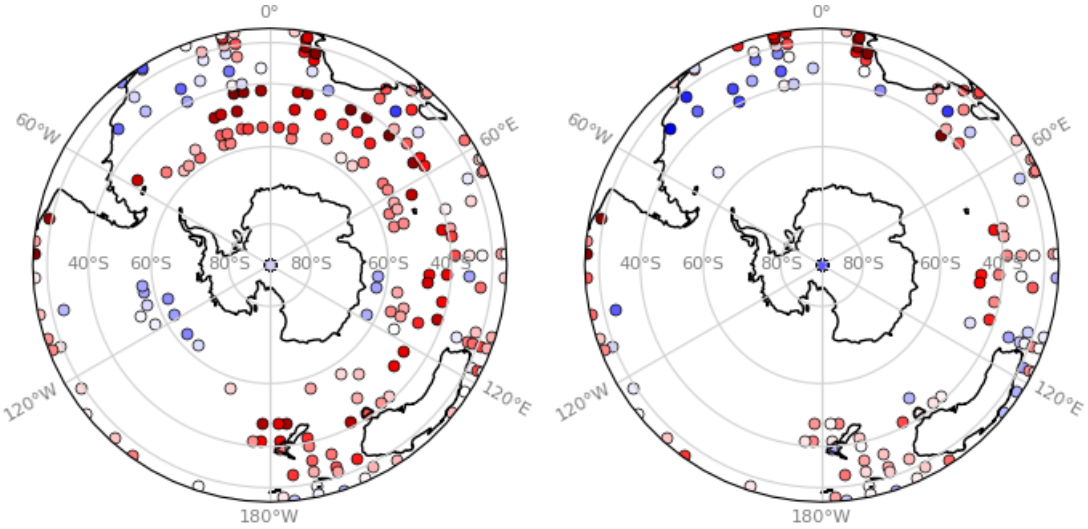

(o) LGM P4-I wind, summer (JFM)

(p) LGM P4-I wind, winter (JAS)

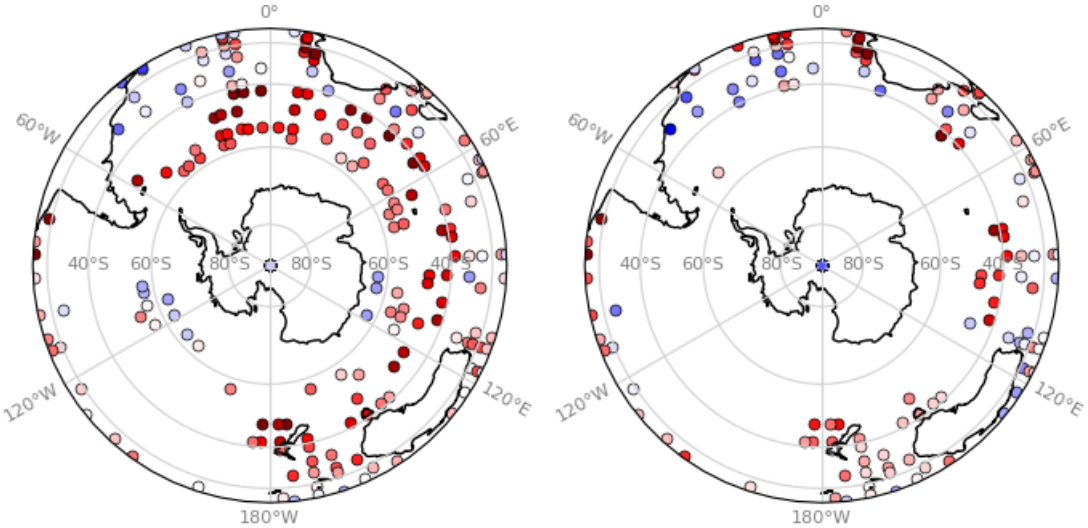

(q) LGM P4-I hosing, summer (JFM)

(r) LGM P4-I hosing, winter (JAS)

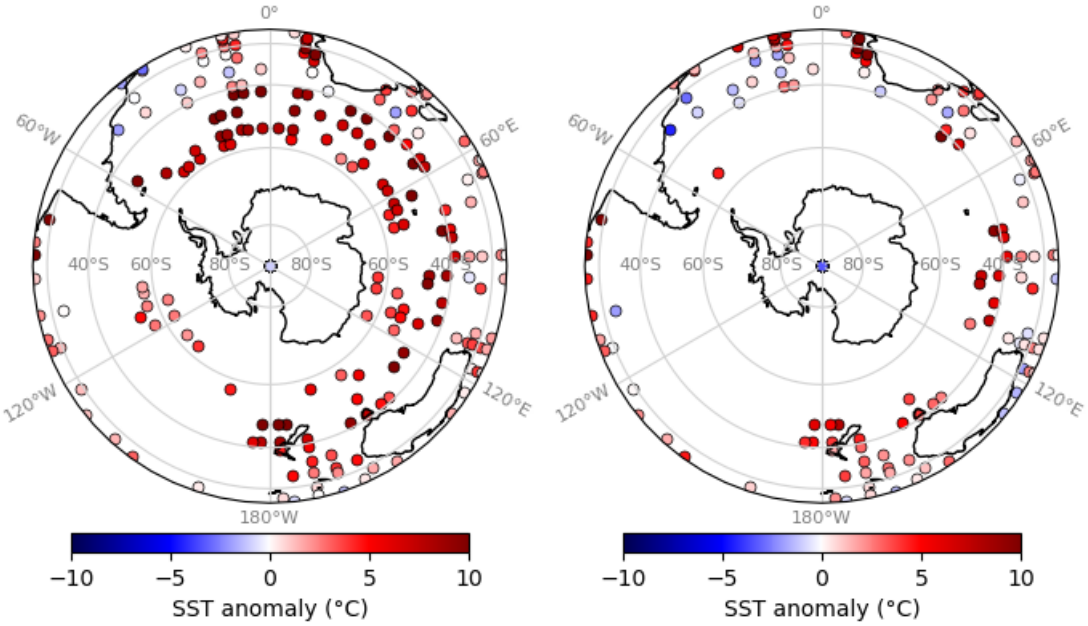

FIGURE S1 – Austral summer (JFM) and winter (JAS) SST anomalies relative to proxy data from the regridded product of MARGO Project Members (2009) (or World Ocean Atlas (1998) for the PI simulation).

(a) PI, summer (JFM)

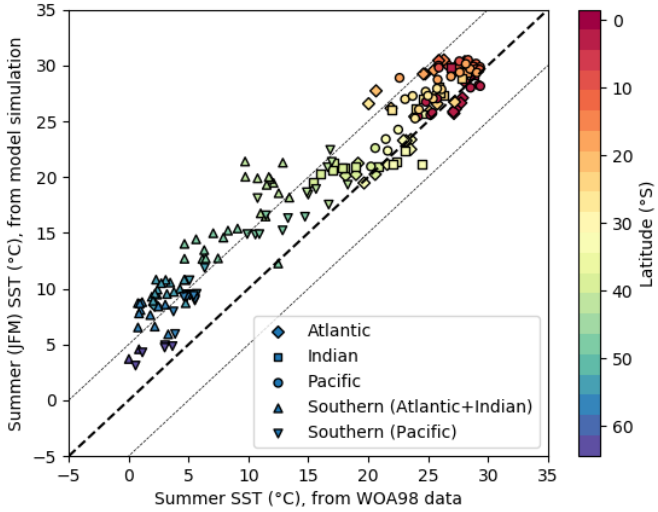

(b) PI, winter (JAS)

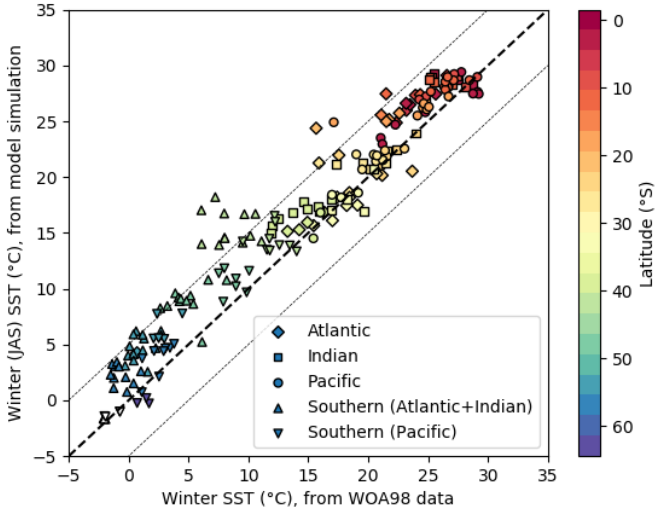

(c) LGM Cold P2, summer (JFM)

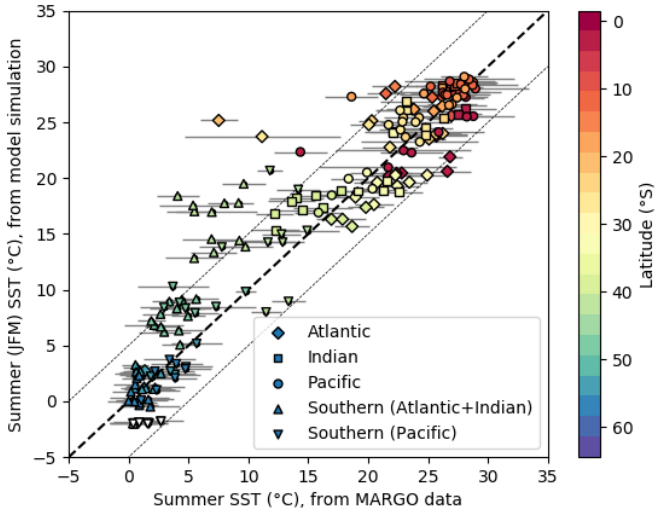

(d) LGM Cold P2, winter (JAS)

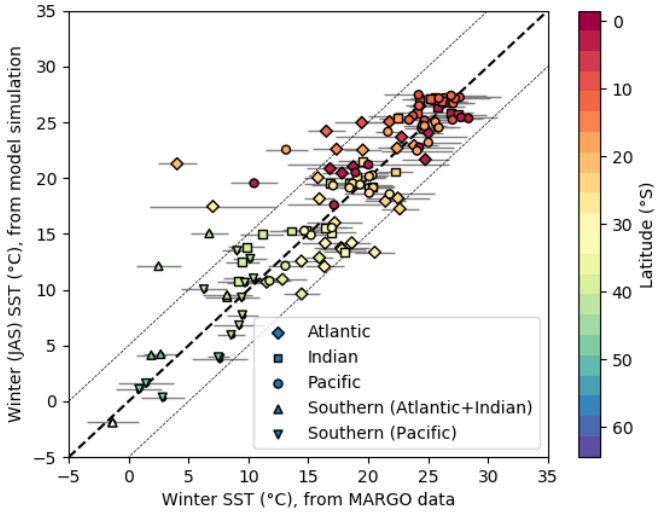

(e) LGM Warm P2, summer (JFM)

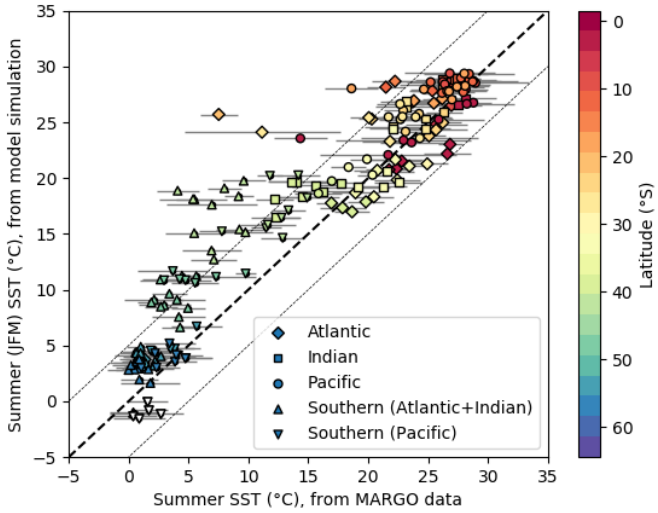

(f) LGM Warm P2, winter (JAS)

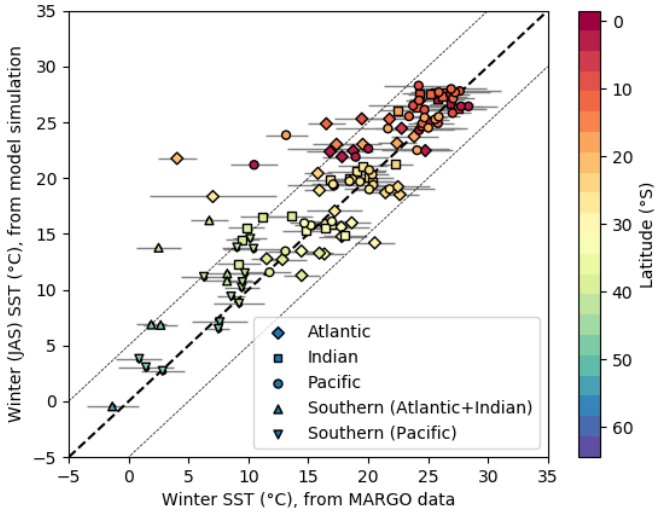

(g) LGM New P2, summer (JFM)

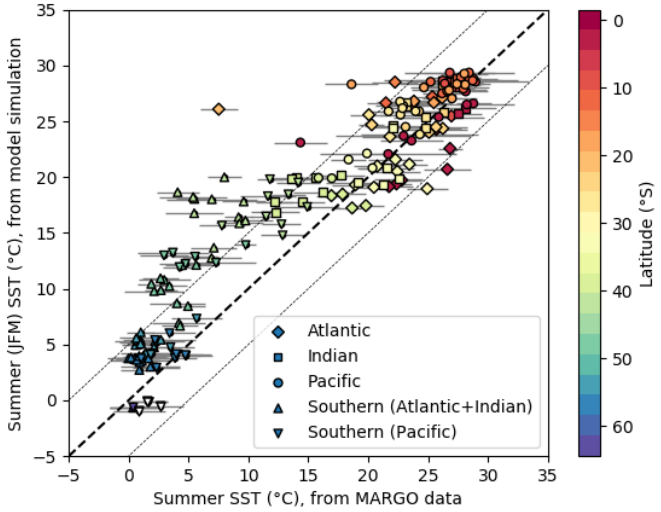

(h) LGM New P2, winter (JAS)

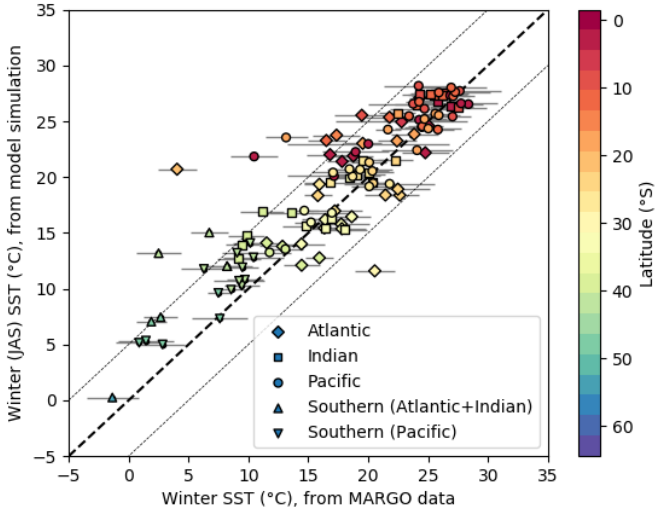

(i) LGM P4-G, summer (JFM)

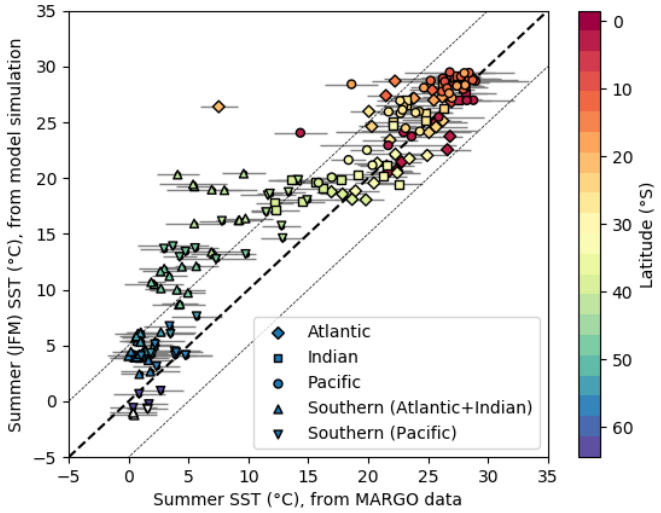

(j) LGM P4-G, winter (JAS)

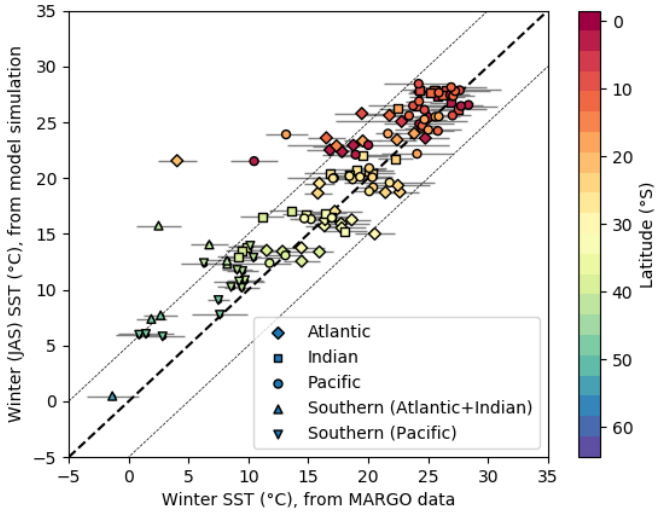

(k) LGM P4-I, summer (JFM)

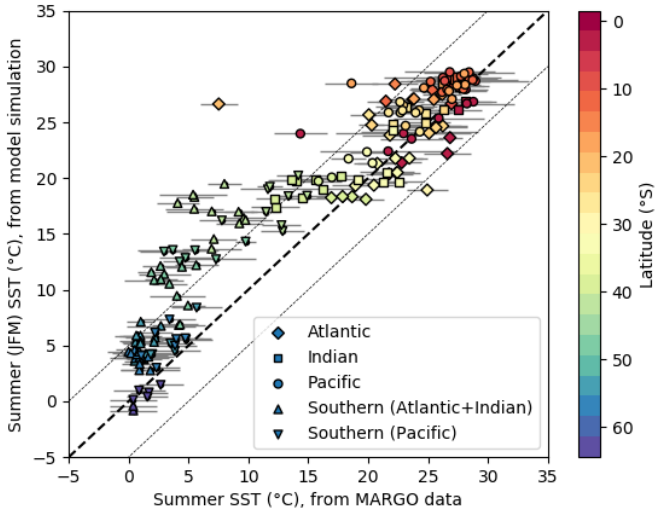

(l) LGM P4-I, winter (JAS)

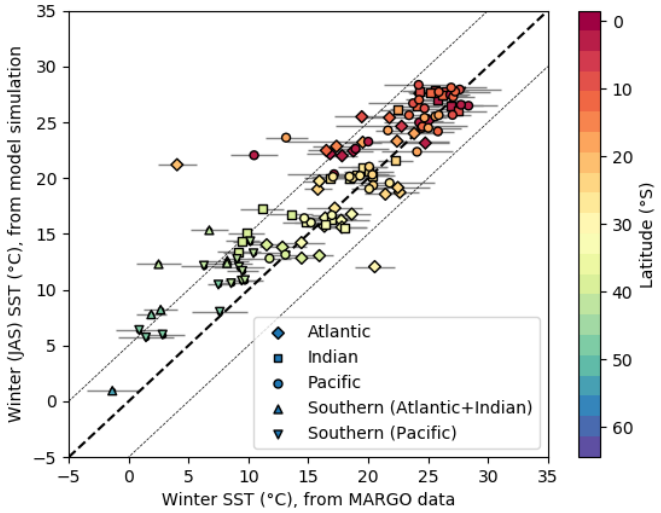

(m) LGM P4-I brines, summer (JFM)

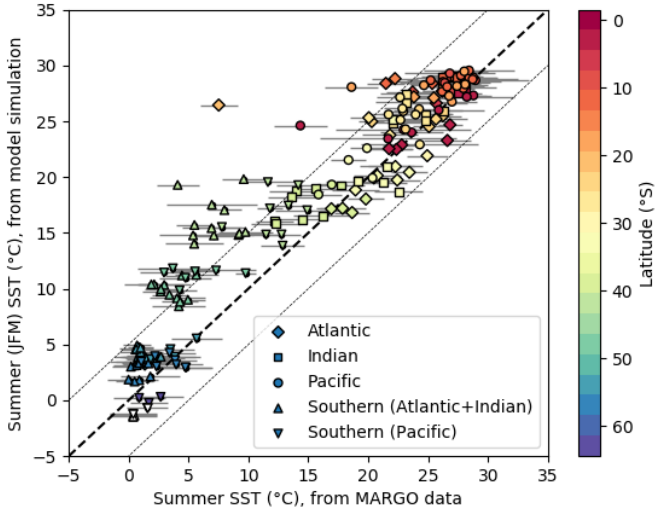

(n) LGM P4-I brines, winter (JAS)

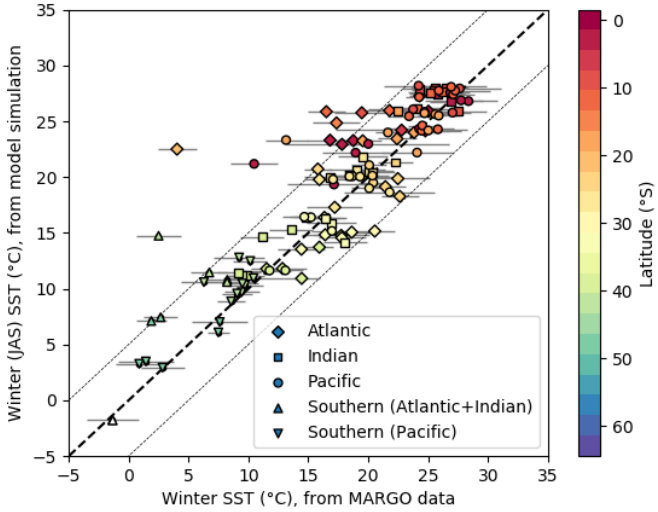

(o) LGM P4-I wind, summer (JFM)

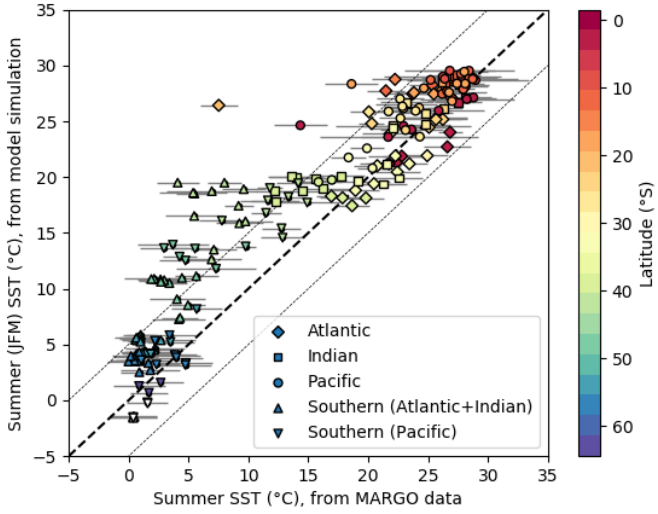

(p) LGM P4-I wind, winter (JAS)

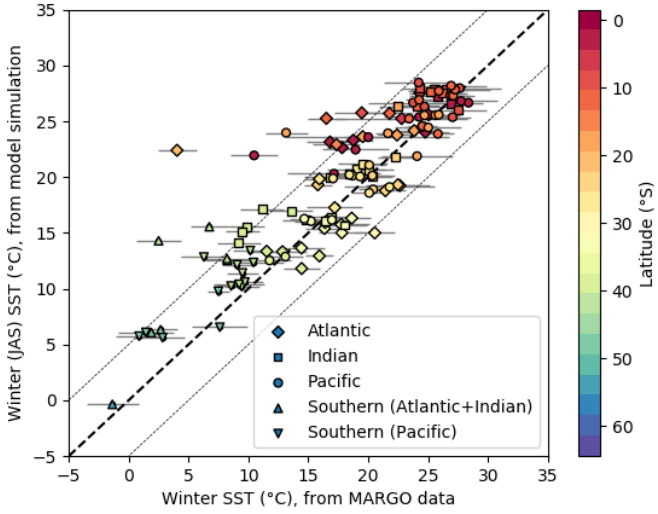

(q) LGM P4-I hosing, summer (JFM)

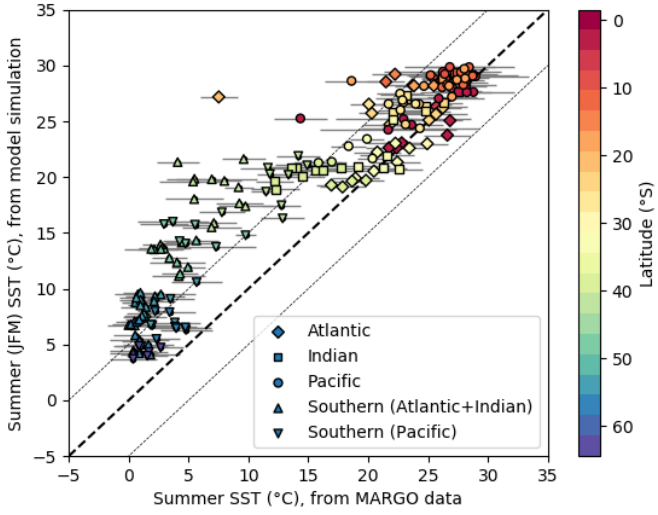

(r) LGM P4-I hosing, winter (JAS)

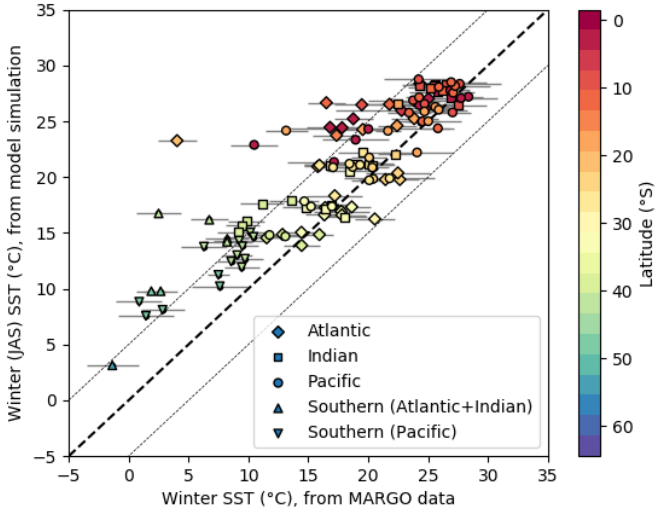

FIGURE S2 – Austral summer (JFM) and winter (JAS) sea-surface temperatures of the Southern Hemisphere in a model versus data diagram, for all simulations. The simulated SSTs are plotted against the SST data from the regridded product (MARGO Project Members (2009) or World Ocean Atlas (1998)) thanks to the aggregation of the coordinates on the nearest ocean grid cell. The 1 :1 line features a perfect model-data agreement (black dashed line), while the grey dotted lines features a 5°C departure from it. The marker style indicates the ocean basin of each core. The marker color shows the latitude of the core, except it is white where the model simulates sea ice in the Southern Ocean. The uncertainties associated with the SST data are plotted by the grey horizontal bars.

(a) Austral summer (JFM)

(b) Austral winter (JAS)

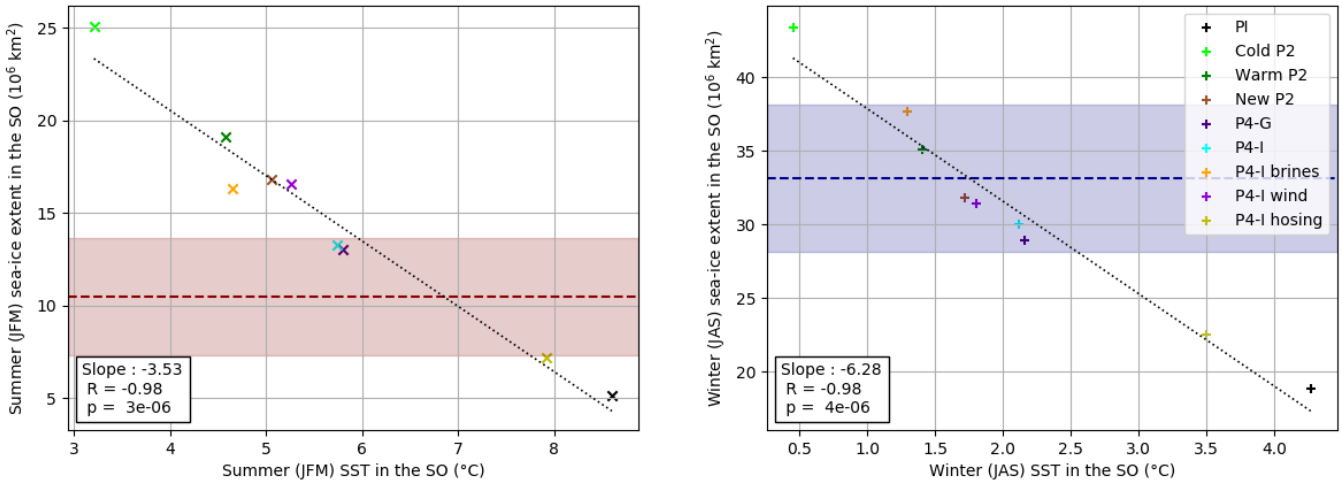

FIGURE S3 – Relationship between the mean SST (averaged up to 36°S) and the sea-ice extent in the Southern Ocean. The LGM sea-ice extent estimated using the proxy data compilation is represented by the red (summer) and the blue (winter) dashed lines (with an indicative error bar of 30% and 15% respectively). The dotted line represents the linear fit to the model results plotted here.

(a) LGM Cold P2, summer (JFM)

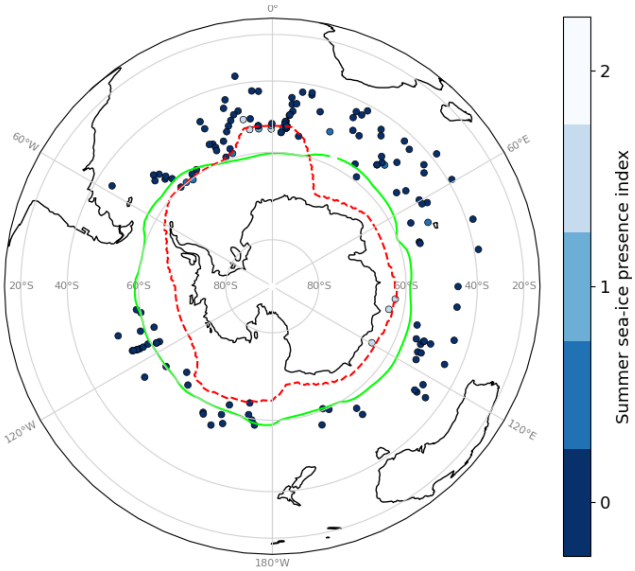

(b) LGM Cold P2, winter (JAS)

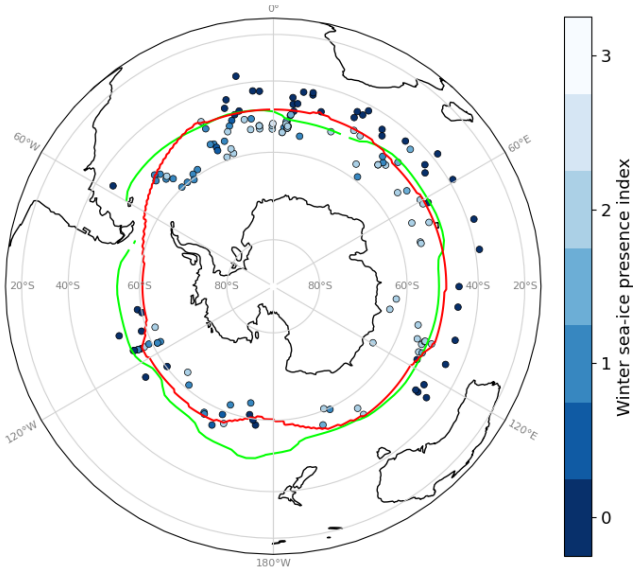

(c) LGM Warm P2, summer (JFM)

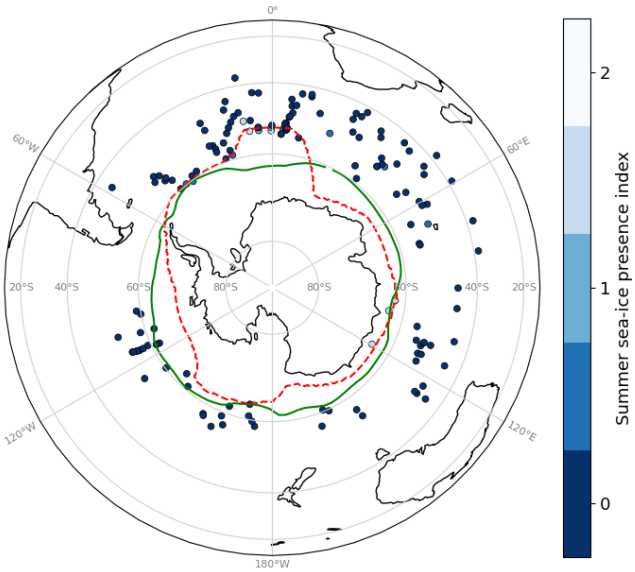

(d) LGM Warm P2, winter (JAS)

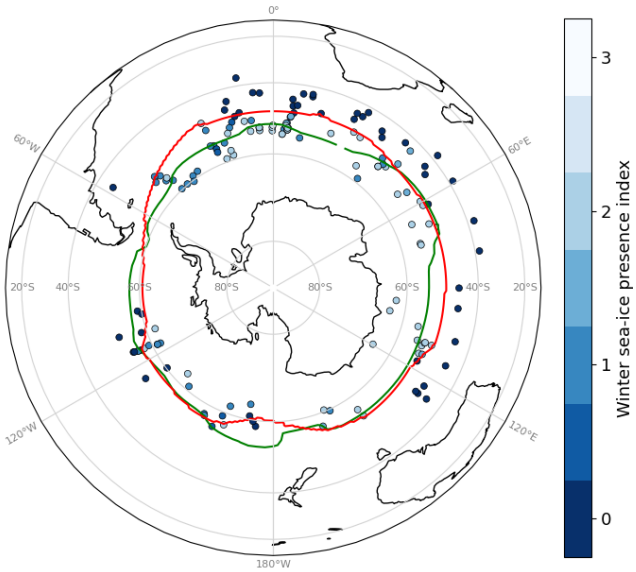

(e) LGM New P2, summer (JFM)

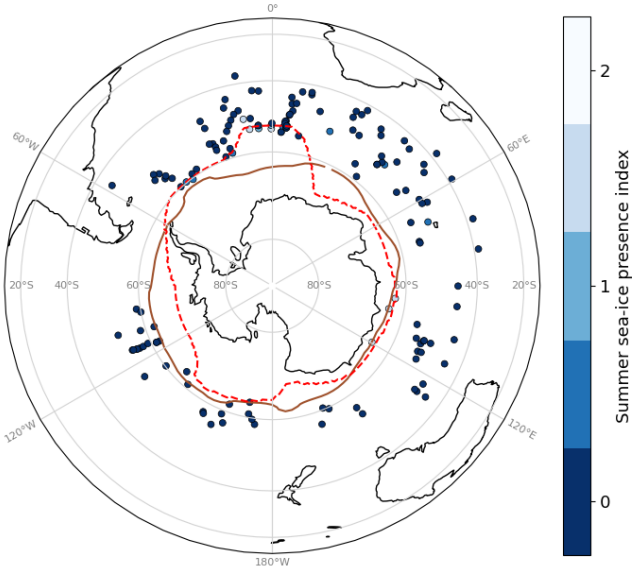

(f) LGM New P2, winter (JAS)

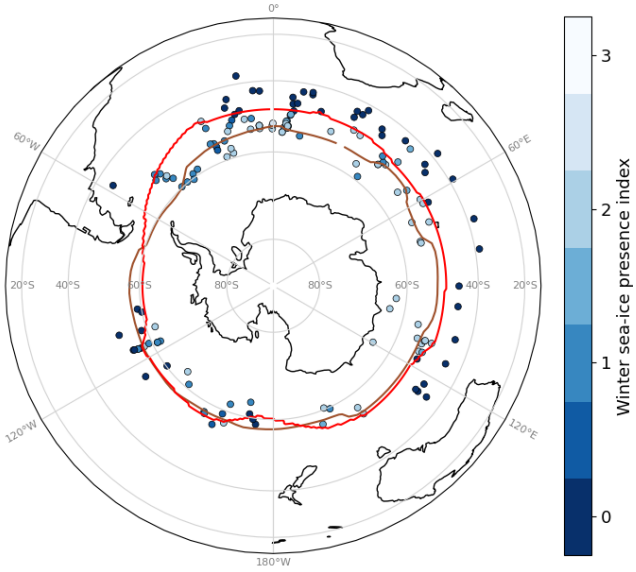

(g) LGM P4-G, summer (JFM)

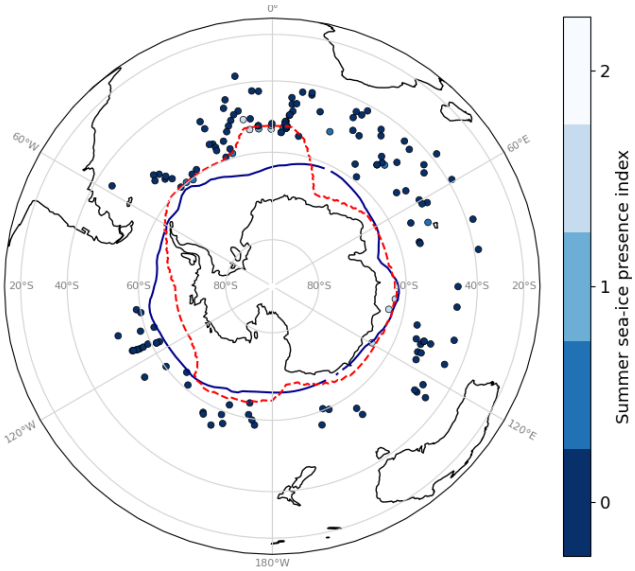

(h) LGM P4-G, winter (JAS)

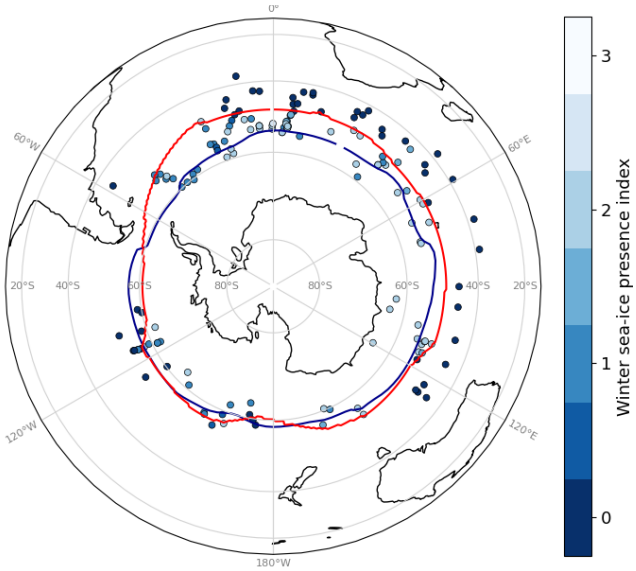

(i) LGM P4-I, summer (JFM)

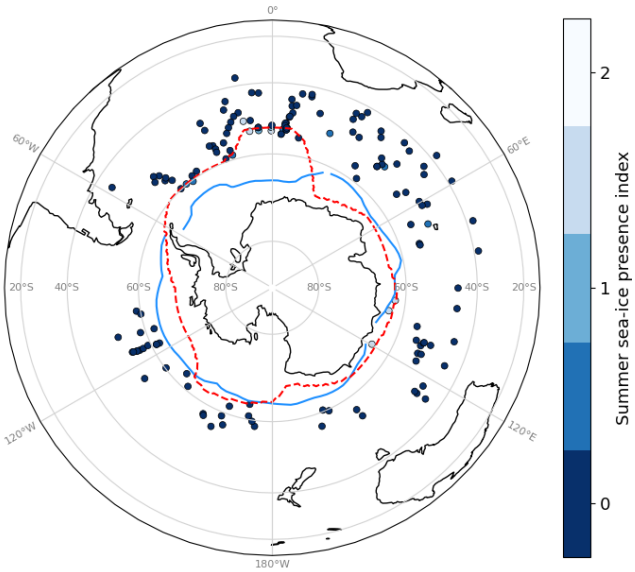

(j) LGM P4-I, winter (JAS)

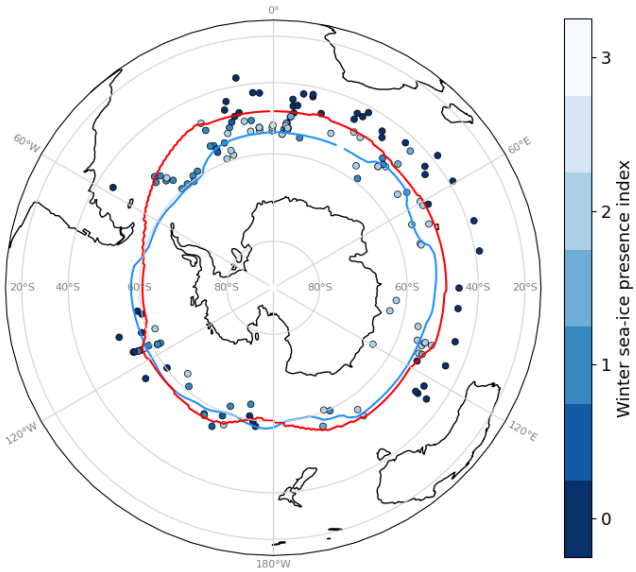

(k) LGM P4-I brines, summer (JFM)

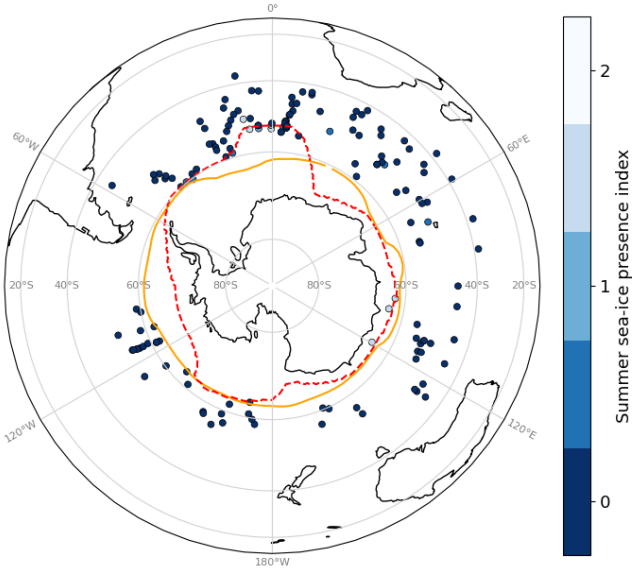

(l) LGM P4-I brines, winter (JAS)

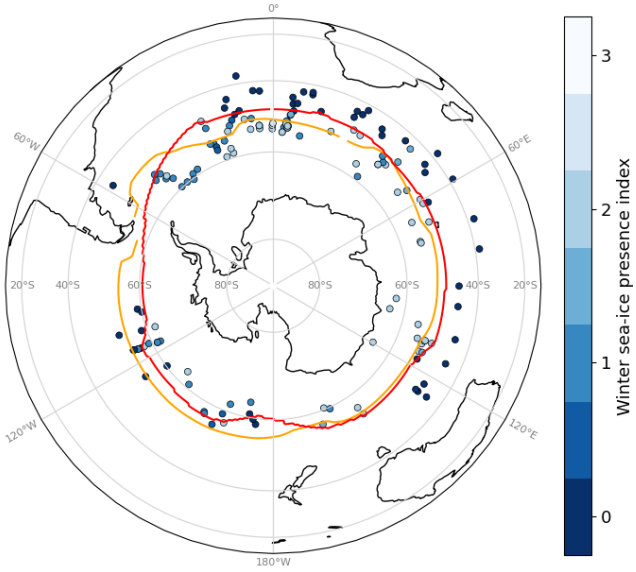

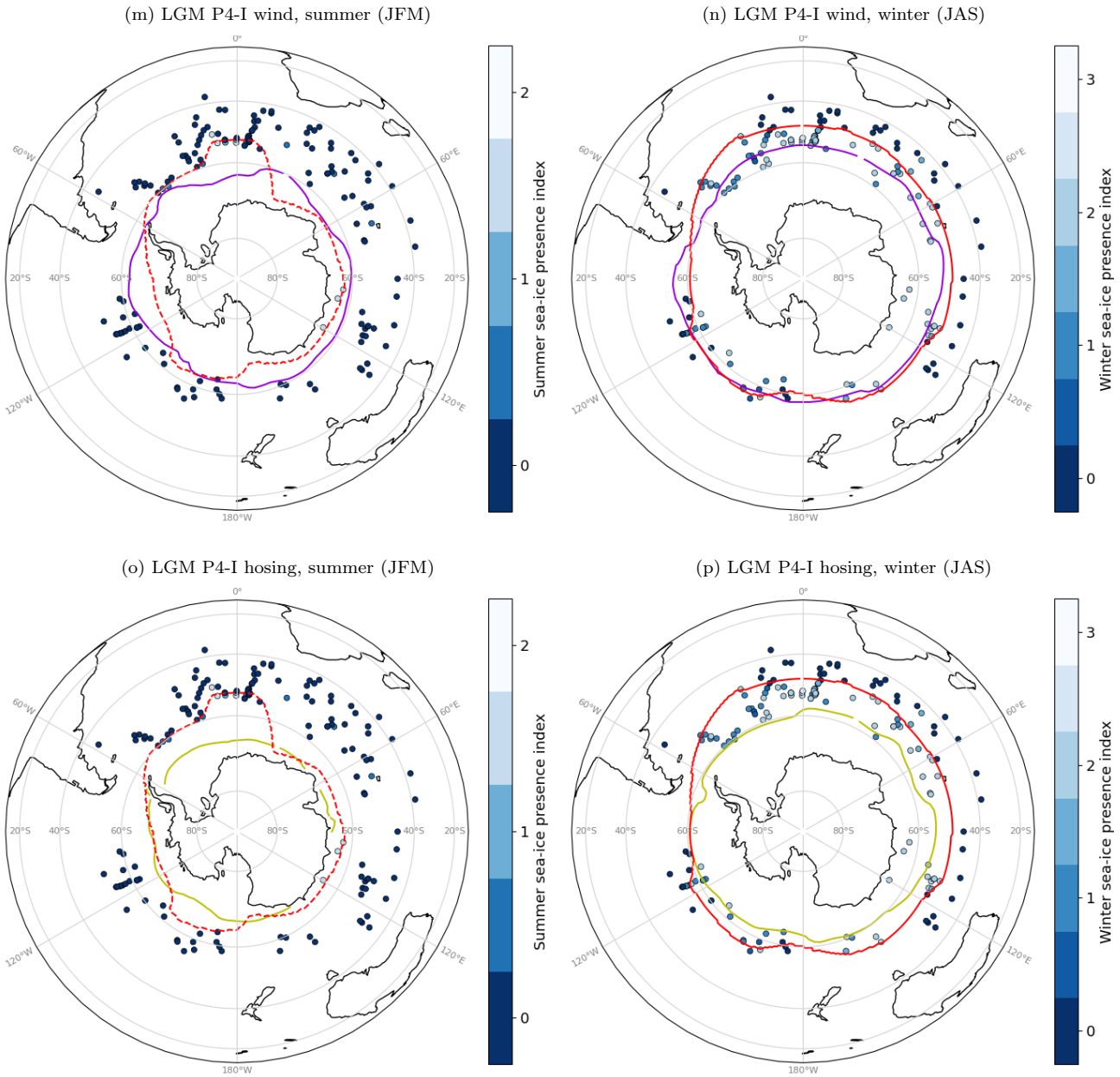

FIGURE S4 – Austral summer (JFM) and winter (JAS) sea-ice edges (at 15% of sea-ice concentration) in the Southern Ocean. The sea-ice presence suggested by marine cores data is represented as an arbitrary index on a blue to white scale, where blue denotes no indication of sea ice in proxies, and white denotes agreement of several proxies on the presence of sea ice. The red lines mark the likely delimitation of the sea-ice presence according to the proxy data (compilation of data from Gersonde et al. (2005), Allen et al. (2011), Ferry et al. (2015), Benz et al. (2016), Xiao et al. (2016), Nair et al. (2019), and Ghadi et al. (2020)). We used a solid red line for the winter months but a dashed line for the summer months as the summer contour is not well-constrained (see Sect. 2.4).

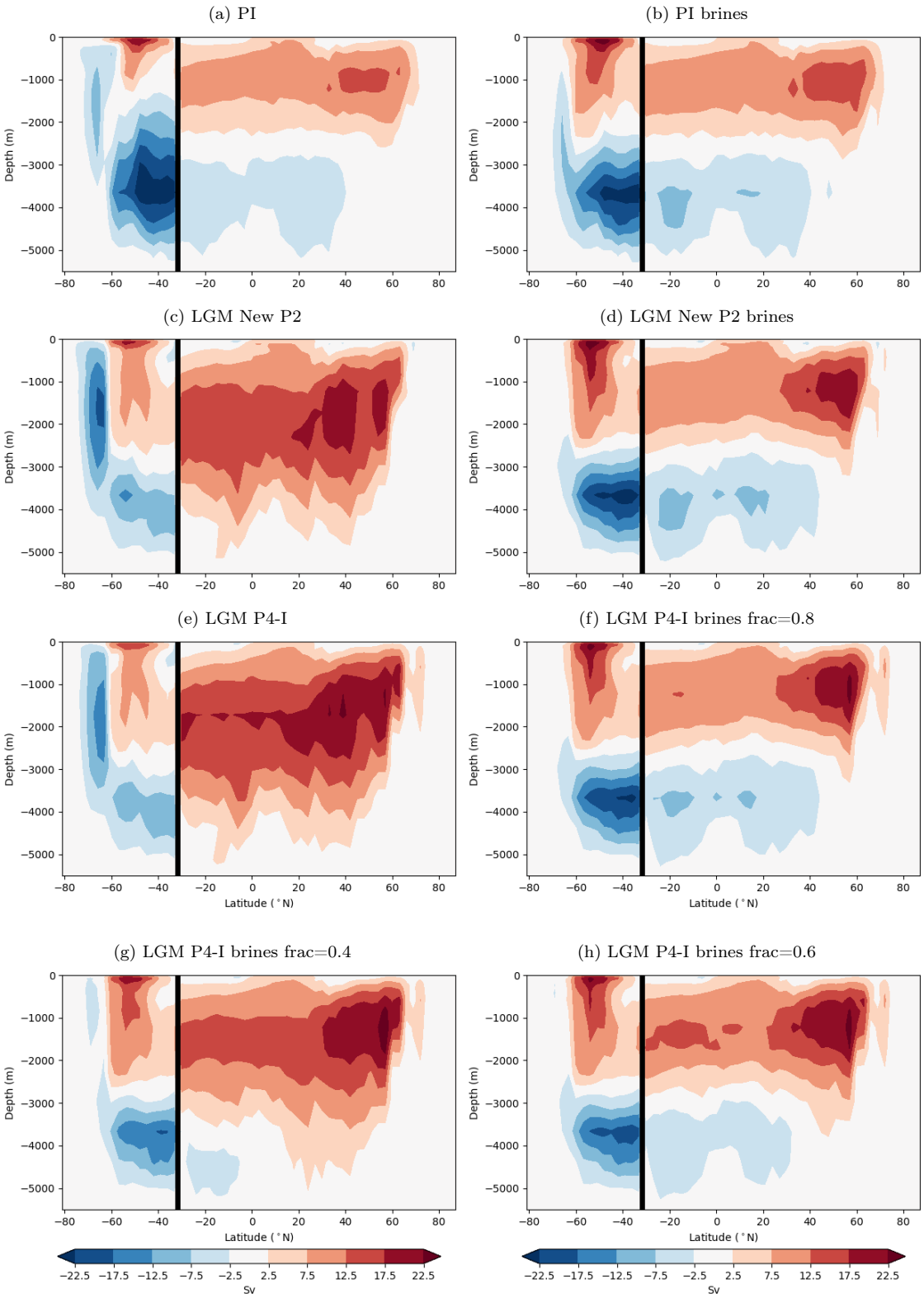

FIGURE S5 – Streamfunctions (Sv) in the Atlantic (North of 32°S) and Southern Ocean basins (South of 32°S). The black vertical line represents the limit between these two basins, chosen at 32°S. This figure shows similar plots as in Figure 7. The streamfunctions of additional simulations using the parameterization of the sinking of brines are displayed to show the effect of the chosen boundary conditions (those of 'PI', 'New P2', or 'P4-I') and of the parameter choice (fraction at 0.4, 0.6 or 0.8) on the streamfunction. For more information, note that the parameter choice and the brine parameterization in general has been discussed in the reviews of Bouttes et al. (2010), which can be found at : https ://cp.copernicus.org/articles/6/575/2010/cp-6-575-2010-discussion.html.

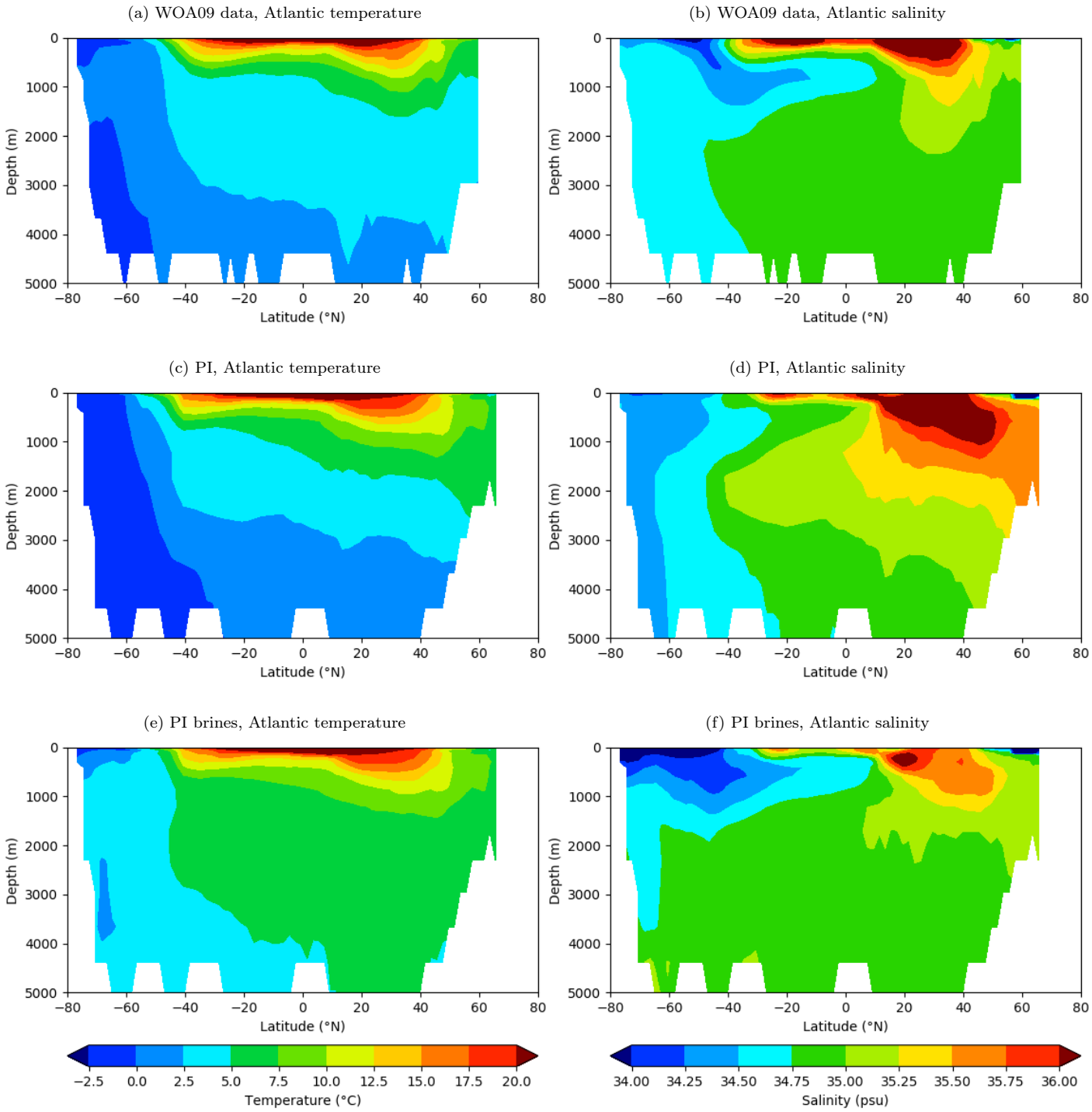

FIGURE S6 – Zonal average of the temperature (a, c, e) and salinity (b, d, f) distribution in the Atlantic ocean. The temperature and salinity distribution simulated at the PI with (e, f) or without (c, d) the parameterization of the sinking of brines is compared to data from the World Ocean Atlas 2009 (Locarnini et al., 2010 ; Antonov et al. 2010).

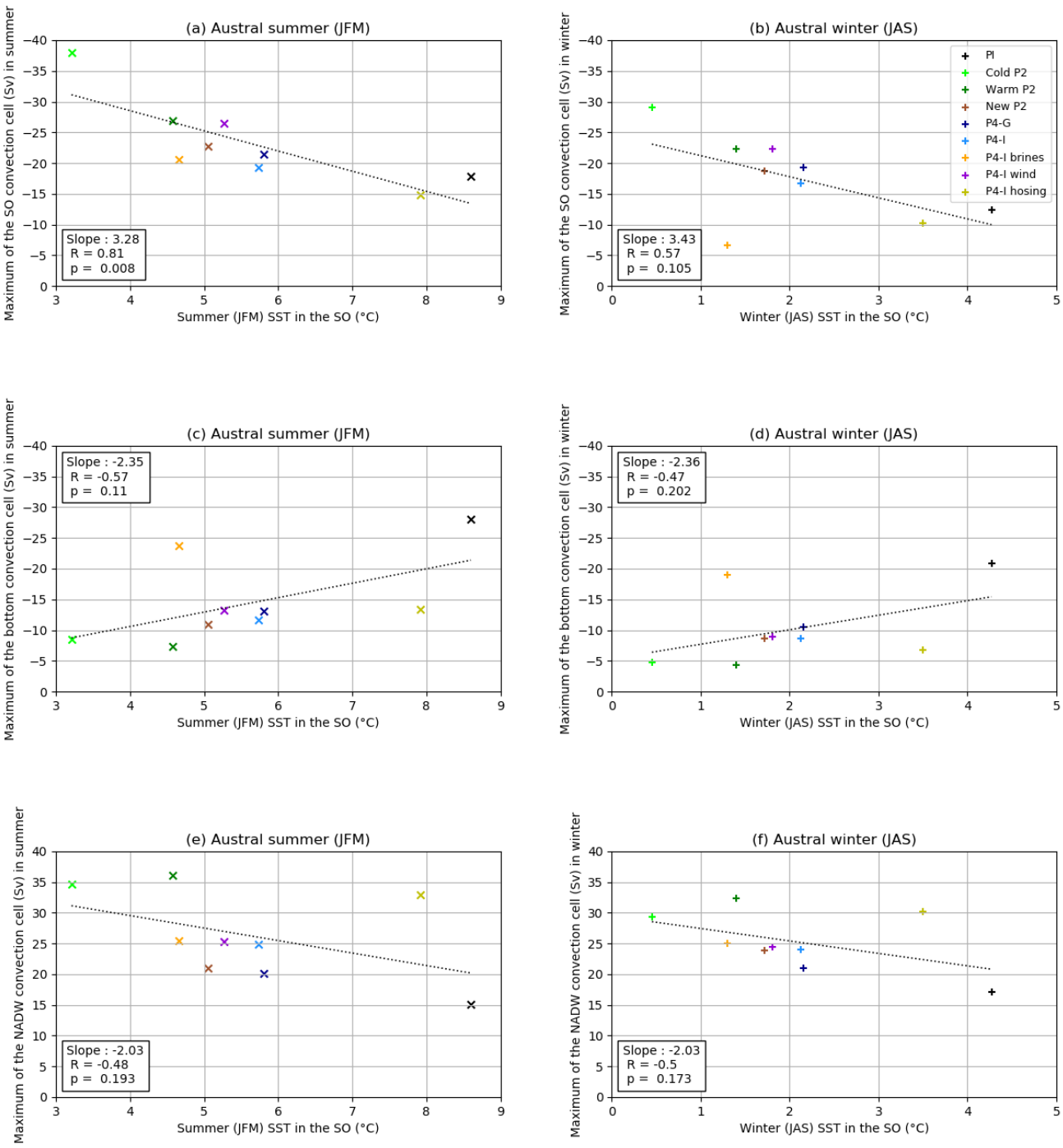

FIGURE S7 – Relationships between the mean SST in the Southern Ocean (averaged up to 36°S) and the Southern Ocean (a, b), bottom (c, d) or NADW (e, f) overturning cell maximum for all simulations. The y-axis is inverted for the two anticlockwise cells (a, b, c, d). The dotted line represents the linear fit to the model results plotted here.

Clim. Past, 17, 1065–1089, 2021
https://doi.org/10.5194/cp-17-1065-2021

Climate of the Past
Open Access
EGU

The PMIP4 Last Glacial Maximum experiments: preliminary results and comparison with the PMIP3 simulations

Masa Kageyama[1], Sandy P. Harrison[2], Marie-L. Kapsch[3], Marcus Lofverstrom[4], Juan M. Lora[5], Uwe Mikolajewicz[3], Sam Sherriff-Tadano[6], Tristan Vadsaria[6], Ayako Abe-Ouchi[6], Nathaelle Bouttes[1], Deepak Chandan[7], Lauren J. Gregoire[8], Ruza F. Ivanovic[8], Kenji Izumi[9], Allegra N. LeGrande[10], Fanny Lhardy[1], Gerrit Lohmann[11], Polina A. Morozova[12], Rumi Ohgaito[13], André Paul[14], W. Richard Peltier[7], Christopher J. Poulsen[15], Aurélien Quiquet[1], Didier M. Roche[1,16], Xiaoxu Shi[10], Jessica E. Tierney[4], Paul J. Valdes[9], Evgeny Volodin[17], and Jiang Zhu[18]

[1]Laboratoire des Sciences du Climat et de l'Environnement/Institut Pierre-Simon Laplace, UMR CEA-CNRS-UVSQ, Université Paris-Saclay, 91191 Gif-sur-Yvette, France
[2]School of Archaeology, Geography and Environmental Science (SAGES), University of Reading, Reading, UK
[3]Max Planck Institute for Meteorology, 20146 Hamburg, Germany
[4]University of Arizona, Tucson, AZ 85721, USA
[5]Yale University, New Haven, CT 06520, USA
[6]Atmospheric and Ocean Research Institute, The University of Tokyo, Kashiwa, Japan
[7]Department of Physics, University of Toronto, 60 St. George Street, Toronto, Ontario M5S1A7, Canada
[8]School of Earth and Environment, University of Leeds, Woodhouse Lane, Leeds, LS2 9JT, UK
[9]School of Geographical Sciences, University of Bristol, University Road, Bristol, BS8 1SS, UK
[10]NASA Goddard Institute for Space Studies, 2880 Broadway, New York, NY 10025, USA
[11]Alfred Wegener Institute, Bremerhaven, Germany
[12]Institute of Geography, Russian Academy of Science, Moscow, Russia
[13]Japan Agency for Marine-Earth Science and Technology, Yokohama, Japan
[14]MARUM – Center for Marine Environmental Sciences and Department of Geosciences, University of Bremen, Bremen, Germany
[15]Department of Earth and Environmental Sciences, University of Michigan, Ann Arbor, MI 48109, USA
[16]Vrije Universiteit Amsterdam, Faculty of Science, Cluster Earth and Climate, de Boelelaan 1085, Amsterdam, the Netherlands
[17]Institute of Numerical Mathematics, Russian Academy of Sciences, Moscow, Russia
[18]Climate and Global Dynamics Laboratory, National Center for Atmospheric Research, Boulder, CO 80305, USA

Correspondence: Masa Kageyama (masa.kageyama@lsce.ipsl.fr)

Received: 31 December 2019 – Discussion started: 23 January 2020
Revised: 21 December 2020 – Accepted: 31 January 2021 – Published: 20 May 2021

Abstract. The Last Glacial Maximum (LGM, ~21 000 years ago) has been a major focus for evaluating how well state-of-the-art climate models simulate climate changes as large as those expected in the future using paleoclimate reconstructions. A new generation of climate models has been used to generate LGM simulations as part of the Paleoclimate Modelling Intercomparison Project (PMIP) contribution to the Coupled Model Intercomparison Project (CMIP). Here, we provide a preliminary analysis and evaluation of the results of these LGM experiments (PMIP4, most of which are PMIP4-CMIP6) and compare them with the previous generation of simulations (PMIP3, most of which are PMIP3-CMIP5). We show that the global averages of the PMIP4 simulations span a larger range in terms of mean annual surface air temperature and mean annual precipitation compared to the PMIP3-CMIP5 simulations, with some PMIP4

simulations reaching a globally colder and drier state. However, the multi-model global cooling average is similar for the PMIP4 and PMIP3 ensembles, while the multi-model PMIP4 mean annual precipitation average is drier than the PMIP3 one. There are important differences in both atmospheric and oceanic circulations between the two sets of experiments, with the northern and southern jet streams being more poleward and the changes in the Atlantic Meridional Overturning Circulation being less pronounced in the PMIP4-CMIP6 simulations than in the PMIP3-CMIP5 simulations. Changes in simulated precipitation patterns are influenced by both temperature and circulation changes. Differences in simulated climate between individual models remain large. Therefore, although there are differences in the average behaviour across the two ensembles, the new simulation results are not fundamentally different from the PMIP3-CMIP5 results. Evaluation of large-scale climate features, such as land–sea contrast and polar amplification, confirms that the models capture these well and within the uncertainty of the paleoclimate reconstructions. Nevertheless, regional climate changes are less well simulated: the models underestimate extratropical cooling, particularly in winter, and precipitation changes. These results point to the utility of using paleoclimate simulations to understand the mechanisms of climate change and evaluate model performance.

1 Introduction

The climate of the Last Glacial Maximum (LGM; ∼ 21 000 years ago) has been a focus of the Paleoclimate Modelling Intercomparison Project (PMIP) since its inception. It is the most recent global cold extreme and as such has been widely documented and used for benchmarking state-of-the-art climate models (Braconnot et al., 2012; Harrison et al., 2014, 2015). The increase in global temperature from the LGM until now (∼ 4 to 6 °C; Annan and Hargreaves, 2015; Friedrich et al., 2016) has been the same order of magnitude as the increase projected by 2100 CE under moderate-to-high emission scenarios. The LGM world was very different from the present one, with large ice sheets covering northern North America and Fennoscandia, in addition to the Greenland and Antarctic ice sheets still present today. These additional ice sheets resulted in a lowering of the global sea level by ∼ 120 m, which induced changes in the land–sea distribution. The closure of the Bering Strait and the exposure of the Sunda and Sahul shelves between southeast Asia and the Maritime Continent are the most prominent of these changes in land–sea geography. Atmospheric greenhouse gas (GHG) concentrations were lower than pre-industrial (PI) values, leading to cooling in addition to that induced by the large ice sheets. The cooling is more pronounced in the high latitudes than in the tropics and greater over land than ocean. The polar amplification and the land–sea contrast signals simulated by the previous generation of paleoclimate simulations (PMIP3 – Coupled Model Intercomparison Project; PMIP3-CMIP5) are similar in magnitude (although opposite in sign) to the signals seen in future projections and have been shown to be consistent with climate observations for the historic period and reconstructions for the LGM (Braconnot et al., 2012; Izumi et al., 2013; Harrison et al., 2014, 2015). However, while the models are able to represent the thermodynamic behaviour that gives rise to these large-scale temperature gradients, they underestimate cooling on land, especially winter cooling, and overestimate tropical cooling over the oceans (Harrison et al., 2014). Thus, one question to be addressed with the new PMIP4-CMIP6 simulations is whether there is any improvement in capturing regional temperature changes. The large temperature changes during the LGM compared to the pre-industrial period make this interval a natural focus for efforts to constrain climate sensitivity but attempts to do this using the PMIP3-CMIP5 simulations were inconclusive (Schmidt et al., 2014; Harrison et al., 2014), in part because of the limited number of LGM simulations available and in part because of the limited range of climate sensitivity sampled by these models. Changes in model configuration have resulted in several of the PMIP4-CMIP6 models having substantially higher climate sensitivity than the PMIP3-CMIP5 versions of the same models, and thus the range of climate sensitivity sampled by the PMIP4-CMIP6 models is much wider. This provides an opportunity to re-examine whether the LGM could provide a strong constraint on climate sensitivity (Renoult et al., 2020; Zhu et al., 2021).

The atmospheric general circulation was strongly modified from its modern-day conditions by changes in coastlines at low latitudes (DiNezio and Tierney, 2013) and by the presence of the Laurentide and Fennoscandian ice sheets (e.g. Laîné et al., 2009; Löfverström et al., 2014, 2016; Ullman et al., 2014; Beghin et al., 2015; Liakka and Löfverström, 2018). These changes in circulation had an impact on precipitation, which was reduced globally (Bartlein et al., 2011) but increased locally, for example, in southwestern North American and in the Mediterranean region (e.g. Kirby et al., 2013; Beghin et al., 2016; Goldsmith et al., 2017; Lora et al., 2017; Lora, 2018; Löfverström and Lora, 2017; Löfverström and Liakka, 2016; Löfverström, 2020; Rehfeld et al., 2020). The interplay between temperature-driven and circulation-driven changes in regional precipitation during the LGM represents a test of the ability of state-of-the-art models to simulate precipitation changes under future scenarios, where both thermodynamic (e.g. related to the Clausius–Clapeyron relationship) and dynamic (e.g. related to changes in the position of the storm tracks and extent of the subtropical anticyclones) effects contribute to changes in the amount and location of precipitation (e.g. Boos, 2012; Scheff and Freirson, 2012; Lora, 2018). Evaluation of the PMIP3-CMIP5 simulations showed that models underestimate the LGM reduction in mean annual precipitation over land (Harrison et al., 2014), reflecting the underestimation of temperature changes in the simulations (Li et al., 2013).

This resulted in an underestimation of the observed aridity (precipitation minus evapotranspiration). While the models reproduced circulation-induced changes in precipitation in western North America, they showed no increase in precipitation south of the North American ice sheet and only limited impact on the precipitation of the circum-Mediterranean region (Harrison et al., 2014; Lora, 2018; Morrill et al., 2018). Thus, one question to be addressed with the new PMIP4-CMIP6 simulations is whether there is any improvement in capturing regional precipitation changes. One complication here is that most of the reconstructions used to evaluate the PMIP3-CMIP5 simulations were pollen based and relied on statistical approaches that do not account for the direct impact of low CO_2 on water-use efficiency (Prentice and Harrison, 2009; Gerhardt and Ward, 2010; Bragg et al., 2013; Scheff et al., 2017) and could therefore be dry biased. However, new methods have been developed that account for this effect (Prentice et al., 2017), and thus it is possible to determine whether accounting for the effect of low CO_2 resolves model–data mismatches in regional precipitation at the LGM.

The LGM boundary conditions also had a strong impact on ocean circulation, as documented via multiple tracers (e.g. Lynch-Stieglitz et al., 2007; Jaccard and Galbraith, 2011; Böhm et al., 2015), which suggest a shallower North Atlantic Deep Water (NADW) cell and expanded Antarctic Bottom Water (AABW). In addition, Gebbie (2014) used a combination of synthesis of multiple tracers measured in sediment cores for the LGM and a global tracer transport model to show that these tracers are compatible with a vertical distribution of NADW and AABW similar to today but that the core of the NADW water mass shoals by 1000 m. None of these proposed reconstructions of glacial circulation are consistent with the PMIP3-CMIP5 model results (Muglia and Schmittner, 2015), which all show a deepening of the Atlantic Meridional Overturning Circulation (AMOC), with NADW reaching the ocean floor in the northern North Atlantic for some models. Previous studies show that this increase in AMOC is related to changes in northern extratropical wind stress due to the presence of the high ice sheets (Oka et al., 2012; Muglia and Schmittner, 2015; Klockmann et al., 2016; Sherriff-Tadano et al., 2018; Galbraith and de Lavergne, 2019). Thus, the simulation of the AMOC, and ocean circulation in general, during the LGM could be highly sensitive to the ice-sheet reconstructions used as boundary conditions (see, e.g. Ullman et al., 2014; Beghin et al., 2016). There is still some uncertainty about the height and shape (although not the extent) of the LGM ice sheets, so the protocol for the LGM PMIP4-CMIP6 experiment takes this uncertainty into account by allowing for alternative ice-sheet configurations (Kageyama et al., 2017) in order to test the sensitivity of LGM climate and ocean circulation to ice-sheet configuration. The PMIP4-CMIP6 LGM experimental protocol also includes changes in other forcings, including vegetation changes and changes in atmospheric dust loadings and their uncertainties. Thus, the new PMIP4-CMIP6 simulations provide opportunities to examine the response of the climate system to multiple forcings, to calculate the impact of individual forcings through sensitivity experiments and to investigate how these forcings combine to produce circulation and climate changes in the marine and terrestrial realms.

In this paper, we present preliminary results from the PMIP4-CMIP6 LGM simulations, compare them to the PMIP3-CMIP5 results (Sect. 3) and evaluate their realism against a range of climatic reconstructions (Sect. 4). We focus on temperature and precipitation, extratropical circulation, energy transport and the AMOC.

2 Material and methods

2.1 PMIP3-CMIP5 and PMIP4-CMIP6 protocols for the LGM simulations

The protocol of the LGM experiments changed between the PMIP3-CMIP5 and PMIP4-CMIP6 phases (Kageyama et al., 2017), partly to accommodate new information about boundary conditions and partly to capitalise on new features of the climate models. The main difference between the PMIP3-CMIP5 and PMIP4-CMIP6 simulations is the specification of the ice sheets. The PMIP3-CMIP5 simulations all used the same ice sheet, which was created as a composite of three separate ice-sheet reconstructions (Abe-Ouchi et al., 2015); the PMIP4-CMIP6 protocol allows modelling groups to use one of three separate ice-sheet reconstructions: the original PMIP3-CMIP5 ice sheet to facilitate comparison with the earlier simulations, ICE-6G_C (Argus et al., 2014; Peltier et al., 2015) and GLAC-1D (Lev Tarasov, personal communication, 2016; Ivanovic et al., 2016). All three reconstructions have similar ice-sheet extent, but the heights of the Laurentide, Fennoscandian and West Antarctica ice sheets differ significantly, by several hundred metres in some places. Comparisons of the simulations made with alternative ice-sheet reconstructions will ultimately allow an assessment of the impact of forcing uncertainties on simulated climates.

2.2 PMIP3, PMIP3-CMIP5, PMIP4 and PMIP4-CMIP6 models

The LGM model output analysed here are from the PMIP4-CMIP6 and PMIP3-CMIP5 *lgm* experiments. We use the corresponding *piControl* experiments as a reference, which are termed "PI" throughout the paper. Some of the models, although following the PMIP3-CMIP5 or PMIP4-CMIP6 protocols, did not formally take part in CMIP (i.e. have not performed the DECK experiments for CMIP6 or have not performed other experiments than PMIP experiments for CMIP5). These are referred to as "PMIP3" and "PMIP4" models in Table 1. We will refer to the full ensemble of PMIP3-CMIP5 and PMIP3-non-CMIP5 experiments as the PMIP3 ensemble and similarly for the PMIP4 ensemble. A

Table 1. PMIP3 and PMIP4 models analysed in the present study. The spin-up duration is only given for the new PMIP4-CMIP6 models.

Model	Climate sensitivity (ΔT^{eq})	Reference	Ice duration (years)	Spin-up phase and rip (f)	PMIP/CMIP	Additional comments
CCSM4	2.9	Brady et al. (2013)	PMIP3		PMIP3-CMIP5 r1i1p1	
CNRM-CM5	3.3	Voldoire et al. (2013)	PMIP3		PMIP3-CMIP5 r1i1p1	
COSMOS-ASO	4.1	Raddatz et al. (2007); Budich et al. (2010), Wetzel et al. (2010)	PMIP3		PMIP3 r1i1p1	
FGOALS-g2	4.4	Zheng and Yu (2013)	PMIP3		PMIP3-CMIP5	
GISS-E2-R	2.1	Ullman et al. (2014)	PMIP3		PMIP3-CMIP5 r1i1p150	PMIP3 ice sheet
GISS-E2-R	2.1	Ullman et al. (2014)	PMIP3		PMIP3-CMIP5 r1i1p151	ICE-5G ice extent but lower Laurentide Ice Sheet altitude
IPSL-CM5A-LR	4.1	Dufresne et al. (2013)	PMIP3		PMIP3-CMIP5 r1i1p1	
MIROC-ESM	4.7	Sueyoshi et al. (2013)	PMIP3		PMIP3-CMIP5 r1i1p1	Initial ocean state was taken from PMIP2 MIROC4m
MPI-ESM-P	3.5		PMIP3		PMIP3-CMIP5 r1i1p1	AO, initial state for spin-up from PMIP2 simulation
MPI-ESM-P	3.5	Adloff et al. (2018)	PMIP3		PMIP3-CMIP5 r1i1p2	AOV
MRI-CGCM3	2.6		PMIP3		PMIP3-CMIP5 r1i1p1	
AWI-ESM1-1-LR (short name: AWIESM1)	3.6	Sidorenko et al. (2015), Lohmann et al. (2020)	ICE-6G_C	1300	PMIP4-CMIP6	
AWI-ESM-2-1-LR (short name AWIESM2)	3.6	Sidorenko et al. (2019)	ICE-6G_C	600	PMIP4-CMIP6	
CESM1.2	3.6	Tierney et al. (2020)	ICE-6GC	1800	PMIP4-CMIP6	
UoT-CCSM4	3.2	Peltier and Vettoretti (2014), Chandan and Peltier (2018), Chandan and Peltier (2017)	ICE-6G_C	2900 years	PMIP4-CMIP6	
HadCM3B-M2.1aD	2.7	Valdes et al. (2017)	GLAC-1D ICE-6G_C PMIP3	400 400 2900	PMIP4-CMIP6	All simulations were initialised from a long (> 5000-year) LGM run that used the same model configuration but ICE5G boundary conditions (ice mask, global orography, bathymetry, land–sea mask) and PMIP3 trace gases. The climatologies were calculated from the 100 years following the spin-up period.
iLOVECLIM1.1.4	3.2 (after 2500 years)	Lhardy et al. (2020)	GLAC-1D ICE-6G_C	5000	PMIP4	5000 years from a PI restart; EMIC
iLOVECLIM1.1.4	3.2 (after 2500 years)	Lhardy et al. (2020)	ICE-6G_C	5000	PMIP4	5000 years from a PI restart; EMIC
INM-CM4-8	2.1	Volodin et al. (2018)	ICE-6G_C	50	PMIP4-CMIP6 r1i1p1f1	
IPSLCM5A2		Sepulchre et al. (2020)	ICE-6G_C	1200	PMIP4-CMIP6	Spin-up from *piControl*
MIROC-ES2L	2.7	Ohgaito et al. (2021) Hajima et al. (2020)	ICE-6G_C	8960	PMIP4-CMIP6 r1i1p1f2	First 6760 years integrated using the MIROC-ES2L physical core; following 2200 years integrated using MIROC-ES2L
MPI-ESM1.2	2.77	Mauritsen et al. (2019)	ICE-6G_c	3850	PMIP4-CMIP6 r1i1p1f1	3850 years after restart from a previous *lgm* simulation.

total of 13 PMIP4 LGM simulations are currently available and slightly more than the 11 LGM simulations in PMIP3 (Table 1). The PMIP3 ensemble includes one model that ran an additional sensitivity test to ice-sheet height (GISS-E2R; Ullman et al., 2014) and one model that ran simulations with and without dynamic vegetation (MPI-ESM-P; Adloff et al., 2018). The PMIP4-CMIP6 ensemble includes three simulations made with updated versions of the models that contributed to PMIP3-CMIP5, specifically IPSLCM, MIROC and MPI-ESM (Table 1). However, the IPSL simulation for PMIP4 does not use the latest IPSLCM6 version specifically developed for CMIP6 due to the impossibility to run the *lgm* experiment with this version. Most of the models that have run the PMIP4-CMIP6 LGM simulations are general circulation models (GCMs) but iLOVECLIM is an Earth system model of intermediate complexity, which is considerably faster than the GCMs. The iLOVECLIM and the HadCM3B-M2.1aD GCMs are the only models in the ensemble to have run simulations using different ice-sheet reconstructions (both models ran with ICE-6G_C and GLAC-1D, and HadCM3B-M2.1aD also ran with the PMIP3 ice sheet). The LGM simulations were either initialised from a previous LGM simulation or were spun up from the pre-industrial state. The length of the spin-up therefore varies (Table 1), as does the length of the equilibrium LGM simulation in these preliminary analyses. The INM-CM4-8 results are from the beginning of an *lgm* simulation and the model is not yet fully equilibrated. All other models have run for several millennia. Our preliminary analyses are based on variables available by 14 December 2020. Although several of the PMIP4-CMIP6 models have higher climate sensitivity than the equivalent models in PMIP3-CMIP5, this is not reflected in the ensemble analysed here. In fact, the PMIP4-CMIP6 ensemble, as of December 2020, has lower climate sensitivities than the PMIP3-CMIP5 models (Table 1): equilibrium sensitivities to a CO_2 doubling from pre-industrial values range from 2.1 to 3.6 °C, (mean: 3.0 °C) in the current PMIP4-CMIP6 ensemble, while the range is from 2.1 to 4.7 °C (mean: 3.4 °C) in the PMIP3-CMIP5 ensemble.

All in all, only a minority of models present in the PMIP3 ensemble ran the PMIP4 simulation, so that the PMIP4 ensemble differs from the PMIP3 one because of the update of these models but mostly because it gathers new models compared to PMIP3. This adds up to the change in protocol from PMIP3 to PMIP4 to explain differences in model results between these two phases of PMIP.

2.3 Sources of information on LGM climate

The PMIP3-CMIP5 model simulations were evaluated against two benchmark datasets: pollen-based reconstructions of seasonal temperature (mean annual temperature – MAT, mean temperature of the coldest month – MTCO, mean temperature of the warmest month – MTWA, growing season temperature indexed by growing degree days above a baseline of 0 °C), mean annual precipitation (MAP) and an index of soil moisture (Bartlein et al., 2011); and a compilation of sea-surface temperature (SST) reconstructions (MARGO Project Members, 2009).

In the Bartlein et al. (2011) dataset, reconstructions at individual pollen sites were averaged to produce an estimate for a $2 \times 2°$ grid; reconstruction uncertainties are estimated as a pooled estimate of the standard errors of the original reconstructions for all sites in each grid cell. Although the Bartlein et al. (2011) dataset has good coverage for some regions, coverage was sparse in the tropics, and there were no reconstructions of LGM climate for Australia. Furthermore, not all of the six climate variables were reconstructed at every site, so statistical comparisons were more robust for some variables than others. The majority of the reconstructions included in the Bartlein et al. (2011) dataset used various sorts of statistical calibrations based on modern-day conditions and therefore do not account for the impact that changes in CO_2 have on water-use efficiency and hence plant distribution. Although Bartlein et al. (2011) were unable to demonstrate a statistically significant difference between statistical reconstructions and model-based inversions (which, in principle, account for the CO_2 effect on plant distribution), their analysis focused on the mid-Holocene where the CO_2 effect is small. There is therefore some concern that the dataset may overestimate aridity at the LGM. Reconstructions which incorporate the effect of CO_2 are now available for Australia (Prentice et al., 2017). Cleator et al. (2020) have used 3-D variational data assimilation techniques with a prior derived from the PMIP3-CMIP5 LGM simulations and the Bartlein et al. (2011) and Prentice et al. (2017) pollen-based reconstructions, and incorporating the Prentice et al. (2017) CO_2 correction, to produce a new global reconstruction of terrestrial climate at the LGM. In addition to accounting for potential effects of low CO_2 on moisture variables at the LGM, this reconstruction produces coherent estimates of seasonal climate variables at many more points than the original pollen-based reconstructions and also extends the geographic coverage.

Tierney et al. (2020) provide a new synthesis of geochemical SST data ($U^{K'}_{37}$, TEX_{86}, Mg/Ca and $\delta^{18}O$) from the LGM (defined as the period from 19 000 to 23 000 years ago) and the late Holocene (defined as the period from 4000 years ago to the present) time periods. This compilation builds upon the MARGO Project Members (2009) collection of $U^{K'}_{37}$ and Mg/Ca data by including new studies published since MARGO was released, as well as expanding the collection to include TEX_{86} and $\delta^{18}O$ of foraminifera. The Tierney et al. (2020) synthesis excludes microfossil-based SST estimates, on the basis that these (1) include no-analogue assemblages (Mix et al., 1999); (2) imply warmer-than-present subtropical gyres, an inference that has been questioned (Crowley, 2000; Telford et al., 2013); and (3) lack Bayesian proxy-system models that were required for the data assimilation technique used by Tierney et al. (2020).

Tierney et al. (2020) use the data along with a model prior from the isotope-enabled Community Earth System Model 1.2 (CESM1.2; Brady et al., 2019) to produce a full-field data assimilation product. Here, we use both the data synthesis and the data assimilation products, labelled "Tierney2020" and "Tierney2020DA", respectively. Data from the LGM and late Holocene, respectively, were calibrated using Bayesian models that fully propagate uncertainties (Tierney and Tingley, 2015; Tierney et al., 2018, 2019; Malevich et al., 2019), yielding a 1000-member posterior distribution of SSTs. These data were sorted from low to high along the ensemble dimension, and then random error representative of site-level downcore uncertainty following the Gaussian distribution $\mathcal{N}(0, 0.5\,^{\circ}\mathrm{C})$ was added back to the matrix. This procedure effectively partitions the error variance; i.e. it assumes that at any given site, absolute uncertainty in SST cancels out in the anomaly calculation, while "relative" uncertainty associated with downcore measurement and nonlinearities in the calibration model is preserved. The data were then averaged within a $5^{\circ} \times 5^{\circ}$ grid and differenced. The standard deviation associated with each grid point is calculated from the differenced ensemble dimension.

In the present work, we also use other available reconstructions, all based on at least part of the initial MARGO Project Members (2009) reconstructions at the core sites: all are global reconstructions, obtained from this dataset via different methods, as summarised by Paul et al. (2021). These datasets are from

- Annan and Hargreaves (2013), who use the MARGO Project Members (2009) dataset, the Bartlein et al. (2019) reconstructions on the continents, as well as the PMIP2 model output to generate a reconstruction of the sea-surface temperatures using multiple linear regression;
- Kurahashi-Nakamura et al. (2017), who use the MARGO Project Members (2009) data, benthic δ^{18}O and δ^{13}C data as well as the MIT General Circulation Model (MITgcm) in combination with the method of Lagrange multipliers/adjoint method to generate a global reconstruction;
- Paul et al. (2021), who produced the GLOMAP2020 dataset based on the floral and faunal assemblage data, as well as various sea-ice reconstructions from MARGO Project Members (2009), together with an optimal gridding method called DIVA to produce monthly global reconstructions. A caveat given in Paul et al. (2021) about this reconstruction is that it may be too warm by 0.5 to 1.0 °C due to impacts of changes in seasonality and in the thermal structure of the ocean that are not taken into account in their reconstructions, as well as the impact due to heterogeneous spatial sampling.

These datasets reflect different approaches and choices of initial datasets (only geochemical data for the Tierney et al. (2020) reconstructions, for which the sites are often close to the coasts or only floral and faunal assemblages for GLOMAP2020), which yields a range a results with illustrate the uncertainty of the SST reconstructions. A crucial difference between the Tierney et al. (2020) synthesis and the other datasets used here is that the former implies more extensive tropical cooling during the LGM (−2.5 °C vs. −1.5 °C for MARGO, −1.2 °C for GLOMAP2020, −1.6 °C for Annan and Hargreaves, 2013, −1.7 °C for Kurahashi-Nakamura et al., 2017). This can be attributed to the exclusion of the microfossil data as well as recalibration of the $U^{K'}_{37}$ proxy with the BAYSPLINE model (Tierney and Tingley, 2018), which corrects for an observed reduced sensitivity of $U^{K'}_{37}$ to SST above approximately 24 °C. The data-assimilated product from Tierney et al. (2020) is even cooler, which might be related to the choice of the global model for the assimilation. A further comparison is presented in Paul et al. (2021).

2.4 Data–model comparisons

We compare the model simulations to paleoclimate data, focusing on large-scale features and regional changes. In these comparisons, the reconstructions are expressed as mean values and the uncertainty by the standard error of the reconstructions. Model outputs were extracted only for the grid cells where there are observations. Model uncertainty is represented by the standard deviation of 10 000 averages over 50 years randomly picked in the ≥ 100-year-long time series of model outputs. Thus, model uncertainty is not, strictly speaking, equivalent to reconstruction uncertainty but merely provides some measure of the variability engendered by sampling the simulated climate.

3 Model results

3.1 Temperature

The global and annual mean temperature in the PMIP4 LGM simulations is between 3.3 and 7.2 °C cooler than the PI simulations (Fig. 1, Table S1). The largest changes in temperature between the LGM and PI simulations (Fig. 2) are found over the Laurentide and Fennoscandian ice sheets, reflecting the significant changes in surface height and albedo caused by the ice sheets. Colder conditions are registered in the northern midlatitudes and high latitudes, partly reflecting the advection of the cold temperature anomalies downwind of the ice sheets. The cooling in the tropics, which results from both the lower atmospheric GHG concentrations and the remote influence of the northern ice sheets, is more muted. As expected, the simulations show larger changes over the land than over ocean. The ratio between the LGM–PI mean surface air temperature anomaly over land and the anomaly over the ocean ranges from 1.0 to 1.6 over the tropics (30° S to 30° N) and from 1.90 to 5.5 for globally averaged temperatures. Zonally averaged temperatures (Fig. 1a) confirm that

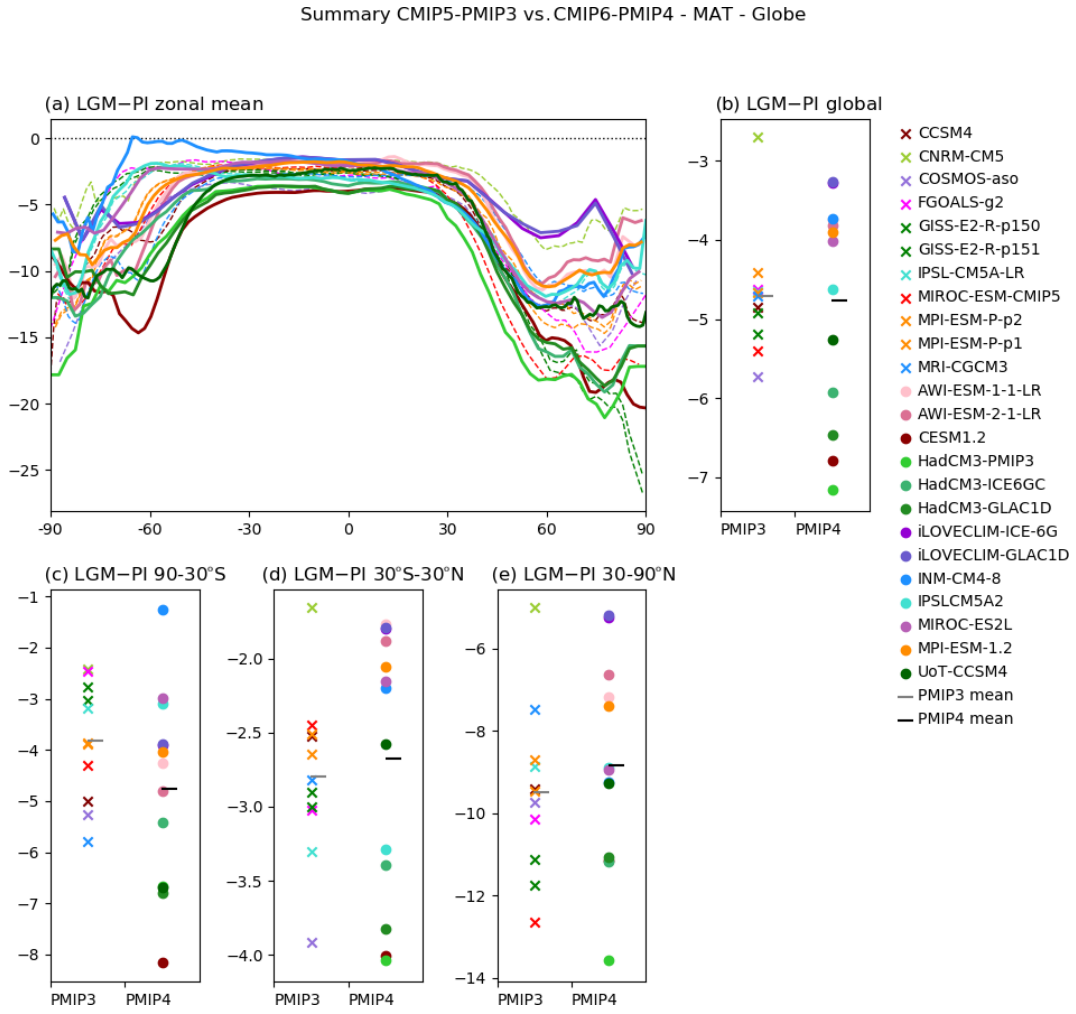

Figure 1. Mean annual surface air temperatures LGM–PI anomalies in °C. **(a)** Zonal means, PMIP3 model results shown as dashed lines, PMIP4 model results shown as thick solid lines; **(b)** global means, PMIP3 model results shown by crosses, PMIP4 models shown by filled circles; averages over **(c)** the southern extratropics (90 to 30° S), **(d)** the tropics (30° S to 30° N) and **(e)** the northern extratropics (30 to 90° N).

the PMIP4 ensemble also shows the expected polar amplification of temperature changes in both the Northern Hemisphere and Southern Hemisphere.

Although the broad-scale patterns of temperature changes are similar, there are differences between the PMIP4 and PMIP3 ensembles. The PMIP4 ensemble average is warmer than the PMIP3 ensemble average (Fig. 2 bottom) over North America, south of the ice sheet, over the Labrador and Nordic Seas and the Tibetan Plateau. On the other hand, the PMIP4 average is colder than the PMIP3 one in regions close to West Antarctica, over some areas of the Laurentide Ice Sheet, over the marine part of the Fennoscandian Ice Sheet and in the North Atlantic and the northern part of the North Pacific. The largest difference between the PMIP3 and PMIP4 averages is over the northern North Atlantic and Nordic Seas, probably reflecting differences in sea-ice cover in these areas. Zonally averaged temperatures (Fig. 1a) show that the PMIP4 global mean annual temperature LGM–PI anomalies spread over a larger range than the PMIP3 ensemble, with a few PMIP4 models (in particular the three HadCM3 simulations and CESM1.2) showing larger cooling than the coldest PMIP3 models. Nonetheless, the multi-model average of the global mean annual temperature LGM–PI anomalies are similar for both ensembles (−4.71 °C for the PMIP3 ensemble, −4.77 °C for the PMIP4 ensemble; see Supplement Table S1).

The northern extratropics are slightly colder in the PMIP3 simulations (multi-model LGM–PI MAT anomaly of −9.5 °C) than in the PMIP4 simulations (multi-model average of −8.8 °C). The minimum cooling and maximum cooling over the PMIP3 and PMIP4 ensembles are also very similar. The PMIP3 and PMIP4 simulations yield similar cooling in the tropics (multi-model average of −2.8 °C for the PMIP3 ensemble and of −2.7 °C for the PMIP4 ensemble, with simi-

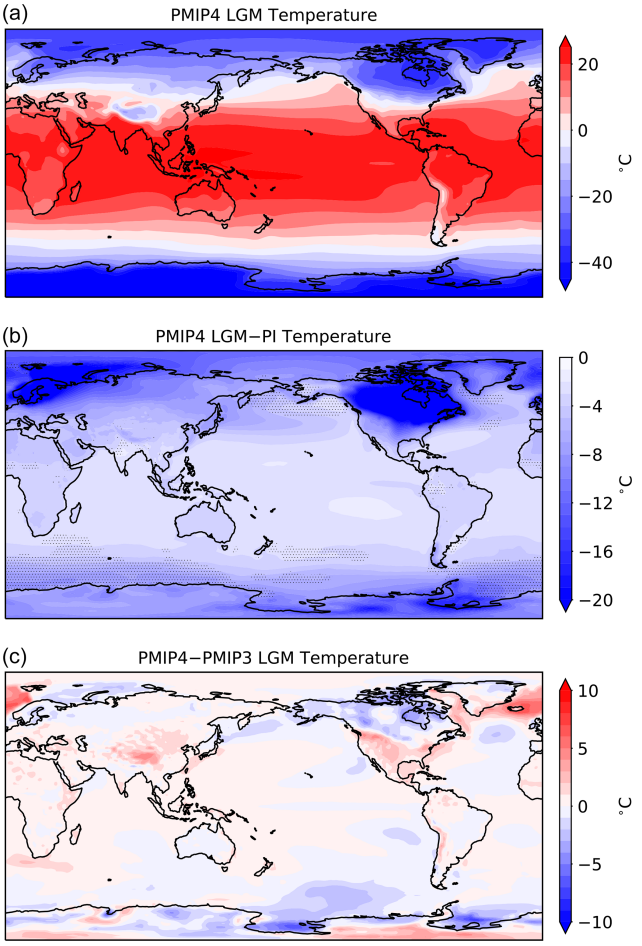

Figure 2. LGM mean annual temperature (in °C) simulated by the ensemble of PMIP4 models **(a)**, LGM–PI mean annual temperature anomaly (in °C) simulated by the same models (middle, where stippling shows where models do not agree on the sign of changes), difference between the PMIP4 and PMIP3 ensembles (in °C, **b**). The PMIP4 average is based on models listed in Table 1, except for iLOVECLIM simulations, which are at lower resolution. The PMIP3 average is based on all PMIP3 models, except the GISS-E2-p151 simulation, which did not use the PMIP3 ice sheet for its boundary conditions.

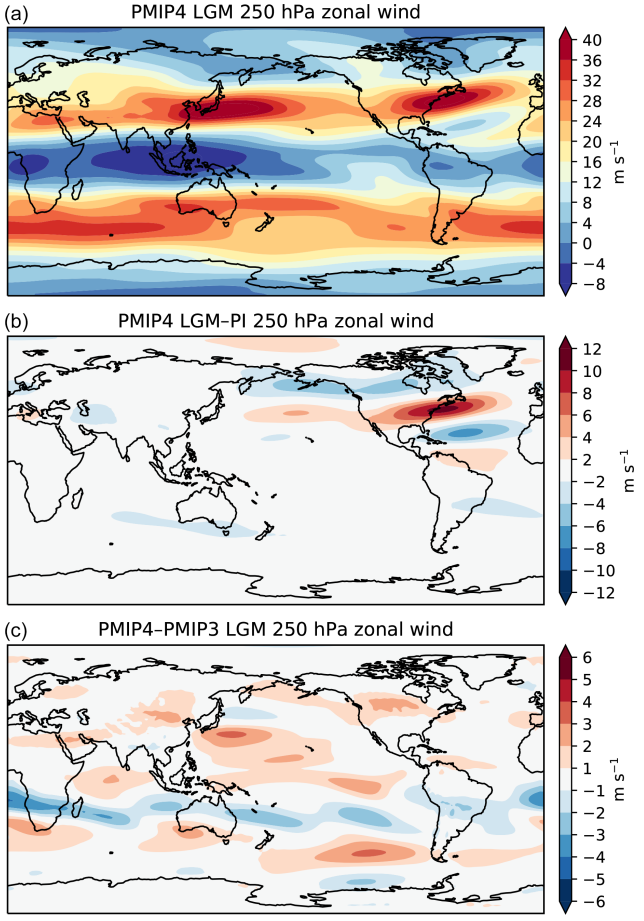

Figure 3. Same as Fig. 2 but for the 250 hPa zonal wind. The PMIP4 average is based on all models listed in Table 1. The PMIP3 average is based on all PMIP3 models in Table 1, except the GISS-E2-p151 simulation, which did not use the PMIP3 ice sheet for its boundary conditions.

lar minima and maxima; see Table S1). However, the cooling of the southern extratropics is more variable in the PMIP4 simulations (−1.2 to approximately −8.15 °C) than in the PMIP3 simulations (−2.4 to approximately −5.8 °C), and its multi-model average is larger for the PMIP4 ensemble (−4.8 °C, compared to −2.8 °C for the PMIP3 ensemble). Therefore, most of the difference in the global average cooling, which ranges from −3.3 to −7.2 °C in the PMIP4 simulations and between −2.7 and −5.7 °C in the PMIP3 simulations, stems from differences in the simulated temperatures over the Southern Hemisphere. It is difficult to assign these differences between the PMIP3 and PMIP4 ensembles to a single reason, since both models and protocols have changed between these two phases. Sensitivity experiments and in-depth study of the experiments carried out with the PMIP3 and PMIP4 protocols but with the same models will be necessary to disentangle the reasons for the differences between the PMIP3 and PMIP4 results. It is in fact rather intriguing that the average cooling over the North American ice sheet is larger in the PMIP4 ensemble, given that both the ICE-6G_C and the GLAC-1D reconstructions yield significantly lower altitudes than the PMIP3 ice-sheet reconstruction, used in all the PMIP3 experiments.

3.2 Atmospheric and oceanic circulation

The PMIP4-CMIP6 models simulate large changes in the Northern Hemisphere upper tropospheric atmospheric circulation (Fig. 3), in response to LGM boundary conditions, in particular over North America and the North Atlantic. The North Atlantic jet stream is narrower and stronger compared to the PI, as shown by an increase reaching more than

$10\,m\,s^{-1}$ in the 250 hPa zonal wind south of the Laurentide Ice Sheet and extending into the North Atlantic, and a decrease in zonal wind to the northwest and southeast of these regions. The strengthening and narrowing of the North Atlantic jet stream was also a characteristic of the PMIP3-CMIP5 simulations (Beghin et al., 2016). However, in the PMIP4-CMIP6 simulations, the jet stream extends further north than in the PMIP3 simulations (Fig. 3, bottom), most prominently near the Laurentide Ice Sheet. This could be because the Laurentide Ice Sheet is lower in the ICE-6G reconstruction than the ice sheet used in the PMIP3-CMIP5 simulations (see, e.g. Ullman et al., 2014; Beghin et al., 2015; Lofverstom et al., 2016) but may also reflect changes in the representation of the zonal winds between the two sets of simulations. This is supported by the fact that there are differences between the PMIP3-CMIP5 and PMIP4 simulations away from the Laurentide Ice Sheet, in particular over the Southern Ocean, where the jet stream is also located more poleward in the PMIP4 than the PMIP3 simulations. Sensitivity experiments using the PMIP3-CMIP5 ice sheets with PMIP4 models, as planned in the PMIP4 LGM experiment protocol (Kageyama et al., 2017), should help resolve the question of whether differences in model treatment or boundary conditions are responsible for the differences in atmospheric circulation between the two ensembles.

The extent of the NADW cell (identified in Fig. 4 by the depths for which the Atlantic meridional overturning streamfunction at 30° N is positive) simulated by PMIP4 models is very similar for LGM and PI, except for iLOVECLIM and IPSLCM5A2, which show a very large deepening of the NADW cell for LGM (Fig. 4). Two of the PMIP4-CMIP6 models (INM-CM4-8 and MIROC-ES2L) show a deep NADW cell reaching the ocean floor in the North Atlantic, whereas five of the PMIP4-CMIP6 models (MPI-ESM1.2, UoT-CCSM4, AWIESM2, CESM1.2, HadCM3) simulate a clear AABW in the North Atlantic. UoT-CCSM4 and CESM1.2 even shows a shallowing of the NADW cell for LGM. The intrusion of AABW cell (defined by negative values in the Atlantic meridional overturning streamfunction at 30° N) into the North Atlantic was shown by some of the PMIP3-CMIP5 simulations (CCSM4, MPI-ESM-1.0P) but not as much as the PMIP4 simulations (AWIESM2, CESM1.2, MPI-ESM-1.2, UoT-CCSM4 and the three HadCM3 simulations, Fig. 4 and Muglia and Schmittner, 2015). Five of the PMIP3-CMIP5 models produced a NADW cell reaching the ocean floor in the North Atlantic and only two had extensive AABW. The maximum strength of the NADW cell itself strengthens in all of the PMIP4 simulations by as much as 11 Sv for IPSLCM5A2. This strengthening is consistent with PMIP3-CMIP5 results and is likely to be associated with the vigorous surface wind over the northern North Atlantic (Muglia and Schmittner, 2015; Sherriff-Tadano and Abe-Ouchi, 2020) and the closure of the Bering Strait (Hu et al., 2015). The strength of the AMOC reduces south of 30° N in UoT-CCSM4 (see Supplement Fig. S2). iLOVECLIM performed simulations of LGM with two different ice-sheet reconstructions (ICE6G, GLAC1D) and shows a weaker NADW cell in GLAC-1D than that produced by ICE-6G_C (Fig. 4). This weakening is likely to be associated with a lower topography of the ice sheet of GLAC1D (e.g. Zhang et al., 2014). On the other hand, HadCM3 was used with the PMIP3, ICE-6G_C and GLAC-1D ice sheets, and the results in terms of AMOC are very similar for the ICE-6G_C and GLAC-1D ice sheets, for which the AMOC slightly strengthens compared to PI, while the AMOC is similar to the PI one for the simulation using the PMIP3 ice sheet.

These circulation changes in the Atlantic Ocean are reflected in the total ocean heat transport (Fig. 5, bottom, the PMIP4 results available for this analysis are from all simulations but the HadCM3 simulations). MPI-ESM1.2 simulates an increase in northward ocean heat transport at all latitudes for the LGM compared to PI, while MIROC-ES2L simulates an increase in this transport from 15° S to 60° N. UoT-CCSM4 and CESM1.2 are the only models simulating a decrease in northward heat transport over a significant range of latitudes, from 50° S to 70° N, in the *lgm* run compared to the *piControl* one. INCM4-CM4-8 simulates increased ocean transport south of 20° N. IPSLCM5A2's ocean transport decreases south of 30° S and between the Equator and 30° N but significantly increases in the southern tropics. All PMIP4 models simulate an increase in northward atmospheric heat transport, in the tropics and up to 50° N, in the *lgm* simulation compared to *piControl*. MIROC-ES2L simulates an increase up to 70° N (Fig. 5, middle). In summary, all models simulate an increase, in their *lgm* run compared to *piControl*, in northward heat transport (Fig. 5, top) in the tropics and northern midlatitudes, although in the UoT-CCSM4 and CESM1.2 models the increase is confined between ∼ 10 and 50° N. This increase in northward heat transport in the tropics and northern midlatitudes during the LGM as compared to PI was also simulated by most PMIP3-CMIP5 models. Given that the magnitude of the heat transport increase is similar in the PMIP4 and PMIP3-CMIP6 simulations, the warmer temperatures at high northern latitudes in the PMIP4-CMIP6 simulations cannot be due to differences in northward ocean heat transport.

3.3 Hydrological cycle

The large-scale gradients in precipitation are similar in the multi-model average of the PMIP4 LGM and PI simulations (Fig. 6, top left), with maximum precipitation in the tropics (Intertropical Convergence Zone (ITCZ) and monsoon regions) and secondary maxima in the midlatitudes, corresponding to the position of the North Pacific, North Atlantic and Southern Ocean storm tracks. The PMIP4 models show a decrease in precipitation between the LGM and PI in all these high-precipitation areas (Fig. 6, bottom left and Fig. 7, top left). There are some regions where precipitation increases

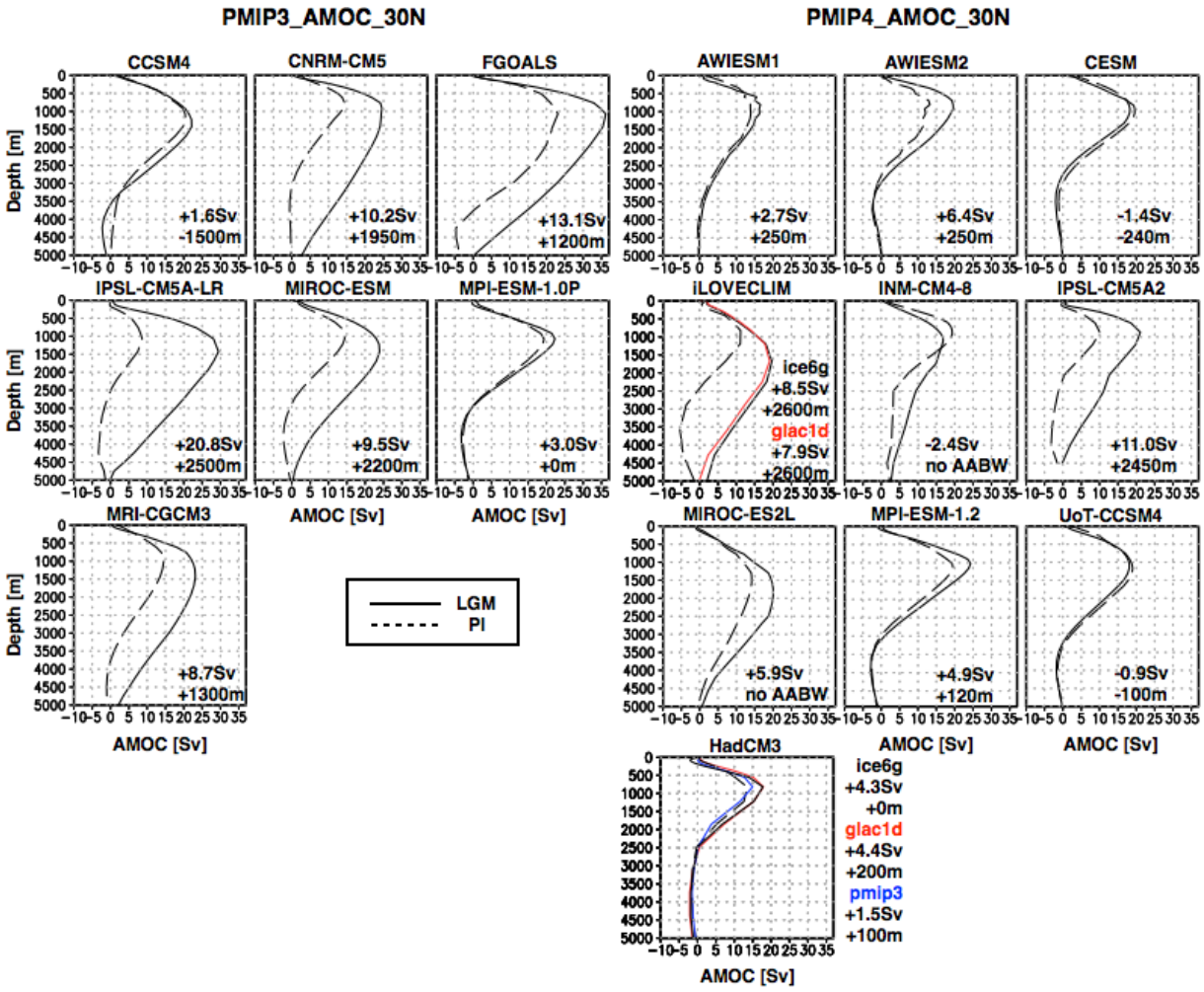

Figure 4. Mean Atlantic Meridional Overturning Circulation (mean meridional stream function for the Atlantic Ocean at 30° N) simulated by the PMIP3 and PMIP4 models for PI and LGM. Numbers in Sv indicate the LGM–PI anomaly in terms of maximum Atlantic meridional overturning streamfunction. Numbers in metres indicate the LGM–PI anomaly in terms of NADW vertical extension, the NADW vertical extent being defined here as the depths over which the mean meridional stream function for the Atlantic Ocean at 30° N is positive.

during the LGM compared to the PI: at least nine PMIP4 models (as shown by the areas which are not stippled) show more precipitation over the subtropical Pacific Ocean and to the south of the Laurentide Ice Sheet, over southern Africa and over the Iberian Peninsula, and some simulate an increase in precipitation over the northern and southern subtropical zones in the Pacific and over the southern subtropical zone in the Atlantic. However, the areas with decreased precipitation are much more extensive than areas with increased precipitation, so zonal averages for the southern extratropics, tropics and northern extratropics (Fig. 7) all show a decrease in precipitation.

The broad-scale patterns of change in precipitation in the PMIP4 simulations are similar to those found in the PMIP3-CMIP5 simulations (Fig. 7, top left). However, the PMIP4 multi-model average is drier than the PMIP3-CMIP5 one (Fig. 6) at the global scale as well as for the southern extratropics and for the tropics. It is similar for both ensembles for the northern extratropics. The geographic patterning in the precipitation changes between the PMIP4 and PMIP3-CMIP5 ensembles (Fig. 6, top right) are complex, particularly in the tropical where the wetter–drier–wetter pattern in the meridional direction suggests differences in ITCZ representation between the two generations of models. This is confirmed by the same figure drawn for the PI (Fig. 6, bottom right), which shows very similar patterns in the PMIP3 vs. PMIP4 anomalies. Both ensembles show a consistent decrease in zonally averaged precipitation in the southern and northern extratropics (Fig. 7). As for the mean annual temperature, the simulated range of precipitation changes is larger for PMIP4 ensemble compared to the PMIP3 one, except for the northern extratropics for which both ensembles show a similar range (Figs. 7 and 2).

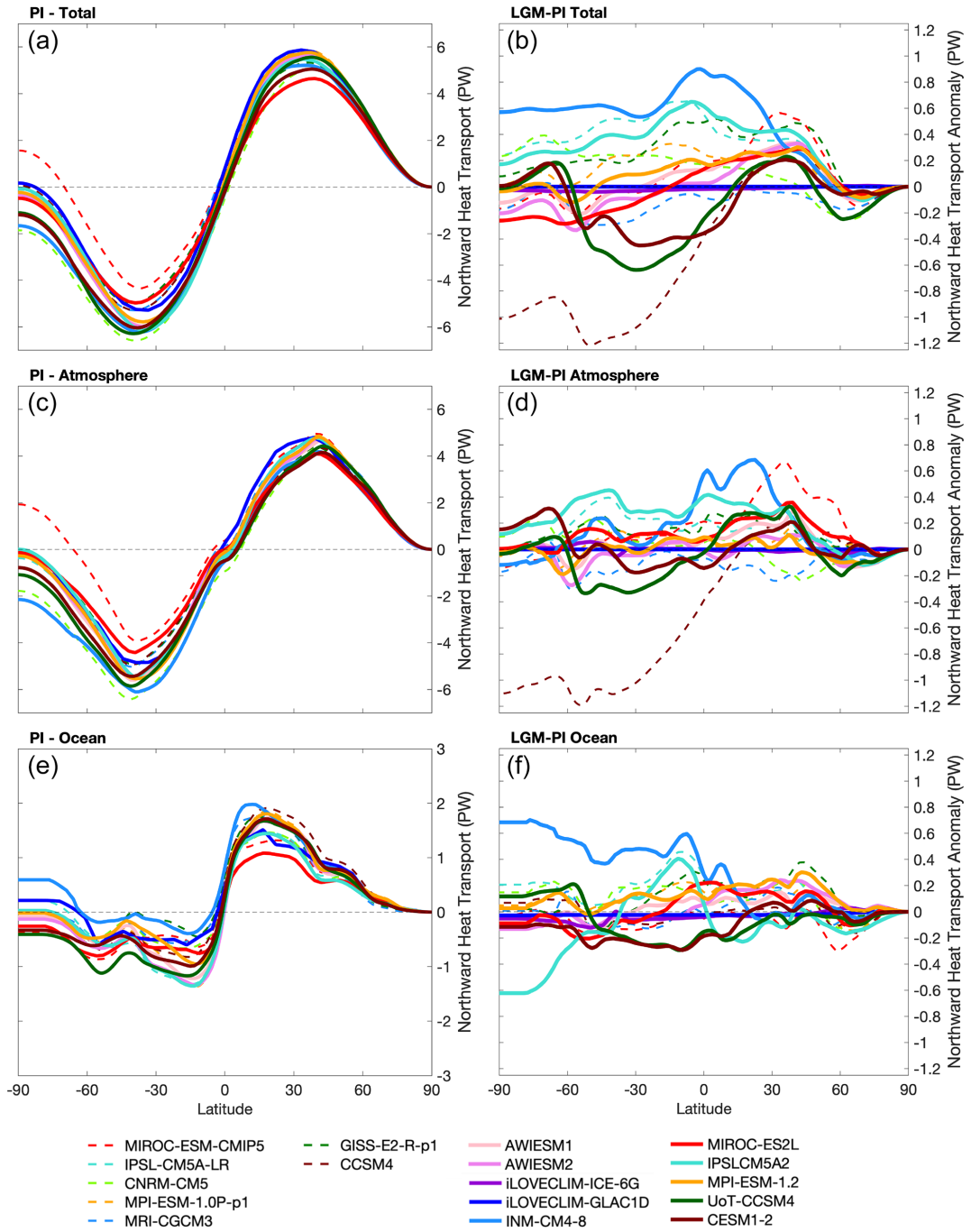

Figure 5. Meridional energy transport for the PI reference state (left-hand side) and LGM–PI anomaly (right-hand side). **(a, b)** Total energy transport, **(c, d)** atmospheric energy transport, **(e, f)** oceanic energy transport.

Evapotranspiration patterns in the PMIP4 LGM and PI simulations are characterised by maximum values in the subtropics and decrease towards high latitudes. The models simulate a global decrease in LGM evapotranspiration relative to the PI that strongly peaks over and around the Northern Hemisphere ice sheets (Fig. 8, left). These results are in agreement with the broad patterns of the PMIP3-CMIP5 ensemble, except for a stronger decrease in evaporation in the northern North Atlantic, which corresponds to the larger average cooling in these regions in the PMIP4 ensemble compared to the PMIP3 ensemble. As a result, net precipitation (precipitation minus evapotranspiration) in the PMIP4 ensemble is higher during the LGM than the PI in the extratropics – particularly over the midlatitude eastern Pacific in

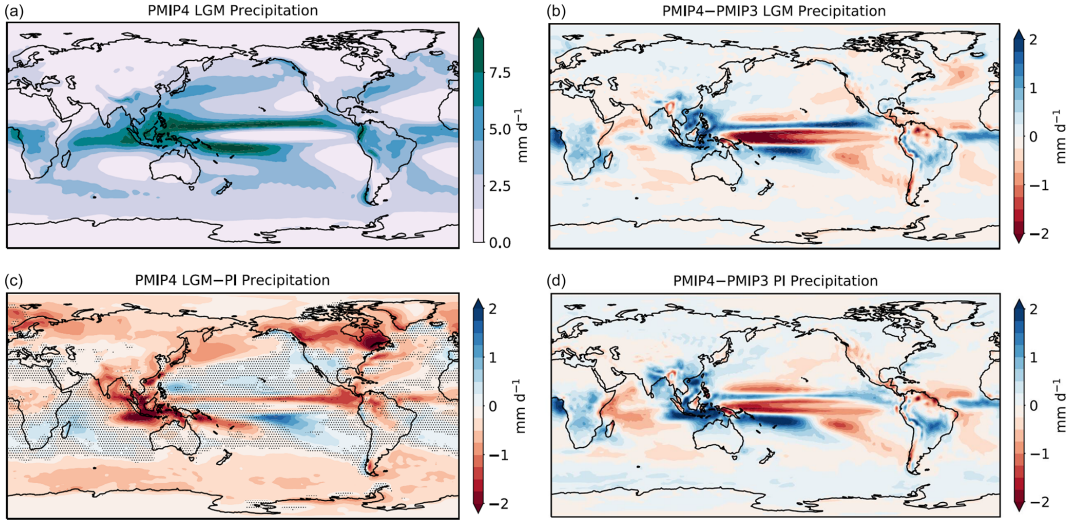

Figure 6. **(a, b)** PMIP4-CMIP6 multi-model LGM mean annual precipitation in mm d^{-1}. **(c)** PMIP4-CMIP6 multi-model LGM–PI mean annual precipitation anomaly (mm d^{-1}) with stippling showing areas where less than nine models agree on the sign of change. **(b)** Difference between the PMIP4-CMIP6 and the PMIP3 multi-model means of the LGM mean annual precipitation (mm d^{-1}). **(d)** Difference between the PMIP4-CMIP6 and the PMIP3 multi-model means of the PI mean annual precipitation (mm d^{-1}).

both hemispheres and over most of North America – with the exception of the North Atlantic, where evaporation decreases are more localised and do not compensate for the reductions in precipitation (Fig. 8, right). This, together with colder temperatures, could help explain why the PMIP4 models simulate a stronger AMOC at the LGM. Substantial reductions in continental net precipitation only occur over tropical South America and high-latitude regions, over the Labrador Sea and its surrounding ice sheets, while Africa, Australia and the midlatitude regions of Eurasia and the Americas see little change or even increased net precipitation.

4 Data–model comparisons

The evaluation of the PMIP3-CMIP5 LGM simulations showed that large-scale climate features, such as the ratio of changes in land–sea temperature, high-latitude temperature amplification and precipitation scaling with temperature, were broadly consistent with modern observations (Braconnot et al., 2012; Izumi et al., 2013; Harrison et al., 2014, 2015).

All PMIP3 and PMIP4 models simulate larger cooling over land than over oceans, on average for the tropics and for the globe. Figure 10 shows averages of model output sampled at sites for which there are reconstructions compared to the averages of the reconstructed values. Since the different reconstructions do not cover the same sites, the averages of the model values at reconstruction sites differ slightly for each dataset. However, for all datasets, the multi-model relationship between the average cooling over land and that over the ocean is approximately linear. Figure 10 allows a comparison between model output and reconstructions averaged over land and over oceans, as well as a comparison of the ratio of the land cooling over the ocean cooling. Although the Cleator et al. (2020) dataset has a larger spatial coverage than the Bartlein et al. (2011) dataset, there is no significant difference between the two datasets for most of the temperature variables across common grid cells (Fig. 9). However, the new reconstructions have a reduced range at the warm end, especially between 0 and 40° N, so that for the averages over the tropics, most simulations are recorded as within or warmer than the land-based reconstructions, while they are within or colder than the Bartlein et al. (2011) reconstructions (Fig. 10, left-hand side). The results for the global averages are fairly consistent for both land-based reconstructions (Fig. 10, right-hand side) but the uncertainty is smaller for the Cleator et al. (2020) dataset. All in all, there are as many simulations within the range of globally averaged reconstructed temperatures of Cleator et al. (2020) as that of Bartlein et al. (2011) but the models outside this range tend to be on the warm side for the Cleator et al. (2020) dataset and both on the warm and cold sides for the Bartlein et al. (2011) dataset.

The reconstructions of the LGM–Late Holocene SST anomalies provided by Tierney et al. (2020) are colder than the MARGO reconstructions in the tropics, and although this removes the apparent cold-bias shown by some simulations, this results in some simulations falling outside the window of reconstructed SSTs at the warm end. This is even more the case if we compare the results to the data-assimilated product from Tierney et al. (2020), which has a global coverage (Fig. 10, left-hand side, bottom line). The results from this latter dataset contrast the results from other global products, as shown in Supplement Fig. S3. These other global datasets (Annan and Hargreaves, 2013; Kurahashi-Nakamura et al.,

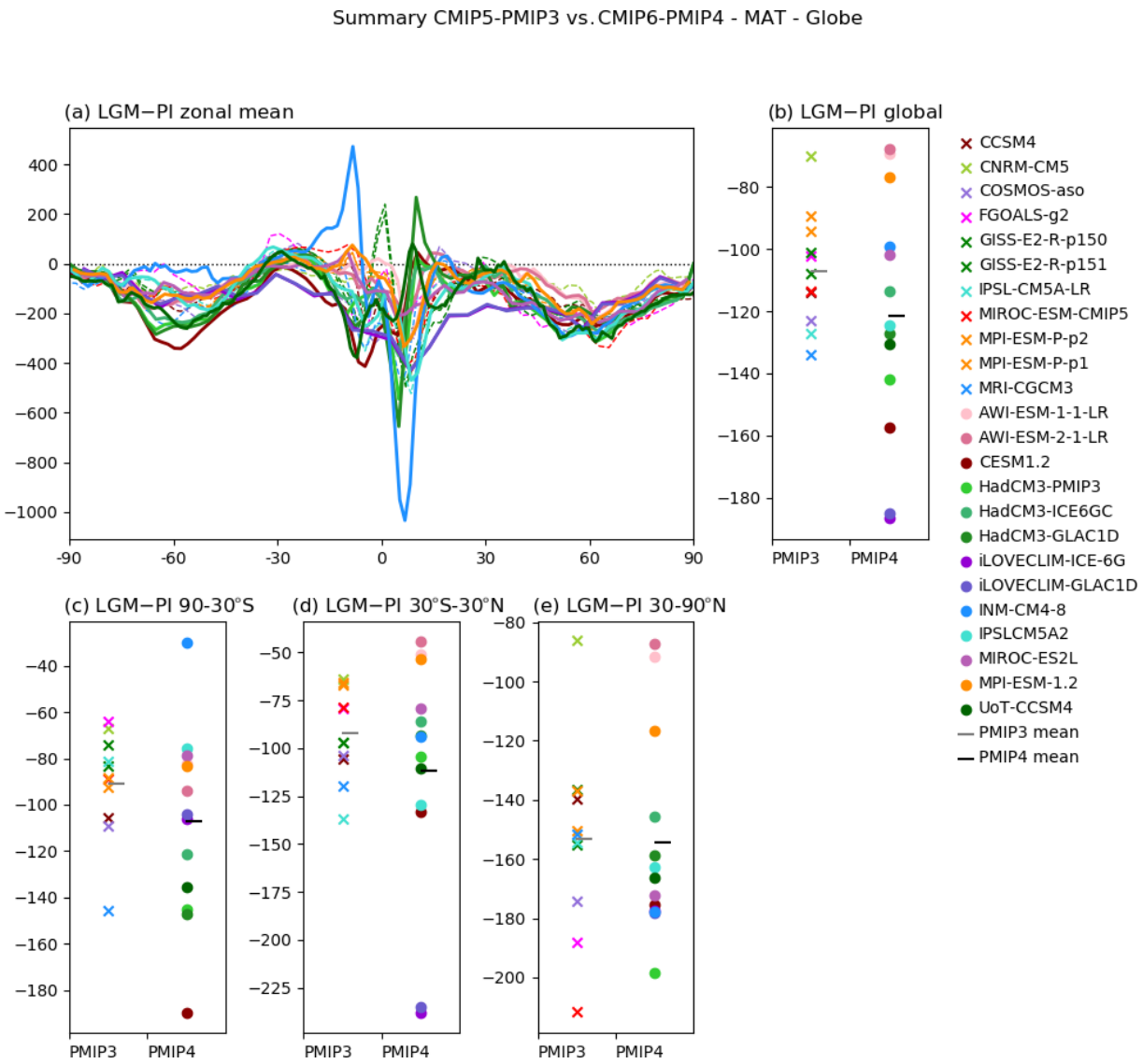

Figure 7. Same as Fig. 1 for mean annual precipitation in mm yr^{-1}.

2017; GLOMAP2020 from Paul et al., 2021) are all derived, at least in part, from the MARGO Project Members (2009) dataset, which might explain their overall consistency with the averages estimated by MARGO Project Members (2009). We have added the warmest estimate (GLOMAP2020) which includes uncertainties in Fig. 10 to obtain a more complete view of the available reconstructions as of 2020, keeping in mind that the authors of the GLOMAP2020 reconstruction estimate that it could be biased by 0.5 to 1.0 °C in the tropics. The simulated mean annual surface air temperature decreases over the tropical oceans stand between these two extremes. This illustrates that model-related uncertainties are comparable with the uncertainties raising from the multiple approaches taken to reconstruct both the continental and oceanic temperatures.

The ratio for the land–sea difference in changes in mean annual temperature in the tropics in the PMIP4 simulations is compatible with the ratio reconstructed from the Bartlein et al. (2011) and MARGO Project Members (2009) datasets. This is also the case if we consider the more recent reconstructions by Cleator et al. (2020) and Tierney et al. (2020), although the multi-model land–sea ratio appears to be smaller than that suggested by the reconstructions. This is the case for both the tropical and global averages. However, it would not be compatible with a land–sea contrast based on the Cleator et al. (2020) dataset and the GLOMAP2020 dataset, even if the warm bias pointed by its authors is taken into account. We are therefore left with large uncertainties on the topic of LGM cooling over land and oceans, from the reconstructions as well as from the models. The uncertainties based on the ensemble of model results and

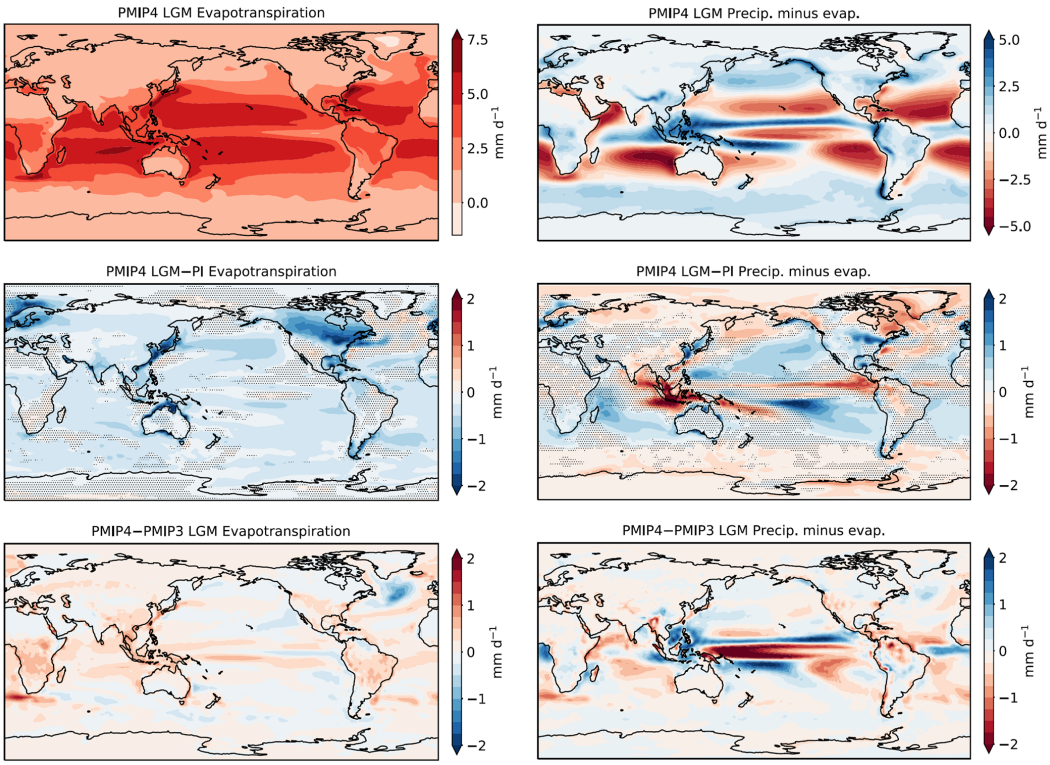

Figure 8. Same as Fig. 2 for mean annual evaporation (left-hand side) and mean annual net precipitation (precipitation–evaporation, right-hand side). All values are in mm d^{-1}. Stippling shows areas where less than nine models agree on the sign of change.

on the ensemble of continental and marine reconstructions are actually very similar.

The amplification of temperature changes at high northern latitudes compared to the tropics is apparent over both the land and the ocean domains, although the amplification appears to be smaller in the new data syntheses (Fig. 11), except of the Tierney et al. (2020) data-assimilated product. For the ocean domain, this could reflect the influence of seasonal production on the extratropical sites, with indicators being more sensitive to summer changes or to changes in the seasonal production cycle. Comparisons of the amplification over land areas with the Bartlein et al. (2011) dataset suggest that the simulated tropical cooling is too large in the PMIP3-CMIP5 simulations, whereas the extratropical cooling was both larger and smaller than that suggested by the reconstructions in both ensembles. Simulated tropical temperatures are more consistent with or warmer than the Cleator et al. (2020) reconstructions, suggesting that the apparent overestimation of tropical cooling in the PMIP3-CMIP5 simulations over land may reflect the paucity of tropical data points in Bartlein et al. (2011). However, the discrepancies between the simulated and reconstructed extratropical land temperatures are still present: there are several PMIP3 and PMIP4 simulations that are much colder than the reconstructions and many which are warmer than the reconstructions. Although polar amplification is more muted over the ocean domain, the comparisons show a similar picture to the land-based comparisons. Simulated tropical ocean temperatures are more compatible with the Tierney et al. (2020) than the MARGO Project Members (2009) synthesis. Simulated extratropical temperature changes in the PMIP3-CMIP5 ensemble mean are considerably colder than those shown by either of these syntheses, but most tend to be on the warm side of the Tierney et al. (2020) data-assimilated product.

The LGM climate is characterised by an increase in temperature seasonality in extratropical regions, with larger changes in winter than in summer (Izumi et al., 2013). This is confirmed by the Cleator et al. (2020) reconstructions. In general, this change in seasonality is reproduced by the models, although the ranges of PMIP4 results for winter are less distinct from their summer counterparts than for the PMIP3 models. The multi-model average seasonality is, however, increased for both ensembles. The simulated cooling in winter temperature is smaller than that indicated by the Bartlein et al. (2011) reconstructions (Fig. 12, top line). This is not the case compared to the Cleator et al. (2020) reconstructions, with which more models are in agreement, except for western Europe, which remains a region of model–data discrepancy. The magnitude of the summer cooling is more consistent between the PMIP4 simulations and the Cleator et al. (2020) reconstructions than between the PMIP3 simulations and the Bartlein et al. (2011) reconstructions in North America, Eu-

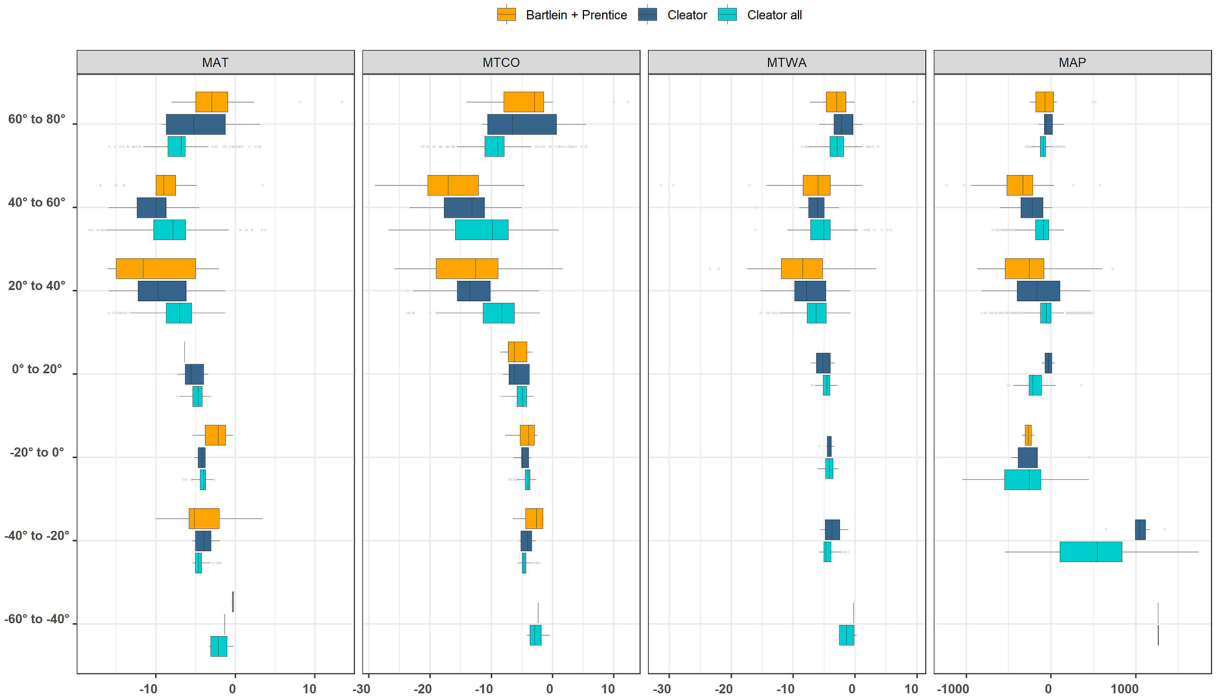

Figure 9. Comparison of terrestrial climate variables from the combined Bartlein et al. (2011) and Prentice et al. (2017) dataset and from the Cleator et al. (2020) reconstruction using data assimilation, averaged over 20° latitudinal bands. The variables are mean annual temperature (MAT), mean temperature of the coldest month (MTCO), mean temperature of the warmest month (MTWA) and mean annual precipitation (MAP). The orange boxplots show the results from the Bartlein et al. (2011) and Prentice et al. (2017) combined dataset, the dark blue boxplots for the reconstructions by Cleator et al. (2020) at sites for which there are reconstructions in the combined dataset, and the green boxplots show the results for the full reconstructions from Cleator et al. (2020).

rope and extratropical Eurasia. Finally, the North Atlantic mean annual cooling simulated by the PMIP4 models spans a larger range that of the PMIP3 ensemble. While the PMIP3 ensemble mean showed temperatures within or above the reconstructed ranges from all oceanic datasets, the PMIP4 ensemble average stands within the range of the reconstructions, with six individual models being within this range, four above and three below. It is therefore quite difficult to determine the cause of the discrepancy in western Europe winter temperatures, which was previously assigned to an underestimation of the North Atlantic cooling. Some of the PMIP4 simulations are in fact much colder over both the North Atlantic and western Europe, and could be studied to further disentangle this model–data disagreement.

Regional changes in the tropics (Fig. 12, bottom line) are more muted than those in the northern extratropics, and seasonality differences are small. We therefore base our comparisons on the mean annual temperature and mean annual precipitation. Both PMIP3 and PMIP4 multi-model averages underestimate MAT cooling over tropical America, which is consistent for both reconstructions. More PMIP4 results stand within the reconstructed range over tropical America. Over tropical Africa, the PMIP3 models were broadly consistent with the Barltein et al. (2011) reconstructed MAP anomaly but underestimate this cooling if we refer to the more recent Cleator et al. (2020) reconstructions. This is also the case for the PMIP4 models, but four simulations (IPSLCM5A2 and the three HadCM3 simulations) are now within the reconstructed range. This is probably related to the simulated tropical SSTs being colder in these simulations. The reconstructed changes in tropical precipitation over America are larger in the Cleator et al. (2020) dataset than in Bartlein et al. (2011), and both PMIP3 and PMIP4 models underestimate the reconstructed drying (Fig. 12). The PMIP4 models, however, all simulate the correct negative sign of the reconstructed precipitation change. There is a large difference between the estimates of precipitation change given by the Bartlein et al. (2011) and the Cleator et al. (2019) datasets for tropical Africa, with the Cleator et al. (2020) reconstructions reducing the drying reconstructed by Bartlein et al. (2011). The ranges of PMIP3 and PMIP4 results are broadly similar over this region, and there are the same number of models (four) within the reconstructed range of Cleator et al. (2020), while no model result was compatible with the Bartlein et al. (2011) reconstructions. All other models underestimate the change or even simulate an increase in precipitation. All in all, the simulated changes in precipitation are therefore more consistent with the newer dataset. Thus, there is no systematic improvement in the sim-

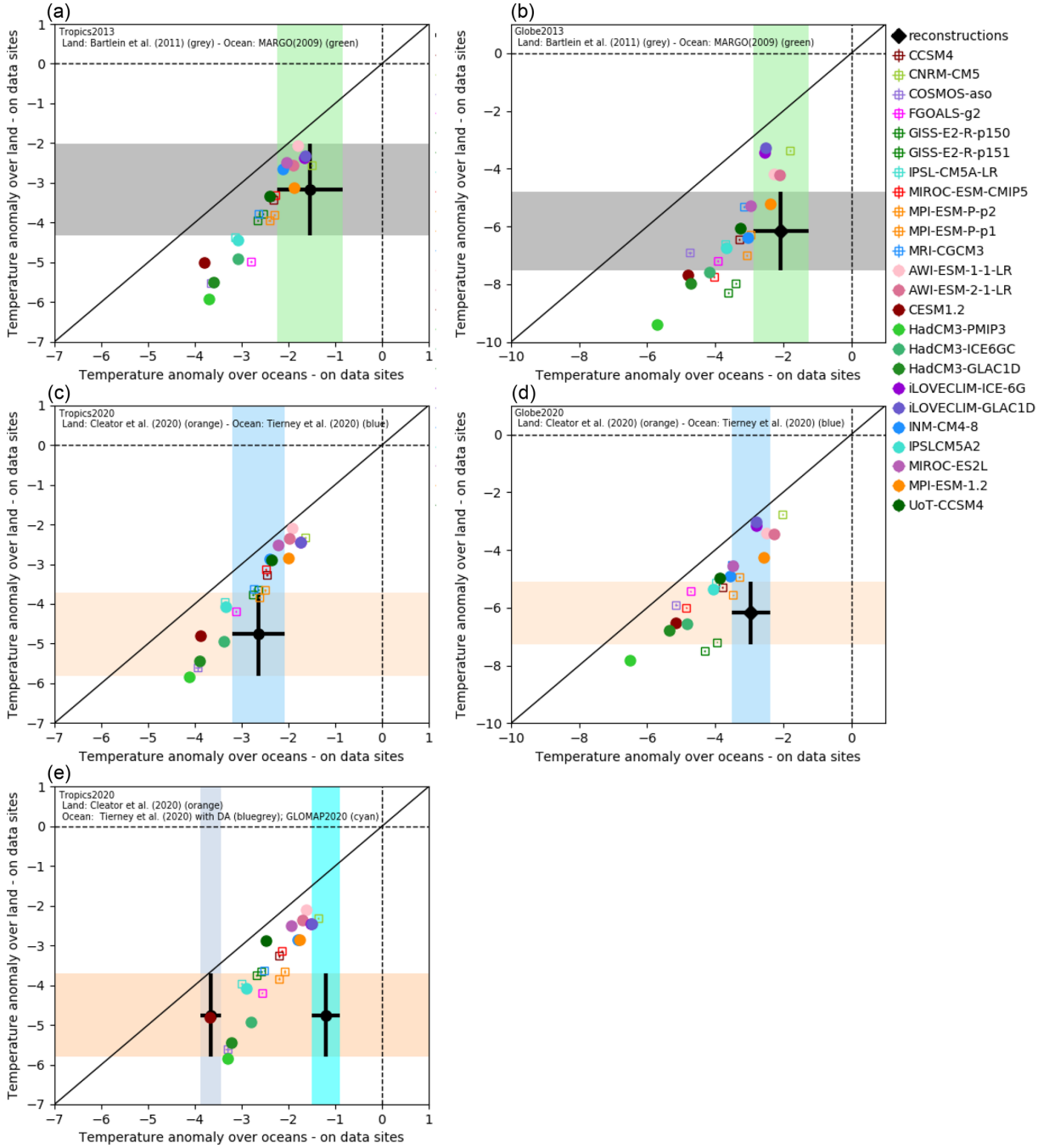

Figure 10. LGM–PI mean annual temperature anomaly over land vs. LGM–PI mean annual temperature anomaly over oceans, averaged over the tropics (30° S–30° N, left-hand side) and over the globe (right-hand side). The model output considered for the averages is taken only on grid points for which there are reconstructions. The top plots are based on the reconstructions used to evaluate the PMIP3-CMIP5 models: the Bartlein et al. (2020) database and the MARGO (2009) SST reconstructions. The bottom plots are based on the most recent reconstructions: Cleator et al. (2020) for terrestrial data and Tierney et al. (2020) for the SSTs.

ulation of tropical climates between the PMIP4 and PMIP3 ensembles.

The six data syntheses can be used to try and constrain the global MAT change from LGM to PI. There is a good correlation between the change in global average MAT over the reconstruction grid points and computed taking all the model grid points into account (Fig. 13). The idea here is therefore to take advantage of this relationship to obtain a range in the global MAT anomaly from the reconstructions. There are models with results below, within and above

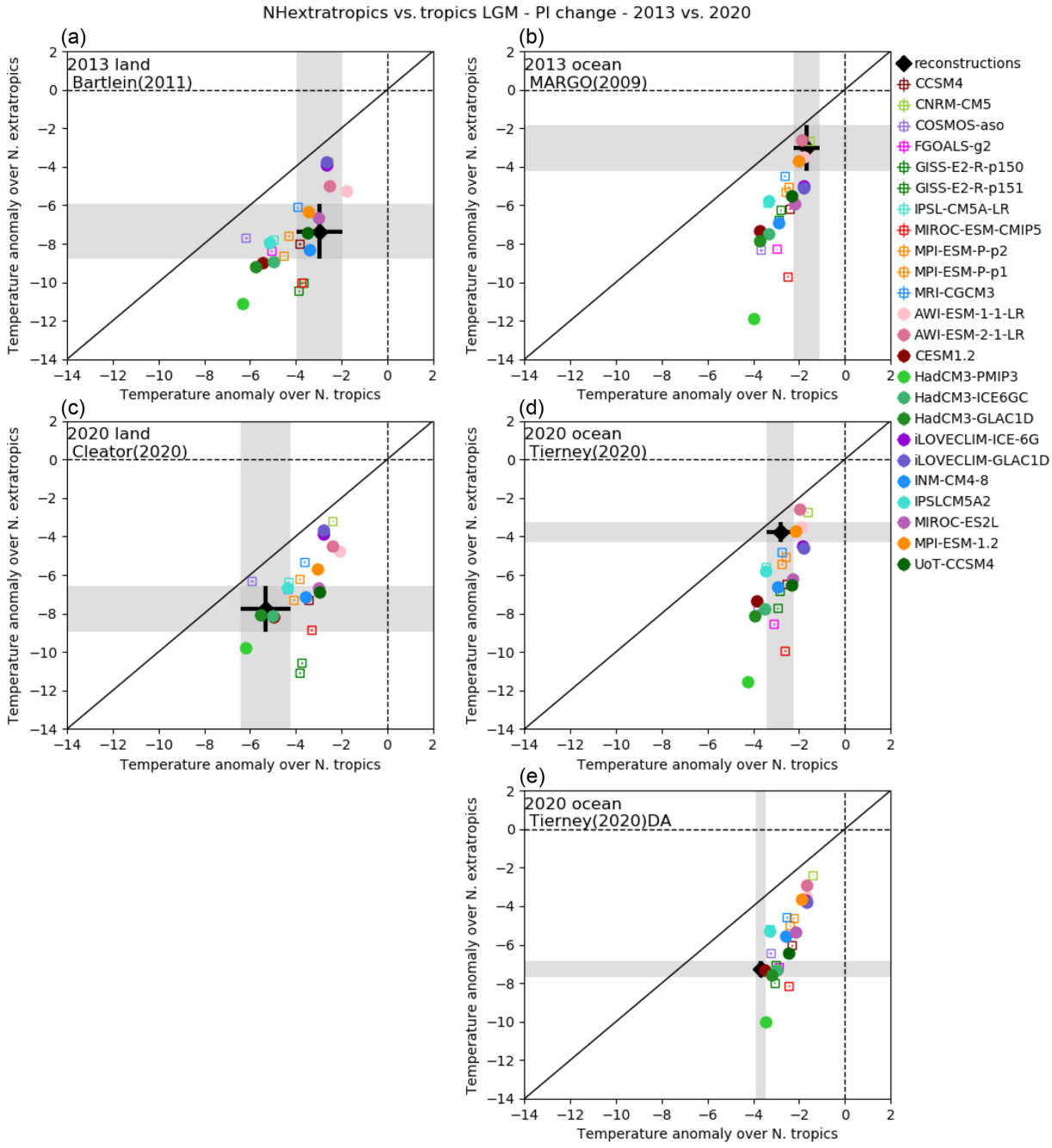

Figure 11. LGM–PI mean annual temperature anomaly over the northern extratropics (30–90° N) vs. over the northern tropics (0–30° N). The model output considered for the averages is taken only on grid points for which there are reconstructions. The four panels are based on the data syntheses of Bartlein et al. (2011) **(a)**, MARGO Project Members (2009) **(b)**, Cleator et al. (2020) **(c)** and Tierney et al. (2020) **(d–e)**.

the average of all of the reconstructions, except MARGO Project Members (2009) and GLOMAP2020, for which no model simulates MAT LGM–PI anomalies above the reconstructed range of values. Retaining only the models which produce changes in MAT consistent with the reconstructions (and reconstruction uncertainty), the globally averaged change in MAT is between −5.7 and −3.7 °C using the Bartlein et al. (2011), between −6.7 and −4.6 °C using the Cleator et al. (2020) datasets, between −4.7 and −3.3 °C for the Tierney et al. (2020) dataset and above −3.9 and −4.4 °C for the MARGO Project Members (2009) and GLOMAP2020 datasets, respectively. Taken altogether, these estimates span a larger range than previous estimates, which indicate changes in MAT of between 4 and 6 °C (Annan and Hargreaves, 2015; Friedrich et al., 2016).

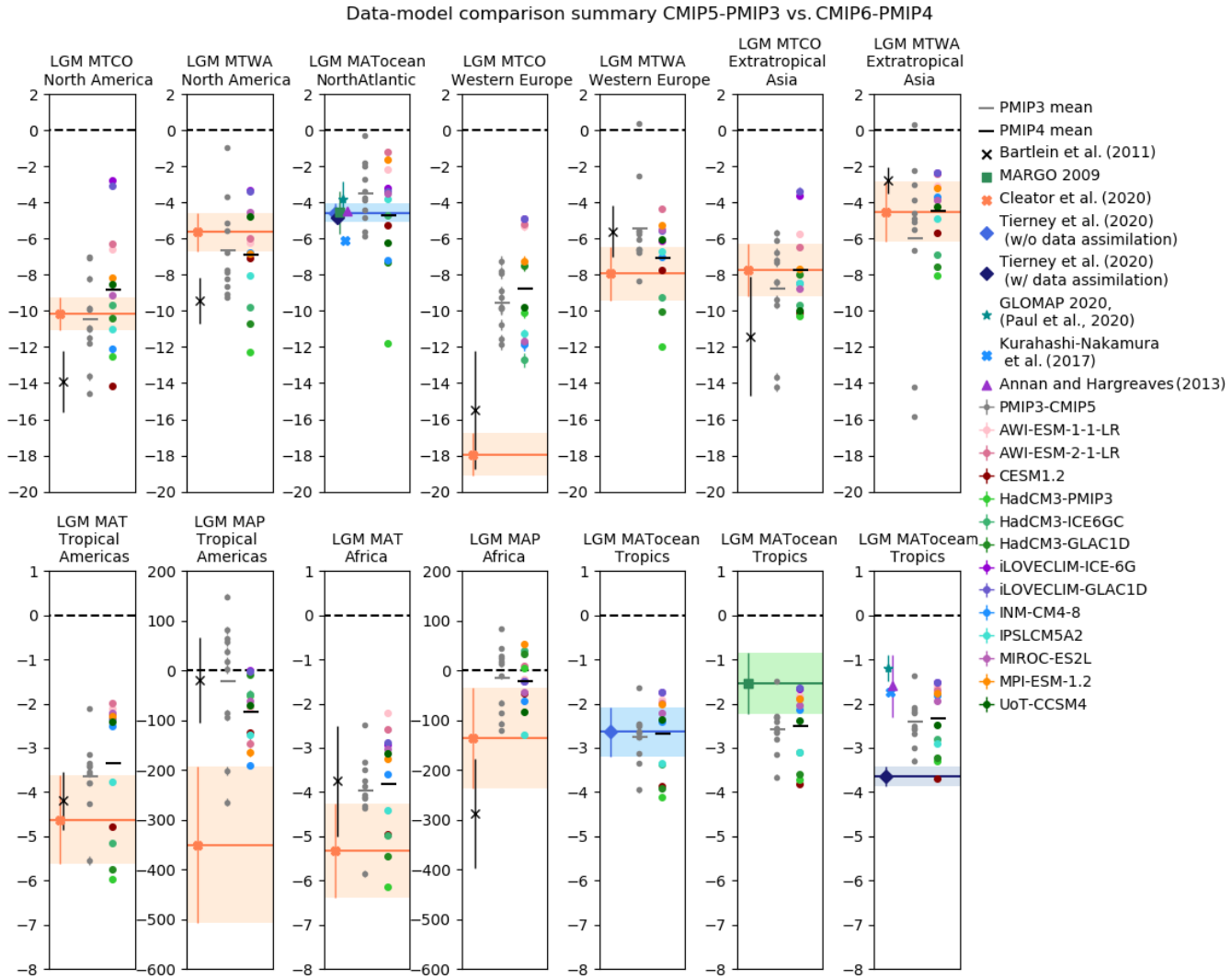

Figure 12. Data–model comparisons for North America (20–50° N, 140–60° W), the North Atlantic Ocean (30–50° N, 60–10° W), western Europe (35–70° N, 10° W–30° E), extratropical Asia (35–75° N), tropical Americas (30° S–30° N, 120–60° W), Africa (35° S–35° N, 10° W–50° E) and tropical oceans (30° S–30° N). MTCO: mean temperature of the coldest month, MTWA: mean temperature of the warmest month, MAT: mean annual temperature, MAP: mean annual precipitation, MATocean: mean annual temperature over the oceans. The error bars for the reconstructions are based on the standard error given at each site: the average and associated standard deviation over the specific area are obtained by computing 10 000 times the average of randomly drawn values in the Gaussian distributions defined at each site by the reconstruction mean and standard error, taken as the standard deviation of the Gaussian. Uncertainty for the model results has been computed based on the 10 000 randomly picked groups of 50 years which were averaged to obtain 10 000 estimates of the 50-year average for a specific region and variable. These were so small that they do not appear on the plots.

5 Conclusions and perspectives

The results from the PMIP4 models differ from those of the PMIP3 ensemble in several ways. The multi-model global cooling is similar in both ensembles but the PMIP4 ensemble range is larger, with four simulations showing colder results than the coldest PMIP3 model. This feature mainly arises from the Southern Hemisphere extratropics, and it is currently difficult to disentangle whether it is due to the PMIP4 model ensemble being largely different from the PMIP3 ensemble or the changes in protocol from PMIP3 to PMIP4 (see also Zhu et al., 2021). The change in the ice sheets appears to have an impact on atmospheric circulation over North America and the North Atlantic. The AMOC increases less in the PMIP4 than in the PMIP3 simulations, and the depth of the NADW cell remains more stable, except for two models, in contrast with more than half the models of the PMIP3-CMIP5 ensemble, which simulated a large deepening of this cell. This could be due to the changes in atmospheric circulation over the North Atlantic, as well as changes in the North Atlantic freshwater balance. Changes in precipi-

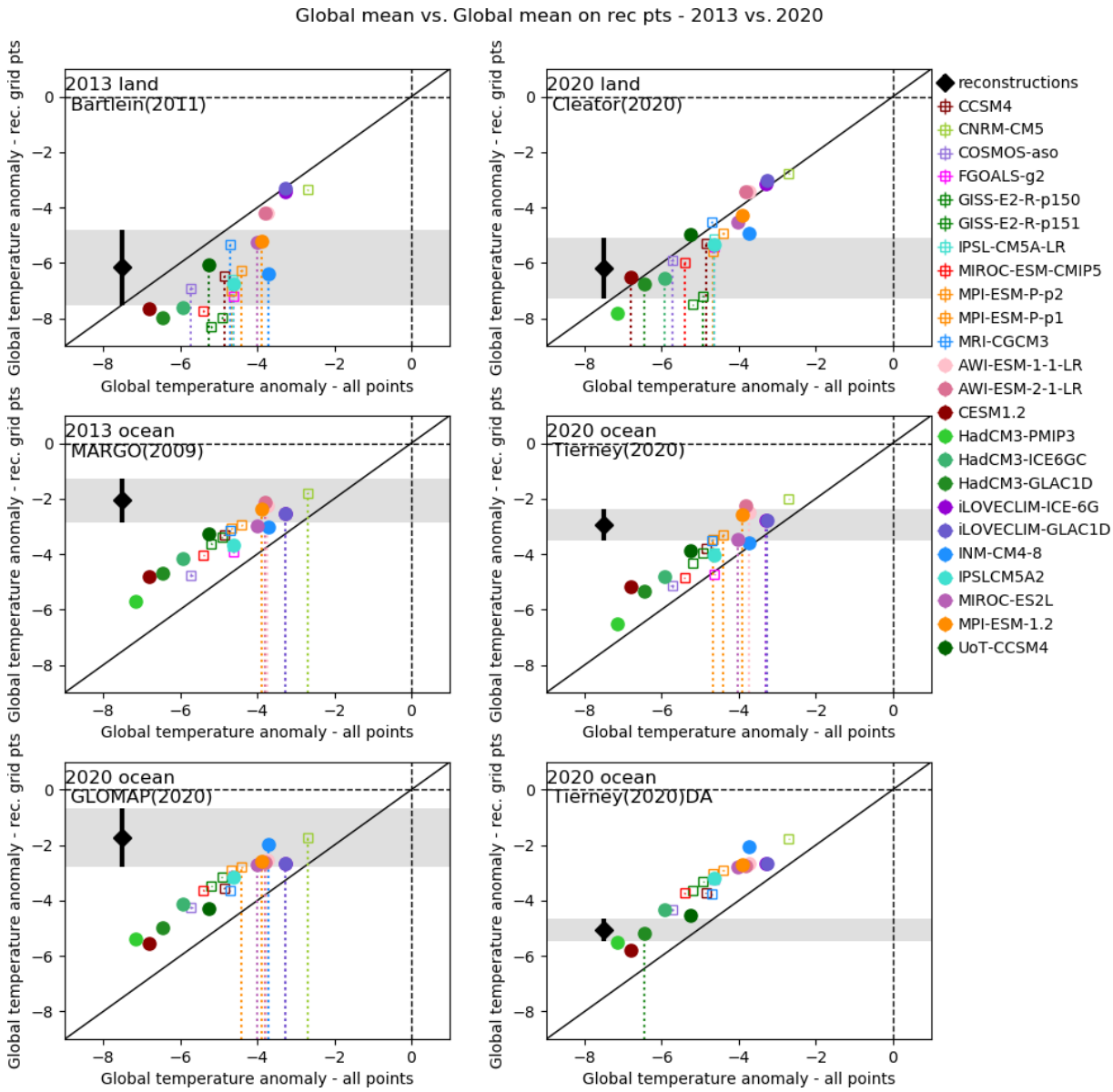

Figure 13. Relationships between global mean temperature changes (x axis, average computed on all model points) and global mean temperature changes for grid points where there are reconstructions (y axis, one plot per dataset). For each plot/dataset, the models whose average falls in the range of the average of the reconstructions are marked by vertical dotted lines down to the x axis.

tation are generally similar for the PMIP3 and PMIP4 ensembles and characterised by less precipitation overall. Reduced evaporation due to colder temperatures partially compensates for the reduction in precipitation, so that areas of negative and significant LGM–PI anomalies in net precipitation (i.e. precipitation minus evaporation) are larger than areas with positive LGM–PI precipitation anomalies. However, both precipitation and net precipitation changes show large spatial heterogeneity and different regional-scale patterns of change between the PMIP4 and PMIP3 ensembles, which appears to be related to the performance of the model ensemble for PI. Additional sensitivity experiments are needed to separate the effects of changes in model configuration and sensitivity on general circulation features, such as the position of the jet streams, from the effects of differences in boundary conditions, such as the improved realism of the ice-sheet configuration.

The PMIP4-CMIP6 ensemble confirms that the models simulate large-scale thermodynamic behaviour common to historical and future simulations, such as land–sea contrast and polar amplification. The results from PMIP3 and PMIP4 align on the same relationships for these large-scale characteristics of climate change. The new reconstructions of Tierney et al. (2020) and Cleator et al. (2020) are in bet-

ter agreement than with the reconstructions from Bartlein et al. (2011) and MARGO Project Members (2009) used to evaluate these features previously (Braconnot et al., 2012; Izumi et al., 2013; Harrison et al., 2014, 2015) for the tropical and global averages. However, global reconstructions of the surface ocean temperatures, such as the Tierney et al. (2020) data-assimilated product, the GLOMAP2020 data by Paul et al. (2021) and the reconstructions by Annan and Hargreaves (2013) and Kurahashi-Nakamura et al. (2017), show a wide range of results in terms of tropical temperatures (from −1 to −4 °C), which prevents firm conclusions on the model–data comparisons based on such global reconstructions. Interestingly, evaluating the uncertainty on tropical cooling from the PMIP model ensemble on the one hand and from the ensemble of continental and marine reconstructions on the other yields very similar results.

The simulated global change in MAT averaged over all the grid cells where reconstructions are available is well correlated with the global average on all model grid points, providing a constraint on the value of the global LGM cooling compared to PI. Using the terrestrial datasets as a constraint indicates a global cooling between −6.7 and −3.7 °C, while using Tierney et al. (2020) as a constraint indicates a global cooling of −4.9 to −3.2 °C, and using the MARGO Project Members (2009) and GLOMAP2020 datasets constrains the global average to be above −3.9 and −4.4 °C, respectively. The constrained range (−6.7 to −3.2 °C) is larger than previous estimates (−4 to −6 °C).

There is no obvious improvement in model performance at a regional scale between the PMIP3 and PMIP4 ensembles. In some cases (e.g. summer temperature over western Europe and extratropical Asia), the PMIP4 ensemble demonstrates a better ability to capture the changes depicted by the reconstructions; in some others (e.g. winter temperatures over Europe, mean annual precipitation over tropical America), the PMIP4 ensemble is still far from the reconstructed values.

Our analyses present a first picture of the PMIP4 LGM experiments. Results from CMIP6 models with high climate sensitivity have only recently become available (Zhu et al., 2021) and will need to be considered in a full assessment of the PMIP4-CMIP6 simulations. Sensitivity experiments, for example, to different ice-sheet configurations, are needed to disentangle the impact of model improvements from those related to using more realistic boundary conditions. Additional planned simulations will also help to disentangle the impacts of changes in vegetation and aerosol loading on the LGM climate. A more systematic evaluation of the simulated climates, using a wider range of paleoenvironmental data, will be helpful in understanding why there are persistent mismatches between the simulations and reconstructions at a regional scale. Nevertheless, this preliminary analysis demonstrates the utility of the PMIP4-CMIP6 simulations in addressing questions about the response of climate to large changes in forcing and illustrates the need to investigate the causes of inter-model differences in these responses.

Data availability. The data shown in this paper can be found on the IPSL repository (https://doi.org/10.14768/de241ea7-4c3d-4b56-8140-5de6940903be, Kageyama, 2021.). The results from the PMIP3-CMIP5 and PMIP4-CMIP6 models can be found on the ESGF (Earth System Grid Federation) website. In particular, the CMIP6 *lgm* runs have the associated DOIs: AWI-ESM-1-1-LR: https://doi.org/10.22033/ESGF/CMIP6.9330 (last access: February 2020, Shi et al., 2020); INM-CM4-8: https://doi.org/10.22033/ESGF/CMIP6.5075 (last access: August 2019, Volodin et al., 2019a); MIROC-ES2L: https://doi.org/10.22033/ESGF/CMIP6.5644 (last access: June 2019, Ohgaito et al., 2019); MPI-ESM1-2-LR: https://doi.org/10.22033/ESGF/CMIP6.6642 (last access: July 2019, Jungclaus et al., 2019). The associated *piControl* simulations have the following DOIs: AWI-ESM-1-1-LR: https://doi.org/10.22033/ESGF/CMIP6.9335 (last access: February 2020, Danek et al., 2020); INM-CM4-8: https://doi.org/10.22033/ESGF/CMIP6.5080 (last access: June 2019, Volodin et al., 2019b); MIROC-ES2L: https://doi.org/10.22033/ESGF/CMIP6.5710 (last access: August 2019, Hajima et al., 2019); MPI-ESM1-2-LR: https://doi.org/10.22033/ESGF/CMIP6.6675 (last access: July 2019, Wieners et al., 2019).

Supplement. The supplement related to this article is available online at: https://doi.org/10.5194/cp-17-1065-2021-supplement.

Author contributions. MK, MLK, UM, SST, TV, AAO, NB, DC, LJG, RFI, KI, ALG, FL, GL, PAM, RO, WRP, CJP, AQ, DMR, XS, PJV, EV and JZ provided the model output presented in this paper. SPH, AP and JET provided new climatic reconstructions. MK, SPH, MLK, ML, JML, SST, TV and AP prepared the figures and wrote the manuscript.

Competing interests. The authors declare that they have no conflict of interest.

Special issue statement. This article is part of the special issue "Paleoclimate Modelling Intercomparison Project phase 4 (PMIP4) (CP/GMD inter-journal SI)". It is not associated with a conference.

Acknowledgements. The authors would like to thank all the modelling groups who provided the PMIP3 and PMIP4 output for this analysis, WCRP, CMIP panel, PCMDI, ESGF infrastructures for sharing data, WCRP and CLIVAR for supporting the PMIP project. Masa Kageyama acknowledges the use of the IPSL (ESPRI – Ensemble de Services Pour la Recherche l'IPSL – computing and data centre (https://mesocentre.ipsl.fr/, last access: April 2021) which is supported by CNRS, Sorbonne Université, Ecole Polytechnique, CNES and through national and international grants) and LSCE storage and computing facilities for the analyses presented in this paper. The IPSL model was run on the Très Grande Infrastructure de Calcul (TGCC) at Commissariat à l'Energie Atomique (gen2212 project). Xiaoxu Shi and Gerrit Lohmann acknowledge

the German Climate Computing Center (DKRZ) for the AWI-ESM simulations. We thank the two reviewers and editor for their helpful comments on the first version of the manuscript.

Financial support. Masa Kageyama is funded by CNRS. Sandy P. Harrison acknowledges funding from the ERC-funded project GC2.0 (Global Change 2.0: Unlocking the past for a clearer future; grant no. 694481). The MPI-M contribution was supported by the German Federal Ministry of Education and Research (BMBF) as a Research for Sustainability initiative (FONA) through the project PalMod (FKZ: grant no. 01LP1504C). Jessica E. Tierney acknowledges funding from the US National Science Foundation (grant no. AGS-1602301) and the Heising-Simons Foundation (grant no. 2016-015). Ruza F. Ivanovic acknowledges partial support from the UK Natural Environment Research Council (grant no. NE/K008536/1) and additionally from UK Research and Innovation (grant no. MR/S016961/1), who also support Lauren J. Gregoire. Christopher J. Poulsen acknowledges funding from the US National Science Foundation (AGS-2002397) and the Heising-Simons Foundation (grant no. 2016-012). Xiaoxu Shi and Gerrit Lohmann acknowledge the support of the PACMEDY and PALMOD2 projects. Ayako Abe-Ouchi acknowledges the financial support from JSPS KAKENHI (grant no. 17H06104) and MEXT KAKENHI (grant no. 17H06323).

Review statement. This paper was edited by Julien Emile-Geay and reviewed by two anonymous referees.

References

Abe-Ouchi, A., Saito, F., Kageyama, M., Braconnot, P., Harrison, S. P., Lambeck, K., Otto-Bliesner, B. L., Peltier, W. R., Tarasov, L., Peterschmitt, J.-Y., and Takahashi, K.: Ice-sheet configuration in the CMIP5/PMIP3 Last Glacial Maximum experiments, Geosci. Model Dev., 8, 3621–3637, https://doi.org/10.5194/gmd-8-3621-2015, 2015.

Adloff, M., Reick, C. H., and Claussen, M.: Earth system model simulations show different feedback strengths of the terrestrial carbon cycle under glacial and interglacial conditions, Earth Syst. Dynam., 9, 413–425, https://doi.org/10.5194/esd-9-413-2018, 2018.

Annan, J. D. and Hargreaves, J. C.: A new global reconstruction of temperature changes at the Last Glacial Maximum, Clim. Past, 9, 367–376, https://doi.org/10.5194/cp-9-367-2013, 2013.

Annan, J. D. and Hargreaves, J. C.: A perspective on model-data surface temperature comparison at the Last Glacial Maximum, Quat. Sci. Rev., 107, 1–10, https://doi.org/10.1016/j.quascirev.2014.09.019, 2015.

Argus, D. F., Peltier, W. R., Drummond, R., and Moore, A. W.: The Antarctica component of postglacial rebound model ICE-6G_C(VM5a) based on GPS positioning, exposure age dating of ice thicknesses, and relative sea level histories, Geophys. J. Int., 198, 537–563, https://doi.org/10.1093/gji/ggu140, 2014.

Bartlein, P. J., Harrison, S.P., Brewer, S., Connor, S., Davis B.A.S., Gajewski, K., Guiot, J., Harrison-Prentice, T. I., Henderson, A., Peyron, O., Prentice, I. C., Scholze, M., Seppä, H., Shuman, B., Sugita, S., Thompson, R. S., Viau, A., Williams, J., and Wu, H.,: Pollen-based continental climate reconstructions at 6 and 21 ka: a global synthesis, Clim. Dynam. 37, 775–802, 2011.

Beghin, P., Charbit, S., Dumas, C., Kageyama, M., and Ritz, C.: How might the North American ice sheet influence the northwestern Eurasian climate?, Clim. Past, 11, 1467–1490, https://doi.org/10.5194/cp-11-1467-2015, 2015.

Beghin, P., Charbit, S., Kageyama, M., Combourieu Nebout, N., Hatté, C., Dumas, C., and Peterschmitt, J.-Y.: What drives LGM precipitation over the western Mediterranean? A study focused on the Iberian Peninsula and northern Morocco, Clim. Dynam., 46, 2611–2631, 2016.

Böhm, E., Lippold, J., Gutjahr, M., Frank, M., Blaser, P., Antz, B., Fohlmeister, J., Frank, N., Andersen, M., B., and Deininger, M.: Strong and deep Atlantic meridional overturning circulation during the last glacial cycle, Nature, 517, 73–76, https://doi.org/10.1038/nature14059, 2015.

Boos, W. R.: Thermodynamic Scaling of the Hydrological Cycle of the Last Glacial Maximum, J. Climate, 25, 992–1006, https://doi.org/10.1175/JCLI-D-11-00010.1, 2012.

Braconnot, P., Harrison, S. P., Kageyama, M., Bartlein, P. J., Masson-Delmotte, V., Abe-Ouchi, A., Otto-Bliesner, B., and Zhao, Y.: Evaluation of climate models using palaeoclimatic data, Nat. Clim. Change, 2, 417–424, 2012.

Brady, E. C., Otto-Bliesner, B. L., Kay, J. E., and Rosenbloom, N.: Sensitivity to Glacial Forcing in the CCSM4, J. Climate, 26, 1901–1925, https://doi.org/10.1175/JCLI-D-11-00416.1, 2013.

Bragg, F. J., Prentice, I. C., Harrison, S. P., Eglinton, G., Foster, P. N., Rommerskirchen, F., and Rullkötter, J.: Stable isotope and modelling evidence for CO_2 as a driver of glacial-interglacial vegetation shifts in southern Africa, Biogeosciences, 10, 2001–2010, https://doi.org/10.5194/bg-10-2001-2013, 2013.

Chandan, D. and Peltier, W. R.: Regional and global climate for the mid-Pliocene using the University of Toronto version of CCSM4 and PlioMIP2 boundary conditions, Clim. Past, 13, 919–942, https://doi.org/10.5194/cp-13-919-2017, 2017.

Chandan, D. and Peltier, W. R.: On the mechanisms of warming the mid-Pliocene and the inference of a hierarchy of climate sensitivities with relevance to the understanding of climate futures, Clim. Past, 14, 825–856, https://doi.org/10.5194/cp-14-825-2018, 2018.

Cleator, S. F., Harrison, S. P., Nichols, N. K., Prentice, I. C., and Roulstone, I.: A new multivariable benchmark for Last Glacial Maximum climate simulations, Clim. Past, 16, 699–712, https://doi.org/10.5194/cp-16-699-2020, 2020.

Crowley, T. J.: CLIMAP SSTs re-revisited, Clim. Dynam., 16, 241–255, 2000

Danek, C., Shi, X., Stepanek, C., Yang, H., Barbi, D., Hegewald, J., and Lohmann, G.: AWI AWI-ESM1.1LR model output prepared for CMIP6 CMIP piControl, Version 20200212, Earth System Grid Federation, https://doi.org/10.22033/ESGF/CMIP6.9335, 2020.

DiNezio, P. and Tierney, J. E.: The effect of sea level on glacial Indo-Pacific climate, Nat. Geosci., 6, 485–491, https://doi.org/10.1038/ngeo1823, 2013.

Galbraith, E. and de Lavergne, C.: Response of a comprehensive climate model to a broad range of external forcings: relevance for deep ocean ventilation and the development of late Cenozoic

ice ages, Clim. Dynam., 52, 653, https://doi.org/10.1007/s00382-018-4157-8, 2019.

Gebbie, G.: How much didGlacial North Atlantic Water shoal?, Paleoceanography, 29, 190–209, https://doi.org/10.1002/2013PA002557, 2014.

Gerhart, L. M. and Ward, J. K.: Plant responses to low [CO_2] of the past. New Phytol., 188, 674–695, 2010.

Goldsmith, Y.. Polissar, P., Ayalon, A., Bar-Matthews, M., Demenocal, P., and Broecker, W. S.: The modern and Last Glacial Maximum hydrological cycles of the Eastern Mediterranean and the Levant from a water isotope perspective, Earth Planet. Sc. Lett., 457, 303–312, https://doi.org/10.1016/j.epsl.2016.10.017, 2017.

Hajima, T., Abe, M., Arakawa, O., Suzuki, T., Komuro, Y., Ogura, T., Ogochi, K., Watanabe, M., Yamamoto, A., Tatebe, H., Noguchi, M., Ohgaito, R., Ito, A., Yamazaki, D., Ito, A., Takata, K., Watanabe, S., Kawamiya, M., and Tachiiri, K.: MIROC MIROC-ES2L model output prepared for CMIP6 CMIP piControl, Version 20190823.Earth System Grid Federation, https://doi.org/10.22033/ESGF/CMIP6.5710, 2019.

Hajima, T., Watanabe, M., Yamamoto, A., Tatebe, H., Noguchi, M. A., Abe, M., Ohgaito, R., Ito, A., Yamazaki, D., Okajima, H., Ito, A., Takata, K., Ogochi, K., Watanabe, S., and Kawamiya, M.: Development of the MIROC-ES2L Earth system model and the evaluation of biogeochemical processes and feedbacks, Geosci. Model Dev., 13, 2197–2244, https://doi.org/10.5194/gmd-13-2197-2020, 2020.

Harrison, S. P., Bartlein, P. J., Brewer, S., Prentice, I. C., Boyd, M., Hessler, I., Holmgren, K., Izumi, K., and Willis, K.: Climate model benchmarking with glacial and mid-Holocene climates, Clim. Dynam., 43, 671–688, 2014.

Harrison, S. P., Bartlein, P. J., Izumi, K., Li, G., Annan, J., Hargreaves, J., Braconnot, P., and Kageyama, M.: Evaluation of CMIP5 palaeo-simulations to improve climate projections, Nat. Clim. Change, 5, 735–743, https://doi.org/10.1038/nclimate2649, 2015.

Hu, A. X., Meehl, G. A., Han, W. Q., Otto-Bliestner, B., Abe-Ouchi, A., and Rosenbloom, N.: Effects of the Bering Strait closure on AMOC and global climate under different background climates, Prog Oceanogr., 132, 174–196, https://doi.org/10.1016/j.pocean.2014.02.004, 2015.

Ivanovic, R. F., Gregoire, L. J., Kageyama, M., Roche, D. M., Valdes, P. J., Burke, A., Drummond, R., Peltier, W. R., and Tarasov, L.: Transient climate simulations of the deglaciation 21-9 thousand years before present (version 1) – PMIP4 Core experiment design and boundary conditions, Geosci. Model Dev., 9, 2563–2587, https://doi.org/10.5194/gmd-9-2563-2016, 2016.

Izumi, K., Bartlein, P. J., and Harrison, S. P.: Consistent large-scale temperature responses in warm and cold climates, Geophys. Res. Lett., 40, 1817–1823, https://doi.org/10.1002/grl.50350, 2013.

Jaccard, S. L. and Galbraith, E. D.: Large climate-driven changes of oceanic oxygen concentrations during the last deglaciation, Nat. Geosci., 5, 151–156, https://doi.org/10.1038/NGEO1352, 2012.

Jungclaus, J., Mikolajewicz, U., Kapsch, M.-L., D'Agostino, R., Wieners, K.-H., Giorgetta, M., Reick, C., Esch, M., Bittner, M., Legutke, S., Schupfner, M., Wachsmann, F., Gayler, V., Haak, H., de Vrese, P., Raddatz, T., Mauritsen, T., von Storch, J.-S., Behrens, J., Brovkin, V., Claussen, M., Crueger, T., Fast, I., Fiedler, S., Hagemann, S., Hohenegger, C., Jahns, T., Kloster, S., Kinne, S., Lasslop, G., Kornblueh, L., Marotzke, J., Matei, D., Meraner, K., Modali, K., Müller, W., Nabel, J., Notz, D., Peters, K., Pincus, R., Pohlmann, H., Pongratz, J., Rast, S., Schmidt, H., Schnur, R., Schulzweida, U., Six, K., Stevens, B., Voigt, A., and Roeckner, E.: MPI-M MPI-ESM1.2-LR model output prepared for CMIP6 PMIP lgm, Version 20190710, Earth System Grid Federation, https://doi.org/10.22033/ESGF/CMIP6.6642, 2019.

Kageyama, M., Albani, S., Braconnot, P., Harrison, S. P., Hopcroft, P. O., Ivanovic, R. F., Lambert, F., Marti, O., Peltier, W. R., Peterschmitt, J.-Y., Roche, D. M., Tarasov, L., Zhang, X., Brady, E. C., Haywood, A. M., LeGrande, A. N., Lunt, D. J., Mahowald, N. M., Mikolajewicz, U., Nisancioglu, K. H., Otto-Bliesner, B. L., Renssen, H., Tomas, R. A., Zhang, Q., Abe-Ouchi, A., Bartlein, P. J., Cao, J., Li, Q., Lohmann, G., Ohgaito, R., Shi, X., Volodin, E., Yoshida, K., Zhang, X., and Zheng, W.: The PMIP4 contribution to CMIP6 – Part 4: Scientific objectives and experimental design of the PMIP4-CMIP6 Last Glacial Maximum experiments and PMIP4 sensitivity experiments, Geosci. Model Dev., 10, 4035–4055, https://doi.org/10.5194/gmd-10-4035-2017, 2017.

Kageyama, M., Braconnot, P., Harrison, S. P., Haywood, A. M., Jungclaus, J. H., Otto-Bliesner, B. L., Peterschmitt, J.-Y., Abe-Ouchi, A., Albani, S., Bartlein, P. J., Brierley, C., Crucifix, M., Dolan, A., Fernandez-Donado, L., Fischer, H., Hopcroft, P. O., Ivanovic, R. F., Lambert, F., Lunt, D. J., Mahowald, N. M., Peltier, W. R., Phipps, S. J., Roche, D. M., Schmidt, G. A., Tarasov, L., Valdes, P. J., Zhang, Q., and Zhou, T.: The PMIP4 contribution to CMIP6 – Part 1: Overview and overarching analysis plan, Geosci. Model Dev., 11, 1033–1057, https://doi.org/10.5194/gmd-11-1033-2018, 2018.

Kageyama, M.: Data plotted in Kageyama et al., 2021 (Climate of the Past), https://doi.org/10.14768/de241ea7-4c3d-4b56-8140-5de6940903be, 2021.

Kirby, M. E., Feakins, S. J., Bonuso, N., Fantozzi, J. M., and Hiner, C. A.: Latest Pleistocene to Holocene hydroclimates from Lake Elsinore, California, Quat. Sci. Rev., 76, 1–15, https://doi.org/10.1016/j.quascirev.2013.05.023, 2013.

Klockmann, M., Mikolajewicz, U., and Marotzke, J.: The effect of greenhouse gas concentrations and ice sheets on the glacial AMOC in a coupled climate model, Clim. Past, 12, 1829–1846, https://doi.org/10.5194/cp-12-1829-2016, 2016.

Kurahashi-Nakamura, T., Paul, A., and Losch, M.: Dynamical reconstruction of the global ocean state during the Last Glacial Maximum, Paleoceanography, 32, 326–350, https://doi.org/10.1002/2016PA003001, 2017.

Laîné, A., Kageyama, M., Salas-Mélia, D., Voldoire, A., Rivière, G., Ramstein, G., Planton, S., and Tyteca, J. Y., Peterschmitt: Northern hemisphere storm tracks during the Last Glacial Maximum in the PMIP2 Ocean-Atmosphere coupled models: energetic study, seasonal cycle, precipitation, Clim. Dynam., 32, 593–614, https://doi.org/10.1007/s00382-008-0391-9, 2009.

Lhardy, F., Bouttes, N., Roche, D. M., Crosta, X., Waelbroeck, C., and Paillard, D.: Impact of Southern Ocean surface conditions on deep ocean circulation at the LGM: a model analysis, Clim. Past Discuss. [preprint], https://doi.org/10.5194/cp-2020-148, in review, 2020.

Li, G., Harrison, S. P., Bartlein, P. J., Izumi, K., Prentice, I. C.: Precipitation scaling with temperature in warm and cold climates: an analysis of CMIP5 simulations, Geophys. Res. Lett., 40, 4018–4024, https://doi.org/10.1002/grl.50730, 2013.

Liakka, J. and Löfverström, M.: Arctic warming induced by the Laurentide Ice Sheet topography, Clim. Past, 14, 887–900, https://doi.org/10.5194/cp-14-887-2018, 2018.

Löfverström, M.: A dynamic link between high-intensity precipitation events in southwestern North America and Europe at the Last Glacial Maximum, Earth Planet. Sc. Lett., 534, 116081, https://doi.org/10.1016/j.epsl.2020.116081, 2020.

Löfverström, M., Caballero, R., Nilsson, J., and Kleman, J.: Evolution of the large-scale atmospheric circulation in response to changing ice sheets over the last glacial cycle, Clim. Past, 10, 1453–1471, https://doi.org/10.5194/cp-10-1453-2014, 2014.

Löfverström, M., Caballero, R., Nilsson, J., and Messori, G.: Stationary Wave Reflection as a Mechanism for Zonalizing the Atlantic Winter Jet at the LGM, J. Atmos. Sci., 73, 3329–3342, https://doi.org/10.1175/JAS-D-15-0295.1, 2016.

Löfverström, M. and Liakka, J.: On the limited ice intrusion in Alaska at the LGM, Geophys. Res. Lett., 43, 11030–11038, https://doi.org/10.1002/2016GL071012, 2016.

Löfverström, M. and Lora, J. M., Abrupt regime shifts in the North Atlantic atmospheric circulation over the last deglaciation, Geophys. Res. Lett., 44, 8047–8055, https://doi.org/10.1002/2017GL074274, 2017.

Lohmann, G., Butzin, M., Eissner, N., Shi, X., and Stepanek, C.: Abrupt climate and weather changes across timescales, Paleoceanogr. Paleoclimatol., 35, e2019PA003782, https://doi.org/10.1029/2019PA003782, 2020.

Lora, J. M., Mitchell, J. L., Risi, C., and Tripati, A. E.: North Pacific atmo- spheric rivers and their influence on western North America at the Last Glacial Maximum, Geophys. Res. Lett., 44, 1051–1059, https://doi.org/10.1002/2016GL071541, 2017.

Lora, J. M.: Components and Mechanisms of Hydrologic Cycle Changes over North America at the Last Glacial Maximum, J. Climate, 31, 7035–7051, https://doi.org/10.1175/JCLI-D-17-0544.1, 2018.

Lynch-Stieglitz, J., Adkins, J. F., Curry, W. B., Dokken, T., Hall, I. R., Herguera, J. C., Hirschi, J. J.-M., Ivanova, E. V., Kissel, C., Marchal, O., Marchitto, T. M., McCave, I. N., McManus, J. F., Mulitza, S., Ninnemann, U., Peeters, F., Yu, E.-F., and Zahn, R.: Atlantic Meridional Overturning Circulation During the Last Glacial Maximum, Science, 316, 66, https://doi.org/10.1126/science.1137127, 2007.

Malevich, S. B., Vetter, L., and Tierney, J. E.: Global core top calibration of δ18O in planktic foraminifera to sea surface temperature, Paleoceanogr. Paleoclimatol., 34, 1292–1315, 2019.

MARGO Project Members: Constraints on the magnitude and patterns of ocean cooling at the Last Glacial Maximum, Nat. Geosci., 2, 127–132, 2009.

Masson-Delmotte, V., Dreyfus, G., Braconnot, P., Johnsen, S., Jouzel, J., Kageyama, M., Landais, A., Loutre, M.-F., Nouet, J., Parrenin, F., Raynaud, D., Stenni, B., and Tuenter, E.: Past temperature reconstructions from deep ice cores: relevance for future climate change, Clim. Past, 2, 145–165, https://doi.org/10.5194/cp-2-145-2006, 2006.

Mauritsen, T., Bader, J., Becker, T., Behrens, J., Bittner, M., Brokopf, R., Brovkin, V., Claussen, M., Crueger, T., Esch, M., Fast, I., Fiedler, S., Fläschner, D., Gayler, V., Giorgetta, M., Goll, D. S., Haak, H., Hagemann, S., Hedemann, C., Hohenegger, C., Ilyina, T., Jahns, T., Jimenéz-de-la-Cuesta, D., Jungclaus, J., Kleinen, T., Kloster, S., Kracher, D., Kinne, S., Kleberg, D., Lasslop, G., Kornblueh, L., Marotzke, J., Matei, D., Meraner, K., Mikolajewicz, U., Modali, K., Möbis, B., Müller, W. A., Nabel, J. E. M. S., Nam, C. C. W., Notz, D., Nyawira, S.-S., Paulsen, H. Peters, K., Pincus, R., Pohlmann, H. Pongratz, J., Popp, M., Raddatz, T. J., Rast, S., Redler, R., Reick, C. H., Rohrschneider, T., Schemann, V., Schmidt, H., Schnur, R., Schulzweida, U., Six, K. D., Stein, L., Stemmler, I., Stevens, B., von Storch, J.-S., Tian, F., Voigt, A., Vrese, P., Wieners, K.-H., Wilkenskjeld, S., Winkler, A., and Roeckner, E.: Developments in the MPI-M Earth System Model version 1.2 (MPI-ESM1.2) and its response to increasing CO_2, J. Adv. Model. Earth Syst., 11, 998–1038, https://doi.org/10.1029/2018MS001400, 2019.

Mix, A. C., Morey, A. E., Pisias, N. G., and Hostetler, S. W.: Foraminiferal faunal estimates of paleotemperature: Circumventing the no-analog problem yields cool ice age tropics, Paleoceanography, 14, 350–359, 1999.

Morrill, C., Lowry, D. P., and Hoell, A.: Thermodynamic and dynamic causes of pluvial conditions during the Last Glacial Maximum in western North America, Geophys. Res. Lett. 45, 335–345, 2018.

Muglia, J. and Schmittner, A.: Glacial Atlantic overturning increased by wind stress in climate models, Geophys. Res. Lett., 42, 9862–9869, https://doi.org/10.1002/2015GL064583, 2015.

Ohgaito, R., Abe-Ouchi, A., Abe, M., Arakawa, O., Ogochi, K., Hajima, T., Watanabe, M., Yamamoto, A., Tatebe, H., Noguchi, M., Ito, A., Yamazaki, D., Ito, A., Takata, K., Watanabe, S., Kawamiya, M., and Tachiiri, K.: MIROC MIROC-ES2L model output prepared for CMIP6 PMIP lgm, Version 20191002, Earth System Grid Federation, https://doi.org/10.22033/ESGF/CMIP6.5644, 2019.

Ohgaito, R., Yamamoto, A., Hajima, T., O'ishi, R., Abe, M., Tatebe, H., Abe-Ouchi, A., and Kawamiya, M.: PMIP4 experiments using MIROC-ES2L Earth system model, Geosci. Model Dev., 14, 1195–1217, https://doi.org/10.5194/gmd-14-1195-2021, 2021.

Oka, A., Hasumi, H., and Abe-Ouchi, A.: The thermal threshold of the Atlantic meridional overturning circulation and its control by wind stress forcing during glacial climate, Geophys. Res. Lett., 39, L09709, https://doi.org/10.1029/2007gl029475, 2012.

Paul, A., Mulitza, S., Stein, R., and Werner, M.: A global climatology of the ocean surface during the Last Glacial Maximum mapped on a regular grid (GLOMAP), Clim. Past, 17, 805–824, https://doi.org/10.5194/cp-17-805-2021, 2021.

Peltier, W. R., Argus, D. F., and Drummond, R.: Space geodesy constrains ice age terminal deglaciation: The global ICE-6G_C(VM5a) model, J. Geophys. Res.-Sol. Ea., 120, 450–487,https://doi.org/10.1002/2014JB011176, 2015.

Peltier, W. R. and Vettoretti, G.: Dansgaard-Oeschger oscillations predicted in a comprehensive model of glacial climate: A "kicked" salt oscillator in the Atlantic, Geophys. Res. Lett., 41, 7306–7313, https://doi.org/10.1002/2014GL061413, 2014.

Prentice, I. C. and Harrison, S. P.: Ecosystem effects of CO_2 concentration: evidence from past climates, Clim. Past, 5, 297–307, https://doi.org/10.5194/cp-5-297-2009, 2009.

Prentice, I. C., Cleator, S. F., Huang, Y. F., Harrison, S. P., and Roulstone, I.: Reconstructing ice – age climates: quantifying low-CO_2 effects on plants, Glob. Planet. Change, 149, 166–176, https://doi.org/10.1016/j.gloplacha.2016.12.012, 2017.

Rehfeld, K., Hébert, R., Lora, J. M., Löfverström, M., and Brierley, C. M.: Variability of surface climate in simula-

tions of past and future, Earth Syst. Dynam., 11, 447–468, https://doi.org/10.5194/esd-11-447-2020, 2020.

Renoult, M., Annan, J. D., Hargreaves, J. C., Sagoo, N., Flynn, C., Kapsch, M.-L., Li, Q., Lohmann, G., Mikolajewicz, U., Ohgaito, R., Shi, X., Zhang, Q., and Mauritsen, T.: A Bayesian framework for emergent constraints: case studies of climate sensitivity with PMIP, Clim. Past, 16, 1715–1735, https://doi.org/10.5194/cp-16-1715-2020, 2020.

Scheff, J. and Frierson, D. M. W.: Robust future precipitation declines in CMIP5 largely reflect the poleward expansion of model subtrop-ical dry zones, Geophys. Res. Lett., 39, L18704, https://doi.org/10.1029/2012GL052910, 2012.

Scheff, J., Seager, R., and Liu, H.: Are glacials dry? Consequences for paleoclimatology and for greenhouse warming. J. Climate, 30, 6593–6609, https://doi.org/10.1175/JCLI-D-16-0854.1, 2017.

Schmidt, G. A., Annan, J. D., Bartlein, P. J., Cook, B. I., Guilyardi, E., Hargreaves, J. C., Harrison, S. P., Kageyama, M., LeGrande, A. N., Konecky, B., Lovejoy, S., Mann, M. E., Masson-Delmotte, V., Risi, C., Thompson, D., Timmermann, A., Tremblay, L.-B., and Yiou, P.: Using palaeo-climate comparisons to constrain future projections in CMIP5, Clim. Past, 10, 221–250, https://doi.org/10.5194/cp-10-221-2014, 2014.

Sepulchre, P., Caubel, A., Ladant, J.-B., Bopp, L., Boucher, O., Braconnot, P., Brockmann, P., Cozic, A., Donnadieu, Y., Dufresne, J.-L., Estella-Perez, V., Ethé, C., Fluteau, F., Foujols, M.-A., Gastineau, G., Ghattas, J., Hauglustaine, D., Hourdin, F., Kageyama, M., Khodri, M., Marti, O., Meurdesoif, Y., Mignot, J., Sarr, A.-C., Servonnat, J., Swingedouw, D., Szopa, S., and Tardif, D.: IPSL-CM5A2 – an Earth system model designed for multi-millennial climate simulations, Geosci. Model Dev., 13, 3011–3053, https://doi.org/10.5194/gmd-13-3011-2020, 2020.

Sherriff-Tadano, S. and Abe-Ouchi, A.: Roles of sea ice–surface wind feedback in maintaining the glacial Atlantic meridional overturning circulation and climate, J. Climate, https://doi.org/10.1175/JCLI-D-19-0431.1, 2020.

Sherriff-Tadano, S., Abe-Ouchi, A., Yoshimori, M., Oka, A., and Chan, W.-L.: Influence of glacial ice sheets on the Atlantic meridional overturning circulation through surface wind change, Clim. Dynam., 50, 2881–2903, https://doi.org/10.1007/s00382-017-3780-0, 2018.

Shi, X., Yang, H., Danek, C., and Lohmann, G.: AWI AWI-ESM1.1LR model output prepared for CMIP6 PMIP lgm, Version 20200212, Earth System Grid Federation, https://doi.org/10.22033/ESGF/CMIP6.9330, 2020.

Sidorenko, D., Rackow, T., Jung, T., Semmler, T., Barbi, D., Danilov, S., Dethloff, K., Dorn, W., Fieg, K., Goßling, H. F., Handorf, D., Harig, S., Hiller, W., Juricke, S., Losch, M., Schröter, J., Sein, D. V., and Wang, Q.: Towards multi-resolution global climate modeling with ECHAM6-FESOM, Part I: model formulation and mean climate, Clim. Dynam., 44, 757–780, https://doi.org/10.1007/s00382-014-2290-6, 2015.

Sidorenko, D., Goessling, H., Koldunov, N., Scholz, P., Danilov, S., Barbi, D., Cabos, W., Gurses, O., Harig, S., Hinrichs, C., Juricke, S., Lohmann, G., Losch, M., Mu, L., Rackow, T., Rakowsky, N., Sein, D., Semmler, T., Shi, X., Stepanek, C., Streffing, J., Wang, Q., Wekerle, C., Yang, H., and Jung, T.: Evaluation of FESOM2.0 Coupled to ECHAM6.3: Preindustrial and HighResMIP Simulations, J. Adv. Model. Earth Sy., 11, 3794–3815, https://doi.org/10.1029/2019MS001696, 2019.

Sueyoshi, T., Ohgaito, R., Yamamoto, A., Chikamoto, M. O., Hajima, T., Okajima, H., Yoshimori, M., Abe, M., O'ishi, R., Saito, F., Watanabe, S., Kawamiya, M., and Abe-Ouchi, A.: Set-up of the PMIP3 paleoclimate experiments conducted using an Earth system model, MIROC-ESM, Geosci. Model Dev., 6, 819–836, https://doi.org/10.5194/gmd-6-819-2013, 2013.

Telford, R. J., Li, C., and Kucera, M.: Mismatch between the depth habitat of planktonic foraminifera and the calibration depth of SST transfer functions may bias reconstructions, Clim. Past, 9, 859–870, https://doi.org/10.5194/cp-9-859-2013, 2013.

Tierney, J. E. and Tingley, M. P.: A TEX 86 surface sediment database and extended Bayesian calibration, Sci. Data, 2, 150029, https://doi.org/10.1038/sdata.2015.29, 2015.

Tierney, J. E. and Tingley, M. P.: BAYSPLINE: A new calibration for the alkenone paleothermometer, Palaeogeogr. Palaeocl., 33, 281–301, 2018.

Tierney, J. E., Malevich, S. B., Gray, W., Vetter, L., and Thirumalai, K.: Bayesian calibration of the Mg/Ca paleothermometer in planktic foraminifera, Palaeogeogr. Palaeocl., 34, 2005–2030, https://doi.org/10.1029/2019PA003744, 2019.

Tierney, J. E., Zhu, J., King, J., Malevich, S. B., Hakim, G. J., and Poulsen, C. J.: Glacial cooling and climate sensitivity revisited, Nature, 584, 569–573, https://doi.org/10.1038/s41586-020-2617-x, 2020.

Ullman, D. J., LeGrande, A. N., Carlson, A. E., Anslow, F. S., and Licciardi, J. M.: Assessing the impact of Laurentide Ice Sheet topography on glacial climate, Clim. Past, 10, 487–507, https://doi.org/10.5194/cp-10-487-2014, 2014.

Valdes, P. J., Armstrong, E., Badger, M. P. S., Bradshaw, C. D., Bragg, F., Crucifix, M., Davies-Barnard, T., Day, J. J., Farnsworth, A., Gordon, C., Hopcroft, P. O., Kennedy, A. T., Lord, N. S., Lunt, D. J., Marzocchi, A., Parry, L. M., Pope, V., Roberts, W. H. G., Stone, E. J., Tourte, G. J. L., and Williams, J. H. T.: The BRIDGE HadCM3 family of climate models: HadCM3@Bristol v1.0, Geosci. Model Dev., 10, 3715–3743, https://doi.org/10.5194/gmd-10-3715-2017, 2017.

Voldoire, A., Sanchez-Gomez, E., Salas y Mélia, D., Decharme, B., Cassou, C., Sénési, S., Valcke, S., Beau, I., Alias, A. Chevallier, M., Déqué, M., Deshayes, J., Douville, H., Fernandez, E., Madec, G., Maisonnave , E., Moine, M.-P., Planton, S., Saint-Martin, D., Szopa, S., Tyteca, S., Alkama, R., Belamari, S., Braun, A., Coquart, L., and Chauvin, F.: The CNRM-CM5.1 global climate model: description and basic evaluation, Clim. Dynam., 40, 2091–2121, https://doi.org/10.1007/s00382-011-1259-y, 2013.

Volodin, E., Mortikov, E., Kostrykin, S., Galin, V., Lykossov, V., Gritsun, A., Diansky, N., Gusev, A., Iakovlev, N., Shestakova, A., and Emelina, S.: Simulation of the modern climate using the INM-CM48 climate model, Russian Journal of Numerical Analysis and Mathematical Modelling, 33, 367–374, https://doi.org/10.1515/rnam-2018-0032, 2018.

Volodin, E., Mortikov, E., Gritsun, A., Lykossov, V., Galin, V., Diansky, N., Gusev, A., Kostrykin, S., Iakovlev, N., Shestakova, A., and Emelina, S.: INM INM-CM4-8 model output prepared for CMIP6 PMIP lgm, Version 20190802, Earth System Grid Federation, https://doi.org/10.22033/ESGF/CMIP6.5075, 2019a.

Volodin, E., Mortikov, E., Gritsun, A., Lykossov, V., Galin, V., Diansky, N., Gusev, A., Kostrykin, S., Iakovlev, N., Shestakova, A., and Emelina, S.: INM INM-CM4-8 model output prepared for CMIP6 CMIP piControl, Version 20190605, Earth System Grid Federation, https://doi.org/10.22033/ESGF/CMIP6.5080, 2019b.

Wieners, K.-H., Giorgetta, M., Jungclaus, J., Reick, C., Esch, M., Bittner, M., Legutke, S., Schupfner, M., Wachsmann, F., Gayler, V., Haak, H., de Vrese, P.,; Raddatz, T., Mauritsen, T., von Storch, J.-S., Behrens, J.,; Brovkin, V., Claussen, M., Crueger, T., Fast, I., Fiedler, S., Hagemann, S., Hohenegger, C., Jahns, T., Kloster, S., Kinne, S., Lasslop, G., Kornblueh, L.,; Marotzke, J., Matei, D., Meraner, K., Mikolajewicz, U., Modali, K., Müller, W. Nabel, J., Notz, Di., Peters, K., Pincus, R., Pohlmann, H., Pongratz, J.,; Rast, S., Schmidt, H., Schnur, R., Schulzweida, U., Six, K., Stevens, B., Voigt, A., and Roeckner, E.: MPI-M MPI-ESM1.2-LR model output prepared for CMIP6 CMIP piControl, Version 20190710, Earth System Grid Federation, https://doi.org/10.22033/ESGF/CMIP6.6675, 2019.

Zhang, X., Lohmann, G., Knorr, G., and Purcell, C.: Abrupt glacial climate shifts controlled by ice sheet changes, Nature, 512, 290–294, https://doi.org/10.1038/nature13592, 2014.

Zhu, J., Otto-Bliesner, B. L., Brady, E. C., Poulsen, C. J., Tierney, J. E., Löfverström, M., and DiNezio, P.: Assessment of equilibrium climate sensitivity of the Community Earth System Model version 2 through simulation of the Last Glacial Maximum, Geophys. Res. Lett., 48, e2020GL091220, https://doi.org/10.1029/2020GL091220, 2021.

Quaternary Science Reviews 240 (2020) 106394

Contents lists available at ScienceDirect

Quaternary Science Reviews

journal homepage: www.elsevier.com/locate/quascirev

Modelling the impact of biogenic particle flux intensity and composition on sedimentary Pa/Th

Lise Missiaen [a, *], Laurie C. Menviel [a], Katrin J. Meissner [a, b], Didier M. Roche [c, d], Jean-Claude Dutay [c], Nathaelle Bouttes [c], Fanny Lhardy [c], Aurélien Quiquet [c, e], Sylvain Pichat [f, g], Claire Waelbroeck [h]

[a] Climate Change Research Centre, University of New South Wales, Sydney, Australia
[b] ARC Centre of Excellence for Climate Extremes, University of New South Wales, Sydney, Australia
[c] Laboratoire des Sciences du Climat et de l'environnement, LSCE/IPSL, CEA-CNRS-UVSQ-Université Paris Saclay, F91-198, Gif sur Yvette, France
[d] Vrije Universiteit Amsterdam, Faculty of Science, Cluster Earth and Climate, de Boelelaan 1085, 1081, HV, Amsterdam, the Netherlands
[e] Institut Louis Bachelier, Chair Energy and Prosperity, Paris, 75002, France
[f] Univ Lyon, ENSL, Univ Lyon 1, CNRS, LGL-TPE, F-69007, Lyon, France
[g] Max Planck Inst Chem, Climate Geochem Dept, Hahn Meitner Weg 1, D-55128, Mainz, Germany
[h] LOCEAN/IPSL, Sorbonne Université-CNRS-IRD-MNHN, UMR7159, Paris, France

ARTICLE INFO

Article history:
Received 23 October 2019
Received in revised form
29 May 2020
Accepted 29 May 2020
Available online 19 June 2020

Keywords:
Ocean circulation
Particle fluxes
Pa/Th
Abrupt climate events

ABSTRACT

There is compelling evidence that millennial climate variability of the last glacial period was associated with significant changes in the Atlantic Meridional Overturning Circulation (AMOC). Several North Atlantic sedimentary Pa/Th records indicate a consistent and large Pa/Th increase across millennial-scale events, which has been interpreted as considerable reduction in North Atlantic Deep Water (NADW) formation. However, the use of sedimentary Pa/Th as a pure kinematic circulation proxy is challenging because Pa and Th are also highly sensitive to changes in particulate flux intensity and composition that might have occurred across these millennial scale events. In this study, we use the Pa/Th enabled iLOVECLIM Earth System Model of intermediate complexity to evaluate the impact of changes in biogenic particle flux intensity and composition on the Atlantic Pa/Th. We find that in our model, changes in Particulate Organic Carbon (POC), and to a lesser extent biogenic opal production, can significantly affect the sedimentary Pa/Th, possibly explaining up to 30% of the observed North Atlantic Pa/Th increase across Heinrich stadial 1. The sedimentary Pa/Th response is also likely sensitive to shifts in the geographical distribution of the particles, especially in high scavenging regions. Our study suggests that a decrease in opal production in the northwest Atlantic can induce a far field Pa/Th increase in a large part of the North Atlantic basin. Therefore, local monitoring of particle fluxes may not be sufficient to rule out any influence of changing particle fluxes on sedimentary Pa/Th records.

1. Introduction

There is compelling evidence that the millennial-scale climate variability of the last glacial period was associated with significant changes in the Atlantic Meridional Overturning Circulation (AMOC) (see (Lynch-Stieglitz, 2017) for a review). The most prominent millennial scale climate events are Heinrich stadials, which correspond to cold North Atlantic periods associated with massive iceberg discharges (see (Hemming, 2004) for a review). The most widely accepted hypothesis to account for the North Atlantic cooling during those stadials involves a reduced poleward heat transport caused by a weakening or shutdown of the AMOC (e.g. (Rahmstorf, 2002)).

Among available proxies, one of the most valuable to reconstruct past changes in AMOC strength is the ($^{231}Pa_{xs,0}/^{230}Th_{xs,0}$), which corresponds to the activity ratio of ^{231}Pa (Pa hereafter) and ^{230}Th (Th hereafter) derived from water column scavenging (subscript "xs") at the time of the deposition (subscript "0") - hereafter simply noted Pa/Th. The two isotopes are produced homogeneously in the water column by decay of their parent U

* Corresponding author.
E-mail address: l.missiaen@unsw.edu.au (L. Missiaen).

https://doi.org/10.1016/j.quascirev.2020.106394
0277-3791/

isotopes at a known and constant ratio, called the production ratio, which is equal to 0.093 (dpm/dpm). The dominant ocean sink of Pa and Th is particle scavenging, while radioactive decay plays a smaller role due to their relatively long half-lives (32 760 years for Pa and 75 380 years for Th). As Pa and Th have distinct particle reactivities, and thus different residence times in the water column, the oceanic circulation can influence the sedimentary Pa/Th ratio. Th is more rapidly scavenged and transferred to the sediments than Pa because of its higher particulate reactivity. Hence, its residence time in the water column (10–40 years (Henderson and Anderson, 2003),) is shorter than that of Pa (50–200 years). Therefore, Pa can be transported further by ocean circulation than Th. It is estimated that about 26% of the Pa (and only 4% of the Th) produced in the North Atlantic is transported southwards, out of the Atlantic basin, in the modern ocean (Deng et al., 2018). The excess Pa is transferred to the sediments in the Southern Ocean, rich in opal, which is known to be a strong scavenger for Pa (Chase et al., 2002; Walter et al., 1997). The sedimentary Pa/Th in North Atlantic cores is therefore lower than the production ratio and any increase towards the production ratio results for a large part from a reduction in southward Pa advection by the AMOC. The use of Pa/Th as a kinematic circulation proxy only holds for the Atlantic basin where Pa transport by ocean circulation is dominant over particle-related Pa transport across the particle flux gradients.

A recent Pa/Th compilation over the last deglaciation (Ng et al., 2018) showed a consistent Pa/Th increase of roughly 0.03 Pa/Th units in the North Atlantic during Heinrich stadial 1 (McManus et al., 2004; Mulitza et al., 2017; Ng et al., 2018). This has been interpreted as an indication of a possible complete AMOC shutdown (off-mode).

However, the use of Pa/Th as a kinematic circulation proxy has been debated (e.g. (Lippold et al., 2012b, 2011, 2009), on the basis that the Pa/Th ratio is not only controlled by circulation strength but also by particle scavenging. Pa and Th scavenging efficiencies and affinities for different sediment components have been intensively studied (e.g. (Chase et al., 2003, 2002; Luo and Ku, 2004, 1999)), recently taking advantage of the GEOTRACES water column database (Hayes et al., 2015b). It has been shown that changes in the particle flux intensity and/or composition can significantly increase or decrease the residence time of Pa, and to a lesser extent that of Th (Chase et al., 2003, 2002; Luo and Ku, 2004). As a consequence, Pa and Th can be transported from low particle flux or low scavenging areas to high particle flux and/or high scavenging areas (across the particle fluxes gradients), which is usually referred to as the boundary scavenging effect (Anderson et al., 1983; François, 2007) and can ultimately modify the sedimentary Pa/Th ratio.

Even if quantitative estimates are still lacking, substantial changes in marine productivity and subsequent changes in both particle composition and flux intensity have been evidenced across the millennial-scale events of the last glacial, from both paleo data (e.g. (Cartapanis et al., 2018, 2016; Kienast et al., 2016)) and modelling studies (e.g. (Mariotti et al., 2012; Menviel et al., 2008; Schmittner, 2005). It has also been proposed that a switch in predominant plankton types from diatom-dominated assemblages (i.e. opal producers) to coccolithophore-dominated assemblages (i.e. $CaCO_3$ producers) could have occurred at low latitudes in relation to changes in the environmental conditions (Brzezinski et al., 2002; Matsumoto et al., 2002). The impact of particle composition on the paleo Pa/Th records has been previously assessed indirectly by analyzing the sediment composition (e.g. (Böhm et al., 2015; Gherardi et al., 2009; Lippold et al., 2012a). These analyses mostly focused on the evolution of the sedimentary opal content as opal is known to strongly affect Pa scavenging. A few recent studies also assessed the evolution of the detrital particle flux and its impact on sedimentary Pa/Th (Burckel et al., 2015; Missiaen et al., 2018; Waelbroeck et al., 2018). Generally, the Pa/Th signal has been considered to be mainly driven by circulation changes if 1) the reconstructed sedimentary opal fluxes are lower than an empirical threshold deduced from observations (see (Lippold et al., 2012a)), and/or 2) there is no significant correlation between the reconstructed particle fluxes and the Pa/Th over the considered time period (e.g. (Böhm et al., 2015; Burckel et al., 2015; Waelbroeck et al., 2018). This approach has several major limitations: 1) the sediment content only represents the preserved particles, which may differ significantly from the export particle production at the deposition time due to changes in remineralization intensity (e.g. (Dunne et al., 2007)) or postdeposition dissolution (Farrell and Prell, 1989; Le and Shackleton, 1992; Richaud et al., 2007; Stephens and Kadko, 1997); 2) only the impact of opal fluxes variations has been systematically investigated although Pa and Th are transferred to the sediments by at least 3 other particles types (POC, $CaCO_3$ and lithogenic); 3) though it has been acknowledged that strong particle flux gradients can induce Pa and Th transport across sub-basins (also called « boundary scavenging » (François, 2007)), the particle composition and flux intensity evolutions have been investigated at the considered core sites only, without taking into account any influence of neighboring or regional productivity changes. The latter could indeed induce changes in Pa or Th concentrations at the considered core site location and therefore bias the sedimentary Pa/Th circulation signal. Such biases have been predicted in theory (François, 2007) and references therein) and confirmed by sensitivity experiments in modelling studies (e.g. (Lippold et al., 2012a; Luo et al., 2010).

Because Pa/Th is a complex but valuable proxy of circulation strength, Pa and Th scavenging has been included into several models of varying complexity over the last decades, with the aim to better understand its behavior. The simplest versions consist in 1D box models (e.g. (Nozaki et al., 1981; Roy-Barman, 2009) and zonally averaged 2D models (Luo et al., 2010; Marchal et al., 2000). More complex studies include a 3D set-up in coarse resolution models (Henderson et al., 1999) and with simplified particle representation (Siddall et al., 2007, 2005). The latest developments consider more sophisticated and interactive particle representations in state-of-the-art climate models (Gu and Liu, 2017; van Hulten et al., 2018), and models of intermediate complexity (Missiaen et al., 2020; Rempfer et al., 2017). Some models also include parametrizations to account for the impact of high magnitude coastal fluxes and bottom sediment remobilization on Pa and Th scavenging (Rempfer et al., 2017). These models offer the opportunity to improve our understanding of Pa and Th behavior with respect to circulation and particle changes. To date, some sensitivity experiments have been performed to investigate the impact of the equilibrium partition coefficient (e.g. (Gu and Liu, 2017; Siddall et al., 2005; van Hulten et al., 2018) and circulation changes (Gu and Liu, 2017; Missiaen et al., 2020; Rempfer et al., 2017; Siddall et al., 2007) but little has been done to investigate the impact of changes in particle flux intensity and composition on the sedimentary Pa/Th ratio with a 3D model. While (Lippold et al., 2012a; Luo et al., 2010) tested the impact of particle flux changes in a 2D model framework (Siddall et al., 2007), described the impact of halving and minimizing the total particle fluxes (POC, $CaCO_3$ and opal) in a hosing experiment with a focus on the North Atlantic. To date there has been no comprehensive study assessing the impact of changes in individual particle composition and fluxes.

In this study, we use the Earth System model of intermediate complexity iLOVECLIM to 1) better constrain the role of biogenic particles on sedimentary Pa/Th ratio in a 3D perspective and 2)

assess the potential impact of large-scale past changes in global particle fluxes on paleo Pa/Th records.

2. Methods

2.1. iLOVECLIM Pa/Th module

We use the Earth System model of intermediate complexity iLOVECLIM, which is a fork development of the LOVECLIM model (Goosse et al., 2010). iLOVECLIM includes modules representing the atmosphere (ECBilt), the ocean (CLIO), the sea ice, and the land vegetation (VECODE). The ocean component (CLIO) consists of a free-surface primitive equation ocean model with a resolution of 3° × 3° (corresponding to 120 longitudinal and 65 latitudinal grid cells) and 20 depth layers. A module computing the evolution of dissolved and particulate ^{230}Th and ^{231}Pa in the ocean has been recently added and is fully described in (Missiaen et al., 2020). This Pa/Th module explicitly computes the input of Pa and Th from U decay, their radioactive decay, and their removal by particle scavenging (i.e. adsorption/desorption and particle settling) following the Bacon and Anderson reversible scavenging model (Bacon and Anderson, 1982). In line with other modelling studies (Gu and Liu, 2017; Rempfer et al., 2017) and for simplicity, we have only considered biogenic particles in this study. Nevertheless, the lithogenic particles have been found to have high scavenging efficiencies on Pa and Th (Hayes et al., 2015b), and to potentially represent a significant amount of the total particle fluxes (Conte et al., 2001), or to form nepheloid layers that affect the Pa and Th behavior at the bottom of the oceans (Costa et al., 2020), and would therefore deserve to be considered in future studies. We consider a single particle size class and three different biogenic particle types: biogenic opal, particulate organic carbon (POC), and calcium carbonate ($CaCO_3$). Like in other Pa/Th models (Gu and Liu, 2017; Rempfer et al., 2017; Siddall et al., 2007, 2005), the particles are given a uniform settling speed of 1000 m/y, in agreement with previous estimations (Anderson et al., 2016; Gdaniec et al., 2018; Krishnaswami et al., 1976). The Pa/Th module is not coupled to iLOVECLIM's biogeochemical model because iLOVECLIM does not simulate the oceanic Si cycle. The Pa/Th module therefore does not use prognostic particle fluxes in this study. Instead, the model uses prescribed and fixed 3D particle fields obtained from a preindustrial simulation with the Ocean General Circulation Model (OGCM) NEMO-PISCES. These fields have been described and validated against observations. In particular, it has been acknowledged that while the $CaCO_3$ and POC concentrations are generally underestimated, the opal concentrations are overestimated, in particular on the western margin along the American coast (see (van Hulten et al., 2018) for details). iLOVECLIM computes the transport (advection and diffusion) of the four tracers (i.e. the dissolved and particulate Pa and Th). The scavenging coefficients used in iLOVECLIM are presented in Table 1 and are discussed in more detail in (Missiaen et al., 2020). The simulated dissolved and particulate Pa and Th patterns as well as sedimentary Pa/Th have been evaluated against the recent GEOTRACES observations (Deng et al., 2014; Hayes et al., 2015a, 2015b) and a core-top compilation (see (van Hulten et al., 2018) and references therein). The model performance in simulating the water column and sedimentary Pa and Th is comparable to state-of-the-art ocean circulation models (see (Missiaen et al., 2020). Our model is computationally efficient, able to simulate 800 years of Pa and Th evolution in about 24 h.

$$Kd_{(i,j)} = \frac{\sigma_{i,j} \times w^s \times \rho_{sw}}{M^{(i)} \times k^{desorp}}$$

where $Kd_{(i,j)}$ is the partition coefficient for isotope i (Pa or Th) for particle type j (POC, $CaCO_3$ or opal), $\sigma_{i,j}$ are the scavenging efficiencies for isotope i of particle j that are obtained after model optimization as described in (Missiaen et al., 2020), w^s is the settling speed, K^{desorp} is the desorption coefficient considered constant and equal to 2.4 y^{-1}, $M^{(i)}$ is the molar mass of particle type i (i.e. 12 g mol^{-1} for POC, 100.08 g mol^{-1} for $CaCO_3$ and 67.3 g mol^{-1} for opal) and ρ_{sw} is the mean density of sea water (constant and fixed to 1.03 10^6 g m^{-3}).

2.2. Experimental design

The model was first equilibrated for 5000 years (control run) under PI boundary conditions with control particle fields as described in (Missiaen et al., 2020; van Hulten et al., 2018). In order to investigate the potential impact of large-scale changes in particle flux intensity and composition on the sedimentary Pa/Th, we perform ten idealized sensitivity experiments in which we vary the prescribed particle fields under pre-industrial (PI) boundary conditions (Table 2). The idealized sensitivity experiments are run for 1000 years each, and the particle flux fields (i.e. concentration times settling speed) are globally increased or decreased by multiplying the particle concentrations by a fixed factor (i.e. preserving the regional patterns of the PI control particles, and keeping the settling speed constant) as described in Table 2. The particle forcing is shown in Fig. 1. Given that the residence time of Pa and Th in the ocean have been estimated to be about 200 and 40 years respectively (Henderson and Anderson, 2003), the duration of our

Table 2
Particle flux forcing applied in sensitivity experiments under PI boundary conditions. The particle fluxes have been altered globally by changing the particle concentration, keeping the settling speed at 1000 m/y. Twice the PI flux is denoted CTRLx2, half the PI flux is denoted CTRL_2.

Simulation name	POC	$CaCO_3$	Opal
CTRL	CTRL	CTRL	CTRL
All_x2	CTRL x2	CTRL x2	CTRL x2
All_2	CTRL/2	CTRL/2	CTRL/2
Opal_x2	CTRL	CTRL	CTRL x2
Opal_2	CTRL	CTRL	CTRL/2
CaCO3_x2	CTRL	CTRL x2	CTRL
CaCO3_2	CTRL	CTRL/2	CTRL
POC_x2	CTRL x2	CTRL	CTRL
POC_2	CTRL/2	CTRL	CTRL
Opal_2_CaCO3_x2	CTRL	CTRL x2	CTRL/2

Table 1
Scavenging coefficients in iLOVECLIM.

a) Sigma coefficients (as parametrized in iLOVECLIM)					
σ_Pa_CaCO3	σ_Pa_POC	σ_Pa_opal	σ_Th_CaCO3	σ_Th_POC	σ_Th_opal
1.87	1.55	7.62	76.83	5.47	3.77
b) Kd equivalents (see (Missiaen et al., 2020))					
Kd_Pa_CaCO3	Kd_Pa_POC	Kd_Pa_opal	Kd_Th_CaCO3	Kd_Th_POC	Kd_Th_opal
8.01 E+06	5.53 E+07	4.86 E+07	3.29 E+08	1.96 E+08	2.40 E+07

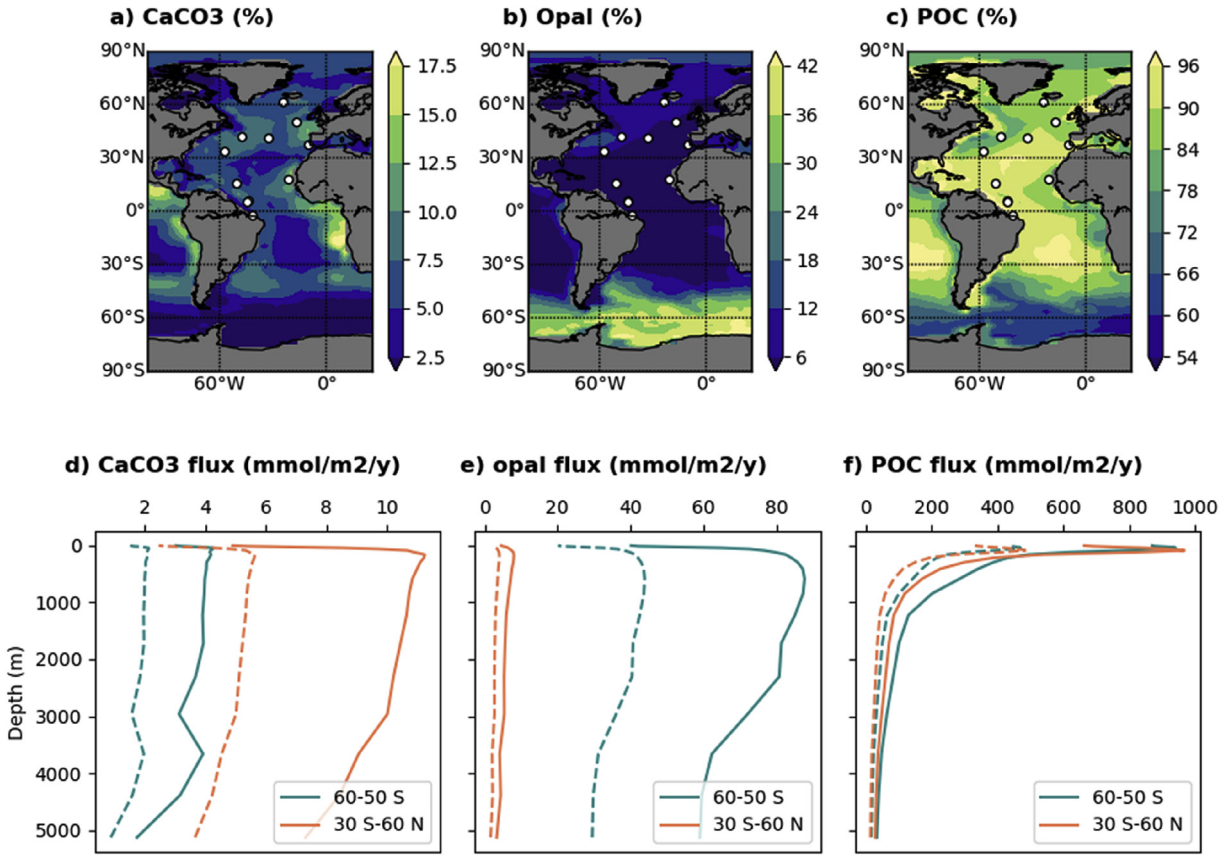

Fig. 1. Particle forcing. Percentage of each particle type obtained by integrating the considered particle concentrations over the water column and normalizing by the sum of the integrated concentrations of all particles ($CaCO_3$ + opal + POC = 100%) for each grid-cell for a) $CaCO_3$, b) opal and c) POC. All particle fields used in this study are derived from a preindustrial simulation performed with NEMO-PISCES (van Hulten et al., 2018) (see methods). The white dots represent the locations of cores with available Pa/Th time series covering Heinrich stadial 1 (Ng et al., 2018). Zonally averaged Atlantic particle profiles expressed as particle fluxes (mmol/m^2/y) for d) $CaCO_3$, e) opal and f) POC. The blue lines represent the average profile between 50°S and 60°S, the orange lines represent the average profile between 30°S and 60°N. The dashed lines represent the particle forcing profiles for halved concentrations. The export particle fluxes at 75 m are presented in Figure S1.

sensitivity simulations is sufficient to reach equilibrium as shown in previous studies (Missiaen et al., 2020; van Hulten et al., 2018). We then compare the last 100 years of each simulation with 100 years of the PI control simulation.

It has been suggested that changes in environmental conditions during episodes of past climate change (such as the last deglaciation) might have triggered a switch between dominant plankton assemblages (namely between diatoms that produce biogenic silica and coccolithophores that mostly produce $CaCO_3$ (Brzezinski et al., 2002; Matsumoto et al., 2002)). The hypothesis states that silicic acid might have been transported towards lower latitudes where it would have enhanced diatom productivity under glacial conditions, knowing that silicic acid availability is a limiting nutrient at low latitudes today. During the last deglaciation, the diatom productivity might therefore have decreased at low latitudes, while the coccolithophore productivity might have increased, as a result of changes in temperature as well as nutrient (and in particular Si) availability. This might have changed the water column $CaCO_3$/opal rain ratio, consistent with large marine ecosystem reorganizations across climatic transitions suggested by modelling studies (e.g. (Bopp et al., 2005; Marinov et al., 2010)). In addition, lower $CaCO_3$ burial rates despite higher sediment accumulation rates (105% of the Holocene mass accumulation rate) have been reported during the Last Glacial Maximum (LGM) (Cartapanis et al., 2018). Although post depositional dissolution cannot be excluded, these results are consistent with reduced coccolithophore production at the LGM. Here, we test the impact of such plankton assemblage changes by globally increasing the $CaCO_3$ concentrations and decreasing the opal concentrations by a factor of 2 assuming that the total productivity (POC) concentration remained constant.

The Pa and Th fluxes to the sediment presented in this study correspond to the Pa or Th activity in the bottom ocean grid cell (deepest flooded grid cell) multiplied by the uniform particle settling speed of 1000 m/y.

Under PI boundary conditions, the simulated AMOC in iLOVECLIM is about 17 Sv with interannual and decadal variability of ± 2 Sv. To account for this variability, we tested the significance of the changes due to particle modifications as follows. We define the natural variability of the sedimentary Pa/Th as its variance (2 sigma) evaluated over the last 100 years of the PI control simulation. Then, we evaluate the significance of the anomaly between the average sedimentary Pa/Th in a perturbed simulation and in the control run over the 100 final years of the simulation. An anomaly is considered to be significant if it exceeds the natural variability (i.e. anomaly >4 sigma).

3. Results

3.1. Pa and Th scavenging in iLOVECLIM under control PI conditions

Before analyzing the impact of changes in particle flux intensity and composition, we start by describing the scavenging of Pa and

Th in the control PI run. We define the normalized Pa and Th flux to the sediments as the ratio of the Pa and Th buried in the sediments to the local production in the overlying water column. In the absence of any Pa or Th transport, the Pa and Th burial would equal the production in the corresponding overlying water column. Therefore, when the normalized fluxes are different from 1, they indicate the extent of Pa and Th transport in the Atlantic either related to the deep circulation or to the particle gradients (Fig. 2). The normalized flux to the sediments ranges between 0.5 and 1.4 for Th (median = 1 (as expected), 1 sigma = 0.34) while it ranges between 0.3 and >2 for Pa (median = 1 (as expected), 1 sigma = 0.76), highlighting that a larger proportion of the Pa is transported within the Atlantic basin compared to Th. The simulated normalized Pa and Th fluxes display a common geographical pattern. The two isotopes are preferentially buried in the sediments along the North American continental margin (between 30°N and 50°N), off the Argentinian coast (between 20°S and 60°S) and off the African coast. Pa is also effectively buried in the Southern Ocean opal belt (between 40°S and 60°S), which is consistent with the transport of Pa from the North Atlantic to the Southern Ocean by the AMOC (Walter et al., 1997). The two isotopes also tend to be transported away from the basin interior (i.e. in the two subtropical gyres - ~10°N to 40°N and ~10°S to 40°S)).

Overall, the regions of effective Pa and Th burial correspond to regions where marine productivity is active and produces large fluxes of biogenic particles (Fig. 2 - Figure S1). In such regions, dissolved Pa and Th are rapidly adsorbed onto the particles because of the high particle fluxes and are actively transferred to the sediments. Consistently, there is a deficit of dissolved Pa and Th, which is dynamically altered by eddy advection and diffusion.

3.2. Impact of globally uniform changes in particle fluxes

In this section we describe the impact of globally uniform changes in particle fluxes on Pa and Th scavenging under PI boundary conditions (see methods). As we obtain quasi symmetric responses for the doubling and halving of particle concentrations, we only discuss the case of reduced particle concentrations. The results of experiments where particle concentrations were doubled are shown in the supporting information (Figures S2, S3 and S5).

3.2.1. Dissolved Pa and Th

Although dissolved Pa and Th activities (hereafter simply designated by dissolved Pa and Th) are not accessible in the paleorecords, their spatial distribution provides insights into the particle type that most effectively scavenges Pa and Th to the sediments in different sub-regions of the Atlantic basin.

As expected, a decrease in the total particle flux (all_2) leads to an increase in dissolved Pa and Th across the entire Atlantic basin, because less Pa and Th is being scavenged and removed from the water column by particles (Fig. 3). In our model, halving the particle content in the whole water column roughly doubles the dissolved Pa and Th activities, suggesting a quasi linear response of the dissolved phase (Fig. 3). The magnitude of the changes in dissolved Pa and Th is sensitive to the type of the altered particles, consistent with the prescribed scavenging affinities (Table 1). Halving POC concentrations (POC_2) increases both the dissolved Pa and Th by ~40% in most of the Atlantic basin. By contrast, changing the opal or $CaCO_3$ concentrations creates region specific responses. Halving the opal concentration (opal_2) results in a 80% increase in dissolved Pa in the Southern Ocean while dissolved Th is increased by ~15% in the Southern Ocean and displays no significant change in the rest of the basin. Finally, halving the $CaCO_3$ concentrations (CaCO3_2) leads to a 15% increase in dissolved Pa and a 50–60% increase in dissolved Th concentrations in most of the Atlantic Ocean (Fig. 3).

We note that $CaCO_3$ and POC are mostly present north of 40°S, with POC being the most abundant particle (Fig. 1). In the Southern Ocean, opal is the most abundant particle while POC and $CaCO_3$ have very low concentrations. The geographical pattern of dissolved Pa and Th variations is closely correlated to particle distribution: the highest changes in dissolved Pa and Th are observed in high particle flux regions such as coastal areas and the Southern Ocean opal belt (i.e. high scavenging intensity regions, see Section 3.1). Halving POC or $CaCO_3$ concentrations leads to an increase in dissolved Pa north 40°S, while halving opal concentrations increases the dissolved Pa in the Southern Ocean and to a lesser extent along the North American coastal margin (between 30°N and 50°N) (Fig. 3). By contrast, decreasing $CaCO_3$ concentrations increases the dissolved Th north of 40°S while decreasing the opal or POC concentrations increases the dissolved Th in the Southern Ocean (Fig. 3).

Our simulations highlight that in our model Pa is mostly

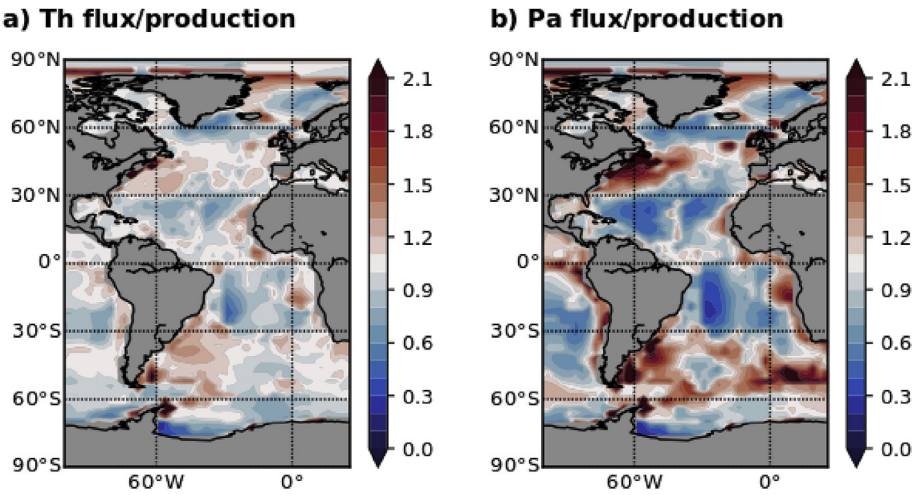

Fig. 2. Pa and Th flux to the sediments normalized to the production in the overlying water column. a) Th flux/production b) Pa flux/Production i.e. ratio between the Pa or flux to the sediment and the production in the overlying water column calculated in each grid cell. Values lower than 1 indicate that Pa and/or Th have been transported away. The areas of high Pa and Th fluxes, in particular along the coast of North America (between ~30°N and 50°N), South America (~30°S –60°S) and the African coast, correspond to regions of high particle fluxes (see Fig. 1).

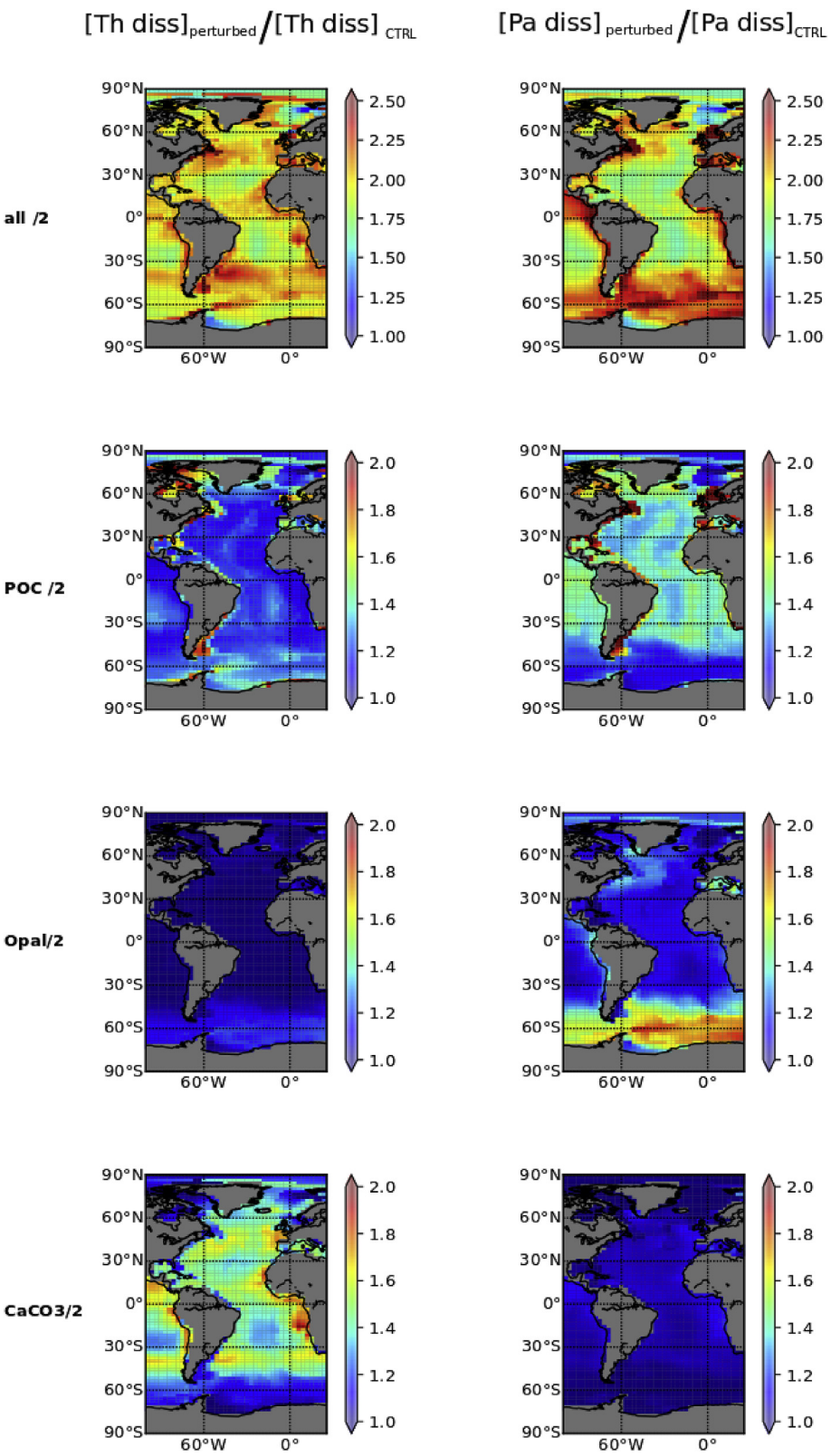

Fig. 3. Ratio between water column integrated dissolved Th and Pa activities ([Pa diss] and [Th diss]) of the corresponding perturbed simulations and the equivalent from the PI control simulation (CTRL). Values equal to 1 indicate no change, values > 1 indicate more dissolved Pa and Th.

transferred to the sediments by opal in the Southern Ocean as well as off the North American coast (between 30°N and 50°N) where our prescribed particle fields contain a relatively high amount of opal. Elsewhere, Pa is transferred to the sediments by POC and to a lesser extent by $CaCO_3$. Th is the element that is most effectively transferred to the sediments by $CaCO_3$ in most of the Atlantic basin. In the Southern Ocean, where there is less $CaCO_3$, Th is scavenged by opal and POC with roughly the same efficiency. This is consistent with the prescribed affinities of Pa and Th for the different particle types (Table 1).

3.2.2. Sedimentary Pa/Th

In this section, we focus our analysis on the modelled sedimentary Pa/Th, which corresponds in our simulations to the ratio of the particulate Pa and Th in the deepest ocean grid cell (see methods). We note that the spatial pattern of sedimentary Pa/Th response is comparable to the spatial pattern of sedimentary Pa (Figures S4 and S5), highlighting the driving role of Pa in the sedimentary Pa/Th response. Contrarily to what we observed for dissolved activities, halving the particle fluxes does not produce a uniform Pa/Th change throughout the whole Atlantic. Instead, the Pa/Th response to particle changes has an interesting geographical pattern that we describe below for our different simulations (all_2, opal_2, CaCO3_2 and POC_2). The results of the simulations in which we multiply the particle fields by 2 are presented in the supplementary material (Figure S3).

Decreasing the total particle concentration (all_2) decreases the sedimentary Pa/Th by about 0.016 in most of the Atlantic basin (Fig. 4). The magnitude of the Pa/Th decrease in coastal regions is about twice as large as in the basin interior. In the Southern Ocean and along the West African coast, decreasing the total particle concentration induces a Pa/Th increase of 0.012–0.02 (Fig. 4). In this simulation, less Pa is transferred to the sediments in the Atlantic basin, leaving more Pa to be transported into the Southern Ocean, where it is scavenged by opal. The same overall sedimentary Pa/Th pattern is observed in the POC_2 experiment, with anomalies of slightly lower amplitude: the Pa/Th decreases by about 0.012 in the major part of the Atlantic basin and increases by about 0.01–0.018 in the South Atlantic, off the West African coast and off the North American coast (between 30°N and 50°N). These changes show that in our simulations POC is the main scavenger particle type for Pa, except south of 40°S, in the Southern Ocean opal belt. Interestingly, according to the scavenging coefficients (Table 1), Pa affinity for POC is not particularly high, especially when compared to its affinity for opal (i.e. Kd_Pa_POC is almost equal to Kd_Pa_opal). But the scavenging intensity is driven by both the affinity and the particle flux (i.e. particle concentration multiplied by the settling speed). The high POC fluxes, which are 12–35 times higher than the opal and $CaCO_3$ fluxes (Fig. 1) in the Atlantic basin north of 40°S, explain the high sensitivity of Pa to changes in POC concentrations. Looking at the POC profiles (Fig. 1), we note that the high concentrations are restricted to the first 300 m and rapidly decrease with depth. Our model therefore suggests that surface productivity changes can significantly affect deep/sedimentary Pa/Th, highlighting the role of POC to effectively transfer the Pa produced in the upper water column to deeper layers.

Though opal is only abundant in the Southern Ocean, a decrease in opal concentration (opal_2) also produces significant sedimentary Pa/Th changes with a slightly more complex geographical pattern. The sedimentary Pa/Th decreases by 0.012–0.02 in the South Atlantic (around 40°S) and off the North American coast (between 30°N and 50°N). There is a minor decrease (around 0.008) along the equator between 10°S and 10°N. Elsewhere, and in particular in the two subtropical gyres, which are depleted in opal, the Pa/Th increases by about 0.01 (Fig. 4).

Finally, halving the $CaCO_3$ concentrations (CaCO3_2) has the least impact on sedimentary Pa/Th (<0.0008), with Pa/Th increasing in the subtropical gyres and decreasing elsewhere. The

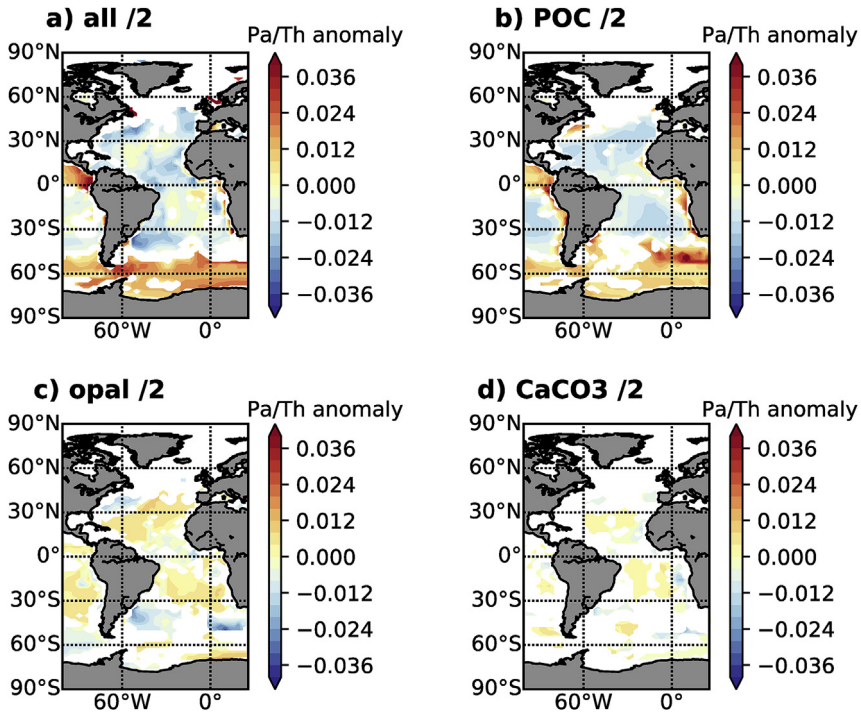

Fig. 4. Sedimentary Pa/Th response to forced global particle flux decrease. Sedimentary Pa/Th anomalies (sensitivities studies − PI control run). The areas in white did not display significant changes compared to the natural variability (i.e. anomalies <4σ − see methods). The changes in all/2 reflect the combination of changes in POC/2, opal/2 and CaCO3/2, even if not clearly apparent on the figure as changes less than 4σ are not shown.

low impact of $CaCO_3$ on Pa/Th is related to the low affinity of Pa for this particle type (Table 1) and to low $CaCO_3$ concentrations (Fig. 1).

To summarize, we have seen that in our simulations POC is the dominant particle that transfers Pa to the sediments in the Atlantic Ocean, while opal is the main scavenger in regions where NEMO-PISCES simulated high opal concentrations, i.e. in the Southern Ocean and along the North American continental margins (between 30°N and 50°N and around 40°S). $CaCO_3$ has the smallest impact on sedimentary Pa/Th, consistent with the low affinity of Pa for $CaCO_3$ (Table 1) and lower particle concentrations. Despite some spatial variability, reducing the particle concentration tends to increase Pa accumulation in the sediments of the open ocean and subtropical gyres. Our study suggests that the sedimentary Pa/Th response to a 50% particle concentration decrease i) exceeds the natural Pa/Th variability under PI conditions, leading to mean Pa/Th changes of 0.01, and ii) strongly depends on the particle fields and their geographical distribution.

3.3. Impact of a change in phytoplankton type

In this section we analyze the results of a simulation where we mimic a global change in plankton community at constant POC production by halving the opal flux and doubling the $CaCO_3$ flux (see methods). This is informative on the respective role of the two particle types in driving sedimentary Pa/Th changes in the different regions of the Atlantic basin. In the opal_2_CaCO3x2 simulation, sedimentary Pa/Th strongly decreases by 0.02 in the Southern Ocean around 40°S and in particular in the southeastern Atlantic basin (Fig. 5). Pa/Th also decreases along the American margin (between 30°N and 50°N) by 0.015 and to a lesser extent between 20°S and the equator where the decrease is less than 0.01. Elsewhere the sedimentary Pa/Th increases, in particular in the North Atlantic between 0 and 40°N by about 0.01 and off the African coast by up to 0.015 (Fig. 5). Overall, the sedimentary Pa/Th pattern in the opal_2_CaCO3x2 simulation is similar to the pattern obtained in the opal_2 simulation in the North Atlantic and in the Southern Ocean (south of 40°S) and to the CaCO3x2 simulation in the equatorial south Atlantic and along the African coast (between 40°S and 20°N) (Fig. 5). The sedimentary Pa/Th is therefore mostly affected by changes in opal flux in the North Atlantic and in the Southern Ocean (south of 40°S), while it is predominantly affected by changes in $CaCO_3$ flux in the equatorial south Atlantic and off the African coast (between 40°S and 20°N).

4. Discussion

4.1. Potential changes in particle fluxes across climatic transitions

There is compelling evidence of marked productivity changes across climatic transitions (e.g. Jaccard et al., 2013; Kohfeld et al., 2005) associated with variations of biogenic particles (POC, CaCO3 and opal) production (e.g. Yamamoto et al., 2019) and burial (Cartapanis et al., 2018, 2016). However, quantitative reconstructions of changes in particle fluxes across climatic transitions are currently limited by 1) the lack of Atlantic-wide compilations of proxy-based reconstructions, 2) discrepancies between model outputs when different models are run under similar boundary conditions (e.g. (Kageyama et al., 2013a, 2013b)). Despite these limitations, both proxy data and climate models consistently suggest a decrease in productivity in the North Atlantic while the productivity might have increased slightly in the Southern Ocean and in equatorial regions during Heinrich stadials (e.g. (Brown and Galbraith, 2016; Mariotti et al., 2012 and references therein, Martínez-García et al., 2014; Straub et al., 2013)). Modelling studies (Brown and Galbraith, 2016; Mariotti et al., 2012) estimate that the export productivity could have decreased by about 50% in the North Atlantic during an Heinrich stadial. In this study we have explored the impact of similar large-scale variations in export productivity by doubling or halving the particle fluxes in our simulations.

4.2. Sensitivity of sedimentary Pa/Th to particles versus circulation changes

A recent compilation of Pa/Th records covering the last deglaciation in the Atlantic basin (Ng et al., 2018) shows that most of the northwest Atlantic cores display a marked ~0.03 Pa/Th units increase between the LGM and Heinrich stadial 1. Such Pa/Th variations have also been observed for other millennial scale events (e.g. Böhm et al., 2015; Burckel et al., 2016, 2015; Waelbroeck et al., 2018). Our sensitivity study shows that a 50% change in biogenic particle flux intensity can lead to a variation in Pa/Th of ~0.01, which corresponds to about 30% of the observed Pa/Th increase across Heinrich stadial 1.

By comparison, in iLOVECLIM, a ~250 years AMOC shutdown under PI boundary conditions causes a consistent Pa/Th increase of about 0.03 in the northwest Atlantic (40°N - 60°N) between 2000 and 3000 m water depth (Missiaen et al., 2020). This is consistent

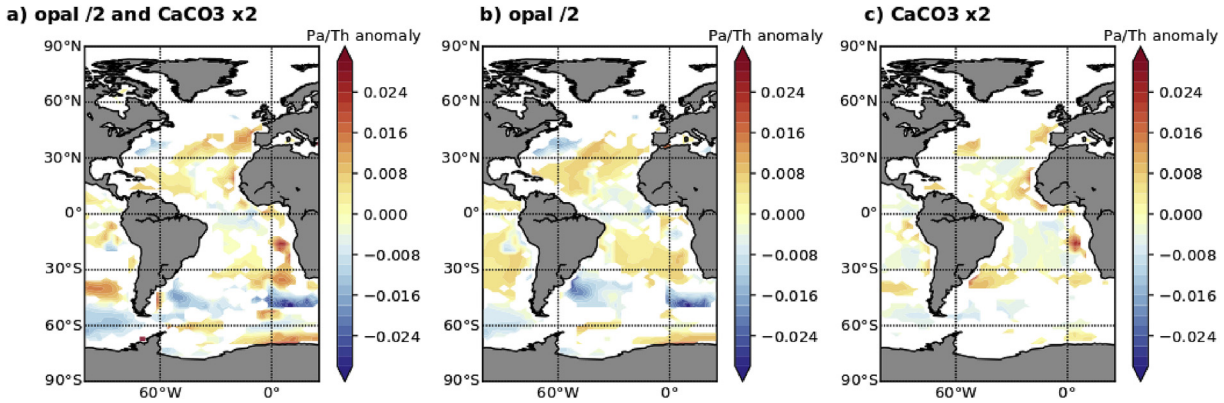

Fig. 5. Effect of a change in plankton community on the sedimentary Pa/Th. As on Fig. 4, sedimentary Pa/Th anomalies are represented (sensitivities studies − PI control run). The areas in white did not display significant changes compared to the natural variability (i.e. anomalies $<4\sigma$ − see methods). Opal concentrations are halved, while $CaCO_3$ concentrations are doubled and POC concentrations are maintained constant.

with the simulated Pa/Th variations obtained in other model studies (Gu and Liu, 2017; Rempfer et al., 2017; Siddall et al., 2007). However, at the Bermuda Rise location (~34°N, 58°W, > 4300 m), where the first Pa/Th time series has been obtained (McManus et al., 2004), the Pa/Th increases by ~ 0.01 in iLOVECLIM, which is less than the observed Pa/Th variation recorded at this location across Heinrich stadial 1. However, this particular hosing experiment is not an analogue to a Heinrich event, because the simulation was integrated under preindustrial (not glacial) boundary conditions, the freshwater was only added to the Nordic Seas, and the AMOC was shut down for a relatively short duration (~300 years), which is shorter than what is observed during Heinrich stadial 1 (>1000 years) (see (Missiaen et al., 2020)). In addition, the Bermuda Rise lies in the transition zone between the coastal region with high particle fluxes and the open ocean in iLOVECLIM (see Fig. 1), complicating direct model-data comparison at this specific location. The particle-induced Pa/Th variations simulated in this study are therefore significant and of the same order of magnitude (30–100%) than the simulated changes obtained during an AMOC shutdown.

It is important to note that the amplitude of Pa/Th variations due to a circulation slowdown was tested in iLOVECLIM with an AMOC strength of ~17 Sv, but a rather shallow NADW (~2500 m) compared to observations (Lozier et al., 2019). As Pa concentrations typically increase with depth (Henderson and Anderson, 2003), the depth of NADW may impact the southward transport of Pa in the model. Any change in the boundary conditions, such as for example the reference climate state (e.g. LGM), and subsequent changes in the Atlantic water masses configuration, will also likely impact the sensitivity of the sedimentary Pa/Th to changes in particle fluxes. In line with previous studies, we find that in regions with sluggish circulation (typically outside of the deep western boundary current), the impact of particle fluxes variations (e.g. in coastal areas) could have an even larger impact on sedimentary Pa/Th. Indeed, in these regions, the particle-induced Pa transport is a dominant process that can overcome the circulation-induced Pa transport (Gu and Liu, 2017).

To date, attempts to achieve quantitative reconstructions of the AMOC strength variations rely on fitting a Pa/Th enabled model to observed Pa/Th variations from Atlantic sediment cores. However, the skill of a Pa/Th model to predict the sedimentary Pa/Th response to abrupt circulation changes depends on its ability to capture the "right" balance between Pa and Th transport by advection and Pa and Th transport induced by particle flux gradients (i.e. the scavenging regime). Future work is therefore needed to further evaluate the sensitivity of iLOVECLIM and other Pa/Th enabled models to circulation and particle fluxes changes.

4.3. Evaluation of the Pa and Th transport in iLOVECLIM

One way to further assess how Pa and Th are transported in a model consists in analyzing the normalized Pa and Th fluxes to the sediments i.e. the ratio between the fluxes to the sediments (particulate Pa and Th) and the local water column production (Fig. 1-see section 3.1). Model studies first estimated that up to 30% of the Th is transported and deposited away from the water column where it has been produced (Henderson et al., 1999). A recent analysis of the new GEOTRACES water column data revised this estimate to ~40% (Hayes et al., 2015a), which was confirmed by the recent review and compilation of ^{230}Th sedimentary data of (Costa et al., 2020). In other words, assuming that Th settles fast enough to stay in the Atlantic basin, the ratio between the Th flux to the sediments and the local water column production should range between ~0.6 and 1.4. In iLOVECLIM, the range of normalized Th flux is slightly wider (from ~0.4 to 1.6) in the PI control simulation, meaning that Th transport (mostly by particle gradients) is likely slightly overestimated. The normalized Th flux from different models embedding Pa and Th has been shown to often resemble the biological productivity pattern as observed here in iLOVECLIM. However, while iLOVECLIM produces normalized Th fluxes relatively close to 1, a larger range in normalized Th fluxes has been evidenced in other models (Costa et al., 2020). Future work is needed to evaluate how the scavenging regimes are represented across different Earth system models embedding Pa and Th isotopes, as well as how the different model structures and parametrization choices influence the sedimentary Pa/Th.

4.4. Impact of far field changes in particle fluxes on Pa/Th records

Our sensitivity experiments highlight that the sedimentary Pa/Th response has a geographical pattern that is tightly related to the geographical distribution of the particles and the spatial distribution of high scavenging intensity areas. In regions where Pa and Th are dominantly scavenged to the sediments by a certain particle type, a greater flux of this particle type increases the Pa/Th ratio (as expected). Where this particle type is not the dominant scavenger, the opposite effect happens. When reducing the scavenging intensity in a neighboring region, the Pa/Th is found to increase outside the main scavenging areas as more Pa can escape from the high scavenging areas and settle down in the open ocean sediments. In particular, our study suggests that an opal production decrease off the North American coast (between 30°N and 50°N - corresponding in our model to a high opal flux area) may induce a significant Pa/Th increase in a large part of the North Atlantic basin, where opal production is low and where most of the available Pa/Th records are located (Figs. 1–4). A decrease in the particle fluxes results in an increase in the residence time of Pa and Th in the water column. The fact that in our model more Pa settles in the North Atlantic when we decrease the particle fluxes globally is due to reduced Pa scavenging along the American coast (between 30°N and 50°N). The presence of opal in the North Atlantic under modern conditions is corroborated by modern observations (van Hulten et al., 2018). Additionally, there is evidence in the sediments for a North Atlantic opal belt (Lippold et al., 2012a; Seiter et al., 2004) south of Iceland while in the model the North Atlantic opal belt is located closer to the North American coast.

The fact that Pa can be burried in the North Atlantic sediments when the general scavenging intensity decreases also suggests that relatively low amounts of Pa are transported towards the Southern Ocean in the central North Atlantic in our model. This may be related to the relatively shallow NADW (lower boundary ~2500 m) compared to observations, given that the highest concentrations of Pa are generally found at greater depths and/or in regions with sluggish circulation outside of the deep western boundary current. Further work is needed to investigate the mechanisms of Pa transport in other Pa/Th enabled models.

From the data side (Gherardi et al., 2009), reported an inverse relationship between the reconstructed diatom flux (hence opal flux) and the sedimentary Pa/Th in core MD95-2027 located in the northwest Atlantic, which is consistent with our sensitivity experiment results. The potential of changes in biogenic particle fluxes and composition to increase the sedimentary Pa/Th ratio has been largely acknowledged in the literature, with a particular concern for opal, for which Pa has a very strong affinity (Chase et al., 2002). The impact of potential changes in opal flux on sedimentary Pa/Th has been assessed by different means. Some studies argued that the opal content of the core(s) remained low (generally < 5 wt %) throughout the studies time interval (Böhm et al., 2015; Lippold et al., 2016, 2012a). Other studies highlighted that there was no

correlation between the Pa/Th and the ^{230}Th-normalized opal flux and/or ^{230}Th-normalized diatom valves flux records in the sediment core (e.g. (Gherardi et al., 2009; Mulitza et al., 2017; Nave et al., 2007). Our study confirms that in addition to the site-specific particle flux variations, the basin-wide and/or regional particle fluxes may have also impacted the paleo Pa/Th records. Revisiting the available Pa/Th records would thus require an extensive basin-wide evaluation of the particle flux evolution and/or evaluation of the Pa budget in the Atlantic basin (Hayes et al., 2014) throughout the deglaciation.

Finally, our sensitivity experiments with iLOVECLIM show that uniform changes in particle concentrations affect the Pa/Th ratio distribution differently depending on the particle type, and our model suggests that changes in POC may influence the sedimentary Pa/Th ratio more than opal. From the observational side, changes in POC concentrations have not been monitored along with the Pa/Th time series, mostly because sedimentary POC content is prone to be modified by post-deposition remineralization processes. In our simulations, the high sensitivity of the sedimentary Pa/Th to POC could potentially originate from two distinct model features: 1) an over-representation of POC concentrations in the particle forcing fields and/or 2) the choice of scavenging coefficients that give Pa and Th high affinity for POC (see Table 1). The prescribed particle concentration fields used in this study have been evaluated against modern data in (van Hulten et al., 2018) and the POC concentrations appear to be slightly overestimated in the upper 200 m of the water column, but generally underestimated in the oligotrophic regions such as the subtropical gyres. Additional observations of particulate concentrations in the water column are required to better assess the quality of the POC representation in NEMO-PISCES. The coefficients are tunable parameters that have been determined using an objective exploration of the parameter space (Missiaen et al., 2020) and set to obtain the best fit between sedimentary Pa/Th, dissolved and particulate water column Pa and Th. The scavenging coefficients that are used in iLOVECLIM are significantly higher than observations (Hayes et al., 2015b). However, decreasing the scavenging coefficients towards the values determined by (Hayes et al., 2015b) dramatically decreases model data agreements in the water column, suggesting that the model needs high scavenging coefficients to remove enough Pa and Th from the water column. This is consistent with the conclusions from previous studies (e.g. Dutay et al., 2009), which found that scavenging coefficients are implicitly inversely scaled to the particle fluxes in order to simulate a scavenging intensity compatible with observations. Further model intercomparison work is needed to investigate whether the high sensitivity of sedimentary Pa/Th to POC is a robust feature across different representations of Pa and Th scavenging in different models.

5. Conclusions and perspectives

We have performed a set of idealized simulations using the Earth System model of intermediate complexity iLOVECLIM in order to study the large-scale relation between sedimentary Pa/Th and biogenic particle fluxes in the water column. Our results show that changes in particle fluxes due to changes in biogenic export productivity can significantly impact sedimentary Pa/Th. Our simulations suggest that the Pa/Th response is sensitive to the geographical distribution of particles and intense scavenging areas; for example, a decrease in the opal fluxes off the North American coast (between 30°N and 50°N), where in our reference preindustrial simulations the opal fluxes are relatively high, induces a sedimentary Pa/Th increase in most of the North Atlantic basin, outside of the high opal scavenging area. Far field changes in opal production might therefore impact the sedimentary Pa/Th, even in low opal production areas. Our simulations show that depending on the particle type, uniform changes in particle fluxes affect the spatial distribution of the Pa/Th ratio differently (Figs. 4–5). They also highlight a potential dominant role of POC in driving Pa/Th changes, followed by opal. Further work is necessary to assess if this result is a robust feature across different models able to simulate the evolution of Pa and Th in the ocean. Halving the particle fluxes, as might have happened during Heinrich stadial 1, leads to a Pa/Th increase of about 0.01, corresponding to ~30% of the observed Pa/Th increase in the North Atlantic across Heinrich stadial 1. This corresponds to at least one third and up to the full amplitude of sedimentary Pa/Th changes simulated during an AMOC shutdown by the same model, suggesting that in this model framework, the sedimentary Pa/Th has a similar sensitivity to circulation and particle flux changes. The ability of a model to capture the amplitude of Pa/Th changes associated with abrupt climate change is related to its ability to capture the right balance between the circulation-related and the particle-related transport, which ultimately depends on the representation of the deep-water circulation, particle fluxes and the scavenging parameters. Further progress in assessing the impact of particle-induced sedimentary Pa/Th changes therefore requires i) a thorough evaluation of past geographical particles patterns, and ii) a skillful representation of the scavenging regime and water mass pathways, which would require an in-depth Pa/Th model intercomparison.

Author contributions

LM, LCM and KJM designed the research. LM, DMR, NB, JCD AQ and FL developed the iLOVECLIM model. LM performed the simulations and data curation. JCD and SP contributed to expert knowledge on Pa/Th. LM wrote the manuscript with the inputs form all the co-authors. CW, KJM and LCM obtained the funding.

Lise Missiaen: Conceptualization, Investigation, Methodology, Validation, Visualization, Writing- original draft. **Laurie C. Menviel**: Supervision, Writing-review and editing, Funding acquisition. **Katrin J. Meissner**: Supervision, Writing-review and editing, Funding acquisition. **Didier M. Roche**: Resources, Methodology, Software, Writing-review and editing. **Nathaelle Bouttes**: Methodology, Software, Writing-review and editing. **Jean-Claude Dutay**: Methodology, Writing-review and editing. **Aurélien Quiquet**: Methodology, Software, Writing-review and editing. **Fanny Lhardy**: Methodology, Software, Writing-review and editing. **Sylvain Pichat**: Writing-review and editing. **Claire Waelbroeck**: Writing-review and editing, Funding acquisition

Code and data availability

The iLOVECLIM source code is based on the LOVECLIM model version 1.2 whose code is accessible at http://www.elic.ucl.ac.be/modx/elic/index.php?id=289. The developments on the iLOVECLIM source code are hosted at https://forge.ipsl.jussieu.fr/ludus but are not publicly available due to copyright restrictions. Access can be granted on demand by request to D. M. Roche (didier.roche@lsce.ipsl.fr).

The model output related to this article will be submitted to https://pangaea.de/.

Declaration of competing interest

The authors declare that they have no conflict of interests.

Acknowledgements

This is a contribution to ERC project ACCLIMATE; the research leading to these results has received funding from the European Research Council under the European Union's Seventh Framework Programme (FP7/2007–2013)/ERC grant agreement 339108. KJM, LCM and LM acknowledge funding from the Australian Research Council grant DP180100048 awarded to KJM and LCM and grant FT180100606 awarded to LCM. We thank S. Moreira and for his help with Python.

Appendix A. Supplementary data

Supplementary data to this article can be found online at https://doi.org/10.1016/j.quascirev.2020.106394.

References

Anderson, R.F., Bacon, M.P., Brewer, P.G., 1983. Removal of 230 Th and 231 Pa at ocean margins. Earth Planet Sci. Lett. 66, 73–90.

Anderson, R.F., Cheng, H., Edwards, R.L., Fleisher, M.Q., Hayes, C.T., Huang, K.-F., Kadko, D., Lam, P.J., Landing, W.M., Lao, Y., 2016. How well can we quantify dust deposition to the ocean? Phil. Trans. Math. Phys. Eng. Sci. 374, 20150285.

Bacon, M.P., Anderson, R.F., 1982. Distribution of thorium isotopes between dissolved and particulate forms in the deep sea. J. Geophys. Res.: Oceans 87, 2045–2056. https://doi.org/10.1029/JC087iC03p02045.

Böhm, E., Lippold, J., Gutjahr, M., Frank, M., Blaser, P., Antz, B., Fohlmeister, J., Frank, N., Andersen, M.B., Deininger, M., 2015. Strong and deep Atlantic meridional overturning circulation during the last glacial cycle. Nature 517, 73–76.

Bopp, L., Aumont, O., Cadule, P., Alvain, S., Gehlen, M., 2005. Response of diatoms distribution to global warming and potential implications: a global model study. Geophys. Res. Lett. 32 https://doi.org/10.1029/2005GL023653.

Brown, N., Galbraith, E.D., 2016. Hosed vs. unhosed: interruptions of the Atlantic Meridional Overturning Circulation in a global coupled model, with and without freshwater forcing. Clim. Past 12, 1663–1679. https://doi.org/10.5194/cp-12-1663-2016.

Brzezinski, M.A., Pride, C.J., Franck, V.M., Sigman, D.M., Sarmiento, J.L., Matsumoto, K., Gruber, N., Rau, G.H., Coale, K.H., 2002. A switch from Si (OH) 4 to NO3− depletion in the glacial Southern Ocean. Geophys. Res. Lett. 29, 5-1-5–4.

Burckel, P., Waelbroeck, C., Gherardi, J.M., Pichat, S., Arz, H., Lippold, J., Dokken, T., Thil, F., 2015. Atlantic Ocean circulation changes preceded millennial tropical South America rainfall events during the last glacial. Geophys. Res. Lett. 42, 411–418.

Burckel, P., Waelbroeck, C., Luo, Y., Roche, D.M., Pichat, S., Jaccard, S.L., Gherardi, J., Govin, A., Lippold, J., Thil, F., 2016. Changes in the geometry and strength of the Atlantic meridional overturning circulation during the last glacial (20-50ka). Clim. Past 12, 2061.

Cartapanis, O., Bianchi, D., Jaccard, S.L., Galbraith, E.D., 2016. Global pulses of organic carbon burial in deep-sea sediments during glacial maxima. Nat. Commun. 7, 10796.

Cartapanis, O., Galbraith, E.D., Bianchi, D., Jaccard, S., 2018. Carbon burial in deep-sea sediment and implications for oceanic inventories of carbon and alkalinity over the last glacial cycle. Clim. Past 14, 1819–1850.

Chase, Z., Anderson, R.F., Fleisher, M.Q., Kubik, P.W., 2003. Scavenging of 230Th, 231Pa and 10Be in the Southern Ocean (SW Pacific sector): the importance of particle flux, particle composition and advection. Deep Sea Res. Part II Top. Stud. Oceanogr. 50, 739–768. https://doi.org/10.1016/S0967-0645(02)00593-3.

Chase, Z., Anderson, R.F., Fleisher, M.Q., Kubik, P.W., 2002. The influence of particle composition and particle flux on scavenging of Th, Pa and Be in the ocean. Earth Planet Sci. Lett. 204, 215–229. https://doi.org/10.1016/S0012-821X(02)00984-6.

Conte, M.H., Ralph, N., Ross, E.H., 2001. Seasonal and interannual variability in deep ocean particle fluxes at the Oceanic Flux Program (OFP)/Bermuda Atlantic Time Series (BATS) site in the western Sargasso Sea near Bermuda. Deep Sea Res. Part II Top. Stud. Oceanogr. 48, 1471–1505. https://doi.org/10.1016/S0967-0645(00)00150-8.

Costa, K.M., Hayes, C.T., Anderson, R.F., Pavia, F.J., Bausch, A., Deng, F., Dutay, J.-C., Geibert, W., Heinze, C., Henderson, G., Hillaire-Marcel, C., Hoffmann, S., Jaccard, S.L., Jacobel, A.W., Kienast, S.S., Kipp, L., Lerner, P., Lippold, J., Lund, D., Marcantonio, F., McGee, D., McManus, J.F., Mekik, F., Middleton, J.L., Missiaen, L., Not, C., Pichat, S., Robinson, L.F., Rowland, G.H., Roy-Barman, M., Tagliabue, A., Torfstein, A., Winckler, G., Zhou, Y., 2020. 230Th normalization: new insights on an essential tool for quantifying sedimentary fluxes in the modern and quaternary ocean. Paleoceanogr. Paleoclimatol. 35, e2019PA003820 https://doi.org/10.1029/2019PA003820.

Deng, F., Henderson, G.M., Castrillejo, M., Perez, F.F., Steinfeldt, R., 2018. Evolution of 231Pa and 230Th in overflow waters of the north Atlantic. Biogeosciences 15, 7299–7313. https://doi.org/10.5194/bg-15-7299-2018.

Deng, F., Thomas, A.L., Rijkenberg, M.J.A., Henderson, G.M., 2014. Controls on seawater 231Pa, 230Th and 232Th concentrations along the flow paths of deep waters in the Southwest Atlantic. Earth Planet Sci. Lett. 390, 93–102. https://doi.org/10.1016/j.epsl.2013.12.038.

Dunne, J.P., Sarmiento, J.L., Gnanadesikan, A., 2007. A synthesis of global particle export from the surface ocean and cycling through the ocean interior and on the seafloor. Global Biogeochem. Cycles 21. https://doi.org/10.1029/2006GB002907.

Dutay, J.-C., Lacan, F., Roy-Barman, M., Bopp, L., 2009. Influence of particle size and type on 231Pa and 230Th simulation with a global coupled biogeochemical-ocean general circulation model: a first approach. G-cubed 10.

Farrell, J.W., Prell, W.L., 1989. Climatic change and CaCO3 preservation: an 800,000 year bathymetric reconstruction from the central equatorial Pacific Ocean. Paleoceanography 4, 447–466.

François, R., 2007. Paleoflux and Paleocirculation from Sediment 230Th and 231Pa/230Th. Proxies in Late Cenozoic Paleoceanography. Elsevier, pp. 681–716.

Gdaniec, S., Roy-Barman, M., Foliot, L., Thil, F., Dapoigny, A., Burckel, P., Garcia-Orellana, J., Masqué, P., Mörth, C.-M., Andersson, P.S., 2018. Thorium and protactinium isotopes as tracers of marine particle fluxes and deep water circulation in the Mediterranean Sea. Mar. Chem. 199, 12–23.

Gherardi, J.M., Labeyrie, L., Nave, S., Francois, R., McManus, J.F., Cortijo, E., 2009. Glacial-interglacial circulation changes inferred from 231Pa/230Th sedimentary record in the North Atlantic region. Paleoceanography 24. https://doi.org/10.1029/2008PA001696 n/a-n/a.

Goosse, H., Brovkin, V., Fichefet, T., Haarsma, R., Huybrechts, P., Jongma, J., Mouchet, A., Selten, F., Barriat, P.-Y., Campin, J.-M., 2010. Description of the Earth system model of intermediate complexity LOVECLIM version 1.2. Geosci. Model Dev. (GMD) 3, 603–633.

Gu, S., Liu, Z., 2017. 231 Pa and 230 Th in the Ocean model of the community Earth system model (CESM1. 3). Geosci. Model Dev. (GMD) 10.

Hayes, C.T., Anderson, R.F., Fleisher, M.Q., Huang, K.-F., Robinson, L.F., Lu, Y., Cheng, H., Edwards, R.L., Moran, S.B., 2015a. 230Th and 231Pa on GEOTRACES GA03, the U.S. GEOTRACES North Atlantic transect, and implications for modern and paleoceanographic chemical fluxes. Deep Sea Res. Part II Top. Stud. Oceanogr. 116, 29–41. https://doi.org/10.1016/j.dsr2.2014.07.007.

Hayes, C.T., Anderson, R.F., Fleisher, M.Q., Serno, S., Winckler, G., Gersonde, R., 2014. Biogeography in 231Pa/230Th ratios and a balanced 231Pa budget for the Pacific Ocean. Earth Planet Sci. Lett. 391, 307–318. https://doi.org/10.1016/j.epsl.2014.02.001.

Hayes, C.T., Anderson, R.F., Fleisher, M.Q., Vivancos, S.M., Lam, P.J., Ohnemus, D.C., Huang, K.-F., Robinson, L.F., Lu, Y., Cheng, H., Edwards, R.L., Moran, S.B., 2015b. Intensity of Th and Pa scavenging partitioned by particle chemistry in the North Atlantic Ocean. Mar. Chem. 170, 49–60. https://doi.org/10.1016/j.marchem.2015.01.006.

Hemming, S.R., 2004. Heinrich events: massive late Pleistocene detritus layers of the North Atlantic and their global climate imprint. Rev. Geophys. 42.

Henderson, G.M., Anderson, R.F., 2003. The U-series toolbox for paleoceanography. Rev. Mineral. Geochem. 52, 493–531. https://doi.org/10.2113/0520493.

Henderson, G.M., Heinze, C., Anderson, R.F., Winguth, A.M.E., 1999. Global distribution of the 230Th flux to ocean sediments constrained by GCM modelling. Deep Sea Res. Oceanogr. Res. Pap. 46, 1861–1893. https://doi.org/10.1016/S0967-0637(99)00030-8.

Jaccard, S.L., Hayes, C.T., Martínez-García, A., Hodell, D.A., Anderson, R.F., Sigman, D.M., Haug, G.H., 2013. Two modes of change in Southern Ocean productivity over the past million years. Science 339, 1419. https://doi.org/10.1126/science.1227545.

Kageyama, M., Braconnot, P., Bopp, L., Caubel, A., Foujols, M.-A., Guilyardi, E., Khodri, M., Lloyd, J., Lombard, F., Mariotti, V., 2013a. Mid-holocene and last glacial maximum climate simulations with the IPSL model—Part I: comparing IPSL_CM5A to IPSL_CM4. Clim. Dynam. 40, 2447–2468.

Kageyama, M., Braconnot, P., Bopp, L., Mariotti, V., Roy, T., Woillez, M.-N., Caubel, A., Foujols, M.-A., Guilyardi, E., Khodri, M., 2013b. Mid-Holocene and last glacial maximum climate simulations with the IPSL model: part II: model-data comparisons. Clim. Dynam. 40, 2469–2495.

Kienast, S.S., Winckler, G., Lippold, J., Albani, S., Mahowald, N.M., 2016. Tracing dust input to the global ocean using thorium isotopes in marine sediments: ThoroMap. Global Biogeochem. Cycles 30, 1526–1541. https://doi.org/10.1002/2016GB005408.

Kohfeld, K.E., Le Quéré, C., Harrison, S.P., Anderson, R.F., 2005. Role of marine biology in glacial-interglacial CO2 cycles. Science 308, 74–78.

Krishnaswami, S., Lal, D., Somayajulu, B.L.K., Weiss, R.F., Craig, H., 1976. Large-volume in-situ filtration of deep Pacific waters: mineralogical and radioisotope studies. Earth Planet Sci. Lett. 32, 420–429.

Le, J., Shackleton, N.J., 1992. Carbonate dissolution fluctuations in the western equatorial pacific during the late quaternary. Paleoceanography 7, 21–42. https://doi.org/10.1029/91PA02854.

Lippold, J., Gherardi, J.-M., Luo, Y., 2011. Testing the 231Pa/230Th paleocirculation proxy: a data versus 2D model comparison. Geophys. Res. Lett. 38 https://doi.org/10.1029/2011GL049282.

Lippold, J., Grützner, J., Winter, D., Lahaye, Y., Mangini, A., Christl, M., 2009. Does sedimentary 231Pa/230Th from the Bermuda Rise monitor past Atlantic meridional overturning circulation? Geophys. Res. Lett. 36.

Lippold, J., Gutjahr, M., Blaser, P., Christner, E., de Carvalho Ferreira, M.L., Mulitza, S., Christl, M., Wombacher, F., Böhm, E., Antz, B., Cartapanis, O., Vogel, H., Jaccard, S.L., 2016. Deep water provenance and dynamics of the (de)glacial

Atlantic meridional overturning circulation. Earth Planet Sci. Lett. 445, 68–78. https://doi.org/10.1016/j.epsl.2016.04.013.
Lippold, J., Luo, Y., Francois, R., Allen, S.E., Gherardi, J., Pichat, S., Hickey, B., Schulz, H., 2012a. Strength and geometry of the glacial Atlantic meridional overturning circulation. Nat. Geosci. 5, 813.
Lippold, J., Mulitza, S., Mollenhauer, G., Weyer, S., Heslop, D., Christl, M., 2012b. Boundary scavenging at the East Atlantic margin does not negate use of 231Pa/230Th to trace Atlantic overturning. Earth Planet Sci. Lett. 333–334, 317–331. https://doi.org/10.1016/j.epsl.2012.04.005.
Lozier, M.S., Li, F., Bacon, S., Bahr, F., Bower, A.S., Cunningham, S.A., de Jong, M.F., de Steur, L., deYoung, B., Fischer, J., Gary, S.F., Greenan, B.J.W., Holliday, N.P., Houk, A., Houpert, L., Inall, M.E., Johns, W.E., Johnson, H.L., Johnson, C., Karstensen, J., Koman, G., Le Bras, I.A., Lin, X., Mackay, N., Marshall, D.P., Mercier, H., Oltmanns, M., Pickart, R.S., Ramsey, A.L., Rayner, D., Straneo, F., Thierry, V., Torres, D.J., Williams, R.G., Wilson, C., Yang, J., Yashayaev, I., Zhao, J., 2019. A sea change in our view of overturning in the subpolar North Atlantic. Science 363, 516–521.
Luo, S., Ku, T.-L., 2004. On the importance of opal, carbonate, and lithogenic clays in scavenging and fractionating 230Th, 231Pa and 10Be in the ocean. Earth Planet Sci. Lett. 220, 201–211.
Luo, S., Ku, T.-L., 1999. Oceanic 231Pa/230Th ratio influenced by particle composition and remineralization. Earth Planet Sci. Lett. 167, 183–195.
Luo, Y., Francois, R., Allen, S.E., 2010. Sediment 231Pa/230Th as a recorder of the rate of the Atlantic meridional overturning circulation: insights from a 2-D model. Ocean Sci. Discuss. 6, 2755–2829.
Lynch-Stieglitz, J., 2017. The Atlantic meridional overturning circulation and abrupt climate change. Ann. Rev. Mar. Sci. 9, 83–104. https://doi.org/10.1146/annurev-marine-010816-060415.
Marchal, O., François, R., Stocker, T.F., Joos, F., 2000. Ocean thermohaline circulation and sedimentary 231Pa/230Th ratio. Paleoceanography 15, 625–641.
Marinov, I., Doney, S.C., Lima, I.D., 2010. Response of ocean phytoplankton community structure to climate change over the 21st century: partitioning the effects of nutrients, temperature and light. Biogeosciences 7, 3941–3959. https://doi.org/10.5194/bg-7-3941-2010.
Mariotti, V., Bopp, L., Tagliabue, A., Kageyama, M., Swingedouw, D., 2012. Marine productivity response to Heinrich events: a model-data comparison. Clim. Past 8, 1581–1598.
Martínez-García, A., Sigman, D.M., Ren, H., Anderson, R.F., Straub, M., Hodell, D.A., Jaccard, S.L., Eglinton, T.I., Haug, G.H., 2014. Iron fertilization of the subantarctic ocean during the last ice age. Science 343, 1347. https://doi.org/10.1126/science.1246848.
Matsumoto, K., Sarmiento, J.L., Brzezinski, M.A., 2002. Silicic acid leakage from the Southern Ocean: a possible explanation for glacial atmospheric pCO2. Global Biogeochem. Cycles 16, 5-1-5–23.
McManus, J.F., Francois, R., Gherardi, J.-M., Keigwin, L.D., Brown-Leger, S., 2004. Collapse and rapid resumption of Atlantic meridional circulation linked to deglacial climate changes. Nature 428, 834–837.
Menviel, L., Timmermann, A., Mouchet, A., Timm, O., 2008. Meridional reorganizations of marine and terrestrial productivity during Heinrich events. Paleoceanography 23. https://doi.org/10.1029/2007PA001445.
Missiaen, L., Bouttes, N., Roche, D.M., Dutay, J.-C., Quiquet, A., Waelbroeck, C., Pichat, S., Peterschmitt, J.-Y., 2020. Carbon isotopes and Pa/Th response to forced circulation changes: a model perspective. Clim. Past 16, 867–883. https://doi.org/10.5194/cp-16-867-2020.
Missiaen, L., Pichat, S., Waelbroeck, C., Douville, E., Bordier, L., Dapoigny, A., Thil, F., Foliot, L., Wacker, L., 2018. Downcore variations of sedimentary detrital (238U/232Th) ratio: implications on the use of 230Thxs and 231Paxs to reconstruct sediment flux and ocean circulation. G-cubed. https://doi.org/10.1029/2017GC007410.
Mulitza, S., Chiessi, C.M., Schefuß, E., Lippold, J., Wichmann, D., Antz, B., Mackensen, A., Paul, A., Prange, M., Rehfeld, K., 2017. Synchronous and proportional deglacial changes in Atlantic Meridional Overturning and northeast Brazilian precipitation. Paleoceanography.
Nave, S., Labeyrie, L., Gherardi, J., Caillon, N., Cortijo, E., Kissel, C., Abrantes, F., 2007. Primary productivity response to Heinrich events in the north Atlantic Ocean and Norwegian sea. Paleoceanogr. Paleoclimatol. 22.
Ng, H.C., Robinson, L.F., McManus, J.F., Mohamed, K.J., Jacobel, A.W., Ivanovic, R.F., Gregoire, L.J., Chen, T., 2018. Coherent deglacial changes in western Atlantic Ocean circulation. Nat. Commun. 9.
Nozaki, Y., Horibe, Y., Tsubota, H., 1981. The water column distributions of thorium isotopes in the western North Pacific. Earth Planet Sci. Lett. 54, 203–216.
Rahmstorf, S., 2002. Ocean circulation and climate during the past 120,000 years. Nature 419, 207. https://doi.org/10.1038/nature01090.
Rempfer, J., Stocker, T.F., Joos, F., Lippold, J., Jaccard, S.L., 2017. New insights into cycling of 231Pa and 230Th in the Atlantic Ocean. Earth Planet Sci. Lett. 468, 27–37. https://doi.org/10.1016/j.epsl.2017.03.027.
Richaud, M., Loubere, P., Pichat, S., Francois, R., 2007. Changes in opal flux and the rain ratio during the last 50,000 years in the equatorial Pacific. Deep Sea Res. Part II Top. Stud. Oceanogr. 54, 762–771.
Roy-Barman, M., 2009. Modelling the effect of boundary scavenging on Thorium and Protactinium profiles in the ocean. Biogeosciences 6, 3091–3107. https://doi.org/10.5194/bg-6-3091-2009.
Schmittner, A., 2005. Decline of the marine ecosystem caused by a reduction in the Atlantic overturning circulation. Nature 434, 628.
Seiter, K., Hensen, C., Schröter, J., Zabel, M., 2004. Organic carbon content in surface sediments—defining regional provinces. Deep Sea Res. Oceanogr. Res. Pap. 51, 2001–2026. https://doi.org/10.1016/j.dsr.2004.06.014.
Siddall, M., Henderson, G.M., Edwards, N.R., Frank, M., Müller, S.A., Stocker, T.F., Joos, F., 2005. 231Pa/230Th fractionation by ocean transport, biogenic particle flux and particle type. Earth Planet Sci. Lett. 237, 135–155. https://doi.org/10.1016/j.epsl.2005.05.031.
Siddall, M., Stocker, T.F., Henderson, G.M., Joos, F., Frank, M., Edwards, N.R., Ritz, S.P., Müller, S.A., 2007. Modeling the relationship between 231Pa/230Th distribution in North Atlantic sediment and Atlantic meridional overturning circulation. Paleoceanography 22. https://doi.org/10.1029/2006PA001358.
Stephens, M.P., Kadko, D.C., 1997. Glacial-Holocene calcium carbonate dissolution at the central equatorial Pacific seafloor. Paleoceanography 12, 797–804.
Straub, M., Tremblay, M.M., Sigman, D.M., Studer, A.S., Ren, H., Toggweiler, J.R., Haug, G.H., 2013. Nutrient conditions in the subpolar North Atlantic during the last glacial period reconstructed from foraminifera-bound nitrogen isotopes. Paleoceanography 28, 79–90. https://doi.org/10.1002/palo.20013.
van Hulten, M., Dutay, J.-C., Roy-Barman, M., 2018. A global scavenging and circulation ocean model of thorium-230 and protactinium-231 with improved particle dynamics (NEMO–ProThorP 0.1). Geosci. Model Dev. (GMD) 11, 3537–3556. https://doi.org/10.5194/gmd-11-3537-2018.
Waelbroeck, C., Pichat, S., Böhm, E., Lougheed, B.C., Faranda, D., Vrac, M., Missiaen, L., Vazquez Riveiros, N., Burckel, P., Lippold, J., Arz, H.W., Dokken, T., Thil, F., Dapoigny, A., 2018. Relative timing of precipitation and ocean circulation changes in the western equatorial Atlantic over the last 45 kyr. Clim. Past 14, 1315–1330. https://doi.org/10.5194/cp-14-1315-2018.
Walter, H.J., Van der Loeff, M.R., Hoeltzen, H., 1997. Enhanced scavenging of 231 Pa relative to 230 Th in the South Atlantic south of the Polar Front: implications for the use of the 231 Pa/230 Th ratio as a paleoproductivity proxy. Earth Planet Sci. Lett. 149, 85–100.
Yamamoto, A., Abe-Ouchi, A., Ohgaito, R., Ito, A., Oka, A., 2019. Glacial CO2 decrease and deep-water deoxygenation by iron fertilization from glaciogenic dust. Clim. Past 15, 981–996. https://doi.org/10.5194/cp-15-981-2019.

Clim. Past, 17, 2179–2199, 2021
https://doi.org/10.5194/cp-17-2179-2021

Climate of the Past
Open Access
EGU

Climate and ice sheet evolutions from the last glacial maximum to the pre-industrial period with an ice-sheet–climate coupled model

Aurélien Quiquet[1,a], **Didier M. Roche**[1,2], **Christophe Dumas**[1], **Nathaëlle Bouttes**[1], **and Fanny Lhardy**[1]

[1]Laboratoire des Sciences du Climat et de l'Environnement, LSCE/IPSL, CEA-CNRS-UVSQ, Université Paris-Saclay, 91191 Gif-sur-Yvette, France
[2]Earth and Climate Cluster, Faculty of Earth and Life Sciences, Vrije Universiteit Amsterdam, Amsterdam, the Netherlands
[a]now at: NumClim Solutions, Palaiseau, France

Correspondence: Aurélien Quiquet (aurelien.quiquet@lsce.ipsl.fr)

Received: 14 April 2021 – Discussion started: 26 April 2021
Revised: 30 August 2021 – Accepted: 7 September 2021 – Published: 19 October 2021

Abstract. The last deglaciation offers an unique opportunity to understand the climate–ice-sheet interactions in a global warming context. In this paper, to tackle this question, we use an Earth system model of intermediate complexity coupled to an ice sheet model covering the Northern Hemisphere to simulate the last deglaciation and the Holocene (26–0 ka). We use a synchronous coupling every year between the ice sheet and the rest of the climate system and we ensure a closed water cycle considering the release of freshwater flux to the ocean due to ice sheet melting. Our reference experiment displays a gradual warming in response to the forcings, with no abrupt changes. In this case, while the amplitude of the freshwater flux to the ocean induced by ice sheet retreat is realistic, it is sufficient to shut down the Atlantic meridional overturning circulation from which the model does not recover within the time period simulated. However, with reduced freshwater flux we are nonetheless able to obtain different oceanic circulation evolutions, including some abrupt transitions between shut-down and active circulation states in the course of the deglaciation. The inclusion of a parameterisation for the sinking of brines around Antarctica also produces an abrupt recovery of the Atlantic meridional overturning circulation, absent in the reference experiment. The fast oceanic circulation recoveries lead to abrupt warming phases in Greenland. Our simulated ice sheet geometry evolution is in overall good agreement with available global reconstructions, even though the abrupt sea level rise at 14.6 ka is underestimated, possibly because the climate model underestimates the millennial-scale temperature variability. In the course of the deglaciation, large-scale grounding line instabilities are simulated both for the Eurasian and North American ice sheets. The first instability occurs in the Barents–Kara seas for the Eurasian ice sheet at 14.5 ka. A second grounding line instability occurs ca. 12 ka in the proglacial lake that formed at the southern margin of the North American ice sheet. With additional asynchronously coupled experiments, we assess the sensitivity of our results to different ice sheet model choices related to surface and sub-shelf mass balance, ice deformation and grounding line representation. While the ice sheet evolutions differ within this ensemble, the global climate trajectory is only weakly affected by these choices. In our experiments, only the abrupt shifts in the oceanic circulation due to freshwater fluxes are able to produce some millennial-scale variability since no self-generating abrupt transitions are simulated without these fluxes.

1 Introduction

The Quaternary has been marked by large sea level oscillations. A gradual sea level fall, associated with an increase in the continental ice sheet volume, characterises prolonged glacial periods lasting for several tens of thousand of years. In turn, short glacial terminations precede interglacial periods that show reduced ice sheets. The study of glacial terminations can help us to understand the mechanisms behind

large-scale ice sheet retreat but also the key role of ice sheets within the global climate system.

During the last deglaciation ($\sim$ 21–7 ka), the sea level rose by about 120 metres to reach approximately its present-day level (Waelbroeck et al., 2002; Lambeck et al., 2014). This rise is mostly explained by the disintegration of the North American and Eurasian ice sheets, while Greenland and Antarctica together probably contributed less than 20 m (Whitehouse et al., 2012; Briggs et al., 2014; Lecavalier et al., 2014; Simms et al., 2019). The extent of the Northern Hemisphere ice sheets across the deglaciation is relatively well known, although it can sometimes present large ($>$ 1 kyr) dating uncertainties (Hughes et al., 2016; Dalton et al., 2020). However, the volume evolution of the individual ice sheets remains weakly constrained. In particular, sea level archives have suggested the presence of abrupt sea level rises standing out from the gradual sea level rise of the deglaciation (Deschamps et al., 2012; Abdul et al., 2016; Harrison et al., 2019). These so-called meltwater pulses suggest large-scale ice sheet instabilities, but the contribution of the different ice sheets to these events remains debated (e.g. Liu et al., 2016).

Parallel to the non-linear ice sheet retreat, the atmosphere and the ocean have also undergone some large and abrupt variations. For example, while atmospheric temperatures above Greenland rise gradually since the Last Glacial Maximum (LGM), they rise abruptly by more than 10 °C in a few decades at the onset of the Bølling–Allerød period at 14.7 ka (Severinghaus and Brook, 1999; Buizert et al., 2014). After 500 years of interglacial conditions, the climate abruptly returns to a cold state during the Younger Dryas (Alley, 2000a) from which the temperatures rise again steadily to reach their Holocene values. The evolution of the oceanic conditions are more uncertain. It seems nonetheless that the North Atlantic Deep Water (NADW) was shallower at the LGM compared to today (Curry and Oppo, 2005). The 3D evolution of the water masses across the deglaciation is difficult to constrain given that different proxies can provide conflicting information (Waelbroeck et al., 2019). However, it is likely that the Atlantic meridional oceanic circulation (AMOC) has not remained constant, with possible rapid transitions from different states: intense, reduced or even shut down (e.g. McManus et al., 2004; Ng et al., 2018).

The succession of events linking the changes in the atmosphere, ocean and ice sheets has yet to be formalised. Bi-directionally coupled ice-sheet–climate models are ideal tools to study these interactions since they can explicitly represent the different climatic feedbacks at play, without having to prescribe ad hoc external scenarios. In such coupling, the climate model provides the climatic forcing fields needed by the ice sheet model and in turn the ice sheet model provides an updated surface topography and ice sheet mask. Several coupled ice-sheet–climate models are now available in the literature, spanning a range of complexities. Given that the ice sheet integrates climate change over long timescales ($>$ 10 kyr), the vast majority of the work that has investigated multi-millennial climate change during the Quaternary has used simplified climate models to reduce the numerical cost (e.g. Calov et al., 2005; Fyke et al., 2011; Huybrechts et al., 2011; Heinemann et al., 2014). However, some general circulation models (GCMs) have also been bi-directionally coupled to ice sheet models (e.g. Vizcaíno et al., 2008; Gregory et al., 2012). In this case, the model is run for short integrations (typically less than 1000 years) or use an asynchronous coupling to speed up the simulations (e.g. Ziemen et al., 2019). With the asynchronous coupling, the climate model is run less frequently than the ice sheet model (e.g. 1 year of climate is used to perform 10 years of ice sheet evolution).

To date, although a fair amount of coupled ice-sheet–climate models exist, only few have been used to simulate the last deglaciation of Northern Hemisphere ice sheets. Thanks to an inexpensive setup in terms of computational cost, the CLIMBER-2 Earth system model of intermediate complexity coupled to the SICOPOLIS ice sheet model has been used in several studies to simulate the last glacial–interglacial cycles (e.g. Ganopolski and Brovkin, 2017) and beyond (Willeit et al., 2019). CLIMBER-2 has also been coupled to an alternative ice sheet model (Charbit et al., 2005; Bonelli et al., 2009). These studies have demonstrated the ability of the model to reproduce the global eustatic sea level reconstructions. They have also brought major improvements in our understanding of the respective role of orbital forcing, greenhouse gas mixing ratio, ice sheets and dust to explain the past climatic variability. However, CLIMBER-2 shows drastic simplifications of the physics of the atmosphere (statistical–dynamical model on a coarse grid of $10^\circ \times \sim 51^\circ$ resolution) and in the ocean (three zonally averaged oceanic basins). Heinemann et al. (2014) used an alternative Earth system model of intermediate complexity, LOVECLIM (Goosse et al., 2010), to simulate the last deglaciation of Northern Hemisphere ice sheets. Compared to CLIMBER-2, LOVECLIM shows a higher spatial resolution in the atmosphere ($\sim 5.6^\circ \times 5.6^\circ$ resolution) and accounts for a general circulation oceanic model (Goosse and Fichefet, 1999). To successfully reproduce the ice sheet evolution Heinemann et al. (2014) have to use a correction of the climatic fields (namely temperature and precipitation). In addition, they use an asynchronous coupling to speed up their simulations. In doing so, they discard the role of freshwater flux to the ocean resulting from ice sheet melting. To our knowledge, no other bi-directionally coupled ice-sheet–climate model has been used to simulate the last deglaciation of Northern Hemisphere ice sheets.

Building on the work of Roche et al. (2014a), we present here the first comprehensive climatic simulations of the last deglaciation with interactive Northern Hemisphere ice sheets using a bi-directional synchronous coupling. We have performed different experiments with varying oceanic conditions to assess their importance in shaping the deglaciation.

In addition, we have performed additional sensitivity experiments using an asynchronous coupling to assess the importance of some modelling choices on our results. In Sect. 2 we present our model, the coupling strategy and the experimental setup. We show our results in terms of atmospheric temperature evolution, oceanic circulation changes and simulated ice sheets in Sect. 3. We discuss further our model limitations and expected improvements in Sect. 4 and conclude in Sect. 5.

2 Methods

2.1 Climate and ice sheet models

*i*LOVECLIM (here in version 1.1) is a code fork of the LOVECLIM 1.2 model (Goosse et al., 2010). The core of the model is a combination of a quasi-geostrophic atmospheric model solved on a T21 ($\sim 5.6° \times 5.6°$) spectral grid (ECBilt, Haarsma et al., 1997; Opsteegh et al., 1998); a free surface oceanic general circulation model on a $3° \times 3°$ spherical grid which includes a thermodynamic sea ice model (CLIO, Goosse and Fichefet, 1999); and a dynamic vegetation and carbon allocation model (VECODE, Brovkin et al., 1997). *i*LOVECLIM has been extensively used to study millennial climate change during the Quaternary. For example, it has proven able to reproduce the glacial–interglacial variability of the hydrological cycle in the tropics (Caley et al., 2014). It has also been used to study Heinrich events during the last glacial period (Roche et al., 2014b) or to investigate the processes responsible for changes in the carbon cycle during the last eight interglacial periods (Bouttes et al., 2018). With a similar model configuration to the one used in this work, *i*LOVECLIM results were included in the fourth phase of the Palaeoclimate Modelling Intercomparison Project (PMIP) contribution to the Coupled Model Intercomparison Project (CMIP) (Kageyama et al., 2021).

Since Roche et al. (2014a), the model has also included a 3D thermomechanically coupled ice sheet model (GRISLI, Ritz et al., 2001; Quiquet et al., 2018a). GRISLI solves the ice sheet mass conservation equation on a Cartesian grid. Like most ice sheet models, deformation is computed with a Glen flow law in which anisotropy is artificially accounted for using a flow enhancement factor (E_f) that facilitates deformation induced by vertical shear. For the entire domain, the velocity field is the sum of velocity driven by vertical shearing (shallow ice approximation, SIA) and the velocity driven by horizontal shearing (shallow shelf approximation, SSA). In doing so, the SSA is used as a sliding law (Bueler and Brown, 2009; Winkelmann et al., 2011). Basal dragging $\boldsymbol{\tau}_\mathrm{b}$ is assumed to follow a linear friction law:

$$\boldsymbol{\tau}_\mathrm{b} = -\beta \boldsymbol{u}_\mathrm{b}, \tag{1}$$

where β is the basal drag coefficient and $\boldsymbol{u}_\mathrm{b}$ is the basal velocity. Cold-based grid points have a virtually infinite friction at the base (5×10^5 Pa yr m^{-1}), while floating ice shelves have no friction. For grid points at the pressure melting point, we use a friction computed from the effective pressure at the base of the ice sheet N:

$$\beta = c_\mathrm{f} N, \tag{2}$$

where c_f is a parameter that has to be calibrated. For the experiments shown here, we impose an ice flux at the grounding line that follows the analytical solution of Tsai et al. (2015). Calving at the ice shelf edge occurs if the ice thickness falls below a critical threshold and if the upstream Lagrangian ice flux does not allow us to maintain an ice thickness above this threshold. The threshold is set here to 250 m. Ice sheet model parameters (enhancement factor, basal drag coefficient and hydraulic conductivity) are calibrated in the same way as in Quiquet et al. (2018a) to reproduce glacial–interglacial Antarctic ice sheet grounding line migration. In addition, we used a map of sediment thickness (Laske and Masters, 1997) to locally reduce basal dragging. We assume that for a sediment thickness greater than 200 m, the basal drag coefficient in Eq. (2) is multiplied by a dimensionless factor of 0.05. Glacial isostatic adjustment is accounted for in GRISLI using an elastic-lithosphere–relaxed-asthenosphere model (Le Meur and Huybrechts, 1996), with a relaxation time of the asthenosphere of 3000 years. The ice sheet model is run here on a Cartesian 40 km grid of the Northern Hemisphere using a Lambert azimuthal equal-area projection.

2.2 Ice sheet model coupling

The inclusion of GRISLI into *i*LOVECLIM has been presented in Roche et al. (2014a). However, the coupling procedure has been largely modified from this work. In particular, we have substantially improved the computation of surface and sub-shelf mass balance. Water conservation between GRISLI and the rest of the climate model has also been considerably improved. Details on this coupling are given in the following, while its schematic representation is shown in Fig. 1. It is important to mention that only the Northern Hemisphere ice sheets are interactively simulated, while the Antarctic ice sheet topography and ice mask remain prescribed at their Last Glacial Maximum following the PMIP4 protocol.

2.2.1 Surface mass balance

In Roche et al. (2014a), the ice sheet surface mass balance (SMB) was computed from the annual mean precipitation and the annual and July mean near-surface air temperature using a positive degree day method (Reeh, 1989). Although computationally inexpensive and easy to implement in a model, this method does not account for some important physical quantities that influence the SMB. In particular, the surface shortwave radiation is only implicitly taken into account through the temperature. Instead, we use here the insolation temperature melt method (ITM) following Pollard

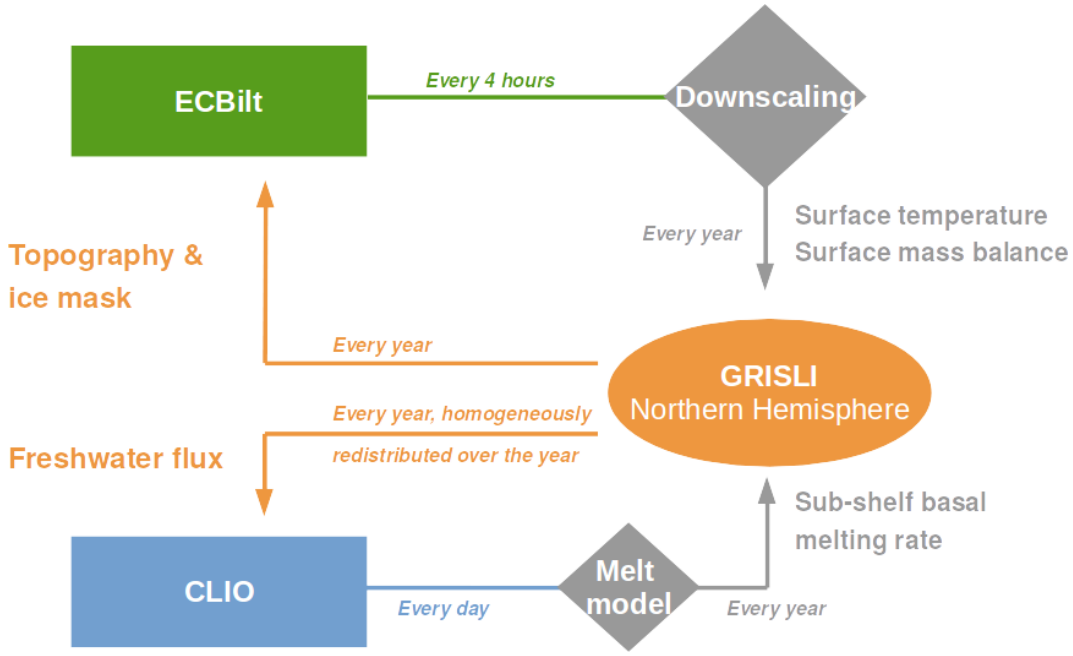

Figure 1. Schematic representation of the coupling between the ice sheet model (GRISLI) and the atmospheric (ECBilt) and the oceanic (CLIO) models.

(1980) and van den Berg et al. (2008). The amount of melt M_s over one time step Δt is in this case

$$M_s = \max\left(\frac{\Delta t}{\rho_w L_m}\left((1-\alpha)\mathrm{SW}_s + c_{rad} + \lambda T_s\right), 0\right), \quad (3)$$

where is the T_s is the near-surface air temperature, SW_s is the shortwave radiation at the surface, α is the surface albedo, ρ_w is the density of liquid water and L_m is the specific latent heat of fusion. λ and c_{rad} are empirical parameters that need calibration. In the literature, this calibration has been performed on observations of present-day glaciers. The λ parameter is generally set to $10\,\mathrm{W\,m^{-2}\,K^{-1}}$ (Pollard, 1980; van den Berg et al., 2008; Robinson et al., 2010). The parameter c_{rad} is less constrained and is adjusted for the region considered (van den Berg et al., 2008). It is set to $-50\,\mathrm{W\,m^{-2}}$ in Pollard (1980), it ranges from -40 to $-60\,\mathrm{W\,m^{-2}}$ in Robinson et al. (2010), whilst it is equal to $-117\,\mathrm{W\,m^{-2}}$ in van den Berg et al. (2008). We used $\lambda = 10\,\mathrm{W\,m^{-2}\,K^{-1}}$ and $c_{rad} = -40\,\mathrm{W\,m^{-2}}$. However, *i*LOVECLIM presents an important warm bias in eastern North America and a cold bias in northern Europe that lead to an unrealistic simulated ice sheet under glacial forcing, a problem also identified in Heinemann et al. (2014). To account for this, we use a local modification of the melt parameter c_{rad} to partially correct these temperature biases. To this aim, we compute the annual mean temperature bias with respect to ERA-Interim (Dee et al., 2011) and use a linear correction in which a $+10\,^{\circ}\mathrm{C}$ bias leads to $c_{rad} = -80\,\mathrm{W\,m^{-2}}$ (instead of the reference value of $-40\,\mathrm{W\,m^{-2}}$).

Because of the gap between the coarse atmospheric model resolution and the ice sheet model resolution, the downscaling of the forcing fields needed by the ice sheet model is a persistent issue in ice-sheet–climate coupling. Here, we make use of the online dynamical downscaling embedded in *i*LOVECLIM (Quiquet et al., 2018b). This allows for the computation on every atmospheric model time step (4 h) of snow, rain and near-surface air temperature at the ice sheet model resolution, explicitly taking into account the high-resolution topography. We used these fields directly to compute a surface mass balance at the resolution of the ice sheet model with the ITM method (Eq. 3). The near-surface air temperature and the SMB are accumulated along the course of the year to generate the yearly forcing fields required by the ice sheet model. We made a few adjustments compared to the downscaling procedure presented in Quiquet et al. (2018b). In particular, some large-scale climate fields are now bi-linearly interpolated onto the high-resolution grid before the energy and moisture computation. This prevents the strong discontinuities that could exist between two sub-grid points belonging to two different large-scale grid cells.

2.2.2 Sub-shelf melt rate

The sub-shelf melt rate in Roche et al. (2014a) was imposed arbitrarily to a homogeneous and constant value for the entire Northern Hemisphere. Instead, we use here a physically based computation of the sub-shelf melt rate following Beckmann and Goosse (2003). For each vertical oceanic layer, z,

we estimate the potential sub-shelf melt rate as

$$M_{\text{shelf}}(z) = \frac{\rho_{\text{w}} c_p \gamma_{\text{T}} F_{\text{g}} \text{TF}(z)}{\rho_{\text{i}} L_m}, \quad (4)$$

where c_p is the specific heat capacity of sea water, ρ_{i} is the density of ice, γ_{T} is the thermal exchange velocity and TF(z) is the thermal forcing at depth z, defined as the difference between the ambient temperature and the temperature of the salinity-dependent freezing point. F_g is a weakly constrained dimensionless parameter and can be changed to explore the response of the ice sheet to different sub-shelf melt sensitivities to oceanic temperature change. In our reference experiment, we chose a parameter value (15×10^{-3}) that produces about $0.1\,\text{m}\,\text{yr}^{-1}$ in the Arctic, a value similar to what the Ross ice shelf is experiencing today in Antarctica. In addition, in order to avoid unrealistic ice shelf expansion over the deep ocean we also impose a high sub-shelf melt rate of $20\,\text{m}\,\text{yr}^{-1}$ where the bathymetry is greater than 1500 m. Also, to mimic the fact that observed melt rates are greater in the vicinity of the grounding line, we double the value of the inferred melt rate in Eq. (4) for the floating points that are in contact with the grounding line. Equation (4) is computed for each oceanic time step (1 d) and integrated over the year in order to provide the yearly forcing needed by the ice sheet model. There is no downscaling of the sub-shelf melt rate to the high-resolution ice sheet model grid, except that the depth of the ice shelf draft is used to determine the vertical layer z in Eq. (4) that produces the melt.

2.2.3 Ice sheet feedbacks

Changes in the ice sheet feed back to the atmospheric and to the oceanic models. On the one hand, at the beginning of each year in the climate model, the ice mask and the orography in the climate model are changed according to the changes computed by the ice sheet model in the previous year. Both fields are aggregated from the ice sheet model resolution (40 km) to the T21 resolution in the same way as in Roche et al. (2014a). There is no partially glaciated grid cell in the atmospheric model: a coarse grid cell is regarded as glaciated (ice mask set to 1) if it contains at least 30 % of sub-grid points with an ice thickness greater than 1 m. The ice mask in the atmospheric model impacts the surface albedo.

On the other hand, freshwater fluxes resulting from the ice sheet melting are transferred to the oceanic model. In Roche et al. (2014a), the total ice sheet volume variation was transferred to the continental routing scheme assuming a uniform distribution over the ice sheet. Only the calving flux was separated from the total volume variation to eventually feed an iceberg model (Bügelmayer et al., 2015). This method has the advantage of ensuring a closed water budget within the model but the spatial information about ice sheet runoff is lost. For this reason, we now explicitly separate the different components of the global volume variation on the ice sheet model side. Basal and surface melt of the grounded part of the ice sheet are transferred to the routing scheme exactly where they occur. The basal melt below the ice shelves are also added to the ocean where they occur but at the surface and not at depth. The calving flux can be either regarded as the basal melt or used to feed the iceberg model. At present, the iceberg model is not activated in our experiments and the calving flux, similarly to the sub-shelf melt, is given at the oceanic surface. Local latent heat release resulting from iceberg melting is taken into account. Since the ice sheet model main time step is 1 year, we do not have access to the seasonal cycle of the freshwater fluxes and their annual value computed by the ice sheet model is homogeneously distributed through the year in the oceanic model.

For the experiments presented here, changes in the ice sheet size do not affect the global ocean volume. The bathymetry in the oceanic model thus remains constant.

2.3 Experimental setup

2.3.1 Boundary and initial conditions

The climate model uses time-varying information of greenhouse gases (Lüthi et al., 2008) and insolation (Berger, 1978). The carbon dioxide mixing ratio evolution and the 65° N insolation in June is depicted in Fig. 3. For the oceanic model, we use a recent implementation of the Last Glacial Maximum bathymetry at 21 ka (Lhardy et al., 2021), which is left unchanged for the duration of the experiments. Topography and ice mask are both provided by the ice sheet model. On the ice sheet model side, in addition to the climate forcings, another forcing is the transient eustatic sea level reconstruction from Waelbroeck et al. (2002).

To define our initial state, we run uncoupled ice sheet and climate experiments. First, we run the climate model using the Last Glacial Maximum boundary conditions for 3000 years. In this case, the ice sheet topography and ice mask correspond to the one of the GLAC-1D reconstructions (Tarasov et al., 2012; Tarasov and Peltier, 2002; Briggs et al., 2014) at 21 ka. The different experiments presented in the rest of the paper are all branched from the simulated climate at the end of this 3000 years. In addition, the last 100 years of this experiment are also used to define a climatological annual surface mass balance and surface temperature. We use this climatology to perform stand-alone ice sheet experiments starting from an ice-free configuration of the Northern Hemisphere. The ice sheet model is run for 200 kyr under this constant climate forcing. In doing so, the model has time to build up ice sheets in equilibrium with the Last Glacial Maximum climate simulated by the climate model. We chose to run such a long spin-up so that the slowly evolving variables, such as the internal temperature field and the basal hydraulic head, are in equilibrium with the simulated glacial climate. In this way, we reduce the initial model drift for the coupled experiments. The simulated ice sheets after this spin-up are presented in Fig. 2a. The extent of the ice sheets generally

agrees well with the geologically constrained reconstruction of GLAC-1D (Fig. 2c) and ICE-6G_C (Fig. 2d, Argus et al., 2014; Peltier et al., 2015) even though it is underestimated in the western part of the Eurasian ice sheet. The climate fields used to build the spun-up ice sheets have been elaborated from the climate model with prescribed GLAC-1D boundary conditions. As such, the spun-up ice sheets should resemble the GLAC-1D reconstructions. If this is generally the case, there is nonetheless an overestimation of the surface elevation of the North American ice sheet. This could indicate a precipitation overestimation in this area or an underestimation of the ice sheet velocities. However, the fact that the Eurasian ice sheet does not present this bias points towards an overestimation of the precipitation. The spun-up ice sheets are used as initial conditions for the ice sheet model in the coupled experiments presented in this paper. All the experiments, including the sensitivity experiments with perturbed parameter values, use the same spun-up climate and ice sheet states.

2.3.2 Description of the experiments

We have performed two sets of experiments to investigate two important points for the simulation of the deglaciation. First, the freshwater fluxes resulting from ice sheet melting likely influenced the climate evolution during the deglaciation since they can have led to abrupt AMOC changes (e.g. Liu et al., 2009; Menviel et al., 2011; Obase and Abe-Ouchi, 2019). Thus, in a first set of experiments, we have performed various synchronously coupled experiments with varying oceanic circulation evolutions. Second, several modelling choices related to the ice sheet model are not well constrained and could also have an influence on the simulated deglaciation. To tackle this problem, in a second set of experiments, we have performed various sensitivity experiments using an asynchronous coupling to reduce the computation cost. More details on these experiments are given in the following.

Our reference experiment (DGL) is an ice-sheet–climate experiment, synchronously coupled. This experiment starts at 26 ka and uses the initial conditions presented in Sect. 2.3.1. The climate and the ice sheets used as initial conditions are not fully consistent between each other since they have been obtained with uncoupled long-term equilibriums. As such, the first 1000 years or so of our experiments have to be discussed with care since part of the response can arise from artefacts due to the start of the coupling.

In addition to this reference experiment, we have performed additional synchronously coupled experiments for the first set of experiments which aims at investigating the importance of oceanic changes in shaping the last deglaciation.

First, we have run experiments in which the amount of freshwater is reduced in order to gradually limit their influence. In DGL_FWF/2 and DGL_FWF/3 we divide the flux resulting from ice sheet melting by 2 and 3, respectively, while in DGL_noFWF this flux is not injected into the ocean.

Second, it has been shown that the simulated NADW at the LGM in the *i*LOVECLIM model is too deep with respect to what oceanic tracers suggest (Lhardy et al., 2021), a feature shared with other PMIP participating models (Kageyama et al., 2021). This bias in the oceanic circulation can affect our results for the deglaciation. One way to provide an alternative oceanic circulation in the model is to use a parameterisation for the sinking of brines (Bouttes et al., 2010) around Antarctica. In this parameterisation, a fraction of the salt rejected by sea ice formation (40 %) is transferred to the deepest oceanic layer. This is done to artificially reproduce the sinking of dense waters induced by sea ice formation along the continental slope of Antarctica since such a process cannot be properly resolved in a $3° \times 3°$ resolution oceanic model. The parameterisation favours vertical stratification around Antarctica, enhancing Antarctic Bottom Water (AABW) and conversely weakening and shallowing of the NADW. Under glacial conditions, this leads to a better agreement with palaeo-data (Lhardy et al., 2021). We have thus performed an experiment in which the parameterisation for the sinking of brines is activated (DGL_brines). The experiments with reduced freshwater flux and with the parameterisation for the sinking of brines are branched from the reference experiment DGL at 21 ka. At that time the ice sheets are not contributing to sea level change (total mass change of 0).

The second set of experiments consists of asynchronously coupled experiments to assess the sensitivity of our results to the modelling choices for the ice sheet model. In these experiments, the forcings (greenhouse gas mixing ratio and orbital forcing) are accelerated with a factor of 5. Acceleration has already been used extensively in the literature (e.g. Jackson and Broccoli, 2003; Gregory et al., 2012; Roberts et al., 2014; Heinemann et al., 2014; Choudhury et al., 2020). The accelerated experiments cover the 26–0 ka time span, but only 5200 years are computed in the climate model instead of the full 26 000 years. In such experiments, the ice sheet model is run for 5 years after 1 year of simulated climate so that only the ice sheet forcings are accelerated but not ice dynamics. This method allows us to significantly reduce the computation time needed to perform multi-millennial experiments. However, accelerated experiments cannot correctly represent the effect of freshwater discharge to the ocean resulting from ice sheet melting since either the flux of water or the mass can be preserved but not both at the same time. Here, we discard completely the role of freshwater flux to the ocean in the accelerated experiments. The ADGL experiments are the accelerated counterpart of the DGL experiments and as such will define the new reference for the accelerated experiments.

The other accelerated experiments are used to assess the sensitivity of our simulated deglaciation to important processes related to ice sheet dynamics: modelling choices for

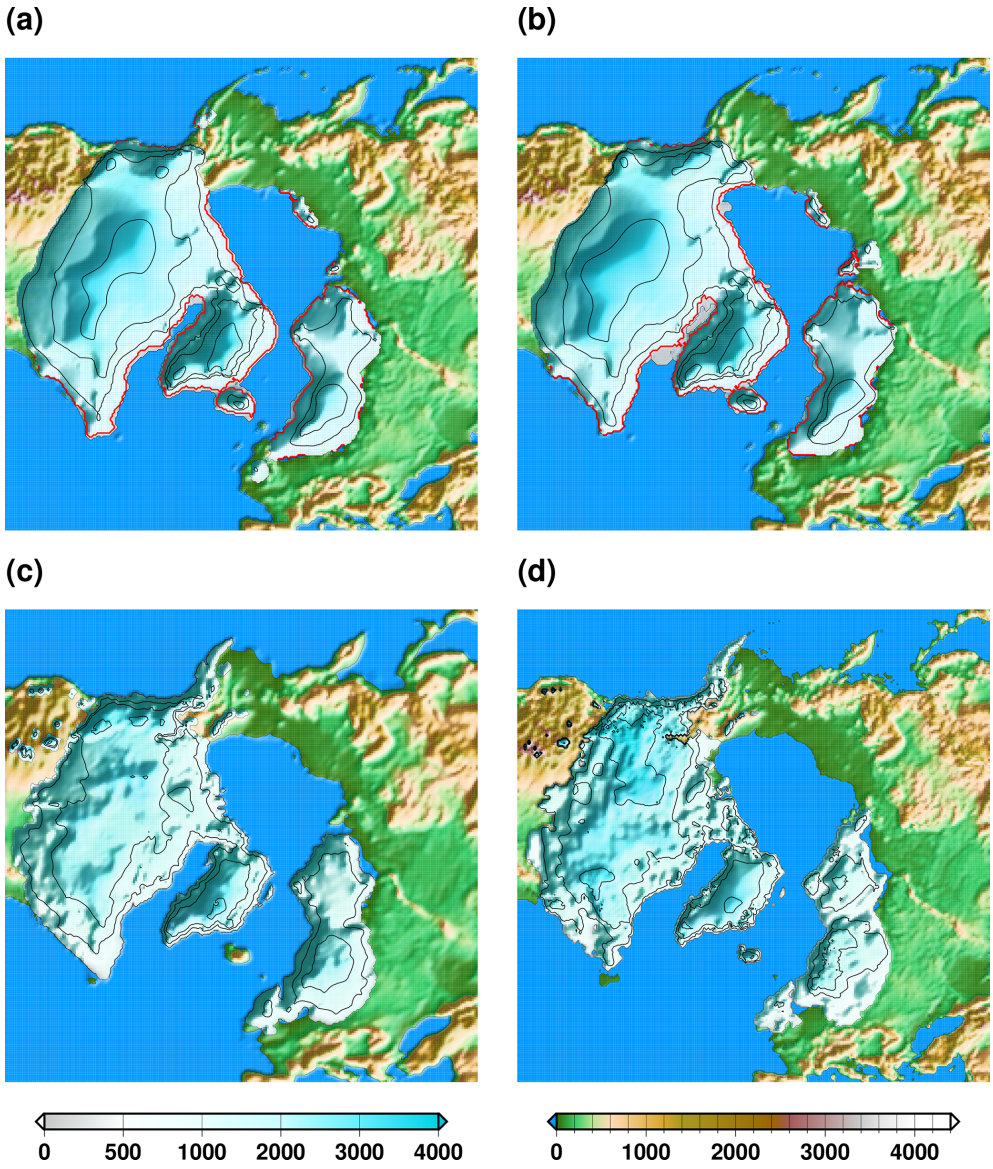

Figure 2. Surface elevation above contemporaneous sea level: **(a)** after the glacial spin-up, **(b)** in the reference deglaciation experiment DGL at 21 ka, **(c)** in the GLAC-1D reconstruction and **(d)** in the ICE-6G_C reconstruction. The colour scale is different for ice-free and ice-covered regions. The simulated ice sheet grounding line is represented by the red line, while the black lines represent isocontours of ice sheet surface elevation (separated by 1000 m).

ice dynamics, for the surface mass balance and for the sub-shelf melt rate.

First, we explore two aspects related to ice dynamics: grounding line dynamics and ice deformation. The ice sheet model GRISLI accounts for two formulations of the flux at the grounding line. For the Antarctic ice sheet, the use of Schoof (2007) instead of Tsai et al. (2015) leads to slower grounding line retreat during deglaciation phases (Quiquet et al., 2018a). For this reason, in the ADGL_schoof experiment we use the Schoof (2007) formulation of the flux at the grounding instead of Tsai et al. (2015). A second aspect for ice dynamics is the choice of the flow enhancement factor E_f, which is a tuned parameter that has consequences for the ice velocity. In the ADGL_ef experiment we use a larger flow enhancement factor (larger velocities) since the simulated North American ice thickness at the LGM is overestimated (Fig. 2).

Then, to explore the sensitivity of our results to the surface mass balance we have performed two experiments in which the weakly constrained melt parameter c_{rad} (Eq. 3) is changed. In ADGL_accplus we use a smaller value for this parameter in order to reduce surface melt to delay the deglaciation. In the ADGL_nocor experiment we use a ho-

mogeneous value of c_{rad} instead of using the spatial heterogeneous value defined from the temperature bias.

Finally, to assess the sensitivity of our results to the subshelf melt rate, in the ADGL_bmbplus we enhance the subshelf melt rate to increase the relative importance of oceanic changes with respect to atmospheric changes.

The list of the different experiments is available in Table 1.

The climate model computes about 850 years in 24 h on a single core of an Intel®Xeon®CPU@3.70 GHz. The computational cost of the ice sheet model is negligible with respect to the rest of the climate model, while the interactive atmospheric downscaling decreases the performance by about 40 % compared to the standard climate model. The coupled synchronous experiments took roughly 1 month to complete, while the asynchronous experiments were approximatively 5 times faster.

3 Results

In this section we first describe the general evolution of the simulated climate in the synchronously coupled experiments before examining the ice sheet changes. Then we examine the results for the accelerated asynchronously coupled experiments to infer the sensitivity of our results to different ice sheet evolutions.

3.1 Climate evolution in the synchronously coupled ice-sheet–climate experiments

The simulated global mean surface temperature evolution for the synchronously coupled ice sheet climate experiments is shown in Fig. 3, together with the strength of the AMOC. In response to the forcings, the different experiments produce a gradual warming from the Last Glacial Maximum towards its maximum value during the Holocene. The glacial–interglacial temperature difference ranges from 3.1 to 3.8 °C and is in good agreement with a palaeo-temperature stack (Shakun et al., 2012), even though *i*LOVECLIM is one of the warmest models at the LGM within the PMIP4 ensemble (Kageyama et al., 2021). The glacial–interglacial temperature difference is mostly explained by the cold temperatures at the LGM resulting from the large ice sheets that induce higher surface elevations and a strong albedo effect. A polar amplification is simulated since the northern and southern high latitudes both show a greater temperature difference from the pre-industrial period compared to the tropics (Fig. 4). This pattern is consistent with recent reconstructions (e.g. Tierney et al., 2020, shown in Fig. 4d), even though with a smaller amplitude in our model. However, our simulated glacial–interglacial temperature difference is within the range of other estimates (4 ± 0.8 °C, Annan and Hargreaves, 2013).

For all the experiments, we simulate a gradual warming with no abrupt climate transitions. If the different experiments show a similar temperature evolution, they also

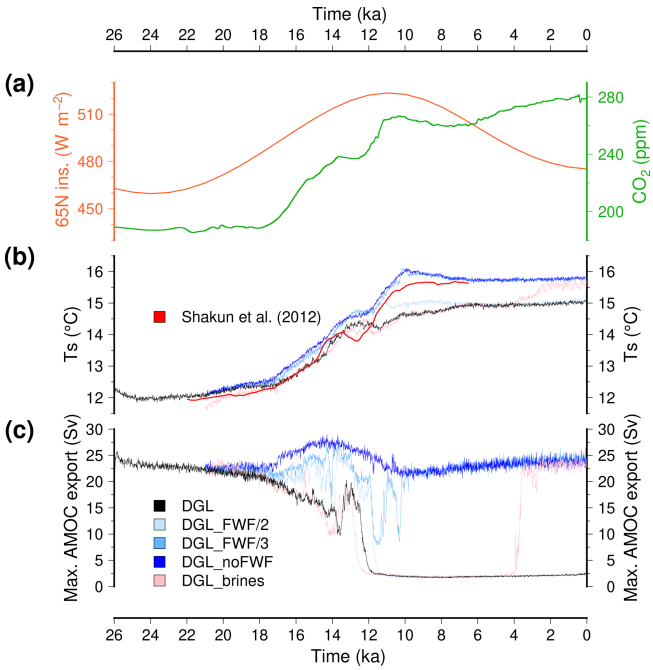

Figure 3. **(a)** Time evolution of the major forcings for the climate model (June insolation at 65° N and carbon dioxide mixing ratio). **(b)** Simulated global mean surface temperature. **(c)** Simulated maximum of the Atlantic stream function. The reference model DGL is in black, while the experiments with reduced freshwater flux to the ocean from ice sheet melting are depicted with blue shading (dark blue for no freshwater flux). The experiments with enhanced brine formation are in pink. Here, we use a 10-year running mean for the model results to smooth interannual variability. In **(b)** we also show the temperature anomaly reconstruction from Shakun et al. (2012) (to which we added 15.5 °C, a typical pre-industrial global mean surface temperature simulated by the model).

display subtle differences. First, the experiments that use a reduced freshwater flux resulting from ice sheet melting present a more rapid warming compared to the reference experiment (e.g. DGL_noFWF with respect to DGL). Second, the experiments show a diverging temperature evolution after around 13 ka. After this date, the reference DGL simulation shows a slight decrease in temperature for about 2 kyr followed by a moderate warming until ∼ 7 ka. By contrast, the experiment in which the freshwater fluxes are discarded (DGL_noFWF) displays a brief period during which the temperature ceases to increase followed by a sharp temperature increase. In this case, the maximal surface temperature is reached at 10 ka after which there is a slight decrease until 7 ka. DGL_FWF/3 shows a very similar temperature change as DGL_noFWF, while DGL_FWF/2 presents similarities with both DGL and DGL_noFWF. This temperature evolution is in overall agreement with the temperature reconstruction of Shakun et al. (2012), which shows a pause in the deglacial warming trends at about 13.5 ka, synchronous with the carbon dioxide plateau. The experiment with the

Table 1. Characteristics of the experiments performed in this study. The accelerated experiments use an ice sheet coupling frequency of 5 years with an acceleration factor for the forcings of 5. The freshwater flux to the ocean resulting from ice sheet melting is either considered (labelled "yes"), discarded ("no") or partially considered (marked with *). Brine rejection due to Southern Ocean sea ice formation is either considered or not. The ice flux at the grounding line in the ice sheet model follows the Tsai et al. (2015) or the Schoof (2007) formulation. The calibrated value for the ice flow enhancement factor, E_f, is 1.8. The parameter c_{rad} in the surface melt model is $-40\,W\,m^{-2}$ in the reference experiments, and its value is locally corrected with a map elaborated from the present-day annual mean surface temperature bias (labelled "variable"). The parameter F_g is used in the linear sub-shelf melt model, set in its reference value at 15×10^{-3}.

Label	Accelerated	Freshwater	Brines	Grounding line flux	E_f (–)	c_{rad} ($W\,m^{-2}$)	F_g (–)
DGL	No	Yes	No	Tsai et al. (2015)	1.8	Variable, −40	15×10^{-3}
DGL_FWF/2	No	Some*	No	Tsai et al. (2015)	1.8	Variable, −40	15×10^{-3}
DGL_FWF/3	No	Some*	No	Tsai et al. (2015)	1.8	Variable, −40	15×10^{-3}
DGL_noFWF	No	No	No	Tsai et al. (2015)	1.8	Variable, −40	15×10^{-3}
DGL_brines	No	Yes	Yes	Tsai et al. (2015)	1.8	Variable, −40	15×10^{-3}
ADGL	Yes	No	No	Tsai et al. (2015)	1.8	Variable, −40	15×10^{-3}
ADGL_schoof	Yes	No	No	Schoof (2007)	1.8	Variable, −40	15×10^{-3}
ADGL_ef	Yes	No	No	Tsai et al. (2015)	3.5	Variable, −40	15×10^{-3}
ADGL_accplus	Yes	No	No	Tsai et al. (2015)	1.8	Variable, −50	15×10^{-3}
ADGL_bmbplus	Yes	No	No	Tsai et al. (2015)	1.8	Variable, −40	150×10^{-3}
ADGL_nocor	Yes	No	No	Tsai et al. (2015)	1.8	Homogeneous, −40	15×10^{-3}

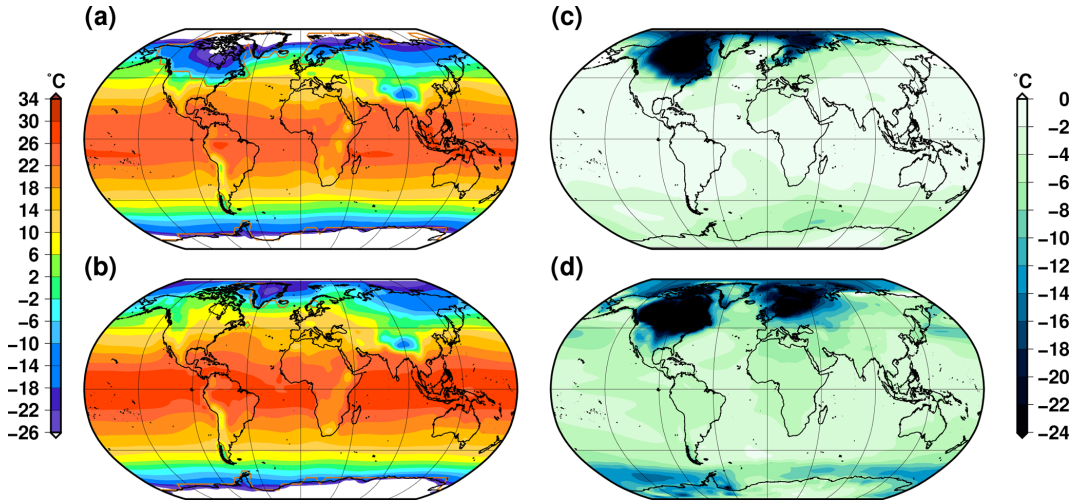

Figure 4. Simulated annual near-surface air temperature in the reference experiment DGL: **(a)** at the Last Glacial Maximum (21 ka) and **(b)** for the pre-industrial period (0 ka). **(c)** Simulated temperature difference between the Last Glacial Maximum and the pre-industrial period **(a–b)**. **(d)** Temperature difference between the Last Glacial Maximum and the pre-industrial period in Tierney et al. (2020).

parameterisation of brines sinking, DGL_brines, displays a comparable temperature evolution to the reference simulation DGL for most of the simulated time period. However, the brine parameterisation induces a cooling of about 0.5 °C in the first years after its activation due to increased sea ice extent around Antarctica. In addition, at 4 ka, the global mean temperature starts to rise again after a relatively steady state for the rest of the Holocene. At 0 ka the temperature in the DGL_brines experiment is close to the temperature in the DGL_noFWF and DGL_FWF/3.

These differences in terms of global mean surface temperature amongst the different experiments are mostly explained by the differences in the state of the simulated Atlantic oceanic circulation. The reference experiment DGL simulates a decrease in the AMOC from the Last Glacial Maximum. After a 50 % reduction in its glacial values, the oceanic circulation strengthens at 13.5 ka for about 500 years before an abrupt collapse. This AMOC collapse is synchronous with the simulated pause in the temperature increase. From 12 ka onwards, the model simulates virtually no meridional overturning circulation. The evolution of the AMOC is drastically different when the freshwater flux to the ocean resulting from ice sheet melting is not considered (DGL_noFWF). In this case, the AMOC remains strong during the whole 26 kyr,

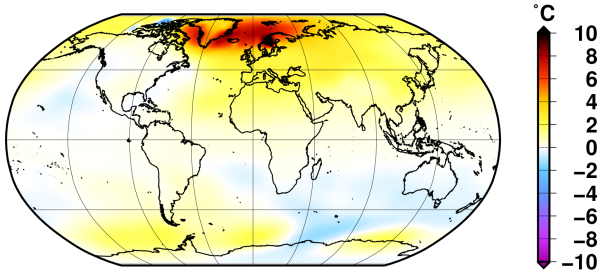

Figure 5. Simulated annual near-surface air temperature difference during the pre-industrial period (0 ka) from the reference experiment DGL and the experiment DGL_noFWF, in which the freshwater flux resulting from ice sheet melting is not applied to the ocean model (DGL_noFWF – DGL).

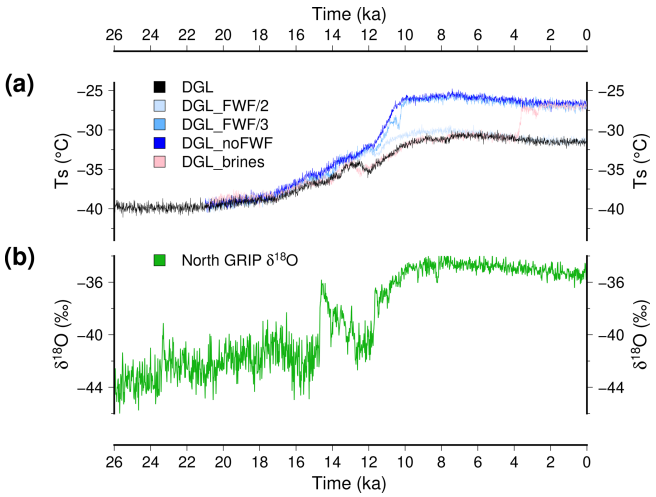

Figure 6. **(a)** Simulated surface temperature at the location of the North GRIP deep ice core. The reference model DGL is in black, while the experiments with reduced freshwater flux to the ocean from ice sheet melting are depicted with blue shading (dark blue for no freshwater flux). The experiments with enhanced brine formation are in pink. Here, we use a 10-year running mean for the model results to smooth interannual variability. **(b)** The isotopic content in δ^{18}O measured at North GRIP (Andersen et al., 2004), which is often regarded as representative of local temperature changes.

with a maximum in the middle of the deglaciation towards 14 ka. This explains why the temperature rises more rapidly during the deglaciation in this experiment compared to the reference DGL experiment. Due to the weak AMOC in this case, the Northern Hemisphere remains colder, which ultimately delays the deglaciation of the ice sheets. The simulated pre-industrial period is also 0.8 °C colder in DGL with respect to DGL_noFWF since the absence of oceanic meridional heat transport results in much colder high latitudes, especially in the North Atlantic (Fig. 5). The release of only half the meltwater flux to the ocean (DGL_FWF/2) does not allow us to maintain an active AMOC during the Holocene either, but the collapse of the AMOC is delayed here with respect to the reference experiment. In addition to the DGL_noFWF experiment, only the experiment in which only one-third of the meltwater flux is released to the ocean (DGL_FWF/3) is able to maintain an active AMOC during the Holocene. In this case, there are several abrupt oscillations in the strength of the circulation from 14 to 10 ka, but the model recovers and simulates an AMOC similar to the DGL_noFWF from 10 ka onwards. For most of the simulated time period, the experiment in which the sinking of brines around Antarctica is parameterised (DGL_brines) shows a very similar evolution than the reference DGL experiment, except that the AMOC shut-down occurs a few centuries earlier. However, at 4 ka the AMOC abruptly recovers and explains the final increase in the global mean temperature.

While some experiments show very abrupt shifts in the ocean, the atmospheric temperature evolution is nonetheless mostly gradual. This is visible at the global scale (Fig. 3b) but also when examining the temperature change above the Greenland ice sheet (Fig. 6a). The local temperature change closely resembles the global mean temperature change, even though with a larger amplitude. There are a few abrupt changes: slightly less than 4 °C in about 200 years at 10.7 ka and at 3.8 ka for the DGL_FWF/3 and DGL_brines experiments, respectively. These are direct consequences of the AMOC recoveries visible in Fig. 3c. These simulated abrupt warming events over the Greenland ice sheet look similar to the ones of the ice core record (Fig. 6b). The North GRIP (North Greenland Ice Core Project) δ^{18}O is generally used to reconstruct the past local temperature changes with a conversion factor of 0.67 ‰ per degree to 0.8 ‰ per degree (e.g. Johnsen et al., 1997; Buizert et al., 2014), suggesting a glacial–interglacial difference of more than 15 °C. On comparable timescales, the Bølling–Allerød warming at 14.7 ka displays a similar temperature change amplitude compared to our simulated abrupt warming events, even though slightly larger. This suggests that, in our model, abrupt changes in the Atlantic oceanic circulation can induce large temperature changes over the Greenland ice sheet, similar to the ones deduced from the ice core records. However, the timing of the simulated abrupt events in the experiments shown here does not correspond to the ones of the ice record.

3.2 Simulated ice sheet changes

The large-scale differences amongst the different experiments discussed in Sect. 3.1 are largely driven by differences in the amount of the freshwater released to the ocean related to ice sheet melting. This freshwater flux is shown in Fig. 7a for the reference experiment DGL. Even though this flux displays some variability, its evolution is generally gradual and shows a maximum around 14 ka where it peaks above 0.3 Sv (1 Sv corresponds to 10^6 m^3 s^{-1}) with 100-year mean values about 0.23 Sv. In Fig. 7a we also show the meltwater flux computed from the ice thickness changes in the

ICE-6G_C and GLAC-1D geologically constrained reconstructions. These fluxes have the same order of magnitude of the simulated flux in the DGL experiment. However, the model fails to reproduce the two distinct accelerations in ice sheet retreat visible in the reconstructions for the meltwater pulse 1A at 14.6 ka (Deschamps et al., 2012) and the meltwater pulse 1B at 11.45 ka (Abdul et al., 2016). Instead, the model produces important fluxes (greater than 0.1 Sv) over a few thousand years. Another way to discuss these fluxes is to integrate them in time to have an idea of the total ice sheet volume evolution through the deglaciation (Fig. 7b). In doing so, we can see that the coupled *i*LOVECLIM-GRISLI model setup produces an ice volume evolution in general agreement with the reconstructions since it lies between the two estimates of ICE-6G_C and GLAC-1D most of the time. However, the coupled model seems to deglaciate too fast since it displays a lower total ice sheet volume than the two reconstructions from 12.5 ka. In Fig. 7b we also show the eustatic sea level reconstruction of Lambeck et al. (2014) which displays a larger ice sheet volume, in particular around the Last Glacial Maximum. Since we do not simulate the Antarctic ice sheet changes, the ice volume shown in this figure only represents the Northern Hemisphere ice sheet volume. Interactive simulation of the Antarctic ice sheet would result in a larger ice volume during the glacial period reducing partially the mismatch with the Lambeck et al. (2014) reconstruction. At the end of the simulation, the model has an overestimation of the present-day ice volume. This overestimation corresponds to about 4.5 m of sea level equivalent and is explained by an overestimation of the Greenland ice sheet volume and remaining small ice sheets in the Ellesmere Island, Iceland, Norway and offshore of Newfoundland (Grand Banks).

The ice volume evolution of individual ice sheets is presented in Fig 8 for both the reference DGL and the DGL_noFWF experiments. In this figure, the individual ice sheet break-up is also represented for the ICE-6G_C and the GLAC-1D reconstructions. The ice volume partitioning is well reproduced. The North American ice sheet is by far the largest contributor for the last glacial sea level fall. At 26 ka, we simulate an ice volume of 81 m of sea level equivalent within the range of the geological reconstructions (75 and 86 m). However, in our experiments, the North American ice sheet volume increases until 20.5 ka where the reconstructions suggest a decline already as early as 26 ka (ICE-6G_C) or 23.8 ka (GLAC-1D). This is mostly due to our methodology used to define the initial state for the coupled experiments. When the coupling starts, at the beginning of our experiments, there is an abrupt change in the climate model in terms of ice mask and surface elevation from GLAC-1D to our spun-up ice sheets. Our spun-up ice sheets at 26 ka (Fig. 2a) show a higher North American ice sheet surface elevation than the GLAC-1D reconstruction used during the climatic spin-up, suggesting an overestimation of the precipitation in this area. When the coupling starts, this precipitation bias is amplified due to higher surface elevation and

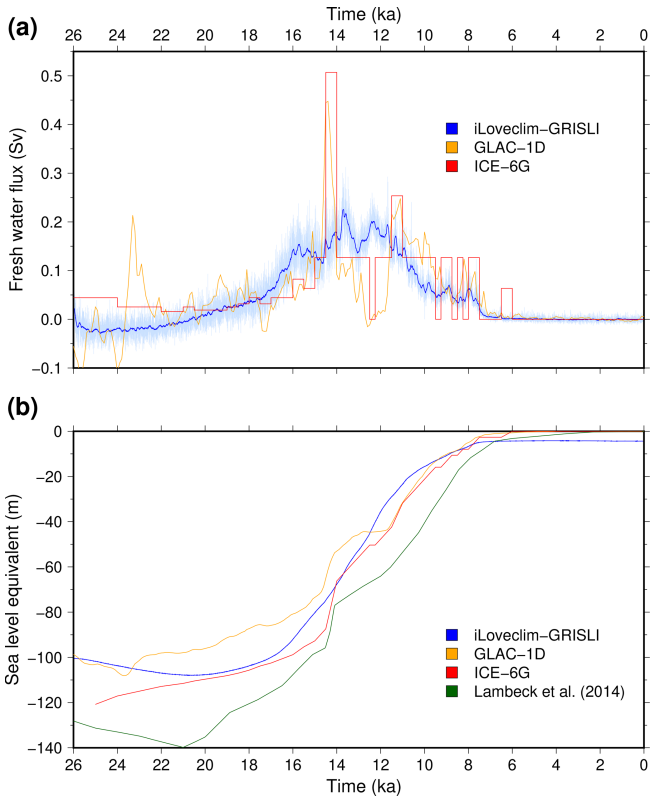

Figure 7. **(a)** Time evolution of the freshwater release to the ocean resulting from the computed change in the Northern Hemisphere ice sheets. The blue curve depicts the values smoothed with a 100-year running mean, while annual values are depicted in light blue. The ice mass change for the two geologically constrained reconstructions of GLAC-1D and ICE-6G_C is depicted in orange and red, respectively. **(b)** Corresponding eustatic sea level evolution.

related increased orographic precipitation. The *i*LOVECLIM climate model likely shows an underestimation of the elevation desertification effect over the ice sheets (Quiquet et al., 2018b). The simulated volume of the Eurasian ice sheet displays a similar evolution than the North American ice sheet with a maximum around the Last Glacial Maximum. This agrees well with the GLAC-1D reconstruction. Given its smaller volume, the absolute rate of volume loss is smaller for the Eurasian ice sheet (1.3 m per millennium) compared to the one of the North American ice sheet (5.7 m per millennium). However, the Eurasian ice sheet has already lost half its volume by 14.5 ka, whereas this occurs at 12.8 ka for the North American ice sheet. The Greenland ice sheet presents only a small volume reduction of 2.6 m of sea level equivalent, in good agreement with the reconstructions. However, the Greenland ice sheet volume at the end of the simulation is largely overestimated compared to the present-day observations (about 40 % volume overestimation). As for the total volume, the individual ice sheets deglaciate faster in the DGL_noFWF experiment. This is particularly visible for the

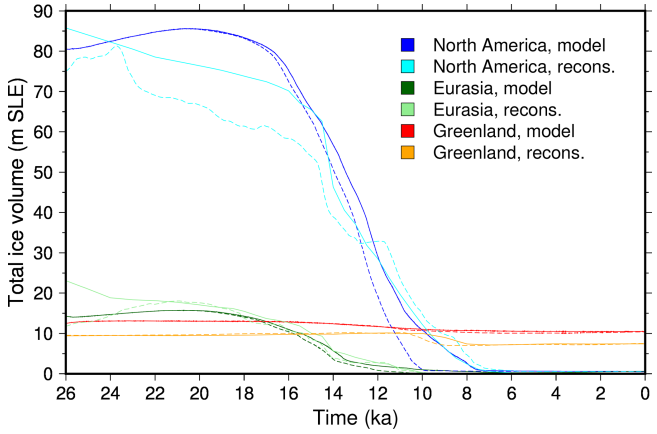

Figure 8. Individual ice sheet contributions to deglacial sea level rise, expressed as metres of sea level equivalent (SLE). For our model experiments, we show the ice volume for the reference experiment DGL (plain lines) and the experiment in which the freshwater flux resulting from ice sheet melting is not released to the ocean DGL_noFWF (dashed lines). For the reconstructions, we show the ICE-6G_C (plain lines) and the GLAC-1D (dashed lines) reconstructions.

North American ice sheet for which there is a difference of 1000 years at about 11 ka.

A map of the simulated ice sheet configuration for selected snapshots is shown in Fig. 9. This figure shows the results for the reference DGL experiment, while the other synchronously coupled experiments show a similar deglacial pattern although with differences in timing. At 26 ka, the North American ice sheet presents some very active ice streams on its northern margin from east to west: the Hudson Strait ice stream, the Lancaster Sound ice stream and the Amundsen Gulf ice stream. In these regions, grounded ice velocities are greater than $500\,\mathrm{m\,yr^{-1}}$. Elsewhere, the ice sheet does not present well-identified ice streams but the margins generally present large velocities, greater than $200\,\mathrm{m\,yr^{-1}}$. The other ice sheets present a smaller ice flow. From 26 to 21 ka, there is only little change in the ice sheet except the Eurasian ice sheet retreat from the British Isles and the development of an ice shelf at the outlet of the Hudson Strait ice stream. The simulated topography at 21 ka (Fig. 2b) is close to the spun-up ice sheets used at 26 ka and generally remains in good agreement with the geologically constrained reconstructions. From 21 ka, we simulate a gradual ice sheet retreat for both the North American and the Eurasian ice sheets. The North American ice sheet mostly retreats in its southern continental part due to decreased surface mass balance related to the gradual warming. The deflected bedrock in this area leads to the apparition of proglacial lakes, already visible at 14 ka. Similarly, at this date, the southern flank of the Eurasian ice sheet also displays proglacial lakes. The eastern part of the Eurasian ice sheet, the Barents–Kara ice sheet, rapidly collapses due to a grounding line instability in the Kara sea. This instability is initiated at about 14.5 ka and results in a complete disintegration of the Barents–Kara ice sheet in about 1.2 ka. Such instability is favoured by the depressed bedrock, with a ~ 300 m deepening in the Kara sea with respect to the present-day bathymetry, resulting in steeper retrograde slopes. Another grounding line instability occurs later for the continental part of the North American ice sheet. The grounding line retreat is clearly visible at 12 ka. This lake-induced instability considerably facilitates the North American ice sheet deglaciation (Quiquet et al., 2021a). At 8 ka, we simulate a very small North American ice sheet and only a relic of the Eurasian ice sheet over the Scandinavian mountains. At this time, the bedrock is still depressed below sea level over the northern most part of America but slowly returns to its present-day value. During the last 1000 years of the simulation, the bedrock uplift rate in the vicinity of the Hudson Bay is about 0.5 to 1.2 m per century, a value comparable to modern observations (Husson et al., 2018). The Greenland ice sheet expands considerably onto the continental shelf during the glacial period and retreats until about 10 ka. It does not display any substantial change in the ice extent during the Holocene, but it displays some ice elevation changes. The ice elevation evolution near the summit shows a maximum at about 10 ka and decreases afterwards in agreement with palaeo-elevation reconstructions at the deep ice core drilling sites (Vinther et al., 2009).

The chronology and pattern of the deglaciation is largely affected by the biases in the climate model. We present these biases in terms of mean annual temperature and total precipitation rate in Fig. 10. To construct this figure we use a reference pre-industrial experiment (with fixed ice sheets), performed with a similar setup to the deglaciation experiments. Notably, this pre-industrial experiment uses the same last glacial oceanic bathymetry with a closed Bering Strait. The Northern Hemisphere topography and ice mask are nonetheless at their present-day reference value for GRISLI (Amante and Eakins, 2009; Bamber et al., 2013). The model presents a cold bias associated with an overestimation of the precipitation in the northwestern part of the North American continent. This explains why this region of the North American ice sheet deglaciates much later than its eastern sector where a warm bias is present. Also, Grand Banks and Iceland remain ice covered at the end of the simulation where the model is generally too cold and too wet. More generally, the climate model tends to overestimate the precipitation over mountainous areas which can induce a positive feedback over some ice caps such as Iceland, Grand Banks, Ellesmere Island and the Scandinavian mountains.

In Fig. 11 we present the rate of total ice mass change and its individual components: surface mass balance, basal mass balance and calving. The total mass change remains positive until 20.5 ka due to a positive integrated surface mass balance, not entirely compensated for by the basal mass loss (mostly sub-shelf melt) and calving. After this date, the total mass change becomes negative for the rest

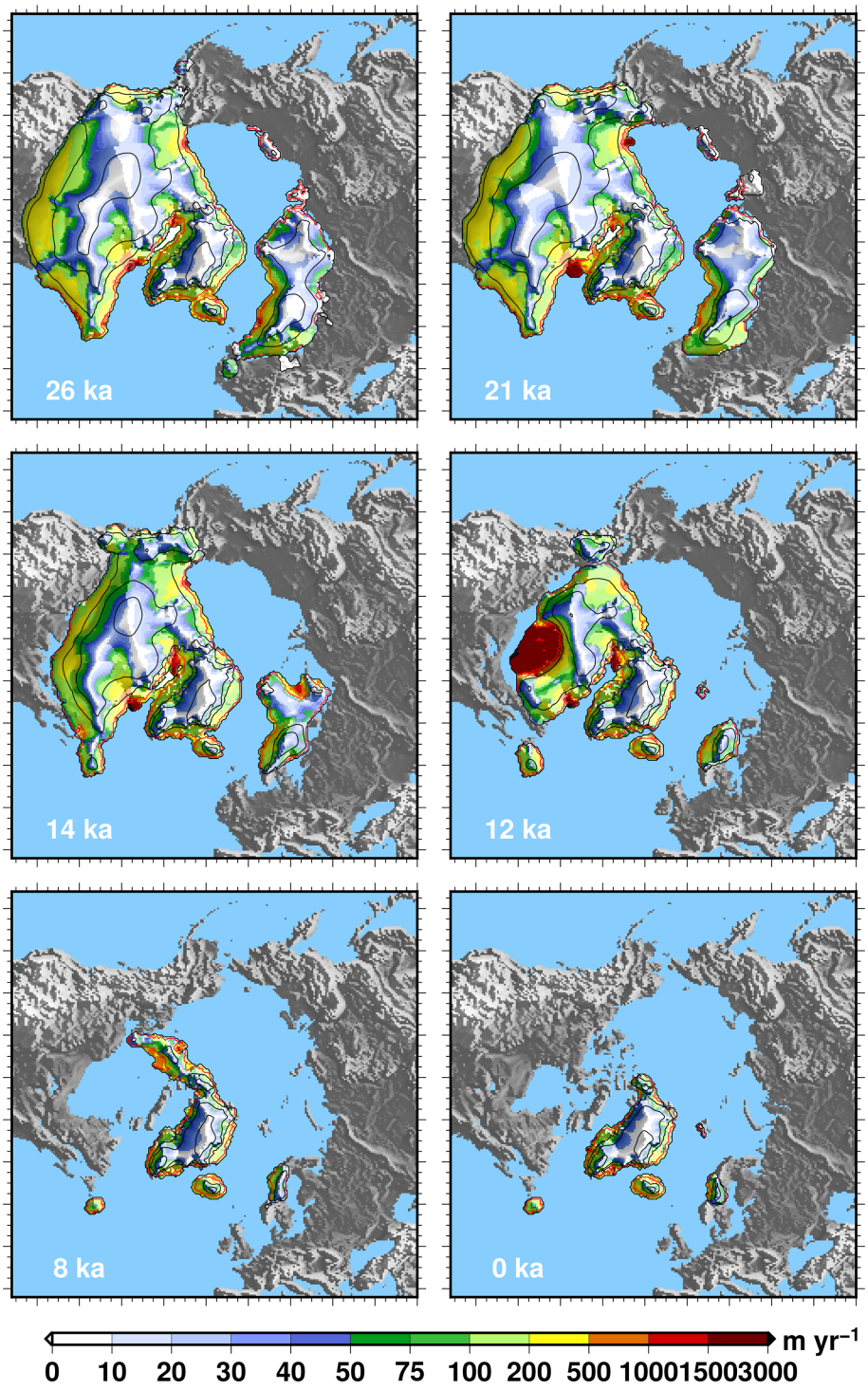

Figure 9. Simulated Northern Hemisphere ice sheets in the reference model for selected snapshots. The simulated ice elevation above contemporaneous eustatic sea level is shown with the black isocontours (separated by 1000 m). The red contour is the ice sheet grounding line. The amplitude of the simulated vertically averaged ice sheet velocity is draped over the surface topography and depicted by the colour palette. Emerged land masses are in grey, while bed elevation below contemporaneous sea level is in blue.

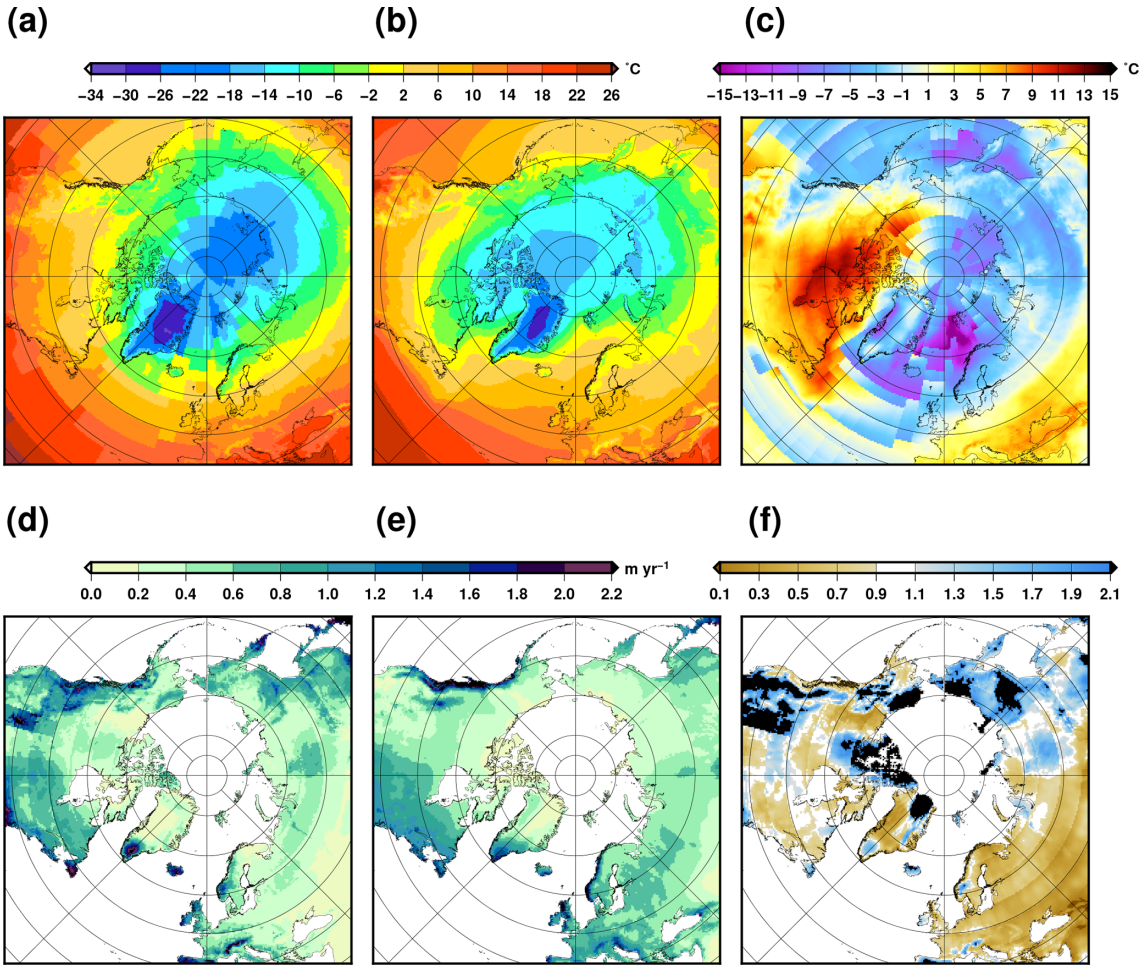

Figure 10. **(a)** Simulated annual near-surface air temperature for a pre-industrial climate experiment using the model configuration used for the deglaciation experiment (i.e. with an LGM ocean bathymetry) but with a present-day topography and ice mask for the Northern Hemisphere. **(b)** Annual near-surface air temperature for the ERA5 climatological mean over 1979–2008. **(c)** Temperature difference **(a–b)**. **(d)** Simulated annual total precipitation rate for the same pre-industrial experiment. **(e)** CRU-CL-v2 annual total precipitation rate. **(f)** Precipitation ratio between the data in panels **(d)** and **(e)**.

of the duration of the experiment. The total mass loss peaks at -9.7×10^3 Gt yr^{-1} at 13.8 ka when surface ablation and loss by calving almost synchronously display a maximum (surface ablation slightly precedes the calving increase). At this date, the mass loss due to the ocean and lake represent more than half the loss by surface mass balance. In fact, if both basal mass loss and calving remain almost constant until 14.5 ka (-1.4×10^3 Gt yr^{-1}), they nonetheless show some variability after this date. These fluxes are maximal at the time of the grounding instabilities shown in Fig. 9 for both the Eurasian (14.5–13.5 ka) and the North American (12.8–10 ka) ice sheets. While the mass loss is primarily driven by surface ablation until 12.8 ka, after this date the oceanic and lake forcing become the major driver for the ice sheet retreat. The total mass loss finally reaches zero (ice sheet equilibrium) at 6.5 ka. The lesser importance of the sub-shelf melt rate for the first phase of the deglaciation could arise from the simple model we use to represent this process. Notably, we use a linear melting rate dependency on temperature change, while a quadratic dependency could best reproduce this process (Favier et al., 2019). A quadratic dependency would result in more sensitive melt rate changes to temperature changes.

3.3 Accelerated experiments to assess specific sensitivities

The aim of this section is to assess the sensitivity of the simulated climate evolution to the choice of critical ice sheet model parameters and assumptions. To do so, we have performed additional experiments in which the forcings are accelerated. Three major sources of uncertainties have been explored: ice sheet mechanics (deformation and grounding line dynamics), surface mass balance and sub-shelf melting rates.

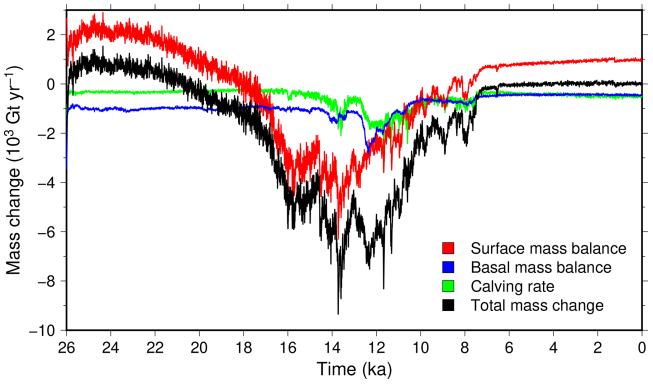

Figure 11. Time evolution of the different contributions to ice sheet mass changes. The total mass change is the sum of the surface mass balance, the basal mass balance and the calving rate.

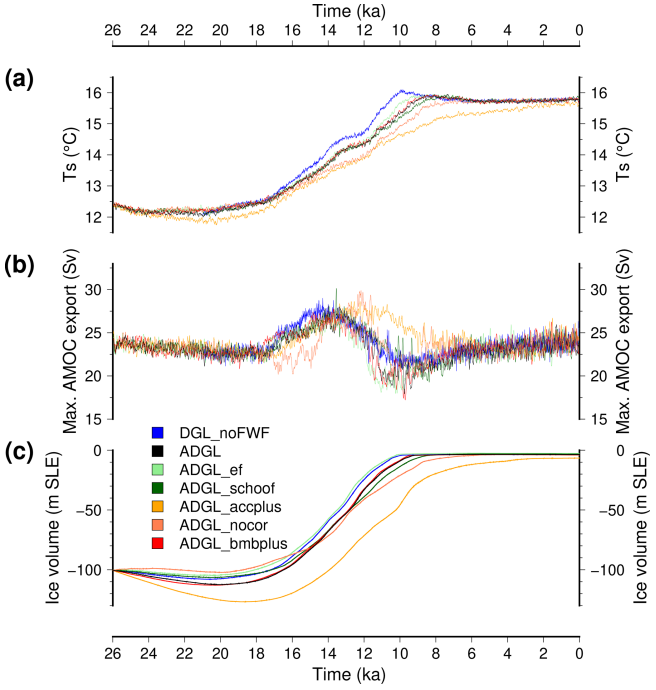

Figure 12. Time evolution of a selection of large-scale climate variables for different sensitivity experiments: **(a)** global mean surface temperature, **(b)** maximum of the Atlantic stream function and **(c)** simulated Northern Hemisphere ice volume. The model that does not account for the freshwater release to the ocean due to ice sheet melting is shown in grey (DGL_noFWF). The other lines are accelerated simulations (factor of acceleration of 5), and they similarly do not account for the freshwater flux to the ocean. The accelerated reference experiment is in blue (ADGL). The dark green line is an experiment in which we use the Schoof (2007) formulation of the flux at the grounding line (ADGL_schoof) instead of Tsai et al. (2015). The light green line is an experiment for which we use a larger enhancement factor (3.5 instead of 1.8, ADGL_ef). The light orange line is a version of the model with a lower c_{rad} coefficient (-50 instead of $-40\,\mathrm{W\,m^{-2}}$, ADGL_accplus) which induces a more positive surface mass balance. The dark orange is for an experiment in which we do not apply the spatial correction of the c_{rad} parameter (ADGL_nocor). The blue line is for an experiment with an increase in sub-shelf melting rate (ADGL_bmbplus).

The evolution of some large-scale climate variables for these additional experiments are shown in Fig. 12. Since we do not feed back the freshwater related to ice sheet melting to the ocean in the accelerated experiments, they have to be compared to the DGL_noFWF experiment. The reference accelerated experiment ADGL (black in Fig. 12) is in fact similar to the DGL_noFWF (blue): rapid temperature increase and active Atlantic circulation throughout the deglaciation. However, the accelerated experiment displays larger ice sheets than the non-accelerated (about 8 m of sea level equivalent at 14 ka) and as a result a colder climate ($\sim 0.4\,^{\circ}$C in global mean surface temperature at 14 ka). If the timing of the ice sheet retreat can be slightly different, the overall pattern of this retreat is only weakly affected by the acceleration factor.

The two experiments related to ice sheet dynamics (ADGL_ef and ADGL_schoof) do present some differences in their simulated ice sheet volume. The increased enhancement factor (ADGL_ef) leads to thinner ice sheets (smaller ice volume) and, as such, deglaciates faster than the reference accelerated experiment (ADGL). The experiment in which we use the formulation of Schoof (2007) instead of Tsai et al. (2015) (ADGL_schoof) also produces a lower ice sheet volume during the glacial period. However, this experiment shows a slower ice sheet retreat during the deglaciation compared to the reference ADGL experiment. This is mostly related to the greater grounding line sensitivity in the formulation of Tsai et al. (2015), already shown in (Quiquet et al., 2018a) for the Antarctic ice sheet. These differences in terms of ice sheet evolution nonetheless only have a limited impact on the climate evolution. The ADGL_ef produces a slightly more rapid warming during the deglaciation (related to the smaller ice sheets), while it is the opposite for the ADGL_schoof (slower ice sheet retreat). The Atlantic circulation is also weakly impacted by the different ice sheet evolution. Only the ADGL_ef produces a slightly earlier decrease in the overturning circulation than the ADGL experiment, while the ADGL_schoof displays insignificant differences.

The two experiments related to modification of the surface mass balance parameters induce larger simulated ice sheet volume differences. Associated with a larger ice sheet surface mass balance, the ADGL_accplus produces larger ice sheet volumes throughout the whole simulated time period. For this experiment the maximal ice volume is reached by circa 19 ka, and it is larger by about 15 m of sea level equivalent than the ADGL experiment. This excess ice also explains the delayed ice sheet retreat: at 10 ka the simulated ice sheets still represent about 45 m drop in eustatic sea level in the ADGL_accplus experiment compared to about 8 m in

the ADGL experiment. This has consequences for the simulated climate: (i) the global mean temperature rises more slowly, eventually reaching a comparable value to the reference simulation at 0 ka; (ii) the phase of very active overturning in the middle of the deglaciation is extended by 2 kyr. Even though the ADGL_accplus experiment displays larger ice sheet volume, the pattern of the ice sheet retreat is similar to the one of the ADGL experiment. By contrast, the ADGL_nocor experiment provides alternative ice sheet histories. In the ADGL experiment the Barents–Kara sector of the Eurasian ice sheet is almost fully deglaciated at 13.5 ka, while it is the case only after 8.5 ka in the ADGL_nocor experiment. Conversely, the North American ice sheet retreats faster in the ADGL_nocor experiment. This is a direct consequence of the cold temperature bias in northern Europe and the warm bias in North America. If the climate evolution is not drastically changed as a result of these different ice sheet chronologies, it nonetheless shows some interesting differences. The overturning circulation remains moderate for a longer time period compared to the ADGL experiment since it increases only after 15 ka (with respect to 17.5 ka in ADGL). As a result the global mean temperature in ADGL_nocor is colder than in ADGL even though it shows smaller ice sheets at least until 15 ka. The oceanic circulation in the model seems largely affected by the Eurasian ice sheet size.

Finally, the experiment in which we increase the sub-shelf melting rate, ADGL_bmbplus, shows only negligible changes with respect to the ADGL experiment. This suggests that, in our model, the ice sheet retreat is mostly driven by surface ablation and not sub-shelf melt.

4 Discussion

We have shown that in our reference experiment the freshwater flux to the ocean resulting from ice sheet melting leads to a progressive weakening of the Atlantic overturning circulation from the Last Glacial Maximum, eventually leading to a complete shut-down without recovery within the time frame of the experiments presented. With different sensitivity experiments in which we modify the amount of freshwater flux released to the ocean, we have shown that we are able to simulate abrupt transitions from collapsed to recovered state of the Atlantic circulation during the deglaciation. Thus, with a reduced freshwater flux, the AMOC can remain active during the Holocene. This suggests that if the model contains the physical elements for rapid changes in the AMOC, it seems nonetheless too sensitive to the amount of freshwater since it is unable to maintain an active oceanic circulation with a realistic amount of freshwater fluxes. Alternative experiments (not discussed here) with the *i*LOVECLIM model in which we used prescribed ice sheet reconstructions (instead of interactive) and freshwater fluxes derived from the GLAC-1D and ICE-6G_C also lead to a shut-down of the overturning circulation. This problem has been identified in other models. For example, freshwater derived from geologically constrained ice sheet reconstructions (ICE-5G, Peltier, 2004) also leads to an AMOC collapse in Bethke et al. (2012), while most of the time idealised freshwater scenarios, which can substantially differ from the reconstructions, are preferred (e.g. Liu et al., 2009; Menviel et al., 2011; He et al., 2013; Obase and Abe-Ouchi, 2019). Transient sensitivity of the simulated AMOC to freshwater flux remains an open question when attempting to simulate the climate evolution across the last deglaciation. For these transient experiments, it would be useful to perform a systematic analysis of the sensitivity of the oceanic circulation to key processes for deep convection, such as the brine rejection during sea ice formation or atmospheric wind stress and also in the way the freshwater flux is imposed on the oceanic model, e.g. considering the depth of the freshwater release, its seasonality or the impact of the iceberg transport.

The simulated temperature change during the deglaciation is generally very gradual with no abrupt transitions. For example, in our experiments over the Greenland ice sheet the local temperature change is strongly correlated to the global mean temperature change and most of the time does not display abrupt events such as the one recorded in ice cores (Alley, 2000b). In fact only the abrupt AMOC recoveries in certain experiments (DGL_FWF/3 at 10.7 ka and DGL_brines at 3.8 ka) are able to produce abrupt temperature changes in Greenland comparable to the ice core record. Since these AMOC recoveries are lacking in the majority of our experiments we generally largely underestimate the millennial-scale variability observed at high latitudes. This variability could largely influence the ice sheet evolution. For example, since the Bølling–Allerød warming is not simulated in our model, we are not able to quantify its impact on the North American or the Eurasian ice sheets (Gregoire et al., 2016; Brendryen et al., 2020).

In addition, within the experiments presented here, only changes in the AMOC related to freshwater flux are able to produce some abrupt temperature changes. For example, all the accelerated experiments, in which this process is not considered, have produced a smooth temperature increase since the LGM. However, these experiments show different ice sheet evolutions with some rapid ice sheet retreat at times. This suggests that in our model and for the time period simulated, external forcing and ice sheet changes alone are not able to produce millennial-scale climate variability without invoking freshwater hosing.

Finally, we have identified a few expected improvements.

First, in our experiments we did not consider the potential changes in the Antarctic ice sheet since we use a constant topography and ice mask in the Southern Hemisphere. Similarly we do not take into account the freshwater flux resulting from Antarctic ice sheet retreat from the Last Glacial Maximum. This simplification was motivated by the fact that an earlier study already identified that freshwater hosing around

Antarctica with our model has a negligible impact on the simulated climate (Roche et al., 2010). In this region, the circumpolar current tends to rapidly dilute the released freshwater leading to a very limited impact on vertical oceanic mixing. However, the gradual retreat of the ice sheet from the continental shelf margin can also facilitate the sinking of brines and as such enhance dense water formation. If the sinking of brines around Antarctica seems to play a moderate role in our experiments, it can nonetheless produce an abrupt AMOC recovery at 3.8 ka, not occurring in the reference experiment. As such, this process should be more thoroughly investigated with, for example, interactive Antarctic topography and bathymetry.

Second, we have used a very simple parameterisation for sub-shelf melt when alternative parameterisations display a better agreement with complex sub-shelf cavity oceanic models (Favier et al., 2019). This process is key for the future of Antarctic ice sheet (Seroussi et al., 2020) and could be equally important for the deglaciation of marine-based sectors of the Northern Hemisphere ice sheets (Petrini et al., 2018; Clark et al., 2020). For this reason, we plan to implement an alternative sub-shelf melt model at the interface between GRISLI and *i*LOVECLIM. However, in our experiments, the main driver for ice sheet retreat is surface mass balance, at least until 12.8 ka. After this date, sub-shelf melt rate becomes important only because grounding line instabilities have been triggered. These instabilities do not seem to be triggered by an artificially high grounding line melting rate since the experiment with higher sub-shelf melt displays a very similar ice sheet evolution. These results could be revisited with a more complex sub-shelf model.

Lastly, we run deglaciation experiments starting from 26 ka assuming that the Northern Hemisphere ice sheets were in equilibrium with the simulated glacial climate. However, the Last Glacial Maximum ice sheets were the results of the long previous glacial period starting from the last glacial inception. Ideally, it would have been best to perform a transient coupled experiment covering this period of time in order to have more realistic ice sheet states. Notably, slowly evolving ice sheet variables such as glacial isostasy or internal temperatures are expected to be affected by a transient spin-up instead of a constant glacial spin-up. However, it currently remains a numerical challenge to perform such a transient spin-up.

5 Conclusions

In this paper, we have presented climate model experiments in which the Northern Hemisphere ice sheets are synchronously coupled to the rest of the system (atmosphere and ocean). For the majority of our experiments, the atmospheric changes are mostly gradual, while the Atlantic overturning circulation displays abrupt changes. In the reference experiment, the model fails at keeping an active circulation during the Holocene. It is only when the freshwater amounts released to the ocean are reduced that we can simulate AMOC shut-downs and recoveries, suggesting too strong a sensitivity of this process in our model. The AMOC recoveries, when simulated, are associated with abrupt warming events in Greenland. The simulated ice sheet evolution is in general agreement with geologically reconstructions even though the retreat is too fast with respect to these reconstructions. The simulated ice sheets present some phases of acceleration in their retreat related to grounding line instabilities. These occur in the Arctic Ocean for the Eurasian ice sheet and in proglacial lakes at the southern margin of the North American ice sheet. However these events are not directly correlated to abrupt climate changes. In addition, we performed various sensitivity experiments in which we did not consider the freshwater released to the ocean but in which we modified some critical aspects of the ice sheet model. If these experiments produce different ice sheet deglacial chronologies they show similar climate trajectories. This suggests that ice sheet geometry changes alone, i.e without freshwater fluxes, are not enough to generate abrupt events in our model.

Data availability. The source data of the figures presented in the main text of the paper are available on the Zenodo repository with the digital object identifier https://doi.org/10.5281/zenodo.5336280 (Quiquet et al., 2021b).

Author contributions. AQ, DMR and CD designed the project. All authors have contributed to the model developments necessary to perform this work. AQ performed the simulations. All authors participated in the analysis of model outputs and the paper writing.

Competing interests. The authors declare that they have no conflict of interest.

Disclaimer. Publisher's note: Copernicus Publications remains neutral with regard to jurisdictional claims in published maps and institutional affiliations.

Acknowledgements. We would like to thank the two referees, Evan Gowan and Javier Blasco, for their insightful comments. Catherine Ritz is warmly thanked for her dedication to the GRISLI ice sheet model. We acknowledge the Institut Pierre Simon Laplace for hosting the *i*LOVECLIM model code under the LUDUS framework project (https://forge.ipsl.jussieu.fr/ludus, last access: 8 October 2021).

Financial support. The research leading to these results has received funding from the SCOR foundation project COASTRISK.

Review statement. This paper was edited by Alessio Rovere and reviewed by Evan Gowan and Javier Blasco.

References

Abdul, N. A., Mortlock, R. A., Wright, J. D., and Fairbanks, R. G.: Younger Dryas sea level and meltwater pulse 1B recorded in Barbados reef crest coral Acropora palmata, Paleoceanography, 31, 330–344, https://doi.org/10.1002/2015PA002847, 2016.

Alley, R. B.: The Younger Dryas cold interval as viewed from central Greenland, Quaternary Sci. Rev., 19, 213–226, https://doi.org/10.1016/S0277-3791(99)00062-1, 2000a.

Alley, R. B.: Ice-core evidence of abrupt climate changes, P. Natl. Acad. Sci. USA, 97, 1331–1334, https://doi.org/10.1073/pnas.97.4.1331, 2000b.

Amante, C. and Eakins, B.: ETOPO1 1 Arc-Minute Global Relief Model: Procedures, Data Sources and Analysis, NOAA Technical Memorandum NESDIS NGDC-24, National Geophysical Data Center, NOAA, 2009.

Andersen, K. K., Azuma, N., Barnola, J.-M., Bigler, M., Biscaye, P., Caillon, N., Chappellaz, J., Clausen, H. B., Dahl-Jensen, D., Fischer, H., Flückiger, J., Fritzsche, D., Fujii, Y., Goto-Azuma, K., Grønvold, K., Gundestrup, N. S., Hansson, M., Huber, C., Hvidberg, C. S., Johnsen, S. J., Jonsell, U., Jouzel, J., Kipfstuhl, S., Landais, A., Leuenberger, M., Lorrain, R., Masson-Delmotte, V., Miller, H., Motoyama, H., Narita, H., Popp, T., Rasmussen, S. O., Raynaud, D., Rothlisberger, R., Ruth, U., Samyn, D., Schwander, J., Shoji, H., Siggard-Andersen, M.-L., Steffensen, J. P., Stocker, T., Sveinbjörnsdóttir, A. E., Svensson, A., Takata, M., Tison, J.-L., Thorsteinsson, T., Watanabe, O., Wilhelms, F., and White, J. W. C.: High-resolution record of Northern Hemisphere climate extending into the last interglacial period, Nature, 431, 147–151, 2004.

Annan, J. D. and Hargreaves, J. C.: A new global reconstruction of temperature changes at the Last Glacial Maximum, Clim. Past, 9, 367–376, https://doi.org/10.5194/cp-9-367-2013, 2013.

Argus, D. F., Peltier, W. R., Drummond, R., and Moore, A. W.: The Antarctica component of postglacial rebound model ICE-6G_C (VM5a) based on GPS positioning, exposure age dating of ice thicknesses, and relative sea level histories, Geophys. J. Int., 198, 537–563, https://doi.org/10.1093/gji/ggu140, 2014.

Bamber, J. L., Siegert, M. J., Griggs, J. A., Marshall, S. J., and Spada, G.: Paleofluvial Mega-Canyon Beneath the Central Greenland Ice Sheet, Science, 341, 997–999, https://doi.org/10.1126/science.1239794, 2013.

Beckmann, A. and Goosse, H.: A parameterization of ice shelf–ocean interaction for climate models, Ocean Model., 5, 157–170, https://doi.org/10.1016/S1463-5003(02)00019-7, 2003.

Berger, A.: Long-Term Variations of Daily Insolation and Quaternary Climatic Changes, J. Atmos. Sci., 35, 2362–2367, https://doi.org/10.1175/1520-0469(1978)035<2362:LTVODI>2.0.CO;2, 1978.

Bethke, I., Li, C., and Nisancioglu, K. H.: Can we use ice sheet reconstructions to constrain meltwater for deglacial simulations?, Paleoceanography, 27, PA2205, https://doi.org/10.1029/2011PA002258, 2012.

Bonelli, S., Charbit, S., Kageyama, M., Woillez, M.-N., Ramstein, G., Dumas, C., and Quiquet, A.: Investigating the evolution of major Northern Hemisphere ice sheets during the last glacial-interglacial cycle, Clim. Past, 5, 329–345, https://doi.org/10.5194/cp-5-329-2009, 2009.

Bouttes, N., Paillard, D., and Roche, D. M.: Impact of brine-induced stratification on the glacial carbon cycle, Clim. Past, 6, 575–589, https://doi.org/10.5194/cp-6-575-2010, 2010.

Bouttes, N., Swingedouw, D., Roche, D. M., Sanchez-Goni, M. F., and Crosta, X.: Response of the carbon cycle in an intermediate complexity model to the different climate configurations of the last nine interglacials, Clim. Past, 14, 239–253, https://doi.org/10.5194/cp-14-239-2018, 2018.

Brendryen, J., Haflidason, H., Yokoyama, Y., Haaga, K. A., and Hannisdal, B.: Eurasian Ice Sheet collapse was a major source of Meltwater Pulse 1A 14,600 years ago, Nat. Geosci., 13, 363–368, https://doi.org/10.1038/s41561-020-0567-4, 2020.

Briggs, R. D., Pollard, D., and Tarasov, L.: A data-constrained large ensemble analysis of Antarctic evolution since the Eemian, Quaternary Sci. Rev., 103, 91–115, https://doi.org/10.1016/j.quascirev.2014.09.003, 2014.

Brovkin, V., Ganopolski, A., and Svirezhev, Y.: A continuous climate-vegetation classification for use in climate-biosphere studies, Ecol. Model., 101, 251–261, https://doi.org/10.1016/S0304-3800(97)00049-5, 1997.

Bueler, E. and Brown, J.: Shallow shelf approximation as a "sliding law" in a thermomechanically coupled ice sheet model, J. Geophys. Res., 114, F03008, https://doi.org/10.1029/2008JF001179, 2009.

Buizert, C., Gkinis, V., Severinghaus, J. P., He, F., Lecavalier, B. S., Kindler, P., Leuenberger, M., Carlson, A. E., Vinther, B., Masson-Delmotte, V., White, J. W. C., Liu, Z., Otto-Bliesner, B., and Brook, E. J.: Greenland temperature response to climate forcing during the last deglaciation, Science, 345, 1177–1180, https://doi.org/10.1126/science.1254961, 2014.

Bügelmayer, M., Roche, D. M., and Renssen, H.: Representing icebergs in the *i*LOVECLIM model (version 1.0) – a sensitivity study, Geosci. Model Dev., 8, 2139–2151, https://doi.org/10.5194/gmd-8-2139-2015, 2015.

Caley, T., Roche, D. M., and Renssen, H.: Orbital Asian summer monsoon dynamics revealed using an isotope-enabled global climate model, Nat. Commun., 5, 5371, https://doi.org/10.1038/ncomms6371, 2014.

Calov, R., Ganopolski, A., Claussen, M., Petoukhov, V., and Greve, R.: Transient simulation of the last glacial inception. Part I: glacial inception as a bifurcation in the climate system, Clim. Dynam., 24, 545–561, https://doi.org/10.1007/s00382-005-0007-6, 2005.

Charbit, S., Kageyama, M., Roche, D., Ritz, C., and Ramstein, G.: Investigating the mechanisms leading to the deglaciation of past continental northern hemisphere ice sheets with the CLIMBER–GREMLINS coupled model, Global Planet. Change, 48, 253–273, https://doi.org/10.1016/j.gloplacha.2005.01.002, 2005.

Choudhury, D., Timmermann, A., Schloesser, F., Heinemann, M., and Pollard, D.: Simulating Marine Isotope Stage 7 with a coupled climate–ice sheet model, Clim. Past, 16, 2183–2201, https://doi.org/10.5194/cp-16-2183-2020, 2020.

Clark, P. U., He, F., Golledge, N. R., Mitrovica, J. X., Dutton, A., Hoffman, J. S., and Dendy, S.: Oceanic forcing of penultimate deglacial and last interglacial sea-level rise, Nature, 577, 660–664, https://doi.org/10.1038/s41586-020-1931-7, 2020.

Curry, W. B. and Oppo, D. W.: Glacial water mass geometry and the distribution of $\delta^{13}C$ of ΣCO_2 in the western Atlantic Ocean, Paleoceanography, 20, PA1017, https://doi.org/10.1029/2004PA001021, 2005.

Dalton, A. S., Margold, M., Stokes, C. R., Tarasov, L., Dyke, A. S., Adams, R. S., Allard, S., Arends, H. E., Atkinson, N., Attig, J. W., Barnett, P. J., Barnett, R. L., Batterson, M., Bernatchez, P., Borns, H. W., Breckenridge, A., Briner, J. P., Brouard, E., Campbell, J. E., Carlson, A. E., Clague, J. J., Curry, B. B., Daigneault, R.-A., Dubé-Loubert, H., Easterbrook, D. J., Franzi, D. A., Friedrich, H. G., Funder, S., Gauthier, M. S., Gowan, A. S., Harris, K. L., Hétu, B., Hooyer, T. S., Jennings, C. E., Johnson, M. D., Kehew, A. E., Kelley, S. E., Kerr, D., King, E. L., Kjeldsen, K. K., Knaeble, A. R., Lajeunesse, P., Lakeman, T. R., Lamothe, M., Larson, P., Lavoie, M., Loope, H. M., Lowell, T. V., Lusardi, B. A., Manz, L., McMartin, I., Nixon, F. C., Occhietti, S., Parkhill, M. A., Piper, D. J. W., Pronk, A. G., Richard, P. J. H., Ridge, J. C., Ross, M., Roy, M., Seaman, A., Shaw, J., Stea, R. R., Teller, J. T., Thompson, W. B., Thorleifson, L. H., Utting, D. J., Veillette, J. J., Ward, B. C., Weddle, T. K., and Wright, H. E.: An updated radiocarbon-based ice margin chronology for the last deglaciation of the North American Ice Sheet Complex, Quaternary Sci. Rev., 234, 106223, https://doi.org/10.1016/j.quascirev.2020.106223, 2020.

Dee, D. P., Uppala, S. M., Simmons, A. J., Berrisford, P., Poli, P., Kobayashi, S., Andrae, U., Balmaseda, M. A., Balsamo, G., Bauer, P., Bechtold, P., Beljaars, A. C. M., van de Berg, L., Bidlot, J., Bormann, N., Delsol, C., Dragani, R., Fuentes, M., Geer, A. J., Haimberger, L., Healy, S. B., Hersbach, H., Hólm, E. V., Isaksen, L., Kållberg, P., Köhler, M., Matricardi, M., McNally, A. P., Monge-Sanz, B. M., Morcrette, J.-J., Park, B.-K., Peubey, C., de Rosnay, P., Tavolato, C., Thépaut, J.-N., and Vitart, F.: The ERA-Interim reanalysis: configuration and performance of the data assimilation system, Q. J. Roy. Meteor. Soc., 137, 553–597, https://doi.org/10.1002/qj.828, 2011.

Deschamps, P., Durand, N., Bard, E., Hamelin, B., Camoin, G., Thomas, A. L., Henderson, G. M., Okuno, J., and Yokoyama, Y.: Ice-sheet collapse and sea-level rise at the Bølling warming 14,600 years ago, Nature, 483, 559–564, https://doi.org/10.1038/nature10902, 2012.

Favier, L., Jourdain, N. C., Jenkins, A., Merino, N., Durand, G., Gagliardini, O., Gillet-Chaulet, F., and Mathiot, P.: Assessment of sub-shelf melting parameterisations using the ocean–ice-sheet coupled model NEMO(v3.6)–Elmer/Ice(v8.3) , Geosci. Model Dev., 12, 2255–2283, https://doi.org/10.5194/gmd-12-2255-2019, 2019.

Fyke, J. G., Weaver, A. J., Pollard, D., Eby, M., Carter, L., and Mackintosh, A.: A new coupled ice sheet/climate model: description and sensitivity to model physics under Eemian, Last Glacial Maximum, late Holocene and modern climate conditions, Geosci. Model Dev., 4, 117–136, https://doi.org/10.5194/gmd-4-117-2011, 2011.

Ganopolski, A. and Brovkin, V.: Simulation of climate, ice sheets and CO_2 evolution during the last four glacial cycles with an Earth system model of intermediate complexity, Clim. Past, 13, 1695–1716, https://doi.org/10.5194/cp-13-1695-2017, 2017.

Goosse, H. and Fichefet, T.: Importance of ice-ocean interactions for the global ocean circulation: A model study, J. Geophys. Res., 104, 23337–23355, https://doi.org/10.1029/1999JC900215, 1999.

Goosse, H., Brovkin, V., Fichefet, T., Haarsma, R., Huybrechts, P., Jongma, J., Mouchet, A., Selten, F., Barriat, P.-Y., Campin, J.-M., Deleersnijder, E., Driesschaert, E., Goelzer, H., Janssens, I., Loutre, M.-F., Morales Maqueda, M. A., Opsteegh, T., Mathieu, P.-P., Munhoven, G., Pettersson, E. J., Renssen, H., Roche, D. M., Schaeffer, M., Tartinville, B., Timmermann, A., and Weber, S. L.: Description of the Earth system model of intermediate complexity LOVECLIM version 1.2, Geosci. Model Dev., 3, 603–633, https://doi.org/10.5194/gmd-3-603-2010, 2010.

Gregoire, L. J., Otto-Bliesner, B., Valdes, P. J., and Ivanovic, R.: Abrupt Bølling warming and ice saddle collapse contributions to the Meltwater Pulse 1a rapid sea level rise, Geophys. Res. Lett., 43, 9130–9137, https://doi.org/10.1002/2016GL070356, 2016.

Gregory, J. M., Browne, O. J. H., Payne, A. J., Ridley, J. K., and Rutt, I. C.: Modelling large-scale ice-sheet–climate interactions following glacial inception, Clim. Past, 8, 1565–1580, https://doi.org/10.5194/cp-8-1565-2012, 2012.

Haarsma, R. J., Selten, F. M., Opsteegh, J. D., Lenterink, G., and Liu, Q.: ECBILT: A coupled atmosphere ocean sea-ice model for climate predictability studies, KNMI technical report TR-195, De Bilt, The Netherlands, 1997.

Harrison, S., Smith, D. E., and Glasser, N. F.: Late Quaternary meltwater pulses and sea level change, J. Quaternary Sci., 34, 1–15, https://doi.org/10.1002/jqs.3070, 2019.

He, F., Shakun, J. D., Clark, P. U., Carlson, A. E., Liu, Z., Otto-Bliesner, B. L., and Kutzbach, J. E.: Northern Hemisphere forcing of Southern Hemisphere climate during the last deglaciation, Nature, 494, 81–85, https://doi.org/10.1038/nature11822, 2013.

Heinemann, M., Timmermann, A., Elison Timm, O., Saito, F., and Abe-Ouchi, A.: Deglacial ice sheet meltdown: orbital pacemaking and CO_2 effects, Clim. Past, 10, 1567–1579, https://doi.org/10.5194/cp-10-1567-2014, 2014.

Hughes, A. L. C., Gyllencreutz, R., Lohne, Ø. S., Mangerud, J., and Svendsen, J. I.: The last Eurasian ice sheets – a chronological database and time-slice reconstruction, DATED-1, Boreas, 45, 1–45, https://doi.org/10.1111/bor.12142, 2016.

Husson, L., Bodin, T., Spada, G., Choblet, G., and Kreemer, C.: Bayesian surface reconstruction of geodetic uplift rates: Mapping the global fingerprint of Glacial Isostatic Adjustment, J. Geodyn., 122, 25–40, https://doi.org/10.1016/j.jog.2018.10.002, 2018.

Huybrechts, P., Goelzer, H., Janssens, I., Driesschaert, E., Fichefet, T., Goosse, H., and Loutre, M.-F.: Response of the Greenland and Antarctic Ice Sheets to Multi-Millennial Greenhouse Warming in the Earth System Model of Intermediate Complexity LOVECLIM, Surv. Geophys., 32, 397–416, https://doi.org/10.1007/s10712-011-9131-5, 2011.

Jackson, C. S. and Broccoli, A. J.: Orbital forcing of Arctic climate: mechanisms of climate response and implications for continental glaciation, Clim. Dynam., 21, 539–557, https://doi.org/10.1007/s00382-003-0351-3, 2003.

Johnsen, S. J., Clausen, H. B., Dansgaard, W., Gundestrup, N. S., Hammer, C. U., Andersen, U., Andersen, K. K., Hvidberg, C. S., Dahl-Jensen, D., Steffensen, J. P., Shoji, H., Sveinbjörnsdóttir, A. E., White, J., Jouzel, J., and Fisher, D.: The $\delta^{18}O$ record along the Greenland Ice Core Project deep ice core and the problem of possible Eemian climatic instability, J. Geophys. Res., 102, 26397–26410, https://doi.org/10.1029/97JC00167, 1997.

Kageyama, M., Harrison, S. P., Kapsch, M.-L., Lofverstrom, M., Lora, J. M., Mikolajewicz, U., Sherriff-Tadano, S., Vadsaria, T., Abe-Ouchi, A., Bouttes, N., Chandan, D., Gregoire, L. J., Ivanovic, R. F., Izumi, K., LeGrande, A. N., Lhardy, F., Lohmann, G., Morozova, P. A., Ohgaito, R., Paul, A., Peltier, W. R., Poulsen, C. J., Quiquet, A., Roche, D. M., Shi, X., Tierney, J. E., Valdes, P. J., Volodin, E., and Zhu, J.: The PMIP4 Last Glacial Maximum experiments: preliminary results and comparison with the PMIP3 simulations, Clim. Past, 17, 1065-1089, https://doi.org/10.5194/cp-17-1065-2021, 2021.

Lambeck, K., Rouby, H., Purcell, A., Sun, Y., and Sambridge, M.: Sea level and global ice volumes from the Last Glacial Maximum to the Holocene, P. Natl. Acad. Sci. USA, 111, 15296–15303, https://doi.org/10.1073/pnas.1411762111, 2014.

Laske, G. and Masters, G.: A Global Digital Map of Sediment Thickness, EOS T. Am. Geophys. Un., 78, F483, 1997.

Lecavalier, B. S., Milne, G. A., Simpson, M. J. R., Wake, L., Huybrechts, P., Tarasov, L., Kjeldsen, K. K., Funder, S., Long, A. J., Woodroffe, S., Dyke, A. S., and Larsen, N. K.: A model of Greenland ice sheet deglaciation constrained by observations of relative sea level and ice extent, Quaternary Sci. Rev., 102, 54–84, https://doi.org/10.1016/j.quascirev.2014.07.018, 2014.

Le Meur, E. and Huybrechts, P.: A comparison of different ways of dealing with isostasy: examples from modeling the Antarctic ice sheet during the last glacial cycle, Ann. Glaciol., 23, 309–317, https://doi.org/10.3189/S0260305500013586, 1996.

Lhardy, F., Bouttes, N., Roche, D. M., Crosta, X., Waelbroeck, C., and Paillard, D.: Impact of Southern Ocean surface conditions on deep ocean circulation during the LGM: a model analysis, Clim. Past, 17, 1139–1159, https://doi.org/10.5194/cp-17-1139-2021, 2021.

Liu, J., Milne, G. A., Kopp, R. E., Clark, P. U., and Shennan, I.: Sea-level constraints on the amplitude and source distribution of Meltwater Pulse 1A, Nat. Geosci., 9, 130–134, https://doi.org/10.1038/ngeo2616, 2016.

Liu, Z., Otto-Bliesner, B. L., He, F., Brady, E. C., Tomas, R., Clark, P. U., Carlson, A. E., Lynch-Stieglitz, J., Curry, W., Brook, E., Erickson, D., Jacob, R., Kutzbach, J., and Cheng, J.: Transient Simulation of Last Deglaciation with a New Mechanism for Bølling-Allerød Warming, Science, 325, 310–314, https://doi.org/10.1126/science.1171041, 2009.

Lüthi, D., Le Floch, M., Bereiter, B., Blunier, T., Barnola, J.-M., Siegenthaler, U., Raynaud, D., Jouzel, J., Fischer, H., Kawamura, K., and Stocker, T. F.: High-resolution carbon dioxide concentration record 650,000–800,000 years before present, Nature, 453, 379–382, https://doi.org/10.1038/nature06949, 2008.

McManus, J. F., Francois, R., Gherardi, J.-M., Keigwin, L. D., and Brown-Leger, S.: Collapse and rapid resumption of Atlantic meridional circulation linked to deglacial climate changes, Nature, 428, 834–837, https://doi.org/10.1038/nature02494, 2004.

Menviel, L., Timmermann, A., Timm, O. E., and Mouchet, A.: Deconstructing the Last Glacial termination: the role of millennial and orbital-scale forcings, Quaternary Sci. Rev., 30, 1155–1172, https://doi.org/10.1016/j.quascirev.2011.02.005, 2011.

Ng, H. C., Robinson, L. F., McManus, J. F., Mohamed, K. J., Jacobel, A. W., Ivanovic, R. F., Gregoire, L. J., and Chen, T.: Coherent deglacial changes in western Atlantic Ocean circulation, Nat. Commun., 9, 2947, https://doi.org/10.1038/s41467-018-05312-3, 2018.

Obase, T. and Abe-Ouchi, A.: Abrupt Bølling-Allerød Warming Simulated under Gradual Forcing of the Last Deglaciation, Geophys. Res. Lett., 46, 11397–11405, https://doi.org/10.1029/2019GL084675, 2019.

Opsteegh, J. D., Haarsma, R. J., Selten, F. M., and Kattenberg, A.: ECBILT: a dynamic alternative to mixed boundary conditions in ocean models, Tellus A, 50, 348–367, https://doi.org/10.3402/tellusa.v50i3.14524, 1998.

Peltier, W.: Global glacial isostasy and the surface of the ice-age earth: The ICE-5G (VM2) model and GRACE, Annu. Rev. Earth Pl. Sc., 32, 111–149, https://doi.org/10.1146/annurev.earth.32.082503.144359, 2004.

Peltier, W. R., Argus, D. F., and Drummond, R.: Space geodesy constrains ice age terminal deglaciation: The global ICE-6G_C (VM5a) model, J. Geophys. Res.-Sol. Ea., 120, 450–487, https://doi.org/10.1002/2014JB011176, 2015.

Petrini, M., Colleoni, F., Kirchner, N., Hughes, A. L. C., Camerlenghi, A., Rebesco, M., Lucchi, R. G., Forte, E., Colucci, R. R., and Noormets, R.: Interplay of grounding-line dynamics and sub-shelf melting during retreat of the Bjørnøyrenna Ice Stream, Scientific Reports, 8, 7196, https://doi.org/10.1038/s41598-018-25664-6, 2018.

Pollard, D.: A simple parameterization for ice sheet ablation rate, Tellus, 32, 384–388, https://doi.org/10.3402/tellusa.v32i4.10593, 1980.

Quiquet, A., Dumas, C., Ritz, C., Peyaud, V., and Roche, D. M.: The GRISLI ice sheet model (version 2.0): calibration and validation for multi-millennial changes of the Antarctic ice sheet, Geosci. Model Dev., 11, 5003–5025, https://doi.org/10.5194/gmd-11-5003-2018, 2018a.

Quiquet, A., Roche, D. M., Dumas, C., and Paillard, D.: Online dynamical downscaling of temperature and precipitation within the iLOVECLIM model (version 1.1), Geosci. Model Dev., 11, 453–466, https://doi.org/10.5194/gmd-11-453-2018, 2018b.

Quiquet, A., Dumas, C., Paillard, D., Ramstein, G., Ritz, C., and Roche, D. M.: Deglacial Ice Sheet Instabilities Induced by Proglacial Lakes, Geophys. Res. Lett., 48, e2020GL092141, https://doi.org/10.1029/2020GL092141, 2021a.

Quiquet, A., Roche, D. M., Dumas, C., Bouttes, N., and Lhardy, F.: Dataset for "Climate and ice sheet evolutions from the last glacial maximum to the pre-industrial period with an ice sheet – climate coupled model", Zenodo [data set], https://doi.org/10.5281/zenodo.5336280, 2021b.

Reeh, N.: Parameterization of Melt Rate and Surface Temperature on the Greenland Ice Sheet, Polarforschung, 59, 113–128, 1989.

Ritz, C., Rommelaere, V., and Dumas, C.: Modeling the evolution of Antarctic ice sheet over the last 420,000 years: Implications for altitude changes in the Vostok region, J. Geophys. Res., 106, 31943–31964, https://doi.org/10.1029/2001JD900232, 2001.

Roberts, W. H. G., Valdes, P. J., and Payne, A. J.: Topography's crucial role in Heinrich Events, P. Natl. Acad. Sci. USA, 111, 16688–16693, https://doi.org/10.1073/pnas.1414882111, 2014.

Robinson, A., Calov, R., and Ganopolski, A.: An efficient regional energy-moisture balance model for simulation of the Greenland Ice Sheet response to climate change, The Cryosphere, 4, 129–144, https://doi.org/10.5194/tc-4-129-2010, 2010.

Roche, D. M., Wiersma, A. P., and Renssen, H.: A systematic study of the impact of freshwater pulses with respect to dif-

ferent geographical locations, Clim. Dynam., 34, 997–1013, https://doi.org/10.1007/s00382-009-0578-8, 2010.

Roche, D. M., Dumas, C., Bügelmayer, M., Charbit, S., and Ritz, C.: Adding a dynamical cryosphere to iLOVECLIM (version 1.0): coupling with the GRISLI ice-sheet model, Geosci. Model Dev., 7, 1377–1394, https://doi.org/10.5194/gmd-7-1377-2014, 2014a.

Roche, D. M., Paillard, D., Caley, T., and Waelbroeck, C.: LGM hosing approach to Heinrich Event 1: results and perspectives from data–model integration using water isotopes, Quaternary Sci. Rev., 106, 247–261, https://doi.org/10.1016/j.quascirev.2014.07.020, 2014b.

Schoof, C.: Ice sheet grounding line dynamics: Steady states, stability, and hysteresis, J. Geophys. Res., 112, F03S28, https://doi.org/10.1029/2006JF000664, 2007.

Seroussi, H., Nowicki, S., Payne, A. J., Goelzer, H., Lipscomb, W. H., Abe-Ouchi, A., Agosta, C., Albrecht, T., Asay-Davis, X., Barthel, A., Calov, R., Cullather, R., Dumas, C., Galton-Fenzi, B. K., Gladstone, R., Golledge, N. R., Gregory, J. M., Greve, R., Hattermann, T., Hoffman, M. J., Humbert, A., Huybrechts, P., Jourdain, N. C., Kleiner, T., Larour, E., Leguy, G. R., Lowry, D. P., Little, C. M., Morlighem, M., Pattyn, F., Pelle, T., Price, S. F., Quiquet, A., Reese, R., Schlegel, N.-J., Shepherd, A., Simon, E., Smith, R. S., Straneo, F., Sun, S., Trusel, L. D., Van Breedam, J., van de Wal, R. S. W., Winkelmann, R., Zhao, C., Zhang, T., and Zwinger, T.: ISMIP6 Antarctica: a multi-model ensemble of the Antarctic ice sheet evolution over the 21st century, The Cryosphere, 14, 3033–3070, https://doi.org/10.5194/tc-14-3033-2020, 2020.

Severinghaus, J. P. and Brook, E. J.: Abrupt Climate Change at the End of the Last Glacial Period Inferred from Trapped Air in Polar Ice, Science, 286, 930–934, https://doi.org/10.1126/science.286.5441.930, 1999.

Shakun, J. D., Clark, P. U., He, F., Marcott, S. A., Mix, A. C., Liu, Z., Otto-Bliesner, B., Schmittner, A., and Bard, E.: Global warming preceded by increasing carbon dioxide concentrations during the last deglaciation, Nature, 484, 49–54, https://doi.org/10.1038/nature10915, 2012.

Simms, A. R., Lisiecki, L., Gebbie, G., Whitehouse, P. L., and Clark, J. F.: Balancing the last glacial maximum (LGM) sea-level budget, Quaternary Sci. Rev., 205, 143–153, https://doi.org/10.1016/j.quascirev.2018.12.018, 2019.

Tarasov, L. and Peltier, W. R.: Greenland glacial history and local geodynamic consequences, Geophys. J. Int., 150, 198–229, https://doi.org/10.1046/j.1365-246X.2002.01702.x, 2002.

Tarasov, L., Dyke, A. S., Neal, R. M., and Peltier, W. R.: A data-calibrated distribution of deglacial chronologies for the North American ice complex from glaciological modeling, Earth Planet. Sc. Lett., 315–316, 30–40, https://doi.org/10.1016/j.epsl.2011.09.010, 2012.

Tierney, J. E., Zhu, J., King, J., Malevich, S. B., Hakim, G. J., and Poulsen, C. J.: Glacial cooling and climate sensitivity revisited, Nature, 584, 569–573, https://doi.org/10.1038/s41586-020-2617-x, 2020.

Tsai, V. C., Stewart, A. L., and Thompson, A. F.: Marine ice-sheet profiles and stability under Coulomb basal conditions, J. Glaciol., 61, 205–215, https://doi.org/10.3189/2015JoG14J221, 2015.

van den Berg, J., van de Wal, R., and Oerlemans, H.: A mass balance model for the Eurasian Ice Sheet for the last 120,000 years, Global Planet. Change, 61, 194–208, https://doi.org/10.1016/j.gloplacha.2007.08.015, 2008.

Vinther, B. M., Buchardt, S. L., Clausen, H. B., Dahl-Jensen, D., Johnsen, S. J., Fisher, D. A., Koerner, R. M., Raynaud, D., Lipenkov, V., Andersen, K. K., Blunier, T., Rasmussen, S. O., Steffensen, J. P., and Svensson, A. M.: Holocene thinning of the Greenland ice sheet, Nature, 461, 385–388, https://doi.org/10.1038/nature08355, 2009.

Vizcaíno, M., Mikolajewicz, U., Gröger, M., Maier-Reimer, E., Schurgers, G., and Winguth, A. M. E.: Long-term ice sheet–climate interactions under anthropogenic greenhouse forcing simulated with a complex Earth System Model, Clim. Dynam., 31, 665–690, https://doi.org/10.1007/s00382-008-0369-7, 2008.

Waelbroeck, C., Labeyrie, L., Michel, E., Duplessy, J. C., McManus, J. F., Lambeck, K., Balbon, E., and Labracherie, M.: Sea-level and deep water temperature changes derived from benthic foraminifera isotopic records, Quaternary Sci. Rev., 21, 295–305, https://doi.org/10.1016/S0277-3791(01)00101-9, 2002.

Waelbroeck, C., Lougheed, B. C., Riveiros, N. V., Missiaen, L., Pedro, J., Dokken, T., Hajdas, I., Wacker, L., Abbott, P., Dumoulin, J.-P., Thil, F., Eynaud, F., Rossignol, L., Fersi, W., Albuquerque, A. L., Arz, H., Austin, W. E. N., Came, R., Carlson, A. E., Collins, J. A., Dennielou, B., Desprat, S., Dickson, A., Elliot, M., Farmer, C., Giraudeau, J., Gottschalk, J., Henderiks, J., Hughen, K., Jung, S., Knutz, P., Lebreiro, S., Lund, D. C., Lynch-Stieglitz, J., Malaizé, B., Marchitto, T., Martínez-Méndez, G., Mollenhauer, G., Naughton, F., Nave, S., Nürnberg, D., Oppo, D., Peck, V., Peeters, F. J. C., Penaud, A., Portilho-Ramos, R. d. C., Repschläger, J., Roberts, J., Rühlemann, C., Salgueiro, E., Goni, M. F. S., Schönfeld, J., Scussolini, P., Skinner, L. C., Skonieczny, C., Thornalley, D., Toucanne, S., Rooij, D. V., Vidal, L., Voelker, A. H. L., Wary, M., Weldeab, S., and Ziegler, M.: Consistently dated Atlantic sediment cores over the last 40 thousand years, Scientific Data, 6, 165, https://doi.org/10.1038/s41597-019-0173-8, 2019.

Whitehouse, P. L., Bentley, M. J., and Le Brocq, A. M.: A deglacial model for Antarctica: geological constraints and glaciological modelling as a basis for a new model of Antarctic glacial isostatic adjustment, Quaternary Sci. Rev., 32, 1–24, https://doi.org/10.1016/j.quascirev.2011.11.016, 2012.

Willeit, M., Ganopolski, A., Calov, R., and Brovkin, V.: Mid-Pleistocene transition in glacial cycles explained by declining CO_2 and regolith removal, Science Advances, 5, eaav7337, https://doi.org/10.1126/sciadv.aav7337, 2019.

Winkelmann, R., Martin, M. A., Haseloff, M., Albrecht, T., Bueler, E., Khroulev, C., and Levermann, A.: The Potsdam Parallel Ice Sheet Model (PISM-PIK) – Part 1: Model description, The Cryosphere, 5, 715–726, https://doi.org/10.5194/tc-5-715-2011, 2011.

Ziemen, F. A., Kapsch, M.-L., Klockmann, M., and Mikolajewicz, U.: Heinrich events show two-stage climate response in transient glacial simulations, Clim. Past, 15, 153–168, https://doi.org/10.5194/cp-15-153-2019, 2019.

Bibliography

A. Abe-Ouchi, F. Saito, M. Kageyama, P. Braconnot, S. P. Harrison, K. Lambeck, B. L. Otto-Bliesner, W. R. Peltier, L. Tarasov, J.-Y. Peterschmitt, and K. Takahashi. Ice-sheet configuration in the CMIP5/PMIP3 Last Glacial Maximum experiments. *Geosci. Model Dev.*, 8:3621–3637, 2015. doi: 10.5194/gmd-8-3621-2015.

A. Abelmann, R. Gersonde, G. Knorr, X. Zhang, B. Chapligin, E. Maier, O. Esper, H. Friedrichsen, G. Lohmann, H. Meyer, and R. Tiedemann. The seasonal sea-ice zone in the glacial Southern Ocean as a carbon sink. *Nature Communications*, 6, 2015. doi: 10.1038/ncomms9136.

J. F. Adkins. The role of deep ocean circulation in setting glacial climates. *Paleoceanography*, 28:539–561, 2013. doi: 10.1002/palo.20046.

J. F. Adkins, K. McIntyre, and D. P. Schrag. The salinity, temperature, and δ^{18}O of the glacial deep ocean. *Science*, 298(5599):1769–1773, 2002. doi: 10.1126/science.1076252.

C. S. Allen, J. Pike, and C. J. Pudsey. Last glacial-interglacial sea-ice cover in the SW Atlantic and its potential role in global deglaciation. *Quat. Sci. Rev.*, 30:2446–2458, 2011. doi: 10.1016/j.quascirev.2011.04.002.

C. Amante and B. W. Eakins. *ETOPO1 1 Arc-Minute Global Relief Model: Procedures, Data Sources and Analysis. NOAA Technical Memorandum NESDIS NGDC-24. National Geophysical Data Center, NOAA*, 2009.

J. D. Annan and J. C. Hargreaves. A new global reconstruction of temperature changes at the Last Glacial Maximum. *Clim. Past*, 9:367–376, 2013. doi: 10.5194/cp-9-367-2013.

J. I. Antonov, D. Seidov, T. P. Boyer, R. A. Locarnini, A. V. Mishonov, H. E. Garcia, O. K. Baranova, M. M. Zweng, and D. R. Johnson. *World Ocean Atlas 2009, Volume 2: Salinity.* Levitus, S., NOAA Atlas NESDIS 69, US Government Printing Office, Washington, D.C., 2010.

D. F. Argus, W. R. Peltier, R. Drummond, and A. W. Moore. The Antarctica component of postglacial rebound model ICE-6G-C (VM5a) based on GPS positioning, exposure age dating of ice thicknesses, and relative sea level histories. *Geophys. J. Int.*, 198:537–563, 2014. doi: 10.1093/gji/ggu140.

J. A. Baker, A. J. Watson, and G. K. Vallis. Meridional Overturning Circulation in a Multibasin Model. Part I: Dependence on Southern Ocean Buoyancy Forcing. *Journal of Physical Oceanography*, 50(5):1159–1178, 2020. doi: 10.1175/JPO-D-19-0135.1.

J. A. Baker, A. J. Watson, and G. K. Vallis. Meridional Overturning Circulation in a Multibasin Model. Part II: Sensitivity to Diffusivity and Wind in Warm and Cool Climates. *Journal of Physical Oceanography*, 51 (6):1813–1828, 2021. doi: 10.1175/JPO-D-20-0121.1.

A. Barthélemy, T. Fichefet, H. Goosse, and G. Madec. Modeling the interplay between sea ice formation and the oceanic mixed layer: Limitations of simple brine rejection parameterizations. *Ocean Modelling*, 86:141–152, 2015. doi: 10.1016/j.ocemod.2014.12.009.

R. L. Beadling, J. L. Russell, R. J. Stouffer, M. Mazloff, L. D. Talley, P. J. Goodman, J.-B. Sallée, H. T. Hewitt, P. Hyder, and A. Pandde. Representation of Southern Ocean Properties across Coupled Model Intercomparison Project Generations: CMIP3 to CMIP6. *Journal of Climate*, 33(15):6555–6581, 2020. doi: 10.1175/JCLI-D-19-0970.1.

E. Behrens, G. Rickard, O. Morgenstern, T. Martin, A. Osprey, and M. Joshi. Southern Ocean deep convection in global climate models: A driver for variability of subpolar gyres and Drake Passage transport on decadal timescales. *J. Geophys. Res.-Oceans*, 121:3905–3925, 2016. doi: 10.1002/2015JC011286.

F. Beny, V. Bout-Roumazeilles, G. R. Davies, C. Waelbroeck, A. Bory, N. Tribovillard, M. Delattre, and R. Abraham. Radiogenic isotopic and clay mineralogical signatures of terrigenous particles as water-mass tracers: New insights into South Atlantic deep circulation during the last termination. *Quaternary Science Reviews*, 228, 2020. doi: 10.1016/j.quascirev.2019.106089.

V. Benz, O. Esper, R. Gersonde, F. Lamy, and R. Tiedemann. Last Glacial Maximum sea surface temperature and sea-ice extent in the Pacific sector of the Southern Ocean. *Quat. Sci. Rev.*, 146:216–237, 2016. doi: 10.1016/j.quascirev.2016.06.006.

B. Bereiter, S. Eggleston, J. Schmitt, C. Nehrbass-Ahles, T. F. Stocker, H. Fischer, S. Kipfstuhl, and J. Chappellaz. Revision of the EPICA Dome C CO_2 record from 800 to 600 kyr before present. *Geophys. Res. Lett.*, 42:542–549, 2015. doi: 10.1002/2014GL061957.

C. J. Berends, B. de Boer, and R. S. W. van de Wal. Reconstructing the evolution of ice sheets, sea level, and atmospheric CO_2 during the past 3.6 million years. *Clim. Past*, 17:361–377, 2021. doi: 10.5194/cp-17-361-2021.

A. Berger. Long-term variations of daily insolation and quaternary climatic changes. *J. Atmos. Sci.*, 35: 2362–2367, 1978. doi: 10.1175/1520-0469(1978)035<2362:LTVODI>2.0.CO;2.

L. Bopp, K. E. Kohfeld, and C. Le Quéré. Dust impact on marine biota and atmospheric CO_2 during glacial periods. *Paleoceanography*, 18(2), 2003. doi: 10.1029/2002PA000810.

N. Bouttes, D. Paillard, and D. M. Roche. Impact of brine-induced stratification on the glacial carbon cycle. *Clim. Past*, 6(5):575–589, 2010. doi: 10.5194/cp-6-575-2010.

N. Bouttes, D. Paillard, D. M. Roche, V. Brovkin, and L. Bopp. Last Glacial Maximum CO_2 and $\delta^{13}C$ successfully reconciled. *Geophys. Res. Lett.*, 38, 2011. doi: 10.1029/2010GL044499.

N. Bouttes, D. M. Roche, V. Mariotti, and L. Bopp. Including an ocean carbon cycle model into iLOVECLIM (v1.0). *Geoscientific Model Development*, 8:1563–1576, 2015. doi: 10.5194/gmd-8-1563-2015.

T. J. Bracegirdle, F. Colleoni, N. J. Abram, N. A. N. Bertler, D. A. Dixon, M. England, V. Favier, C. J. Fogwill, J. C. Fyfe, I. Goodwin, H. Goosse, W. Hobbs, J. M. Jones, E. D. Keller, A. L. Khan, S. J. Phipps, M. N. Raphael, J. Russell, L. Sime, E. R. Thomas, M. R. van den Broeke, and I. Wainer. Back to the future : using long-term observational and paleo-proxy reconstructions to improve model projections of Antarctic climate. *Geosciences*, 9(6), 2019. doi: 10.3390/geosciences9060255.

P. Braconnot, B. Otto-Bliesner, S. Harrison, S. Joussaume, J.-Y. Peterchmitt, A. Abe-Ouchi, M. Crucifix, E. Driesschaert, T. Fichefet, C. D. Hewitt, M. Kageyama, A. Kitoh, A. Laîné, M.-F. Loutre, O. Marti, U. Merkel, G. Ramstein, P. Valdes, S. L. Weber, Y. Yu, and Y. Zhao. Results of PMIP2 coupled simulations of the Mid-Holocene and Last Glacial Maximum – Part 1: experiments and large-scale features. *Clim. Past*, 3:261–277, 2007. doi: 10.5194/cp-3-261-2007.

P. Braconnot, S. P. Harrison, M. Kageyama, P. J. Bartlein, V. Masson-Delmotte, A. Abe-Ouchi, B. Otto-Bliesner, and Y. Zhao. Evaluation of climate models using palaeoclimatic data. *Nature Climate Change*, 2: 417–424, 2012.

L. I. Bradtmiller, J. F. McManus, and L. F. Robinson. $^{231}Pa/^{230}Th$ evidence for a weakened but persistent Atlantic meridional overturning circulation during Heinrich Stadial 1. *Nature Communications*, 5, 2014. doi: 10.1038/ncomms6817.

R. D. Briggs, D. Pollard, and L. Tarasov. A data-constrained large ensemble analysis of Antarctic evolution since the Eemian. *Quat. Sci. Rev.*, 103:91–115, 2014. doi: 10.1016/j.quascirev.2014.09.003.

V. Brovkin, A. Ganopolski, and Y. Svirezhev. A continuous climate-vegetation classification for use in climate-biosphere studies. *Ecol. Model.*, 101:251–261, 1997.

V. Brovkin, J. Bendtsen, M. Claussen, A. Ganopolski, C. Kubatzki, V. Petoukhov, and A. Andreev. Carbon cycle, vegetation, and climate dynamics in the Holocene: Experiments with the CLIMBER-2 model. *Global Biogeochem. Cy.*, 16, 2002a. doi: 10.1029/2001GB001662.

V. Brovkin, M. Hofmann, J. Bendtsen, and A. Ganopolski. Ocean biology could control atmospheric δ^{13}C during glacial-interglacial cycle. *Geochem. Geophy. Geosyst.*, 3(1027), 2002b. doi: 10.1029/2001GC000270.

V. Brovkin, A. Ganopolski, D. Archer, and S. Rahmstorf. Lowering of glacial atmospheric CO_2 in response to changes in oceanic circulation and marine biogeochemistry. *Paleoceanography*, 22(PA4202), 2007. doi: 10.1029/2006PA001380.

K. Bryan and L. J. Lewis. A water mass model of the world ocean. *J. Geophys. Res.*, 84:2503–2517, 1979.

P. J. Buchanan, R. J. Matear, A. Lenton, S. J. Phipps, Z. Chase, and D. M. Etheridge. The simulated climate of the Last Glacial Maximum and insights into the global marine carbon cycle. *Clim. Past*, 12(12):2271–2295, 2016. doi: 10.5194/cp-12-2271-2016.

E. Böhm, J. Lippold, M. Gutjahr, M. Frank, P. Blaser, B. Antz, J. Fohlmeister, N. Frank, M. B. Andersen, and M. Deininger. Strong and deep Atlantic meridional overturning circulation during the last glacial cycle. *Nature*, 517:73–76, 2015. doi: 10.1038/nature14059.

M. Bügelmayer, D. M. Roche, and H. Renssen. Representing icebergs in the iLOVECLIM model (version 1.0) – a sensitivity study. *Geosci. Model Dev.*, 8:2139–2151, 2015. doi: 10.5194/gmd-8-2139-2015.

T. Caley and D. M. Roche. δ^{18}O water isotope in the iLOVECLIM model (version 1.0) – Part 3: A palaeo-perspective based on present-day data-model comparison for oxygen stable isotopes in carbonates. *Geoscientific Model Development*, 6:1505–1516, 2013. doi: 10.5194/gmd-6-1505-2013.

J.-M. Campin. *Modélisation tridimensionnelle de la circulation générale océanique lors du dernier maximum glaciaire*. PhD thesis, Université Catholique de Louvain, 1997.

J.-M. Campin and H. Goosse. Parameterization of density-driven downsloping flow for a coarse-resolution ocean model in z-coordinate. *Tellus*, 51A:412–430, 1999. doi: 10.3402/tellusa.v51i3.13468.

D. Castellana, S. Baars, F. W. Wubs, and H. A. Dijkstra. Transition Probabilities of Noise-induced Transitions of the Atlantic Ocean Circulation. *Scientific Reports*, 9(1):1–7, 2019. doi: 10.1038/s41598-019-56435-6.

Y. Chavaillaz, F. Codron, and M. Kageyama. Southern westerlies in LGM and future (RCP4.5) climates. *Clim. Past*, 9:517–524, 2013. doi: 10.5194/cp-9-517-2013.

M. Claussen, L. A. Mysak, A. J. Weaver, M. Crucifix, T. Fichefet, M. F. Loutre, S. L. Weber, J. Alcamo, V. A. Alexeev, A. Berger, R. Calov, A. Ganopolski, H. Goosse, G. Lohman, F. Lunkeit, I. I. Mohkov, V. Petoukhov, P. Stone, , and Z. Wang. Earth System Models of Intermediate Complexity: closing the gap in the spectrum of climate system models. *Clim. Dynam.*, 18:579–586, 2002. doi: 10.1007/s00382-001-0200-1.

X. Crosta, A. Sturm, L. Armand, and J.-J. Pichon. Late Quaternary sea ice history in the Indian sector of the Southern Ocean as recorded by diatom assemblages. *Mar. Micropaleontol.*, 50:209–223, 2004. doi: 10.1016/S0377-8398(03)00072-0.

W. B. Curry and D. W. Oppo. Glacial water mass geometry and the distribution of δ^{13}C of $\sum CO_2$ in the western Atlantic Ocean. *Paleoceanography*, 20(PA1017):317–341, 2005. doi: 10.1029/2004PA001021.

A. M. De Boer and A. M. Hogg. Control of the glacial carbon budget by topographically induced mixing. *Geophys. Res. Lett.*, 41:4277–4284, 2014. doi: 10.1002/2014GL059963.

C. de Lavergne, G. Madec, J. Le Sommer, A. J. G. Nurser, and A. C. Naveira Garabato. On the Consumption of Antarctic Bottom Water in the Abyssal Ocean. *Journal of Physical Oceanography*, 46(2):635–661, 2016. doi: 10.1175/JPO-D-14-0201.1.

C. de Lavergne, C. Vic, G. Madec, F. Roquet, A. F. Waterhouse, Y. Cuypers, P. Bouruet-Aubertot, B. Ferron, and T. Hibiya. A Parameterization of Local and Remote Tidal Mixing. *Journal of Advances in Modeling Earth Systems*, 12, 2020. doi: 10.1029/2020MS00206.

A. de Vernal, R. Gersonde, H. Goosse, M.-S. Seidenkrantz, and E. W. Wolff. Sea ice in the paleoclimate system : the challenge of reconstructing sea ice from proxies – an introduction. *Quat. Sci. Rev.*, 79:1–8, 2013. doi: 10.1016/j.quascirev.2013.08.009.

K. A. Donohue, K. L. Tracey, D. R. Watts, M. P. Chidichimo, and T. K. Chereskin. Mean Antarctic Circumpolar Current transport measured in Drake Passage. *Geophys. Res. Lett.*, 43:11760–11767, 2016. doi: 10.1002/2016GL070319.

S. M. Downes, R. Farneti, P. Uotila, S. M. Griffies, S. J. Marsland, D. Bailey, E. Behrens, M. Bentsen, D. Bi, A. Biastoch, C. Böning, A. Bozec, V. M. Canuto, E. Chassignet, G. Danabasoglu, S. Danilov, N. Diansky, H. Drange, P. G. Fogli, A. Gusev, A. Howard, M. Ilicak, T. Jung, M. Kelley, W. G. Large, A. Leboissetier, M. Long, J. Lu, S. Masina, A. Mishra, A. Navarra, A. J. George Nurser, L. Patara, B. L. Samuels, D. Sidorenko, P. Spence, H. Tsujino, Q. Wang, and S. G. Yeager. An assessment of Southern Ocean water masses and sea ice during 1988–2007 in a suite of interannual CORE-II simulations. *Ocean Model.*, 94:67–94, 2015. doi: 10.1016/j.ocemod.2015.07.022.

J. C. Duplessy, N. J. Shackleton, R. G. Fairbanks, L. Labeyrie, D. Oppo, and N. Kallel. Deepwater source variations during the last climatic cycle and their impact on the global deepwater circulation. *Paleoceanography*, 3:343–360, 1988. doi: 10.1029/PA003i003p00343.

K. Döös and D. J. Webb. The Deacon cell and the other meridional cells of the Southern Ocean. *Journal of Physical Oceanography*, 24(2):429–442, 1994.

M. Eide, A. Olsen, U. S. Ninnemann, and T. Johannessen. A global ocean climatology of preindustrial and modern ocean δ^{13}C. *Global Biogeochemical Cycles*, 31:515–534, 2017. doi: 10.1002/2016GB005473.

J. Emile-Geay and G. G. Madec. Geothermal heating, diapycnal mixing and the abyssal circulation. *Ocean Sci.*, 5:203–217, 2009.

O. Esper and R. Gersonde. New tools for the reconstruction of Pleistocene Antarctic sea ice. *Palaeogeography, Palaeoclimatology, Palaeoecology*, 399:260–283, 2014. doi: 10.1016/j.palaeo.2014.01.019.

T. Extier. *Climate and low latitude water cycle variations during the Quaternary : a model-data approach*. PhD thesis, Université Paris Saclay, 2019.

V. Eyring, S. Bony, G. A. Meehl, C. A. Senior, B. Stevens, R. J. Stouffer, and K. E. Taylor. Overview of the Coupled Model Intercomparison Project Phase 6 (CMIP6) experimental design and organization. *Geosci. Model Dev.*, 9:1937–1958, 2016. doi: 10.5194/gmd-9-1937-2016.

R. Ferrari, M. F. Jansen, J. F. Adkins, A. Burke, A. L. Stewart, and A. F. Thompson. Antarctic sea ice control on ocean circulation in present and glacial climates. *P. Natl. Acad. Sci.*, 111(24):8753–8758, 2014. doi: 10.1073/pnas.1323922111.

A. J. Ferry, X. Crosta, P. G. Quilty, D. Fink, W. Howard, and L. K. Armand. First records of winter sea ice concentration in the southwest Pacific sector of the Southern Ocean. *Paleoceanography*, 30:1525–1539, 2015. doi: 10.1002/2014PA002764.

F. Fetterer, K. Knowles, W. Meier, and M. Savoie. Sea Ice Index. Electronic., 2012. URL http://nsidc.org/data/seaiceindex/.

T. Fichefet and M. A. Morales Maqueda. Sensitivity of a global sea ice model to the treatment of ice thermodynamics and dynamics. *J. Geophys. Res.*, 102:12609–12646, 1997. doi: 10.1029/97JC00480.

E. Freeman, L. C. Skinner, C. Waelbroeck, and D. Hodell. Radiocarbon evidence for enhanced respired carbon storage in the Atlantic at the Last Glacial Maximum. *Nature communications*, 7, 2016. doi: 10.1038/ncomms11998.

T. Friedrich, A. Timmermann, T. Decloedt, D. S. Luther, and A. Mouchet. The effect of topography-enhanced diapycnal mixing on ocean and atmospheric circulation and marine biogeochemistry. *Ocean Modelling*, 39:262–274, 2011. doi: 10.1016/j.ocemod.2011.04.012.

E. Galbraith and C. de Lavergne. Response of a comprehensive climate model to a broad range of external forcings: relevance for deep ocean ventilation and the development of late Cenozoic ice ages. *Clim. Dynam.*, 52(1-2):653–679, 2019. doi: 10.1007/s00382-018-4157-8.

G. Gebbie. How much did Glacial North Atlantic Water shoal? *Paleoceanography*, 29:190–209, 2014. doi: 10.1002/2013PA002557.

P. R. Gent and J. C. McWilliams. Isopycnal mixing in ocean general circulation models. *J. Phys. Oceanogr.*, 20:150–155, 1990. doi: 10.1175/1520-0485(1990)020<0150:IMIOCM>2.0.CO;2.

R. Gersonde and U. Zielinski. The reconstruction of late Quaternary Antarctic sea-ice distribution—the use of diatoms as a proxy for sea-ice. *Palaeogeography, Palaeoclimatology, Palaeoecology*, 162:263–286, 2000. doi: 10.1016/S0031-0182(00)00131-0.

R. Gersonde, X. Crosta, A. Abelmann, and L. Armand. Sea-surface temperature and sea ice distribution of the Southern Ocean at the EPILOG Last Glacial Maximum — a circum-Antarctic view based on siliceous microfossil records. *Quat. Sci. Rev.*, 24(7–9):869–896, 2005. doi: 10.1016/j.quascirev.2004.07.015.

H. Goosse. *Climate System Dynamics and Modelling*. Cambridge University Press, 2015.

H. Goosse and T. Fichefet. Importance of ice-ocean interactions for the global ocean circulation: a model study. *J. Geophys. Res.*, 104:23337–23355, 1999. doi: 10.1029/1999JC900215.

H. Goosse and V. Zunz. Decadal trends in the Antarctic sea ice extent ultimately controlled by ice–ocean feedback. *The Cryosphere*, 8:453–470, 2014. doi: 10.5194/tc-8-453-2014.

H. Goosse, J.-M. Campin, T. Fichefet, and E. Deleersnijder. Sensitivity of a global ice-ocean model to the Bering Strait throughflow. *Clim. Dynam.*, 13:349–358, 1997a. doi: 10.1007/s003820050170.

H. Goosse, T. Fichefet, and J.-M. Campin. The effects of the water flow through the Canadian Archipelago in a global ice-ocean model. *Geophys. Res. Lett.*, 24:1507–1510, 1997b. doi: 10.1029/97GL01352.

H. Goosse, E. Deleersnijder, T. Fichefet, and M. H. England. Sensitivity of a global coupled ocean-sea ice model to the parameterization of vertical mixing. *Journal of Geophysical Research Atmospheres*, 1041(C6): 13681–13696, 1999. doi: 10.1029/1999JC900099.

H. Goosse, J.-M. Campin, E. Deleersnijder, T. Fichefet, P.-P. Mathieu, M. A. Morales Maqueda, and B. Tartinville. Description of the CLIO model version 3.0. 2000. URL https://www.researchgate.net/publication/253170859_Description_of_the_CLIO_model.

H. Goosse, V. Brovkin, T. Fichefet, R. Haarsma, P. Huybrechts, J. Jongma, A. Mouchet, F. Selten, P. Y. Barriat, J. M. Campin, E. Deleersnijder, E. Driesschaert, H. Goelzer, I. Janssens, M. F. Loutre, M. A. Morales Maqueda, T. Opsteegh, P. P. Mathieu, G. Munhoven, E. J. Pettersson, H. Renssen, D. M. Roche, M. Schaeffer, B. Tartinville, A. Timmermann, and S. L. Weber. Description of the Earth system model of intermediate complexity LOVECLIM version 1.2. *Geosci. Model Dev.*, 3(2):603–633, 2010. doi: 10.5194/gmd-3-603-2010.

H. Goosse, D. M. Roche, A. Mairesse, and M. Berger. Modelling past sea ice changes. *Quat. Sci. Rev.*, 79: 191–206, 2013. doi: 10.1016/j.quascirev.2013.03.011.

H. Goosse, J. E. Kay, K. C. Armour, A. Bodas-Salcedo, H. Chepfer, D. Docquier, A. Jonko, P. J. Kushner, O. Lecomte, F. Massonnet, H.-S. Park, F. Pithan, G. Svensson, and M. Vancoppenolle. Quantifying climate feedbacks in polar regions. *Nat. Commun.*, 9:1–13, 2018. doi: 10.1038/s41467-018-04173-0.

J. Gottschalk, N. Vázquez Riveiros, C. Waelbroeck, L. C. Skinner, E. Michel, J.-C. Duplessy, D. Hodell, and A. Mackensen. Carbon isotope offsets between benthic foraminifer species of the genus *Cibicides (Cibicidoides)* in the glacial sub-Antarctic Atlantic. *Paleoceanography*, 31:1583–1602, 2016. doi: 10.1002/2016PA003029.

J. Gottschalk, G. Battaglia, H. Fischer, T. L. Frölicher, S. L. Jaccard, A. Jeltsch-Thömmes, F. Joos, P. Köhler, K. J. Meissner, L. Menviel, C. Nehrbass-Ahles, J. Schmitt, A. Schmittner, L. C. Skinner, and T. F. Thomas F. Stocker. Mechanisms of millennial-scale atmospheric CO_2 change in numerical model simulations. *Quaternary Science Reviews*, pages 30–74, 2020. doi: 10.1016/j.quascirev.2019.05.013.

W. R. Gray, C. de Lavergne, R. C. J. Wills, L. Menviel, P. Spence, M. Holzer, M. Kageyama, and E. Michel. Poleward shift in the Southern Hemisphere westerly winds synchronous with the deglacial rise in CO_2. *Nature*, in review, 2021. doi: 10.21203/rs.3.rs-404786/v1.

S. Gu, Z. Liu, J. Zhang, J. Rempfer, F. Joos, and D. W. Oppo. Coherent Response of Antarctic Intermediate Water and Atlantic Meridional Overturning Circulation During the Last Deglaciation: Reconciling Contrasting Neodymium Isotope Reconstructions From the Tropical Atlantic. *Paleoceanography*, 32:1036–1053, 2017. doi: 10.1002/2017PA003092.

S. Gu, Z. Liu, D. W. Oppo, J. Lynch-Stieglitz, A. Jahn, J. Zhang, and L. Wu. Assessing the potential capability of reconstructing glacial Atlantic water masses and AMOC using multiple proxies in CESM. *Earth and Planetary Science Letters*, 541, 2020. doi: 10.1016/j.epsl.2020.116294.

M. P. Hain, D. M. Sigman, and G. H. Haug. Carbon dioxide effects of Antarctic stratification, North Atlantic Intermediate Water formation, and subantarctic nutrient drawdown during the last ice age: Diagnosis and synthesis in a geochemical box model. *Global Biogeochem. Cy.*, 24(GB4023), 2010. doi: 10.1029/2010GB003790.

T. Hesse, M. Butzin, T. Bickert, and G. Lohman. A model-data comparison of δ^{13}C in the glacial Atlantic Ocean. *Paleoceanography*, 26(PA3220), 2011. doi: 10.1029/2010PA002085.

C. Heuzé. Antarctic Bottom Water and North Atlantic Deep Water in CMIP6 models. *Ocean Sci.*, 2021. doi: 10.5194/os-2020-66.

C. Heuzé, K. J. Heywood, D. P. Stevens, and J. K. Ridley. Southern Ocean bottom water characteristics in CMIP5 models. *Geophys. Res. Lett.*, 40(7):1409–1414, 2013. doi: 10.1002/grl.50287.

C. Heuzé, J. K. Ridley, D. Calvert, D. P. Stevens, and K. J. Heywood. Increasing vertical mixing to reduce Southern Ocean deep convection in NEMO3.4. *Geosci. Model Dev.*, 8:3119–3130, 2015. doi: 10.5194/gmd-8-3119-2015.

K. J. Heywood, S. Schmidtko, C. Heuzé, J. Kaiser, T. D. Jickells, B. Y. Queste, D. P. Stevens, M. Wadley, A. F. Thompson, S. Fielding, D. Guihen, E. Creed, J. K. Ridley, and W. Smith. Ocean processes at the Antarctic continental slope. *Phil. Trans. R. Soc. A*, 372(20130047), 2014. doi: 10.1098/rsta.2013.0047.

M. Hieronymus, J. Nycander, J. Nilsson, K. Döös, and R. Hallberg. Oceanic Overturning and Heat Transport: The Role of Background Diffusivity. *Journal of Climate*, 32, 2019. doi: 10.1175/JCLI-D-18-0438.1.

W. R. Hobbs, R. Massom, S. Stammerjohn, P. Reid, G. Williams, and W. Meier. A review of recent changes in Southern Ocean sea ice, their drivers and forcings. *Global and Planetary Change*, 143:228–250, 2016. doi: 10.1016/j.gloplacha.2016.06.008.

K. Homola, A. J. Spivack, R. W. Murray, R. Pockalny, S. D'Hondt, and R. Robinson. Deep North Atlantic Last Glacial Maximum Salinity Reconstruction. *Paleoceanography and Paleoclimatology*, accepted, 2021. doi: 10.1029/2020PA004088.

F. Hourdin, T. Mauritsen, A. Gettelman, J.-C. Golaz, V. Balaji, Q. Duan, D. Folini, D. Ji, D. Klocke, Y. Qian, F. Rauser, C. Rio, L. Tomassini, M. Watanabe, and D. Williamson. The art and science of climate model tuning. *American Meteorological Society*, pages 589–602, 2017. doi: 10.1175/BAMS-D-15-00135.1.

J. N. W. Howe, A. M. Piotrowski, T. L. Noble, S. Mulitza, C. M. Chiessi, and G. Bayon. North Atlantic Deep Water Production during the Last Glacial Maximum. *Nat. Commun.*, 7(11765):1–8, 2016. doi: 10.1038/ncomms11765.

A. Hu, G. A. Meehl, B. L. Otto-Bliesner, C. Waelbroeck, W. Han, M.-F. Loutre, K. Lambeck, J. X. Mitrovica, and N. Rosenbloom. Influence of Bering Strait flow and North Atlantic circulation on glacial sea-level changes. *Nature Geoscience*, 3:118–121, 2010. doi: 10.1038/NGEO729.

P. Hyder, J. M. Edwards, R. P. Allan, H. T. Hewitt, T. J. Bracegirdle, J. M. Gregory, R. A. Wood, A. J. S. Meijers, J. Mulcahy, P. Field, K. Furtado, A. Bodas-Salcedo, K. D. Williams, D. Copsey, S. A. Josey, C. Liu, C. D. Roberts, C. Sanchez, J. Ridley, L. Thorpe, S. C. Hardiman, M. Mayer, D. I. Berry, and S. E. Belcher. Critical Southern Ocean climate model biases traced to atmospheric model cloud errors. *Nat. Commun.*, 9 (3625), 2018. doi: 10.1038/s41467-018-05634-2.

Intergovernmental Panel on Climate Change. *Climate Change 2013 – The Physical Science Basis: Working Group I Contribution to the Fifth Assessment Report of the Intergovernmental Panel on Climate Change*. Cambridge University Press, 2014. doi: 10.1017/CBO9781107415324.

R. F. Ivanovic, L. J. Gregoire, M. Kageyama, D. M. Roche, P. J. Valdes, A. Burke, R. Drummond, W. R. Peltier, and L. Tarasov. Transient climate simulations of the deglaciation 21–9 thousand years before present (version 1) – PMIP4 Core experiment design and boundary conditions. *Geosci. Model Dev.*, 9:2563–2587, 2016. doi: 10.5194/gmd-9-2563-2016.

M. F. Jansen. Glacial ocean circulation and stratification explained by reduced atmospheric temperature. *PNAS*, 114(1):45–50, 2017. doi: 10.1073/pnas.1610438113.

M. F. Jansen and L.-P. Nadeau. The Effect of Southern Ocean Surface Buoyancy Loss on the Deep-Ocean Circulation and Stratification. *Journal of Physical Oceanography*, 46, 2016. doi: 10.1175/JPO-D-16-0084.1.

H. L. Johnson, P. Cessi, D. P. Marshall, F. Schloesser, and M. A. Spall. Recent Contributions of Theory to Our Understanding of the Atlantic Meridional Overturning Circulation. *Journal of Geophysical Research: Oceans*, 124:5376–5399, 2019. doi: 10.1029/2019JC015330.

S. Joussaume and K. E. Taylor. Status of the Paleoclimate Modeling Intercomparison Project (PMIP). *Proceedings of the first international AMIP scientific conference*, pages 425–430, 1995.

M. Kageyama, S. Albani, P. Braconnot, S. P. Harrison, P. O. Hopcroft, R. F. Ivanovic, F. Lambert, O. Marti, W. R. Peltier, J.-Y. Peterschmitt, D. M. Roche, L. Tarasov, X. Zhang, E. C. Brady, A. M. Haywood, A. N. LeGrande, D. J. Lunt, N. M. Mahowald, U. Mikolajewicz, K. H. Nisancioglu, B. L. Otto-Bliesner, H. Renssen, R. A. Tomas, Q. Zhang, A. Abe-Ouchi, P. J. Bartlein, J. Cao, Q. Li, G. Lohmann, R. Ohgaito, X. Shi, E. Volodin, K. Yoshida, X. Zhang, and W. Zheng. The PMIP4 contribution to CMIP6 – Part 4: Scientific objectives and experimental design of the PMIP4-CMIP6 Last Glacial Maximum experiments and PMIP4 sensitivity experiments. *Geosci. Model Dev.*, 10:4035–4055, 2017. doi: 10.5194/gmd-10-4035-2017.

M. Kageyama, P. Braconnot, S. P. Harrison, A. M. Haywood, J. H. Jungclaus, B. L. Otto-Bliesner, J.-Y. Peterschmitt, A. Abe-Ouchi, S. Albani, P. J. Bartlein, C. Brierley, M. Crucifix, A. Dolan, L. Fernandez-Donado, H. Fischer, P. O. Hopcroft, R. F. Ivanovic, F. Lambert, D. J. Lunt, N. M. Mahowald, W. R. Peltier, S. J. Phipps, D. M. Roche, G. A. Schmidt, L. Tarasov, P. J. Valdes, Q. Zhang, and T. Zhou. The PMIP4 contribution to CMIP6 – Part 1: Overview and over-arching analysis plan. *Geoscientific Model Development*, 11:1033–1057, 2018. doi: 10.5194/gmd-11-1033-2018.

M. Kageyama, S. P. Harrison, M.-L. Kapsch, M. Löfverström, J. M. Lora, U. Mikolajewicz, S. Sherriff-Tadano, T. Vadsaria, A. Abe-Ouchi, N. Bouttes, D. Chandan, A. N. LeGrande, F. Lhardy, G. Lohmann, P. A. Morozova, R. Ohgaito, W. R. Peltier, A. Quiquet, D. M. Roche, X. Shi, A. Schmittner, J. E. Tierney, and E. Volodin. The PMIP4-CMIP6 Last Glacial Maximum experiments: preliminary results and comparison with the PMIP3-CMIP5 simulations. *Clim. Past*, 2021. doi: 10.5194/cp-2019-169.

R. Key, A. Kozyr, C. Sabine, K. Lee, R. Wanninkhof, J. Bullister, R. Feely, F. Millero, C. Mordy, and T.-H. Peng. A global ocean carbon climatology: Results from GLODAP. *Global Biogeochem. Cy.*, 18(GB4031), 2004.

S. Khatiwala, A. Schmittner, and J. Muglia. Air-sea disequilibrium enhances ocean carbon storage during glacial periods. *Science Advances*, 5(6), 2019. doi: 10.1126/sciadv.aaw4981.

D. C. Kitover, R. van Balen, D. M. Roche, J. Vandenberghe, and H. Renssen. Advancement toward coupling of the VAMPER permafrost model within the Earth system model iLOVECLIM (version 1.0): description and validation. *Geosci. Model Dev.*, 8:1445–1460, 2019. doi: 10.5194/gmd-8-1445-2015.

M. Klockmann, U. Mikolajewicz, and J. Marotzke. The effect of greenhouse gas concentrations and ice sheets on the glacial AMOC in a coupled climate model. *Clim. Past*, pages 1829–1846, 2016. doi: 10.5194/cp-12-1829-2016.

R. Knutti, D. Masson, and A. Gettelman. Climate model genealogy: Generation CMIP5 and how we got there. *Geophys. Res. Lett.*, 40:1194–1199, 2015. doi: 10.1002/grl.50256.

H. Kobayashi and A. Oka. Response of Atmospheric pCO_2 to Glacial Changes in the Southern Ocean Amplified by Carbonate Compensation. *Paleoceanography and Paleoclimatology*, 33:1206–1229, 2018. doi: 10.1029/2018PA003360.

K. E. Kohfeld and A. Ridgwell. In *Surface Ocean-Lower Atmosphere Processes, Volume 187*, chapter Glacial-interglacial variability in atmospheric CO_2. 2009. doi: 10.1029/2008GM000845.

K. E. Kohfeld, R. M. Graham, A. M. de Boer, L. C. Sime, E. W. Wolff, C. Le Quéré, and L. Bopp. Southern Hemisphere Westerly Wind Changes during the Last Glacial Maximum: Paleo-data Synthesis. *Quaternary Science Reviews*, 68:76–95, 2013.

T. Kuhlbrodt, A. Griesel, M. Montoya, A. Levermann, M. Hofmann, and S. Rahmstorf. On the driving processes of the Atlantic meridional overturning circulation. *Rev. Geophys.*, 45:RG2001, 2007. doi: 10.1029/2004RG000166.

T. Kurahashi-Nakamura, A. Paul, and M. Losch. Dynamical reconstruction of the global ocean state during the Last Glacial Maximum. *Paleoceanography*, 32:326–350, 2017.

K. Lambeck, H. Rouby, A. Purcell, Y. Sun, and M. Sambridge. Sea level and global ice volumes from the Last Glacial Maximum to the Holocene. *P. Natl. Acad. Sci.*, 111(43):15296–15303, 2014. doi: 10.1073/pnas.1411762111.

F. Lhardy, N. Bouttes, D. M. Roche, A. Abe-Ouchi, Z. Chase, K. Crichton, R. Ivanovic, M. Jochum, M. Kageyama, H. Kobayashi, L. Menviel, J. Muglia, R. Nuterman, A. Oka, A. Schmittner, G. Vettoretti, and A. Yamamoto. A first intercomparison of the simulated LGM carbon results within PMIP-carbon: role of the ocean boundary conditions. *Paleoceanography and Paleoclimatology*, 36(10), 2021a. doi: 10.1029/2021PA004302.

F. Lhardy, N. Bouttes, D. M. Roche, X. Crosta, C. Waelbroeck, and D. Paillard. Impact of Southern Ocean surface conditions on deep ocean circulation during the LGM: a model analysis. *Clim. Past*, 17:1139–1159, 2021b. doi: 10.5194/cp-17-1139-2021.

J. Lippold, Y. Luo, R. Francois, S. E. Allen, J. Gherardi, S. Pichat, B. Hickey, and H. Schulz. Strength and geometry of the glacial Atlantic Meridional Overturning Circulation. *Nature Geoscience*, 5, 2012. doi: 10.1038/NGEO1608.

J. Lippold, M. Gutjahr, P. Blaser, E. Christner, M. L. de Carvalho Ferreira, S. Mulitza, M. Christl, F. Wombacher, E. Böhm, B. Antz, O. Cartapanis, H. Vogel, and S. L. Jaccard. Deep water provenance and dynamics of the (de)glacial Atlantic meridional overturning circulation. *Earth and Planetary Science Letters*, 445:68–78, 2016. doi: 10.1016/j.epsl.2016.04.013.

W. Liu and A. V. Fedorov. Global Impacts of Arctic Sea Ice Loss Mediated by the Atlantic Meridional Overturning Circulation. *Geophysical Research Letters*, 46:944–952, 2019. doi: 10.1029/2018GL080602.

R. A. Locarnini, A. V. Mishonov, J. I. Antonov, T. P. Boyer, H. E. Garcia, O. K. Baranova, M. M. Zweng, and D. R. Johnson. *World Ocean Atlas 2009, Volume 1: Temperature*. Levitus, S., NOAA Atlas NESDIS 68, US Government Printing Office, Washington, D.C., 2010.

L. Loulergue, A. Schilt, R. Spahni, V. Masson-Delmotte, T. Blunier, B. Lemieux, J. M. Barnola, D. Raynaud, T. F. Stocker, and J. Chappellaz. Orbital and millennial-scale features of atmospheric CH_4 over the past 800 000 year. *Nature*, 453:383–386, 2008. doi: 10.1038/nature06950.

A. Lourantou, J. V. Lavric, P. Köhler, J.-M. Barnola, D. Paillard, E. Michel, D. Raynaud, and J. Chappellaz. Constraint of the CO_2 rise by new atmospheric carbon isotopic measurements during the last deglaciation. *Global Biogeochem. Cycles*, 24(GB2015), 2010. doi: 10.1029/2009GB003545.

F. Lucazeau. Analysis and Mapping of an Updated Terrestrial Heat Flow Data Set. *Geochemistry, Geophysics, Geosystems*, 20:4001–4024, 2019. doi: 10.1029/2019GC008389.

J. Lynch-Stieglitz. The Atlantic Meridional Overturning Circulation and Abrupt Climate Change. *Annual Review of Marine Science*, 9:83–104, 2017. doi: 10.1146/annurev-marine-010816-060415.

J. Lynch-Stieglitz, J. F. Adkins, W. B. Curry, T. Dokken, I. R. Hall, J. C. Herguera, J. J.-M. Hirschi, E. V. Ivanova, C. Kissel, O. Marchal, T. M. Marchitto, I. N. McCave, J. F. McManus, S. Mulitza, U. Ninnemann, F. Peeters, E.-F. Yu, and R. Zahn. Atlantic Meridional Overturning Circulation During the Last Glacial Maximum. *Science*, 316:66–69, 2007. doi: 10.1126/science.1137127.

L. Ma, B. Wang, and J. Jian Cao. Impacts of atmosphere–sea ice–ocean interaction on Southern Ocean deep convection in a climate system model. *Climate Dynamics*, 2020. doi: 10.1007/s00382-020-05218-1.

A. Mackensen, H.-W. Hubberten, T. Bickert, G. Fischer, and D. K. Fütterer. The δ^{13}C in benthic foraminiferal tests of *Fontbotia wuellerstorfi* (Schwager) Relative to the δ^{13}C of dissolved inorganic carbon in Southern Ocean Deep Water: Implications for glacial ocean circulation models. *Paleoceanography*, 8(5):587–610, 1993. doi: 10.1029/93PA01291.

T. Maksym. Arctic and Antarctic Sea Ice Change: Contrasts, Commonalities, and Causes. *Annual Review of Marine Science*, 11:187–213, 2019. doi: 10.1146/annurev-marine-010816-060610.

MARGO Project Members. Constraints on the magnitude and patterns of ocean cooling at the Last Glacial Maximum. *Nat. Geosci.*, 2:127–132, 2009. doi: 10.1038/NGEO411.

J. Marshall and K. Speer. Closure of the meridional overturning circulation through Southern Ocean upwelling. *Nat. Geosci.*, 5(3):171–180, 2012. doi: 10.1038/ngeo1391.

B. Marzeion, A. Levermann, and J. Mignot. The Role of Stratification-Dependent Mixing for the Stability of the Atlantic Overturning in a Global Climate Model. *Journal of Physical Oceanography*, 37:2672–2681, 2007. doi: 10.1175/2007JPO3641.1.

A. Marzocchi and M. F. Jansen. Connecting Antarctic sea ice to deep-ocean circulation in modern and glacial climate simulations. *Geophys. Res. Lett.*, 44(12):6286–6295, 2017. doi: 10.1002/2017GL073936.

A. Marzocchi and M. F. Jansen. Global cooling linked to increased glacial carbon storage via changes in Antarctic sea ice. *Nature geoscience*, 12:1001–1005, 2019. doi: 10.1038/s41561-019-0466-8.

K. Matthes, B. Funke, M. E. Andersson, L. Barnard, J. Beer, P. Charbonneau, M. A. Clilverd, T. Dudok de Wit, M. Haberreiter, A. Hendry, C. H. Jackman, M. Kretzschmar, T. Kruschke, M. Kunze, U. Langematz, D. R. Marsh, A. C. Maycock, S. Misios, C. J. Rodger, A. A. Scaife, A. Seppälä, M. Shangguan, M. Sinnhuber, K. Tourpali, I. Usoskin, M. van de Kamp, P. T. Verronen, and S. Versick. Solar forcing for CMIP6 (v3.2). *Geosci. Model Dev.*, 10(6):2247–2302, 2017. doi: 10.5194/gmd-10-2247-2017.

G. D. McCarthy, D. A. Smeed, W. E. Johns, E. Frajka-Williams, B. I. Moat, D. Rayner, M. O. Baringer, C. S. Meinen, J. Collins, and H. L. Bryden. Measuring the Atlantic Meridional Overturning Circulation at 26N. *Progress in Oceanography*, 130:91–111, 2015. doi: 10.1016/j.pocean.2014.10.006.

V. L. Meccia and U. Mikolajewicz. Interactive ocean bathymetry and coastlines for simulating the last deglaciation with the Max Planck Institute Earth System Model (MPI-ESM-v1.2). *Geosci. Model Dev.*, 11:4677–4692, 2018. doi: 10.5194/gmd-11-4677-2018.

G. A. Meehl, J. M. Arblaster, C. T. Y. Chung, M. M. Holland, A. DuVivier, L. Thompson, D. Yang, and C. M. Bitz. Sustained ocean changes contributed to sudden Antarctic sea ice retreat in late 2016. *Nature Communications*, pages 10–14, 2019. doi: 10.1038/s41467-018-07865-9.

A. J. S. Meijers. The Southern Ocean in the Coupled Model Intercomparison Project phase 5. *Phil. Trans. R. Soc. A*, 372(20130296), 2014. doi: 10.1098/rsta.2013.0296.

L. Menviel, F. Joos, and S. P. Ritz. Simulating atmospheric CO_2 , ^{13}C and the marine carbon cycle during the Last Glacial-Interglacial cycle: possible role for a deepening of the mean remineralization depth and an increase in the oceanic nutrient inventory. *Quaternary Science Reviews*, 56:46–68, 2012. doi: 10.1016/j.quascirev.2012.09.012.

L. Menviel, J. Yu, F. Joos, A. Mouchet, K. J. Meissner, and M. H. England. Poorly ventilated deep ocean at the Last Glacial Maximum inferred from carbon isotopes: A data-model comparison study. *Paleoceanography*, 32:2–17, 2017. doi: 10.1002/2016PA003024.

L. C. Menviel, P. Spence, L. C. Skinner, K. Tachikawa, T. Friedrich, L. Missiaen, and J. Yu. Enhanced Mid-depth Southward Transport in the Northeast Atlantic at the Last Glacial Maximum Despite a Weaker AMOC. *Paleoceanography and Paleoclimatology*, 35(e2019PA003793), 2020. doi: 10.1029/2019PA003793.

F. Mesinger and A. Arakawa. Numerical methods used in atmospheric models. *WMO-ISCU Joint Organizing Committee, GARP Publications Series*, 17, 1976.

L. Missiaen, N. Bouttes, D. M. Roche, J.-C. Dutay, A. Quiquet, C. Waelbroeck, S. Pichat, and J.-Y. Peterschmitt. Carbon isotopes and Pa/Th response to forced circulation changes: a model perspective. *Climate of the Past*, 16:867–883, 2020a. doi: 10.5194/cp-16-867-2020.

L. Missiaen, L. Menviel, K. J. Meissner, D. M. Roche, J.-C. Dutay, N. Bouttes, F. Lhardy, A. Quiquet, S. Pichat, and C. Waelbroeck. Modelling the impact of biogenic particle flux intensity and composition on sedimentary Pa/Th. *Quaternary Science Reviews*, 240, 2020b. doi: 10.1016/j.quascirev.2020.106394.

A. C. Mix, E. Bard, and R. Schneider. Environmental processes of the ice age: land, oceans, glaciers (EPILOG). *Quaternary Science Reviews*, 20(4):627–657, 2001. doi: 10.1016/S0277-3791(00)00145-1.

B. I. Moat, D. A. Smeed, E. Frajka-Williams, D. G. Desbruyères, C. Beaulieu, W. E. Johns, D. Rayner, A. Sanchez-Franks, M. O. Baringer, D. Denis Volkov, L. C. Jackson, and H. L. Bryden. Pending recovery in the strength of the meridional overturning circulation at 26° N. *Ocean Sci.*, 16:863–874, 2020. doi: 10.5194/os-16-863-2020.

A. L. Morée, J. Schwinger, U. S. Ninnemann, A. Jeltsch-Thömmes, I. Bethke, and C. Heinze. Evaluating the biological pump efficiency of the Last Glacial Maximum ocean using δ^{13}C. *Clim. Past*, 17:753–774, 2021. doi: 10.5194/cp-17-753-2021.

J. Muglia and A. Schmittner. Glacial Atlantic overturning increased by wind stress in climate models. *Geophys. Res. Lett.*, 42(22):9862–9869, 2015. doi: 10.1002/2015GL064583.

J. Muglia and A. Schmittner. Carbon isotope constraints on glacial Atlantic meridional overturning: Strength vs depth. *Quaternary Science Reviews*, 257, 2021. doi: 10.1016/j.quascirev.2021.106844.

J. Muglia, C. J. Somes, L. Nickelsen, and A. Schmittner. Combined Effects of Atmospheric and Seafloor Iron Fluxes to the Glacial Ocean. *Paleoceanography*, 32, 2017. doi: 10.1002/2016PA003077.

J. Muglia, L. C. Skinner, and A. Schmittner. Weak overturning circulation and high Southern Ocean nutrient utilization maximized glacial ocean carbon. *Earth and Planetary Science Letters*, 496:47–56, 2018. doi: 10.1016/j.epsl.2018.05.038.

A. Nair, R. Mohan, X. Crosta, M. Manoj, M. Thamban, and V. Marieu. Southern Ocean sea ice and frontal changes during the Late Quaternary and their linkages to Asian summer monsoon. *Quat. Sci. Rev.*, 213: 93–104, 2019. doi: 10.1016/j.quascirev.2019.04.007.

M. Ödalen, J. Nycander, K. I. C. Oliver, L. Brodeau, and A. Ridgwell. The influence of the ocean circulation state on ocean carbon storage and CO_2 drawdown potential in an Earth system model. *Biogeosciences*, 15: 1367–1393, 2018. doi: 10.5194/bg-15-1367-2018.

A. Oka, A. Abe-Ouchi, M. O. Chikamoto, and T. Ide. Mechanisms controlling export production at the LGM: Effects of changes in oceanic physical fields and atmospheric dust deposition. *Global Biogeochem. Cy.*, 25 (GB2009), 2011. doi: 10.1029/2009GB003628.

A. Oka, H. Hasumi, and A. Abe-Ouchi. The thermal threshold of the Atlantic meridional overturning circulation and its control by wind stress forcing during glacial climate. *Geophysical Research Letters*, 39(L09709), 2012. doi: 10.1029/2007gl029475.

J. D. Opsteegh, R. J. Haarsma, F. M. Selten, and A. Kattenberg. ECBilt: A dynamic alternative to mixed boundary conditions in ocean models. *Tellus A*, 50(3):348–367, 1998. doi: 10.1034/j.1600-0870.1998.t01-1-00007.x.

B. L. Otto-Bliesner, C. D. Hewitt, T. M. Marchitto, E. Brady, A. Abe-Ouchi, M. Crucifix, S. Murakami, and S. L. Weber. Last Glacial Maximum ocean thermohaline circulation: PMIP2 model intercomparisons and data constraints. *Geophys. Res. Lett.*, 34(12):1–6, 2007. doi: 10.1029/2007GL029475.

D. Paillard and F. Parrenin. The Antarctic ice sheet and the triggering of deglaciations. *Earth and Planetary Science Letters*, 227:263–271, 2004. doi: 10.1016/j.epsl.2004.08.023.

T.-W. Park, Y. Deng, M. Cai, J.-H. Jeong, and R. Zhou. A dissection of the surface temperature biases in the Community Earth System Model. *Clim. Dyn.*, 43:2043–2059, 2014. doi: 10.1007/s00382-013-2029-9.

C. L. Parkinson and D. J. Cavalieri. Antarctic sea ice variability and trends, 1979–2010. *Cryosphere*, 6:871–880, 2012. doi: 10.5194/tc-6-871-2012.

W. R. Peltier. Global glacial isostasy and the surface of the ice-age Earth: the ICE-5G (VM2) model and GRACE. *Annu. Rev. Earth Pl. Sc.*, 32:111–149, 2004. doi: 10.1146/annurev.earth.32.082503.144359.

W. R. Peltier, D. F. Argus, and R. Drummond. Space geodesy constrains ice age terminal deglaciation: The global ICE-6G-C (VM5a) model. *J. Geophys. Res.-Sol. Ea.*, 120:450–487, 2015. doi: 10.1002/2014JB011176.

C. D. Peterson, L. E. Lisiecki, and J. V. Stern. Deglacial whole-ocean δ^{13}C change estimated from 480 benthic foraminiferal records. *Paleoceanography*, 29:549–563, 2014. doi: 10.1002/2013PA002552.

F. Pöppelmeier, P. Blaser, M. Gutjahr, S. L. Jaccard, M. Frank, L. Max, and J. Lippold. Northern-sourced water dominated the Atlantic Ocean during the Last Glacial Maximum. *Geology*, 48(8), 2020. doi: 10.1130/G47628.1.

A. Quiquet, D. M. Roche, C. Dumas, and D. Paillard. Online dynamical downscaling of temperature and precipitation within the iLOVECLIM model (version 1.1). *Geoscientific Model Development*, 11:453–466, 2018. doi: 10.5194/gmd-11-453-2018.

A. Quiquet, D. M. Roche, C. Dumas, N. Bouttes, and F. Lhardy. Climate and ice sheet evolutions from the last glacial maximum to the pre-industrial period with an ice sheet − climate coupled model. *Climate of the Past*, 17:2179–2199, 2021. doi: 10.5194/cp-17-2179-2021.

S. Rahmstorf. Ocean circulation and climate during the past 120,000 years. *Nature*, 419, 2002.

A. C. Ravelo and C. Hillaire-Marcel. In C. Hillaire–Marcel and A. De Vernal, editors, *Proxies in Late Cenozoic Paleoceanography*, chapter The Use of Oxygen and Carbon Isotopes of Foraminifera in Paleoceanography, pages 735–764. 2007. doi: 10.1016/S1572-5480(07)01023-8.

A. T. Roach, K. Aagaard, C. H. Pease, S. A. Salo, T. Weingartner, V. Pavlov, and M. Kulakov. Direct measurements of transport and water properties through the Bering Strait. *J. Geophys. Res.: Oceans*, 100 (C9), 1995.

D. M. Roche. δ^{18}O water isotope in the iLOVECLIM model (version 1.0) – Part 1: Implementation and verification. *Geoscientific Model Development*, 6:1481–1491, 2013. doi: 10.5194/gmd-6-1481-2013.

D. M. Roche and T. Caley. δ^{18}O water isotope in the iLOVECLIM model (version 1.0) – Part 2: Evaluation of model results against observed δ^{18}O in water samples. *Geoscientific Model Development*, 6:1493–1504, 2013. doi: 10.5194/gmd-6-1493-2013.

D. M. Roche, T. M. Dokken, H. Goosse, H. Renssen, and S. L. Weber. Climate of the Last Glacial Maximum: sensitivity studies and model-data comparison with the LOVECLIM coupled model. *Clim. Past*, 3(2):205–224, 2007. doi: 10.5194/cpd-2-1105-2006.

D. M. Roche, X. Crosta, and H. Renssen. Evaluating Southern Ocean sea-ice for the Last Glacial Maximum and pre-industrial climates: PMIP-2 models and data evidence. *Quat. Sci. Rev.*, 56:99–106, 2012. doi: 10.1016/j.quascirev.2012.09.020.

D. M. Roche, C. Dumas, M. Bügelmayer, S. Charbit, and C. Ritz. Adding a dynamical cryosphere to iLOVECLIM (version 1.0): coupling with the GRISLI ice-sheet model. *Geoscientific Model Development*, 7:1377–1394, 2014. doi: 10.5194/gmd-7-1377-2014.

D. M. Roche, C. Waelbroeck, B. Metcalfe, and T. Caley. FAME (v1.0): a simple module to simulate the effect of planktonic foraminifer species-specific habitat on their oxygen isotopic content. *Geoscientific Model Development*, 11:3587–3603, 2018. doi: 10.5194/gmd-11-3587-2018.

A. Schilt, M. Baumgartner, J. Schwander, D. Buiron, E. Capron, J. Chappellaz, L. Loulergue, S. Schüpbach, R. Spahni, H. Fischer, and T. F. Stocker. Atmospheric nitrous oxide during the last 140 000 years. *Earth Planet. Sc. Lett.*, 300:33–43, 2010. doi: 10.1016/j.epsl.2010.09.027.

G. A. Schmidt, J. D. Annan, P. J. Bartlein, B. I. Cook, E. Guilyardi, J. C. Hargreaves, S. P. Harrison, M. Kageyama, A. N. LeGrande, B. Konecky, S. Lovejoy, M. E. Mann, V. Masson-Delmotte, C. Risi, D. Thompson, A. Timmermann, L.-B. Tremblay, and P. P. Yiou. Using palaeo-climate comparisons to constrain future projections in CMIP5. *10.5194/cp-10-221-2014*, 10:221–250, 2014. doi: Clim.Past.

A. Schmittner, J. A. M. Green, and S.-B. Wilmes. Glacial ocean overturning intensified by tidal mixing in a global circulation model. *Geophys. Res. Lett.*, 42:4014–4022, 2015. doi: 10.1002/2015GL063561.

P. Sepulchre, A. Caubel, J.-B. Ladant, L. Bopp, O. Boucher, P. Braconnot, P. Brockmann, A. Cozic, Y. Donnadieu, J.-L. Dufresne, V. Estella-Perez, C. Ethé, F. Fluteau, M.-A. Foujols, G. Gastineau, J. Ghattas, D. Hauglustaine, F. Hourdin, M. Kageyama, M. Khodri, O. Marti, Y. Meurdesoif, J. Mignot, A.-C. Sarr, J. Servonnat, D. Swingedouw, S. Szopa, and D. Tardif. IPSL-CM5A2 – an Earth system model designed for multi-millennial climate simulations. *Geosci. Model Dev.*, 13:3011–3053, 2020. doi: 10.5194/gmd-13-3011-2020.

S. Sherriff-Tadano and A. Abe-Ouchi. Roles of Sea Ice–Surface Wind Feedback in Maintaining the Glacial Atlantic Meridional Overturning Circulation and Climate. *Journal of Climate*, 33, 2020. doi: 10.1175/JCLI-D-19-0431.1.

S. Sherriff-Tadano, A. Abe-Ouchi, M. Yoshimori, A. Oka, and W.-L. Chan. Influence of glacial ice sheets on the Atlantic meridional overturning circulation through surface wind change. *Climate Dynamics*, 50:2881–2903, 2018. doi: 10.1007/s00382017-3780-0.

S. Sherwood, M. J. Webb, J. D. Annan, K. C. Armour, P. M. Forster, J. C. Hargreaves, G. Hegerl, S. A. Klein, K. D. Marvel, E. J. Rohling, M. Watanabe, T. Andrews, P. Braconnot, C. S. Bretherton, G. L. Foster, Z. Hausfather, A. S. von der Heydt, R. Knutti, T. Mauritsen, J. R. Norris, C. Proistosescu, M. Rugenstein, G. A. Schmidt, K. B. Tokarska, and M. D. Zelinka. An assessment of Earth's climate sensitivity using multiple lines of evidence. *Reviews of Geophysics, American Geophysical Union*, 2020. doi: 10.1029/2019RG000678.

S.-I. Shin, Z. Liu, B. L. Otto-Bliesner, J. E. Kutzbach, and S. J. Vavrus. Southern Ocean sea-ice control of the glacial North Atlantic thermohaline circulation. *Geophys. Res. Lett.*, 30(2), 2003. doi: 10.1029/2002GL015513.

D. M. Sigman and E. A. Boyle. Glacial/interglacial variations in atmospheric carbon dioxide. *Nature*, 407:859–869, 2000. doi: 10.1038/35038000.

D. M. Sigman, M. P. Hain, and G. H. Haug. The polar ocean and glacial cycles in atmospheric CO_2 concentration. *Nature*, 466:47–55, 2010. doi: 10.1038/nature09149.

E. L. Sikes, K. A. Allen, and D. C. Lund. Enhanced $\delta^{13}C$ and $\delta^{18}O$ Differences Between the South Atlantic and South Pacific During the Last Glaciation: The Deep Gateway Hypothesis. *Paleoceanography*, 32:1000–1017, 2017. doi: 10.1002/2017PA003118.

K. D. Six and E. Maier-Reimer. Effects of plankton dynamics on seasonal carbon fluxes in an ocean general circulation model. *Global Biogeochem. Cy.*, 10:559–583, 1996.

L. C. Skinner. Glacial-interglacial atmospheric CO_2 change: a possible "standing volume" effect on deep-ocean carbon sequestration. *Clim. Past*, 5:537–550, 2009.

L. C. Skinner, F. Primeau, E. Freeman, M. de la Fuente, P. A. Goodwin, J. Gottschalk, E. Huang, I. N. McCave, T. L. Noble, and A. E. Scrivner. Radiocarbon constraints on the glacial ocean circulation and its impact on atmospheric CO_2. *Nat. Commun.*, 8, 2017. doi: 10.1038/ncomms16010.

D. A. Smeed, G. D. McCarthy, S. A. Cunningham, E. Frajka-Williams, D. Rayner, W. E. Johns, C. S. Meinen, M. O. Baringer, B. I. Moat, A. Duchez, and H. L. Bryden. Observed decline of the Atlantic meridional overturning circulation 2004–2012. *Ocean Sci.*, 10:29–38, 2014. doi: 10.5194/os-10-29-2014.

D. A. Smeed, S. A. Josey, C. Beaulieu, W. E. Johns, B. I. Moat, E. Frajka-Williams, D. Rayner, C. S. Meinen, M. O. Baringer, H. L. Bryden, and G. D. McCarthy. The North Atlantic Ocean is in a state of reduced overturning. *Geophysical Research Letters*, 45:1527–1533, 2017. doi: 10.1002/2017GL076350.

K. Stein, A. Timmermann, E. Y. Kwon, and T. Friedrich. Timing and magnitude of Southern Ocean sea ice/carbon cycle feedbacks. *PNAS*, 2020. doi: 10.1073/pnas.1908670117.

B. B. Stephens and R. F. Keeling. The influence of Antarctic sea ice on glacial-interglacial CO_2 variations. *Nature*, 404:171–174, 2000.

X. Sun and K. Matsumoto. Effects of sea ice on atmospheric pCO_2 : A revised view and implications for glacial and future climates. *Journal of Geophysical Research*, 115(G02015), 2010. doi: 10.1029/2009JG001023.

A. Tagliabue, L. Bopp, D. M. Roche, N. Bouttes, J.-C. Dutay, R. Alkama, M. Kageyama, E. Michel, and D. Paillard. Quantifying the roles of ocean circulation and biogeochemistry in governing ocean carbon-13 and atmospheric carbon dioxide at the last glacial maximum. *Clim. Past*, 5:695–706, 2009. doi: 10.5194/cp-5-695-2009.

A. Tagliabue, O. Aumont, and L. Bopp. The impact of different external sources of iron on the global carbon cycle. *Geophys. Res. Lett.*, 41:920–926, 2014. doi: 10.1002/2013GL059059.

L. Tarasov and W. R. Peltier. Greenland glacial history and local geodynamic consequences. *Geophy. J. Int.*, 150:198–229, 2002.

L. Tarasov, A. S. Dyke, R. M. Neal, and W. R. Peltier. A data-calibrated distribution of deglacial chronologies for the North American ice complex from glaciological modeling. *Earth Planet. Sc. Lett.*, 315-316:30–40, 2012. doi: 10.1016/j.epsl.2011.09.010.

J. E. Tierney, J. Zhu, J. King, S. B. Malevich, G. J. Hakim, and C. J. Poulsen. Glacial cooling and climate sensitivity revisited. *Nature*, 584:569–573, 2020. doi: 10.1038/s41586-020-2617-x.

J. R. Toggweiler, J. L. Russell, and S. R. Carson. Midlatitude westerlies, atmospheric CO_2, and climate change during the ice ages. *Paleoceanography*, 21(PA2005), 2006. doi: 10.1029/2005PA001154.

D. J. Ullman, A. N. LeGrande, A. E. Carlson, F. S. Anslow, and J. M. Licciardi. Assessing the impact of laurentide ice sheet topography on glacial climate. *Clim. Past*, 10:487–507, 2014. doi: 10.5194/cp-10-487-2014.

A. J. Watson, G. K. Vallis, and M. Nikurashin. Southern Ocean buoyancy forcing of ocean ventilation and glacial atmospheric CO_2. *Nature geoscience*, 2015. doi: 10.1038/NGEO2538.

S. L. Weber, S. S. Drijfhout, A. Abe-Ouchi, M. Crucifix, M. Eby, A. Ganopolski, S. Murakami, B. Otto-Bliesner, and W. R. Peltier. The modern and glacial overturning circulation in the Atlantic ocean in PMIP coupled model simulations. *Clim. Past*, 3:51–64, 2007.

S.-B. Wilmes, A. Schmittner, and J. A. M. Green. Glacial Ice Sheet Extent Effects on Modeled Tidal Mixing and the Global Overturning Circulation. *Paleoceanography and Paleoclimatology*, 34:1437–1454, 2019. doi: 10.1029/2019PA003644.

D. J. Wilson, T. Struve, T. van de Flierdt, T. Chen, T. Li, A. Burke, and L. F. Robinson. Sea-ice control on deglacial lower cell circulation changes recorded by Drake Passage deep-sea corals. *Earth and Planetary Science Letters*, 544, 2020. doi: 10.1016/j.epsl.2020.116405.

R. A. Woodgate. Increases in the Pacific inflow to the Arctic from 1990 to 2015, and insights into seasonal trends and driving mechanisms from year-round Bering Strait mooring data. *Prog. Oceanogr.*, 160:124–154, 2018. doi: 10.1016/j.pocean.2017.12.007.

N. Wunderling, J. F. Donges, J. Kurths, and R. Winkelmann. Interacting tipping elements increase risk of climate domino effects under global warming. *Earth Syst. Dynam.*, 12:601–619, 2021. doi: 10.5194/esd-12-601-2021.

W. Xiao, O. Esper, and R. Gersonde. Last glacial-Holocene climate variability in the Atlantic sector of the Southern Ocean. *Quat. Sci. Rev.*, 135:115–137, 2016. doi: 10.1016/j.quascirev.2016.01.023.

A. Yamamoto, A. Abe-Ouchi, R. Ohgaito, A. Ito, and A. Akira Oka. Glacial CO_2 decrease and deep-water deoxygenation by iron fertilization from glaciogenic dust. *Clim. Past*, 15(3):981–996, 2019. doi: 10.5194/cp-15-981-2019.

List of Figures

List of Tables

Acronyms

AABW Antarctic Bottom Water.

AAIW Antarctic Intermediate Water.

ACC Antarctic Circumpolar Current.

AGCM Atmosphere General Circulation Model.

AMOC Atlantic Meridional Overturning Circulation.

AOGCM Atmosphere−Ocean General Circulation Model.

BCs Boundary Conditions.

CLIMAP Climate Long-Range Investigation, Mapping and Prediction.

CMIP Coupled Model Intercomparison Project.

DIC Dissolved Inorganic Carbon.

DOC Dissolved Organic Carbon.

EMIC Earth system Model of Intermediate Complexity.

ENSO El Niño−Southern Oscillation.

ESM Earth System Model.

GCM General Circulation Model.

GLODAP Global Ocean Data Analysis Project.

IPCC Intergovernmental Panel on Climate Change.

LGM Last Glacial Maximum.

MARGO Multiproxy Approach for the Reconstruction of the Glacial Ocean Surface.

MLD Mixed Layer Depth.

NADW North Atlantic Deep Water.

OGCM Atmosphere General Circulation Model.

PI pre-industrial.

PMIP Paleoclimate Modelling Intercomparison Project.

RMSE Root Mean Square Error.

SAT Surface Air Temperature.

SO Southern Ocean.

SS Sea Salinity.

SSS Sea Surface Salinity.

SST Sea Surface Temperature.

ST Sea Temperature.

WCRP World Climate Research Program.

WOA World Ocean Atlas.

université PARIS-SACLAY

ÉCOLE DOCTORALE
Sciences de l'Environnement d'Île-de-France (SEIF)

Titre: Rôle de la glace de mer australe sur la circulation océanique profonde et le cycle du carbone au Dernier Maximum Glaciaire

Mots clés: circulation océanique profonde, glace de mer, contenu en carbone, modélisation des paléo-climats

Résumé: La période froide du Dernier Maximum Glaciaire était caractérisée, en regard de notre climat moderne, par une couverture de glace de mer australe accrue, une circulation profonde Atlantique moins profonde et une plus faible concentration en CO_2 dans l'atmosphère. Ces différences sont bien connues grâce aux observations indirectes mais difficiles à représenter dans les simulations issues des modèles de climat. En effet, ces modèles simulent fréquemment une concentration en CO_2 atmosphérique trop élevée, une circulation océanique trop profonde dans l'Atlantique et une banquise présentant une distribution trop circulaire dans l'océan austral ainsi qu'une étendue hivernale et une amplitude saisonnière trop faibles. Ces désaccords modèle-données observés au Dernier Maximum Glaciaire remettent en cause la représentation numérique de certains processus climatiques essentiels. Plusieurs études soulignent le rôle majeur de la glace de mer australe sur la capacité de stockage de carbone de l'océan et la circulation océanique profonde. Je me suis donc focalisée sur cette région pour mieux comprendre les processus associés à ce stockage. Grâce aux simulations réalisées avec le modèle système terre iLOVECLIM, j'ai pu démontrer que les incertitudes liées à la représentation des calottes polaires ont un impact limité sur les variables examinées ici. En revanche, d'autres choix de conditions aux limites (affectant le volume de l'océan, l'ajustement de l'alcalinité) peuvent entraîner des modifications importantes du contenu total en carbone de l'océan. Je montre également que l'utilisation d'une paramétrisation simple de la plongée des saumures résultant de la formation de glace de mer permet d'améliorer significativement la simulation de la glace de mer australe, de la circulation océanique profonde et de la concentration en CO_2 atmosphérique. Un ensemble de simulations incluant l'impact de différentes paramétrisations océaniques est utilisé pour montrer que la circulation océanique très profonde simulée par notre modèle ne peut être attribuée à une glace de mer australe insuffisante. En revanche, les processus de convection dans l'océan austral semblent clefs pour améliorer à la fois la glace de mer australe, la circulation océanique profonde et la concentration en CO_2 atmosphérique au Dernier Maximum Glaciaire.

Title: Role of Southern Ocean sea ice on deep ocean circulation and carbon cycle at the Last Glacial Maximum

Keywords: deep ocean circulation, sea ice, carbon sequestration, paleoclimate modelling

Abstract: Compared to the present-day climate, the cold period of the Last Glacial Maximum was characterized by an expanded sea-ice cover in the Southern Ocean, a shoaled Atlantic deep ocean circulation and a lower atmospheric CO_2 concentration. These changes are well-documented by indirect observations but difficult to represent in simulations of climate models. Indeed, these models tend to simulate a too high atmospheric CO_2 concentration, a too deep Atlantic deep ocean circulation, and a sea-ice cover with a too circular distribution in the Southern Ocean and a too small winter extent and seasonal amplitude. The model-data discrepancies observed at the Last Glacial Maximum call into question the model representation of some important climate processes. Several studies have underlined the crucial role of the Southern Ocean sea ice on ocean carbon storage capacity and deep circulation. I have therefore focussed on this region to improve our understanding of the processes associated with this storage. Thanks to simulations performed with the Earth System Model iLOVECLIM, I have demonstrated that the uncertainties related to ice sheet reconstructions have a limited impact on the variables examined in this study. In contrast, other choices of boundary conditions (influencing the ocean volume and alkalinity adjustment) can yield large changes of carbon sequestration in the ocean. I also show that a simple parameterization of the sinking of brines consequent to sea-ice formation significantly improves the simulated Southern Ocean sea ice, deep ocean circulation and atmospheric CO_2 concentration. A set of simulations including the effects of diverse ocean parameterizations is used to show that the too deep ocean circulation simulated by our model cannot be attributed to an insufficient sea-ice cover, whereas convection processes in the Southern Ocean seem crucial to improve both the Southern Ocean sea ice, the deep ocean circulation and the atmospheric CO_2 concentration at the Last Glacial Maximum.

Maison du doctorat de l'Université Paris-Saclay
2e étage aile ouest, École normale supérieure Paris-Saclay
4 avenue des Sciences,
91190 Gif-sur-Yvette, France